



Design and Construction Guidelines for Thermally Insulated Concrete Pavements

Minnesota
Department of
Transportation

**RESEARCH
SERVICES**

Office of
Policy Analysis,
Research &
Innovation

Lev Khazanovich, Principal Investigator
Department of Civil Engineering
University of Minnesota

January 2013

Research Project
Final Report 2013-02



Your Destination... Our Priority



To request this document in an alternative format, please contact the Affirmative Action Office at 651-366-4723 or 1-800-657-3774 (Greater Minnesota); 711 or 1-800-627-3529 (Minnesota Relay). You may also send an e-mail to ADArequest.dot@state.mn.us.

(Please request at least one week in advance).

Technical Report Documentation Page

1. Report No. MN/RC 2013-02	2.	3. Recipients Accession No.	
4. Title and Subtitle Design and Construction Guidelines for Thermally Insulated Concrete Pavements		5. Report Date January 2013	
		6.	
7. Author(s) L. Khazanovich, J.T. Balbo, L. Johanneck, R. Lederle, M. Marasteanu, P. Saxena, D. Tompkins, M. Vancura, M. Watson, J. Harvey, N.J. Santero, and J. Signore		8. Performing Organization Report No.	
9. Performing Organization Name and Address Department of Civil Engineering Pavements Research Center University of Minnesota University of California 500 Pillsbury Dr. SE 1353 S. 46 th St, Bldg. 452 Minneapolis, MN 55455 Richmond, CA 94804		10. Project/Task/Work Unit No. CTS Project #2008036, TPF-5(149)	
		11. Contract (C) or Grant (G) No. (C) 89261 (WO) 90	
12. Sponsoring Organization Name and Address Minnesota Department of Transportation Research Services 395 John Ireland Boulevard, MS 330 St. Paul, MN 55155		13. Type of Report and Period Covered Final Report	
		14. Sponsoring Agency Code	
15. Supplementary Notes http://www.lrrb.org/pdf/201302.pdf			
16. Abstract (Limit: 250 words) <p>The report describes the construction and design of composite pavements as a viable design strategy to use an asphalt concrete (AC) wearing course as the insulating material and a Portland cement concrete (PCC) structural layer as the load-carrying material. These pavements are intended for areas with heavy trucks and problem soils to increase the service life and minimize maintenance. The project focused specifically on thermally insulated concrete pavements (TICPs) (that is, composite thin AC overlays of new or structurally sound existing PCC pavements) and developed design and construction guidelines for TICPs. Specific research objectives include determining behavior of the layers of the TICP system, understanding life-cycle costs and the feasibility of TICPs, and incorporating the results into design and construction guidelines. Both construction and design guidelines are considered in light of the construction and performance of TICP test sections at the Minnesota Road Research project (MnROAD).</p>			
17. Document Analysis/Descriptors Composite pavements, Asphalt pavements, Concrete pavements, Pavement design, Paving, Highway engineering		18. Availability Statement No restrictions. Document available from: National Technical Information Services, Alexandria, Virginia 22312	
19. Security Class (this report) Unclassified	20. Security Class (this page) Unclassified	21. No. of Pages 323	22. Price

Design and Construction Guidelines for Thermally Insulated Concrete Pavements

Final Report

Prepared by:

Lev Khazanovich, Jose T. Balbo, Luke Johannek, Rita Lederle, Mihai Marasteanu,
Priyam Saxena, Derek Tompkins, Mary Vancura, and Mark Watson

Department of Civil Engineering
University of Minnesota

John Harvey, Nicholas J. Santero, and James Signore

Pavement Research Center
University of California

January 2013

Published by:

Minnesota Department of Transportation
Research Services
395 John Ireland Boulevard, MS 330
St. Paul, Minnesota 55155

This report documents the results of research conducted by the authors and does not necessarily represent the views or policies of the Minnesota Department of Transportation, the University of Minnesota, or the University of California. This report does not contain a standard or specified technique.

The authors, the Minnesota Department of Transportation, the University of Minnesota, and the University of California do not endorse products or manufacturers. Trade or manufacturers' names appear herein solely because they are considered essential to this report.

Acknowledgments

This research was supported by the Federal Highway Administration (FHWA) Pooled Fund Project TPF-5(149), which was funded by the Minnesota Department of Transportation (MnDOT), the California Department of Transportation (Caltrans), the Washington Department of Transportation, and the FHWA. The authors thank all members of the TPF-5(149) technical panel for their review and encouragement throughout the various stages of the project work; particularly important to the success of the project were Tim Clyne of MnDOT and Nadarajah Sivanewaran of FHWA, who contributed helpful comments and revisions in the development of this final report and other project documents.

Furthermore, the authors acknowledge the Strategic Highway Research Program (SHRP2) Project R21 “Composite Pavements,” which provided useful composite pavement data and additional insight into design and construction issues for composite pavements. The authors thank the Minnesota Road Research facility (MnROAD) and the University of California Pavement Research Center (UCPRC) for their assistance in obtaining useful pavement data for this project work.

Table of Contents

Chapter 1. Introduction.....	1
Chapter 2. MEPDG and Climate Modeling Validation and Analysis.....	2
2.1. Effect of Climate Data and Climate Modeling on MEPDG Predictions for Composite Pavements	2
2.1.1 <i>Enhanced Integrated Climatic Model</i>	4
2.1.2 <i>EICM Validation</i>	19
2.1.3 <i>Design Characteristics</i>	38
2.1.4 <i>Conclusions on EICM Data Quality</i>	48
2.2. Characterization of Unbound Materials in the MEPDG and DARWin-ME	50
2.2.1 <i>Level 3 Stiffness Characterization for Design Procedures</i>	51
2.2.2 <i>Effects of EICM Inputs for Unbound Layers</i>	55
2.2.3 <i>Consistency of Base Stiffness for Different Pavement Types</i>	60
2.2.4 <i>Subgrade Characterization Recommendations for Pavement Design</i>	62
Chapter 3. Response Model for Combined Thermal and Traffic Loading	64
3.1. Background.....	64
3.1.1 <i>Components of Stress under Temperature Curling</i>	64
3.1.2 <i>MEPDG Rapid Solutions for Predicting Critical PCC Bottom Surface Stresses</i>	67
3.1.3 <i>Adoption of the Fatigue Cracking Model for Composite Pavements in MEPDG</i>	75
3.1.4 <i>Asphalt Characterization</i>	76
3.1.5 <i>Limitations of the Structural Modeling of Composite Pavements in the MEPDG</i> ...	79
3.2. Finite Element Analysis of Composite Pavement Incorporating a Viscoelastic Layer	80
3.2.1 <i>Viscoelastic Material Representation of Asphalt Concrete</i>	80
3.2.2 <i>Development of Finite Element Model for the Analysis of Viscoelastic Slab-on-Grade</i>	85
3.2.3 <i>Extension of the FE Model to Multi-Layered Composite Pavements</i>	96
3.2.4 <i>Step-by-Step Procedure for Computing the Stresses in the Composite Pavement</i> .	100
3.2.5 <i>Validation of the Finite Element Model</i>	102
3.3. Stress Solutions Using the 2-Moduli Approach	119
3.3.1 <i>AC Moduli under Traffic Loads and Temperature Gradients</i>	120
3.3.2 <i>The 2-Moduli Approach</i>	121
3.3.3 <i>Stress Computation Procedure using the 2-Moduli Approach</i>	122
3.3.4 <i>Brief Formulation for the FE Model Based on the 2-Moduli Approach</i>	126

3.3.5	<i>Step-by-Step Procedure for Computing the Combined Stresses</i>	127
3.3.6	<i>Verification of the Combined Stress Obtained using the 2-Moduli Approach</i>	130
3.3.7	<i>Comparison of the Stress Solution using the 2-Moduli Approach with the Stress Solution using the MEPDG Process</i>	135
3.4.	Development of a Framework for Implementation of the 2-Moduli Approach into MEPDG	137
3.4.1	<i>Simplification of the Structural System</i>	138
3.4.2	<i>Equivalency Techniques for Multi-Layered Pavements</i>	143
3.5.	The 2-Moduli Approach in Summary.....	146
3.5.1	<i>Research Findings</i>	146
3.5.2	<i>Recommendations for the Future Research</i>	147
Chapter 4.	Design and Analysis of TICP	148
4.1.	HMA-PCC Rutting Models	148
4.1.1	<i>MEPDG Rutting Model</i>	148
4.1.2	<i>CalME Rutting Model</i>	151
4.1.3	<i>TPF-5(149) M-E Design to Mitigate Rutting in TICP</i>	154
4.1.4	<i>Validation of TPF-5(149) Procedure for Rutting in TICP</i>	161
4.1.5	<i>Sensitivity Analysis of TPF-5(149) Procedure for Rutting in TICP</i>	170
4.2.	HMA-PCC Reflective Cracking Models	172
4.2.1	<i>Original MEPDG Reflective Cracking Model</i>	173
4.2.2	<i>CalME Reflective Cracking Model</i>	174
4.2.3	<i>TPF-5(149) Procedure for Predicting Reflective Cracking in TICP</i>	175
4.2.4	<i>Validation of TPF-5(149) Procedure for Reflection Cracking</i>	179
4.2.5	<i>Sensitivity Analysis of TPF-5(149) Procedure for Reflection Cracking</i>	183
4.3.	JPCP Cracking Models for HMA-PCC	188
4.3.1	<i>MEPDG Transverse Cracking Model for JPCP</i>	189
4.3.2	<i>Modifications to JPCP Transverse Cracking Model for HMA-PCC Projects and Incorporation into the MEPDG</i>	189
4.3.3	<i>Sensitivity Analysis of Modified MEPDG JPCP Transverse Cracking Model</i>	191
4.3.4	<i>Confirmation of TPF-5(149) Modifications to MEPDG JPCP Transverse Cracking Model for HMA-PCC Projects</i>	194
4.4.	JPCP Faulting Models for HMA-PCC.....	195
4.4.1	<i>MEPDG JPCP Faulting Model</i>	196
4.4.2	<i>Modifications of MEPDG Faulting Model for HMA-PCC and Incorporation into the MEPDG Procedure</i>	197

4.4.3	<i>Validation and Sensitivity Analysis of Modified MEPDG Faulting Model for HMA-PCC</i>	199
4.5.	Guidelines to TPF-5(149) Procedure for Design and Analysis of TICP	203
4.5.1	<i>Creating MEPDG Project File</i>	203
4.5.2	<i>Execute MEPDG Analysis for TICP Project</i>	205
4.5.3	<i>Execute TPF 5(149) Analysis for TICP Project</i>	205
4.5.4	<i>Interpret Design Outputs</i>	205
4.6.	Design and Analysis Discussion and Conclusions	206
Chapter 5.	Construction Practices for HMA-PCC Composite Pavements	208
5.1.	Construction Practices for HMA-PCC Composite Pavements	209
5.1.1	<i>JPCP Construction</i>	209
5.1.2	<i>RCC Construction</i>	219
5.1.3	<i>HMA Overlay Construction</i>	224
5.2.	AC Mix Design for HMA-PCC	239
5.2.1	<i>Important Performance Concerns for AC-over-PCC</i>	239
5.2.2	<i>Asphalt Concrete Mixtures for AC-PCC</i>	242
5.2.3	<i>AC Overlay Mix Design Selection</i>	245
Chapter 6.	Life Cycle Cost Analysis Case Studies	251
6.1.	Background Information for Caltrans Case Studies	251
6.2.	Reconstruction of truck lanes on I-15 in California	253
6.2.1	<i>Caltrans I-70 Case Study Results</i>	256
6.3.	Construction of New Pavement Lanes on State Route 70 in California	259
6.3.1	<i>Caltrans State Route 70 Case Study Results</i>	262
6.4.	Construction of Two Lanes on a Major Highway or Interstate in Minnesota	266
6.4.1	<i>Minnesota Case Study Results</i>	268
6.5.	Structural Analysis and LCCA	271
Chapter 7.	Conclusions and Recommendations	272
References		274
Appendix A: Construction Practices Survey		

List of Tables

Table 2-1: Transverse cracking percentage in PCC layer of AC/PCC projects, organized by environmental conditions.....	12
Table 2-2: Predicted distresses for AC/PCC projects in Southern California.....	14
Table 2-3: Predicted distresses for locations near Long Island, New York.....	15
Table 2-4: Predicted cracking values.....	17
Table 2-5: Percent slabs cracked in AC/PCC projects for additional locations.....	19
Table 2-6: Percentage of un-flagged data in MnROAD Cells 106 & 206.....	26
Table 2-7: Depths of sensor pairings located in Cell 106.....	27
Table 2-8: Effect of PCC thermal conductivity on transverse cracking in PCC layer.....	38
Table 2-9: Effect of AC thermal conductivity on transverse cracking in PCC layer.....	38
Table 2-10: Effect of PCC heat capacity on transverse cracking in PCC layer.....	39
Table 2-11: Effect of AC heat capacity on transverse cracking in PCC layer.....	39
Table 2-12: Effect of the coefficient of thermal expansion in the PCC layer on predicted pavement performance of an AC/PCC pavement.....	40
Table 2-13: Effect of the coefficient of thermal expansion in the PCC layer on predicted pavement performance of a PCC pavement.....	40
Table 2-14: Effect of PCC thickness for an AC/PCC composite pavement with a 2-in AC layer.....	41
Table 2-15: Effect of PCC thickness for an AC/PCC composite pavement with a 3-in AC layer.....	41
Table 2-16: Effect of joint spacing on predicted pavement performance.....	42
Table 2-17: Effect of slab width on predicted pavement performance.....	43
Table 2-18: MEPDG default gradation values for A-1-a and A-3 base layers.....	45
Table 2-19: Resilient modulus (MR) for various subgrades computed using CBR and CBR* in the MEPDG and DARWin-ME.....	53
Table 2-20: Alligator cracking and total rutting after 20 years as predicted by the MEPDG and DARWin-ME for 4" flexible pavement with an A-1-a base and various subgrades and material parameter inputs.....	54
Table 2-21: Inputs for base and subgrade variation.....	55
Table 3-1: Parameters of the Kelvin-Voigt model for the plate and Winkler foundation.....	105
Table 3-2: Layer properties for the elastic analysis.....	110

Table 3-3: Kelvin-Voigt parameters for the viscoelastic surface layer.	111
Table 3-4: Layer properties for multi-layered composite pavements.	111
Table 3-5: Parameters of the Kelvin-Voigt element for the viscoelastic plate.	113
Table 3-6: Prony series coefficients for material models 1 and 2.	115
Table 3-7: Layer properties for the baseline composite pavement.	118
Table 3-8: Structural details of the composite pavement analyzed in the MEPDG.	120
Table 3-9: Temperature profile for the composite pavement.	130
Table 3-10: Layer properties for the composite pavement.	131
Table 3-11: Material properties for the AC layer.	131
Table 3-12: Deflections and stress at the bottom of the PCC layer at slab center.	132
Table 3-13: Deflections and stress at the bottom of the PCC layer at an edge node.	132
Table 3-14: Deflections and stress at the bottom of the PCC layer at slab edge.	133
Table 3-15: Deflections and stress at the bottom of the PCC layer at an interior node.	133
Table 3-16: Temperature profile for the composite pavement.	134
Table 3-17: Layer properties for the composite pavement.	135
Table 3-18: Deflections and stresses at the top of the PCC layer at slab edge.	135
Table 3-19: Layer properties for the composite pavement.	136
Table 3-20: Layer properties for the composite pavement.	139
Table 3-21: Temperature profile for the composite pavement.	140
Table 3-22: Layer properties for slabs SL1 and SL2.	145
Table 3-23: Deflections and stress at the bottom of the PCC layer at slab edge.	146
Table 4-1: Model coefficients for CalME fatigue model.	155
Table 4-2: Model coefficients for CalME rutting model.	155
Table 4-3: HVS loading program for example section.	163
Table 4-4: Section 609HB temperature summary for air and pavement.	165
Table 4-5: MnROAD Cell 106/206 design in summary.	169
Table 4-6: Assigned values for H_{eff} , c , and d in original MEPDG reflective cracking model (from AASHTO 2008).	174
Table 5-1: Checklist of design and construction activities for concrete pavements (adapted from Grogg and Smith, 2001).	217
Table 5-2: Recommended aggregate gradation for RCC mixes (from ACI 1995).	221

Table 5-3: Sieve sizes used to define fine and coarse mixes in AASHTO M 323 (from Christensen and Bonaquist 2006).	243
Table 6-1: Caltrans Case 1 JPCP maintenance and rehabilitation schedule.....	254
Table 6-2: Caltrans Case 1 TICP Design 1 maintenance and rehabilitation schedule.....	255
Table 6-3: Caltrans Case 1 TICP Design 2 maintenance and rehabilitation schedule.....	256
Table 6-4: Caltrans Case 1: Change of PCC thickness in TICP pavement for same NPV as JPCP with 1:1 costs.	257
Table 6-5: Caltrans Case 1: Change of PCC thickness in TICP pavement for same NPV as JPCP with 0.8:1 costs.	258
Table 6-6: Caltrans Case 1: Change of PCC life in TICP pavement for same NPV as JPCP with 1:1 costs.	259
Table 6-7: Caltrans Case 1: Change of PCC life in TICP pavement for same NPV as JPCP with 0.8:1 costs.	259
Table 6-8: Caltrans Case 2 JPCP truck lane maintenance and rehabilitation schedule.	260
Table 6-9: Caltrans Case 2 TICP Design 1 maintenance and rehabilitation schedule.....	261
Table 6-10: Caltrans Case 2 TICP Design 2 maintenance and rehabilitation schedule.....	262
Table 6-11: Caltrans Case 2 Change of PCC thickness in TICP pavement for same NPV as JPCP with 1:1 costs.	263
Table 6-12: Caltrans Case 2 Change of PCC thickness in TICP pavement for same NPV as JPCP with 0.8:1 costs.	264
Table 6-13: Caltrans Case 2 Change of PCC life in TICP pavement for same NPV as JPCP with 1:1 costs.	265
Table 6-14: Caltrans Case 2 Change of PCC life in TICP pavement for same NPV as JPCP with 0.8:1 costs.	265
Table 6-15: MN Case 3 bituminous pavement M & R schedule for ESALs > 7 million.....	267
Table 6-16: MN Case 3 concrete pavement M & R schedule.	268
Table 6-17: MN Case 3 range of concrete and asphalt costs used for the LCCA.	268
Table 6-18: MN Case 3 breakeven range for the cost of TICP concrete as a percentage of JPCP concrete.	271

List of Figures

Figure 2-1: Heat transfer between pavement and air on a sunny day (NCHRP 2004).....	5
Figure 2-2: Frequency distribution of predicted IRI values for composite pavement structure....	8
Figure 2-3: Frequency distribution of predicted IRI values for rigid pavement structure.....	9
Figure 2-4: Frequency distribution of predicted rutting values for composite pavement structure.	9
Figure 2-5: Frequency distribution of predicted rutting values for single layer flexible pavement structure.....	10
Figure 2-6: Frequency distribution of predicted transverse cracking values for composite pavement structure.....	11
Figure 2-7: Frequency distribution of predicted transverse cracking values for rigid pavement structure.....	11
Figure 2-8: MEPDG locations of AC/PCC projects – icon color determined by transverse cracking percentage.....	12
Figure 2-9: Wide range of predicted cracking in the Los Angeles metropolitan area.....	13
Figure 2-10: Wide range of predicted cracking in Long Island, New York.....	15
Figure 2-11: Additional locations selected for MEPDG climate data file interpolation for locations in Minnesota.....	18
Figure 2-12: Location of weather stations listed by MEPDG for Minnesota.....	18
Figure 2-13: Design cross-section of MnROAD Cells 106, 206, 113, 213, and 313 (MnDOT 2010).....	21
Figure 2-14: Screen capture of computer code comments defining data flags.....	22
Figure 2-15: Temperature vs. time plot for Cell 106, sensor 28.....	23
Figure 2-16: Flag vs. time plot for Cell 106, sensor 28.....	23
Figure 2-17: Temperature vs. time plot for Cell 106, sensor 28, January 2009.....	24
Figure 2-18: Temperature vs. time plot for Cell 106, sensor 28, June 2009.....	25
Figure 2-19: ΔT Histograms for cell 106 sensor pairings, organized vertically by season.....	28
Figure 2-20: Hourly AC surface temperatures from Cell 106 (in red) and hourly JPCP surface temperatures from Cell 213 (in blue), illustrating the albedo effect.....	29
Figure 2-21: Hourly PCC temperature differences throughout AC-over-PCC (Cell 106 in red) and JPCP (Cell 113 in blue) thicknesses illustrating the insulating effect of an AC overlay.	30

Figure 2-22: Close detail of hourly temperature differences throughout PCC slab thickness for AC-over-PCC (Cell 106 in red) and JPCP (Cell 113 in blue).	31
Figure 2-23: Thermal gradients at similar locations in AC-over-PCC (Cell 106 in red) and JPCP (Cell 313 in blue).	32
Figure 2-24: Simulated thermal gradients for AC-over-PCC and JPCP structures and their measured analogues from MnROAD (Cells 106 and 113, respectively).....	33
Figure 2-25: Measured versus modeled cumulative frequency distribution for thermal gradient through JPCP pavement in July with $k = 1.25 \text{ BTU / hr-ft-}^\circ\text{F}$	34
Figure 2-26: Measured versus modeled cumulative frequency distribution for thermal gradient through JPCP pavement in July with $k = 0.94 \text{ BTU / hr-ft-}^\circ\text{F}$	35
Figure 2-27: Measured versus modeled cumulative frequency distribution for thermal gradient through JPCP pavement in March with $k = 1.25 \text{ BTU / hr-ft-}^\circ\text{F}$, which is the MEPDG default value.....	36
Figure 2-28: Measured versus modeled cumulative frequency distribution for thermal gradient through JPCP pavement in March with $k = 0.94 \text{ BTU / hr-ft-}^\circ\text{F}$, the adjusted thermal conductivity value.....	36
Figure 2-29: Measured versus modeled cumulative frequency distribution for thermal gradient through JPCP pavement in July with $k = 0.85 \text{ BTU / hr-ft-}^\circ\text{F}$	37
Figure 2-30: Effect of PCC thickness for an AC/PCC composite pavement with 2-in AC layer.	41
Figure 2-31: Effect of PCC thickness for an AC/PCC composite pavement with 3-in AC layer.	42
Figure 2-32: Correction factor as a function of the degree of saturation (24).	44
Figure 2-33: Resilient modulus for three base layers: A-1-a, A-3, and A-3 (modified).....	46
Figure 2-34: Coefficient of subgrade reaction for three base layers: A-1-a, A-3, and A-3 (modified).	47
Figure 2-35: Effect of base layer material for an AC/PCC composite pavement.....	48
Figure 2-36: Predicted cracking for a rigid pavement with different subgrades and an A-1-a (a) in Minneapolis analyzed with DARWin-ME, (b) in Champaign analyzed with DARWin-ME.....	56
Figure 2-37: Modulus of subgrade reaction, k , under a rigid pavement with different bases and an A-6 subgrade in Minneapolis analyzed with a) the MEPDG and b) DARWin-ME.	57
Figure 2-38: Percentage of slabs cracked with time for a rigid pavement analyzed in the MEPDG v1.1 and DARWin-ME, with identical inputs.	58

Figure 2-39: Seasonally adjusted resilient modulus of the base layer under a flexible pavement with different bases and an A-6 subgrade in Champaign analyzed with a) the MEPDG and b) DARWin-ME.....	59
Figure 2-40: Predicted alligator cracking for a flexible pavement with different bases and an A-6 subgrade (a) in Minneapolis analyzed with DARWin-ME, and (b) in Champaign analyzed with DARWin-ME.....	60
Figure 2-41: Seasonally adjusted resilient modulus for the case of various 9” total thickness pavements with an A-1-a base in Champaign Illinois computed using a) the MEPDG v1.1 and b) DARWin-ME.....	61
Figure 3-1: Modes of JPCP fatigue damage in the MEPDG: Top-down (at left) and bottom-up (at right) cracking as initiated by different combinations of wheel and thermal loads.....	64
Figure 3-2: Schematics for (a) original multi-layered system, (b) single slab system A, and (c) two-slab system B.	72
Figure 3-3: Structural model for (a) NNA1 (corresponding to single axle load) and (b) NNA2 (corresponding to tandem axle load).....	73
Figure 3-4: Structural model for (a) NNB1 (corresponding to single axle single wheel load) and (b) NNB2 (corresponding to single wheel load).....	74
Figure 3-5: Conversion of a composite pavement to an equivalent PCC structure.	75
Figure 3-6: (a) Effective length and (b) effective depth for single axle in a conventional flexible pavement.	78
Figure 3-7: Stress-strain responses under different load durations (adopted from Chen 2000)..	79
Figure 3-8: Schematic representation of Boltzman’s superposition principle (adopted from <i>UMN Online Lecture 2011</i>).	80
Figure 3-9: Schematic of generalized N -term Kelvin-Voigt model.....	82
Figure 3-10: Finite element $ijkl$	86
Figure 3-11: Spring idealization of Winkler foundation using concentrated springs at the nodes of the plate element.	93
Figure 3-12: Mesh and load configuration for the composite pavement subjected to a wheel load.	105
Figure 3-13: Comparison of deflections for a viscoelastic plate placed on a viscoelastic Winkler foundation.	106
Figure 3-14: Stress at the bottom of the viscoelastic plate placed on viscoelastic Winkler foundation.	106
Figure 3-15: Comparison of deflections for a viscoelastic plate with simply supported corners.	108

Figure 3-16: Mesh and loading configuration for the composite pavement subjected to a single-axle dual-wheel load.	109
Figure 3-17: Stress from three-layered analysis versus single- or two-layered analyses.	110
Figure 3-18: Stress versus time for cases 4 and 6 using the viscoelastic FE model.	112
Figure 3-19: Stress versus time for case 5 using the viscoelastic FE model.	112
Figure 3-20: Deflection versus time for a factorial of dashpot viscosities of the Kelvin-Voigt element.	114
Figure 3-21: Stress versus time for a factorial of dashpot viscosities of the Kelvin-Voigt element.	114
Figure 3-22: Schematic for (a) material model 1 and (b) material model 2.	115
Figure 3-23: Creep compliance for material models 1 and 2.	116
Figure 3-24: Deflection of the plate incorporating material models 1 and 2.	117
Figure 3-25: Stress at the bottom of the plate incorporating material models 1 and 2.	117
Figure 3-26: PCC bottom stresses versus AC thickness.	118
Figure 3-27: Asphalt dynamic modulus using the MEPDG versus pavement age.	121
Figure 3-28: System 1.	122
Figure 3-29: System 1 under positive temperature gradient $T(z)$ only.	123
Figure 3-30: System 2.	123
Figure 3-31: System 2 under fictitious force F_{fict}	124
Figure 3-32: System 2 under mid-slab traffic load F and fictitious force F_{fict}	124
Figure 3-33: Kelvin-Voigt model connected to an elastic spring in series.	125
Figure 3-34: Mesh and load configuration for the composite pavement subjected to SADW edge loading.	134
Figure 3-35: Comparison of stress using the 2-moduli approach and the MEPDG procedure.	137
Figure 3-36: The original composite pavement system.	140
Figure 3-37: System A.	141
Figure 3-38: System B.	141
Figure 3-39: Comparison of PCC bottom stresses in the original composite pavement system using the <i>2-moduli approach</i> and simplified systems A and B.	142
Figure 4-1: Temperature quintiles used by MEPDG to determine HMA sublayer dynamic modulus (from AASHTO 2008).	149
Figure 4-2: GUI for extracting MEPDG project input information (at left) and extracting calibration constants (at right).	155

Figure 4-3: MEPDG file "_space.dat", specifying pavement structure.	156
Figure 4-4: MEPDG input file specifying number of months between construction and traffic open.	157
Figure 4-5: MEPDG input file for temperature.	158
Figure 4-6: One of three MEPDG files used to obtain traffic inputs.	159
Figure 4-7: MEPDG files used to obtain dynamic modulus of AC layer.	160
Figure 4-8: MEPDG temporary file describing monthly modulus values for all layer and sublayers in the TICP project.	161
Figure 4-9: The HVS apparatus at UCPRC.	162
Figure 4-10: Section 609HB load history.	163
Figure 4-11: Daily average outside air temperatures.	164
Figure 4-12: Daily average inside air temperatures.	164
Figure 4-13: Daily average temperatures at surface and various depths of Section 609HB.	165
Figure 4-14: Illustration of maximum rut depth and average deformation of a leveled profile.	166
Figure 4-15: Evolution of Section 609HB rutting profile.	166
Figure 4-16: Average deformation for Section 609HB.	167
Figure 4-17: Summary of measured rutting (average deformation) observed at the UCPRC facility for HVS testing.	167
Figure 4-18: Summary of predicted rutting (average deformation) from TPF-5(149) procedure described in this report.	168
Figure 4-19: Comparison of TPF-5(149) procedure and unmodified MEPDG procedure predictions for rutting (average deformation) and observed rutting at MnROAD Cells 106 and 206.	169
Figure 4-20: Comparison of TPF-5(149) procedure and unmodified MEPDG procedure predictions for rutting (average deformation) and observed rutting at MnROAD Cell 70.	170
Figure 4-21: TPF-5(149) procedure for rutting, sensitivity to climate.	171
Figure 4-22: TPF-5(149) procedure for rutting, sensitivity to HMA overlay thickness.	172
Figure 4-23 TPF-5(149) procedure predicted 20-year M+H severity reflective cracking performance for MnROAD Cells 106 and 206.	180
Figure 4-24: The first two years of MnROAD Medium and High (M+H) severity reflection cracking data versus TPF-5(149) modeled M+H performance and Original MEPDG modeled performance.	181
Figure 4-25: Predicted 20-year Low, Medium, and High (L+M+H) severity reflective cracking performance for MnROAD Cells 106 and 206 according to TPF-5(149) procedure.	182

Figure 4-26: First two years of MnROAD Low, Medium, and High (L+M+H) severity reflection cracking data versus TPF-5(149) modeled L+M+H performance.....	182
Figure 4-27: Influence of climate file on TPF-5(149) procedure for M+H reflective cracking.	184
Figure 4-28: Influence of climate file on TPF-5(149) procedure for L+M+H severity reflective cracking.....	184
Figure 4-29: First 40 months of predicted L+M+H severity reflective cracking by TPF-5(149) procedure for five climate files.....	185
Figure 4-30: Influence of HMA overlay thickness on TPF-5(149) procedure for M+H severity reflective cracking.....	186
Figure 4-31: Influence of HMA overlay thickness on TPF-5(149) procedure for L+M+H severity reflective cracking.....	186
Figure 4-32: Influence of dowels on TPF-5(149) procedure for M+H severity reflective cracking for project using Seattle, WA, climate file.....	187
Figure 4-33: Influence of dowels on TPF-5(149) procedure for L+M+H severity reflective cracking for project using Seattle, WA, climate file.....	188
Figure 4-34: Propagation of fatigue cracking in a composite pavement.....	188
Figure 4-35: Predicted JPCP transverse performance for three JPCP projects (according to original MEPDG) and a HMA-PCC project (according to TPF-5(149) procedure).....	191
Figure 4-36: Comparison of 9-inch JPCP project and model predictions for PCC transverse cracking according to original MEPDG and TPF-5(149) procedures.....	192
Figure 4-37. Influence of HMA overlay thickness on predicted JPCP transverse cracking for a HMA-PCC project.....	193
Figure 4-38: Influence of climate on JPCP transverse cracking for a HMA-PCC project.....	193
Figure 4-39. Predicted JPCP transverse cracking in HMA-PCC projects for Minneapolis, MN, and Pullman, WA, according to the original and TPF-5(149) modified MEDPG.....	194
Figure 4-40. Predicted transverse cracking in MnROAD Cells 106 and 206 according to the original MEPDG and TPF-5(149) procedures.....	195
Figure 4-41: Comparison of predicted faulting for HMA-PCC and JPCP projects using MEPDG modified according to TPF-5(149).....	199
Figure 4-42: Effect of 1-inch dowels in HMA-PCC projects for Minneapolis, MN, and Pullman, WA.....	200
Figure 4-43: Influence of climate on predicted faulting in HMA-PCC using TPF-5(149) modified MEPDG for HMA-PCC project with 1-inch dowels.....	201
Figure 4-44: Influence of climate on predicted faulting in HMA-PCC using TPF-5(149) modified MEPDG for HMA-PCC project without dowels.....	201

Figure 4-45: Influence of HMA overlay thickness on predicted faulting in HMA-PCC using TPF-5(149) modified MEPDG for HMA-PCC project with 1-inch dowels.....	202
Figure 4-46: Influence of HMA overlay thickness on predicted faulting in HMA-PCC using TPF-5(149) modified MEPDG for HMA-PCC project without dowels.....	203
Figure 5-1: Curing of concrete pavements is critical; water cure eliminates built-in temperature gradients, high zero-stress temperature, and excessive shrinkage.....	211
Figure 5-2: Dowels can be placed within acceptable tolerances, field measurement every day is critical.	212
Figure 5-3: Tie bar placement is important and should be measured every day.	213
Figure 5-4: Quality construction is critical and contractor pay incentives are very helpful.....	216
Figure 5-5: Recommended aggregate gradation for RCC (from ACI 1995).	221
Figure 5-6: Typical RCC paving operation: dump truck unloads mix into an asphalt paver, a roller follows close behind to ensure adequate compaction (from Portland Cement Association, 2012).	222
Figure 5-7: Relation between compaction (measured as % air free density) and strength (from Schrader, 1992).	223
Figure 5-8: End dump of HMA into paver hopper (Mahoney, Pavement Interactive.com).....	226
Figure 5-9: HMA head in auger (Mahoney, Pavement interactive.com).	227
Figure 5-10: Screed movement with material head variation.....	228
Figure 5-11: Raveled longitudinal joint (Brown, 2006).	229
Figure 5-12: Proper rolling of free edge (Benson and Scherocman 2006).	230
Figure 5-13: Proper overlap of hot mat onto cold mat (Benson and Scherocman 2006).	231
Figure 5-14: Rolling of hot mat for joint compaction (Benson and Scherocman 2006).	232
Figure 5-15: Sawing joints in the AC layer which correspond to the joints in the underlying PCC layer (left) and sealing the newly sawn joints (from Rao et al 2011).	233
Figure 5-16: Illinois tollway saw-and-seal (Elsefi 2011).	233
Figure 5-17: SMA over PCC along A93 in Germany, rectangular patch repair visible next to red traffic diversion truck (Rao SHRP 2010).....	235
Figure 5-18: View of statistical QC/QA process (Hand and Epps 2006).	237
Figure 5-19: Plates randomly placed under HMA mat.....	238
Figure 5-20: Shoveling material from above plates.....	238
Figure 5-21: Examples of AC overlays to rehabilitate existing rigid pavements, here for a repaired PCC slab (at left) and rubblized PCC pavement (at right) (from Christensen and Bonaquist 2011).	239

Figure 5-22: Illustration of net effects of binder stiffness and overlay thickness on fatigue life [from Harvey et al. 2004].	241
Figure 5-23: Recommended low temperature PG grade from LTPPBind (from Bennert 2009).	247
Figure 5-24: Time in years until reflective cracking occurs in AC overlays of PCC pavements and recommended low temperature PG grade from LTPPBind (from Bennert 2009).	247
Figure 5-25: TTI overlay tester to investigate mix design influence on reflective cracking (from Zhou and Scullion 2003).	248
Figure 5-26: Overlay binder content to optimize resistance to rutting and fatigue cracking from Zhou et al (2006).	249
Figure 6-1: The ratio of the NPV of TICP to the NPV of JPCP, which are dependent on asphalt cost, JPCP concrete cost, TICP concrete cost as a percentage of JPCP concrete cost, and discount rate.	270

Executive Summary

The Federal Highway Administration Pooled Fund Project TPF-5(149) was designed to investigate important aspects of a special kind of composite pavement referred to in this study as thermally insulated concrete pavements (TICP). These pavements featured a newly constructed Portland cement concrete (PCC) pavement overlaid with an asphalt concrete (AC) layer, intended both as a renewable wearing course and as an insulating layer to reduce the magnitude of thermal loading in the structural PCC layer. The TPF-5(149) project investigated three important aspects of TICPs:

- structural modeling and design/analysis guidelines;
- construction guidelines; and
- life cycle cost analysis (LCCA) comparisons.

The design and analysis effort placed an emphasis on the use of the American Association of State Highway and Transportation Officials (AASHTO) Mechanistic-Empirical Pavement Design Guide (MEPDG) and the use of composite pavement data collected at the Minnesota Road Research facility (MnROAD) and the University of California Pavement Research Center (UCPRC). In addition, the construction guidelines were informed by the construction of composite pavement test sections at MnROAD and UCPRC. Some of these composite pavements were sections created under the Strategic Highway Research Program (SHRP2) R21 “Composite Pavements” study.

Overall, the TPF-5(149) project led to research products that have immediate application in the design and construction of composite pavements. The applicability of the results extends past TICP and into general AC overlays of PCC pavements: the design, analysis, and construction research in TPF-5(149) can be applied for some aspects rehabilitation (AC overlays of PCC) as easily as new construction (TICP). The following summary highlights notable research in each of three project research directions outlined earlier.

Design and Analysis

The design and analysis effort of TPF-5(149) was a significant undertaking that resulted in the following research.

1. TPF-5(149) investigated the applicability of the existing MEPDG for the design of TICP, which included:
 - a. a review of the climatic models used by the MEPDG for AC overlays of PCC pavement projects and
 - b. a review of the use of a single-load, duration-dependent AC dynamic modulus to characterize the behavior of the AC layer.
2. The development of mechanistic-empirical models for reflective cracking, rutting, faulting, and transverse cracking for composite pavements, which included the evaluation of:
 - a. the original MEPDG models and

- b. reflective cracking and asphalt rutting models developed for the Caltrans mechanistic-empirical pavement design procedure (CalME).
3. The development of a companion program for the MEPDG that allows a user to design and analyze a composite pavement project using the TPF-5(149) mechanistic-empirical models.

A few highlights of this research that have immediate impact on pavement engineering are summarized here. The early evaluation of the MEPDG uncovered significant issues with the Enhanced Integrated Climate model (EICM) in MEPDG and its use of climate data. This led to faulty predictions in transverse cracking in AC overlay projects in the MEPDG. TPF-5(149) uncovered the source of these problems and made recommendations to the developer of the MEPDG to correct that issue; some of these corrections were incorporated into AASHTO's next generation M-E procedure, DARWin-ME.

Furthermore, the TPF-5(149) research team found that the use of a single-load, duration-dependent AC dynamic modulus to characterize the behavior of the AC layer was insufficient for composite pavements subjected to a combination of traffic loads and temperature curling. The research found that the MEPDG can significantly underestimate the stress in composite pavements subjected to a combination of traffic loading and temperature curling. A stress computation procedure called the *2-moduli approach* was developed. This approach can be implemented into the MEPDG, although additional research efforts, such as additional training of the neural networks in the MEPDG, are required.

Finally, the most notable product of the TPF-5(149) project in design and analysis is the developed companion software to the MEPDG. This software is immediately applicable to current composite pavement design given that it:

- incorporates the developed TPF-5(149) M-E models, which are tailored specifically to the MEPDG framework (i.e. MEPDG inputs and parameters);
- provides the user with the flexibility to choose performance models to be used, and this choice comes with the convenience of not requiring a large number of different input parameters per choice;
- allows the designer to incorporate the results of different material characterization procedures (such as the CalME rutting test protocol and the Texas Transportation Institute (TTI) overlay tester) in the design process;
- uses models for faulting that allow the designer to quantify the effect of dowels on the long-term performance of composite pavements, which cannot be done with the current MEPDG models.

As a result, TPF-5(149) project has advanced the design and analysis of composite pavements in terms of both M-E modeling and improving the MEPDG, the most popular and readily available M-E design tool for pavement engineers.

Construction

The project research involved a review of AC overlay construction on concrete pavements. This includes both standard PCC pavements, such as jointed plain concrete pavement (JPCP), and

roller compacted concrete pavement (RCC). Important aspects of JPCP and RCC construction were reviewed for the research and described in this report, and the construction of the AC overlay is described and illustrated in full. This included QA/QC procedures and interviews with experts in pavements to gather their input on important construction concerns. The guidelines developed also included a review of AC mix design criteria for AC overlays and guidelines for the selection of the AC mix to be used in the finished overlay. Criteria considered for mix design include the mitigation of reflective cracking, minimizing rutting, and mitigating low-temperature cracking. The construction guidelines developed in this research have benefited greatly from participation in, and observations of, the construction of TICP and AC-PCC pavements at MnROAD and UCPRC for the TPF-5(149) and Strategic Highway Research Program 2 (SHRP2) R21 projects. These experiences enriched the developed guidelines and made it possible to provide very specific guidelines on certain techniques, such as the use of saw-and-seal on TICP.

Life-Cycle Cost Analysis

The life cycle cost analysis (LCCA) procedure was adopted for cost comparison of newly constructed JPCP and TICP pavements and it accounts various factors in the construction and maintenance of these pavements over the intended service life. The cost efficiency of TICP depends on many factors. For example, as the cost of asphalt increases, other materials in the TICP (most notably the concrete used for the structural layer), must decrease make the TICP competitive with its JPCP equivalent in cost. However, the reduction of cost of the PCC layer through thickness or strength reduction should not jeopardize the structural performance of the TICP. The LCCA case study determined that if the construction cost (per cubic yard, for instance) of the PCC layer of the TICP is the same as the cost of the PCC layer in the JPCP and the cost of the AC layer is 80 percent of the 2009 cost (as assumed earlier), then only one of the TICP designs considered was a cost-effective alternative to JPCP. However, if construction costs for the PCC layer are reduced, then TICP other design alternatives were also potentially cost competitive.

Chapter 1. Introduction

The FHWA Pooled Fund Project TPF-5(149) focused on the design, cost analysis, construction, and analysis of AC overlays of newly constructed PCC pavements. These pavements were termed “thermally insulated” in light of the benefits of the AC overlay relative to environmental/climatic effects on performance. Thermally insulated concrete pavements (TICPs) consist of a concrete pavement structure (jointed or continuously reinforced) covered by an asphalt layer during construction (before opening to traffic) or soon after construction to address ride quality or surface characteristic issues.

Ahead of the TPF-5(149) research, TICPs were thought to possibly combine the structural longevity of PCC pavements with the serviceability of AC pavements. This would involve benefits such as the simplification of PCC design and construction through a thinner PCC layer due to reduced stresses in the concrete from the insulating effects of the asphalt layer, simplified finishing and simplified joint formation techniques. The main objective of the TPF-5(149) research was to perform life cycle cost analysis comparisons and develop design and construction guidelines for TICPs. The study initially had the following secondary objectives:

1. Validation of the structural and climatic models of the Mechanistic-Empirical Pavement Design Guide (MEPDG) for asphalt overlays of concrete pavements.
2. Investigation of applicability of the MEPDG for design of TICPs.
3. Investigation of applicability of reflective cracking and asphalt rutting models developed in California.
4. Development of recommendations for feasibility analysis of newly constructed TICPs or thin overlays of the existing concrete pavements.

The final report describes the project research in fulfillment of these objectives in the following six chapters:

- Chapter 2, Life cycle cost analysis;
- Chapter 3, MEPDG and climate modeling validation and analysis;
- Chapter 4, Response Model for Combined Thermal and Traffic Loading;
- Chapter 5, Performance models and design for the MEPDG;
- Chapter 6, Construction practices; and
- Chapter 7, Conclusions.

Chapter 2. MEPDG and Climate Modeling Validation and Analysis

The current state-of-the-art in pavement design and performance prediction is the Mechanistic-Empirical Pavement Design Guide (MEPDG) (NCHRP 2004). However, empirical design procedures prior to the Mechanistic-Empirical Pavement Design Guide (MEPDG), such as AASHTO-93, were unable to fully account for climatic effects on pavement performance. AASHTO-93 is an empirical pavement design procedure that correlates inputs to serviceability. While the AASHTO procedure has been useful in designing pavements in the past, its empirical nature results in numerous shortcomings that can be addressed by a mechanistic-empirical approach. Though the earliest design models for roadways considered mainly the effects of traffic loading, these models soon evolved to account for the influence of climate and other environmental effects. To that end, modern pavement engineers consider the so-called environmental load to be as critical to design and performance as the volume and type of vehicles traveling a roadway.

The MEPDG was released to the public in 2004, and since that time state and local transportation agencies and other institutions have worked diligently to further understand this significant advance in pavement design and performance prediction. While the incorporation of climate and environment into the MEPDG models is far from comprehensive, the developers of MEPDG took a major step toward accounting for environmental effects through the incorporation of the Enhanced Integrated Climatic Model (EICM). EICM uses hourly climatic data files to predict temperature and moisture profiles, frost heave, and other climate-related phenomena important to MEPDG's analysis of a given pavement system. Although many aspects of the MEPDG modeling and design inputs have been the subject of a great deal of research, very little of the MEPDG dealing with environmental effects and its impact on pavement performance prediction has been a subject of an in-depth analysis in the past. This chapter discusses TPF-5(149) investigations into the influence of EICM.

2.1. Effect of Climate Data and Climate Modeling on MEPDG Predictions for Composite Pavements

Climatic factors, such as precipitation, temperature, and freeze-thaw cycles together with the material characteristics of pavement, such as susceptibility to moisture and freeze-thaw damage, layer drainage, and, in the case of composite pavements, infiltration potential of the pavement on which the pavements are constructed, have a major impact on long term pavement performance (Oh et al 2006).

Climatic factors affect behavior of all layers in the pavement system. The properties of asphalt are dependent on temperature. At low temperatures, asphalt becomes hard and brittle; at high temperatures asphalt becomes soft and more viscous (Mamlouk and Zaniewski 2006). As temperature increases, asphalt becomes less elastic and more viscous, and the modulus of the asphalt layer(s) is significantly reduced. Consequently, the pavement cannot support loads as effectively as it can at lower temperatures. At high temperatures, asphalt is prone to rutting, and at extreme low temperatures it is susceptible to thermal cracking.

Unlike asphalt, concretes do not see a significant reduction in moduli or flexural strength within the same temperature range. Instead, temperature and moisture gradients in the concrete layer induce stresses and strains by distorting the shape of the slab. If caused by a temperature gradient, these distortions are known as curling; if caused by a moisture gradient, these distortions are known as warping. When these distortions are restrained by dowels, self-weight of the slab, and soil support, stresses and strains are induced (Yu et al 1998, Ruiz et al 2008). Curling and warping both consist of two parts: a built-in, permanent component, and a transitory component that varies continuously with changing climatic conditions.

Temperature and moisture fluctuations affect the behavior of unbound layers. An increase in moisture content causes soils to become less stiff. As subsurface temperatures drop below the freezing point, moisture in the unbound pavement layers freezes into ice lenses that bind the aggregate particles together. This leads to an increase in the strength and stiffness of the unbound pavement layers and subgrade soil. When the ice lenses thaw, the moisture increase in the soil can lead to weakened support for the pavement structure (Selezneva et al 2008). Better accounting for these effects will allow pavement engineers to design better, longer-lasting, and more sustainable pavements. However, previous empirical design procedures, such as AASHTO-93, were unable to fully account for these effects.

AASHTO-93 is an empirical pavement design procedure that correlates inputs to serviceability. Two separate design procedures, flexible and rigid, exist for AASHTO-93. The AASHTO-93 procedure was developed at one location and therefore cannot adequately represent climatic effects from locations with different climatic conditions. The procedure has only two environmental inputs: drainage and the seasonal variation of subgrade support. Although these are important effects to consider, alone they are not adequate.

While the AASHTO procedure has been useful in designing pavements in the past, its empirical nature results in numerous shortcomings that can be addressed by a mechanistic-empirical approach. The recently developed MEPDG has addressed this limitation and incorporated a comprehensive Enhanced Integrated Climatic Model as part of the MEPDG design process and design software. The MEPDG uses an incremental damage approach, which allows for the consideration of climatic effects and an hourly evaluation of material properties throughout the design life of the pavement.

Since its introduction, numerous studies have been conducted evaluating sensitivity of the MEPDG pavement performance models to the design input parameters (Hall and Beam 2005, Graves and Mahboub 2006, Kannekanti and Harvey 2006), but no comprehensive sensitivity study of the effects of climate on pavement performance predictions made by the MEPDG has been made. This study aims to fill this gap. Included is a brief description of the Enhanced Integrated Climatic Model, a sensitivity study of the effect of climate for 610 stations located across the United States, and analysis at the national, regional, and local levels. The effects of climate file generation using both station-specific information and virtual station generation through interpolation are also examined.

2.1.1 Enhanced Integrated Climatic Model

The Enhanced Integrated Climatic Model (EICM) is a one-dimensional coupled heat and moisture flow program that simulates changes in pavement and subgrade characteristics and behavior in conjunction with environmental conditions over numerous years of service (Zapata and Houston 2008). It simulates the upper boundary conditions of a pavement-soil system by generating patterns of rainfall, solar radiation, cloud cover, wind speed, and air temperature (Birgisson et al 2000). The EICM is comprised of three main components: a climate-materials structural model (CMS Model), a frost-heave and settlement model (CRREL model) developed at the United States Army Cold Regions Research and Engineering Laboratory, and an infiltration-drainage model (ID model) developed at Texas A & M Universities' Texas Transportation Institute (Richter 2006). The EICM predicts temperature, resilient modulus adjustment factors, pore water pressure, water content, frost and thaw depths, and frost heave throughout the complete pavement and subgrade profile for the entire design life of the pavement structure (Zaghoul et al 2006).

Originally designed for the FHWA in 1989 at Texas A & M University, it was developed as the Integrated Climatic Model (ICM). Larson and Dempsey revised the original model in 1997, and subsequently released ICM version 2.0 (Larson and Dempsey 1997). The EICM was adapted for use in the MEPDG and underwent several major modifications under the NCHRP 1-37A study. Version 2.1 is currently referred to as the Enhanced Integrated Climatic Model (EICM).

The EICM requires information about following five weather-related parameters on an hourly basis throughout the design life of the pavement:

- Air temperature
- Wind speed
- Percent sunshine
- Precipitation
- Relative Humidity

Air temperature, wind speed, and percent sunshine are used to estimate the heat transfer between the road and the atmosphere, as illustrated in Figure 2-1.

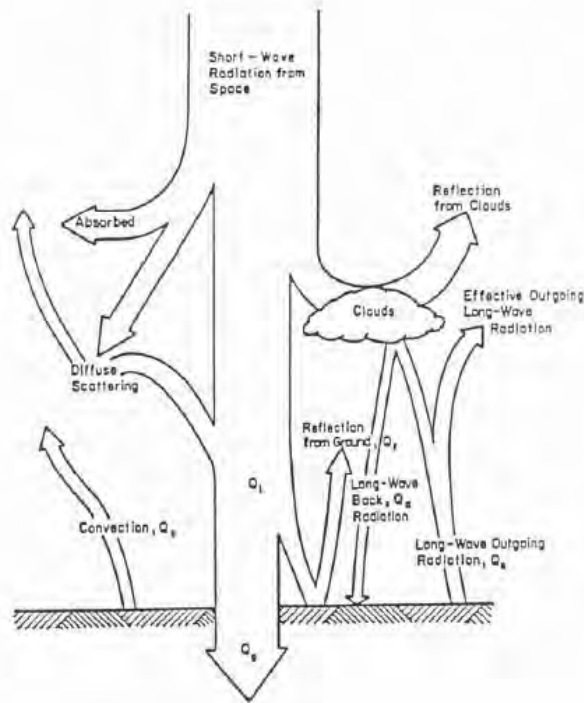


Figure 2-1: Heat transfer between pavement and air on a sunny day (NCHRP 2004).

Temperatures throughout the pavement structure are dominated by atmospheric conditions at the surface. While measuring air temperatures is relatively simple, there is not a direct correspondence between the air temperatures and pavement surface temperatures. To estimate the pavement temperature, the energy balance at the surface used in the CMS model is described in the *Guide for Mechanistic-Empirical Design of New and Rehabilitated Structures* (NCHRP 2004). The Design Guide predicts pavement temperature for every hour based on the following equation.

$$Q_i - Q_r + Q_a - Q_e \pm Q_c \pm Q_h \pm Q_g = 0$$

where,

Q_i = Incoming short wave radiation.

Q_r = Reflected short wave radiation.

Q_a = Incoming long wave radiation.

Q_e = Outgoing long wave radiation.

Q_c = Convective heat transfer.

Q_h = Effects of transpiration, condensation, evaporation, and sublimation.

Q_g = Energy absorbed by the ground.

The convective heat transfer between the pavement and air is affected by the wind speed. Convective heat transfer occurs when the air temperature and pavement surface temperature are

not equal. Heat is always transferred from warm to cold, and results in either a gain or loss of heat to or from the pavement. Convection is directly dependent on wind speed, with higher wind speeds resulting in higher convection rates.

Percent sunshine is used in the calculation of heat balance at the pavement surface, and can be thought of as a numerical representation of cloud cover. Incoming shortwave radiation is largely responsible for daytime radiation heating and is dependent on the angle of the sun and the amount of cloud cover. The angle of the sun is dependent on the latitude, date, and time of day.

The EICM does not consider precipitation when determining the surface heat flux boundary conditions. However, precipitation data is used by the EICM to determine the infiltration of moisture in rehabilitated pavements. All precipitation that falls in a month where the average temperature is below 0°C is assumed to be snow. Relative humidity values are used to model both JPCP and CRCP moisture gradients.

The EICM requires this information on an hourly basis throughout the entire life of the pavement to make temperature and moisture predictions at all depths and throughout the life cycle of the pavement. Because the mechanical properties of materials and distress development are greatly impacted by temperature and moisture, the EICM software provides a distinct advantage over previous procedures (NCHRP 2006). To satisfy the requirements for hourly data on the previously mentioned parameters, the EICM uses climatic data obtained from the National Climatic Data Center (NCDC) for 851 stations located across the United States. Stations exist in all 50 states.

EICM Climatic Database

The 851 stations available in the design guide have varying amounts of climate data. The stations with the largest files have 116 months of hourly data. The design guide requires a minimum of 24 months of climatic data for computational purposes (Larson and Dempsey 1997). If the design life is longer than the available climate file, the hourly data is recycled and used again – a pavement designed for 10 years with a 5 year climate file would use the 5-year climate data twice; for instance, the climate for years 1 and 6 would be identical.

A station with more climatic data would likely better represent the climatic conditions at that location. Since environmental conditions need to be accounted for over the entire design period of the pavement, data from only 24 months, the minimum amount of climate data required by the MEPDG, may not represent the climatic conditions well for a particular location. It is widely known that any given year a particular season can be unusually warm or cold, or have above or below average rainfall. If a relatively small number of months are used to represent climate data, it becomes sensitive to outliers, which could be either abnormal weather conditions, or poor data. Even so, 116 months may not be sufficient to represent the climatic conditions at one location. The World Meteorological Organization (WMO) uses periods of 30 consecutive 4 years for long-term climate averages. The 30-year time period was viewed by WMO as being sufficiently long to address concerns about year-to-year variations (UK Meteorological Office 2009).

Station locations in the EICM database are well-distributed geographically across the US, and cover a comprehensive range of climates. In this study, to quantify the number of locations

existing in different climates, the stations were categorized by freezing index (FI) and Mean Annual Rainfall. The thresholds for the categories were:

- Wet > 25" in rainfall/yr
- Freeze > 200 FI

The number of stations in each category is as follows:

- Dry – No Freeze region: 77 stations
- Dry – Freeze region: 136 stations
- Wet – No Freeze region: 164 stations
- Wet – Freeze region: 233 stations

Hence, the stations are climatologically well-distributed, with a significant number of stations existing in all four categories. This well-distributed, comprehensive climatic data was used to conduct a sensitivity analysis and determine the effect of climatic on pavement performance predictions.

Analysis of Climatic Inputs on MEPDG Predictions

In this study, a single pavement structure was analyzed at a large number of locations. The structure tested at each location was identical, the only variable being the climatic file. A new climate file (.icm) was generated for a specific station with complete climate data. Out of the 851 available stations, 610 had complete climate data. The MEPDG does not allow a user to generate a new climate file if the station is missing one or more months of data without using data from nearby stations. This is discussed at length in the later section, *Effect of Climate File Generation*. The number of months of data in the climate files is variable – not all complete files have the same number of months of data. The maximum number of months in a climate file was 116, the minimum number of months in a climate file used was 38.

In order to represent all of the effects that climate has on a pavement structure, a composite pavement, asphalt concrete over Portland cement concrete (AC over PCC), was selected for the MEPDG trial design. Six-hundred ten (610) simulations of composite pavements were conducted. No stations with missing data were used, and no interpolation between stations was done. The following three pavement structures were considered:

- Flexible pavement: 9-in thick AC 58-28PG
- Rigid pavement: 9-in thick PCC, 1.25-in doweled joints
- Composite pavement: 2-in thick AC 58-28PG over 7-in thick JPCP
 - No pre-existing distresses were present in the PCC layer

For all three pavement structures the following inputs were used:

- Design life: 20 years
- Average Annual Daily Truck Traffic (AADTT): 3200
- Joint spacing: 15ft
- Dowels: 1.25-in diameter, 12-in spacing

- Granular Base: 6-in
- Subgrade: A-6
- Water table depth: 5ft
- All other inputs were MEPDG default values

The asphalt performance grade is the same at all locations. This report does not suggest that the same performance grade binder should be used at all locations across the country. Instead, the same binder was used to quantify the effects of climatic on predicted pavement performance given the same pavement structure.

The analysis of the results of the 610 MEPDG runs were performed in three categories: national, regional, and local. Outputs of interest were: reported transverse cracking, IRI, and AC rutting.

National. The frequency distributions for predicted transverse cracking in the PCC layer, IRI, and AC rutting at the end of the project design life are used below in the discussion of the importance of climate in performance prediction. For each distress, relevant examples from two of the three available projects are used, beginning with the discussion of IRI and Figures 2-2 and 2-3.

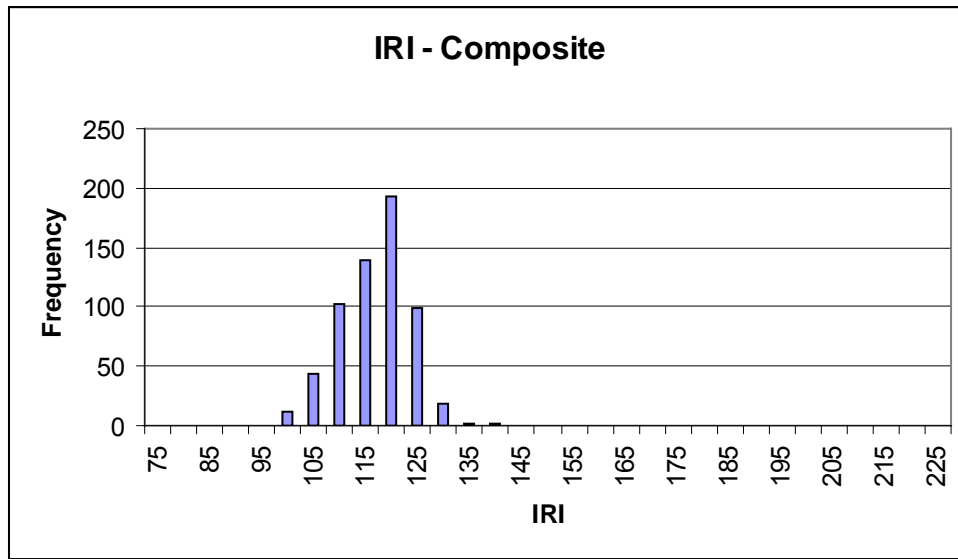


Figure 2-2: Frequency distribution of predicted IRI values for composite pavement structure.

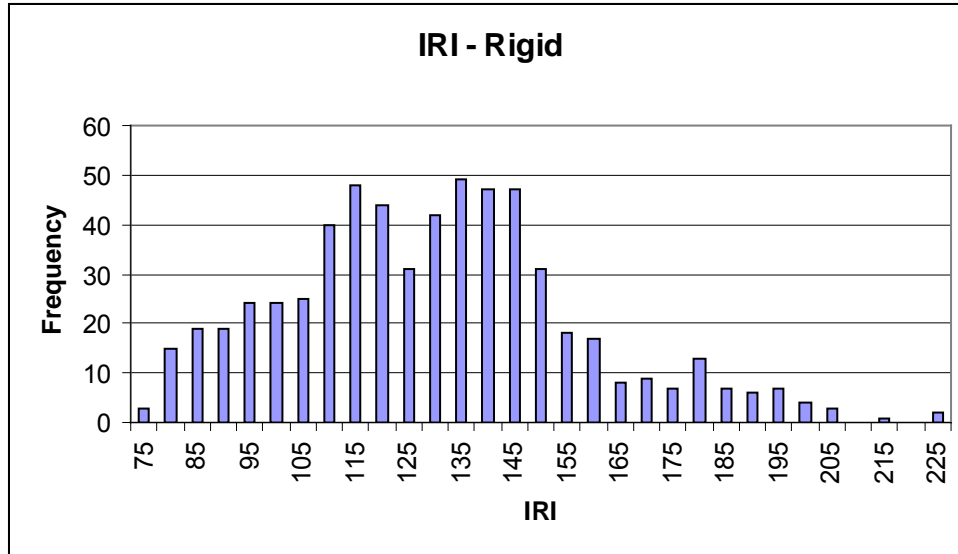


Figure 2-3: Frequency distribution of predicted IRI values for rigid pavement structure.

The predicted IRI values for the composite structure in Figure 2-2 did not appear to be excessively sensitive to the environmental conditions (note also that the flexible and composite IRI results were very similar). The rigid structure was more sensitive and had more extreme predicted values. A key difference in the reported IRI for AC/PCC and an equivalent single-layer PCC system may lie in the fact that joint faulting is not currently taken into consideration when determining IRI for composite pavements.

Figures 2-4 and 2-5 illustrate the predicted performance in AC rutting of all pavements associated with the 610 climate files for an AC/PCC pavement and an equivalent single-layer AC system.

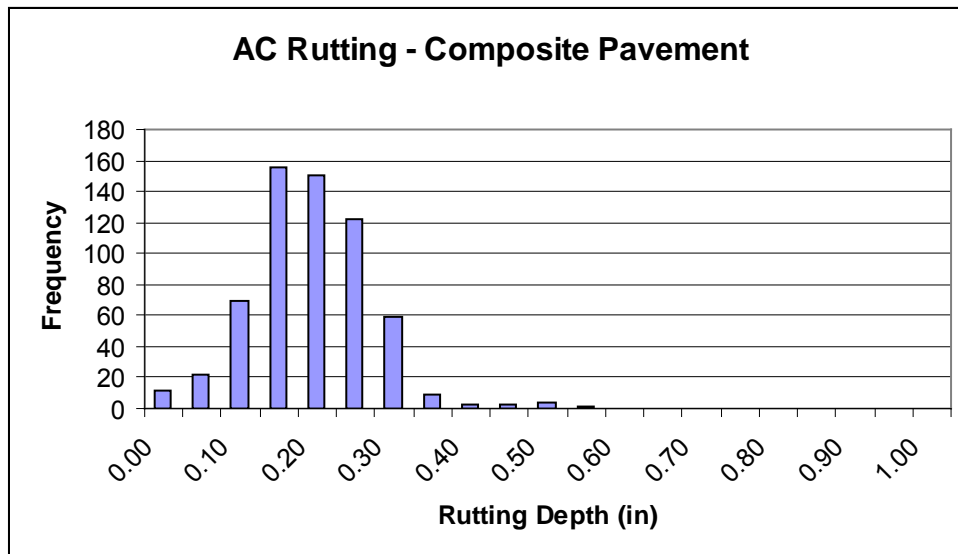


Figure 2-4: Frequency distribution of predicted rutting values for composite pavement structure.

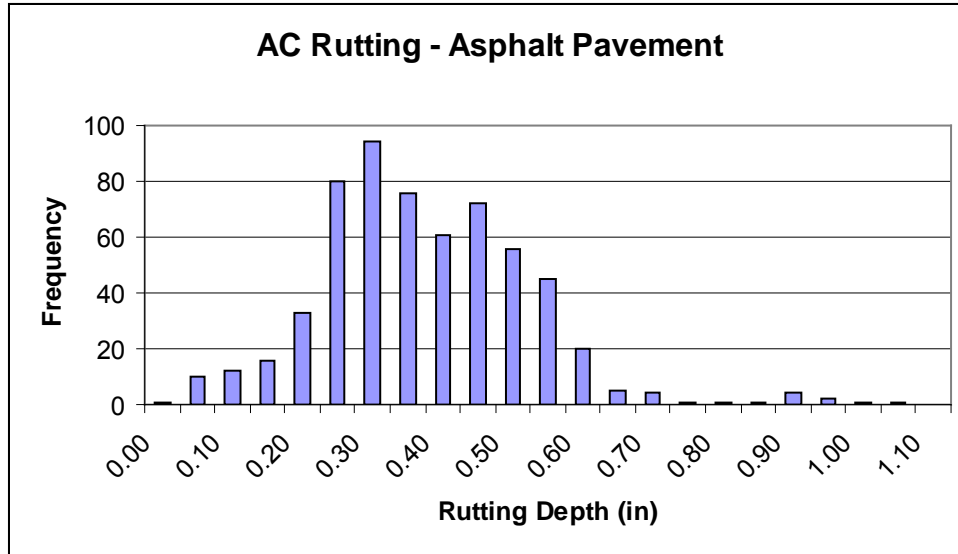


Figure 2-5: Frequency distribution of predicted rutting values for single layer flexible pavement structure.

As illustrated in Figures 2-4 and 2-5, the composite pavement had less extreme values in AC rutting than the 9” single-layer AC pavement, and the single-layer AC equivalent also experienced more rutting in general. This behavior is attributed largely to the rutting being confined to the AC layer in the composite pavement; that is, no base or subgrade rutting was present due to the PCC layer. The histograms of Figures 4 and 5 suggest that, according to the MEPDG predictions, an AC/PCC pavement is less sensitive to climate in AC rutting than an equivalent single-layer AC system.

Finally, the analysis of the effect of the location (climate) on predicted transverse PCC cracking for an AC/PCC pavement and an equivalent single-layer PCC system is reported in Figures 2-6 and 2-7.

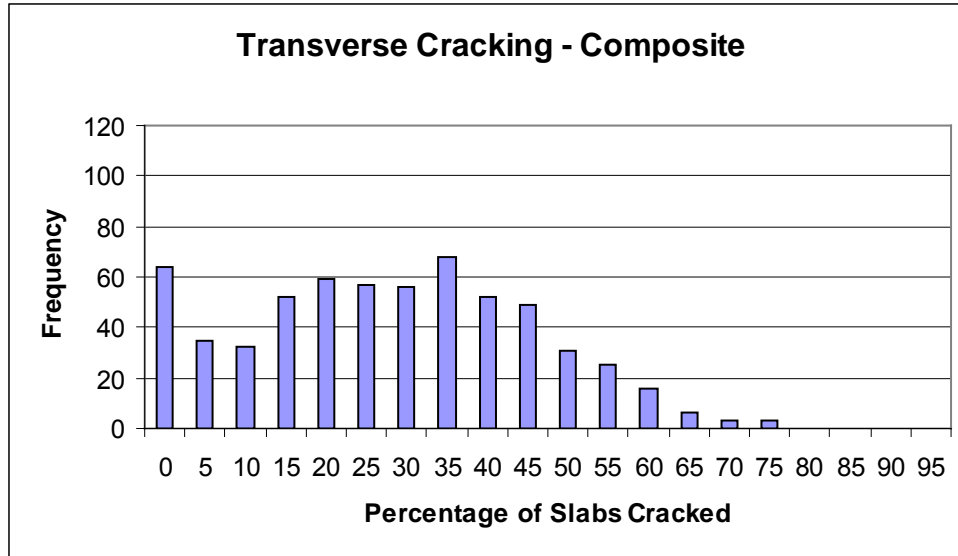


Figure 2-6: Frequency distribution of predicted transverse cracking values for composite pavement structure.

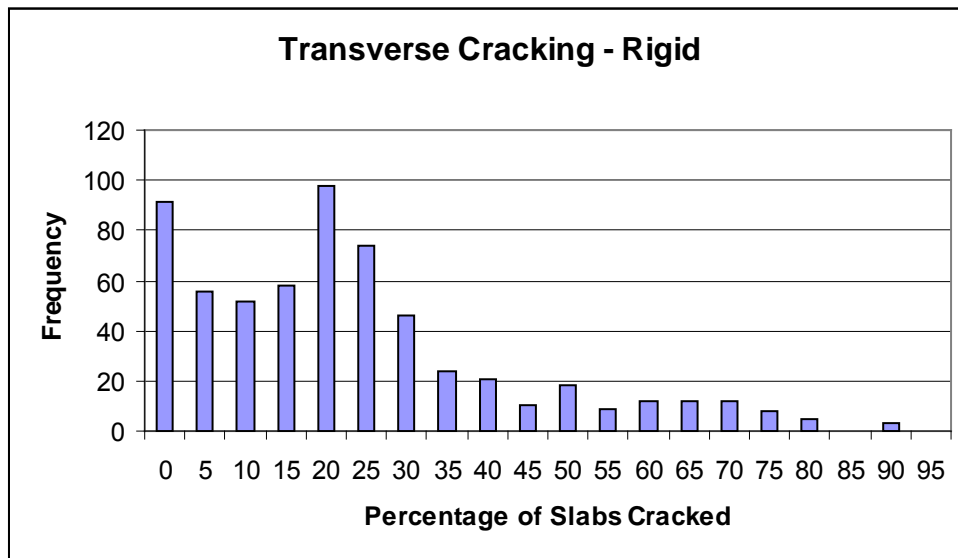


Figure 2-7: Frequency distribution of predicted transverse cracking values for rigid pavement structure.

Visible in Figures 2-6 and 2-7, the climate has a significant effect on predicted transverse cracking in the PCC layer. This is evident by the wide ranges of values predicted. The minimum values reported for the composite structure were 0.0% in Cold Bay and Bethel, AK, and the maximum value was 79.1% in Nogales, AZ. The less extreme values predicted for the composite structure are likely a result of the asphalt layer insulating the PCC layer from extreme temperature variations. Based on the analysis at the national level, it was clear to the researchers that the prediction of transverse cracking in the PCC layer of the composite system was deserving of further attention.

Regional. The predicted cracking output of all 610 stations is organized by the environmental conditions and the predicted cracking percentage, as seen in Table 2-1.

Table 2-1: Transverse cracking percentage in PCC layer of AC/PCC projects, organized by environmental conditions.

No. of Stations		Predicted Cracking Percentage			
Climate	No. of Stations	0-15%	16-25%	26-40%	40%<
Wet – Freeze	233	63	39	93	38
Wet - No Freeze	164	47	14	30	73
Dry – Freeze	136	26	28	42	40
Dry - No Freeze	77	14	13	15	35

In order to better understand the previous table-and charts, the values were analyzed by region.

To determine if there were any patterns or tendencies associated with the predicted performance and the region the station was located in, the results were plotted on Google Earth, as seen in Figure 2-8. Each icon represents a station; the icon colors seen in the following figures are associated with the percentage of transverse cracking in the PCC layer:

- Blue: < 16% slabs cracked
- Green: 16% to 25.9% slabs cracked
- Yellow: 26% to 40% slabs cracked
- Red: > 40% slabs cracked

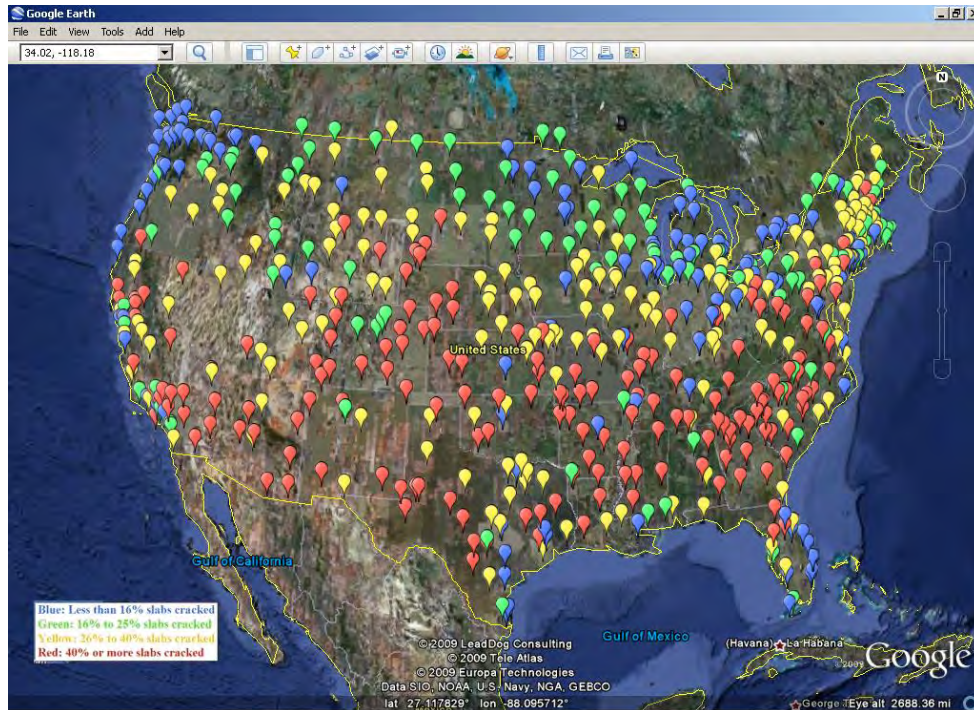


Figure 2-8: MEPDG locations of AC/PCC projects – icon color determined by transverse cracking percentage.

There are some general trends that are visible when looking at the map of the lower 48 states, such as: higher cracking appears to be at stations with a warmer climate and lower cracking appears at stations with a colder climate. Stations along the coast in California, Florida, Oregon, and Washington exhibit a low predicted cracking percentage. Inland locations across the southern United States generally have a higher predicted cracking percentage, as seen in Figure 2-8 in the states of Arizona, Georgia, and Texas. Stations in close proximity to other stations do not always have similar predicted values. This was examined in detail in the following section.

Local. It was observed that for some stations in close proximity, there was a high variation in predicted values. In this example, the MEPDG predicted 3.8% cracking using climate data from LAX International Airport in Los Angeles, CA. The MEPDG predicted 62.7% cracking for Burbank, CA, approximately 18.64 miles away. Given that all other parameters are held constant, this difference of 58.9% should be attributed to the difference in climate data for these two locations. While there is a difference in elevation of 408 ft. between the two stations, the overall climate characteristics are otherwise similar. A possible explanation for this anomaly is that the climate data used was of poor quality, resulting in poor predictions. There are several stations in relatively close proximity, with a wide range of predicted cracking, visible in Figure 2-9.

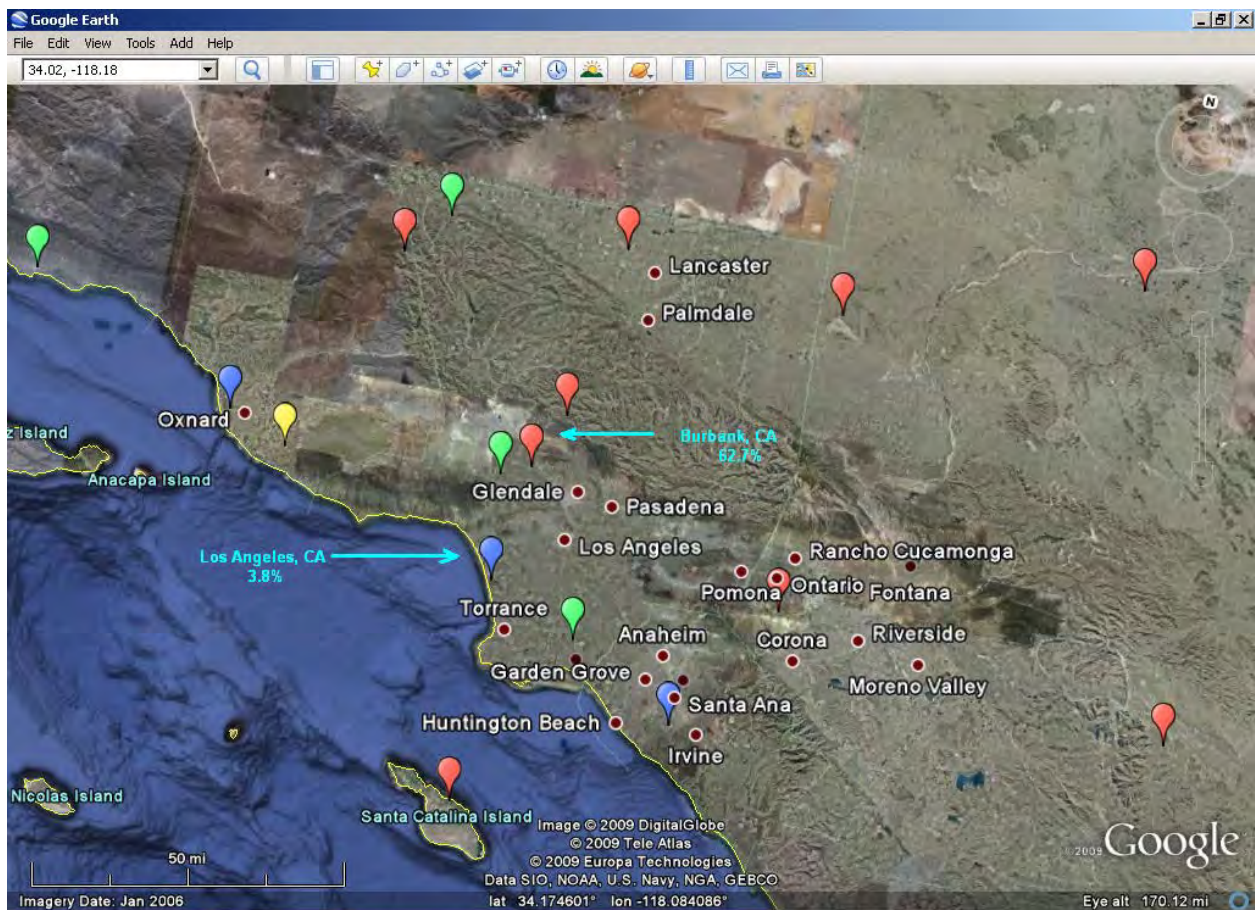


Figure 2-9: Wide range of predicted cracking in the Los Angeles metropolitan area.

Figure 2-9 illustrates the pattern, or lack thereof, in cracking predictions from the MEPDG. This is visible at several locations throughout the United States. Table 2-2 lists all distresses for each location in Figure 2-9. Generally, stations with higher predicted transverse cracking values also had higher values of predicted rutting. This may be due to the AC layer becoming soft, and unable to support loads effectively, resulting in higher stresses in the PCC layer. However, there was no direct link between the amount of predicted transverse cracking in the PCC layer and predicted AC rutting.

This phenomenon was not unique to southern California. Additional analysis of predicted transverse cracking along the 118-mile length of Long Island in New York was conducted, with the results illustrated in Figure 2-10 and Table 2-3. While some variation is expected, a difference of 32.6% within ten miles (35.7% for Central Park to 3.1% for La Guardia) is difficult to attribute to differences in climate given the proximity of the weather stations used for these project files. To eliminate this 32.6% difference in predicted cracking, the pavement at Central Park would require an additional 5 to 10 percent in PCC thickness to have performance equivalent to that of the pavement at La Guardia. The performance of these designs at locations within 10 miles of one another is very unusual.

Table 2-2: Predicted distresses for AC/PCC projects in Southern California.

Location	IRI (in/mi)	Transverse Cracking (%)	AC Cracking		AC Thermal Fracture (ft/mile)	Total Rutting (in)	# of Months of Data	Elev. (ft)	Mean Annual Temp (F)	Mean Annual Precip (in)
			Top-Down (ft/mile)	Bot-Up (%)						
Avalon	118.8	47.1	0	0	169.3	0.21	68	1613	59.84	13.32
Burbank	121.3	62.7	0	0	126.7	0.24	94	734	63.44	13.06
Camarillo	110.9	31.1	0	0	126.7	0.15	77	67	60.23	13.14
Chino	122.5	64	0	0	126.7	0.23	95	682	62.16	10.92
Daggett	130.1	61.9	0.2	0	126.7	0.44	67	1928	67.81	5.72
Lancaster	126.6	59.3	0.1	0	126.7	0.32	63	2371	62.37	10.19
Long Beach	110.1	23.5	0	0	126.7	0.17	114	37	63.37	12.14
Los Angeles	103	3.8	0	0	126.7	0.11	108	326	62.08	14.17
Los Angeles	123.7	66.3	0	0	126.7	0.28	80	185	63.41	14.7
Ontario	116.3	45.5	0	0	126.7	0.21	94	904	63.92	11.17
Oxnard	105.3	14.6	0	0	126.7	0.11	96	68	59.41	10.81
Palm Springs	130.9	67.7	0.2	0	126.7	0.49	65	447	74.9	3.74
Palmdale	125.8	61.9	0	0	126.7	0.31	95	2562	62.14	6.19
Sandberg	113.4	22.1	0	0	126.7	0.19	116	4519	55.39	13.92
Santa Ana	106.9	14.9	0	0	126.7	0.15	85	52	62.87	10.62
Santa Barbara	109	23	0	0	126.7	0.12	95	15	58.3	17.01
Santa Monica	108.5	20.6	0	0	126.7	0.15	65	192	61.68	12.94

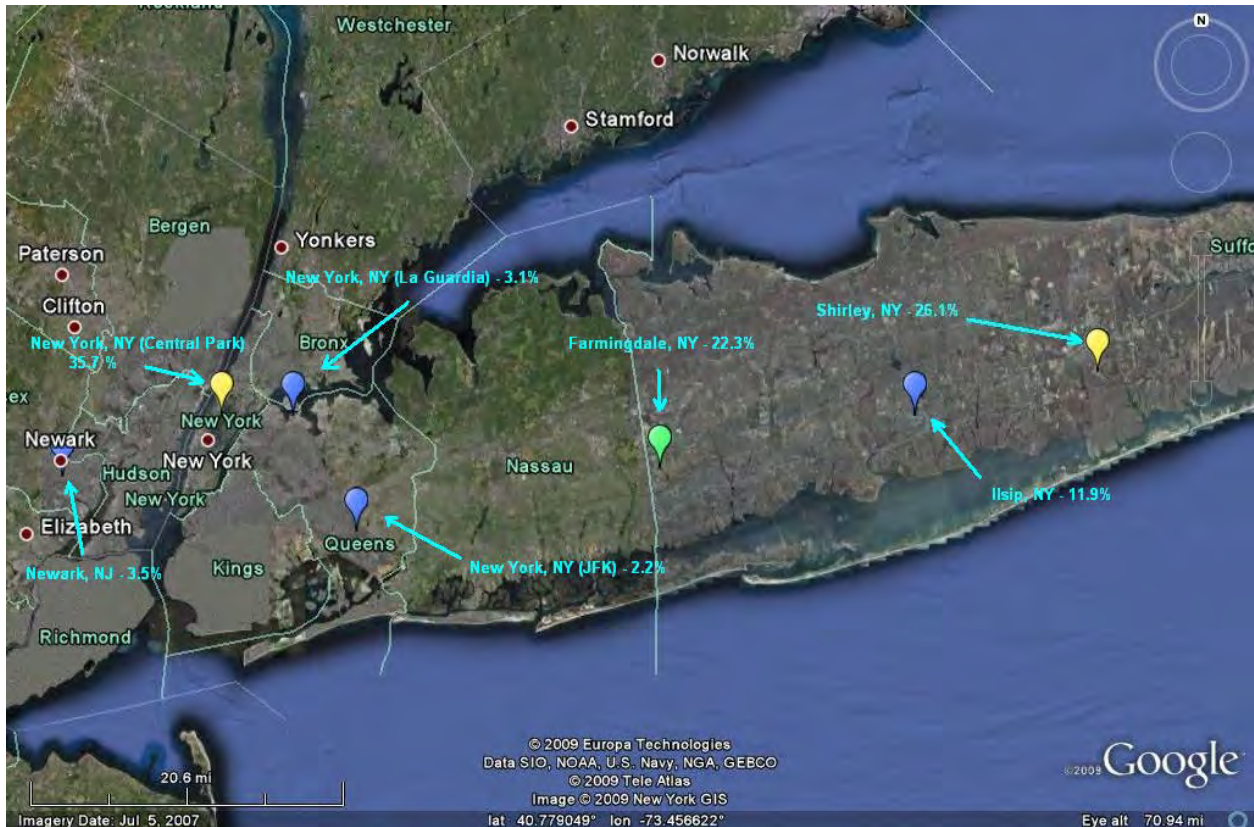


Figure 2-10: Wide range of predicted cracking in Long Island, New York.

Table 2-3: Predicted distresses for locations near Long Island, New York.

Location	IRI (in/mi)	Transverse Cracking (%)	AC Cracking		AC Thermal Fracture (ft/mile)	# of Months of Data	Elev. (ft)	Mean Annual Temp (F)	Mean Annual Precip (in)
			Top-Down (ft/mile)	Bot-Up (%)					
Newark, NJ	110.4	3.5	0	0	126.7	116	28	55.26	42.35
Farmingdale, NY	116	22.3	0	0	126.7	79	74	52.93	42.06
IIsip, NY	112.5	11.9	0	0	126.7	79	144	52.36	38.81
New York, NY (Central Park)	121.2	35.7	0	0	126.7	116	161	55.02	44.43
New York, NY (JFK)	108.9	2.2	0	0	126.7	116	32	54.15	39.58
New York, NY (La Guardia)	110.1	3.1	0	0	126.7	116	39	55.63	42.88
Shirley, NY	117.2	26.1	0	0	126.7	77	71	52.12	41.16

Again, large variation exists in the predicted cracking values among these stations. While there are stations whose extremes act as “outliers” relative to the aggregate data in Tables 2 and 3 (e.g. mean annual temperature for Palm Springs; elevation for Sandberg; and mean annual precipitation for Palm Springs in the southern California example), by and large the stations represented in Tables 2 and 3 are very similar climatically, within each table. Hence, the

researchers are hesitant to attribute the wide variation in the predicted cracking to climate. Rather, the researchers propose that inconsistencies in climate data may be responsible for these differences as a hypothesis for future work regarding MEPDG prediction of AC/PCC performance.

Effect of Climate File Generation

The MEPDG allows the user to select a design location either with or without an existing weather station. If the location specified does not have a weather station, the EICM will interpolate data from nearby existing stations to create a virtual weather station. The user may select up to six nearby stations for interpolation. If a nearby station has an incomplete climatic file, additional stations may need to be selected. Three different combinations of selected stations are presented in this section.

1. Nearest only – Only the first weather station (out of the six listed) was selected. This station was always closest to the location (latitude, longitude, and elevation) entered.
2. All except nearest – Five out of the six listed weather stations were selected. This selection did not include the first (nearest) weather station.
3. All – All six weather stations were selected.

The effect of the number of weather stations used to generate a climatic file was examined. The output was recorded in terms of predicted transverse cracking in the concrete layer. Design specifications are listed below.

- Composite pavement: 2-in thick AC 58-28PG over 7-in thick JPCP
- Design life: 20 years
- AADTT: 3200
- Joint spacing: 15 ft,
- Dowels: 1.25-in diameter, 12-in spacing
- Granular Base: 6-in
- Subgrade: A-6
- Water table depth: 5ft
- All other inputs were MEPDG default values

The locations were selected away from the mountainous regions of the US and covered a wide geographic area in terms of climate. MEPDG factorials were run for these locations with the same pavement structure as described above. MEPDG defaults were used for inputs other than those listed. The factorials were run for two scenarios for a given location: 1) using the nearest climate station data as the only input or 2) using interpolated climate data from nearby climatic stations (not including the nearest station). Table 2-4 provides the percent of cracked slabs after 20 years of the opening of traffic.

This self-consistency test was conducted as a primary evaluation of data quality. If all the weather stations in the MEPDG database were of high quality, then the MEPDG predictions should not depend on the way the interpolated weather station is generated. Table 2-4 illustrates that although the cracking predictions are very close for station climatic data and interpolated climatic data at some locations, for other locations the cracking predictions are dramatically

different. The inconsistency in the results indicates that there are some issues with the climatic database, and that the interpolation option may yield inaccurate results depending upon the quality of the climatic data of the nearby locations. A significant difference in predicted cracking indicates that the climatic data is markedly different between the station nearest the location and the surrounding stations. It is known that some of the existing weather stations have incomplete hourly climatic data (.hcd) files. It is thought that the missing weather stations can cause unreliable MEPDG predictions.

Table 2-4: Predicted cracking values.

Locations	Lat.	Long.	Elev.	% Cracking after 20 years for weather station	
				Nearby station only	Interpolated climate
Columbus, OH	39.59	-82.53	849	6.4	30.9
Grand Forks, ND	47.57	-97.11	842	9.9	11.0
Fort Wayne, IN	41.01	-85.13	806	12.3	20.1
San Antonio, TX	29.32	-98.28	821	17.5	36.2
Madison, WI	43.08	-89.21	860	18.1	17.1
Oshkosh, WI	43.59	-88.34	816	22.9	19.3
Cedar Rapids, IA	41.53	-91.43	870	24.2	27.1
Ann Arbor, MI	42.13	-83.44	836	27.7	12.2
Joplin, MO	37.09	-94.3	985	37.6	35.9
Lawrence, KS	39.01	-95.13	833	43.0	28.8
Oak Ridge, TN	36.01	-84.14	916	51.5	22.3
Atlanta, GA	33.22	-84.34	837	58.9	19

In addition, the researchers conducted a separate local study (in the state of Minnesota) of the effect of climatic file generation, through the corresponding MEPDG interpolation function, on MEPDG predictions of transverse cracking in the PCC layer. The design specifications for the pavement system under consideration are listed below. The target distress was 20% transverse cracking in the PCC layer at 90% reliability. Inputs other than those listed below were MEPDG default values.

- Composite pavement: 2-in thick AC 58-28PG over 7-in thick JPCP
- Joint spacing: 15 ft,
- Dowels: 1.25-in diameter, 12-in spacing
- Design Life: 20 years
- AADTT: 1300
- Granular Base, 8-in
- Subgrade, A-6
- Water table depth – 5ft
- All other inputs were MEPDG default values

The MEPDG was executed for two different locations in Minnesota (Minneapolis and St. Cloud) approximately 60 miles apart. The climatic files used for these two locations were generated by creating a virtual weather station for each location, using all six available stations for interpolation. A large discrepancy in the transverse cracking predicted for these locations was observed: the MEPDG predicted 20.3% of slabs cracked in Minneapolis, and 60.2% of slabs cracked in St. Cloud. To study the effect further, seven additional locations were selected between Minneapolis and St. Cloud as shown in Figure 2-11. The weather stations used for

interpolation for each of the seven additional locations were selected from those made available by the MEPDG, illustrated in Figure 2-12.

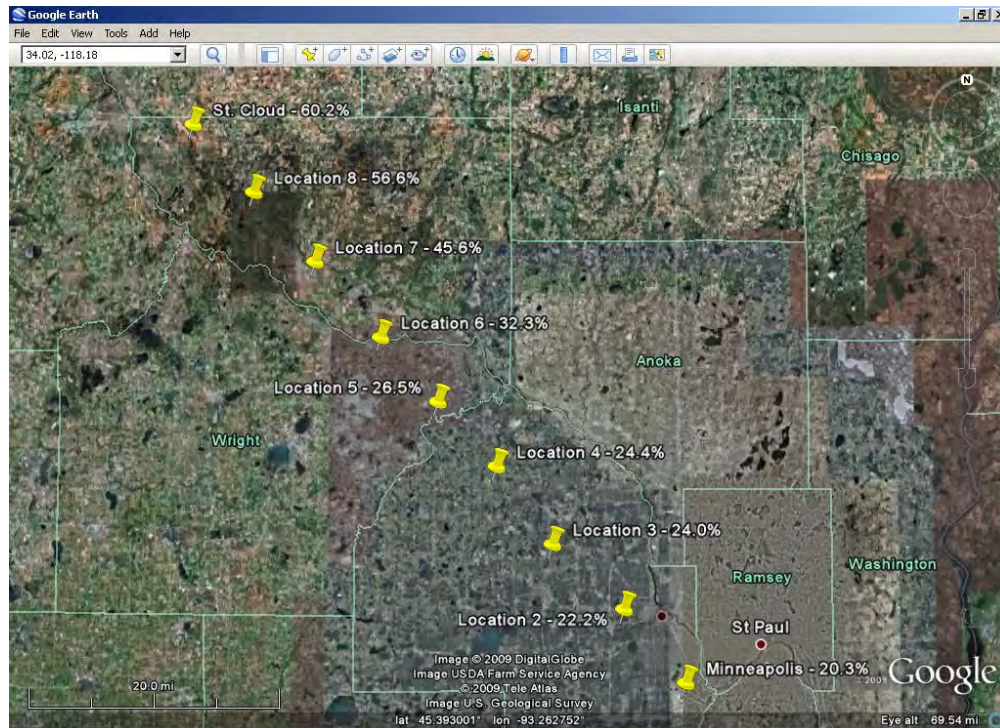


Figure 2-11: Additional locations selected for MEPDG climate data file interpolation for locations in Minnesota.

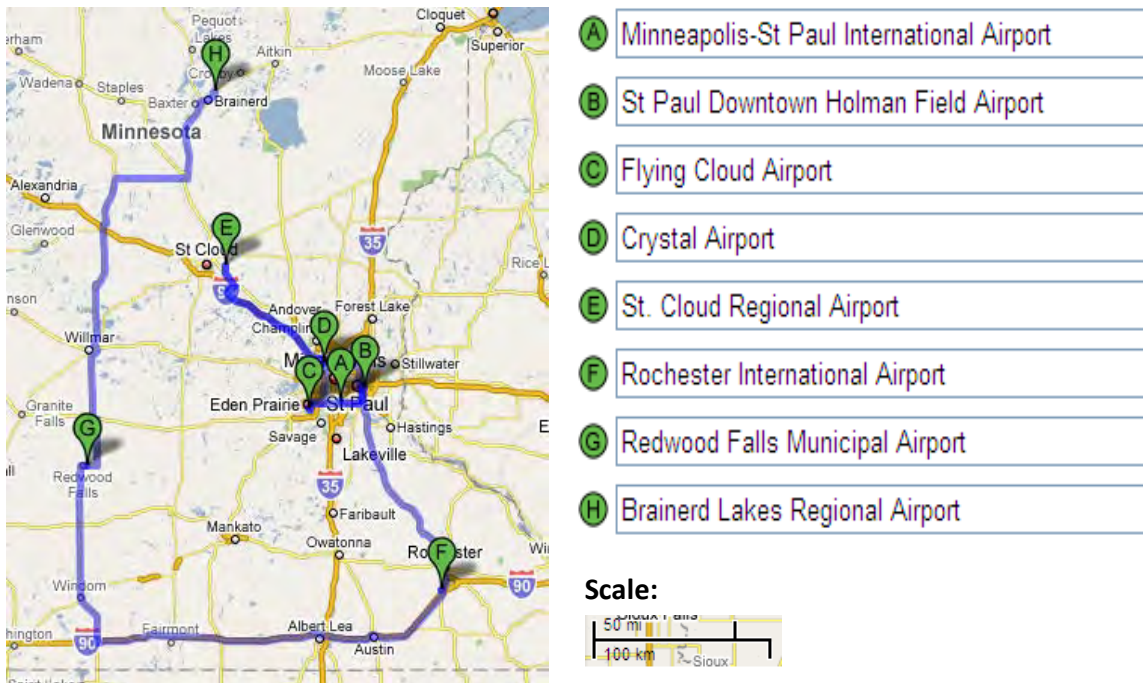


Figure 2-12: Location of weather stations listed by MEPDG for Minnesota.

Table 2-5 documents the percent slabs cracked for the nine locations after 20 years.

Table 2-5: Percent slabs cracked in AC/PCC projects for additional locations.

Locations	Lat.	Long.	% Cracking after 20 years using all weather stations
Minneapolis	44.53	-93.14	20.3
Location 2	44.581	-93.20	22.2
Location 3	45.027	-93.261	24.0
Location 4	45.08	-93.325	24.4
Location 5	45.125	-93.383	26.5
Location 6	45.17	-93.44	32.3
Location 7	45.223	-93.506	45.6
Location 8	45.272	-93.568	56.6
St. Cloud	45.32	-94.03	60.2

Table 2-5 illustrates that in moving along the 60 miles from Minneapolis to St. Cloud, the MEPDG predicts a substantially higher percentage of cracked slabs. Given that the climate from Minneapolis to St. Cloud is not substantially different, this indicates that there is a problem with the St. Cloud station. The largest difference is between Location 6 and Location 7, a difference of 13.3%. It is likely due to the St. Cloud station having missing climate data. It is already known that the St. Cloud climate file is missing one month of data, and it is possible that there are other months that may have poor quality or altogether missing data. The other five stations negated some of the effect of the St. Cloud station until the desired location was within an area where the St. Cloud station was weighted heavier. It is thought that the use of weather stations with missing or incomplete climatic data causes unreliable MEPDG predictions. It is recommended that the weather stations with missing data be eliminated from the MEPDG database.

2.1.2 EICM Validation

Pavement temperature is not constant in time or through depth. Temperatures throughout the pavement structure are dominated by the atmospheric conditions at the surface. The surface of the pavement is subject to more environmental effects and its temperature will fluctuate more than the temperature at the bottom of the structure.

Factors affecting the top surface temperature of a pavement are: incoming short-wave radiation, reflected short-wave radiation, incoming long-wave radiation, outgoing long-wave radiation, convective heat transfer, condensation, evaporation, sublimation, precipitation; and the temperature of the layer(s) immediately beneath bound layer(s) (NCHRP 2004). The bottom of a Portland cement concrete (PCC) slab is affected by the temperature of the layers directly beneath the slab and from energy transferred by conduction from the surface. Although the temperature at the bottom of the slab is ultimately influenced by the conditions at the top surface, it is not directly subjected to the factors that affect the surface temperature. Consequently, pavement temperature is not constant in time and through depth. In particular, temperature variations are especially high at the surface. These variations affect the behavior of rigid pavement structures.

Like almost all other materials, when concrete is heated it expands in size. If the temperature at the top of a concrete slab is unequal to the temperature at the bottom of the slab, different layers

of the slab want to expand to varying degrees. The warmer layer attempts to expand more than the cooler layer, but if the shape of the slab is restrained due to foundation support, dowels, tie bars, and self-weight, stresses are induced (Yu et al 1998). These stresses are known as thermal, or curling, stresses. Tensile stresses at the bottom of the PCC layer occur when the top of the slab is warmer than the bottom, which occurs most commonly during diurnal periods; these stresses are known as daytime curling stresses. Tensile stresses at the bottom of the PCC layer are the main cause of transverse cracking in PCC pavements. Thermal stresses can significantly contribute to cracking and failure of a PCC layer. Therefore, with all other factors equal, a reduction in the temperature difference in the PCC layer would result in lower thermal stresses and less transverse cracking. Thermal stresses can also contribute to other types of distress in rigid pavements. If the bottom of the slab is warmer than the top, the edges of the slab attempt to curl upward. Generally occurring during the night, this nighttime curling stress contributes to joint faulting. Thus, thermal gradients in a PCC pavement are undesirable. Limiting the environmental effects at the top of a PCC slab would reduce the temperature fluctuations at the surface. Because the bottom of the slab does not respond as quickly as the surface does to temperature changes, limiting these effects would reduce thermal gradients.

An asphalt concrete (AC) overlay is a common rehabilitation technique of concrete pavements. Thick AC overlays are used to rehabilitate degrading PCC pavements and improve structural capacity of the existing pavements. Thin AC overlays are used for rehabilitation of structurally sound PCC pavements to cover up surface defects, reduce noise attributed to traffic, and improve ride quality. It has been suggested that the placing of a thin asphalt layer on top of a PCC layer provides an insulating effect (Nishizawa et al 2009). It has been observed by other researchers that an asphalt layer placed on top of an existing PCC pavement can improve pavement performance. While there is a stiffness contribution to the pavement structure from a thin asphalt layer, the improvements in pavement performance suggest that stiffness alone cannot be fully responsible.

This section examines the quality of field data recorded at pavement sections at MnROAD, the thermal insulating effects of AC over PCC overlays, and evaluates the accuracy of predictions of pavement temperature from the MEPDG using MnROAD data. Although thermal stresses can contribute to several types of pavement distresses, transverse cracking is the primary measure of pavement performance used.

MnROAD Data and Data Analysis

To analyze the EICM performance of predicted temperature distributions, a baseline needs to be established; in this case, measured data served as the benchmark. This section details the efforts of temperature data screening and analysis. Temperature measurements from composite and rigid pavement sections were retrieved, and the data was screened to prevent the use of data with questionable quality, to assure that only data that was representative of the actual conditions was used.

The temperature data used in this section was retrieved from the “mainline” test sections along I-94 at the Minnesota Road Research facility (MnROAD). MnROAD is a full-scale cold-region pavement testing facility constructed in 1994 and administered by the Minnesota Department of Transportation (Mn/DOT). MnROAD is located near Albertville, MN along US Interstate 94.

The full-scale testing facilities at MnROAD consist of over 35 sections (or cells) distributed over a west-bound stretch of I-94, a low-volume road loop, and a farm loop. Each of the test cells represents experiments in road research, from pavement materials and design to emerging construction technologies. The test cells are continuously monitored by thousands of live sensors, including more than 1000 thermocouples located at various depths of pavement sections (MnDOT 2010). Data from these sensors are catalogued and maintained in Mn/DOT's database (Tompkins and Khazanovich 2007).

This study utilized a full year of hourly pavement temperature data, extracted from five test cells along the MnROAD mainline sections, a 3.5-mile stretch of I-94 that carries an average of 26,400 vehicles daily. Those five test cells are three thin concrete cells (113, 213, and 313) and two composite AC-over-PCC cells (106 and 206). The design for each of these cells is illustrated in Figure 2-13.

113	213	313	106	206
5"	5.5"	6"	2"64-34	2"64-34
5"Cl 1 Stab Agg	5"Cl 1 Stab Agg	5"Cl 1 Stab Agg	5"	5"
5"	4.5"	4"	6"Cl 1 Stab Agg	6"Cl 1 Stab Agg
Class 5	Class 5	Class 5	6"	6"
Clay	Clay	Clay	Class 5	Class 5
heavy turf	heavy turf	heavy turf	Clay	Clay
15'x12'	15'x12'	15'x12'	Mesabi 4.75 SuperP	Mesabi 4.75 SuperP
			15'x12'	15'x12'
			1"	no dowels
			dowel	
Oct 08	Oct 08	Oct 08	Oct 08	Oct 08
Current	Current	Current	Current	Current

Figure 2-13: Design cross-section of MnROAD Cells 106, 206, 113, 213, and 313 (MnDOT 2010).

As evident from Figure 2-13, the designs of the two sets of test cells are very similar, the main difference between the five cells being the presence of an AC overlay. This difference is at the core of the comparison that uses the data, which is to investigate the difference in thermal readings through overlaid and exposed PCC.

Data Quality Testing. Temperature data from MnROAD was filtered using a program under development by the University of Minnesota, Mn/DOT, and the Minnesota Local Road Research

Board for mining of various pavement data (Barnes 2009). This program subjected the temperature data to different tests to identify missing data, insufficient data for a given day, sensor outliers, data subset outliers, and in so doing flagged suspect data.

Temperature data that appears to be erroneous to the statistical software is flagged. There are fourteen different “flags”, each of which represents a different data test failure. Figure 2-14 is a screen capture of the computer code comments, which define the data flags.

```
In this section we define constants for each of the flags.
%-----

% Missing data flags
FLAG_MISSING_DATA           = 1;    % missing data
FLAG_NOT_YET_OPERATIONAL    = 2;    % missing data at the beginning
FLAG_DEACTIVATED            = 3;    % missing data at the end
FLAG_TOO_SPARSE_DAY        = 4;    % not enough data in any day

% Time-series based
FLAG_OUT_OF_RANGE           = 5;    % sensor outliers with annual & diurnal fit
FLAG_NEIGHBORHOOD_OUTLIERS = 6;    % sensor outliers with local neighborhood
fit
FLAG_LAG_ONE_OUTLIERS       = 7;    % sensor outliers in lag one

% Subset-based flags
FLAG_POINT_EXTREMES         = 8;    % subset outliers, record-by-record
FLAG_DAILY_RANGE            = 9;    % subset daily range outliers, day-by-day
FLAG_DAILY_EXTREMES         = 10;   % subset daily extreme outliers, day-by-day

% Sensor-by-sensor consistency
FLAG_INTERMITTENT_DATA      = 11;   % too many flagged data points around
FLAG_INCONSISTENT_DAY       = 12;   % too small of a fraction of good data,
day-by-day
FLAG_INCONSISTENT_WEEK      = 13;   % too small of a fraction of good data,
week-by-week
FLAG_INCONSISTENT_MONTH     = 14;   % too small of a fraction of good data,
month-by-month
```

Figure 2-14: Screen capture of computer code comments defining data flags.

This subsection provides a detailed example of the data testing and analysis of temperature data quality from Cells 106 and 206. The intent is to provide the reader a description of the types of quality checks and analysis the data were subject to, not to cover each cell and sensor combination used in the analysis in the later sections in this report.

Temperature data from 48 sensors in cell 106 and 16 sensors in 206 were tested. In some cases, such as cell 106 sensor 28, it is clear there was a problem starting in mid-June 2009, as seen in Figure 2-15; flagged data is green, un-flagged is blue.

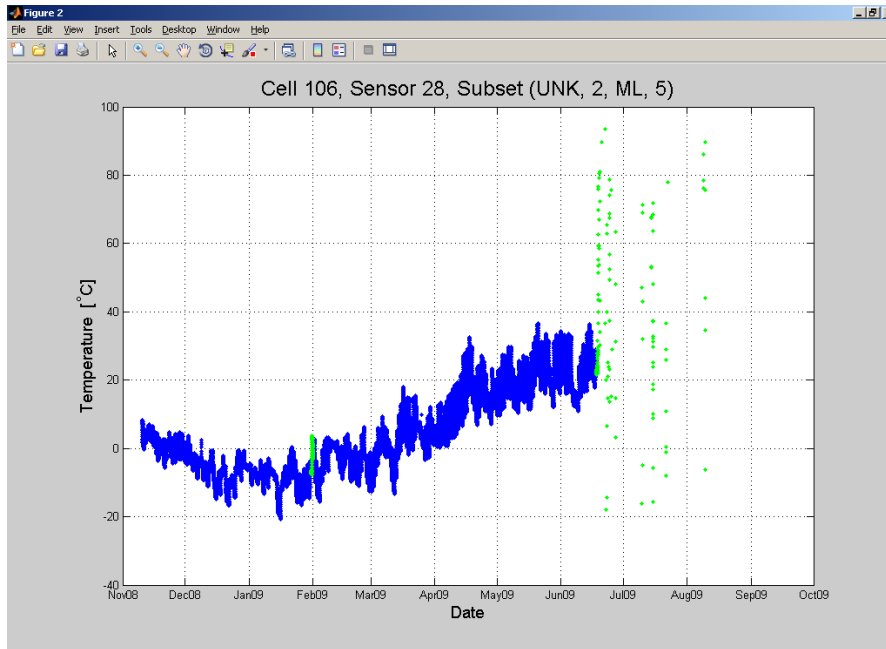


Figure 2-15: Temperature vs. time plot for Cell 106, sensor 28.

Not all temperature versus time plots are as revealing at first glance. Additionally, small sections of data may be flagged, with the sensor then resuming proper function. Note the period at the end of January 2009 that is flagged in Figure 2-15. A visual inspection does not always provide a clear explanation of what statistical quality check the data is violating. To account for this, another output consists of a plot of flags versus time, visible in Figure 2-16. The flag present is plotted along the ordinate, with time plotted on the abscissa.

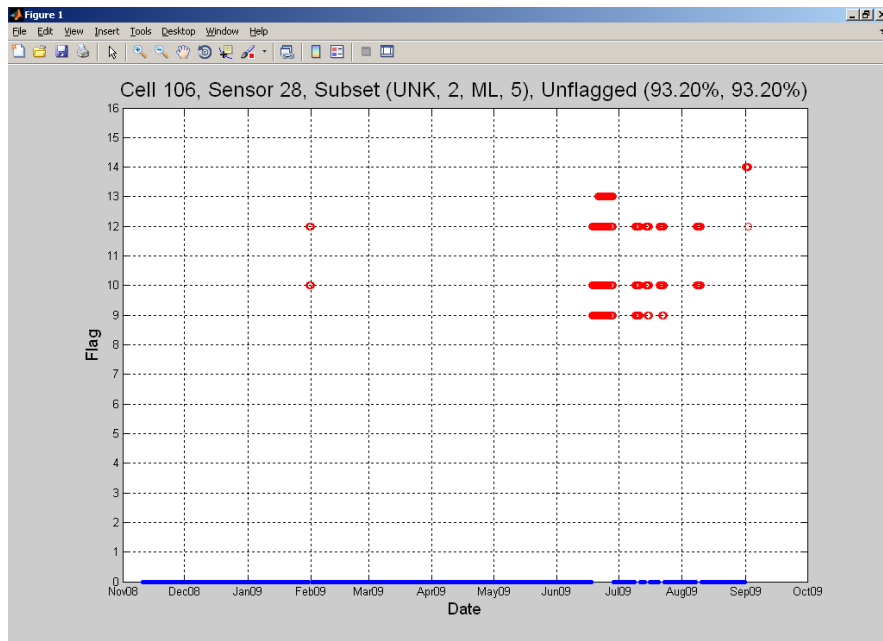


Figure 2-16: Flag vs. time plot for Cell 106, sensor 28.

The flags present in late January 2009, 10 and 12, indicate that the data has daily extreme outliers, and is inconsistent from day to day, respectively. This means the daily maximum and minimum values are too extreme, and there is too small a fraction of good data, day to day. The data flagged in mid-June has the following flags present: 9 (daily range), 10 (daily extremes), 12 (inconsistent day to day), 13 (inconsistent week to week), 14 (inconsistent month to month). Closer examination of the data flagged in January reveals what is likely the problem, which can be seen in Figure 2-17.

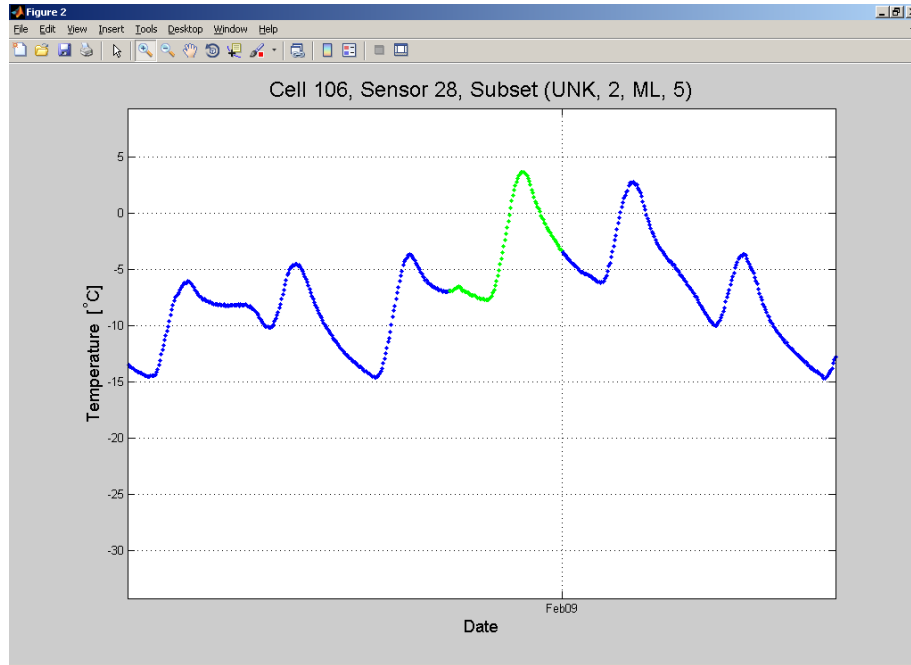


Figure 2-17: Temperature vs. time plot for Cell 106, sensor 28, January 2009.

The minimum value was “expected” to be lower than what was recorded. This is visible where the data is first flagged, which is plotted in green. Expected values are determined by other observations in the same subset. Sensors in the same subset are located at a similar depth and in a similar material. Even though the data appears acceptable upon initial inspection, especially when observing a large amount of data from longer time period, the software indicated there was a problem.

Figure 2-18 is a close-up of temperature data from the same cell/sensor combination in mid-June. The sensor malfunction is clearly visible.

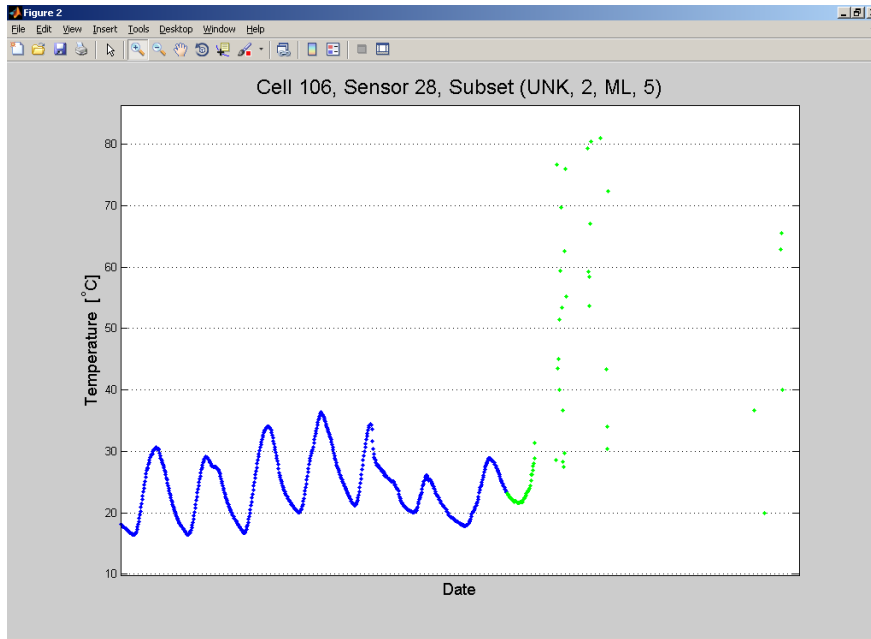


Figure 2-18: Temperature vs. time plot for Cell 106, sensor 28, June 2009.

Table 2-6 indicates the percentage of un-flagged data for each temperature sensor in cell 106 and cell 206. This information is calculated during the data analysis, and is visible on the flag versus time plots.

It should be noted that in some cases the percentage of un-flagged data might be misleading if that the only output considered in determining the quality of the data retrieved from a specific sensor. That is, flagged data is not necessarily evenly distributed throughout time. For cell 28, 93.20% of the data is un-flagged. Given the high percentage of flagged data, the user may think that entire time period should be discarded. However, inspection of the temperature and flag graphs indicate that the data is reliable and of high quality until about the middle of June 2009.

In summary, temperature data was analyzed from MnROAD test sections 106 & 206. The temperature data was screened, and data that was suspected to be erroneous was flagged. A table indicating the percentage of un-flagged data from each sensor in cell 106 & 206 was presented.

Table 2-6: Percentage of un-flagged data in MnROAD Cells 106 & 206.

Cell	Sensor	Unflagged
106	1	98.95%
106	2	99.29%
106	3	99.29%
106	4	99.29%
106	5	99.29%
106	6	99.29%
106	7	99.63%
106	8	98.28%
106	9	98.61%
106	10	98.95%
106	11	98.95%
106	12	99.29%
106	13	99.29%
106	14	99.29%
106	15	99.63%
106	16	99.29%
106	17	98.28%
106	18	91.51%
106	19	88.80%
106	20	98.28%
106	21	94.22%
106	22	85.42%
106	23	93.54%
106	24	96.92%
106	25	98.28%
106	26	98.28%
106	27	98.28%
106	28	93.20%
106	29	99.29%
106	30	99.63%
106	31	99.63%
106	32	99.63%
106	33	99.63%
106	34	99.63%
106	35	99.63%
106	36	99.63%
106	37	99.63%
106	38	99.63%
106	39	98.28%
106	40	98.61%
106	41	98.61%
106	42	98.61%
106	43	98.61%
106	44	99.29%
106	45	99.63%
106	46	88.13%
106	47	98.95%
106	48	98.61%

Cell	Sensor	Unflagged
206	1	98.07%
206	2	98.83%
206	3	98.83%
206	4	98.07%
206	5	98.07%
206	6	98.07%
206	7	98.07%
206	8	98.07%
206	9	99.21%
206	10	99.21%
206	11	99.21%
206	12	99.21%
206	13	98.83%
206	14	98.83%
206	15	99.21%
206	16	99.21%

Consistency Between Similar Sensor Pairs. The following analysis was performed for Cell 106. The difference in temperature was determined for four similar sensor pairings; the temperature of the uppermost sensor located in the PCC layer of the pavement structure minus the temperature of the bottom sensor in the PCC layer. The four sensor pairings that were analyzed in Cell 106 were:

- 104 and 106
- 112 and 114
- 120 and 122
- 128 and 130.

These sensors were selected because they were the sensors located closest to the top and bottom of the PCC layer. The pairings were selected because the sensors are similar in that they are located at the same depth, and in the exact same pavement structure, but at varying locations.

Table 2-7: Depths of sensor pairings located in Cell 106.

Cell	Model	Sensor	Depth (ft)	Depth (in)
106	TC	104	0.208	2.496
106	TC	106	0.5	6
106	TC	112	0.208	2.496
106	TC	114	0.5	6
106	TC	120	0.208	2.496
106	TC	122	0.5	6
106	TC	128	0.208	2.496
106	TC	130	0.5	6

The depth listed in the Table 2-7 is from the top surface of the pavement. Cell 106 is an AC/PCC composite pavement structure, with a 2-in AC layer on top of a 5-in PCC layer. It is noted that the “top” sensors were located approximately ½ - in below the top surface of the PCC layer, and the “bottom” sensors were located 1-in above the bottom surface of the PCC layer.

The difference in temperature between the top and bottom sensors were determined for each sensor pairing, and plotted in the histograms found in Figure 2-19.

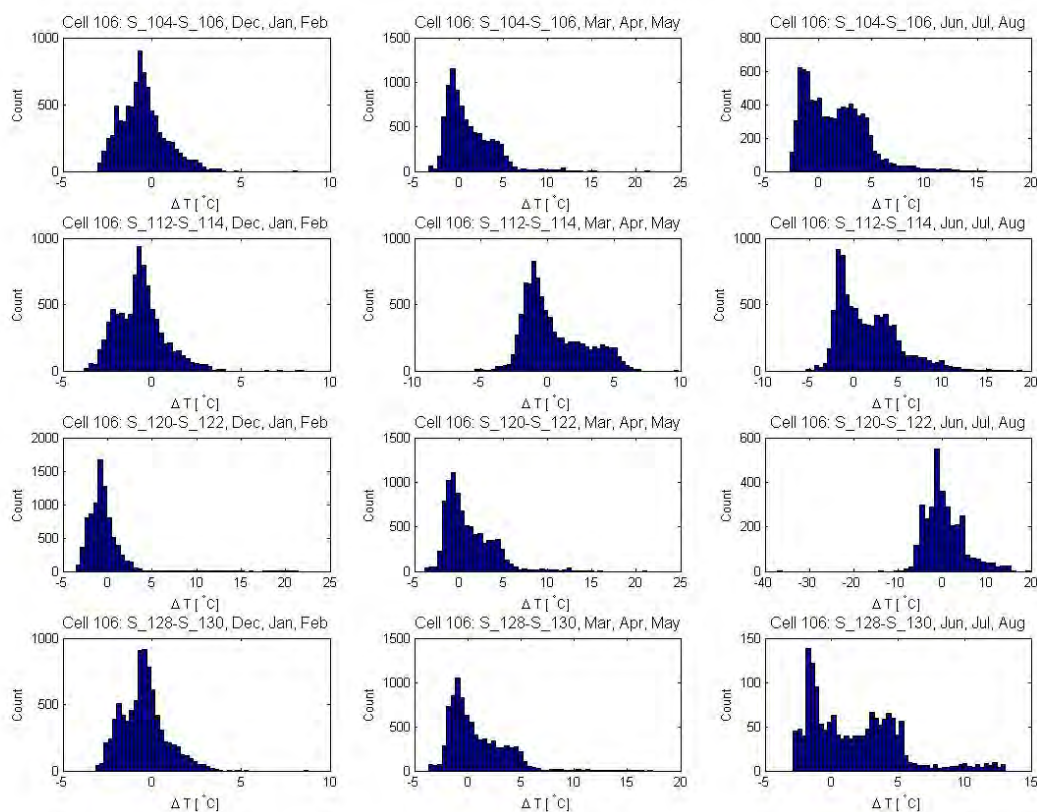


Figure 2-19: ΔT Histograms for cell 106 sensor pairings, organized vertically by season.

The ΔT “bins,” located in Figure 2-19 on the X-axis, indicate the difference in temperature from the top and bottom sensors. The “count” or frequency, located on the Y-axis, represents the number of observations that occurred in each particular bin. The data covered a 9-month time span: December 2008 – August 2009. The histograms are organized in rows according to sensor pairing (e.g. sensors 104-106 are located in the top row), and in columns according to season (e.g. each histogram in the leftmost column represents data from the months of Dec, Jan, and Feb, and so forth).

Given the organization of the histograms, it is expected that the histograms should look somewhat similar within each column, since the columns are representations of temperature differences from the same season, as observed by different sensor pairings.

It is noted that the differences in temperature from the top to the bottom of the PCC layer are more pronounced in the summer months, when the pavement structure is subjected to longer and more intense periods of incoming solar radiation. During periods where the incoming radiation is less intense (Dec, Jan, Feb) the differences in temperature are not as large.

Temperature data screening was completed for each cell and sensor combination used in the analyses in the following sections of this report. Results varied between sensors, but for the vast

majority of the sensors only 1% to 2% of the temperature data was flagged as potentially problematic. No flagged data (i.e. no questionable data) was used in the analysis described in this report. Given the high volume and sometimes suspect nature of temperature data, screening the data allowed the researchers to compare temperature data from the sensors with confidence.

Field Data Analysis. A preliminary analysis of the thermal data meets expectations in many regards. For instance, a natural comparison of an AC-over-PCC pavement with its single-layer counterpart is to investigate the albedo effect. Surface albedo is the effect of color on the degree of absorption of solar radiation and thereby surface temperature. Surfaces with a darker color absorb more incoming solar radiation, and thus have a lower albedo; hence, AC surfaces typically have a lower albedo than that of PCC. Accounting for the albedo effect, one would expect that the surface of the AC-over-PCC pavement would have higher maximum and daytime temperatures than that of a single-layer PCC pavement. This was confirmed with data from MnROAD Cells 106 (AC over PCC) and 213 (JPCP), as illustrated in Figure 2-20.

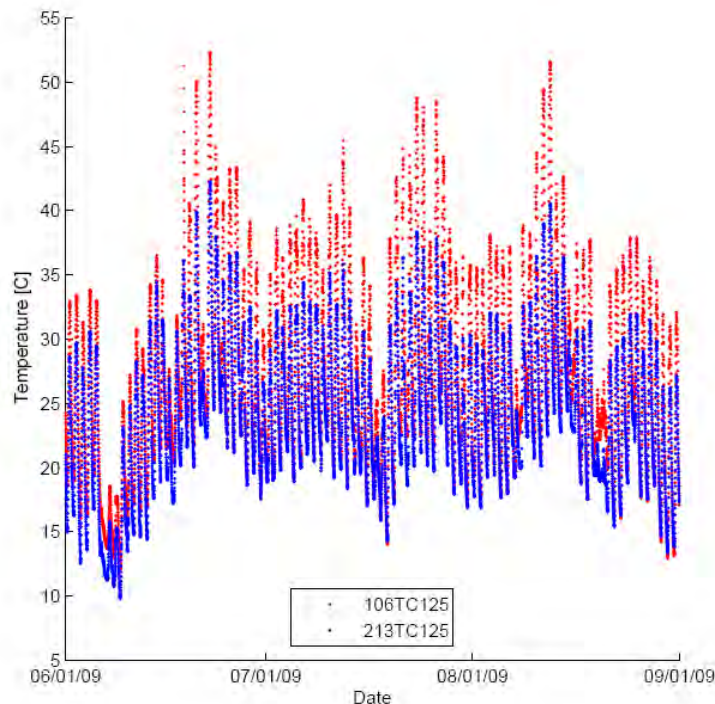


Figure 2-20: Hourly AC surface temperatures from Cell 106 (in red) and hourly JPCP surface temperatures from Cell 213 (in blue), illustrating the albedo effect.

Note in Figure 2-20 that the AC surface temperatures are clearly higher than the PCC surface temperatures. All other factors being equal, these increased surface temperatures due to albedo lead to greater positive temperature gradients in the AC-PCC system, assuming the temperature near the base is the same in both systems. (Here a positive thermal gradient is one in which the temperature at the surface exceeds that near the base.)

Larger thermal gradients in the composite system do not necessarily create a larger thermal gradient through the PCC slab itself. The presence of the AC overlay may create an insulating

effect, wherein the gradient in the PCC slab in the composite system is less severe than its exposed JPCP counterpart. Figure 2-21 is a plot of temperature differences between the top and bottom of the PCC slabs in an exposed JPCP pavement (Cell 113) and an AC-over-PCC pavement (Cell 106). For Cell 113, the PCC only slab, temperature data is recorded at 0.5 inches and 4 inches from the pavement surface; for Cell 106, the data is taken from thermocouples located at 2.5 inches and 6 inches from the surface. In both cases, the gradient through the PCC slab is described for a vertical distance of 3.5 inches.

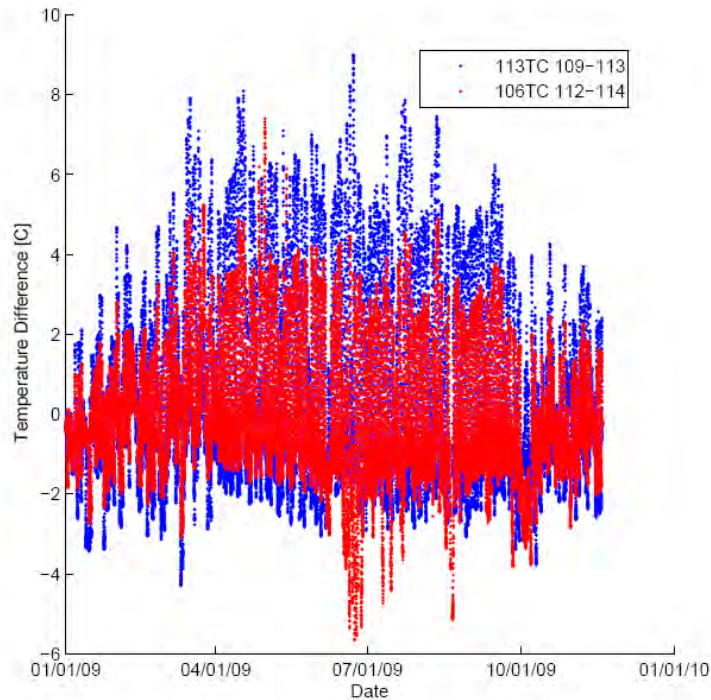


Figure 2-21: Hourly PCC temperature differences throughout AC-over-PCC (Cell 106 in red) and JPCP (Cell 113 in blue) thicknesses illustrating the insulating effect of an AC overlay.

It is clear in Figure 2-21 that the thermal gradient for the PCC slab is less in magnitude in the AC-PCC composite structure than in the exposed JPCP. This effect can be more closely observed in Figure 2-22, which illustrates hourly detail on the thermal gradient in the same PCC slabs (in Cells 113 and 106) over a two-week span (July 24 – August 7, 2009).

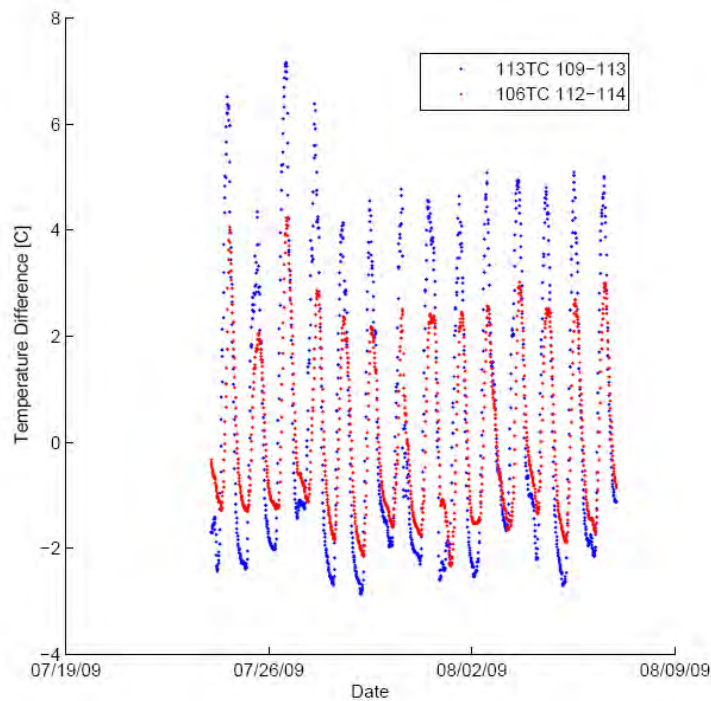


Figure 2-22: Close detail of hourly temperature differences throughout PCC slab thickness for AC-over-PCC (Cell 106 in red) and JPCP (Cell 113 in blue).

As implied through the use of various time periods for the hourly data of Figures 20, 21, and 22, the insulating phenomenon of AC overlays will be observed for all seasons. While the effect is more pronounced in the summer months, when solar radiation and daytime heating are at a maximum, the effect remains observable even in the winter months (which are depicted, in part, in Figure 2-21).

It could be suggested that since the sensors used in Figure 2-21 were located 0.5 inches from the top of the PCC slab – 0.5 inches from the pavement surface for JPCP Cell 113 and 2.5 inches from the pavement surface for AC/PCC Cell 106 – and not at similar absolute depths, the reduction in temperature differences could be attributed to the effect of the sensor location. To disprove this explanation, Figure 2-23 examines thermal gradients for similar overall depths in the composite and JPCP structures. This comparison differs from the comparison visible in Figure 2-21, as both upper locations are at an absolute depth of 2.5 inches below the pavement surface. The bottom locations for this analysis are 5.5 inches for the JPCP Cell 113 and 6 inches for the AC/PCC Cell 106. The vertical distance assumed for each thermal gradient, then, is 3 inches for Cell 113 and 3.5 inches for Cell 106.

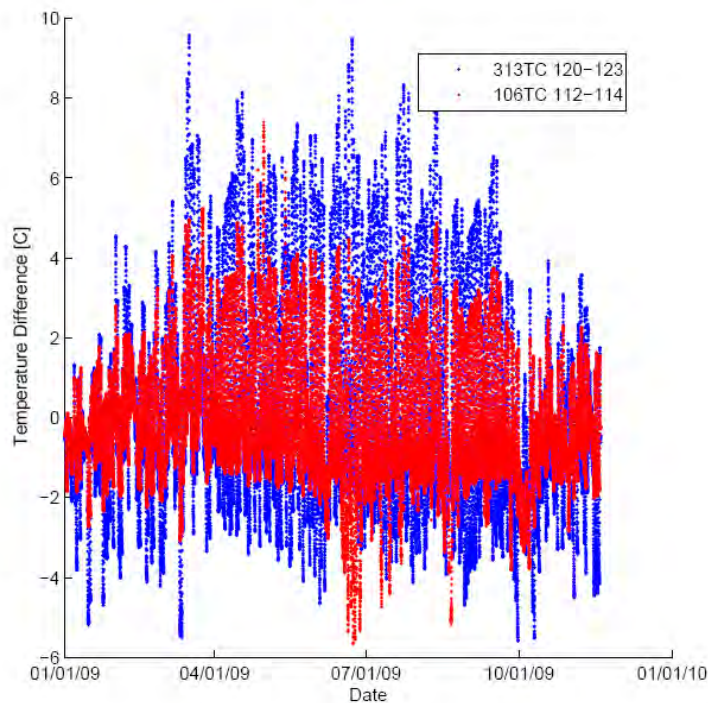


Figure 2-23: Thermal gradients at similar locations in AC-over-PCC (Cell 106 in red) and JPCP (Cell 313 in blue).

Figure 2-23 confirms the insulating effect of the asphalt layer. The plot shows that even over a slightly greater vertical distance of 0.5 inches, whose additional thickness would increase the magnitude of the thermal gradient, the AC/PCC Cell 106 has markedly lower temperature differences. If temperature distributions were not affected by the asphalt layer, this comparison would yield similar results for each system at the indicated depths. Hence, the insulating effect is not an artifact of selective data analysis.

The EICM simulations also predict that an AC overlay reduces temperature gradients in the PCC layer directly beneath it. Figure 2-24 compares cumulative frequency distribution of simulated data for July from MEPDG and cumulative frequency distribution of measured data for July from MnROAD. The figure reveals that both the data analysis of temperature data and climatic modeling support the hypothesis that the AC overlay significantly alters the temperature distributions in an underlying PCC slab. Moreover, Figure 2-24 shows good qualitative agreements between the EICM predictions and measured data. In the next section, a quantitative comparison between measured and predicted temperature differences is conducted.

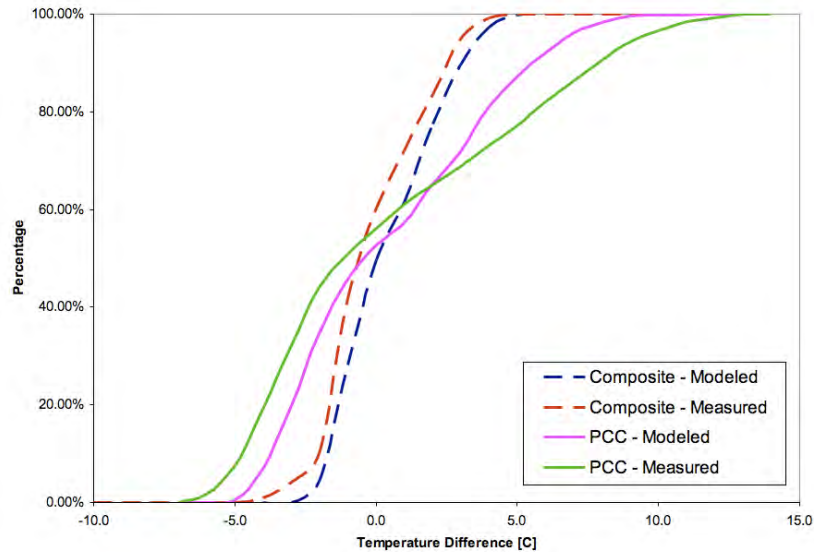


Figure 2-24: Simulated thermal gradients for AC-over-PCC and JPCP structures and their measured analogues from MnROAD (Cells 106 and 113, respectively).

MEPDG and EICM Sensitivity to Thermal Conductivity

To date, there have been few large-scale comparisons of EICM predictions for thermal gradients through pavement slabs with measured data. At the outset of this discussion, it should be noted that the EICM uses historical climatic data and does not use or produce climatic forecasts. The climatic data used to produce the modeled data was recorded from a 9 year 8 month period spanning from 1996 – 2006, ending nearly three full years prior to the temperature measurements recorded at MnROAD in 2009. Thus, it is not expected that the modeled data from any single year or an average of years of modeled data will match with the one year of measured data used in this report.

The aim in this discussion of EICM, then, is to better understand the model and the key parameters that drive its predictions for climate – and consequently, predictions of pavement performance for the MEPDG. One parameter that has received little notice given its relative obscurity in pavement research is thermal conductivity. This parameter is often left untouched by pavement engineers; however, as was illustrated earlier for predictions of transverse cracking, its influence can be far reaching in terms of MEPDG performance predictions. The following discussion attempts to characterize the influence of this parameter on EICM predictions.

Measured temperature differences through a JPCP pavement (MnROAD Cell 113) and modeled temperature differences for a JPCP pavement (from MEPDG and EICM) were plotted in a cumulative frequency distribution, visible in Figure 2-25. For this initial comparison, the MEPDG default thermal conductivity value of 1.25 BTU / hr-ft-°F was used for the PCC in the JPCP. The plot represents the temperature distributions for one month (July) of measured data from MnROAD and the minimum and maximum predicted values of seven simulated instances of the same month from seven years of modeled climate data from EICM/MEPDG.

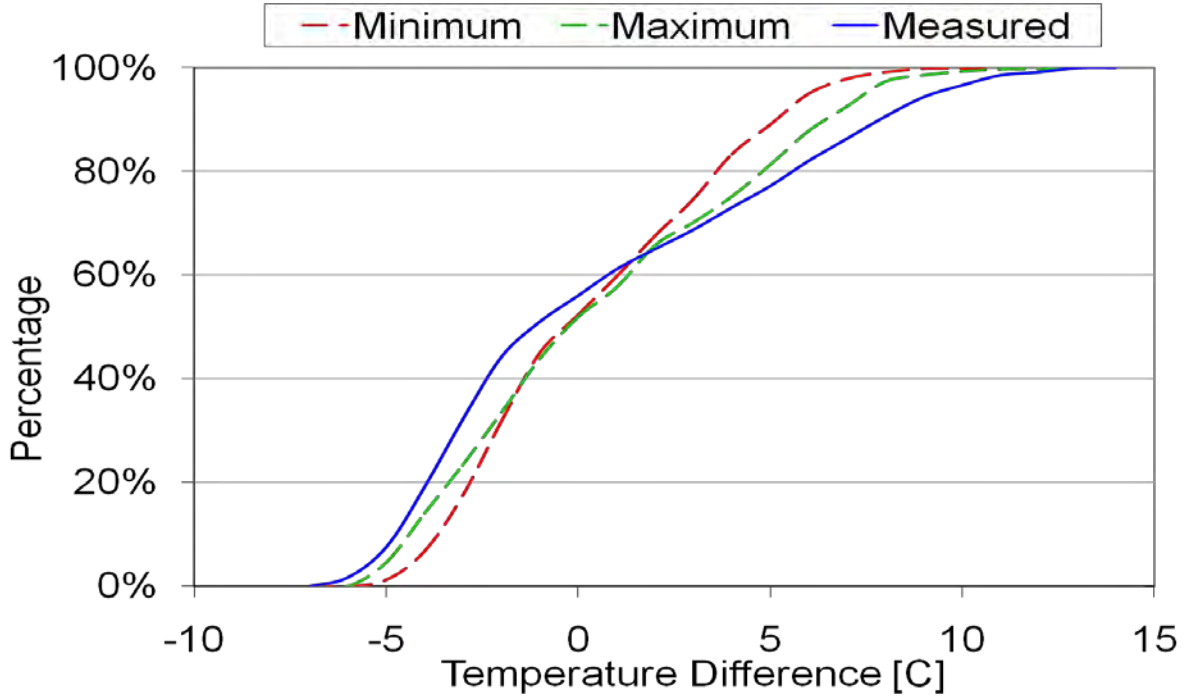


Figure 2-25: Measured versus modeled cumulative frequency distribution for thermal gradient through JPCP pavement in July with $k = 1.25 \text{ BTU / hr-ft-}^\circ\text{F}$.

As can be seen from Figure 2-25, the MEPDG underestimates frequencies of positive and negative temperature gradients that were measured in the PCC cells at MnROAD. For example, the EICM predicts that the temperature differences between the top and the bottom surfaces of the PCC should be less than $+7^\circ\text{C}$ more than 95% percent of time. The MnROAD measurements show that temperature differences less than $+7^\circ\text{C}$ occurred only 86.3% of time, therefore 13.7% of the temperature differences recorded were greater than $+7^\circ\text{C}$. Similarly, the EICM predicts that the temperature difference between the top and the bottom surfaces of the PCC should be less than -3°C 22.4% of time. The MnROAD measurements show that the temperature differences less (more negative) than -3°C occurred 32.3% of time.

One explanation for this difference is that the reduced temperature differences in the modeled data are, in part, a result of the MEPDG forcing an unnecessarily high value for thermal conductivity on EICM – that is, the thermal conductivity does not match that Cell 113 at MnROAD (the actual value of which is unknown, as it would be for most as-designed or in-field pavements).

The thermal conductivity input was adjusted a lower value of $k = 0.94 \text{ BTU / hr-ft}^\circ\text{F}$. Figure 2-26 illustrates a similar comparison as Figure 2-25, but with this new value for the thermal conductivity.

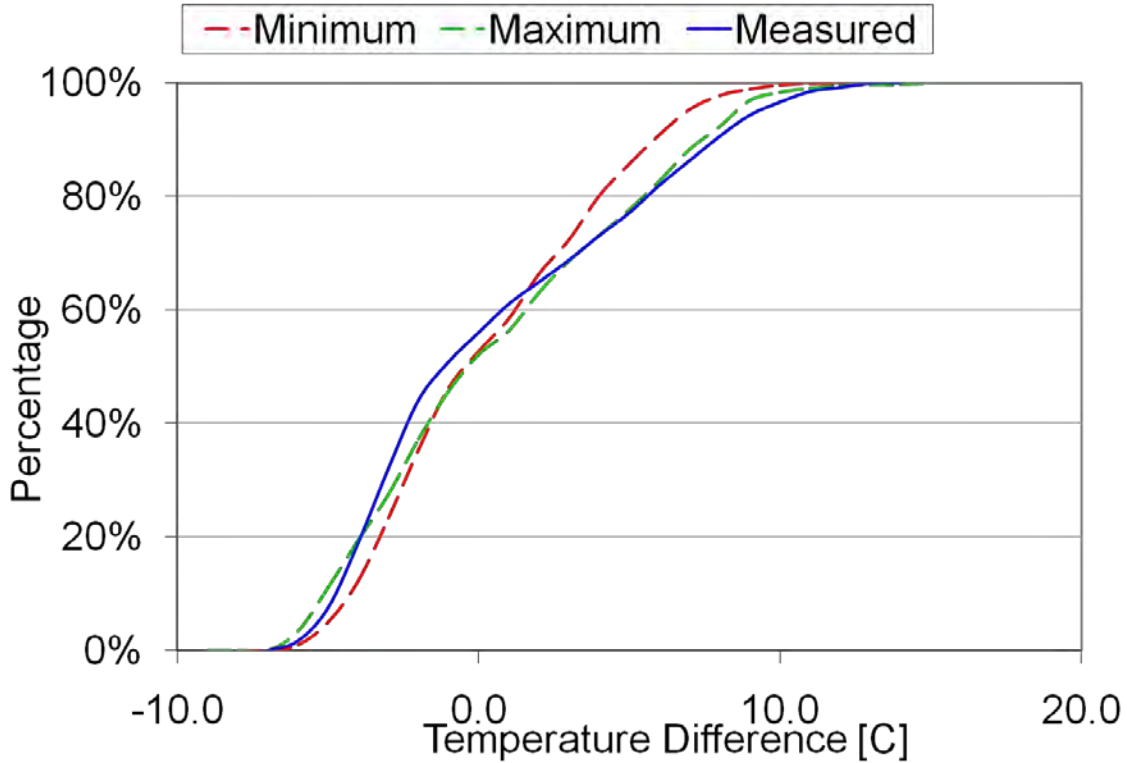


Figure 2-26: Measured versus modeled cumulative frequency distribution for thermal gradient through JPCP pavement in July with $k = 0.94$ BTU / hr-ft-°F.

Here it is evident that the lower value of $k = 0.94$ BTU / hr-ft-°F for the thermal conductivity input brings the simulated minimum and maximum thermal gradients closer to the measured cumulative frequency distribution from MnROAD. To confirm that the adjusted thermal conductivity value improved on the model using the MEPDG default value, other months were examined. Figures 27 and 28 provide a comparison of modeled and measured data from the month of March for the MEPDG default value for thermal conductivity and the comparing the default thermal conductivity value and the adjusted value of $k = 0.94$ BTU / hr-ft-°F.

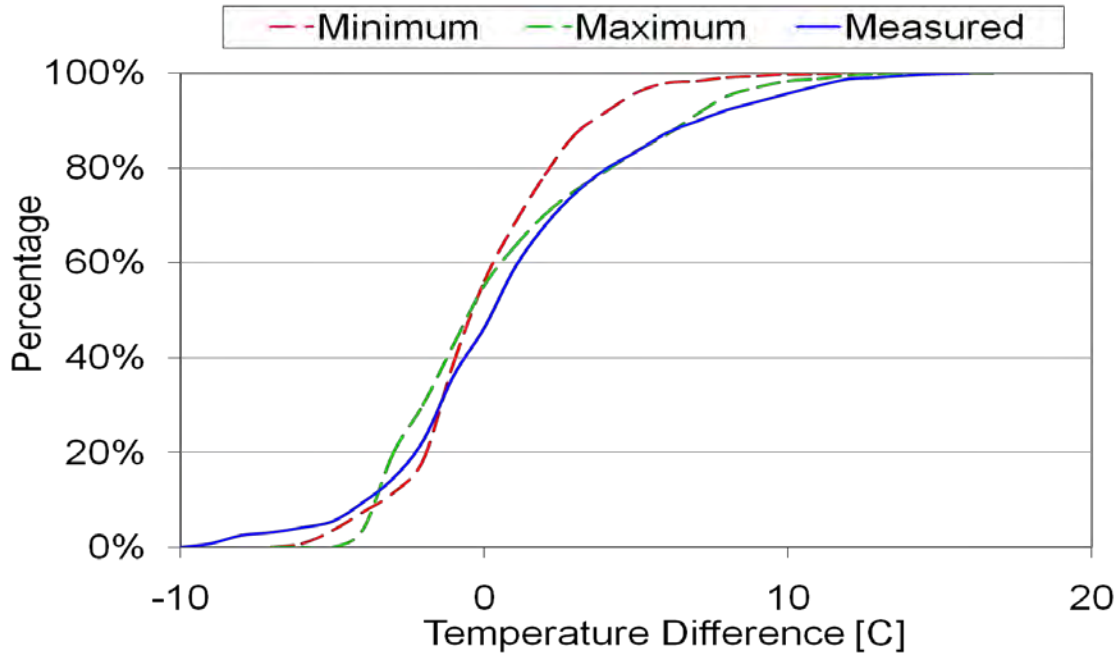


Figure 2-27: Measured versus modeled cumulative frequency distribution for thermal gradient through JPCP pavement in March with $k = 1.25 \text{ BTU / hr-ft-}^\circ\text{F}$, which is the MEPDG default value.

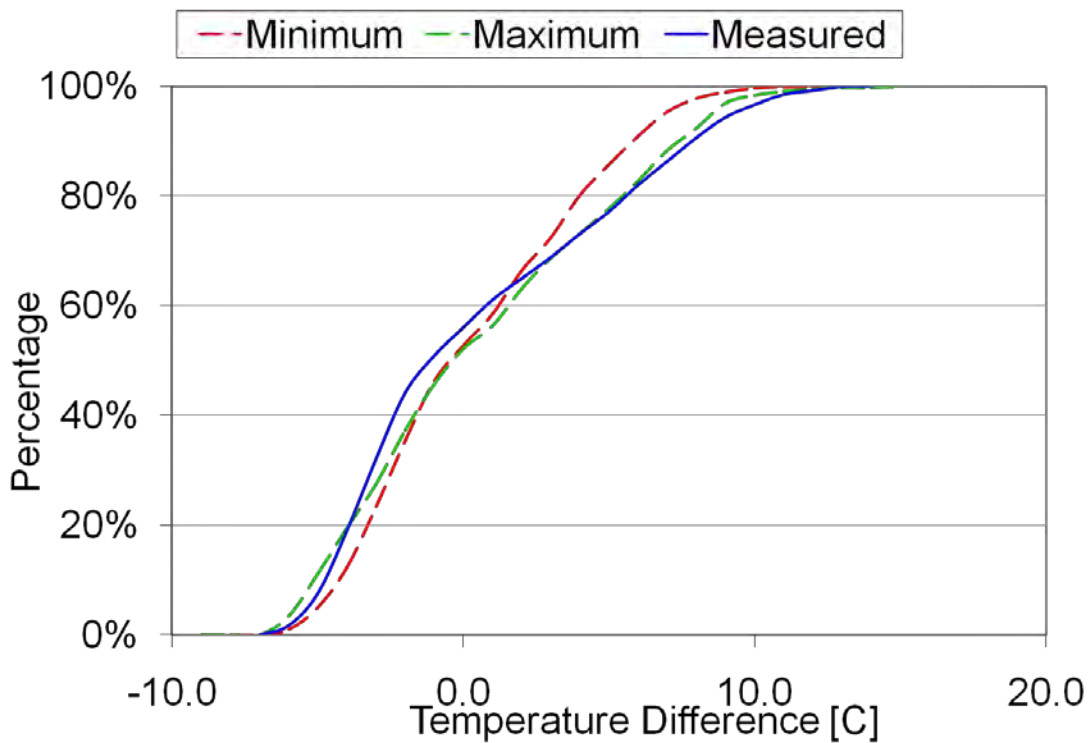


Figure 2-28: Measured versus modeled cumulative frequency distribution for thermal gradient through JPCP pavement in March with $k = 0.94 \text{ BTU / hr-ft-}^\circ\text{F}$, the adjusted thermal conductivity value.

The analysis for March and July are indicative of similar analyses performed for other months, all of which suggested that a reduction of the MEPDG default thermal conductivity input value resulted in better agreement between the measured data and the modeled thermal gradients.

Further analysis found, however, that the relationship between measured data and modeled data began to deteriorate for values of thermal conductivity that were less than $k = 0.94 \text{ BTU / hr-ft-}^\circ\text{F}$. Figure 2-29 is representative of modeled data using a thermal conductivity input less than $0.94 \text{ BTU / hr-ft-}^\circ\text{F}$ – for this figure, $k = 0.85 \text{ BTU / hr-ft-}^\circ\text{F}$ for the simulated data, which is illustrated against the measured MnROAD data from July once again.

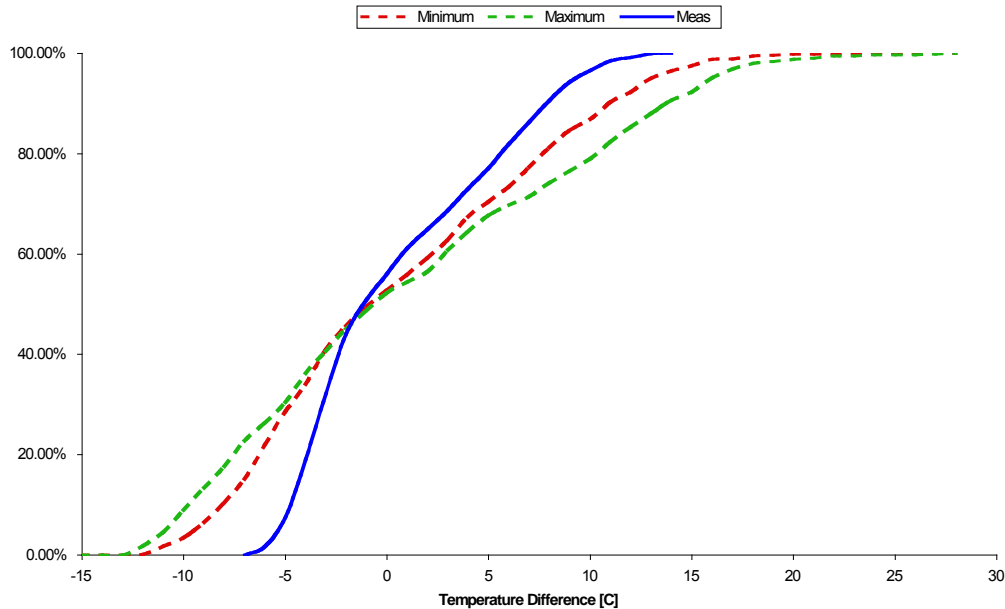


Figure 2-29: Measured versus modeled cumulative frequency distribution for thermal gradient through JPCP pavement in July with $k = 0.85 \text{ BTU / hr-ft-}^\circ\text{F}$.

As evident in Figure 2-29, the thermal conductivity input value of $0.85 \text{ BTU / hr-ft-}^\circ\text{F}$ results in modeled data that is in poor agreement with the measured data collected at MnROAD. This is especially evident by noting the range of values along the abscissa.

Hence, by adjusting the thermal conductivity input to a value lower than the MEPDG default of $1.25 \text{ BTU / hr-ft-}^\circ\text{F}$, the predictions of temperature gradients were found to agree better with measured data from MnROAD for PCC slab in JPCP pavements. Furthermore, a range of values were tested for the thermal conductivity, and the analysis found that a value of $0.94 \text{ BTU / hr-ft-}^\circ\text{F}$ produced the best fit of modeled data to the measured MnROAD data. Although agreement between the measured and modeled data varied from month to month, the value of $0.94 \text{ BTU / hr-ft-}^\circ\text{F}$ produced the best results for each month. While this value does not produce an exact fit and is not intended to, given the nature of EICM modeling and inherent variability in any data set, the modifications to the thermal conductivity input represent an improvement over the default value.

It is important to note that only one PCC pavement structure was considered in this analysis. A similar analysis for other MnROAD concrete sections will be conducted in the future.

2.1.3 Design Characteristics

Characterization of Thermal Properties in EICM

Several EICM material properties may affect EICM temperature predictions and subsequently MEPDG performance predictions. This section examines the sensitivity of the EICM and the MEPDG pavement performance predictions to the following EICM thermal property inputs: thermal conductivity and heat capacity.

Thermal Conductivity. The thermal conductivity is a material characteristic indicating the ability of a material to transfer heat. Heat energy is transferred to or from the pavement surface by convection, radiation, or conduction. Materials with a lower rate of thermal conductivity resist the transfer of heat energy. The conduction of heat energy from the surface and from below is what directly influences the temperature in the PCC layer. The MEPDG recommends the following default values of thermal conductivity:

- AC: 0.67 BTU / hr-ft-°F
- PCC: 1.25 BTU / hr-ft-°F

The sensitivity of the thermal conductivity input on predicted transverse cracking was tested for a 2-inch AC over 7-inch PCC composite pavement. Annual Average Daily Truck Traffic was set to 7420, to reach a target of 20% transverse cracking over a 20-year design life using all default values. The location selected was the Minneapolis – St. Paul International Airport; all other MEPDG default values were used. The AC layer thermal conductivity was held constant at the MEPDG default for the model runs where the PCC thermal conductivity was adjusted, and *vice versa*. Results from the MEPDG model runs are listed in Tables 8 and 9.

Table 2-8: Effect of PCC thermal conductivity on transverse cracking in PCC layer.

Thermal Conductivity - PCC	% Cracking
1.38	15.8
(default) 1.25	20.0
1.13	25.6
1.00	32.0
0.94	35.6
0.85	41.0

Table 2-9: Effect of AC thermal conductivity on transverse cracking in PCC layer.

Thermal Conductivity - AC	% Cracking
0.80	30.1
(default) 0.67	20.0
0.54	20.3

It can be observed from Tables 2-8 and 2-9 that the thermal conductivity values can substantially influence the amount of predicted transverse cracking. The differences in the amount of predicted transverse cracking are a result of variations in temperature distributions in the PCC layer. The EICM predicts that the thermal conductivity of the AC and PCC layers are capable of significantly altering the temperature distributions in the PCC layer; consequently, these temperature distributions have a noteworthy effect on predicted pavement performance.

Heat Capacity. Heat capacity is the amount of heat energy required to change the temperature of a material a specified amount. Less energy is required to raise the temperature of a material with a lower heat capacity. The MEPDG recommends the following default values of heat capacity:

- PCC: 0.35 BTU / lb-°F
- AC: 0.23 BTU / lb-°F

Using the same inputs and design employed in the thermal conductivity analysis, the sensitivity of the heat capacity input on predicted transverse cracking was examined. The results are listed in Tables 10 and 11.

Table 2-10: Effect of PCC heat capacity on transverse cracking in PCC layer.

Heat Capacity - PCC	% Cracking
0.35	12.2
(default) 0.28	20.0
0.21	32.1

Table 2-11: Effect of AC heat capacity on transverse cracking in PCC layer.

Heat Capacity - AC	% Cracking
0.29	15.2
(default) 0.23	20.0
0.17	25.8

As can be observed in tables 10 and 11, an increase in heat capacity results in a reduction of predicted transverse cracking predicted by the MEPDG. This was true for both the AC and PCC layer in the structure. This is attributed to the material being able to contain more heat energy without changing temperature, which resulted in a lower thermal gradient in the pavement structure as compared to a material with a lower heat capacity. A change in heat capacity in the PCC layer had a larger effect on predicted transverse cracking when compared to a similar change in the AC layer.

Coefficient of Thermal Expansion. A third PCC thermal property input is provided by the MEPDG, namely, the *coefficient of thermal expansion*, which is the change in volume of a substance per unit temperature. Although it is an important parameter to consider when predicting rigid pavement performance, the coefficient of thermal expansion does not affect the temperature distribution throughout the pavement structure. Rather, the temperature distribution influences how much of an effect the coefficient of thermal expansion has. Large temperature variations in the PCC layer will result in greater expansion and contraction, which may result in thermal stresses and cracking. The sensitivity to the coefficient of thermal expansion of the PCC layer was examined for both a PCC and AC/PCC structure, and the results are listed in Tables 12

and 13. The MEPDG recommends the following default values for the coefficient of thermal expansion:

- PCC: 5.5 per °F * 10⁻⁶

Table 2-12: Effect of the coefficient of thermal expansion in the PCC layer on predicted pavement performance of an AC/PCC pavement.

Coefficient of Thermal Expansion (PCC)	% Cracking
4.125	13.3
5.5	20.0
6.875	30.7

Table 2-13: Effect of the coefficient of thermal expansion in the PCC layer on predicted pavement performance of a PCC pavement.

Coefficient of Thermal Expansion (PCC)	% Cracking
4.125	3.3
5.5	20.0
6.875	78.7

As expected, a decrease in the coefficient of thermal expansion of the PCC layer resulted in lower predicted transverse cracking values from the MEPDG. It is important to note that the composite AC/PCC structure was far less sensitive than the PCC-only rigid pavement to differences in the coefficient of thermal expansion of the PCC layer. This appears to be due to the insulating effect of the AC layer. When the PCC layer is exposed it is subjected to greater temperature fluctuations; greater fluctuations and extreme temperatures exposed to a PCC layer with a high coefficient of thermal expansion results in higher cracking.

Characterization of Design Features

AC and PCC Layer Thickness. In this sub-section, a sensitivity analysis of layer thicknesses of an AC/PCC pavement is conducted. The effect of PCC layer thickness on a composite structure was evaluated at two different AC thicknesses. The following inputs were common to all cases examined for the sensitivity analyses in this section:

- Design life: 20 years
- Climate input file: Minneapolis – St. Paul, MN Int’l Airport (MSP)
- Joint spacing: 15ft
- Dowels: 1-in diameter, 12-in spacing
- Granular Base: A-1-a, 6-in
- Subgrade: A-6
- Water table depth: 5ft
- All other inputs were MEPDG default values

The Annual Average Daily Truck Traffic (AADTT) was set for a target of 20% cracked slabs in the PCC layer for two composite structures: a 2-in AC over 7-in PCC, and a 3-in AC over 6-in PCC structure. In each case, the AC thickness was held constant, and the PCC was adjusted +/- 2-in at 1-in increments. The results are listed in Tables 14 & 15 and Figures 30 & 31.

Table 2-14: Effect of PCC thickness for an AC/PCC composite pavement with a 2-in AC layer.

AC Thickness	PCC Thickness	Traffic	% Cracking
2	5	7420	99.8
2	6	7420	89.3
2	7	7420	20
2	8	7420	0.2
2	9	7420	0

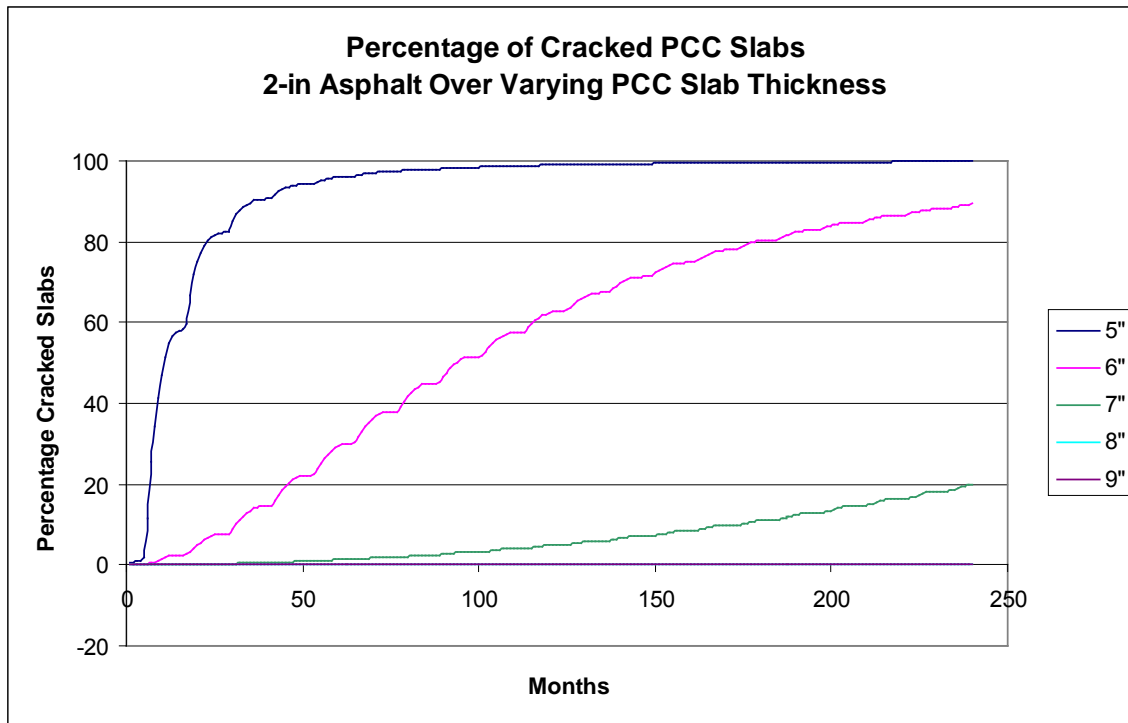


Figure 2-30: Effect of PCC thickness for an AC/PCC composite pavement with 2-in AC layer.

Table 2-15: Effect of PCC thickness for an AC/PCC composite pavement with a 3-in AC layer.

AC Thickness	PCC Thickness	Traffic	% Cracking
3	4	4325	99.9
3	5	4325	96.9
3	6	4325	20
3	7	4325	0.3
3	8	4325	0

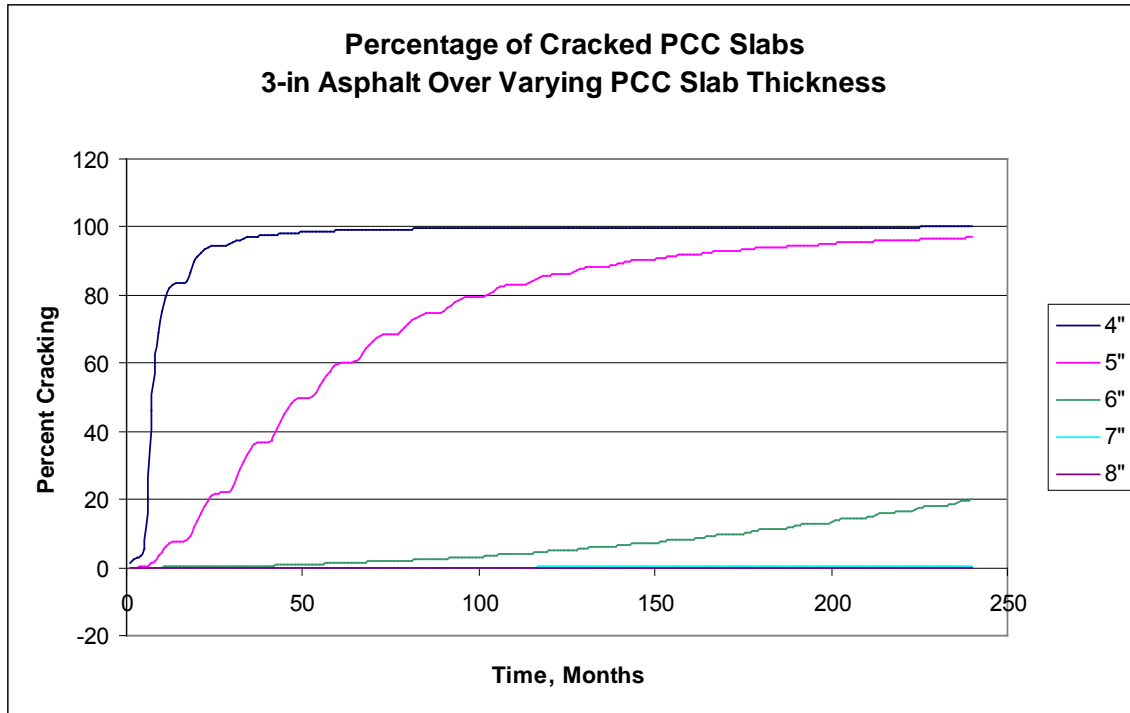


Figure 2-31: Effect of PCC thickness for an AC/PCC composite pavement with 3-in AC layer.

The results indicate that the predicted pavement performance of an AC/PCC composite structure is very sensitive to the thickness of the PCC layer. It is also noted that a 9-in AC/PCC composite pavement with a 7-in PCC layer will support much more traffic, over 3000 AADTT, than a 9-in AC/PCC composite structure with a 6-in PCC layer.

Slab Width and Joint Spacing. The effect of slab width and joint spacing were examined, with the results listed in Tables 16 and 17.

Table 2-16: Effect of joint spacing on predicted pavement performance.

Slab Length	% Cracking	
	AC/PCC Pavement	PCC Pavement
12'	0	0.8
15'	20	20
17'	68.1	75.3
19'	91.1	98.4

The predicted percentage of cracked slabs increased as the joint spacing, or slab length, increased. As joint spacing increased, the predictions for the composite structure were slightly less than the rigid structure. Both structures had a dramatic increase in cracking as joint spacing increased. As joint spacing increased two feet from 15 feet to 17 feet, predicted cracking increased from 20% to 68.1% (AC/PCC) and from 20% to 75.3% (PCC).

Table 2-17: Effect of slab width on predicted pavement performance.

Slab Width	% Cracking	
	AC/PCC Pavement	PCC Pavement
12'	20	20
12.5'	2.3	3
13'	0.1	0.3
13.5	0.1	0.3
14'	0.1	0.3

The effect of slab width was essentially the same for the composite and rigid structures, with the composite structure predicted to exhibit slightly less cracking than the rigid structure. As width of the slab increased, the predicted percentage of cracked slabs decreased. This was expected, as a wheel load located farther from the edge (which is the case for a widened slab) produces less tensile stress than the same load located at the slab edge.

Properties of Base and Subgrade. The MEPDG permits accounting for seasonal variation in properties of unbound materials by adjustment of the resilient moduli for each design period (month) (Khazanovich et al 2006). The user has two options:

- Provide the resilient modulus for each design period or
- Provide resilient modulus for the optimum moisture content.

If the second option is selected, the Enhanced Integrated Climatic Model incorporated into the MEPDG software predicts seasonal variation in the moisture content of the unbound layers (Larson and Dempsey 1997). Then, the MEPDG software adjusts the moduli for the other moisture conditions using the following model (Witczak et al 2000a, Witczak et al 2000b):

$$M_R = 10^{a + \frac{b-a}{1 + \text{EXP}(\beta + k_S \cdot (S - S_0))}} M_{Ropt}$$

where

- M_R = resilient modulus at any degree of saturation;
- S = degree of saturation while testing the material;
- M_{Ropt} = resilient modulus at optimum water content and maximum dry density;
- S_0 = degree of saturation at optimum water content;
- a = minimum of $\log\left(\frac{M_R}{M_{Ropt}}\right)$;
- b = maximum of $\log\left(\frac{M_R}{M_{Ropt}}\right)$;
- β = location parameter, obtained as a function of a and b ;
- k_S = regression parameter.

For fine-grained materials, the Guide recommends the following model parameters:

$$a = -0.5934, b=0.4, \beta = -0.3944, k_S = 6.1324.$$

Figure 2-32 presents the correction factor for the moisture condition for the various degrees of saturation. One can observe that increase in moisture content decreases resilient modulus.

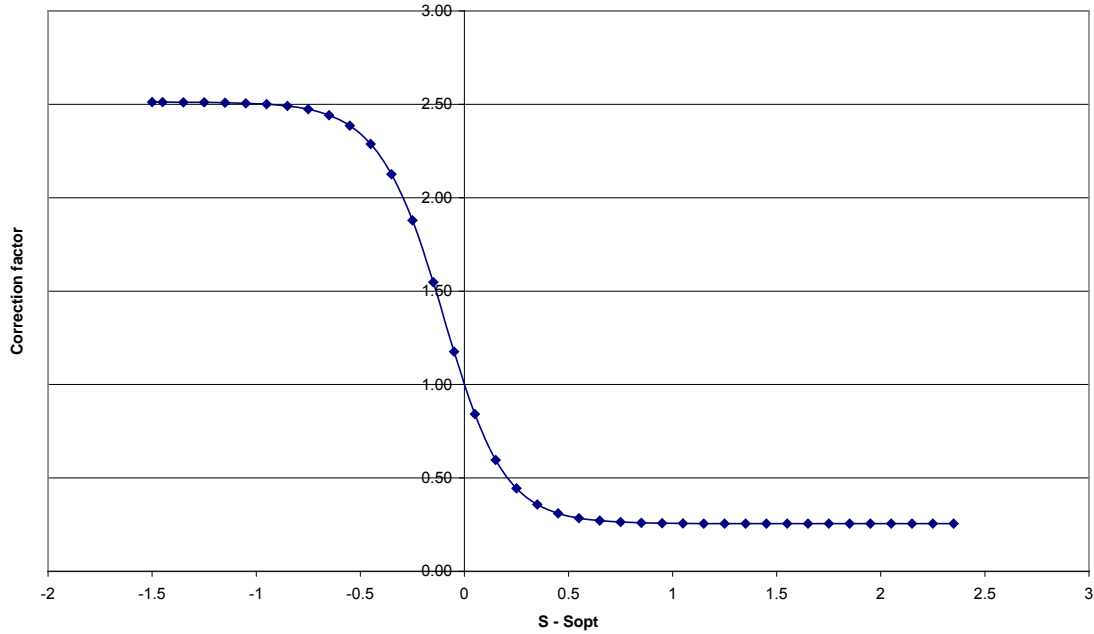


Figure 2-32: Correction factor as a function of the degree of saturation (24).

The effect of the base properties on several modeled parameters was examined. Two base layers were considered with default resilient modulus values: A-1-a and A-3. Additionally, an A-3 base was modified by adjusting the resilient modulus value from 16,000 psi to 40,000 psi, which is the default value used by the EICM for an A-1-a base layer. Table 2-18 shows the default gradation values used by the MEPDG for the A-1-a and A-3 base materials.

Table 2-18: MEPDG default gradation values for A-1-a and A-3 base layers.

Sieve	Percent Passing	
	A-1-a	A-3
#200	8.7	5.2
#80	12.9	33
#40	20	76.8
#10	33.8	94.3
#4	44.7	95.3
3/8"	57.2	96.6
1/2"	63.1	97.1
3/4"	72.7	98
1"	78.8	98.6
1 1/2"	85.8	99.2
2"	91.6	99.7
3 1/2"	97.6	99.9

Figures 33 present the modeled resilient modulus for the three base layers under consideration over the time period of one year, from January to December. Figure 2-34 shows the corresponding coefficients of subgrade reaction for these systems.

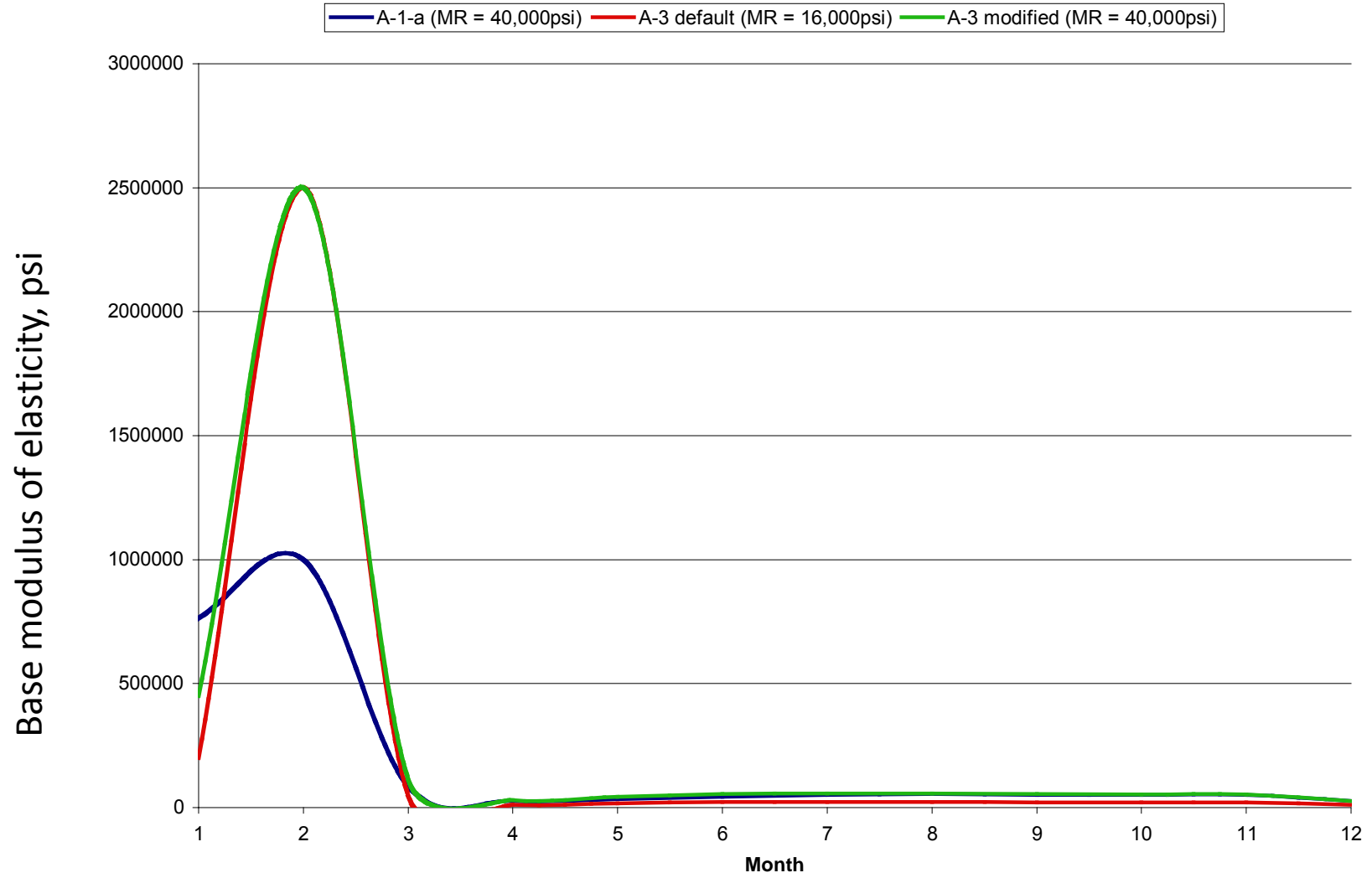


Figure 2-33: Resilient modulus for three base layers: A-1-a, A-3, and A-3 (modified).

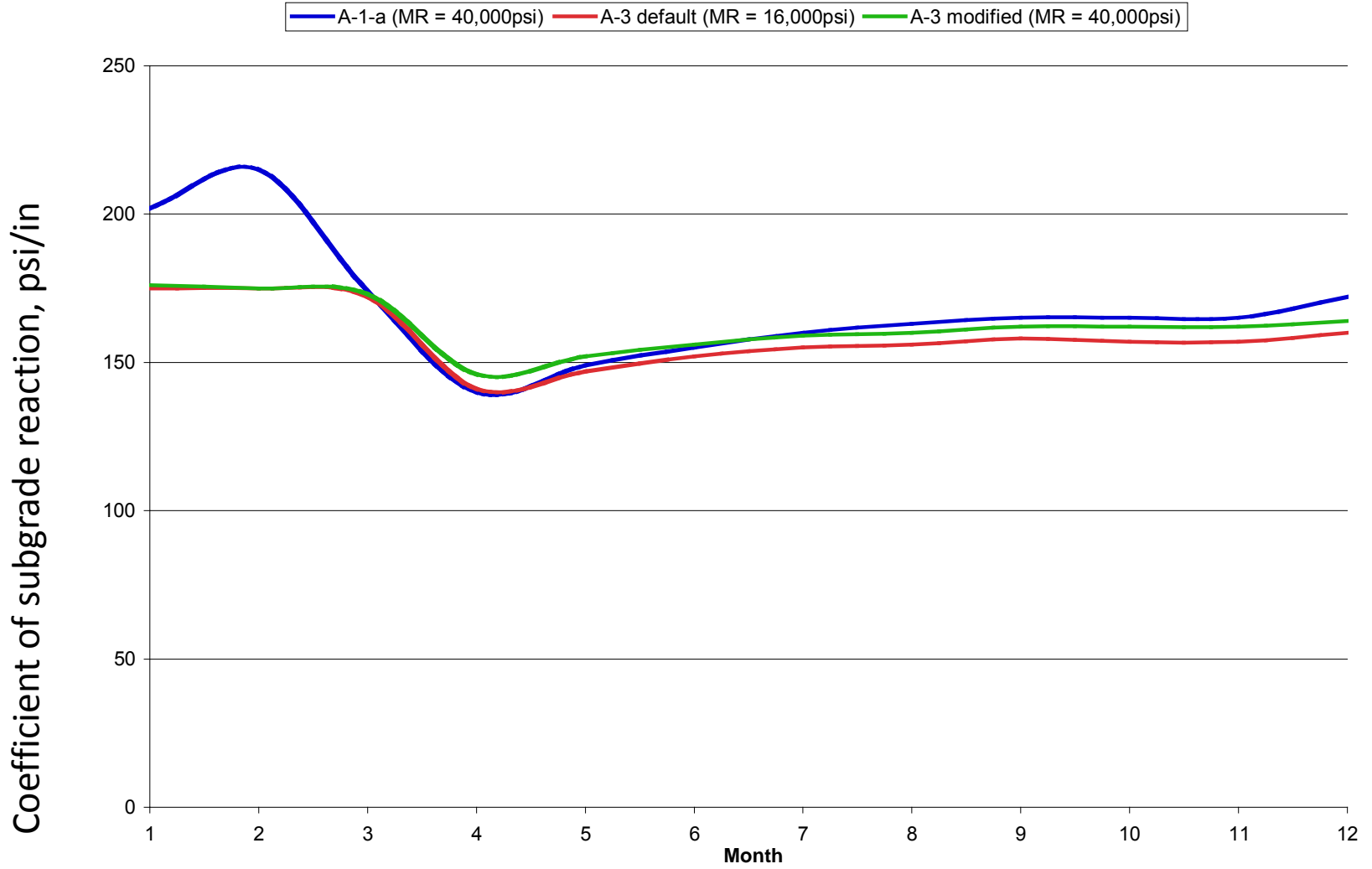


Figure 2-34: Coefficient of subgrade reaction for three base layers: A-1-a, A-3, and A-3 (modified).

Figures 33 and 34 demonstrate that the gradation of the base layer has an equal or greater effect on the modeled resilient modulus in comparison to the input value for resilient modulus at optimum moisture content.

As a result, Figure 2-35 demonstrates that gradation affects predicted cracking in the PCC layer more than the resilient modulus at optimum moisture content.

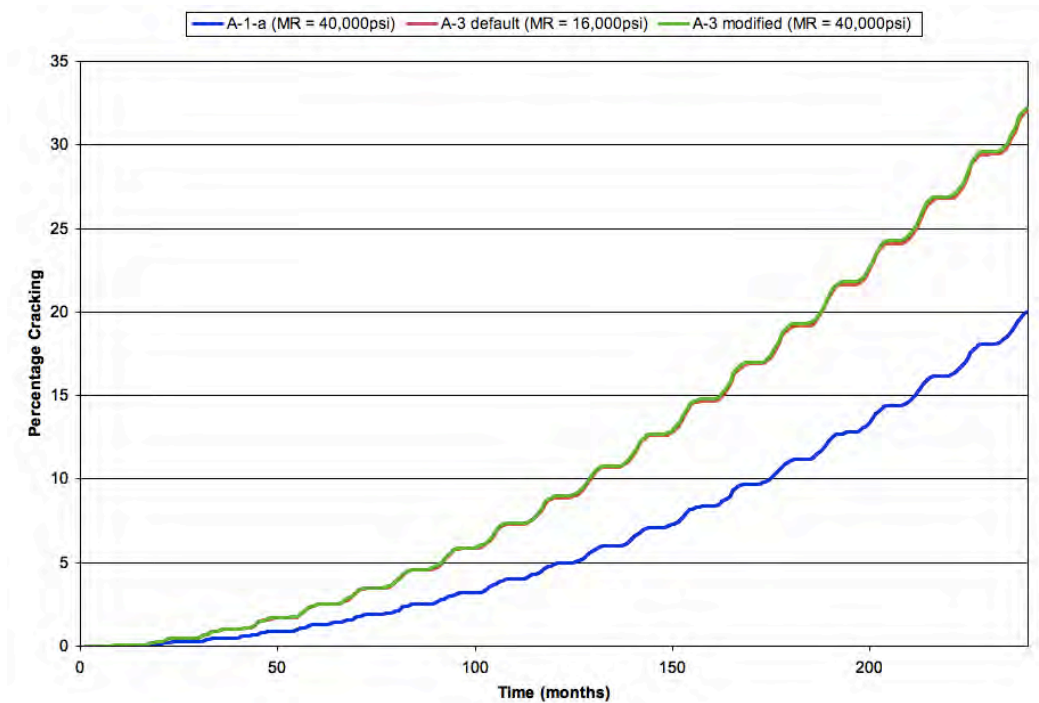


Figure 2-35: Effect of base layer material for an AC/PCC composite pavement.

2.1.4 Conclusions on EICM Data Quality

While many aspects of the MEPDG modeling and design inputs have been the subject of a great deal of research, very little of the MEPDG dealing with climate and its impact on pavement performance prediction has been a subject of an in-depth analysis in the past. The dual focus of this report was an analysis of the effect of climate on MEPDG predictions, and the thermal characteristics of a composite pavement system and the modeling of these characteristics relative to measured environmental conditions.

First, a comprehensive sensitivity study of the effect of climate on the MEPDG performance prediction was conducted. Pavement performance was simulated at more than 600 locations across the US using the climatic database data supplied by the MEPDG.

It was found that the environment has a significant impact on predicted pavement performance. A pavement may perform exceptionally good or bad, depending upon where it is located and the conditions it subjected to. A limited analysis was performed comparing trends by region. These trends were found to be reasonable. Nevertheless, differences in predicted pavement performance among stations with similar environmental conditions were greater than expected.

This illustrates the importance of high-quality climatic data to obtain reliable pavement performance predictions. Therefore, there is a need for both a vigorous data check and data cleaning in the climatic database.

The quality of the climate data in the database is non-uniform, and the MEPDG allows stations with low-quality data to be used. Although the MEPDG does not permit stations with missing data to be used alone, these stations can be used when creating a virtual weather station through interpolation. The report demonstrated that the use of incomplete weather stations may only decrease the quality of predictions. Thus, it is recommended that all stations with incomplete data be removed from the database.

While the database verification may take substantial time and resources, a simple, practical approach for the evaluation of data quality is suggested. A pavement structure is tested using climate data from one station; the same structure is tested using a virtual weather station, which incorporates data from nearby stations. If these tests yield significantly different results, one of the following may be the case: a nearby station has low-quality data, or, the station used in the stand-alone test has low-quality data. This test will hold true for locations where there are no significant changes in climate or elevation. This test may not be reliable in mountainous regions.

If data quality is improved and uniform for each testing station, MEPDG performance 9 and would likely improve, and produce more reliable results. Data improvement will be a result of: cleaning data, and making the data from each station uniform and of high quality; and having more data, to eliminate year-to-year variations.

The other primary focus of this study examined measured and modeled temperature distributions in the PCC layer of JPCP and AC-over-PCC pavement structures. Hourly temperature data recorded from AC/PCC composite and JPCP cells located at MnROAD were collected and filtered to remove suspect measurements. This data was then used to investigate the effects of climate on these two pavement systems and validate expectations as an initial check of data quality. Measured data indicated diurnal AC surface temperatures were markedly higher than those of a PCC surface due to albedo. Despite the overall greater temperature difference through the full depth of the AC/PCC structure, temperature records showed the thermal gradient in a PCC layer was significantly less if an AC overlay was present. This effect is thought to contribute to the longevity and improved performance of the underlying PCC structure. EICM simulations were also found to reproduce the insulating effect of an AC overlay observed in the MnROAD data for composite test cells.

Furthermore, the research summarized in this report examined the sensitivity of the EICM and MEPDG to thermal conductivity input values for the AC and PCC layers. It was found that these parameters significantly influenced predicted pavement performance for MEPDG simulations, and this discovery led to further investigation of the influence of thermal conductivity on EICM predictions for thermal gradients through a simulated pavement system. A quantitative comparison of modeled and measured temperature data was conducted. The EICM simulations produced temperature distributions smaller than the measured distributions when the MEPDG default thermal conductivity value of PCC, $k = 1.25 \text{ BTU / hr-ft-}^\circ\text{F}$, value was used. Several PCC thermal conductivity values were tested; the highest agreement between the measured and

modeled data for a 6-in thick MnROAD test section occurred with a PCC thermal conductivity of 0.94 BTU / hr-ft-°F.

Finally, the authors note that adjustments to the MEPDG thermal property inputs in routine design should only be done with care. Solo improvement in prediction of the temperature distribution in the pavement structure does not necessarily lead to improvement in pavement performance predictions if the performance prediction models had been calibrated for the MEPDG default material thermal properties. Therefore, it is important to make evaluation of the MEPDG material thermal properties a part of a MEPDG local calibration process.

2.2. Characterization of Unbound Materials in the MEPDG and DARWin-ME

Unbound materials are commonly used in the construction of flexible, rigid, and composite pavements. Examples of unbound materials include granular base and unmodified subgrade soil. The goals of this study were to explore the characterization of unbound materials, and to evaluate the consistency in predicting pavement performance between different input parameters and different input levels in the Mechanistic-Empirical Pavement Design Guide, specifically in the MEPDG v1.1 (*MEPDG 2009*) and DARWin-ME v1.1 software (*DARWin-ME 2011*). These programs are realizations of the same mechanistic-empirical design procedure and, theoretically, should provide the same results, excluding certain conditions for which DARWin-ME was modified in order to address known issues.

Within both programs, there are three levels of input based on the level of detail with which a given parameter can be characterized. Level 3 uses default parameters for most inputs, and is the least detailed. Level 2 requires testing of the materials to be used in construction, but correlations are allowed. Level 1 is the most detailed, and requires direct testing (*NCHRP 2004*). However, if the same material is characterized using different input levels, the results should not be significantly different.

Unbound materials are characterized in the MEPDG through seasonally adjusted resilient moduli. Typically, a user provides the information required to obtain a resilient modulus at the optimum moisture content and the information required to adjust the modulus for seasonal effects (i.e. moisture content variation, freezing and thawing, etc.). The MEPDG subdivides the unbound layers into sublayers to account for variation of material conditions with depth to make these calculations.

When Level 3 inputs are used, the MEPDG provides a default value of resilient modulus at the optimum moisture content for the material type selected and options for specifying different material types in both the base layer and the subgrade. For Level 2 inputs in the MEPDG, the user provides either the resilient modulus at the optimum moisture content or the results of other soils tests, such as the California bearing ratio (CBR), or dynamic cone penetrometer (DCP). The MEPDG then automatically converts the results of these tests to the resilient modulus (*NCHRP 2004*). However, this conversion procedure may result in an erroneous correction for the moisture content.

For unbound materials, additional information, such as the sieve analysis, unit weight, plasticity index, etc. (*Zapata and Houston 2008*) must also be provided to enable seasonal adjustment

based on climatic analysis. These inputs are collectively referred to as “gradation” in practice, though it is important to remember that this includes much more than the particle size distribution of the soil. Calculations are made within the enhanced integrated climatic model (EICM) (Larson and Dempsey 2003).

Various sensitivity studies evaluated the effect of resilient modulus at the optimum moisture content on the predicted pavement distresses (ex. Hall and Beam 2005). However, other types of characterization of unbound materials have not been sufficiently examined in the past. This paper aims to fill this gap. In addition, the paper identifies issues in the software related to unbound material characterization in the MEPDG v1.1 and DARWin-ME.

2.2.1 Level 3 Stiffness Characterization for Design Procedures

In the MEPDG, the user provides information about an unbound material by selecting the soil type, its classification as either a base material or a subgrade, and its stiffness. At Level 2 inputs, the stiffness is provided as either the resilient modulus at the optimum moisture content, or the result of a test such as the California Bearing Ratio (CBR), which is then automatically correlated to a value of resilient modulus. Table 2-19 shows the default values of resilient modulus at the optimum moisture content for various subgrade materials according to the AASHTO classification, as provided by both the MEPDG v1.1 (MEPDG 2009) and DARWin-ME v1.1 (DARWin-ME 2011). This table also shows values of in-situ CBR for the same soil types, taken as an average of a range of values from Appendix CC-1 of the MEPDG (NCHRP 2004) and the corresponding value of resilient modulus that both the MEPDG and DARWin-ME calculate based on the provided CBR using the following equation:

$$MR = 2555 * CBR^{0.64} \quad [2-1]$$

By comparing the values of resilient modulus computed using CBR to those provided as default values for the soil type, a significant discrepancy can be seen. A possible explanation of these discrepancies is that the ranges of CBR values Appendix CC-1 are given for typical in-situ conditions, whereas the MEPDG inputs should be provided for the optimum moisture content.

Analysis of Table 2-19 also shows that the value of resilient modulus computed from CBR for some of the subgrades is higher than the default resilient modulus at the optimum moisture content, while the value of resilient modulus computed from CBR for other subgrades is lower than the default resilient modulus at the optimum moisture content. For typical pavements analyzed in the MEPDG, the climatic modeling predicts that, most of the time, the top four feet of some subgrades (ex. A-6) are below optimum moisture content, so it's seasonally adjusted resilient moduli are lower than the resilient modulus at the optimum moisture content. At the same time, the MEPDG predicts that the top four feet of other subgrades (ex. A-3) are above optimum moisture content, so the adjusted resilient moduli are above the resilient modulus at the optimum moisture content.

This supports the notion that the CBR values from Appendix CC-1 are for typical in-situ conditions, and that use of these values along with equation 1 does not result in the resilient modulus at the optimum moisture content. Since the software (either MEPDG v 1.1 or

DARWin-ME) automatically applies the seasonal correction factors to calculated resilient moduli, such a correction would lead to erroneous results if the subgrade is characterized using CBR for in-situ conditions.

If the chosen Level 2 input parameter is the result of an in-situ test, and a conventional relationship between this parameter and the resilient modulus is to be used to provide an MEPDG input, the this parameter should be adjusted to the optimum moisture content condition. Alternatively, the relationship between certain Level 2 parameters and the resilient modulus should be modified to predict the resilient modulus for the optimum moisture content. A previous study by Sadasivam and Mallela (*Sadasivam and Mallela 2012*) noted the same need for correction due to the difference in optimum and in-situ moisture conditions in the design of flexible rehabilitation and proposed a solution for obtaining pseudo-optimum values. However, they did not extend their study to apply to the case of new pavements or to pavement types other than flexible. In this study, equations were derived to calculate the pseudo-optimum or adjusted value of CBR and DCP which should be input into the MEPDG to avoid erroneously correcting for the moisture content of the in-situ soil. A derivation is presented below to obtain a pseudo-optimum CBR value, called CBR*. This procedure is then extended to obtain equations for pseudo-optimum DCP (DCP*)

The MEPDG recommended CBR values (CBR_{typ}) were found by averaging the maximum and minimum CBR values for each soil type, taken from Table 2-3 of Appendix CC-1 of the MEPDG (*NCHRP 2004*). From Table 28 of the Mechanistic-Empirical Pavement Design Interim Manual of Practice (*FHWA 2007*), default values for the resilient modulus (MR) at the optimum moisture content for each soil type were obtained. These values were used to calculate the CBR_{rec} using the MEPDG relation:

$$CBR = \left(\frac{MR}{2555} \right)^{1/0.64} \quad [2-2]$$

The relationship between CBR_{typ} and CBR_{rec} given by a power function obtained using regression analysis defines the adjusted, or pseudo-optimum, CBR value, CBR*. This CBR* value can be used as input into the MEPDG:

$$CBR^* = 10.225 * (CBR)^{0.1751} \quad [2-3]$$

Using [2-3], the pseudo-optimum CBR was calculated for each soil type from CBR_{typ} . The resilient modulus was then found using [2-1], call this value MR*. By substituting equation [2-3] into equation [2-1], an equation for resilient modulus at the optimum moisture content in terms of the CBR for a typical in-situ condition can be obtained, which accounts for the need to adjust the CBR can be obtained:

$$MR = 1131.2 * CBR^{1.121} \quad [2-4]$$

Table 2-19 shows the resilient modulus computed with both CBR and CBR*. Both DARWin-ME and the MEPDG obtained the same values of computed resilient modulus using CBR*, and these values match the actual resilient modulus much more closely than the resilient modulus computed by these programs using the regular CBR value.

Table 2-19: Resilient modulus (MR) for various subgrades computed using CBR and CBR* in the MEPDG and DARWin-ME.

Subgrade	MR ^a (psi)	CBR ^b	MR computed with CBR (psi)	CBR*	MR* (psi)
A-1-a	18000	70	38748	21.6	18200
A-1-b	18000	47.5	30233	20.2	17500
A-2-4	16500	30	22529	18.6	16600
A-2-5	16000	22.5	18741	17.7	16100
A-2-6	16000	17.5	15956	16.9	15600
A-2-7	16000	15	14457	16.5	15400
A-3	16000	25	20048	18.0	16300
A-4	15000	15	14457	16.5	15400
A-6	14000	10	11153	15.3	14700
A-7-6	13000	3	5161	12.4	12800

a from (MEPDG 2009)

b from (Hall and Beam 2005)

The MEPDG handles DCP inputs differently than those for CBR. Rather than being converted directly into a resilient modulus, DCP is first converted into a CBR value. Then, the calculated CBR is used to find a calculated resilient modulus. In this case, the correlation between DCP and CBR does not need adjustment, but the CBR to resilient modulus calculation must be corrected as described above. By combining the DCP to CBR relation of:

$$CBR = \frac{292}{DCP^{1.12}} \quad [2-7]$$

with the adjusted CBR to resilient modulus relation given in [2-4], an equation for resilient modulus in terms of DCP which accounts for the need to adjust the DCP can be obtained:

$$MR = 2137.5 \left(\frac{1}{(0.8464 + 1.749 * DCP)^{1.12}} \right)^{0.1121} \quad [2-8]$$

The equation for the pseudo DCP, DCP*, which can be used as input into the MEPDG, is then:

$$DCP^* = 0.1749 * DCP + .8464 \quad [2-9]$$

The MEPDG and DARWin-ME should be modified to use equations [2-4] and [2-8] when converting in-situ CBR and DCP, respectively, to resilient modulus at the optimum moisture content. In the meantime, designers can use the uncorrected software programs by manually computing CBR* or DCP* from soil test results with equations [2-3] and [2-9] respectively, and entering that value into the field for CBR or DCP, respectively.

To determine the effect of implementing these changes on pavement performance in both the MEPDG and DARWin-ME, standard test cases for a 4-inch flexible pavement with 8” of A-1-a base and 1200 average annual daily truck traffic (AADTT) were run using Level 2 and Level 3 inputs with the same soil types. For each case, one run was conducted with a typical resilient modulus Level 3 input, and two runs were conducted at Level 2 inputs: one using a typical value of CBR and another using CBR*, see Table 2-19.

Results of the program runs, using MR, CBR and CBR* as inputs, are shown in Table 2-20. Trends in the results were similar for both DARWin-ME and the MEPDG. When CBR was used as an input and moisture corrections were not accounted for (i.e. when the standard value of CBR was used), pavements with an A-3 subgrade were predicted to experience fewer distresses than if the pavement were designed using either the standard resilient modulus value or the adjusted CBR, CBR*. Conversely, pavements with an A-6 subgrade were predicted to experience more distresses when designed using the uncorrected CBR compared with those designed using either resilient modulus or CBR*. For both subgrade types, pavements designed using CBR* were found to have negligible differences from those designed using resilient modulus.

Table 2-20: Alligator cracking and total rutting after 20 years as predicted by the MEPDG and DARWin-ME for 4” flexible pavement with an A-1-a base and various subgrades and material parameter inputs.

Climate	Subgrade type	Input Level	Input type	MEPDG		DARWin-ME	
				Alligator Cracking (%)	Rutting (in)	Alligator Cracking (%)	Rutting (in)
MN	A-3	Level 2	CBR	7.4	0.67	4	0.58
		Level 3	MR	8.1	0.72	4.4	0.63
		Level 2	CBR*	8.1	0.72	4.4	0.62
IL	A-3	Level 2	CBR	8.7	0.75	4.8	0.65
		Level 3	MR	9.6	0.8	5.3	0.69
		Level 2	CBR*	9.5	0.8	5.3	0.69
MN	A-6	Level 2	CBR	14.4	0.87	8.5	0.76
		Level 3	MR	13.1	0.79	7.7	0.69
		Level 2	CBR*	12.9	0.78	7.5	0.68
IL	A-6	Level 2	CBR	16.2	0.94	9.9	0.8
		Level 3	MR	14.9	0.86	8.9	0.74
		Level 2	CBR*	14.6	0.85	8.8	0.73

2.2.2 Effects of EICM Inputs for Unbound Layers

Several different material properties factor into the performance of an unbound material layer within a pavement system. The seasonally adjusted resilient modulus, Poisson's ratio, unit weight, and coefficient of lateral pressure are used to compute the critical response of the pavement. Gradation is often used to predict moisture content, which is in turn used by the EICM to calculate the seasonally adjusted resilient modulus, based on the user supplied resilient modulus at optimum moisture content (*NCHRP 2004*). Therefore, it is expected that both the gradation and the resilient modulus of the unbound material would affect pavement performance. However, a cursory investigation of the effect of base properties on pavement performance found that this is not always the case in the MEPDG (*Johanneck 2011*). Another study found that the EICM is particularly sensitive to gradation as an input (*Zapata and Houston 2008*). These findings motivated a wider study of how the input parameters of gradation and resilient modulus affect the material properties of the base and subgrade layers, as well as the performance of the overall pavement system within the MEPDG and DARWin-ME.

To compare the effects of resilient modulus and gradation, test cases were run in both the MEPDG and DARWin-ME on three typical pavement structures. By varying the gradation and resilient modulus of the unbound layers, it was possible to determine the effects of these factors on the pavement performance. For the test cases, the standard rigid pavement was a 7" JPCP with 1" diameter dowels; the standard flexible pavement was 4" of PG58-28 asphalt; and the standard composite pavement used was a 7" JPCP with 1" diameter dowels overlaid with 2" of PG58-28 asphalt. For all three pavement types, an 8" granular base and a semi-infinite subgrade was specified. The unbound materials for the base were A-1-a and A-3, while the subgrade materials were A-3 and A-6. To determine the role of gradation versus resilient modulus (MR), one case used a material with properties as of an A-3 base material except the resilient modulus at the optimum moisture content which was assigned to be equal to that of the A-1-a material; this material was denoted A-3M. Similarly, one case used an A-6 subgrade modified to have the same resilient modulus as the A-3 material; this material was denoted A-6M. The variations in base and subgrade are shown in Table 2-21.

Table 2-21: Inputs for base and subgrade variation.

Inputs						
		Base material	MR (psi)	Subgrade material	MR (psi)	
Base variation		A-1-a	40000	A-6	14000	
		A-3	29000			
		A-3M	40000			
Subgrade variation		A-1-a	40000	A-3	16000	
				A-6	14000	
				A-6M	16000	
Material Properties						
Use	Material	MR (psi)	Plasticity Index	% Passing #200	% Passing #4	Diameter D ₆₀ (mm)

Base	A-1-a	40000	1	8.7	44.7	10.82
	A-3	29000	0	5.2	95.3	0.3255
	A-3M	40000	0	5.2	95.3	0.3255
Subgrade	A-3	16000	0	5.2	95.3	0.3255
	A-6	14000	16	63.2	93.5	0.05364
	A-6M	16000	16	63.2	93.5	0.05364

Traffic levels were 3200 AADTT for the rigid and composite pavements, and 1200 AADTT for the flexible pavement. Default values were used for all other inputs. All test cases were run in Champaign Illinois using the standard EICM climate data file, and in Minneapolis Minnesota, using a modified EICM climate file which removed erroneous data. The need to adjust for incorrect climate data in order to ensure the accuracy of the MEPDG has been shown previously (*Johanneck and Khazanovich 2010*).

Figure 2-36 shows the DARWin-ME predicted cracking of the rigid pavement case over time for different subgrades. From this figure, it can be seen that gradation of the subgrade plays a more dominant role than resilient modulus in determining the amount of cracking for rigid pavements. For all cases shown in this figure, the amount of cracking predicted for an A-6 subgrade and an A-6M subgrade (A-6 material with the resilient modulus of an A-3 material) were very similar. The A-3 material had less predicted cracking, particularly for the cases in Minnesota. The same trends were observed for composite pavements. When the base type was held constant and the subgrades varied, it was found that cracking was either dependent on resilient modulus or on a combination of resilient modulus and gradation, depending on the location and the program used.

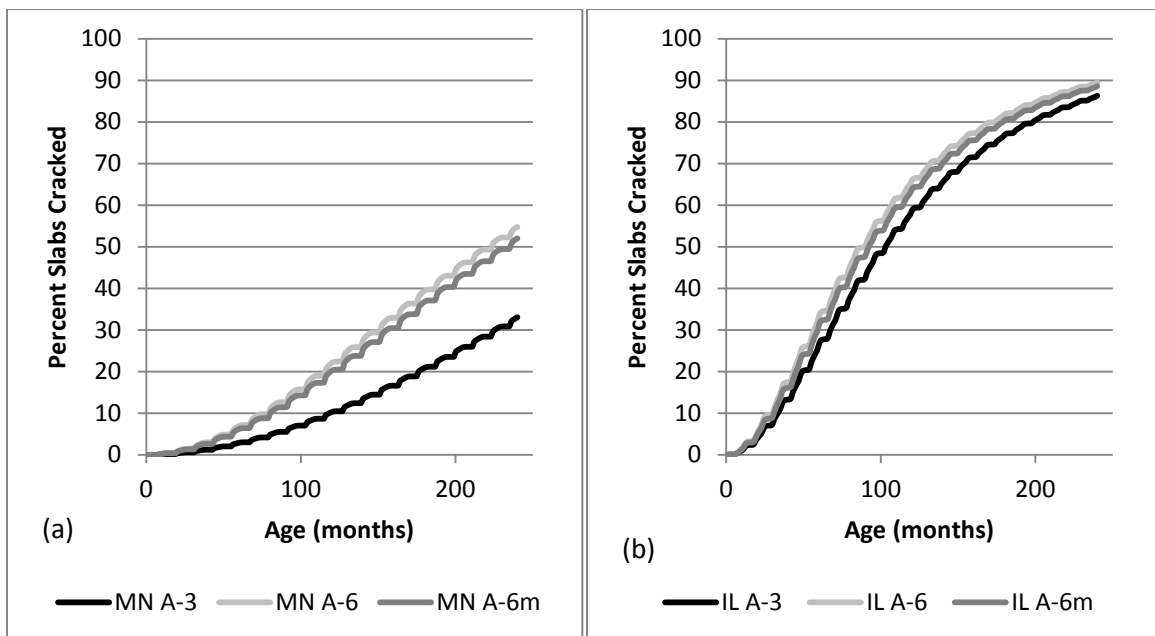


Figure 2-36: Predicted cracking for a rigid pavement with different subgrades and an A-1-a (a) in Minneapolis analyzed with DARWin-ME, (b) in Champaign analyzed with DARWin-ME.

The dependence of cracking on gradation shown in Figure 2-36 can be partially explained by examining how the modulus of subgrade reaction (also called k-value) varies with changes in gradation and resilient modulus. This variation is illustrated in Figure 2-37, which shows the predicted modulus of subgrade reaction over time in Minneapolis. Similar results were found in Champaign, and for composite pavements in both locations. From this figure, it can be seen that the k-value predicted for the cases with an A-3 and A-3M (A-3 gradation and A-1-a resilient modulus) bases match each other fairly well, while the case with the A-1-a base has different values, particularly in winter.

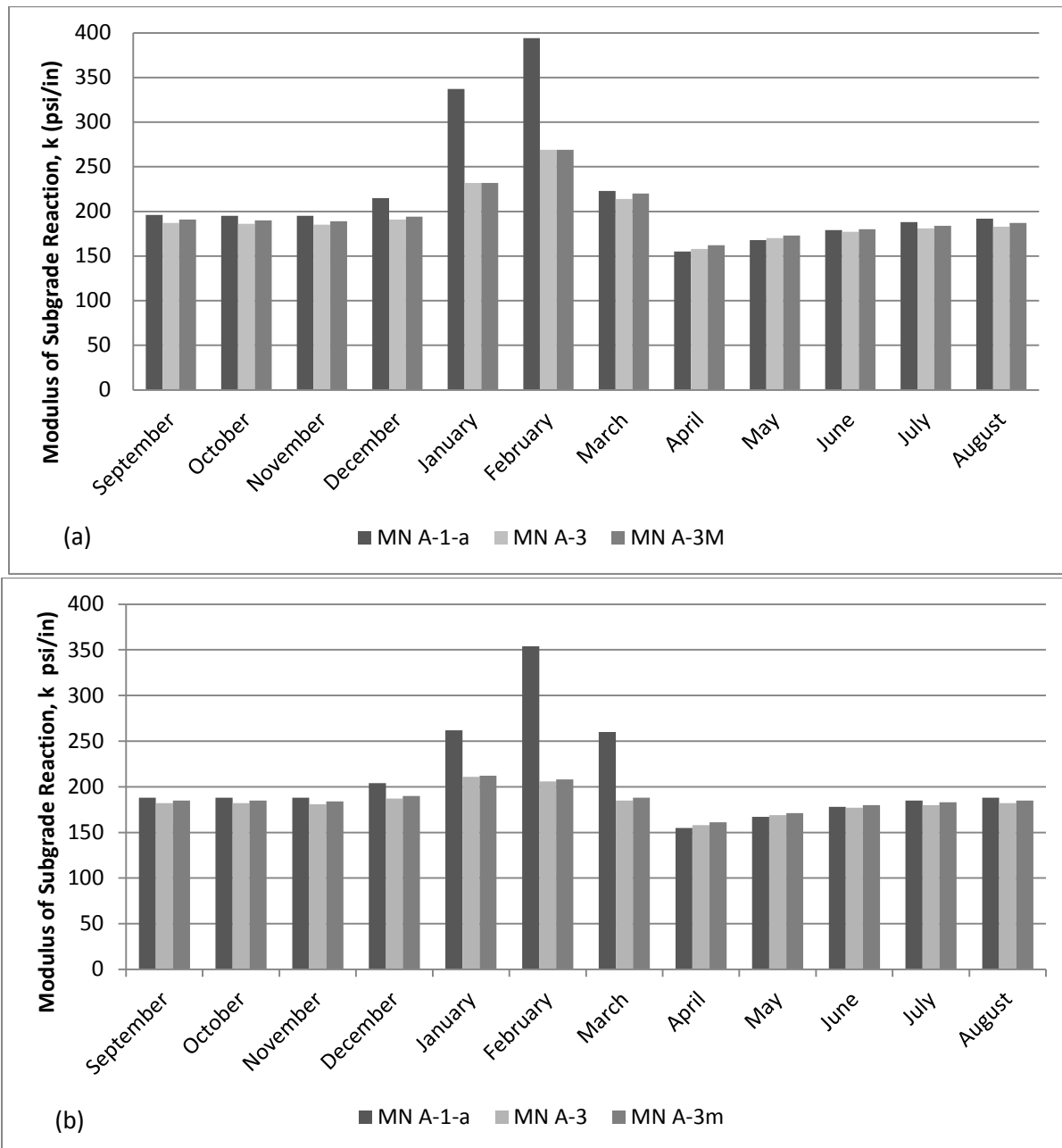


Figure 2-37: Modulus of subgrade reaction, k, under a rigid pavement with different bases and an A-6 subgrade in Minneapolis analyzed with a) the MEPDG and b) DARWin-ME.

It is also worth noting that the value for the k-value predicted by DARWin-ME can be significantly different from the k-values predicted by the MEPDG v1.1 for the same conditions. This discrepancy can be attributed to a difference in the sub-layering procedure used by the MEPDG and DARWin-ME for calculation of seasonal adjustment of the base and subgrade properties and k-value calculation (ARA 2012). The DARWin-ME uses fewer sublayer in moisture content adjustment than was used in the MEPDG v 1.1 and that specified in Chapter 3.3 (NCHRP 2004) and 3.4 (6) of the MEPDG. This modification of the sublayering procedure has not been adequately publicized and because of that it did not receive a proper attention from the pavement community. Figure 2-38 demonstrates that this modification can result in a substantial difference in the predicted pavement performance. This figure shows the predicted cracking of a standard rigid pavement in Minneapolis Minnesota with time, analyzed in both the MEPDG and DARWin-ME, with identical inputs.

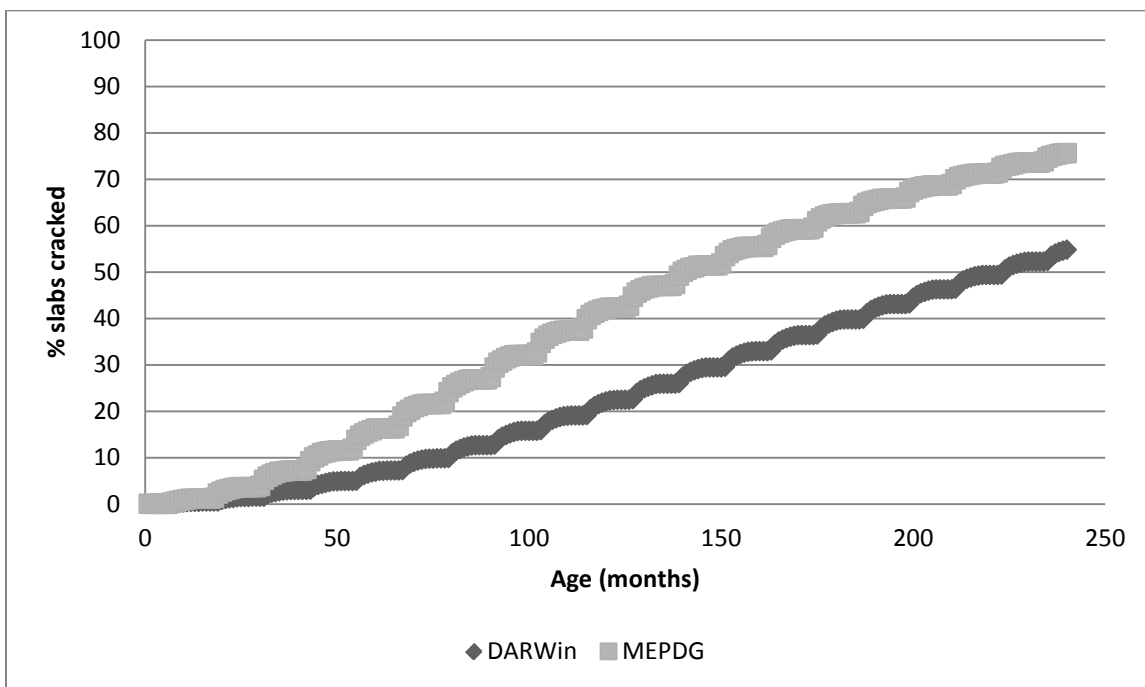


Figure 2-38: Percentage of slabs cracked with time for a rigid pavement analyzed in the MEPDG v1.1 and DARWin-ME, with identical inputs.

Figure 2-38 shows the seasonally adjusted resilient modulus for a flexible pavement in Champaign. It can be seen that resilient modulus appears to be a more dominant factor in the calculation of seasonally adjusted resilient modulus for flexible pavements when compared with gradation. The value of seasonally adjusted resilient modulus for an A-3M base (A-3 material with an A-1-a modulus) is much close to the value for an A-1-a material than an A-3 material. The results for the Minneapolis case showed similar trends.

Comparison of the resilient moduli from DARWin-ME and MEPDG v 1.1 shows that the predicted moduli are similar for the month not affected by freezing and thawing. However, for the winter and spring months the difference can be quite significant. This effect should be carefully investigated.

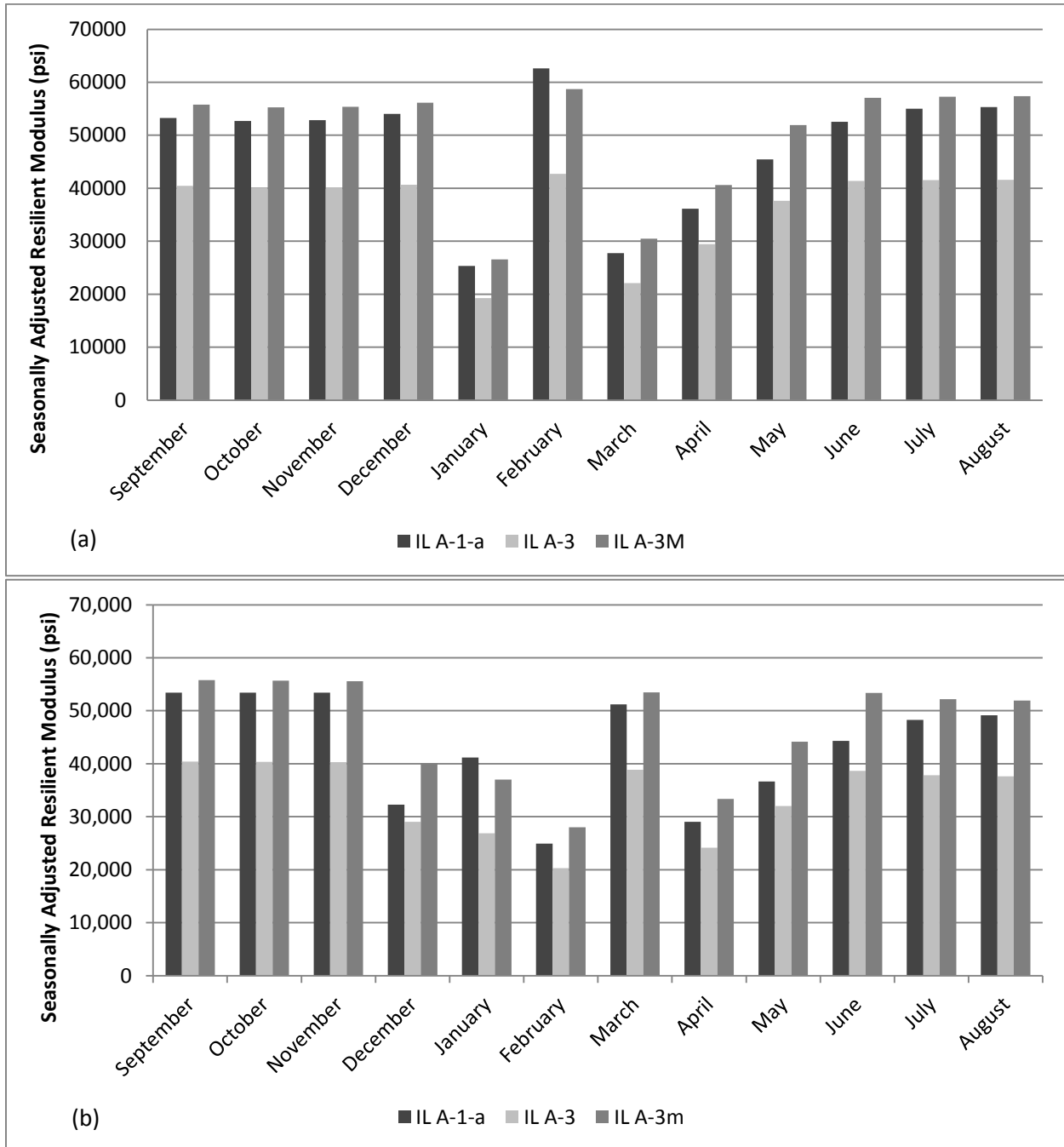


Figure 2-39: Seasonally adjusted resilient modulus of the base layer under a flexible pavement with different bases and an A-6 subgrade in Champaign analyzed with a) the MEPDG and b) DARWin-ME.

The effect of base stiffness on the alligator cracking was evaluated. As expected, an increase in the base stiffness resulted in lower cracking (i.e. the A-3 base exhibited more cracking than A-1-a and A-3M bases). It is interestingly to note that the A-3-M base exhibited slightly less cracking than A-1-a base. This was found to be true for both the MEPDG and DARWin-ME. Also, when the base layer was held constant and the subgrade type was varied, alligator cracking

was found to be dependent on gradation and not resilient modulus. Rutting was found to be dependent on a combination of gradation and resilient modulus, regardless of whether the base or the subgrade was varied.

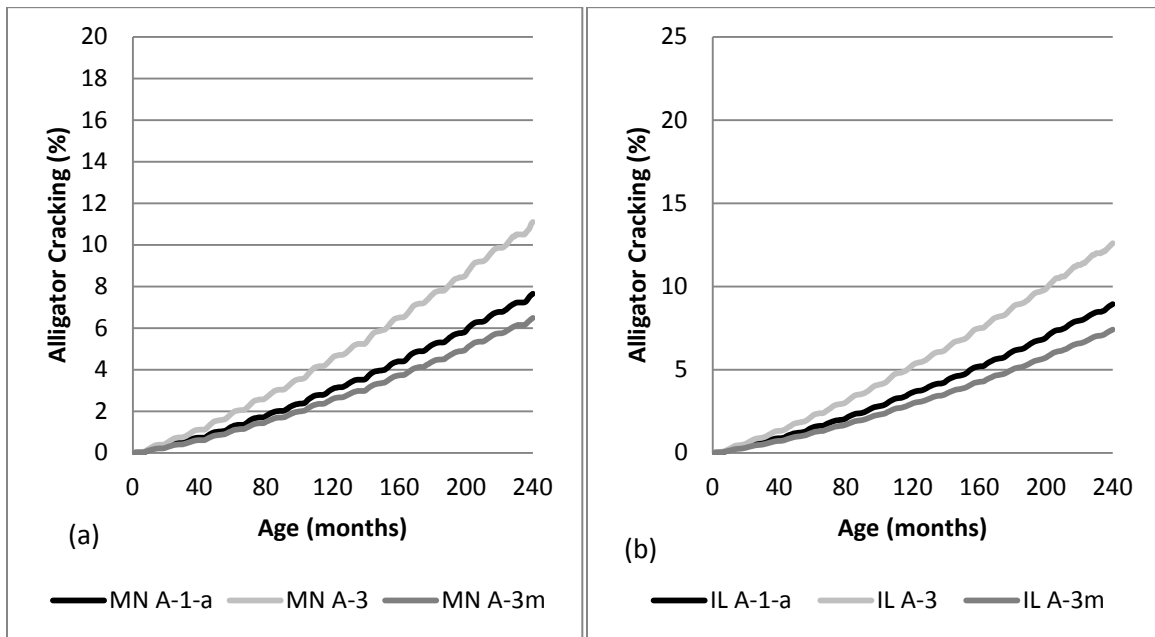


Figure 2-40: Predicted alligator cracking for a flexible pavement with different bases and an A-6 subgrade (a) in Minneapolis analyzed with DARWin-ME, and (b) in Champaign analyzed with DARWin-ME.

The examples presented above as well as others not shown for the sake of brevity demonstrate an importance of the unbound material properties on pavement performance prediction by the MEPDG and DARWin-ME. A full sensitivity analysis should also be conducted to investigate this effect further.

2.2.3 Consistency of Base Stiffness for Different Pavement Types

Another area investigated in this study was the consistency with which the MEPDG and DARWin-ME compute the stiffness of underlying layers for different pavement types. The stiffness of the base, as quantified by the seasonally adjusted resilient modulus, should depend on a combination of the user specified resilient modulus at the optimum moisture content, soil parameters such as gradation, and on the temperature and moisture content of the soil, which in turn is affected by the thickness and thermal properties of the layers above. The seasonally adjusted resilient modulus should not depend on other material properties of those overlying layers, such as their stiffness.

To test whether or not this was indeed the case, test cases were run in the MEPDG and DARWin-ME for a 2" asphalt overlay on 7" of PCC (denoted AC/PCC), a 2" asphalt overlay on 7" of asphalt (denoted AC/AC) with the same thermal properties as the PCC, and a 9" standard asphalt pavement (denoted AC), again with the same thermal properties as the PCC. To match the thermal properties of PCC, the thermal conductivity of the asphalt was changed to 1.25 and

the heat capacity to 0.28, which are the default thermal properties for PCC. In all three cases, an 8” base, semi-infinite A-6 subgrade, and AADTT of 3200 were used. Runs were conducted for A-1-a and A-3 bases, with Minneapolis Minnesota and Champaign Illinois climates, as described above. All other parameters were left at their default values. Results of this investigation are shown for the case of an A-1-a base in Champaign Illinois in Figure 2-41. Similar results were found for the A-3 base, and the Minneapolis Minnesota climate.

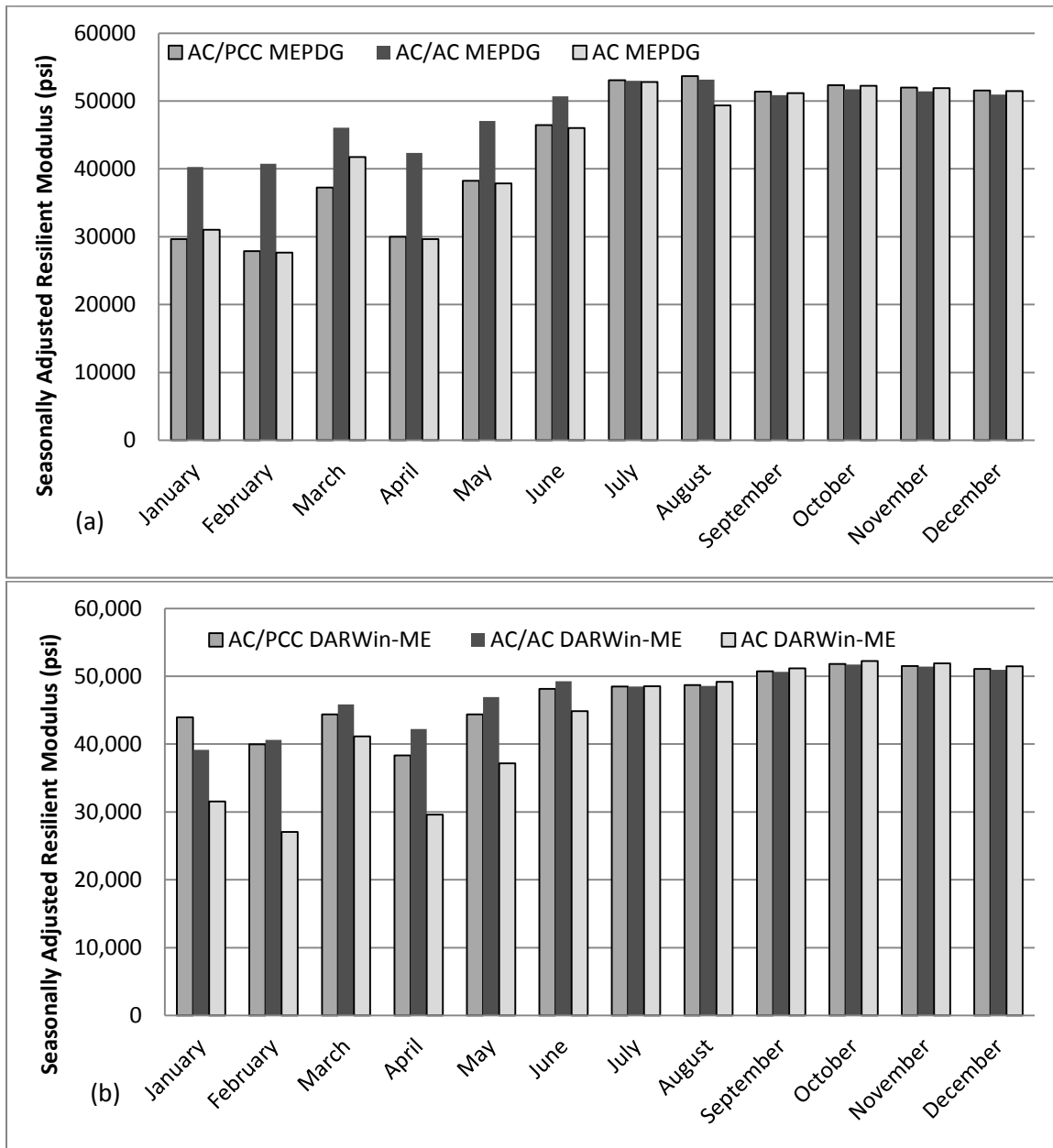


Figure 2-41: Seasonally adjusted resilient modulus for the case of various 9” total thickness pavements with an A-1-a base in Champaign Illinois computed using a) the MEPDG v1.1 and b) DARWin-ME.

By comparing the seasonally adjusted resilient moduli for the AC/AC, AC/PCC, and AC in Figure 2-40a, computed with the MEPDG, and Figure 2-40b, computed with DARWin-ME, it can be seen that the values and the differences between the three pavement types do not match. For example, the MEPDG predicts that the seasonally adjusted resilient modulus of an AC/AC pavement will always be higher than that of an AC/PCC or AC pavement from January through June, at which point they become similar for the remainder of the year. DARWin-ME predicts that the AC/PCC pavement will have higher moduli from February through June. However, the difference in values of moduli between the AC/AC and AC/PCC pavements is predicted to be much smaller by DARWin-ME than by the MEPDG for these months.

From Figure 2-40, it can be seen that there is indeed a difference between the seasonally adjusted resilient modulus of the base layer under different pavements of the same thickness and same thermal properties. This is potentially due to the differences in the sub layering procedure between the two programs, as described earlier. Though determining which of these is the case is outside the scope of this project, the cause of these discrepancies should be investigated in the future, and resolved in later editions of the software.

2.2.4 Subgrade Characterization Recommendations for Pavement Design

Summary of Findings

In this study, the characterization of unbound materials in the MEPDG v1.1 and DARWin-ME was evaluated. The effect of stiffness (resilient modulus) and gradation (soil type) on various program outputs were compared, and gradation was found to be an influential parameter in both programs, influencing many of the outputs for all pavement types. In light of this, it is particularly important to ensure that gradation of all unbound materials is accurately measured.

The DARWin base and subgrade sub-layering for seasonal stiffness adjustment due to moisture and freezing/thawing effects differs from those described in Chapters 3.3 and 3.4 of the MEPDG and implemented in the MEPDG v 1.1 software. This may result in significant difference in predicted subgrade k-values and, subsequently, pavement distresses.

Consistency in the management of resilient modulus between Level 2 and Level 3 inputs was also examined. The Level 2 inputs were found to erroneously correct for moisture content because input data is assumed to be at optimum moisture content, while the results of soil testing is for in-situ conditions. Corrective equations were developed to estimate pseudo-optimum values of CBR, and DCP, which, when automatically corrected for moisture content within the software, produce the correct value of resilient modulus.

Finally, the consistency of the computed seasonally adjusted resilient modulus of the base layer between different pavement types was investigated. In theory, an unbound material should have the same resilient modulus under different pavement types as long as those pavements have the same thickness and thermal properties. However, it was determined that this is not the case in both the MEPDG and DARWin-ME. Test cases run on typical composite pavements, both AC over AC, AC over PCC, and standard flexible pavements found different seasonally adjusted resilient moduli even though all pavements had the same thickness and thermal properties.

Recommendations to the AASHTO Task Force

Based on the findings of this study, several recommendations can be made. Some of these recommendations can be implemented immediately, while others will require further study or correction within the code of a software program.

Immediate Recommendations. It was shown in this study that both the MEPDG and DARWin-ME erroneously correct for moisture content when data from in-situ materials testing, such as CBR and DCP tests, is used for correlation with resilient modulus. This study presented equations which can be used to obtain pseudo-optimum values, so that when moisture corrections are applied, the correct value of resilient modulus will be obtained. The equations presented for the pseudo CBR*, and DCP* should be used when Level 2 inputs are provided for unbound materials in either program.

Given an importance of seasonal stiffness adjustments for unbounded materials found in this study, it is important to have updated documentation on the sub-layering procedure. Therefore, Chapters 3.3 and 3.4 of the MEPDG should be updated to reflect the modifications.

Long Term Recommendations. The finding that gradation plays a much larger role in determining pavement performance than resilient modulus warrants further investigation. Study results clearly showed that gradation does play such an important role in the prediction of pavement distresses, but a sensitivity analysis should be conducted to confirm this.

An unbound material should have the same resilient modulus under different pavement types as long as those pavements have the same thickness and thermal properties. A correction should be made in both the MEPDG and the DARWin-ME programs for the fact that the seasonally adjusted resilient modulus is different for the unbound material layer under two pavements with identical thickness and the thermal properties.

Chapter 3. Response Model for Combined Thermal and Traffic Loading

3.1. Background

The MEPDG contains distress prediction models corresponding to various distresses in a pavement, which can be used to predict the design life. One such distress model for predicting PCC cracking in a composite pavement was adopted directly from the fatigue cracking model of a new jointed plain concrete pavement (JPCP), as illustrated in Figure 3-1. JPCP is a class of rigid pavements that do not contain distributed steel to control random cracking and may or may not contain transverse joint load transfer devices (i.e., dowels) (*AASHTO 2008*).

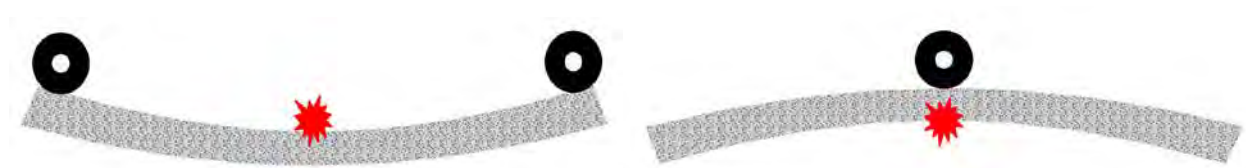


Figure 3-1: Modes of JPCP fatigue damage in the MEPDG: Top-down (at left) and bottom-up (at right) cracking as initiated by different combinations of wheel and thermal loads.

The MEPDG cracking model for composite pavements computes the critical bending stresses in the PCC layer based on the assumption that the AC layer behavior is elastic and its modulus changes on a monthly basis. However, this adaptation is an over-simplification of the actual cracking process as it does not account for the key material property of composite pavements i.e. the viscoelastic behavior of asphalt and its high sensitivity to temperature and loading duration. The major goal of this research is to address this limitation of the MEPDG cracking model in the PCC layer of a composite pavement.

Furthermore, an additional challenge in developing modifications for the MEPDG is the need for computational efficiency. The MEPDG calculates the stress in the PCC layer for every hour of the pavement design life (ex. each hour over 20 years). In this regard, the MEPDG is comprehensive and, as a result, computationally demanding. A secondary goal for this research is to develop a computationally efficient process to account for the cracking behavior in the PCC layer.

3.1.1 Components of Stress under Temperature Curling

Rigid and composite pavements are subjected to bending stresses under temperature gradients and traffic loads. A non-linear distribution of temperature through the depth of the PCC slab closely represents the temperature distribution in an in-situ pavement. During the daytime the slab is under a positive thermal gradient (i.e., the temperature at the top of the PCC layer is greater than the temperature at the bottom of the PCC layer), and during nighttime, the slab is under negative thermal gradient (i.e., the temperature at the bottom of the layer is greater than the temperature at the top of the layer).

Khazanovich (1994) demonstrated the existence of an additional stress attributed to the non-linear temperature distribution through a PCC layer that acts on single or multi-layered pavement systems so as to produce stresses that are self-equilibrating in nature. Consider a slab on an elastic foundation subjected to an arbitrary temperature distribution. The arbitrary temperature distribution may be linear or non-linear through the thickness of the slab but does not vary in the plane of the slab. Also, the slab is free to contract or expand in the horizontal directions. According to Thomlinson (1940) any arbitrary temperature distribution, $T(z)$ can be divided into three components, namely:

1. The constant-strain-causing temperature component, T_C
2. The linear-strain-causing temperature component, T_L
3. The nonlinear-strain-causing temperature component, T_{NL}

Since the arbitrary temperature distribution may vary along the depth of the slab, it must be noted that each of these three components may also vary along the depth of the slab. The constant-strain-causing temperature component, T_C , produces horizontal strains that are constant through the depth of the slab. These strains do not produce stress when the slab is unrestrained in the horizontal directions. Khazanovich (1994) defined the constant-strain-causing temperature component, T_C as follows:

$$T_c(z) = T_o + \frac{\sum_{i=1}^l \int_h \alpha(z)E(z)[T(z) - T_o]dz}{\alpha(z) \sum_{i=1}^l \int_h E(z)dz} \quad (3-1)$$

where

- z = distance to the point of interest from the neutral axis
- T_o = reference temperature of the layer at which there are no temperature-related stresses or strains in the layer
- l = total number of layers in the multi-layered system
- E = Young's modulus
- α = coefficient of thermal expansion
- $T(z)$ = arbitrary temperature distribution

It implies from Equation (3-1) that if the coefficient of thermal expansion is constant through the depth of the slab then the constant-strain-causing temperature component will also be constant.

The linear-strain-causing temperature component, T_L , produces horizontal strains that are linearly distributed along the depth of the slab. Due to the linear distribution of strains, T_L produces bending stresses that can be solved for by using any finite element (FE)-based method. The temperature component, T_L , is defined as follows:

$$T_L(z) = T_o + \frac{z}{\alpha(z)} \frac{\sum_{i=1}^l \int_h E(z) [T(z) - T_o] z dz}{\sum_{i=1}^l \int_h E(z) z^2 dz} \quad (3-2)$$

As before, Equation (3-2) implies that if the coefficient of thermal expansion is constant through the depth of the slab then the linear-strain-causing temperature component will be linear through the depth of the slab. The difference between the total temperature distribution and the reference temperature is equal to the sum of the differences of the individual temperature components and the reference temperature defined as follows:

$$T(z) - T_o = [T_c(z) - T_o] + [T_L(z) - T_o] + [T_{NL}(z) - T_o] \quad (3-3)$$

Knowing the constant and linear strain-causing temperature components, T_L and T_C , the nonlinear-strain-causing temperature component, T_{NL} , can be written as:

$$T_{NL}(z) - T_o = T(z) - [T_c(z) - T_o] - [T_L(z) - T_o] - T_o \quad (3-4)$$

For slabs modeled using linear elastic material models, the corresponding stress at any depth z according to Hooke's law is given as:

$$\sigma_{NL}(z) = -\frac{E(z)\alpha(z)}{(1-\mu)} (T_{NL}(z) - T_o) \quad (3-5)$$

where

μ = Poisson's ratio of the layer

Appendix A provides the analytical solution for calculating the self-equilibrating, non-linear stress, σ_{NL} .

Traffic loads are generally modeled as either concentrated or distributed pressure loads that cause bending stresses. Therefore, the total stress at any point in the slab due to combined traffic loading and temperature curling is given as:

$$\sigma_{Total}(z) = \sigma_{bending}(z) + \sigma_{NL}(z) \quad (3-6)$$

For computing the total stress at a critical location in the PCC layer, bending stresses due to traffic loads and linear-strain-causing temperature component T_L should be added to the self-equilibrating stresses due to the non-linear-strain-causing temperature component T_{NL} . The following section documents the procedure adopted by MEPDG to compute the bending stresses due to traffic loads and the linear-strain-causing temperature component.

3.1.2 MEPDG Rapid Solutions for Predicting Critical PCC Bottom Surface Stresses

The MEPDG identified 30 input parameters to evaluate the JPCP fatigue cracking model. It states that "... an attempt to run all combinations of all 30 input parameters would require analysis of more than 2×10^{14} cases if each parameter is allowed to have just 3 values" (*AASHTO 2009*). For the analysis of a composite pavement, the independent number of input parameters will be even higher due to additional AC properties, and this will further increase the total number of cases to be analyzed. Therefore, a need was identified for developing rapid solutions for calculating PCC stresses in the MEPDG. As a result, a method was developed to compute rigorous yet efficient solutions. The method is based on the following concepts:

1. Slab equivalency concept, and
2. Development of artificial neural networks (NNs).

Slab Equivalency Concept

The concept of slab equivalency was adopted by the MEPDG to reduce the number of independent parameters affecting PCC stresses without introducing any additional error. According to this concept, a multi-layered pavement system could be simplified by using an equivalent transformed section in the form of a single layer slab (*Ioannides et al. 1992*). The solution of a multi-layered system could be developed from the solution for the equivalent single layer slab.

The equivalent single layer slab must exhibit the same deflection profile as the multi-layered slab if the load and the foundation properties (k-value) are the same. This concept employs three equivalency conditions namely, 1) equivalent thickness, 2) equivalent temperature gradient, and 3) equivalent slab. The MEPDG documents application of this theory for the analysis of a JPCP with a base layer. The following equations (11 to 19) demonstrate the equivalency concept for a bonded PCC-base composite system. Similar equations are also provided in the MEPDG documentation for an unbonded PCC-base system.

Equivalent Thickness. Ioannides et al. (1992) presented an equivalent thickness solution for a multi-layered pavement system. The transformation involved flexural stiffness D , with an assumption that the Poisson's ratio of all the layers and that of the equivalent layer were equal, i.e.

$$D_{eqn} = D_{PCC} + D_{Base} \quad (3-7)$$

if,

$$\mu_{eqn} = \mu_{PCC} = \mu_{Base} \quad (3-8)$$

where:

D = flexural stiffness given as:

$$D = \frac{E h^3}{12(1 - \mu^2)} \quad (3-9)$$

E = Young's modulus
 h = layer thickness
 μ = Poisson's ratio

According to Khazanovich (1994) the governing equation of the transformation (equation 7) can also be written in terms of moment in each plate M , as follows:

$$M_{eqn} = M_{PCC} + M_{Base} \quad (3-10)$$

For a fully bonded PCC-base system, the neutral axis of the bonded system, assuming the origin is at the top of the PCC layer, is given as follows:

$$x = \frac{\int_0^h E(z)z dz}{\int_0^h E(z) dz} = \frac{E_{PCC} h_{PCC} \left(\frac{h_{PCC}}{2} \right) + E_{Base} h_{Base} \left(h_{PCC} + \frac{h_{Base}}{2} \right)}{E_{PCC} h_{PCC} + E_{Base} h_{Base}} \quad (3-11)$$

where:

x = location of the neutral axis from the top of PCC layer

The thickness and modulus of the equivalent single layer slab can be established in terms of the thicknesses and moduli of the corresponding multi-layered slab by combining equations (7) to (11) as follows:

$$E_{eff} h_{eff}^3 = E_{PCC} h_{PCC}^3 + E_{Base} h_{Base}^3 + 12 \left[E_{PCC} h_{PCC} \left(\frac{h_{PCC}}{2} - x \right)^2 + E_{Base} h_{Base} \left(h_{PCC} + \frac{h_{Base}}{2} - x \right)^2 \right] \quad (3-12)$$

Since the properties of the equivalent slab depend on the product of its Young's modulus (E) and thickness cubed (h^3), either of the two parameters can be assumed to be equal to a reasonable value. The other parameter can then be expressed in terms of the assumed parameter and properties of the multi-layered slab system. For example, the thickness of the equivalent single-layer slab that has the same modulus of elasticity and Poisson's ratio as the PCC layer of the composite slab is given as:

$$h_{eff} = \sqrt[3]{h_{PCC}^3 + \frac{E_{Base}}{E_{PCC}} h_{Base}^3 + 12 \left[h_{PCC} \left(\frac{h_{PCC}}{2} - x \right)^2 + \frac{E_{Base}}{E_{PCC}} h_{Base} \left(h_{PCC} + \frac{h_{Base}}{2} - x \right)^2 \right]} \quad (3-13)$$

Equation (3-13) represents the equivalent thickness of the single-layer slab that can replace the multi-layered slab while maintaining the same deflection profile and modulus of subgrade reaction (k-value) under loading.

Equivalent Linear Temperature Gradient. Thomlinson (1940) introduced the concept of equivalent temperature gradient for a single-layer slab. Khazanovich (1994) and Ioannides and Khazanovich (1998) later generalized the concept for a non-uniform, multi-layered slab. The MEPDG documentation states that “if two slabs have the same plane-view geometry, flexural stiffness, self-weight, boundary conditions, and applied pressure, and rest on the same foundation, then these slabs have the same deflection and bending moment distributions if their through-the-thickness temperature distributions satisfy the following condition” (AASHTO 2009):

$$\int_{h_A} E_A(z)\alpha_A(z)(T_A(z) - T_{0,A})zdz = \int_{h_B} E_B(z)\alpha_B(z)(T_B(z) - T_{0,B})zdz \quad (3-14)$$

where

- A and B = subscripts denoting the two slabs
- z = distance from the neutral axis
- T_0 = temperature at which these slabs are assumed to be flat
- α = coefficient of thermal expansion
- E = modulus of elasticity
- h = slab thickness

Khazanovich (1994) also states that “[A]s a corollary, two temperature distributions are equivalent only if their respective linear strain components are identical.” Therefore, Equation (3-14) can be employed for replacing the curling analysis of a multi-layered slab with the curling analysis of a single-layer equivalent slab. The temperature distribution in the single-layer equivalent slab is chosen to be a linear function of depth and can be expressed in terms of temperature distributions of the PCC and base layers as follows:

$$\Delta T_{L,eff} = \frac{-12}{h_{eff}^2} \left(\int_{-x}^{h_{PCC}-x} [T(z) - T_0]zdz + \frac{\alpha_{Base} E_{Base}}{\alpha_{PCC} E_{PCC}} \int_{h_{PCC}-x}^{h_{PCC}+h_{Base}-x} [T(z) - T_0]zdz \right) \quad (3-15)$$

where:

- $\Delta T_{L,eff}$ = difference between the top and bottom surface temperatures of the equivalent slab
- $T(z)$ and T_0 = temperature distributions and reference temperature respectively,
- α_{PCC} and α_{Base} = coefficients of thermal expansion of the PCC and base layers, respectively

Korenev’s Equivalent Slab. Korenev and Chernigovskaya (1962) proposed an equivalency concept for circular slabs resting on a Winkler foundation and subjected to traffic loads and

temperature curling. According to this concept, the stress distribution in a slab of known dimensions, properties, loading conditions, and temperature gradients is related to the stress distribution in another slab by Equation (3-16), if the following are the same (*Khazanovich et al. 2001*):

- Ratio of the slab characteristic dimension to the radius of relative stiffness (L/l),
- The total applied load to the slab self-weight (P/Q), and
- Korenev's non-dimensional temperature gradient ϕ .

$$\sigma_1 = \frac{h_2 \gamma_1 l_1^2}{h_1 \gamma_2 l_2^2} \sigma_2 \quad (3-16)$$

where:

σ , h , γ , and l = temperature stress, thickness, unit-weight, and radius of relative stiffness of a given slab, respectively

MEPDG adopts the Korenev's non-dimensional temperature gradient to combine many factors that affect curling stresses into one parameter (*Khazanovich et al. 2001, AASHTO 2009*). It is defined as:

$$\phi = \frac{2\alpha(1+\mu)l^2}{h^2} \frac{k}{\gamma} \Delta T_L \quad (3-17)$$

where:

α , μ , l , γ , h = coefficient of thermal expansion, Poisson's ratio, radius of relative stiffness, unit-weight, and thickness of the slab, respectively

k = modulus of subgrade reaction

ΔT_L = linear temperature difference between the top and bottom surface of the slab

Korenev's slab equivalency concept was modified for the analysis of rectangular slabs. It was found that if the following conditions are fulfilled, then the concept holds true for rectangular slab as well (*AASHTO 2009*):

$$\begin{aligned} l_1 &= l_2 \\ L_1 &= L_2 \\ \phi_1 &= \phi_2 \\ \frac{AGG_1}{k_1 l_1} &= \frac{AGG_2}{k_2 l_2} \\ \frac{P_1}{\gamma_1 h_1} &= \frac{P_2}{\gamma_2 h_2} \\ s_1 &= s_2 \end{aligned} \quad (3-18)$$

where:

l = radius of relative stiffness

L = joint spacing

ϕ = Korenev's nondimensional temperature gradient

AGG = aggregate interlock between the main lane and the shoulder

P = axle weight

γ = PCC slab unit weight

h = PCC thickness

s = distance between slab edge and outer wheel edge

Khazanovich et al. (2001) states that if these conditions hold true for the top surface of continuously reinforced concrete pavements (CRCP), then Korenev's slab equivalency concept can be applied to CRCP.

In summary, the number of independent parameters affecting PCC stresses in a multi-layered system can be reduced by using an equivalent single layer slab and equivalent linear temperature gradient. Once the stresses in the equivalent system are solved for, the stresses in the multi-layered system can be computed using Korenev's equivalent slab method.

MEPDG Neural Networks for Computing PCC Stresses

The purpose of building and training artificial neural networks (NNs) is to essentially create an exhaustive database corresponding to a variety of combinations of design and loading parameters. This database can then be referred quickly for an almost instantaneous prediction of responses. Several NN models were proposed for predicting responses in airfield jointed concrete pavements (Hausmann et al. 1997; Ceylan et al. 1998, 1999, 2000) that basically eliminated the need for using FE based programs such as ILLI-SLAB (Tabatabaie and Barenberg 1980).

MEPDG uses a modified MS-HARP neural network architecture (Banan and Hjelmstad 1994, Khazanovich and Roesler 1997) to further reduce the computational time while computing the PCC stresses. An analysis of three loading scenarios, namely *i*) traffic loading only, *ii*) temperature loading only, and *iii*) combined traffic and temperature loading found that "there is a certain interaction between traffic and temperature loadings such that stresses from traffic loading and temperature gradient cannot be simply superimposed" (AASHTO 2009). In light of this observation, MEPDG substituted the original multi-slab system by a combination of two simpler systems as follows:

- A single slab (system A)
- A two-slab system (system B) (i.e., single slab with shoulder)

Schematics for the original system, system A, and system B are presented in Figure 3-2.

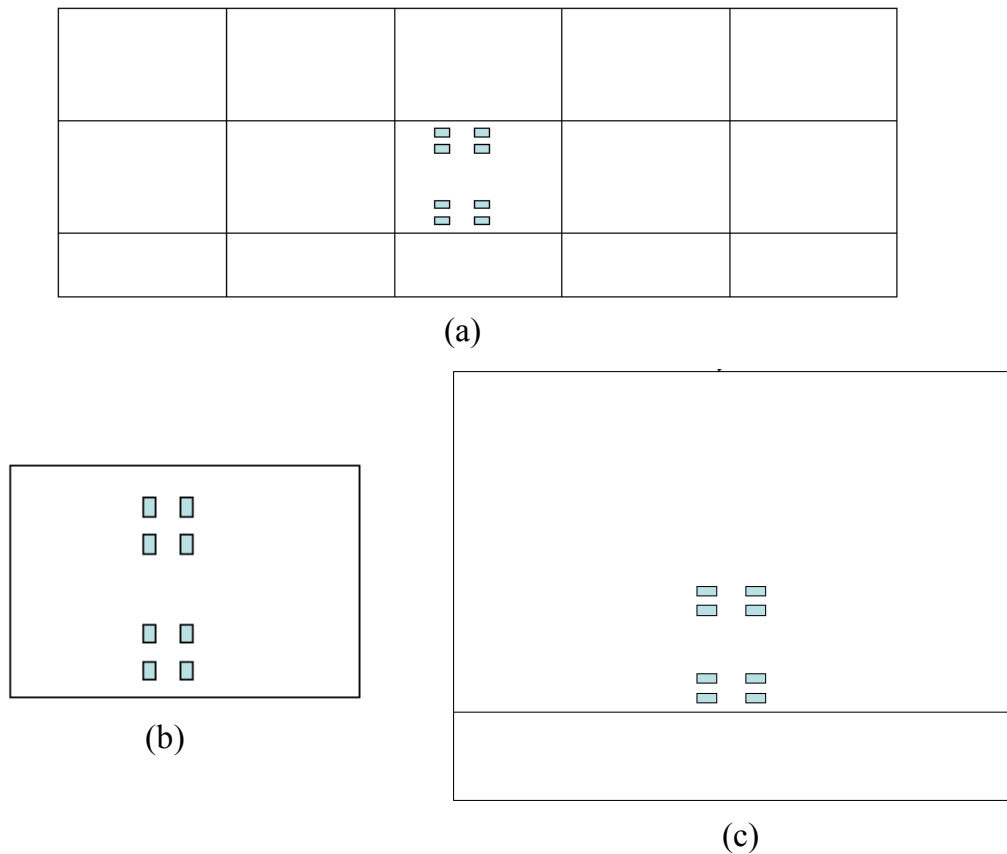


Figure 3-2: Schematics for (a) original multi-layered system, (b) single slab system A, and (c) two-slab system B.

Neural Network NNA for Temperature Curling and Traffic Stresses. The length of single slab system A is equal to the transverse joint spacing of the original system, its width equals the truck lane width of the original system, and its thickness equals the slab thickness of the original system. Two neural networks NNA1 and NNA2 were trained each using a factorial of 14175 ISLAB2000 runs to compute stresses corresponding to temperature curling and single axle loading, and temperature curling and tandem axle loading, respectively. Figure 3-3 presents the structural model for NNA1 and NNA2.

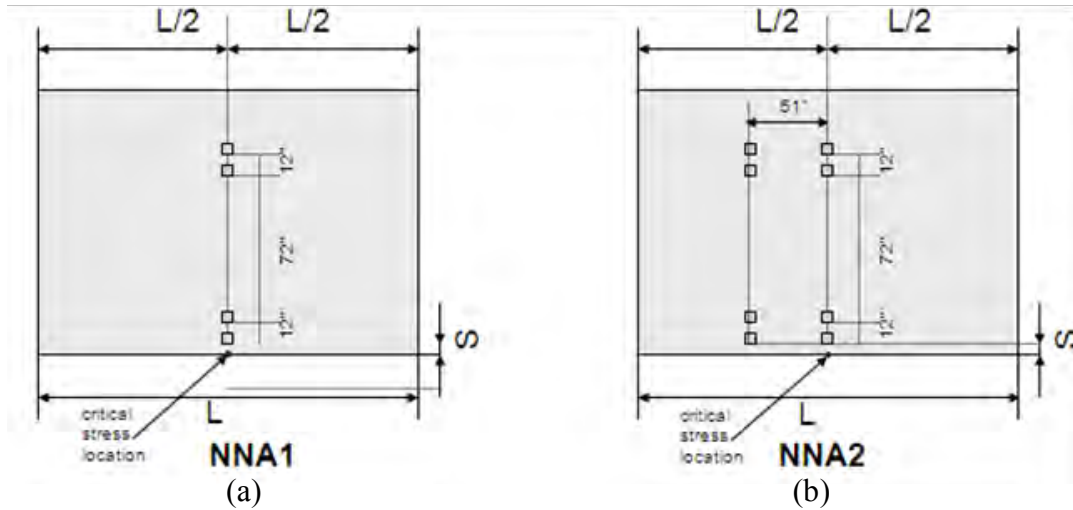


Figure 3-3: Structural model for (a) NNA1 (corresponding to single axle load) and (b) NNA2 (corresponding to tandem axle load).

Neural networks NNA1 and NNA2 were trained to calculate the stresses in system A for three loading conditions, namely:

- Stress due to axle loading, P only, $\sigma^A(P,0)$,
- Curling stress due to equivalent linear temperature loading only (expressed in terms of Korenev's nondimensional temperature gradient ϕ), $\sigma^A(0,\phi)$, and
- Stress due to combined axle and linear temperature loading, $\sigma^A(P,\phi)$.

It should be noted that NNA1 and NNA2 account for neither the tire-footprint geometry nor the shoulder load transfer efficiency (LTE). Also, the stress due to the linear temperature loading $\sigma^A(0,\phi)$ is equal to the curling component of the bending stress, i.e., when no axle load is present (AASHTO 2009).

NNB for Traffic-only Stresses in the Equivalent Slab. System B is a two-slab system that has a sufficiently large slab length to ignore slab size effects, its width equals the truck lane width of the original system, and its thickness equals the slab thickness of the original system. NNs based on system B account for the tire-footprint geometry and the effect of shoulder support. These NNs consider axle loading but not temperature curling. The stresses in the system B were computed for two (2) conditions, namely:

- No load transfer between the slabs in the system B $\sigma^B(0)$, and
- The LTE between the slabs in the system B is equal to shoulder LTE $\sigma^B(LTE_{sh})$.

For single axle loading, all the wheels in the axle are used for computing the stress using neural network NNB1. In case of tandem or tridem axle loading, an additional neural network NNB2 computes the stresses from the remaining wheels (four for a tandem axle and eight for a tridem).

The final stress is obtained by superimposing stresses from NNB1 and NNB2 for the given LTE (either 0 or LTE_{sh}).

Neural networks NNB1 and NNB2 were trained using a factorial of 24300 ISLAB2000 runs and 910 ISLAB2000 runs, respectively. Figure 3-4 presents the structural model for NNB1 and NNB2.

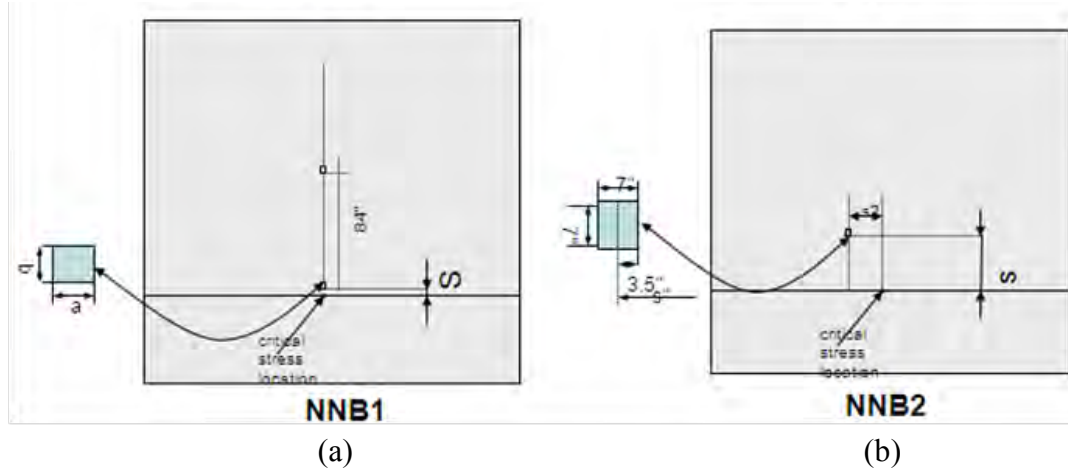


Figure 3-4: Structural model for (a) NNB1 (corresponding to single axle single wheel load) and (b) NNB2 (corresponding to single wheel load).

The total stress in the equivalent slab is then expressed as a combination of stresses from NNA and NNB as follows:

$$\sigma_{comb} = \left[\left(\sigma^A(P, \phi) - \sigma^A(0, \phi) - \sigma^A(P, 0) + \sigma^B(0) \right) \times \frac{\sigma^B(LTE_{sh})}{\sigma^B(0)} \right] + \sigma^A(0, \phi) \quad (3-19)$$

Finally, the stress at the bottom of the PCC layer in the composite pavement is calculated as follows:

$$\sigma_{PCC,bend} = \frac{2 * (h_{PCC} - x)}{h_{eff}} \sigma_{comb} \quad (3-20)$$

$$\sigma_{PCC} = \sigma_{PCC,bend} + \sigma_{NL,PCC,bot} \quad (3-21)$$

where:

σ_{PCC} = total stress at the bottom of the PCC slab

$\sigma_{PCC,bend}$ = bending stress at the bottom of the PCC slab

$\sigma_{NL,PCC,bot}$ = stress at the bottom of the PCC layer caused by the nonlinear strain component of the temperature distribution

So far in this section a review of the MEPDG fatigue cracking model for JPCP was presented. A comprehensive appraisal of the PCC surface stresses due to traffic and temperature loading was performed. And finally, the method adopted by MEPDG to derive rapid solutions through the use of neural networks was discussed. With this as the underlying theory, the focus of discussion now shifts to the adoption of the JPCP fatigue cracking model for composite pavements, presented below.

3.1.3 Adoption of the Fatigue Cracking Model for Composite Pavements in MEPDG

The adoption of the JPCP fatigue cracking model for composite pavements was evaluated by two criteria:

1. Does the physical transformation of the multi-layered composite system to an equivalent system satisfy all the conditions of equivalency previously discussed?
2. Does the stress-strain analysis under traffic loads and temperature curling change due to the inclusion of viscoelastic material properties of the AC layer?

MEPDG adopts the transformed sections concept to convert the composite pavement to an equivalent single layer PCC slab placed directly on the same subgrade as the composite pavement. A representation of the MEPDG composite pavement transformation is shown in Figure 3-5.

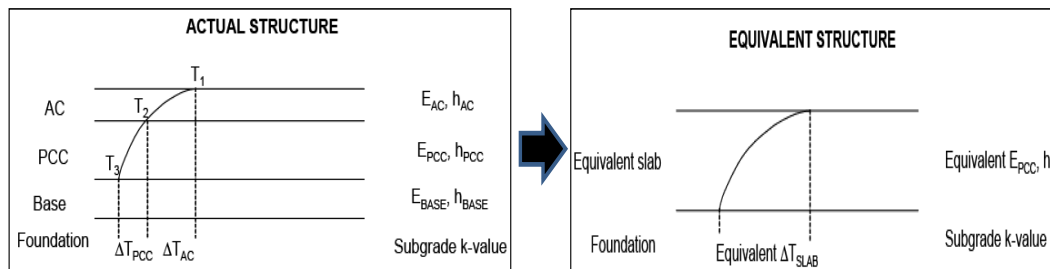


Figure 3-5: Conversion of a composite pavement to an equivalent PCC structure.

Equations for equivalent thickness (13) and equivalent linear temperature gradient (15) were employed such that the thicknesses, moduli, and temperature distributions of the AC and PCC layers were expressed in terms of the thickness, modulus, and the linear temperature gradient of the equivalent structure. The following assumptions were made to define the equivalent structure (*AASHTO 2009*):

1. The deflection basin of the equivalent structure is same as the original composite structure under the same conditions of traffic and temperature loading, and
2. The equivalent temperature gradient must induce the same magnitude of moments in the equivalent structure as that in the PCC slab of the original composite structure.

In the case of JPCP, the material response of the constituent layers (PCC and base) is assumed to be elastic. However, due to the introduction of AC layer, the material response for composite pavements is not purely elastic anymore. Asphalt is a viscoelastic material with a load-deflection response dependent on both the elastic and the viscous components of the material property. Asphalt undergoes creep or relaxation depending upon the loading criterion. Under

constant strain, the stress in asphalt dissipates with time. However, the rate of dissipation, also referred to as stress relaxation, is dependent on the temperature at which the asphalt is kept. At high temperatures, stress relaxation occurs quickly whereas at low temperatures, stress relaxation may take several hours or days (*Nesnas and Nunn, 2004*). MEPDG simplifies the representation of asphalt through the use of a single time-temperature dependent dynamic modulus.

It was identified under this research that the use of a single dynamic modulus may introduce certain limitations in the stress computation process and eventually fatigue cracking computations. In order to better understand the limitations due to the use of a single dynamic modulus, a brief review of computation of AC dynamic modulus under MEPDG framework is presented next.

3.1.4 Asphalt Characterization

Viscoelastic Behavior of Asphalt Concrete

Several researchers have demonstrated that the constitutive equation (relationship between stresses and strains) of asphalt is dependent on time (*Saal et al. 1950, 1958; Van der Poel 1958; Sayegh 1967; Monismith et al. 1962, 1992; Marasteanu and Anderson 2000*). The viscoelastic behavior of asphalt is represented by physical models such as the Maxwell model, the Kelvin-Voigt model, and their generalized forms that are combinations of elastic springs and viscous dashpots. The Maxwell model is a combination of springs and dashpots in series while the Kelvin-Voigt model is a combination of springs and dashpots in parallel. By themselves, the simple Maxwell or Kelvin-Voigt models do not represent the linear viscoelastic behavior of AC adequately. Therefore, more complex models consisting of a combination of several Maxwell and/or Kelvin-Voigt models provide greater flexibility in modeling the response of the viscoelastic material (*Mase 1970*).

If a material is modeled using several Kelvin-Voigt models connected in series the creep compliance of that material has the form of a Prony series which will be defined in Part 3.3. The Prony series coefficients are generally used as input parameters in finite element based programs such as ABAQUS (*ABAQUS 1997*), ANSYS (*ANSYS 2004*), and NIKE3D (*Maker et al. 1995*). The Prony series has been used by many researchers to characterize AC behavior (*Soussou et al. 1970; Daniel 1998; Park et al. 1999, 2001; Di Benedetto et al. 2004, 2007; Elseifi et al. 2006; Zofka 2007, Wang 2007, Zofka et al. 2008, Marasteanu et al. 2009*). For example, Di Benedetto et al. (2004) proposed a 15-element generalized Kelvin-Voigt model using a Prony series to represent the creep compliance of asphalt. The high number of Kelvin-Voigt elements was adopted to cover the entire range of AC behavior under various temperatures and loading frequencies.

The viscoelastic behavior of AC is highly sensitive to the temperature and the rate of loading of the AC material. With an increase in temperature, the stiffness of the AC layer reduces. Similar behavior is observed when the AC layer is subjected to low frequency loads (i.e. long loading rates). The stiffness of the AC layer increases with a decrease in temperature or when subjected to high frequency loads. The stiffness of the AC layer, under a certain loading frequency, can be “shifted” to replicate the stiffness under another frequency by “shifting” the temperature of the analysis. This behavior of asphalt concrete is termed as the time-temperature superposition. The

effect of temperature and loading frequency is most commonly represented by asphalt master curves that are based on the time-temperature superposition principles (*Bahia et al. 1992, Christensen and Anderson 1992, Gordon and Shaw 1994, Marasteanu and Anderson 1999, Rowe 2001, Pellinen and Witczak 2002, Ping and Xiao 2007*).

Characterization of Asphalt in the MEPDG

The MEPDG characterizes the viscoelastic behavior of the AC layer using a load duration-dependent dynamic modulus. The dynamic modulus of asphalt is computed using a master curve of sigmoidal shape, at a reference temperature of 70°F, as shown by the following equations (*Pellinen and Witczak 2002*):

$$\log(E_{AC}) = \delta + \frac{\alpha}{1 + \exp(\beta + \gamma \log(t_r))} \quad (3-22)$$

where:

E_{AC} = dynamic modulus of asphalt
 $\delta, \alpha, \beta,$ and γ = parameters based on the volumetric property of the asphalt mix
 t_r = reduced time, which accounts for the effects of temperature and the rate of loading given as:

$$\log(t_r) = \log(t) - c * (\log(\eta) - \log(\eta_{TR})) \quad (3-23)$$

where:

t = actual loading time
 $c = 1.255882$
 η and η_{TR} = viscosities at temperature T and reference temperature T_R , respectively

The MEPDG utilizes Odemark's method of equivalent thickness (MET) to calculate the actual loading time t . According to this method, any layer of a pavement system can be transformed into an equivalent layer. The transformation is valid as long as both the layers (original and equivalent) have the same flexural stiffness. Maintaining the flexural stiffness ensures that the transformation does not influence the stresses and strains below the transformed layer.

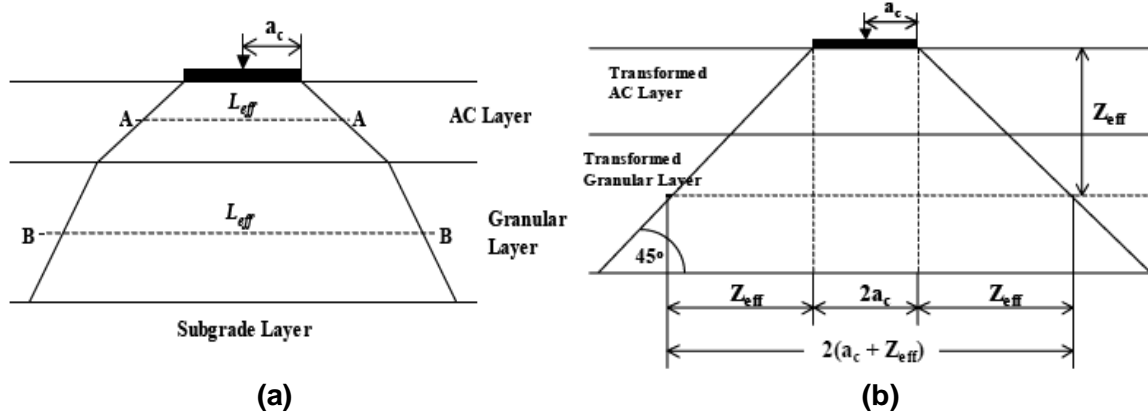


Figure 3-6: (a) Effective length and (b) effective depth for single axle in a conventional flexible pavement.

Using Odemark's MET, both the AC and base layers are transformed into equivalent subgrade layers, i.e., the moduli of the transformed AC and the transformed base layers are equal to the subgrade modulus (Figure 3-6). For simplicity, the stress distribution for a typical subgrade soil is assumed to be at 45° (AASHTO 2009). The effective depth (Z_{eff}), effective length (L_{eff}), and loading time (t) at the mid-depth of the transformed layer are given as:

$$Z_{eff} = \sum_{i=1}^{n-1} \left(h_i * \sqrt[3]{\frac{E_i}{E_{SG}}} \right) + \frac{h_n}{2} * \sqrt[3]{\frac{E_n}{E_{SG}}} \quad (3-24)$$

$$L_{eff} = 2 * (a_c + Z_{eff}) \quad (3-25)$$

$$t = \frac{L_{eff}}{17.6 * V_s} \quad (3-26)$$

where:

- n = layer to be transformed
- h = thickness of a layer
- E = modulus of the layer
- E_{SG} = modulus of the subgrade layer
- a_c = radius of contact area
- V_s = speed of the vehicle

Equations (23) to (26) demonstrate that the asphalt behavior is dependent on the duration of the loads. A traffic load is nearly instantaneous; the duration at highway speeds ranges between 0.01 sec. to 0.05 sec. Under traffic loads asphalt behaves practically as an elastic material as it does not undergo relaxation. On the other hand, the temperature gradient functions like a long-term load, which is applied over the duration of few hours. The long-term load response could be termed as quasi-elastic as the modulus increases to the asymptotes of the long-term asphalt

modulus. From Figure 3-7 it can be inferred that the instantaneous modulus of asphalt is significantly different than the long-term modulus.

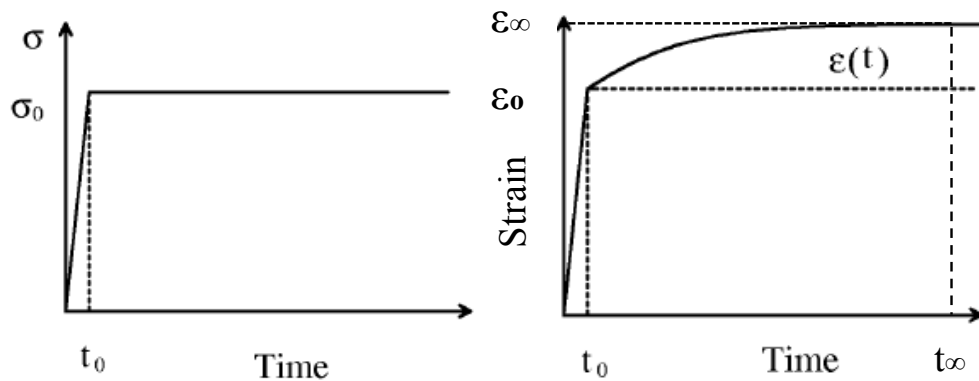


Figure 3-7: Stress-strain responses under different load durations (adopted from Chen 2000).

MEPDG considers only one value of the AC modulus (the dynamic modulus), so the distress computation process due to traffic loads and temperature gradients is over-simplified. There is a need to re-evaluate the characterization of AC layer to account for stress computation under a combination of traffic loads and temperature gradients.

3.1.5 Limitations of the Structural Modeling of Composite Pavements in the MEPDG

As stated before, the adopted fatigue cracking model seems reasonable in its approach towards computing the stress in the PCC layer of a composite pavement. However, an analysis of the AC modulus confirms that there are limitations that need to be considered in this study. These limitations are addressed in the following sections.

Use of a Single Dynamic Modulus of Asphalt

The viscoelastic behavior of AC is dependent on the duration of the loads. As described in the preceding section, asphalt behaves practically as an elastic material under instantaneous traffic loads, whereas, under temperature gradients, the long-term load response of AC is quasi-elastic. The instantaneous modulus of asphalt is significantly different than the long-term modulus. Therefore, a single dynamic modulus is not representative of the combination of traffic load and temperature curling that causes cracking in the PCC layer of a composite pavement.

Assumption that the AC Modulus Changes on a Monthly Basis

The fatigue cracking model for composite pavements is based on the assumption that the AC modulus changes on a monthly basis. Pavements experience changes in temperature, and correspondingly, stresses, throughout a 24-hour cycle. Since AC is highly sensitive to temperature, its modulus should also change depending on the magnitude of the temperature change. However, as the modulus of asphalt is assumed to change on a monthly basis, the computed stresses in the PCC layer do not reflect the actual stresses due to the changes in the stiffness of the AC throughout the month. In order to improve the accuracy of predicted PCC

stresses and corresponding fatigue cracking, it is of utmost importance to address the limitations identified in this section.

3.2. Finite Element Analysis of Composite Pavement Incorporating a Viscoelastic Layer

In this section, a finite element (FE)-based model of a multi-layered composite pavement structure is presented. The asphalt concrete (AC) layer is considered to be viscoelastic while all other constructed layers (primarily Portland cement concrete [PCC] and base) are elastic. The developed FE model is a generalization of ISLAB2000 (*Khazanovich et al. 2000*), a widely used computer program for the analysis of rigid pavements. The rationale for selecting ISLAB2000 was based on the fact that the Mechanistic Empirical Pavement Design Guide (MEPDG) uses the ISLAB2000 framework for structural modeling of concrete pavements and asphalt overlays, and the results of this study could be incorporated into the next versions of the MEPDG.

This section details representation of the AC viscoelastic material, formulation of a FE slab-on-grade model incorporating viscoelastic layers, validation of the FE model using simple examples, and documentation on the sensitivity of the FE model to internal parameters.

3.2.1 Viscoelastic Material Representation of Asphalt Concrete

The stress or strain at a given time in a viscoelastic material depends on the history of the stress or strain at all times preceding the time of interest. The constitutive equation for linear viscoelastic materials is described by Boltzman's superposition principle. According to this principle, the strain (or stress) in a viscoelastic material is the sum or superposition of all strains (or stresses) acting on the material at different times as shown in Figure 3-8 (*Osswald and Menges, 2003*).

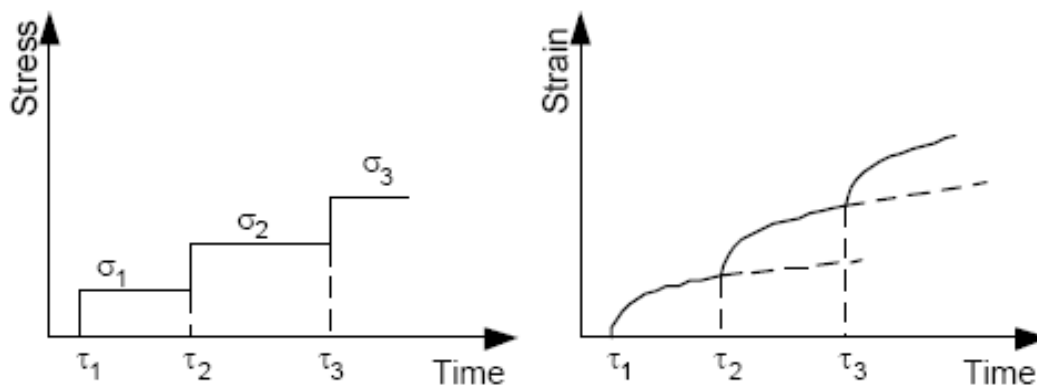


Figure 3-8: Schematic representation of Boltzman's superposition principle (adopted from *UMN Online Lecture 2011*).

The strain at any time t can be expressed mathematically as:

$$\varepsilon(t) = J(t - \tau_1)\sigma_1 + J(t - \tau_2)(\sigma_2 - \sigma_1) + \dots + J(t - \tau_i)(\sigma_i - \sigma_{i-1}) \quad (3-27)$$

where:

$\varepsilon(t)$ = strain at time t

σ_i = applied stress at time τ_i

$J(t)$ = creep compliance of the material defined as the strain under unit stress at any time t , written as follows:

$$J(t) = \frac{\varepsilon(t)}{\sigma_0} \quad (3-28)$$

Equation (3-27) can also be written in the Volterra integral equation form as:

$$\varepsilon(t) = \int_{-\infty}^t J(t - \tau) d\sigma(\tau) = \int_{-\infty}^t J(t - \tau) \dot{\sigma}(\tau) d\tau \quad (3-29)$$

It can be deduced from Equation (3-29) that the creep compliance function characterizes the viscoelastic behavior. Under constant stress, the strain time history can be measured in a laboratory creep test. One of the ways to determine the creep compliance function is by fitting the laboratory measured strain data into a functional form. Several researchers have used linear or non-linear optimization techniques to minimize the least square error between a linear or non-linear model, used to fit the creep compliance function, and the measured test data (*Schapery 1974, Johnson and Quigley 1992, Hill 1993, Chen 2000*).

Of the many available functional forms, a commonly adopted method uses the Prony series [i.e. $\sum_{i=1}^N \alpha_i (e^{-\lambda_i t})$] to represent the creep compliance. The advantage of using the Prony series is two-fold. First, the Prony series has a very simple physical interpretation in the form of a physical model composed of springs and dashpots. Second, the viscoelastic constitutive equation can be expressed in differential form instead of the integral form given by Equation (3-29). The differential form of the viscoelastic constitutive equation can be effectively incorporated into numerical techniques and finite element algorithms (*Zienkiewicz and Taylor 1967, Lesieutre and Govindswamy 1996, Johnson et al. 1997, Johnson 1999, Chen 2000*).

Consider the creep compliance function $J(t)$ in the Prony series form given as:

$$J(t) = \alpha_0 + \sum_{i=1}^N \alpha_i (1 - e^{-\frac{t}{\lambda_i}}) \quad (3-30)$$

where:

N = number of terms in the Prony series
 $\alpha_0, \alpha_i,$ and λ_i = coefficients defining the Prony series
 t = time

Assume that the material is stress-free for time $t < 0$. Integration of Equation (3-29) by parts leads to the following relationship:

$$\varepsilon(t) = \frac{\sigma(t)}{E_0} - \int_0^t \frac{\partial J(t-\tau)}{\partial \tau} \sigma(\tau) d\tau \quad (3-31)$$

$$E_0 = \frac{1}{J(0)} \quad (3-32)$$

where:

E_0 = instantaneous modulus of the material
 $J(0)$ = creep compliance at time $t = 0$

If the Prony series coefficients $\alpha_0, \alpha_i,$ and λ_i are expressed as follows:

$$\alpha_0 = \frac{1}{E_0} \quad \alpha_i = \frac{1}{E_i} \quad \lambda_i = \frac{\eta_i}{E_i} \quad (3-33)$$

where:

E_i = spring stiffness for term i
 η_i = dashpot viscosity for term i
 λ_i = relaxation time for term i

the Prony series has a simple physical interpretation in the form of a model consisting of an elastic spring connected in series with a generalized Kelvin-Voigt model as shown in Figure 3-9.

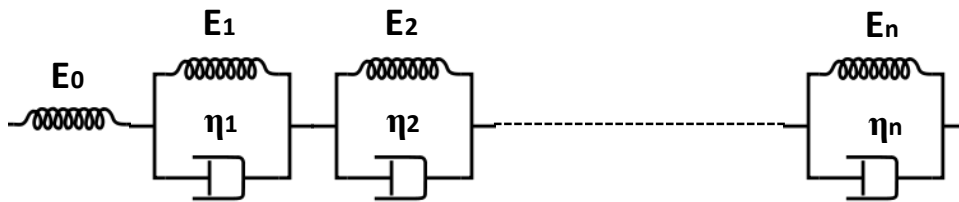


Figure 3-9: Schematic of generalized N -term Kelvin-Voigt model.

The creep compliance function of this model can be written based on equations (3-30) and (3-33) as follows (*Ferry 1970*):

$$J(t) = \frac{1}{E_0} + \sum_{i=1}^N \frac{1}{E_i} \left(1 - e^{-\frac{E_i t}{\eta_i}} \right) \quad (3-34)$$

Another advantage of defining the creep compliance function in terms of the Prony series is that it allows for replacing the integral stress-strain relationship (Equation (3-31)) by a differential relationship where the total strain at any time t is given as:

$$\varepsilon(t) = \varepsilon^{el}(t) + \varepsilon^{cr}(t) = \frac{\sigma(t)}{E_0} + \sum_{i=1}^N \varepsilon_i^{cr}(t) \quad (3-35)$$

where:

ε^{el} = elastic component of strain
 ε^{cr} = creep component of strain

Substituting Equation (3-34) in Equation (3-31) gives the total strain at any time t as:

$$\varepsilon(t) = \frac{\sigma(t)}{E_0} + \sum_{i=1}^N \int_0^t \frac{1}{\eta_i} e^{-\frac{E_i(t-\tau)}{\eta_i}} \sigma(\tau) d\tau \quad (3-36)$$

By differentiating the creep component of the total strain given by the integral Equation (3-36) for any i -th term of the Prony series with respect to time t :

$$\dot{\varepsilon}_i^{cr}(t) = \frac{1}{\eta_i} \sigma(t) - \frac{E_i}{\eta_i} \int_0^t \frac{1}{\eta_i} e^{-\frac{E_i(t-\tau)}{\eta_i}} \sigma(\tau) d\tau \quad (3-37)$$

Substituting the i -th creep strain term from Equation (3-36) into Equation (3-37):

$$\dot{\varepsilon}_i^{cr}(t) = \frac{1}{\eta_i} \sigma(t) - \frac{E_i}{\eta_i} \varepsilon_i^{cr}(t) \quad (3-38)$$

For a very small interval of time, assuming that the elastic stress $\sigma(t)$ does not change within the time interval, the increment of creep strain during the time interval can be approximated by generalizing Equation (3-38) for all terms of the Prony series as follows:

$$\Delta \varepsilon^{cr}(t) \cong \sum_{i=1}^n \left[\left(\sigma(t) - E_i \varepsilon_i^{cr}(t) \right) \frac{\Delta t}{\eta_i} \right] \quad (3-39)$$

where:

$\Delta \varepsilon^{cr}(t)$ = increment of creep strain
 Δt = increment of time

The total strain at the end of any time interval Δt is the sum of the strain at the start of the time interval and the increment of creep strain during the time interval, given as:

$$\varepsilon(t_{j+1}) = \varepsilon(t_j) + \Delta\varepsilon^{cr}(t_j) \quad (3-40)$$

where:

$$\begin{aligned} t_j &= \text{the start of the time increment} \\ t_{j+1} &= \text{the end of the time increment} \end{aligned}$$

At the initial time t_1 (i.e. $j = 0$), the creep strain $\varepsilon^{cr}(t_1) = 0$ and Equation (3-35) become the elastic stress-strain relationship. The increment of creep strain at any time t is dependent on the applied stress during that time interval, the creep strain at the start of the time interval in the individual Kelvin-Voigt elements, the spring stiffness and dashpot viscosity of the Kelvin-Voigt elements, and the time interval Δt_j . This implies that the differential formulation of the creep compliance function does not require storage of the entire strain history.

Analogous to the elastic constitutive Equation (3-Timoshenko 1970), the three-dimensional viscoelastic relationship between stresses σ_{mn} and strains ε_{mn} can be written as:

$$\varepsilon_{mn} = \tilde{J}[(1 + \mu)\sigma_{mn} - \mu\sigma_{kk}\delta_{mn}] \quad (3-41)$$

where:

$$\begin{aligned} m, n, \text{ and } k &= \text{spatial dimensions } x, y, \text{ and } z, \text{ respectively} \\ \mu &= \text{Poisson's ratio} \\ \delta_{mn} &= \text{Kronecker delta function given as follows:} \end{aligned}$$

$$\delta_{mn} = \begin{cases} 1, & m = n \\ 0, & m \neq n \end{cases} \quad (3-42)$$

\tilde{J} is a creep compliance operator defined as follows:

$$\tilde{J}f(t) = \frac{f(t)}{E_0} - \int_0^t \frac{\partial J(t-\tau)}{\partial \tau} f(\tau) d\tau \quad (3-43)$$

The increment of creep strain at the end of the time interval Δt for a three-dimensional analysis can be written by combining equations (3-39) and (3-41) as follows:

$$\Delta\varepsilon_{mn}^{cr}(t) \cong \sum_{i=1}^N \left[\left\{ \begin{aligned} &\tilde{J}\{(1 + \mu)\sigma_{mn}(t) - \mu\sigma_{kk}\delta_{mn}(t)\} \\ &- \tilde{J}^{-1}\left\{ E_i \varepsilon_{mn}^{cr}(t) + \frac{\mu}{1 + \mu} E_i \varepsilon_{kk}^{cr}(t) \delta_{mn} \right\} \end{aligned} \right\} \left\{ \begin{aligned} &\Delta t \\ &\eta_i \end{aligned} \right\} \right] \quad (3-44)$$

The following section describes a finite element model based on the viscoelastic constitutive equation presented herein.

3.2.2 Development of Finite Element Model for the Analysis of Viscoelastic Slab-on-Grade

The finite element method is an efficient tool for computing the unknown variables (such as displacements or forces) for an engineering problem (*Cook et al. 1974, Reddy 1984*). Several FE codes developed specifically for pavement analysis (such as ILLI-SLAB [*Tabatabaie and Barenberg 1980*], WESLIQID [*Chou 1981*], KENSLAB [*Huang 1993*]) are based on plate theory for modeling pavement layers. The plate theory is traditionally adopted for modeling of concrete layers because the horizontal dimensions of a pavement slab are considerably greater than its thickness, and the high stiffness of PCC makes bending the main mode of deformation. This justifies the use of medium-thick plates to model pavement layers.

The Kirchhoff-Love plate theory is an extension of the Euler-Bernoulli beam theory for bending of isotropic and homogenous medium-thick plates. The fundamental assumptions of the plate theory are summarized as follows (*Timoshenko and Woinowsky-Krieger 1959*):

1. The deflection of the mid-surface of the plate is small in comparison to the thickness of the plate.
2. Straight lines initially normal to the mid-surface remain straight and normal to that surface after bending.
3. No mid-surface straining or in-plane straining, stretching, or contracting occurs due to bending.
4. The component of stress normal to the mid-surface is negligible.

In this section, the formulation of a FE model for a slab-on-grade is presented. A viscoelastic plate is placed on a Winkler foundation that could be elastic or viscoelastic. The plate is subjected to traffic loads (in form of a uniformly distributed load over the tire footprint area) and thermal loads (in form of an arbitrary temperature profile varying through the thickness of the plate). The viscoelastic problem is converted into a series of elastic problems such that fictitious loads act on the plate depending on the stress history in the viscoelastic plate. Although readily available in literature (*Zienkiewicz and Taylor 1967, Cook et al. 1974, Ugural and Fenster 2003*), part of the formulation includes a solution for elastic plates subjected to thermal loads, provided for the sake of completeness.

Formulation of the Finite Element Model

A four-node rectangular plate element $ijkl$, as shown in Figure 3-10, was selected to represent the elements of the pavement layer. The coordinate system adopted to develop the formulation is also marked in Figure 3-10. The element has three degrees of freedom at each node.

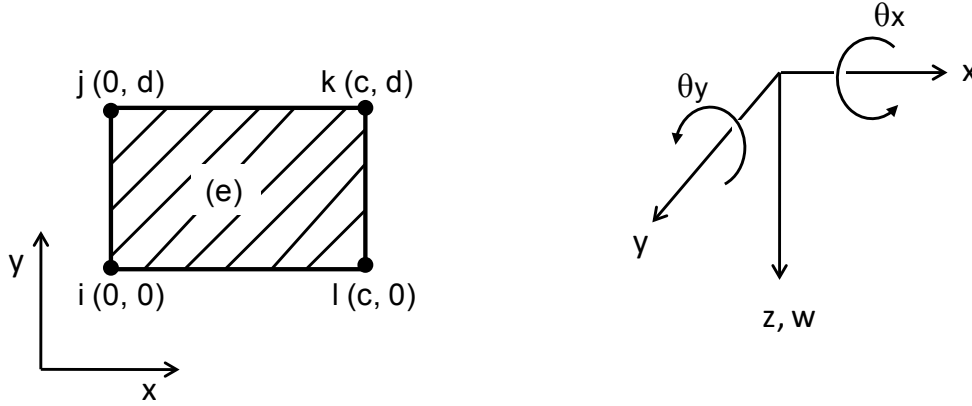


Figure 3-10: Finite element $ijkl$.

From the assumptions of medium-thick plate theory, it is deduced that the vertical shear strains γ_{xz} and γ_{yz} and the normal strain ϵ_z due to vertical loading may be neglected. Thus, the remaining strains at any given point in the plate can be written in terms of displacements as:

$$\epsilon_x = \frac{\partial u}{\partial x} \quad \epsilon_y = \frac{\partial v}{\partial y} \quad \gamma_{xy} = \frac{\partial u}{\partial y} + \frac{\partial v}{\partial x} \quad (3-45)$$

where:

u , v , and w = deflections in the x , y , and z directions, respectively
 ϵ and γ = normal and shear strains, respectively

Since only slab bending is considered, the horizontal deflections can be written in terms of the slopes at the mid-surface given as:

$$u = -z \frac{\partial w}{\partial x} \quad v = -z \frac{\partial w}{\partial y} \quad (3-46)$$

where:

z = distance from the neutral axis of the plate

The strains for an element in the plate can be re-written in matrix form by combining equations (45) and (46) as follows:

$$\{\epsilon\}_e = z \{\kappa\}_e \quad (3-47)$$

$$\{\kappa\}_e = \left\{ -\frac{\partial^2 w}{\partial x^2} \quad -\frac{\partial^2 w}{\partial y^2} \quad -2 \frac{\partial^2 w}{\partial x \partial y} \right\}^T \quad (3-48)$$

where:

subscript e = an individual element in the plate
 κ = curvatures of the element

Further, if the plate is elastic, the stress-strain relationship is given by Hooke's law as follows:

$$\sigma_x = \frac{E}{1-\mu^2}(\varepsilon_x + \mu\varepsilon_y) - \frac{E}{1-\mu^2}(\varepsilon_{0x} + \mu\varepsilon_{0y}) \quad (3-49a)$$

$$\sigma_y = \frac{E}{1-\mu^2}(\varepsilon_y + \mu\varepsilon_x) - \frac{E}{1-\mu^2}(\varepsilon_{0y} + \mu\varepsilon_{0x}) \quad (3-49b)$$

$$\tau_{xy} = \frac{E}{2(1+\mu)}\gamma_{xy} - \frac{E}{2(1+\mu)}\gamma_{0xy} \quad (3-49c)$$

where:

E = Young's modulus
 μ = Poisson's ratio
 ε_0 and γ_0 = normal and shear components of initial strains, respectively
 σ and τ = normal and shear stresses, respectively

The stresses produce bending and twisting moments that can be represented using the following relationships:

$$M_x = \int_{-h/2}^{h/2} z \sigma_x dz \quad M_y = \int_{-h/2}^{h/2} z \sigma_y dz \quad M_{xy} = \int_{-h/2}^{h/2} z \tau_{xy} dz \quad (3-50)$$

Combining equations (48), (49), and (50) leads to the following relationship between the moments in the element and curvatures:

$$\{M\}_e = [D]\{\{\kappa\}_e - \{\kappa_0\}_e\} \quad (3-51)$$

$$[D] = \frac{Eh^3}{12(1-\mu^2)} \begin{bmatrix} 1 & \mu & 0 \\ \mu & 1 & 0 \\ 0 & 0 & (1-\mu)/2 \end{bmatrix} \quad (3-52)$$

where:

$[D]$ = plate flexural stiffness matrix
 κ_0 = initial curvatures due to inelastic strains
 h = plate thickness

The displacement of a node i can be defined using Equation (3-46) as:

$$\{\delta_i\} = \{\theta_{yi} \quad \theta_{xi} \quad w_i\}^T = \left\{ \left(\frac{\partial w}{\partial x} \right)_i \quad \left(\frac{\partial w}{\partial y} \right)_i \quad w_i \right\}^T \quad (3-53)$$

where:

θ_y and θ_x = slopes about the x-axis and y-axis, respectively

Therefore, the displacement of the four-node element $ijkl$ can be written as:

$$\{\delta\}_e = \{\theta_{yi} \quad \theta_{xi} \quad w_i \quad \theta_{yj} \quad \theta_{xj} \quad w_j \quad \theta_{yk} \quad \theta_{xk} \quad w_k \quad \theta_{yl} \quad \theta_{xl} \quad w_l\}^T \quad (3-54)$$

A fourth-order polynomial is commonly used to represent the displacement function in the following form (*Zienkiewicz and Taylor 1967, Khazanovich 1994, Khazanovich et al. 2000*):

$$w = a_1 + a_2x + a_3y + a_4x^2 + a_5xy + a_6y^2 + a_7x^3 + a_8x^2y + a_9xy^2 + a_{10}y^3 + a_{11}x^3y + a_{12}xy^3 \quad (3-55)$$

The curvatures of the plate element are related to the displacements by the following equations:

$$\{\kappa\}_e = [B]\{\delta\}_e \quad (3-56)$$

where:

$[B]$ = strain-displacement matrix (*Zienkiewicz and Taylor 1967*)

The equation of equilibrium for nodal forces can be written by minimizing the total potential energy for all the elements of the system as follows:

$$\sum_1^{ne} \{\Delta\delta\}_e^T \left(\int_{\Omega^e} z^2 [B]^T [\bar{D}] ([B]\{\delta\}_e - \{\kappa_0\}_e) dV - \int_{\Omega^e} [N]^T \{F\}_e dV \right) = 0 \quad (3-57a)$$

or, writing Equation (3-57a) in terms of a single plate element, we have:

$$\int_{\Omega^e} z^2 [B]^T [\bar{D}] [B] dV \{\delta\}_e = \int_{\Omega^e} [N]^T \{F\}_e dV + \int_{\Omega^e} z^2 [B]^T [\bar{D}] \{\kappa_0\}_e dV \quad (3-57b)$$

where:

$[\bar{D}]$ = material property matrix given as:

$$[\bar{D}] = \frac{E}{(1-\mu^2)} \begin{bmatrix} 1 & \mu & 0 \\ \mu & 1 & 0 \\ 0 & 0 & (1-\mu)/2 \end{bmatrix} \quad (3-58)$$

The left hand side of Equation (3-57b) represents the product of stiffness and deflection of the plate element. The stiffness of the plate element is defined in terms of the element stiffness matrix given as:

$$[k]_e = \int_{\Omega^e} z^2 [B]^T [\bar{D}] [B] dV = \int_{A^e} [B]^T [D] [B] dA \quad (3-59)$$

where:

$[k]_e$ = element stiffness matrix
 V and A = volume and the area of the element, respectively

The right hand side of Equation (3-57b) represents the force acting on the plate element due to external loads and initial strains. The first term $\{F\}_e$ is the element force vector due to external loads and self-weight of the plate, and the second term is the element force vector due to inelastic curvatures, given as:

$$\{F_0\}_e = \int_{\Omega^e} z^2 [B]^T [\bar{D}] \{\kappa_0\}_e dV \quad (3-60)$$

The deflections at all the nodes in the plate are computed using Equation (3-57a). After the deflections in the plate are determined, the total strain in the element is calculated using equations (47) and (56) as shown in Equation (3-61). Further, the stress in the element is computed in terms of elastic strains as shown in Equation (3-62).

$$\{\varepsilon(x, y, z)\}_e = z[B] \{\delta\}_e \quad (3-61)$$

$$\{\sigma(x, y, z)\}_e = [\bar{D}] (\{\varepsilon(x, y, z)\}_e - \{\varepsilon_0(x, y, z)\}_e) \quad (3-62)$$

The stresses at any node of the plate are obtained by averaging the stresses from the adjoining nodes when two or more elements share a common node. It should be noted that the initial strains ε_0 could be equal to the thermal strains and/or viscoelastic creep strains as discussed next.

Thermal Loading

Consider a temperature distribution $T(z)$ throughout the plate thickness that is a linear function of depth and can be expressed as follows:

$$T(z) = \frac{\Delta T}{h} z \quad (3-63)$$

where:

h = thickness of the plate

z = distance from the neutral axis of the plate

ΔT = difference of the temperatures between the top and bottom of the plate

The inelastic curvatures due to the temperature variation in the plate are given as:

$$\{\kappa_{therm}\} = \{\alpha T(z) \quad \alpha T(z) \quad 0\}^T = \left\{ \alpha \left(\frac{\Delta T}{h} \right) \quad \alpha \left(\frac{\Delta T}{h} \right) \quad 0 \right\}^T \quad (3-64)$$

where:

α = coefficient of thermal expansion

If the slab is free to expand or contract, then the force due to inelastic curvatures F_{therm} can be written using Equation (3-60) as follows:

$$\{F_{therm}\} = \int_{\Omega^e} z^2 [B]^T [\bar{D}] \left\{ \frac{\alpha \Delta T}{h} \quad \frac{\alpha \Delta T}{h} \quad 0 \right\}^T dV \quad (3-65)$$

Since the temperature gradient ΔT does not vary along the horizontal direction of the slab, Equation (3-65) can be simplified as:

$$\{F_{therm}\} = \left(\int_{A^e} [B]^T [D] dA \right) \left\{ \frac{\alpha \Delta T}{h} \quad \frac{\alpha \Delta T}{h} \quad 0 \right\}^T \quad (3-66)$$

Viscoelastic Analysis

Unlike thermal strains, which do not vary along the horizontal direction of the plate element, the creep strains are a function of the spatial coordinates of the plate element. Therefore, for a three-dimensional analysis, the increment of creep strains given by Equation (3-44) is rewritten for the i -th Kelvin-Voigt element as follows:

$$\begin{aligned} \Delta \varepsilon_{ix}^{cr}(t_j) \cong & \left[\sigma_x(t_j) - \frac{E_i}{(1-\mu^2)} \left\{ \varepsilon_{ix}^{cr}(t_j) + \mu \varepsilon_{iy}^{cr}(t_j) \right\} \right] * \frac{\Delta t_j}{\eta_i} \\ & - \mu \left[\sigma_y(t_j) - \frac{E_i}{(1-\mu^2)} \left\{ \varepsilon_{iy}^{cr}(t_j) + \mu \varepsilon_{ix}^{cr}(t_j) \right\} \right] * \frac{\Delta t_j}{\eta_i} \end{aligned} \quad (3-67a)$$

$$\Delta \varepsilon_{iy}^{cr}(t_j) \cong \left[\sigma_y(t_j) - \frac{E_i}{(1-\mu^2)} \{ \varepsilon_{iy}^{cr}(t_j) + \mu \varepsilon_{ix}^{cr}(t_j) \} \right] * \frac{\Delta t_j}{\eta_i} - \mu \left[\sigma_x(t_j) - \frac{E_i}{(1-\mu^2)} \{ \varepsilon_{ix}^{cr}(t_j) + \mu \varepsilon_{iy}^{cr}(t_j) \} \right] * \frac{\Delta t_j}{\eta_i} \quad (3-67b)$$

$$\Delta \gamma_{ixy}^{cr}(t_j) \cong 2(1+\mu) \left[\tau_{xy}(t_j) - \frac{E_i}{2(1+\mu)} \gamma_{ixy}^{cr}(t_j) \right] * \frac{\Delta t_j}{\eta_i} \quad (3-67c)$$

where:

$\varepsilon_{ix}^{cr}(t_j)$ and $\varepsilon_{iy}^{cr}(t_j)$ = normal creep strains in the x and y directions, respectively
 $\gamma_{ixy}^{cr}(t_j)$ = shear creep strain
 σ_x and σ_y = normal stresses in the x and y directions, respectively
 τ_{xy} = shear stress

At any time t_{j+1} , consider a gradient of creep strain in the plate such that the creep strains at any depth z are a linear function of depth. Analogous to Equation (3-64), the inelastic curvatures due to creep strains at any time t_{j+1} can be written as:

$$\kappa^{cr}(t_{j+1}) = \frac{\varepsilon_{bot}^{cr}(t_{j+1}) - \varepsilon_{top}^{cr}(t_{j+1})}{h} \quad (3-68)$$

where:

$\kappa^{cr}(t_{j+1})$ = inelastic curvatures due to creep strains at the end of the time interval
 $\varepsilon_{bot}^{cr}(t_{j+1})$ = creep strain at the bottom of the plate element at the end of the time interval
 $\varepsilon_{top}^{cr}(t_{j+1})$ = creep strain at the top of the plate element at the end of the time interval

Due to the presence of inelastic curvatures at any time t_{j+1} , it can be said that fictitious forces, accounting for the viscoelastic creep strains, act on the plate element at any time t_{j+1} . Using Equation (3-60), the “creep” force is written as follows:

$$\{F_{creep}(t_{j+1})\} = \int_{\Omega^e} z^2 [B]^T [\bar{D}] \{ \kappa_x^{cr}(t_{j+1}) \quad \kappa_y^{cr}(t_{j+1}) \quad \kappa_{xy}^{cr}(t_{j+1}) \}^T dV \quad (3-69)$$

where:

κ_x^{cr} , κ_y^{cr} , and κ_{xy}^{cr} = normal and shear components of the inelastic curvatures due to creep strains in the x -direction, y -direction, and xy plane, respectively, at any time t_{j+1}

Since the inelastic curvatures due to creep strains are a function of the spatial coordinates of the plate element, approximating functions are used to represent the curvatures at any point in the plate in terms of nodal inelastic curvatures. The following functions were adopted:

$$N_1 = \left(1 - \frac{x}{c}\right) \left(1 - \frac{y}{d}\right) \quad (3-70a)$$

$$N_2 = \left(1 - \frac{x}{c}\right) \left(\frac{y}{d}\right) \quad (3-70b)$$

$$N_3 = \left(\frac{x}{c}\right) \left(\frac{y}{d}\right) \quad (3-70c)$$

$$N_4 = \left(\frac{x}{c}\right) \left(1 - \frac{y}{d}\right) \quad (3-70d)$$

where:

$N_1, N_2, N_3,$ and N_4 = approximating functions for inelastic curvatures due to creep strains at nodes $i, j, k,$ and $l,$ respectively of the element shown in Figure 3-10

The fictitious creep force given in Equation (3-69) can be re-written using Equation (3-70) as follows:

$$\{F_{creep}(t_{j+1})\} = \int_{\Omega^e} z^2 [B]^T [\bar{D}] \{\kappa^{cr}(t_{j+1})\} \{N\}^T dV \quad (3-71)$$

where:

κ^{cr} = matrix containing the normal and shear components of the inelastic curvature due to creep strains at nodes $i, j, k,$ and l of the plate element, i.e.

$$\{\kappa^{cr}\} = \begin{bmatrix} \kappa_x^{cr i} & \kappa_x^{cr j} & \kappa_x^{cr k} & \kappa_x^{cr l} \\ \kappa_y^{cr i} & \kappa_y^{cr j} & \kappa_y^{cr k} & \kappa_y^{cr l} \\ \kappa_{xy}^{cr i} & \kappa_{xy}^{cr j} & \kappa_{xy}^{cr k} & \kappa_{xy}^{cr l} \end{bmatrix} \quad (3-72)$$

and, $\{N\}$ is the vector containing approximating functions, as follows:

$$\{N\} = \{N_1 \quad N_2 \quad N_3 \quad N_4\} \quad (3-73)$$

FE Formulation of the Winkler Foundation

The FE model developed under this research provides a generalization of the current framework for the commercial package ISLAB2000 (Khazanovich *et al.* 2000). ISLAB2000 incorporates many subgrade models (such as Winkler [1861], Pasternak [1954], and Kerr-Vlasov [1964]) that provide the foundation support for the slab. Among them, the Winkler foundation is the simplest foundation model, which is defined using a proportionality constant between the applied pressure and plate deflection at any point. ISLAB2000 utilizes two idealizations for the Winkler foundation: the spring formulation and the energy-consistent Winkler formulation (Khazanovich *et al.* 2000). The energy consistent Winkler formulation permits the use of a coarser mesh and significantly less computational resources than would be required by the spring foundation to achieve the same level of accuracy. This was an important feature of the past when memory requirements and computational time were significant considerations in the slab-on-grade analysis. Recent advances in computer technology have made these factors less important. While the energy-consistent Winkler formulation is more efficient, the spring formulation permits a simpler implementation of the analysis of separation of the slab from the foundation in the case of curling or void analysis. If the mesh size is sufficiently fine, then there is no significant difference between the results from spring and energy-consistent formulations of the Winkler foundation in ISLAB2000.

Under this research, the spring formulation of the Winkler foundation is adopted to model the foundation support. This formulation of the Winkler foundation models the foundation with concentrated springs at the nodes of the plate element as shown in Figure 3-11.

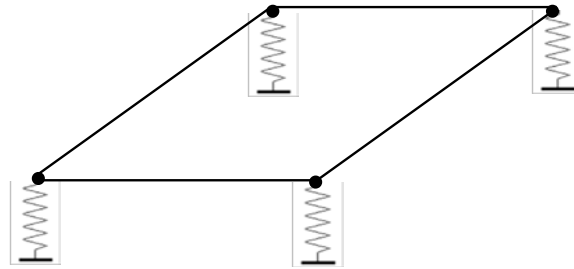


Figure 3-11: Spring idealization of Winkler foundation using concentrated springs at the nodes of the plate element.

The stiffness of the foundation is defined as a product of the coefficient of subgrade reaction and the area of the subgrade (Khazanovich *et al.* 2000). Since a four-node finite element $ijkl$ is used to represent the plate element, the foundation stiffness at each node of the element corresponding to the degree of freedom representing vertical deflection can be written as follows:

$$\left[K_{dd \text{ foundation}} \right]_e = \begin{cases} k_{\text{subgrade}} * \frac{A_e}{4} & \text{for } d \in (3, 6, 9, 12) \\ 0 & \text{otherwise} \end{cases} \quad (3-74)$$

where:

- $[K_{dd \text{ foundation}}]_e$ = stiffness of the foundation supporting the plate element
- k_{subgrade} = coefficient of subgrade reaction
- A_e = area of the element
- d = local degree of freedom corresponding to vertical deflection at element nodes

The foundation stiffness matrix $[K_{\text{foundation}}]_e$ is added to the element stiffness matrix $[k]_e$ in order to incorporate the boundary conditions for the slab-on-grade analysis when the element node is in contact with the foundation. An approach similar to that in ISLAB2000 is adopted to model the separation of the slab from the foundation for curling analysis. For an out of contact node, no contribution from the foundation is considered by setting the stiffness of the spring equal to zero (Khazanovich et al. 2000).

Viscoelastic Winkler Foundation. The foundation model can also incorporate a viscoelastic analysis similar to that presented for the plate in the preceding section. Analogous to Equation (3-67), the increment of creep deflections in the viscoelastic Winkler foundation can be written as follows:

$$\Delta w_{\text{foundation}}^{cr}(t_j) \cong \sum_{i=1}^n [\sigma_{\text{foundation}}(t_j) - k_i w_{\text{foundation}}^{cr}(t_j)] * \frac{\Delta t_j}{\eta_i} \quad (3-75)$$

where:

- $\Delta w_{\text{foundation}}^{cr}$ = increment of creep deflections in the foundation at the end of time interval Δt_j
- $\sigma_{\text{foundation}}$ = stress acting on the foundation at time t_j
- k_i and η_i = spring stiffness and dashpot viscosity of the i -th term of the Prony series
- μ = Poisson's ratio

The total creep deflections in the viscoelastic Winkler foundation at any time t_{j+1} are given by adding the creep deflections at time t_j and the increment of creep deflections during the time interval Δt_j . The fictitious forces acting on the foundation at any time t_j due to the presence of creep deflections are computed as:

$$F_{\text{foundation}}^{cr}(t_j) = k_{\text{subgrade}} * A_e * w_{\text{foundation}}^{cr}(t_j) \quad (3-76)$$

where:

- $w_{\text{foundation}}^{cr}(t_j)$ = total creep deflections in the viscoelastic Winkler foundation at any time t_j

It must be noted that the fictitious Winkler foundation creep force acts on each spring in contact with the nodes of the plate element. The foundation creep force acts only in the degree of

freedom corresponding to the vertical deflection of the plate, or in other words, the foundation creep force is equal to zero for the rotational degree of freedom.

Assembling the Global Matrix and Computing Stresses Based on the Time-Discretized Viscoelastic Analysis

The equilibrium equation for all elements of the plate can be expressed from Equation (3-57a) as follows:

$$[K]\{\delta\} = \{F\} + \{F_0\} \quad (3-77)$$

where:

- $[K]$ = global stiffness matrix
- $\{\delta\}$ = global displacement vector
- $\{F\}$ = global force vector consisting of forces due to traffic loads and self-weight of the slab
- $\{F_0\}$ = local force vector due to inelastic strains such as thermal strain and viscoelastic creep strains from the plate and/or foundation

The global stiffness matrix $[K]$ is assembled by adding the terms of element stiffness matrix $[k]_e$ and the foundation stiffness matrix $[K_{dd \text{ foundation}}]_e$ corresponding to the element $ijkl$ into a global matrix at the corresponding global degrees of freedom over the total number of elements. Similarly, the global force vectors $\{F\}$ and $\{F_0\}$ are also assembled by adding the terms of the element force vectors at corresponding global degrees of freedom over all the elements. Equation (3-77) can be re-written at any time step t_j as follows:

$$\{\delta(t_j)\} = [K]^{-1} \left(\{F(t_j)\} + \{F_{therm}(t_j)\} + \{F_{creep}(t_j)\} \right) \quad (3-78)$$

Thus, the nodal displacements of the plate at time step t_j are calculated by multiplying the inverse of the global stiffness matrix $[K]$ and the sum of the load vector $\{F(t_j)\}$, temperature load vector $\{F_{therm}(t_j)\}$, and the fictitious creep load vector $\{F_{creep}(t_j)\}$ at time step t_j . The load and the temperature load vectors depend on the magnitude of the external loads and temperature at time t_j , respectively, whereas the creep load vector depends on the stress time history. The stiffness matrix $[K]$ from the previous time step is initially used in the next time step analysis. This permits avoiding an additional inversion of the stiffness matrix, which is the most computationally expensive step. However, if the contact conditions are changed at any node (i.e. the deflection changed its sign from the previous time step) then the foundation stiffness matrix should be updated and the corresponding global stiffness matrix $[K]$ should be computed.

Once the global displacements are calculated from Equation (3-78), the element displacement can be extracted using the global degrees of freedom corresponding to each node of the element. The stresses are computed at the end of each time interval from Equation (3-62) as follows:

$$\{\sigma(t_j)\}_e = [\bar{D}]\left(\{\varepsilon(t_j)\} - \{\varepsilon_{therm}\} - \{\varepsilon_{tot}^{cr}(t_j)\}\right)_e \quad (3-79)$$

The formulation of the FE model for a single layer slab-on-grade was presented in this section. The next section presents the extension of this model to multi-layered pavements.

3.2.3 Extension of the FE Model to Multi-Layered Composite Pavements

The FE model presented in the preceding section was developed based on the Kirchhoff-Love plate theory for a single layer plate placed on the Winkler foundation. Pavements, on the other hand, are multi-layered systems with different bonding conditions between the various layers. The interface condition between two layers in contact may vary from zero friction (fully unbonded) to full friction (fully bonded). In this study, only extreme cases (fully bonded and fully unbonded) were considered. In the case of composite pavements defined as a system of AC over PCC over base layers, two layer interfaces exist – one between the AC and PCC layers and other between the PCC and base layers. This leads to four sets of interface conditions: bonded-bonded, unbonded-unbonded, bonded-unbonded, and unbonded-bonded.

As discussed in Part 3.2, multi-layered pavements can be transformed into single layer systems using the method of equivalent thickness (MET). As long as certain conditions are fulfilled that include equality of deflection profiles and equality of modulus of subgrade reaction between the multi-layered slab-on-grade and equivalent single layer slab-on-grade, the stress solution of the multi-layered slab can be expressed in terms of the stress solution of the equivalent slab (*Ioannides et al. 1992*). Thus, the plate theory is used to calculate stresses in the equivalent single layer slab, which are further used to compute the stresses in the layers of a multi-layered slab.

In this section, the equivalency equations between the composite pavement and an equivalent single layer slab are presented for bonded-bonded interface conditions of the composite slab. The equivalency equations for other interface conditions are detailed in Appendix A.

Equivalent Single Layer Slab

Either the thickness or the modulus of the equivalent single layer slab can be computed by equating the equivalent slab's flexural stiffness to the flexural stiffness of the composite pavement if the Poisson's ratio of all the layers of the composite pavement and that of the equivalent layer are equal (*Ioannides et al. 1992*). The thickness (or modulus) can be computed from the following equation if the modulus (or thickness) is known.

$$\frac{E_{eq} h_{eq}^3}{(1-\mu^2)} = \frac{1}{(1-\mu^2)} \left(\frac{E_{AC} h_{AC}^3 + E_{PCC} h_{PCC}^3 + E_{Base} h_{Base}^3 + \left[E_{AC} h_{AC} \left(\frac{h_{AC}}{2} - x \right)^2 + E_{PCC} h_{PCC} \left(h_{AC} + \frac{h_{PCC}}{2} - x \right)^2 + E_{Base} h_{Base} \left(h_{AC} + h_{PCC} + \frac{h_{Base}}{2} - x \right)^2 \right]}{12} \right) \quad (3-80)$$

where:

$E_{eq}, E_{AC}, E_{PCC}, E_{Base}$ = Young's moduli of the equivalent, AC, PCC, and base layers, respectively

$h_{eq}, h_{AC}, h_{PCC}, h_{Base}$ = thicknesses of the equivalent, AC, PCC, and base layers, respectively

x = distance of the neutral axis of the composite pavement from the top of the AC layer

The unit weight of the equivalent single layer is calculated as:

$$\gamma_{eq} = \frac{h_{AC}\gamma_{AC} + h_{PCC}\gamma_{PCC} + h_{Base}\gamma_{Base}}{h_{eq}} \quad (3-81)$$

where:

$\gamma_{eq}, \gamma_{AC}, \gamma_{PCC}, \gamma_{Base}$ = unit weights of the equivalent, AC, PCC, and base layers, respectively

Equivalent Linear Temperature Gradient in the Equivalent Single Layer Slab

It has been shown by Khazanovich (1994) that bending of a multi-layered pavement due to an arbitrary temperature distribution throughout the pavement system can be described by the bending of an equivalent single layer slab subjected to a linear temperature gradient. The equivalent linear temperature gradient in the equivalent single layer slab was approximated in terms of the temperature data of the multi-layered pavement as follows:

$$\Delta T_{eq} = \frac{-12}{h_{eq}^2} + \frac{\alpha_{AC} E_{AC} h_{AC}}{\alpha_{eq} E_{eq} 24} \sum_{i=1}^4 \left((T_i - T_{oACi}) * \left((3i-2) * \frac{h_{AC}}{4} - 3x \right) + (T_{i+1} - T_{oACi+1}) * \left((3i-1) * \frac{h_{AC}}{4} - 3x \right) \right) + \frac{\alpha_{PCC} E_{PCC} h_{PCC}}{\alpha_{eq} E_{eq} 60} \sum_{i=1}^{10} \left(T_i * \left((3i-2) * \frac{h_{PCC}}{10} - 3(x - h_{AC}) \right) + T_{i+1} * \left((3i-1) * \frac{h_{PCC}}{10} - 3(x - h_{AC}) \right) \right) - \frac{\alpha_{PCC} E_{PCC} T_{11}}{\alpha_{eq} E_{eq} 2} h_{PCC} (h_{PCC} + 2h_{AC} - 2x) \quad (3-82)$$

where:

ΔT_{eq} = difference between the top and bottom surface temperatures of the equivalent single layer slab

T_i and T_{oi} = temperature and reference temperature at point i , respectively

α_{eq} , α_{AC} , α_{PCC} and α_{Base} = coefficients of thermal expansion of the equivalent, AC, PCC and base layers, respectively

Appendix A details the procedure for calculating the equivalent linear temperature gradient given in Equation (3-82).

Equivalent Linear Creep Strain Gradient in the Equivalent Single Layer Slab

Analogous to an arbitrary temperature profile that can be expressed in terms of an equivalent linear temperature gradient; the arbitrary creep strain profile of the composite pavement can also be expressed as an equivalent linear creep strain gradient present in the equivalent single layer slab. Therefore, analogous to Equation (3-82) for equivalent linear temperature gradient, the equivalent linear creep strain gradient can be written as:

$$\Delta T^{cr} = \frac{-12}{h_{eq}^2} \left(\frac{E_{AC}}{E_{eq}} \frac{h_{AC}}{24} \sum_{i=1}^4 \left((\varepsilon_i^{cr} - \varepsilon_{oACi}^{cr}) * \left((3i-2) * \frac{h_{AC}}{4} - 3x \right) + (\varepsilon_{i+1}^{cr} - \varepsilon_{oACi+1}^{cr}) * \left((3i-1) * \frac{h_{AC}}{4} - 3x \right) \right) \right) \quad (3-83)$$

where:

ΔT^{cr} = difference between the top and bottom surface creep strains in the equivalent single layer slab

ε_i^{cr} and ε_{oi}^{cr} = creep strains and the reference creep strains at point i , respectively

Additional Stresses in the Composite Pavements Due to Non-linear-strain-causing Temperature and Non-linear-strain-causing Creep Strains Components

As discussed in Part 3.2, it was shown by Khazanovich (1994) that any arbitrary temperature profile could be separated into three components: constant-strain-causing temperature component, linear-strain-causing temperature component, and nonlinear-strain-causing temperature component. The constant-strain-causing temperature component does not cause stresses if the pavement is free to expand and contract. The linear-strain-causing temperature component produces bending stresses that can be calculated from the FE solution for bending of an equivalent single layer slab subjected to an equivalent linear temperature gradient determined from Equation (3-82). The nonlinear-strain-causing temperature component produces self-equilibrating stresses.

The total temperature at any point in the slab can be presented in terms of the various temperature components. Therefore, the nonlinear-strain-causing temperature component is given as:

$$T_{NL}(z) - T_o(z) = T(z) - [T_c(z) - T_o(z)] - [T_L(z) - T_o(z)] - T_o(z) \quad (3-84)$$

where:

T = temperature at the point of interest in the composite pavement
 z = depth of the point of interest from the neutral axis,
 T_o = reference temperature
 T_c = constant-strain-causing temperature component
 T_L = linear-strain-causing temperature component
 T_{NL} = nonlinear-strain-causing temperature component

The stress due to the nonlinear-strain-causing temperature component, σ_{NL} is equal to:

$$\sigma_{NL}(z) = -\frac{E(z)\alpha(z)}{(1-\mu)}(T_{NL}(z) - T_o(z)) \quad (3-85)$$

where:

E , α , and μ = Young's modulus, coefficient of thermal expansion, and Poisson's ratio, respectively, at the point of interest

For the case of a single layer viscoelastic slab, creep strains are linear through the slab thickness. However, for a multi-layer slab, this is not necessarily the case. Similarly to the nonlinear-strain-causing temperature component, the nonlinear-strain-causing creep strain component is defined as:

$$\{\varepsilon_{NL}^{cr}(z)\} - \{\varepsilon_0^{cr}(z)\} = \{\varepsilon^{cr}(z)\} - [\{\varepsilon_c^{cr}(z)\} - \{\varepsilon_0^{cr}(z)\}] - [\{\varepsilon_L^{cr}(z)\} - \{\varepsilon_0^{cr}(z)\}] - \{\varepsilon_0^{cr}(z)\} \quad (3-86)$$

where:

ε^{cr} = creep strain at the point of interest in the composite pavement
 z = depth of the point of interest from the neutral axis
 ε_0^{cr} = reference creep strain
 ε_c^{cr} = constant-strain-causing creep strain component
 ε_L^{cr} = linear-strain-causing creep strain component
 ε_{NL}^{cr} = nonlinear-strain-causing creep strain component

The stress due to the nonlinear-strain-causing creep strain component, σ_{NL}^{cr} is given as:

$$\{\sigma_{NL}^{cr}(z)\} = -[\bar{D}](\{\varepsilon_{NL}^{cr}(z)\} - \{\varepsilon_0^{cr}(z)\}) \quad (3-87)$$

where:

$[\bar{D}]$ = material property matrix defined in Equation (3-58)

Total Stress in the Composite Pavements

Finally, the total stress at any point in the multi-layered composite pavement at any time t can be written as:

$$\sigma(x, y, z, t) = \beta(z) * \sigma_{eq}(x, y, t) + \sigma_{NL}(z) + \sigma_{NL}^{cr}(x, y, z, t) \quad (3-88)$$

$$\beta(z) = \frac{2z}{h_{eq}} \frac{E(z)}{E_{eq}} \quad (3-89)$$

where:

β = is the factor that converts the linear bending stresses at the bottom of the equivalent single layer slab to the linear bending stresses in the multi-layered slab at the depth of interest z

σ_{eq} = stress at the bottom surface of the equivalent single layer slab

σ_{NL} = stress due to the nonlinear-strain-causing temperature component at the depth of interest

σ_{NL}^{cr} = stress due to the nonlinear-strain-causing creep stain component at the depth of interest

3.2.4 Step-by-Step Procedure for Computing the Stresses in the Composite Pavement

In this section, the step-by-step procedure used to develop the FE code based on the FE formulation is presented. The FE code was programmed using the programming language FORTRAN 90 (*Visual Numerics, Inc. 1997*) and the commercial package MATHEMATICA (*Wolfram Research, Inc. 1988*).

Step 1: Read inputs. The input file format mirrors an ISLAB2000 input file. The inputs required for the analysis of composite pavements include slab size, mesh configuration, layer properties, interface conditions, properties of the Winkler foundation, temperature profile, and traffic loading. Additional inputs such as number and size of time increments and coefficients of the Prony series for representing the viscoelastic AC layer (or viscoelastic Winkler foundation, if present) were also included in the input file.

Step 2: Determine the equivalent single layer slab parameters. The thickness and unit weight for an equivalent single layer slab with a Young's modulus of 4.0E+6 psi and coefficient of thermal expansion of 5.5E-6 1/°F are computed depending on the interface conditions of the composite pavement. Also, the equivalent linear temperature gradient in the equivalent single layer slab

and the corresponding non-linear-strain-causing temperature stresses in the composite pavement are computed. Appendix A details the procedure adopted in this step for different interface conditions in the composite pavement.

Step 3: Generate a finite element mesh. A finite element mesh consisting of regular four-node rectangular plate elements with three degrees of freedom per node is generated over the dimensions of the equivalent single layer slab.

Step 4: Compute the stiffness matrix. The element stiffness matrix $\{K\}_e$ is computed using Equation (3-59). The boundary conditions present due to contact of the equivalent single layer slab with the spring formulation of the Winkler foundation are enforced on the element stiffness matrix. Finally, the global stiffness matrix $[K]$ is generated by assembling the element stiffness matrix for each element at the appropriate global degree of freedom. The global stiffness matrix is generated in sparse format.

Step 5: Compute the global force vector. The forces due to traffic loading, self-weight of the slab, thermal strains, and creep strains are computed at time t_j . At the initial time t_1 , the fictitious forces due to creep strains are equal to zero. The global forces acting on the equivalent single layer slab are calculated by adding all the forces at the appropriate degree of freedom for each element.

Step 6: Compute displacements. Using Cholesky's factorization, the system of equations (78) is solved to find the global displacements.

Step 7: Check contact condition. The contact between the equivalent single layer slab and the Winkler foundation is checked using the vertical displacement of the nodes. If the vertical displacement at a plate node is positive, it indicates that the node is in contact with the foundation. If the vertical displacement at a node is negative, it indicates that node is not in contact with the foundation. The change in sign of a nodal displacement between one time step and the next implies that the contact condition at the node has changed. The foundation stiffness matrix $[K_{dd \text{ foundation}}]_e$ is then revised for those nodes and the global stiffness matrix $[K]$ is updated to reflect the change. Steps 4 and 6 are repeated if the contact condition changes between any two time steps.

Step 8: Compute stresses in the equivalent single layer slab. The total strain and elastic stress in the equivalent single layer slab are computed using equations (61) and (79), respectively, at time t_j .

Step 9: Compute creep strains. The increment of creep strains corresponding to the i -th term of the Kelvin-Voigt element are computed using Equation (3-67) at time t_j . The resulting creep strain for each Kelvin-Voigt element and the total creep strain in the equivalent single layer slab at time t_j are updated.

Step 10: Calculate nodal stresses. The average stress at each node at the top and bottom of the equivalent single layer slab is computed at time t_j . Further, the stresses for each layer of the composite pavement system are computed. For example, the total stresses at the top and bottom of the PCC layer of the composite pavement are calculated as follows:

$$\sigma_{PCC,Top} = \frac{2 * (-x + h_{AC})}{h_{eq}} \sigma_{eq} + \sigma_{NL,top} + \sigma_{NL,top}^{cr} \quad (3-90)$$

$$\sigma_{PCC,Bot} = \frac{2 * (h_{PCC} + h_{AC} - x)}{h_{eq}} \sigma_{eq} + \sigma_{NL,bot} + \sigma_{NL,bot}^{cr} \quad (3-91)$$

Repeat steps 5 to 10 for the next time t_{j+1} .

Step 11: Output results. The displacement and stresses in the composite pavement at each node are printed in ISLAB2000 output format.

3.2.5 Validation of the Finite Element Model

The FE model presented in the preceding sections has the capability of analyzing a multi-layered pavement incorporating elastic and/or viscoelastic layers placed over an elastic or a viscoelastic Winkler foundation. This section presents simple examples validating the finite element implementation. The following cases are considered:

1. A viscoelastic plate placed on a viscoelastic Winkler foundation,
2. A viscoelastic plate with simply supported corners,
3. Verification of formation for multi-layered slabs, and
4. Sensitivity of the viscoelastic FE model to internal parameters.

Viscoelastic Plate on Viscoelastic Winkler Foundation

To verify the FE code, a semi-analytical solution is obtained for a viscoelastic plate placed on the viscoelastic Winkler foundation when the creep compliance functions of the viscoelastic plate and the viscoelastic Winkler foundation are proportional. The semi-analytical solution is compared with the finite element solution.

The governing equation for an elastic plate resting on an elastic Winkler foundation has the following form (*Timoshenko and Woinowsky-Krieger 1959*):

$$D_0 \nabla^4 w(x) + k_0 w(x) = p(x) \quad (3-92)$$

where:

w = deflection of the plate

k_0 = coefficient of subgrade reaction of the Winkler foundation

p = load per unit area acting on the plate

x = spatial coordinates x , y , and z

D_0 = stiffness of the plate given as follows:

$$D_0 = \frac{E_0 h^3}{12(1 - \mu^2)} \quad (3-93)$$

where:

E_0 = Young's modulus of the plate
 h = thickness of the plate
 μ = Poisson's ratio

Consider a viscoelastic plate resting on a viscoelastic Winkler foundation. The governing equation for the plate can be written as (Li et al. 2009):

$$\tilde{D}\nabla^4 w(x,t) + \tilde{k}w(x,t) = p(x,t) \quad (3-94)$$

where:

$w(x,t)$ = deflection of the viscoelastic plate at time t
 $p(x,t)$ = load per unit area acting on the viscoelastic plate at time t
 \tilde{D} = stiffness of the viscoelastic plate, is an operator defined as:

$$\tilde{D}f(t) = \frac{E_0 h^3}{12(1-\mu^2)} \tilde{J}^{*-1} f(t) = D_0 \tilde{J}^{*-1} f(t) \quad (3-95)$$

\tilde{k} = operator of subgrade reaction of the viscoelastic foundation relating the deflection of the subgrade with the history of the applied pressure at the same point.

Assume that the operator of subgrade reaction has the following form:

$$\tilde{k}f(t) = k_0 \tilde{J}^{*-1} f(t) \quad (3-96)$$

The operator \tilde{J}^* is the normalized creep compliance operator defined using equations (32) and (43) as follows:

$$\tilde{J}^* f(t) = \frac{\tilde{J}f(t)}{J(0)} \quad (3-97)$$

The creep compliance of operators \tilde{D} and \tilde{k} is proportional. By substituting equations (95) and (96) in (94), we get:

$$D_0 \tilde{J}^{*-1} \nabla^4 w(x,t) + k_0 \tilde{J}^{*-1} w(x,t) = p(x,t) \quad (3-98a)$$

or

$$D_0 \nabla^4 (\tilde{J}^{*-1} w(x,t)) + k_0 (\tilde{J}^{*-1} w(x,t)) = p(x,t) \quad (3-98b)$$

Now, a fictitious deflection w_1 is introduced such that:

$$w_1(x, t) = \tilde{J}^{*-1} w(x, t) \quad (3-99)$$

Substituting Equation (3-99) into Equation (3-98) results in:

$$D_0 \nabla^4 w_1(x, t) + k_0 w_1(x, t) = p(x, t) \quad (3-100)$$

For any time t , Equation (3-100) is identical to the governing equation for an elastic plate placed on the elastic Winkler foundation. If the plate is loaded so that:

$$\begin{aligned} p(x, t) &= p_0(x)H(t) \\ H(t) &= \begin{cases} 1 & \text{if } t \geq 0 \\ 0 & \text{if } t < 0 \end{cases} \end{aligned} \quad (3-101)$$

where:

$H(t)$ = Heaviside step function, then the deflection of the plate has the following form:

$$w_1(x, t) = w_1(x)H(t) \quad (3-102)$$

If a solution of the elastic problem is obtained analytically or numerically, then the solution of the corresponding viscoelastic problem can be obtained as follows:

$$w(x, t) = \tilde{J}^*(w_1(x)H(t)) \quad (3-103)$$

It can be also easily shown that for this boundary value problem the stresses in the viscoelastic plate are proportional to the applied loading. Since the applied load does not change in time for $t \geq 0$, the stresses in the viscoelastic slab do not vary with time for $t \geq 0$.

To verify the finite element program, a semi-analytical solution was obtained and compared with the finite element solution in which a 15 ft long, 12 ft wide, and 9 in-thick viscoelastic plate was placed on a viscoelastic Winkler foundation. The plate was loaded with a constant 100 psi pressure acting at the center of the slab over a footprint of 60 in x 48 in. An uniform mesh of element size equal to 6 in was generated on the plate surface. The load and mesh configuration are shown in Figure 3-12.

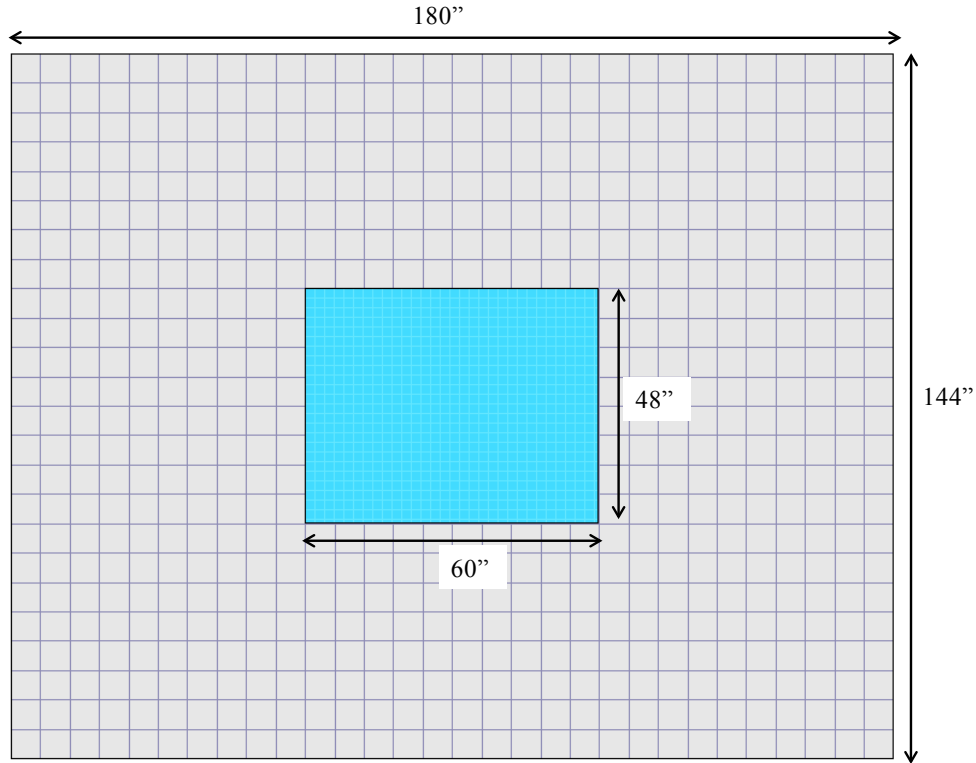


Figure 3-12: Mesh and load configuration for the composite pavement subjected to a wheel load.

The creep compliance of the viscoelastic material is represented by a Prony series in the form of a two-term generalized Kelvin-Voigt model presented in Figure 3-9. Table 3-1 lists the parameters of the Kelvin-Voigt model used to define the creep compliance function for the viscoelastic plate and the viscoelastic Winkler foundation.

Table 3-1: Parameters of the Kelvin-Voigt model for the plate and Winkler foundation.

Instantaneous modulus		Normalized creep compliance parameters			
Viscoelastic plate	Viscoelastic Winkler foundation	Spring stiffness		Dashpot viscosity	
E_0 , psi	k_0 , psi/in	E_1^*	E_2^*	η_1^*	η_2^*
4.0e6	100	0.0238	0.0254	2.8269	0.2494

The FE solution is obtained by executing the FE code for a viscoelastic plate placed on a viscoelastic Winkler foundation. The semi-analytical solution for deflections at any time t is derived by multiplying the elastic deflections at the initial time $t = 0$ obtained from the FE solution with the operator \tilde{J}^* , as given in Equation (3-103). Figure 3-13 presents the deflections computed using the FE model and the semi-analytical solution for a total time of 400 seconds. A good agreement is found between the deflections obtained from the semi-analytical solution and the FE solution.

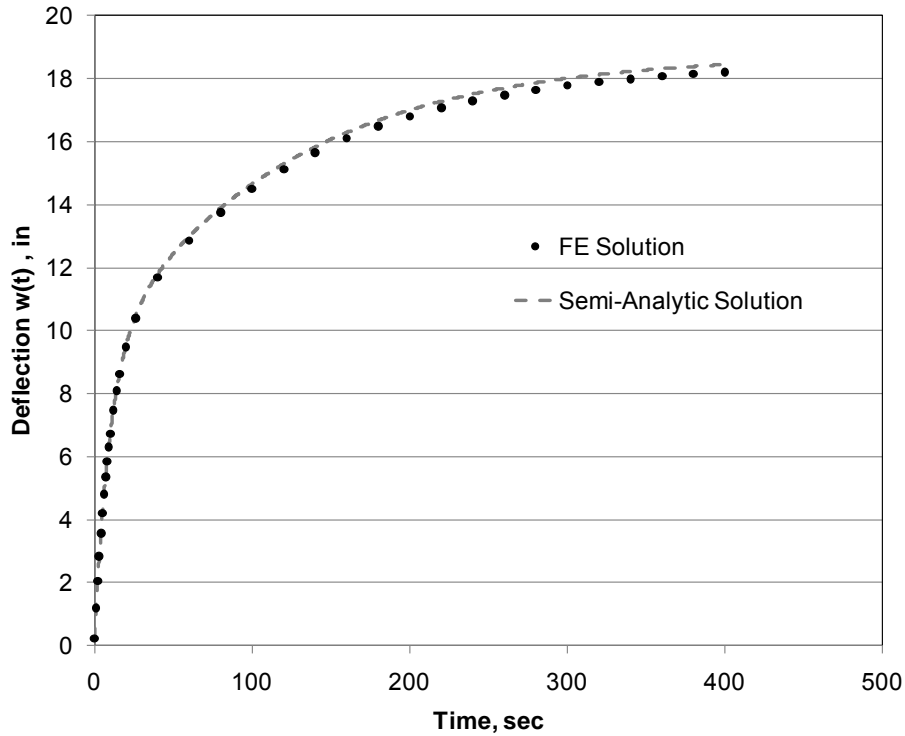


Figure 3-13: Comparison of deflections for a viscoelastic plate placed on a viscoelastic Winkler foundation.

Figure 3-14 presents the bottom surface stress at the center of the plate computed using the FE model for a total time of 400 seconds.

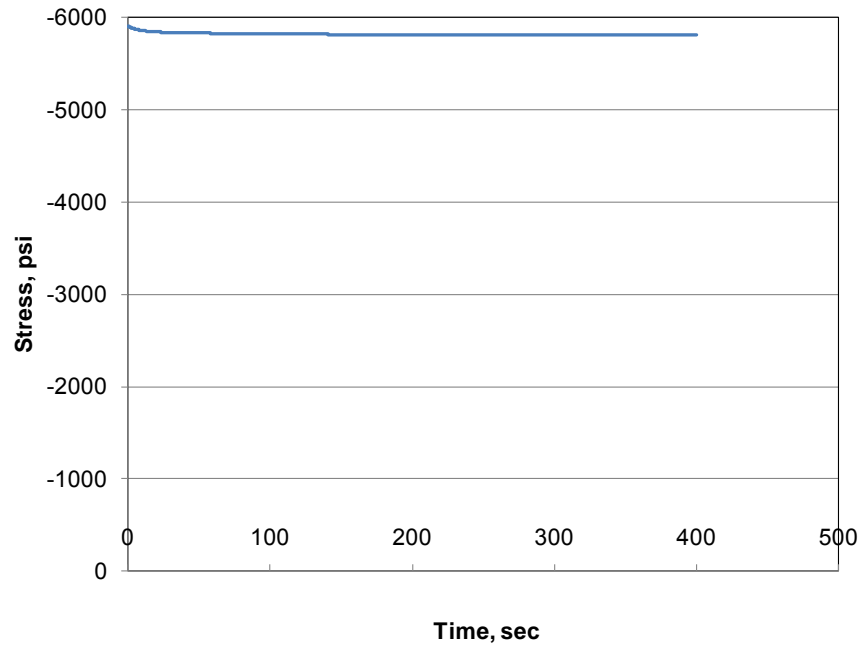


Figure 3-14: Stress at the bottom of the viscoelastic plate placed on viscoelastic Winkler foundation.

A small variation is observed in the stresses at the bottom of the viscoelastic plate during the initial increments of time. Since the time is discretized into small intervals, the observed error is attributed to the size of the time interval selected.

Viscoelastic Plate with Simply Supported Corners

Consider a viscoelastic plate supported at the corners so that the vertical deflections of the corners are equal to zero. The solution of the plate can be derived if appropriate boundary conditions are satisfied. The governing equation and the boundary conditions are given as follows:

$$\tilde{D}\nabla^4 w(x,t) = p(x,t) \quad (3-104)$$

and

$$w(x,t) = 0 \quad \text{for } x \in S \quad (3-105)$$

where:

- \tilde{D} = stiffness operator for the viscoelastic plate defined by Equation (3-95)
- $w(x,t)$ = deflection of the plate at time t
- $p(x,t)$ = applied load at time t and is defined by Equation (3-101)
- S = set of spatial coordinates at which the boundary conditions are imposed

Applying equations (3-95) and (3-99) to Equation (3-104) yields the following equation:

$$D_0\nabla^4 (\tilde{J}^{*-1} w(x,t)) = p(x,t) \quad (3-106a)$$

or

$$D_0\nabla^4 (w_1(x,t)) = p(x,t) \quad (106b)$$

Multiplying both sides of Equation (3-105) by the operator \tilde{J}^* from the left and applying Equation (3-99) leads to the following:

$$\tilde{J}^{*-1} w(x,t) = \tilde{J}^{*-1} 0 \quad \text{for } x \in S \quad (3-107a)$$

or

$$w_1(x,t) = 0 \quad \text{for } x \in S \quad (3-107b)$$

Equations (106b) and (107b) are identical to the governing equation and boundary condition, respectively, for an elastic plate with simply supported corners. This implies that Equation (3-103), which relates the viscoelastic deflections to the elastic deflections as a function of the

operator \tilde{J}^* at any time t , is also a solution for a viscoelastic plate with simply supported corners. The solution given by Equation (3-103) is used to verify the FE solution for a viscoelastic plate with simply supported corners.

A 15 ft long, 12 ft wide, and 9 in thick viscoelastic plate with simply supported corners is analyzed using the FE model. The plate is loaded with a 100 psi pressure over a footprint of 60 in x 48 in at all times as shown in Figure 3-12. The creep compliance function for the viscoelastic plate is defined using the parameters of the Kelvin-Voigt model presented in Table 3-1.

The FE solution for the deflections of the viscoelastic plate with simply supported corners is obtained by executing the FE code. The semi-analytical solution for deflections at any time t is derived by multiplying the elastic deflections at the initial time $t = 0$ obtained from the FE solution with the operator \tilde{J}^* . Figure 3-15 presents the comparison of deflections computed using the FE model and the semi-analytical solution for a total time of 400 seconds.

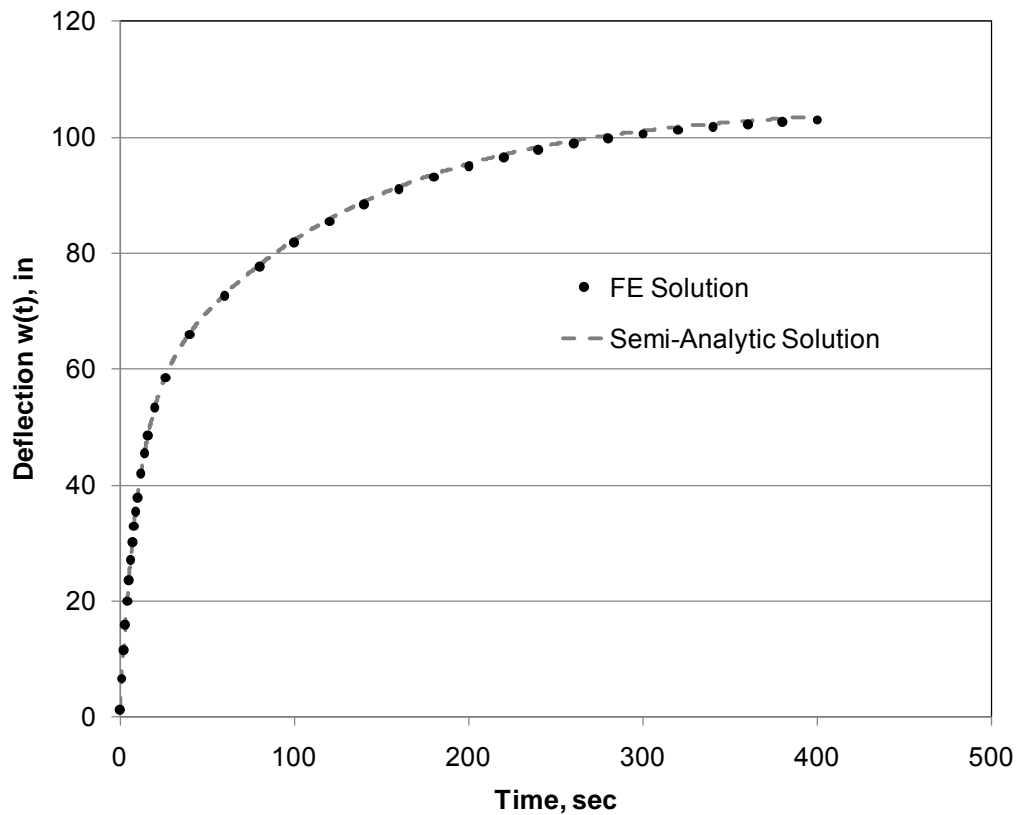


Figure 3-15: Comparison of deflections for a viscoelastic plate with simply supported corners.

The deflections obtained from the semi-analytical solution and the FE solution for a viscoelastic plate with simply supported corners match well.

Verification of the Formation for Multi-Layered Slabs

The FE code has built-in functionality to analyze single-layer, two-layered and three-layered pavements. To verify the ability of the FE code to analyze a multi-layered slab-on-grade, several verification examples were considered. A multi-layered composite slab resting on an elastic Winkler foundation was loaded with 100 psi of pressure acting in the form of a single axle dual wheel configuration. The size of the slab was 180 in x 144 in. The coefficient of subgrade reaction for the elastic Winkler foundation was equal to 100 psi/in. A uniform mesh of element size 6 in x 6 in was generated as shown in Figure 3-16.

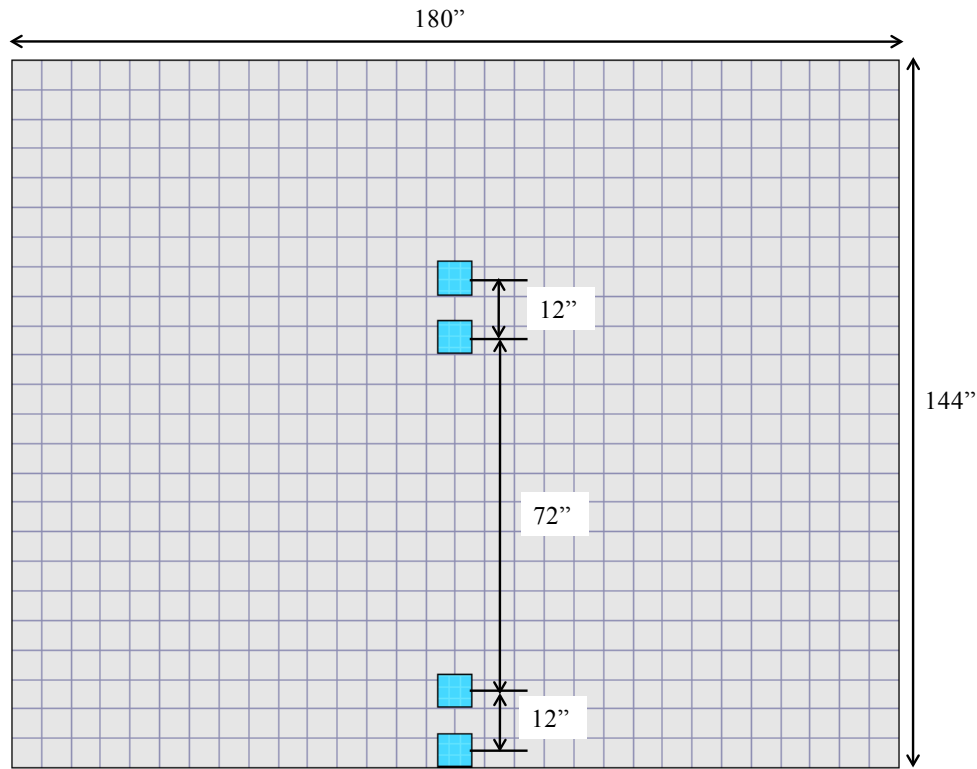


Figure 3-16: Mesh and loading configuration for the composite pavement subjected to a single-axle dual-wheel load.

Elastic and viscoelastic analyses were conducted to verify the ability of the FE code to analyze a multi-layered slab-on-grade. If the FE code is robust, the stresses at a particular point obtained from the analysis of a three-layered pavement system and a corresponding single-layer (or two-layered) system must be equal. It must be noted that all the layers of the three-layered slab and the layer(s) of the corresponding single or two-layered slab should have the same Poisson's ratio μ .

The elastic analysis was conducted at the initial time ($t = 0$). Table 3-2 presents the layer properties for the following cases considered for the elastic analysis:

- Case 1 – To verify the ability of the FE code to analyze single-layer systems, a three-layer slab-on-grade is compared with a corresponding single-layer slab-on-grade when all

layers have the same material properties. In this case, the thickness of the corresponding single-layer slab is equal to the sum of the thicknesses of all the layers of the three-layer slab.

- Case 2 – To verify the ability of the FE code to analyze two-layered systems, a three-layer slab-on-grade was compared with a corresponding two-layer slab-on-grade. The first and second layers of the three-layer slab had the same material properties, and the thickness of the first layer of the corresponding two-layer slab was equal to the sum of the thicknesses of the first and second layers of the three-layer slab.
- Case 3 – The ability of the FE code to analyze a three-layer system is verified when one of the layers is eliminated by setting its thickness equal to zero. In this case, a corresponding two-layer slab-on-grade is analyzed with the same layer thicknesses and material properties as those for the second and third layers of the three-layer slab.

Table 3-2: Layer properties for the elastic analysis.

	Three-layered pavement		Single- / two-layered pavement	
Case 1	h1 = 9 in	E = 4.0E+06 psi	h = 20 in	E = 4.0E+06 psi
	h2 = 5 in	E = 4.0E+06 psi		
	h3 = 6 in	E = 4.0E+06 psi		
Case 2	h1 = 9 in	E = 4.0E+06 psi	h1 = 14 in	E = 4.0E+06 psi
	h2 = 5 in	E = 4.0E+06 psi		
	h3 = 6 in	E3 = 4.0E+04 psi	h2 = 6 in	E2 = 4.0E+04 psi
Case 3	h1 = 0 in	E1 = 2.0E+05 psi	h1 = 5 in	E1 = 4.0E+06 psi
	h2 = 5 in	E2 = 4.0E+06 psi	h2 = 6 in	E2 = 4.0E+04 psi
	h3 = 6 in	E3 = 4.0E+04 psi		

Figure 3-17 presents the comparison of stresses at the bottom of the second layer of a three-layered system at the center of the slab.

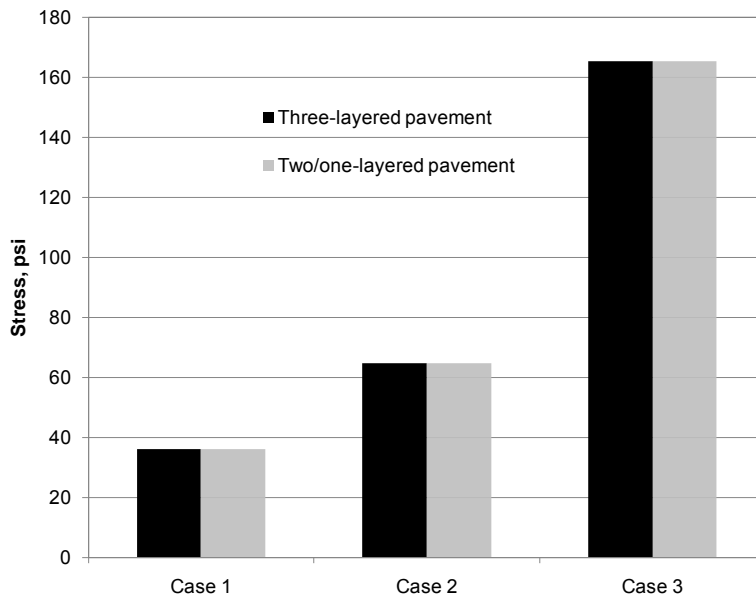


Figure 3-17: Stress from three-layered analysis versus single- or two-layered analyses.

Next, a viscoelastic analysis is conducted with a 9 in thick viscoelastic surface layer (layer 1) for the multi-layered slab. The creep compliance function for the first layer is represented using the generalized two-term Kelvin-Voigt model. The parameters of the Kelvin-Voigt model are presented in Table 3-3.

Table 3-3: Kelvin-Voigt parameters for the viscoelastic surface layer.

Element #	Spring stiffness, psi	Dashpot viscosity, psi-sec
0	200000	--
1	95265	11307535
2	101500	997600

For all the cases in the viscoelastic analysis, the stresses from a three-layered pavement system are compared with the stresses from a corresponding two-layered system.

- Case 4 – The ability of the FE code to perform a viscoelastic analysis for multi-layered systems was verified. The second and third layers of the three-layered slab have the same material properties. The thickness of the second layer of a corresponding two-layer slab was equal to the sum of thicknesses of the second and third layers of the three-layer slab.
- Case 5 – The ability of the FE code to perform a viscoelastic analysis was verified when the second layer of the three-layer slab was eliminated by setting its thickness equal to zero. In this case, a corresponding two-layered slab-on-grade was analyzed with layer thicknesses and material properties the same as those for the first and third layers of the three-layer slab.
- Case 6 – This case is similar to case 5 but the third layer of the three-layer slab was eliminated by setting its thickness equal to zero.

Table 3-4 presents the properties of the underlying layers of the multi-layered pavements considered for the viscoelastic analysis.

Table 3-4: Layer properties for multi-layered composite pavements.

	Three-layered pavement (3LS)		Two-layered pavement (2LS)	
Case 4	h2 = 5 in	E2 = 4.0E+06 psi	h2 = 11 in	E2 = 4.0E+06 psi
	h3 = 6 in	E3 = 4.0E+06 psi		
Case 5	h2 = 0 in	E2 = 4.0E+06 psi	h2 = 6 in	E2 = 4.0E+04 psi
	h3 = 6 in	E3 = 4.0E+04 psi		
Case 6	h2 = 5 in	E2 = 4.0E+06 psi	h2 = 5 in	E2 = 4.0E+06 psi
	h3 = 0 in	E3 = 4.0E+04 psi		

Figures 18 and 19 present the comparison of stresses at the bottom of the viscoelastic surface layer (layer 1) at the center of the slab.

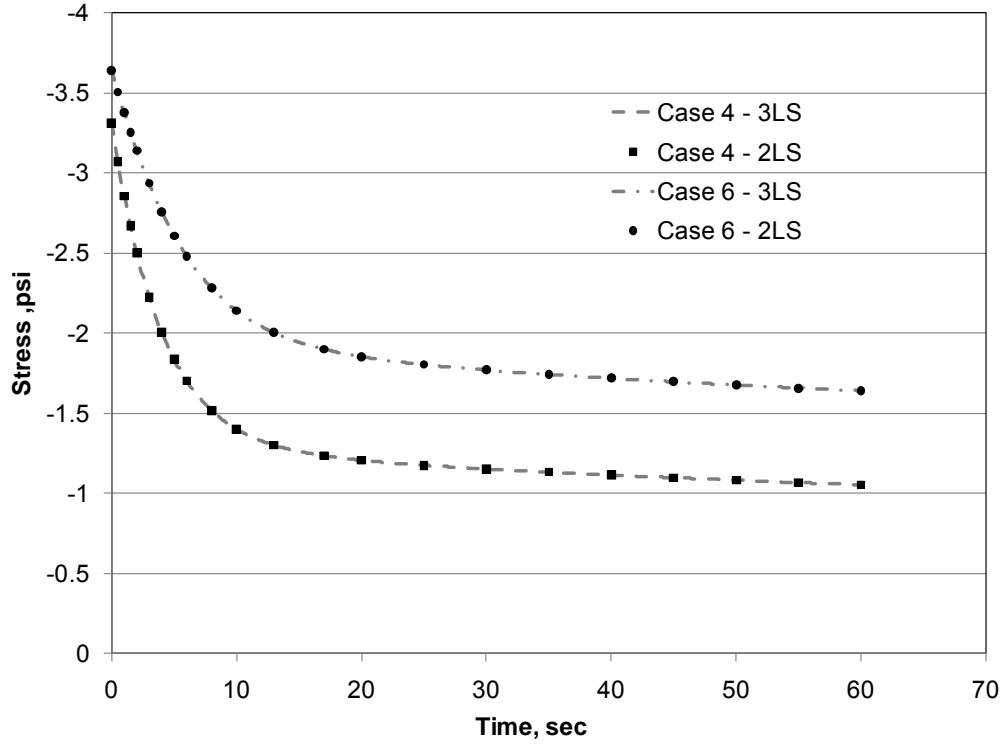


Figure 3-18: Stress versus time for cases 4 and 6 using the viscoelastic FE model.

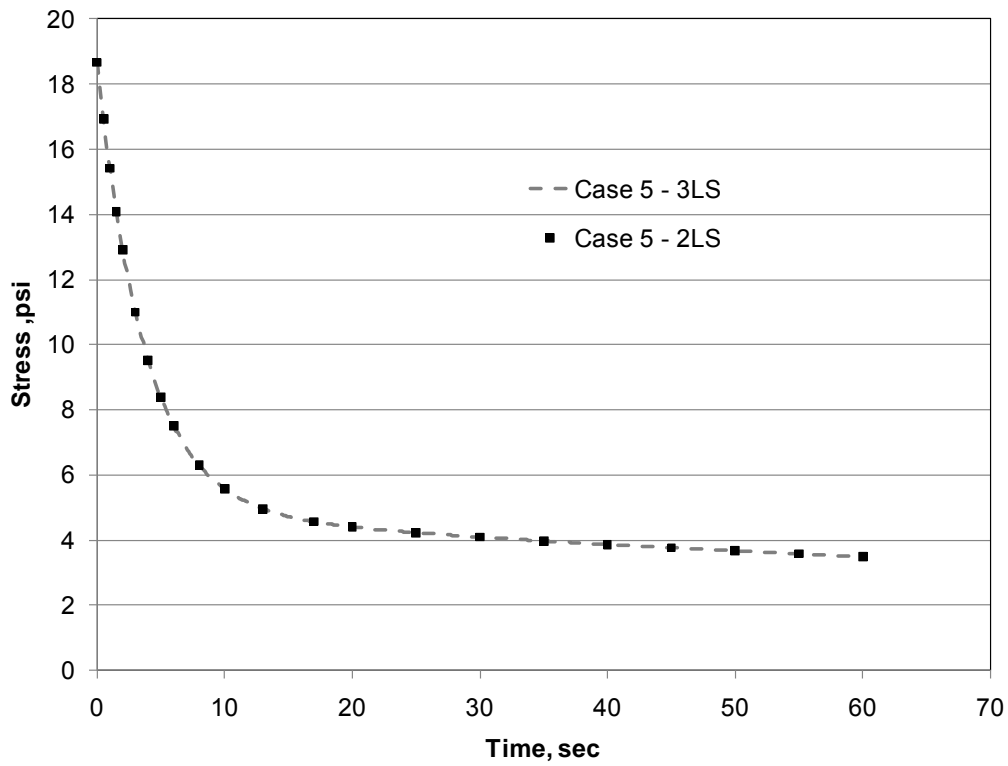


Figure 3-19: Stress versus time for case 5 using the viscoelastic FE model.

Excellent agreement is obtained between the stress from the three-layered analyses and that from the single- or two-layered analyses for all cases.

Sensitivity of the Viscoelastic FE Model to Internal Parameters

The sensitivity of the FE model to the following internal parameters was verified:

1. Implementation of creep compliance function using the Prony series
 - a. Parameters of the Kelvin-Voigt element
 - b. Number of Kelvin-Voigt elements
2. Presence of the viscoelastic layer

Sensitivity of the FE Model to Parameters of Kelvin-Voigt Element. As established previously, the creep compliance function is commonly expressed in the form of an N -term Prony series. For each term of the Prony series there are two coefficients defining the stress-strain relationship of a viscoelastic material. These coefficients can be interpreted as the spring stiffness and dashpot viscosity of commonly adopted physical models such as the Kelvin-Voigt model. In this example, sensitivity of the FE model to the parameters of the Kelvin-Voigt model is verified.

Consider the single layer viscoelastic plate with geometry, mesh, and loading geometry as shown in Figure 3-12. The plate rests on an elastic Winkler foundation with a coefficient of subgrade reaction equal to 100 psi/in. The viscoelastic material characterization of the plate is defined using the spring and dashpot properties of a one-term Kelvin-Voigt element connected to an elastic spring, presented in Table 3-5.

Table 3-5: Parameters of the Kelvin-Voigt element for the viscoelastic plate.

Element #	Spring stiffness, psi	Dashpot viscosity, psi-sec
0	98988.175	--
1	95265	1.0E+04 to 1.0E+07

The dashpot viscosity of the Kelvin-Voigt element is varied between 1.0E+04 psi-sec and 1.0E+07 psi-sec (1.0E+04, 1.0E+05, 2.0E+05, 4.0E+05, 1.0E+06, 1.0E+07). Deflections and stresses in the plate under the applied load are computed using the FE model. Figures 20 and 21 show the deflections and top surface stresses at the plate center versus time, respectively, for the factorial of dashpot viscosities of the Kelvin-Voigt element.

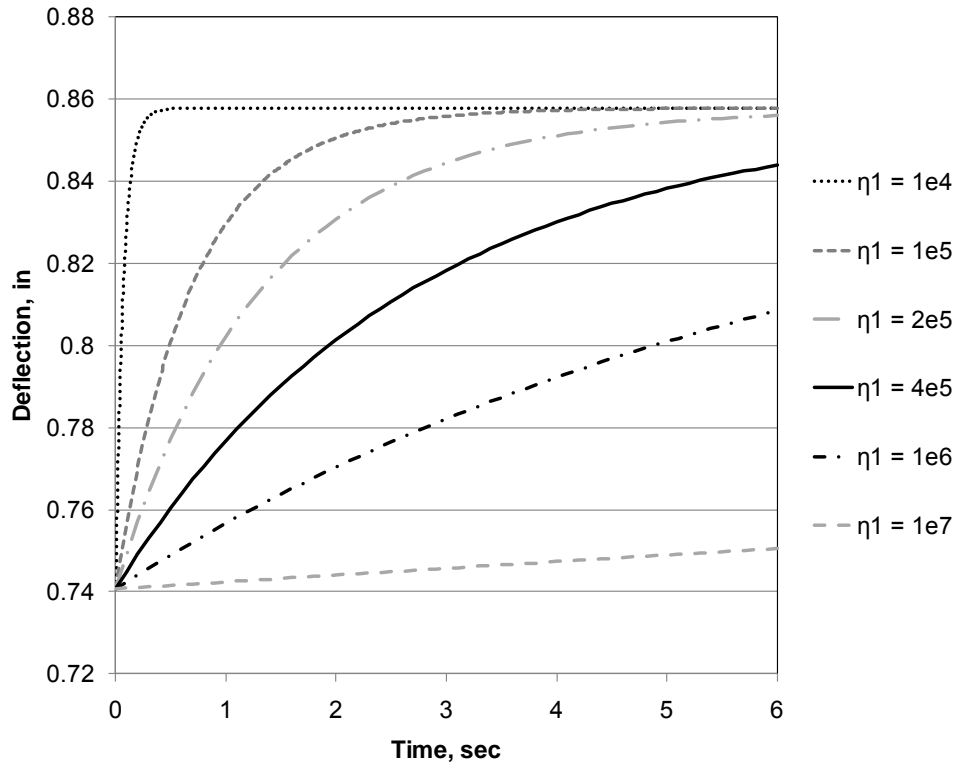


Figure 3-20: Deflection versus time for a factorial of dashpot viscosities of the Kelvin-Voigt element.

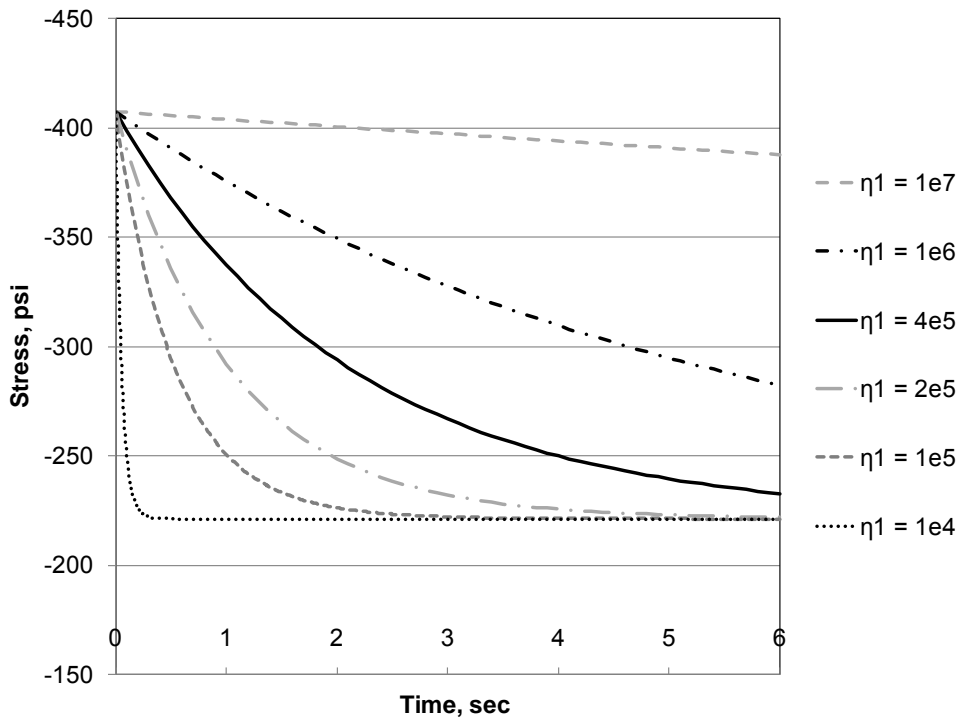


Figure 3-21: Stress versus time for a factorial of dashpot viscosities of the Kelvin-Voigt element.

The deflection and stress for the factorial of dashpot viscosities vary between the deflection and stress for the extreme values of the viscosity considered. Therefore, it can be said that the viscoelastic FE model is not sensitive to the parameters of the Kelvin-Voigt element.

Sensitivity of the FE Model to the Number of Kelvin-Voigt Elements. Consider the single layer viscoelastic plate presented in Figure 3-12. The plate rests on an elastic Winkler foundation with the coefficient of subgrade reaction equal to 100 psi/in. To verify the sensitivity of the viscoelastic FE model on the number of Kelvin-Voigt elements adopted to represent the creep compliance function, the viscoelastic behavior of the plate is defined using two material models considered as follows:

1. Material model 1 – a single Kelvin-Voigt model attached to an elastic spring in series as shown in Figure 3-13(a), and
2. Material model 2 – a two-element generalized Kelvin-Voigt model attached to an elastic spring in series as shown in Figure 3-13(b).

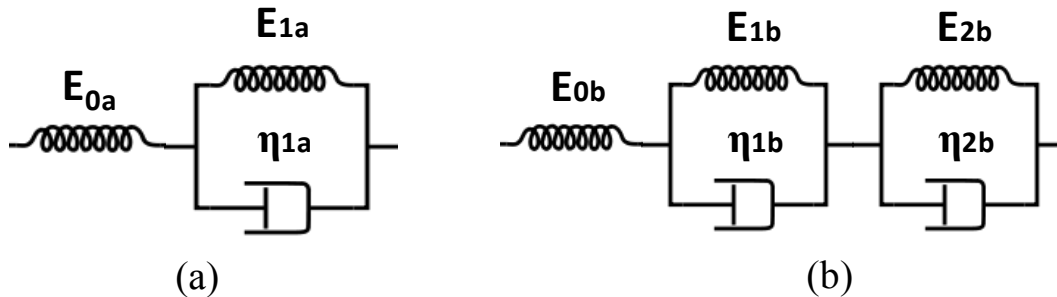


Figure 3-22: Schematic for (a) material model 1 and (b) material model 2.

The parameters of material models 1 and 2 are presented in Table 3-6. Material model 2 is an extension of material model 1. Under certain conditions described below, the creep compliance functions defined by material models 1 and 2 can be exactly equal. In such cases, the deflections and stresses at any node between slabs incorporating material models 1 and 2 should also be exactly equal.

Table 3-6: Prony series coefficients for material models 1 and 2.

Element #	Material Model 1		Material Model 2	
	Spring stiffness, psi	Dashpot viscosity, psi-sec	Spring stiffness, psi	Dashpot viscosity, psi-sec
0	E_{0a}	--	200000	--
1	95265	2.0E+05	95265	2.0E+05
2			101500	η_{2b}

The instantaneous modulus E_{0a} for material model 1 can be expressed using the parameters of material model 2 when the following conditions are present:

$$\frac{1}{E_{0a}} = \frac{1}{E_{0b}} \quad \text{when } \eta_{2b} \text{ is a large value} \quad (3-108)$$

$$\frac{1}{E_{0a}} = \frac{1}{E_{0b}} + \frac{1}{E_{2b}} \quad \text{when } \eta_{2b} \text{ is a small value} \quad (3-109)$$

where:

E_{0a} = instantaneous modulus of material model 1

E_{0b} = instantaneous modulus of material model 2

E_{2b} and η_{2b} = spring stiffness and dashpot viscosity of the second Kelvin-Voigt element of material model 2, respectively

Two values for the dashpot viscosity of the second Kelvin-Voigt element of material model 2 are considered (a) $\eta_{2b} = 1.0\text{E}+13$ and (b) $\eta_{2b} = 1.0\text{E}+03$. The creep compliance function (Equation (3-34)) is plotted for material models 1 and 2 in Figure 3-23 when the instantaneous modulus E_{0a} varies with the dashpot viscosity η_{2b} .

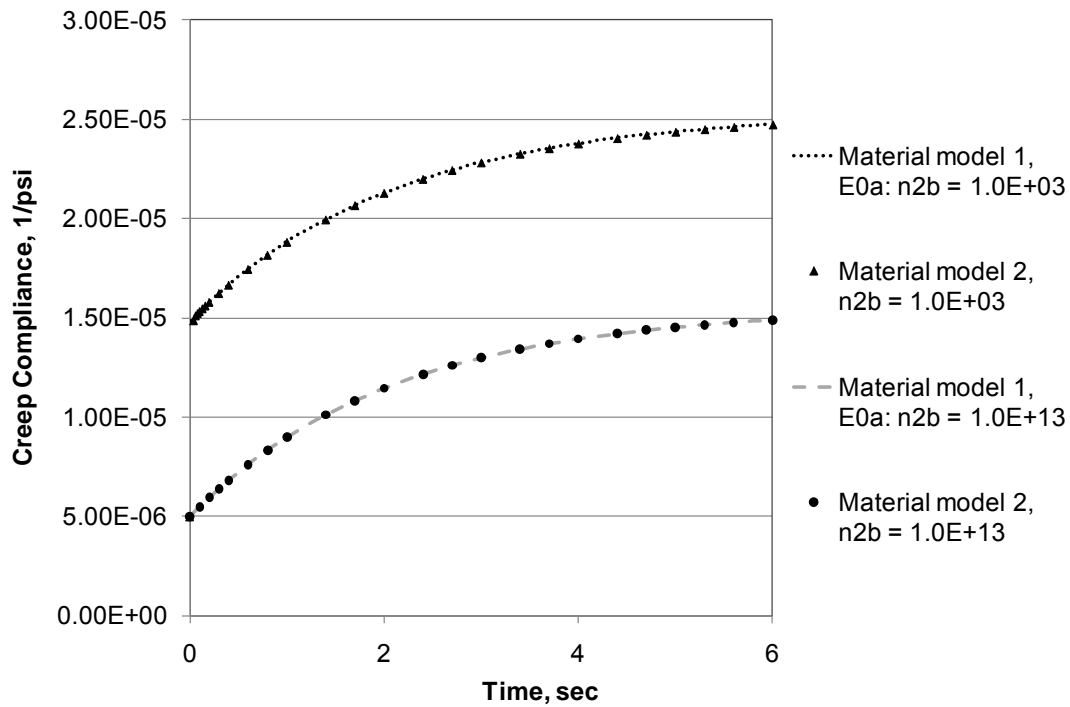


Figure 3-23: Creep compliance for material models 1 and 2.

Further, deflections and stresses in the plate under the applied load are calculated using the FE model. Figures 24 and 25 plot the deflections and bottom surface stresses at the slab center versus time, respectively, for material models 1 and 2.

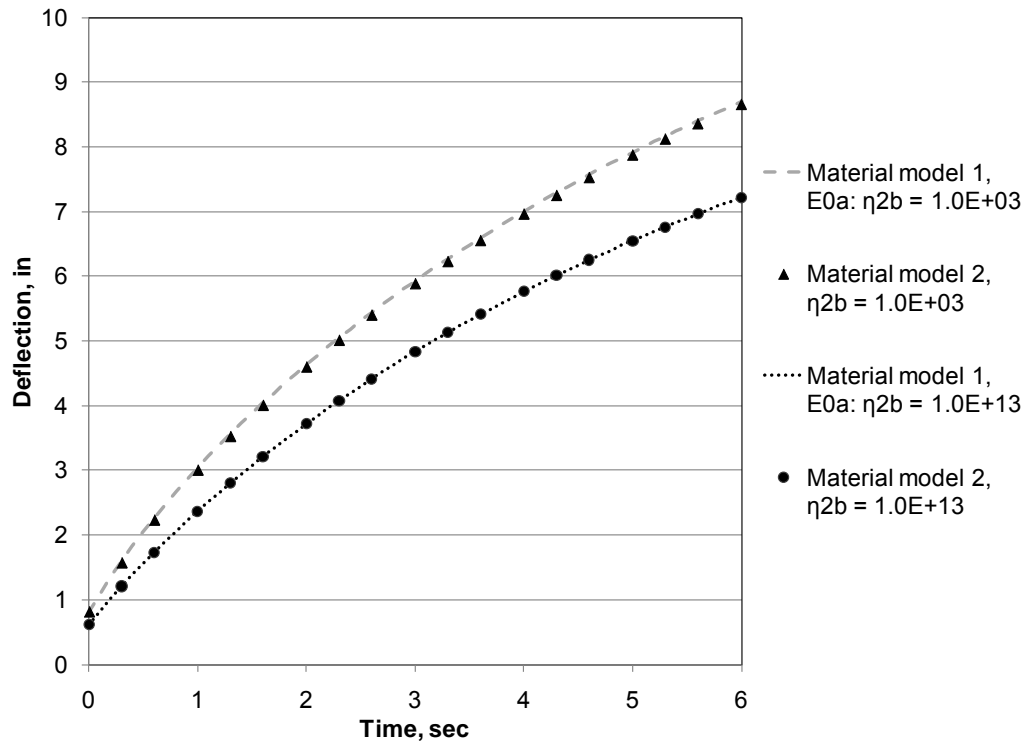


Figure 3-24: Deflection of the plate incorporating material models 1 and 2.

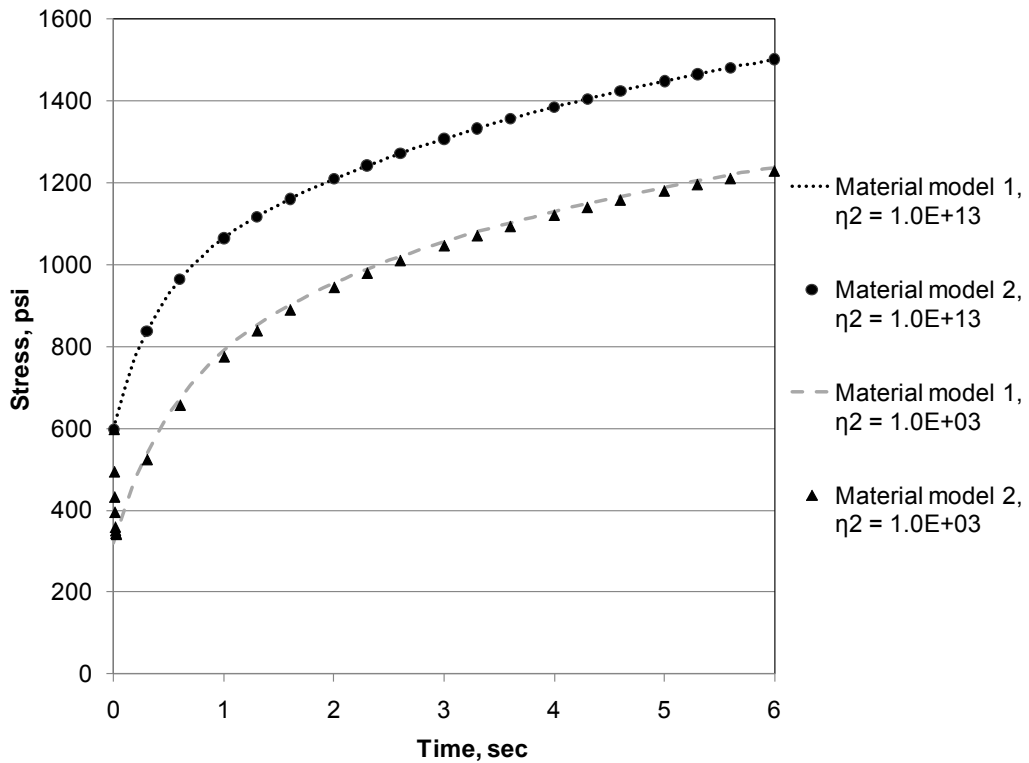


Figure 3-25: Stress at the bottom of the plate incorporating material models 1 and 2.

Excellent agreement is obtained for the creep compliance, deflection, and stress between material models 1 and 2. Therefore, it can be established that the viscoelastic FE model is not sensitive to the number of Kelvin-Voigt elements used in the representation of the creep compliance function.

Sensitivity of the FE Model to the Presence of Viscoelastic Layer. The sensitivity of the FE model to the presence of the viscoelastic AC layer is verified by varying the thickness of the AC layer of the composite pavement. A composite pavement with slab geometry, foundation support, mesh configuration, and wheel loading the same as those presented in Figure 3-16 for this example. A factorial of thicknesses for the AC layer is considered varying between 0 and 9 in (0, 1, 2, 3, 4, 5, 6, 7, 8, and 9). The layer properties for the baseline case are given in Table 3-7. All the layer interfaces are fully bonded. Additionally, an elastic two-layer system consisting of fully bonded PCC and base layers is also considered. The thicknesses and material properties for the PCC and base layers are same as those of the composite pavement.

Table 3-7: Layer properties for the baseline composite pavement.

	Material definition	Thickness, h (in)	Layer modulus, E (psi)	Poisson's ratio, μ	Unit weight, γ (lb/in³)
AC	Viscoelastic	9	Reference Table 3-3	0.15	0.087
PCC	Elastic	5	4.0E+06	0.15	0.087
Base	Elastic	6	4.0E+04	0.15	0.087

Figure 3-26 presents the FE results for PCC bottom stresses at the center of the slab at different times of the viscoelastic analysis. The elastic PCC bottom stresses at the center of the slab from the two-layer system are also shown in the Figure.

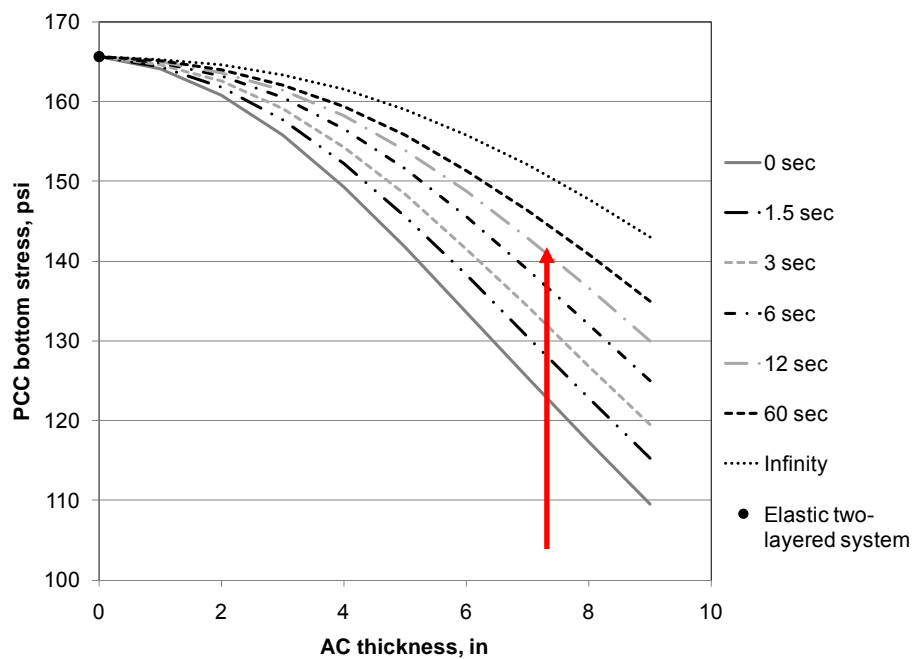


Figure 3-26: PCC bottom stresses versus AC thickness.

As expected, lower values of stress at the bottom of PCC layer are obtained for thicker AC layers at any time t . The stress in the PCC layer converges to the PCC stresses from the elastic two-layer system when the thickness of the AC layer tends to zero at any time t . Also, for any thickness of the AC layer, the stress solution converges as time increases to the stress at infinite time. The difference between the stress at time $t = 0$ and time t at infinity is most prominent for thicker AC layers, and the difference reduces as the thickness of the viscoelastic AC layer reduces.

Thus, the FE model developed under this research is capable of analyzing pavements that incorporate elastic or viscoelastic layers and is not sensitive to the internal parameters used to develop the FE model.

3.3. Stress Solutions Using the 2-Moduli Approach

The Mechanistic Empirical Pavement Design Guide (MEPDG) uses a load duration-dependent dynamic modulus to characterize the constitutive relationship for asphalt concrete (AC). The loading duration for traffic loads depends on the vehicle speed. For a typical interstate pavement with vehicle speeds of roughly 60 mph, the loading duration ranges between 0.01 sec and 0.05 seconds. The analysis of fatigue cracking (i.e. cracking due to repeated traffic loads) in the AC layer for flexible pavements does not involve temperature-induced stresses, which develop much more slowly. The cracking due to temperature gradients is computed separately using a thermal cracking model developed for flexible pavements.

In the case of composite pavements, there is an interaction between curling, which is a rigid pavement phenomenon, and deformations due to traffic loading. Temperature gradients and traffic loads both cause bending stresses that cannot be simply added when composite pavements are subjected to a combination of temperature gradients and instantaneous traffic loads. This is so because temperature curling causes a separation of the slab from the subgrade making the system to behave non-linearly. Moreover, the loading durations of the temperature gradients and fast moving traffic loads are significantly different. Therefore, for the case of composite pavements in the MEPDG framework, the material representation of the AC layer using a single dynamic modulus seems to be an over-simplification.

A finite element (FE)-based model incorporating the viscoelastic behavior of the AC layer in composite pavements was presented in Part 3.2. Although that FE model provides a robust framework for analyzing the viscoelastic slab-on-grade problems, it requires providing the creep compliance of the pavement layer(s), which is not a direct input or output of the MEPDG. In order to maintain compatibility with the MEPDG framework, a procedure is developed such that two different moduli are used to represent the AC layer for different loading durations determined using the MEPDG process. The *2-moduli approach* shall substitute for the time-discretized viscoelastic analysis presented in Part 3.3 by a combination of three elastic solutions such that the total stresses in the pavement are computed as a combination of the stresses from these three solutions.

Part 3.3 discusses the difference in the MEPDG prediction for AC moduli under traffic loads and temperature gradients, the *2-moduli approach* developed to replace the time-discretized viscoelastic analysis, a stress computation procedure for combined stresses under traffic loads

and temperature gradients using the *2-moduli approach*, and verification of the stresses using simple examples.

3.3.1 AC Moduli under Traffic Loads and Temperature Gradients

One of the limitations identified in the adoption of the jointed plain concrete pavement (JPCP) fatigue cracking model for composite pavements was the use of a single load duration-dependent dynamic modulus to characterize the stress-strain relationship in the viscoelastic AC layer. A preliminary investigation, presented in Part 3.2 suggested that the AC modulus may be significantly different under fast moving traffic loads and temperature loading. The MEPDG assumes the temperature gradient to be a step function of time with duration of one hour. Therefore, to maintain consistency with the MEPDG, the duration of temperature loads is selected to be one hour. An analysis of the AC dynamic modulus, based on the MEPDG guidelines, was conducted and the results are presented herein.

In the following example, the AC modulus of a composite pavement located in Minneapolis, MN as prescribed by the MEPDG is analyzed. The pavement structure and layer thicknesses are given in Table 4-8. All other inputs are taken as the MEPDG defaults.

Table 3-8: Structural details of the composite pavement analyzed in the MEPDG.

Layer No.	Type	Material	Thickness, (in)
1	Wearing	AC	4
2	Structural	PCC	6
3	Base	A-1-a	8
4	Subgrade	A-6	Semi-infinite

In the MEPDG, the AC dynamic modulus is calculated for the 3rd quintile monthly AC temperatures at the mid-depth of the AC layer obtained from Enhanced Integrated Climatic Model (EICM) outputs. The AC dynamic modulus is calculated using equations (22) and (23) for the loading time t corresponding to (a) the MEPDG default traffic speed of 60 mph, and (b) 3600 seconds (i.e., one hour of temperature loading). Figure 3-27 illustrates the MEPDG-generated dynamic modulus of the AC layer versus pavement age corresponding to the traffic duration and temperature duration for the first two years of the design life of the composite pavement.

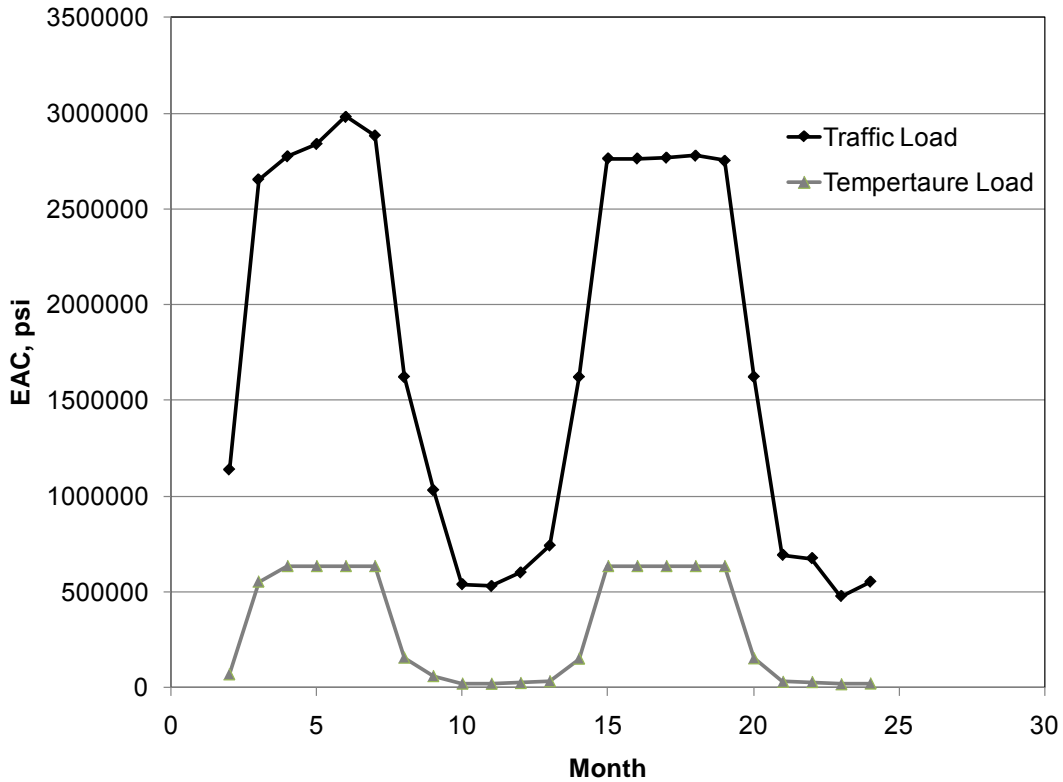


Figure 3-27: Asphalt dynamic modulus using the MEPDG versus pavement age.

It can be established from Figure 3-27 that the AC dynamic modulus is significantly different under typical traffic load durations and one hour of temperature loading. Therefore, for composite pavements under combined traffic and temperature loading, the use of a single dynamic modulus to characterize the stress-strain relationship in the viscoelastic AC layer may be insufficient.

3.3.2 The 2-Moduli Approach

Consider a composite pavement subjected to an arbitrary temperature distribution throughout the slab thickness acting on the time interval $0 < t < t_T$ and axle loading at the end of the time interval. As was demonstrated above, the AC dynamic modulus is significantly different under typical traffic loads and temperature gradients. It is proposed that two separate AC dynamic modulus should be considered as follows:

1. The traffic-duration-dependent dynamic modulus, $EACL$, that characterizes the pavement response under typical traffic loads
2. The temperature-duration-dependent dynamic modulus, $EACT$, that characterizes the pavement response for the duration of temperature loads, t_T .

The stresses obtained by executing separately the curling analysis and the traffic load analysis cannot be simply added to obtain the stress under a combination of traffic loads and temperature curling (AASHTO 2008). This is due to the fact that the slab-foundation interaction is non-linear. Under compression, the deformation of the slab-foundation increases linearly with an increase in

surface pressure, but the slab-foundation cannot resist vertical upward movement. The curling of the slab due to the daytime temperature gradient causes a void under the center of slab as a result of separation from the foundation. The night-time temperature gradient causes a void under the edges of the slab. Hence, due to non-linear interaction of slab with the foundation, two different loading cases (and resulting stresses) cannot be linearly superimposed to mimic the combined loading.

To account for the effect of load duration dependency of the AC layer and non-linear slab foundation interaction, a procedure that involves a combination of solutions of three elastic boundary value problems (BVP) is developed. This procedure is presented next.

3.3.3 Stress Computation Procedure using the 2-Moduli Approach

The *2-moduli approach* is an alternative to the more involved viscoelastic analysis presented in Part 3.3. This method is a combination of three elastic BVPs. The first elastic BVP considers slab curling only and uses the long-term AC modulus, E_{ACT} to characterize the AC stiffness. The second elastic BVP involves determination of the stress field in the composite pavement subjected to curling with the AC layer characterized by the short-term AC modulus, E_{ACL} , and having the same deflection profile as that determined by the first elastic solution. In the third elastic BVP, the short-term AC modulus, E_{ACL} , is used to determine the stress field from the combined effect of curling and axle loading. The total stresses in the pavement are computed as a combination of the stresses from these three solutions.

The First Elastic Problem

Problem 1 models a three-layer system of AC, PCC, and base layers as shown in Figure 3-28. The system rests on the spring idealization of an elastic Winkler foundation. The AC layer is modeled as an elastic material with an elastic modulus corresponding to the temperature-duration-dependent modulus, E_{ACT} . The PCC and base layers are elastic with the modulus of elasticity equal to E_{PCC} and E_{Base} , respectively. The thicknesses of the AC, PCC, and base layers are h_{AC} , h_{PCC} , and h_{Base} , respectively. The unit weights of the AC, PCC, and base layers are γ_{AC} , γ_{PCC} , and γ_{Base} , respectively. All of the layers have Poisson's ratio equal to μ . The coefficient of thermal expansion for the AC layer is α_{AC} while that for the PCC and base layers is selected as α_{PCC} . The interface conditions between the layers could be either fully bonded or unbonded.

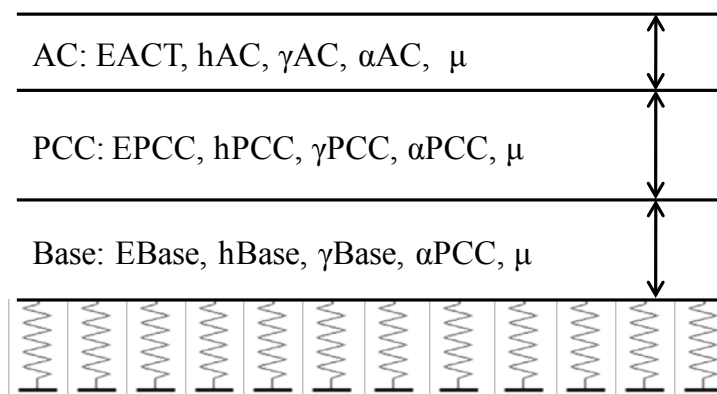


Figure 3-28: System 1.

The pavement system of problem 1 is subjected to a positive temperature gradient $T(z)$ as shown in Figure 3-29. The deflection profile of the slab under the temperature gradient $T(z)$ is recorded. The stress at the bottom of the PCC layer at the mid-slab location under temperature gradient $T(z)$ is denoted as σ_1 . Solutions detailing the computation of this stress are discussed later in the section.

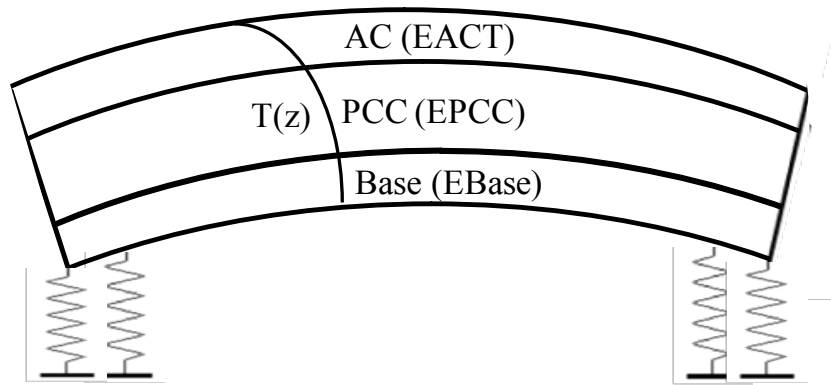


Figure 3-29: System 1 under positive temperature gradient $T(z)$ only.

The Second Elastic Problem

Problem 2 has the same three-layer structure and material properties as problem 1 except that the AC layer is modeled as an elastic material with elastic modulus corresponding to the traffic-duration-dependent modulus, $EACL$. The pavement system of problem 2 is presented in Figure 3-30. The layer interface conditions are the same as those chosen in problem 1.

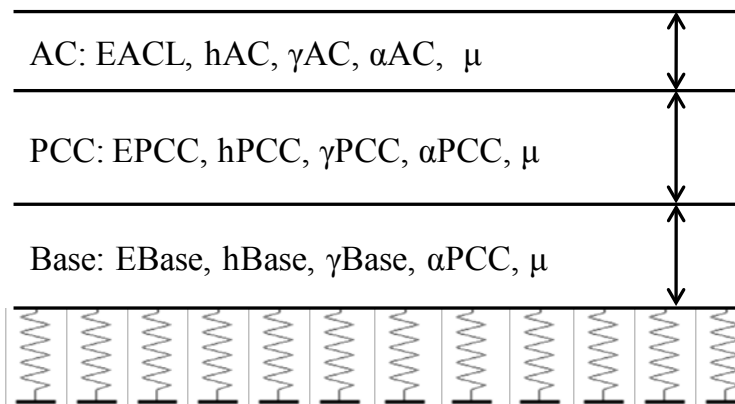


Figure 3-30: System 2.

Assume that a fictitious force F_{fict} acts on the pavement system such that its deflection profile is exactly the same as that from problem 1, i.e. the deflection at each node of system 2 is exactly equal to the deflection at the corresponding node in system 1. Since the deflection profile does not change between problems 1 and 2, it ensures that the subgrade below system 2 is under the same stress distribution as the subgrade below system 1, and that the contact area between the slab and foundation did not change. This ensures that the non-linear behavior of the slab-foundation interaction is properly accounted for. Figure 3-31 presents system 2 under a fictitious

force F_{fict} . The stress resulting from the fictitious force F_{fict} at the bottom of the PCC layer at the mid-slab location is denoted as σ_2 . Solutions detailing the computation of this stress are discussed later in the section.

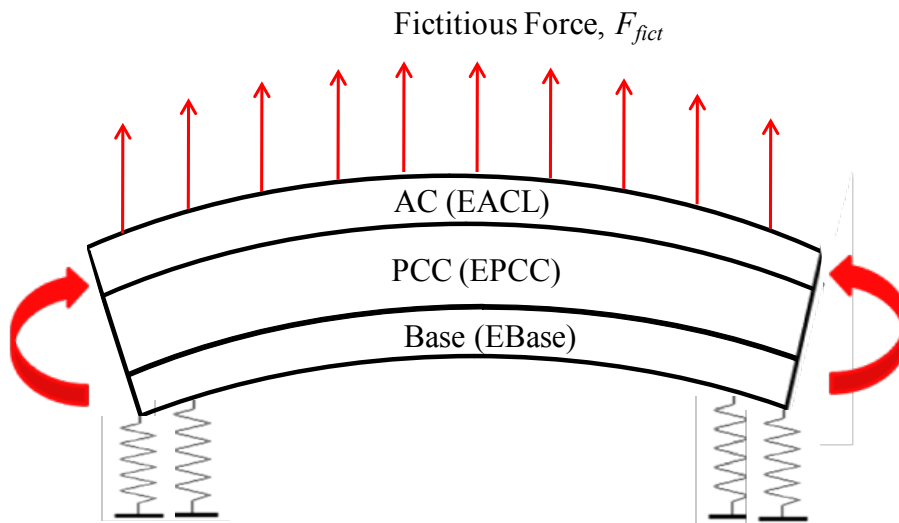


Figure 3-31: System 2 under fictitious force F_{fict} .

The Third Elastic Problem

Since system 2 characterizes the AC layer with an elastic modulus corresponding to the traffic-duration-dependent modulus, $EACL$, in Problem 3, the traffic load F can be superimposed on top of the fictitious load, F_{fict} as shown in Figure 3-32. The stress at the bottom of the PCC layer at the mid-slab location due to the total load is denoted as σ_3 . Solutions detailing the computation of this stress are discussed later in the section.

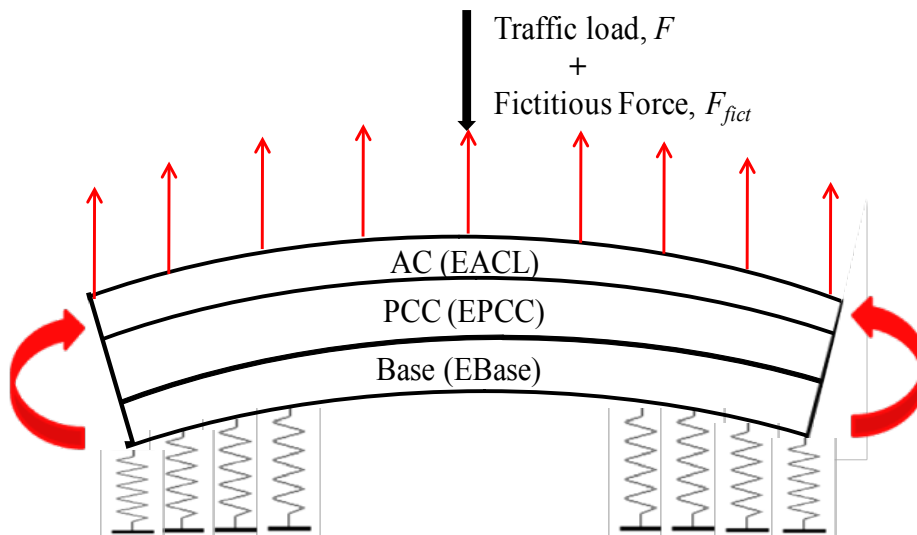


Figure 3-32: System 2 under mid-slab traffic load F and fictitious force F_{fict} .

Combined Stress

Finally, to obtain the stress distribution in the pavement due to the combined effect of temperature and axle loading, solutions of the three elastic problems are combined as follows:

$$\sigma_{2M} = \sigma_1 + (\sigma_3 - \sigma_2) \quad (3-110)$$

where:

σ_{2M} = combined stress at a given location,
 σ_1 = stress at the given location from the first elastic solution,
 σ_2 = stress at the given location from the second elastic solution, and
 σ_3 = stress at the given location from the third elastic solution.

It should be noted that the combined stress (Equation (3-110)) is an approximation of the viscoelastic boundary value problem if the viscoelastic properties of the AC layer are as follows (Figure 3-33):

$$J(t) = \frac{1}{E_0} + \frac{1}{E_1} \left(1 - e^{-\frac{E_1 t}{\eta_1}} \right)$$

$$\frac{1}{E_0} = \frac{1}{EACL}$$

$$\frac{1}{E_1} = \frac{1}{EACT} - \frac{1}{EACL}$$

$$\frac{\eta_1}{E_1} \ll t_T \quad (3-111)$$

where:

t_T = duration of the temperature loading prior to application of the axle load.

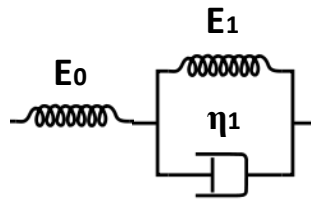


Figure 3-33: Kelvin-Voigt model connected to an elastic spring in series.

Several examples verifying this statement are presented later in the section. The next section presents the FE formulation to obtain the elastic solutions of the BVPs discussed above.

3.3.4 Brief Formulation for the FE Model Based on the 2-Moduli Approach

The *2-moduli approach* has been incorporated into a FE code, and it is similar to the viscoelastic FE model presented in Part 3.3. In this section, the main differences of the formulation are highlighted. The variables of these equations follow the definitions and notations used in Part 3.3.

Recall system 1 considered in the first elastic problem, which considers curling of the composite pavement and where the long-term AC modulus $EACT$ is used to characterize the AC layer. The equilibrium equation for system 1 can be expressed as follows:

$$[K_1]\{\delta\} = \{F_{therm}\} \quad (3-112)$$

where:

$[K_1]$ = global stiffness matrix for system 1 with long-term AC modulus $EACT$
 $\{F_{therm}\}$ = global force vector due to temperature distribution $T(z)$
 $\{\delta\}$ = global displacement vector of system 1

The global stiffness matrix $[K_1]$ and the global thermal force vector $\{F_{therm}\}$ are assembled using the procedure described in the Part 3.3 section entitled *Development of a Finite Element Model for the Analysis of Viscoelastic Slab-on-Grade*. The displacements of the slab, δ_1 can be written as:

$$\{\delta_1\} = [K_1]^{-1} \{F_{therm}\} \quad (3-113)$$

Since system 1 is subjected to the temperature distribution $T(z)$, elastic stress in an element of system 1 can be calculated as:

$$\{\sigma_1\}_e = [\bar{D}_T] (\{\varepsilon_1\} - \{\varepsilon_{therm}\})_e \quad (3-114)$$

where:

subscript e = an individual elements in a plate
 $\{\sigma_1\}$ = elastic stress from the first elastic solution
 $[\bar{D}_T]$ = material property matrix corresponding to modulus $EACT$ and is given by Equation (3-58)
 $\{\varepsilon_1\}$ = total strain corresponding to the global displacements δ_1 and is given by Equation (3-61)
 $\{\varepsilon_{therm}\}$ = thermal strain given by equations (3-47) and (3-64)

System 2, considered in the second elastic problem, characterizes the viscoelastic AC layer using the short-term modulus $EACL$. The deflection profile of system 2 due to the application of a fictitious force F_{fict} must be exactly the same as that of system 1. Therefore, the fictitious force F_{fict} can be computed as follows:

$$\{F_{fict}\} = [K_2]\{\delta_1\} \quad (3-115)$$

where:

K_2 = global stiffness matrix for system 2 with the short-term AC modulus $EACL$

Since no initial strains act on system 2 and the global displacements of system 2 are exactly the same as those of system 1, the elastic stress in an element of system 2 can be calculated as follows:

$$\{\sigma_2\}_e = [\bar{D}_L]\{\varepsilon_1\}_e \quad (3-116)$$

where:

$\{\sigma_2\}$ = elastic stress from the second elastic solution

$[\bar{D}_L]$ = material property matrix corresponding to the modulus $EACL$ computed using Equation (3-58)

In the third elastic problem, system 2 is subjected to traffic loads F along with the fictitious force F_{fict} . The global displacements δ under a combination of loads can be computed as follows:

$$\{\delta\} = [K_2]^{-1}(\{F\} + \{F_{fict}\}) \quad (3-117)$$

where:

$\{F\}$ = global force vector due to traffic loads, and

$\{F_{fict}\}$ = global fictitious force vector from the second elastic solution

The elastic stress from the third elastic problem can be calculated as follows:

$$\{\sigma_3\}_e = [\bar{D}_L]\{\varepsilon_T\}_e \quad (3-118)$$

where:

$\{\sigma_3\}$ = elastic stress from the third elastic solution

$\{\varepsilon_T\}$ = total strain corresponding to the global displacements δ

Finally, using Equation (3-110) the combined stresses are calculated in the pavement.

3.3.5 Step-by-Step Procedure for Computing the Combined Stresses

A step-by-step procedure used to develop the second FE code for computing the combined stresses using the three elastic solutions is presented.

Steps 1 through 8 given in the Part 3.3 section entitled *Step-by-Step Procedure for Computing the Stresses in the Composite Pavement* are repeated for an equivalent single layer slab 1 corresponding to system 1 and an equivalent single layer slab 2 corresponding to system 2. The modifications applied to these steps are noted below.

Step 1: Read inputs. In place of the creep compliance parameters for the viscoelastic FE inputs, the short-term AC modulus $EACL$ and long-term AC modulus $EACT$ are given in the input file.

Step 2: Determine parameters of equivalent single layer slab 1 corresponding to system 1. The thickness and unit weight for an equivalent single layer slab 1 are computed depending on the short-term AC modulus $EACT$ and the interface conditions of system 1.

Step 5: Compute the global force vector for the equivalent single layer slab 1. The global force vector due to the thermal strains and self-weight of the slab is computed at the appropriate degree of freedom for each element.

Step 9: Calculate nodal stresses for the first elastic solution. Stresses for each layer of the composite pavement system are computed. For example, the total stress at the bottom of the PCC layer of the composite pavement for the first elastic solution is calculated as follows:

$$\sigma_{PCC,Bot_1} = \frac{2 * (h_{PCC} + h_{AC} - x_1)}{h_{eq_1}} \sigma_{eq_1} + \sigma_{NL,bot} \quad (3-119)$$

where:

σ_{PCC,Bot_1} and σ_{eq_1} = elastic stresses at the bottom of the PCC layer of system 1 and at the bottom of equivalent single layer slab 1, respectively

h_{eq_1} , h_{AC} , and h_{PCC} = thicknesses of the equivalent single layer slab 1, AC, and PCC layers, respectively

x_1 = distance of the neutral axis of system 1 from the top of the AC layer

$\sigma_{NL,bot}$ = stress due to the nonlinear-strain-causing temperature component

Step 10: Determine parameters of equivalent single layer slab 2 corresponding to system 2. The thickness and unit weight for an equivalent single layer slab 2 are computed depending on the long-term AC modulus $EACL$ and the interface conditions of system 2 (which are the same as those chosen for system 1).

Step 11: Compute the stiffness matrix. Repeat step 4 to generate the global stiffness matrix $[K_2]$ corresponding to system 2.

Step 12: Compute the fictitious force vector in the equivalent single layer slab 2. The global fictitious force vector acting on equivalent single layer slab 2 is computed using the global displacements from the first elastic solution according to Equation (3-115).

Step 13: Compute stresses in the equivalent single layer slab 2. Repeat step 8 to obtain the stresses in the equivalent single layer slab 2 corresponding to the second elastic problem.

Step 14: Calculate nodal stresses for the second elastic solution. Stress for each layer of the composite pavement system is computed. For example, the total stress at the bottom of the PCC layer of the composite pavement for the second elastic solution is calculated as follows:

$$\sigma_{PCC,Bot_2} = \frac{2 * (h_{PCC} + h_{AC} - x_2)}{h_{eq_2}} \sigma_{eq_2} \quad (3-120)$$

where:

σ_{PCC,Bot_2} and σ_{eq_2} = elastic stresses at the bottom of the PCC layer of system 2 and at the bottom of equivalent single layer slab 2, respectively
 h_{eq_2} = thickness of the equivalent single layer slab 2
 x_2 = distance of the neutral axis of system 2 from the top of the AC layer

Step 15: Compute the global force vector for the third elastic solution. The global force vector is computed by adding the traffic loading to the fictitious force acting on system 2 at the appropriate degree of freedom for each element.

Step 16: Compute displacements for the third elastic solution. Same as step 6.

Step 17: Check contact condition. Same as step 7.

Step 18: Compute stresses in the equivalent single layer slab 2. Repeat step 8 to obtain the stresses in the equivalent single layer slab 2 corresponding to the third elastic problem.

Step 19: Calculate nodal stresses for the third elastic solution. The stress for each layer of the composite pavement system is computed. For example, the total stress at the bottom of the PCC layer of the composite pavement for the third elastic solution is calculated as follows:

$$\sigma_{PCC,Bot_3} = \frac{2 * (h_{PCC} + h_{AC} - x_2)}{h_{eq_2}} \sigma_{eq_3} \quad (3-121)$$

where:

σ_{PCC,Bot_3} and σ_{eq_3} = elastic stresses at the bottom of the PCC layer of system 2 and at the bottom of equivalent single layer slab 2, respectively, for the third elastic solution

Step 20: Compute combined stress. The combined stress from the three elastic solutions is calculated using Equation (3-110).

Step 21: Output results. The displacements and combined stresses in the composite pavement at each node are printed in ISLAB2000 output format.

3.3.6 Verification of the Combined Stress Obtained using the 2-Moduli Approach

The stress computation procedure presented previously is verified using simple examples for the following cases:

1. Comparison with the viscoelastic FE model (presented in Part 3.3) for a fictitious tire footprint
2. Comparison with the viscoelastic FE model for a typical tire footprint.
3. Comparison of the combined stress obtained using the *2-moduli approach* with a simple addition of stresses obtained by executing separately the curling analysis and the traffic load analysis, to confirm the presence of non-linear slab-foundation interaction.

Comparison with the Viscoelastic FE Model – Example 1

A three-layered composite pavement placed on an elastic Winkler foundation is loaded with a single wheel load that has a tire footprint of 60 in x 48 in and tire pressure of 100 psi. The wheel load is applied at the center of the slab. A uniform mesh consisting of 6 in x 6 in elements is generated in the horizontal plane. Both interfaces (AC-PCC and PCC-base) are fully bonded. Figure 3-12 shows the mesh and loading configuration for the composite pavement under this wheel load.

The composite pavement is also subjected to a non-linear temperature distribution given in Table 3-9. The temperature profile is adopted from a typical MEPDG hourly thermal distribution for the AC and PCC layers. To maintain consistency with the MEPDG, the temperature in the base layer is assumed to be constant and equal to the temperature at the bottom of layer 2. The depth of the temperature data point in a layer is given from the top of the corresponding layer.

Table 3-9: Temperature profile for the composite pavement.

Layer		No. of temperature data points										
		1	2	3	4	5	6	7	8	9	10	11
AC	Reference temperature = 55.90 °F											
	Depth, in	0.0	1.0	2.0	3.0	4.0						
	Temp., °F	90.9	86.0	81.0	76.4	71.8						
PCC	Reference temperature = 55.90 °F											
	Depth, in	0.0	0.8	1.6	2.4	3.2	4.0	4.8	5.6	6.4	7.2	8.0
	Temp., °F	71.8	69.0	66.9	64.8	63.0	61.4	60.0	58.7	57.6	57.0	55.9

The material properties for the constituent layers of the composite pavement are presented in Table 3-10.

Table 3-10: Layer properties for the composite pavement.

Layer	Thickness, h (in)	Layer modulus, E (psi)	Poisson's ratio, M	Unit weight, γ (lb/in ³)	Coefficient of thermal expansion, α (1/°F)
AC	4	$EACT = 39448.9$	0.15	0.087	1.65E-05
		$EACL = 2.0E+05$			
PCC	8	4.0E+06	0.15	0.087	5.50E-06
Base	0	4.0E+04	0.15	0.087	5.50E-06

The AC layer of the composite pavement is represented by (a) the creep compliance function using a two-term generalized Kelvin-Voigt model when the stresses are computed using the viscoelastic FE model presented in Part 3.3 and (b) the moduli $EACL$ and $EACT$ when stresses are computed using the *2-moduli approach*. The traffic-duration-dependent AC modulus $EACL$ is equal to the instantaneous modulus of the generalized Kelvin-Voigt model. The temperature-duration-dependent AC modulus $EACT$ is equal to the inverse of creep compliance computed using the generalized Kelvin-Voigt model at the end of one hour of loading. Table 3-11 presents the material properties of the AC layer for the viscoelastic FE model and the *2-moduli approach*.

Table 3-11: Material properties for the AC layer.

	Element #	Spring stiffness, psi	Dashpot viscosity, psi-in
Viscoelastic FE Model	0	200000	
	1	95265	11307535
	2	101500	997600
2-Moduli Approach		AC Modulus, psi	
	$EACL$	200000	
	$EACT$	39448.9	

The viscoelastic FE solution is obtained by executing the FE code presented in Part 3.3 for the composite pavement configuration detailed herein. The temperature distribution is applied for 3600 seconds (1 hour) during which the creep strains and corresponding fictitious creep forces develop in the AC layer. At the end of one hour, the wheel load is applied to the pavement.

The combined stress using the *2-moduli approach* was obtained by executing the stress computation procedure detailed in above. Tables 12 and 13 present the deflections and longitudinal stresses from the viscoelastic FE model at the end of the load application and the three elastic solutions for select nodes at the bottom of the PCC layer.

Table 3-12: Deflections and stress at the bottom of the PCC layer at slab center.

	Location, in		Deflection, in	Rotation		Longitudinal Stress, psi
	X	Y		θ_y	θ_x	
Three elastic solution						
# 1	90	72	-0.0054	0.00	0.00	78.65
# 2	90	72	-0.0054	0.00	0.00	-96.61
# 3	90	72	0.2401	0.00	0.00	1947.8
Combined stress						2123.06
Viscoelastic FE solution	90	72	0.2401	0.00	0.00	2122.84
% Error						-0.01%

Table 3-13: Deflections and stress at the bottom of the PCC layer at an edge node.

	Location, in		Deflection, in	Rotation		Longitudinal Stress, psi
	X	Y		θ_y	θ_x	
Three elastic solution						
# 1	90	0	0.0188	-0.0007	0.00	74.35
# 2	90	0	0.0188	-0.0007	0.00	-101.04
# 3	90	0	0.1220	0.0015	0.00	716.08
Combined stress						891.462
Viscoelastic FE solution	90	0	0.1220	0.0015	0.00	891.461
% Error						-0.00015%

The stress from the viscoelastic FE solution and the combined stress from three elastic solutions match very well at the both the center of the slab and the edge node as shown by the .01% and .00015% errors, respectively.

Comparison with the Viscoelastic FE Model – Example 2

Consider the three-layered composite pavement presented previously. The pavement is loaded with a single-axle dual-wheel (SADW) load that has a tire footprint of 7 in x 7 in and tire pressure of 100 psi. The SADW load is applied at the mid-slab location such that one of the wheels is at the edge of the slab. The pavement is also subjected to the temperature distribution given in Table 3-9. Figure 3-15 shows the mesh and loading configuration for the composite pavement under the SADW load. The layer properties of the composite pavement are given in Tables 10 and 11 above. The AC layer is represented in the manner similar to example 1 using (a) the creep compliance function for the viscoelastic FE model and (b) moduli *EACL* and *EACT* for the *2-moduli approach*. Tables 14 and 15 present the deflections and longitudinal stresses obtained using the viscoelastic FE model and the three elastic solutions for select nodes at the bottom of the PCC layer.

Table 3-14: Deflections and stress at the bottom of the PCC layer at slab edge.

	Location, in		Deflection, in	Rotation		Longitudinal Stress, psi
	X	Y		θ_y	θ_x	
Three elastic solution						
# 1	90	0	0.0188	-0.0007	0.00	74.35
# 2	90	0	0.0188	-0.0007	0.00	-101.04
# 3	90	0	0.0466	-0.0011	0.00	268.11
Combined stress						443.5
Viscoelastic FE solution	90	0	0.0466	-0.0011	0.00	443.3
% Error						-0.046%

Table 3-15: Deflections and stress at the bottom of the PCC layer at an interior node.

	Location, in		Deflection, in	Rotation		Longitudinal Stress, psi
	X	Y		θ_y	θ_x	
Three elastic solution						
# 1	72	54	-0.0034	-0.00015	0.00008	69.44
# 2	72	54	-0.0034	-0.00015	0.00008	-106.09
# 3	72	54	0.0106	-0.00026	-0.00004	-21.51
Combined stress						154.02
Viscoelastic FE solution	72	54	0.0106	-0.00026	-0.00004	153.76
% Error						-0.169%

The stress from the viscoelastic FE solution and the combined stress from the three elastic solutions match fairly well at both the center of the slab and the interior node as shown by the .046% and .169% errors, respectively. The slight difference noted in both the examples is attributed to the accumulation of error due to the length of time interval considered in the viscoelastic FE solution.

Comparison with Simple Addition of the Stresses

To confirm that the stress in a pavement is not a direct addition of stresses due to traffic load and temperature gradient, a typical composite pavement slab placed on an elastic Winkler foundation is considered. A 15 ft long by 12 ft wide pavement slab is loaded with single-axle dual-wheel (SADW) loads at the edge of the slab as shown in Figure 3-34. The SADW loads have a tire footprint of 7 in x 7 in and tire pressure of 100 psi. A uniform mesh consisting of 6 in x 6 in elements is generated. The modulus of subgrade reaction for the Winkler foundation is equal to 100 psi/in. The interface between the AC and PCC layers of the composite pavement is fully bonded while that between the PCC and base layers is fully unbonded.

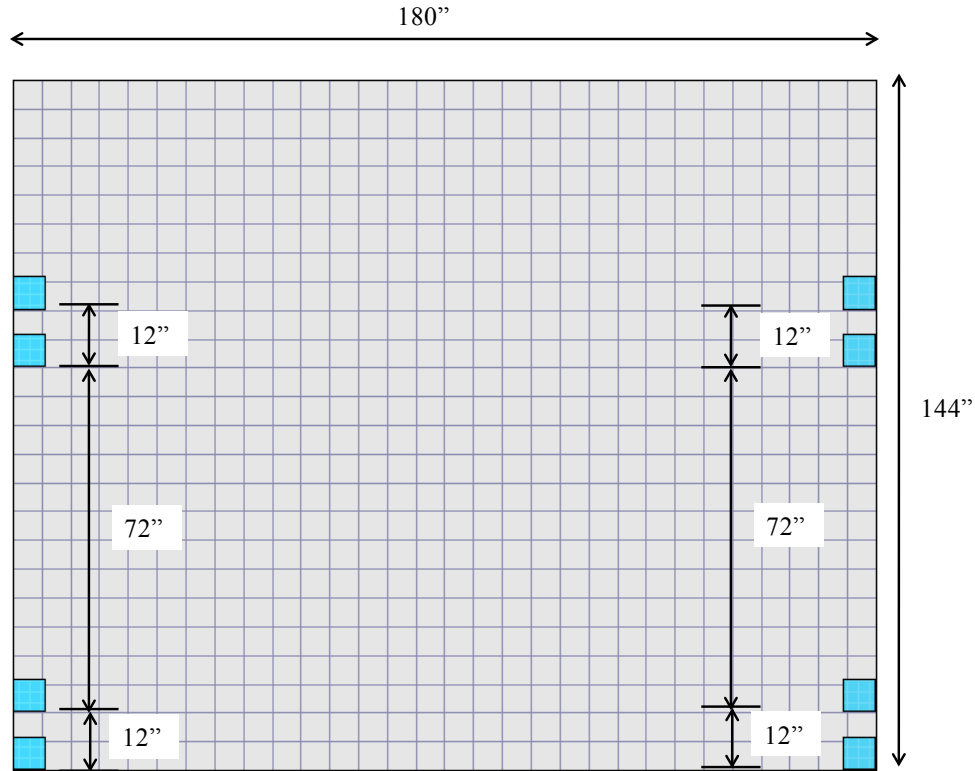


Figure 3-34: Mesh and load configuration for the composite pavement subjected to SADW edge loading.

The composite pavement is also subjected to a non-linear night-time temperature distribution given in Table 3-16.

Table 3-16: Temperature profile for the composite pavement.

Layer		No. of temperature data points										
		1	2	3	4	5	6	7	8	9	10	11
AC	Reference temperature = 55.90 °F											
	Depth, in	0.0	0.5	1.0	1.5	2.0						
	Temp., °F	40.9	46.0	49.0	52.9	57.8						
PCC	Reference temperature = 55.90 °F											
	Depth, in	0.0	0.7	1.4	2.1	2.8	3.5	4.2	4.9	5.6	6.3	7.0
	Temp., °F	57.8	60.2	62.5	64.7	66.9	68.0	70.9	72.8	74.5	76.2	78.8

The material properties for the constituent layers of the composite pavement are presented in Table 3-17.

Table 3-17: Layer properties for the composite pavement.

Layer	Thickness, h (in)	Layer modulus, E (psi)	Poisson's ratio, μ	Unit weight, γ (lb/in ³)	Coefficient of thermal expansion, α (1/°F)
AC	2	$E_{ACT} = 39448.9$	0.15	0.087	1.65E-05
		$E_{ACL} = 2.0E+05$			
PCC	7	4.0E+06	0.15	0.087	5.50E-06
Base	6	4.0E+04	0.15	0.000	5.50E-06

The stress in the pavement is computed using the *2-moduli approach* presented above. Further, the stress is computed when the composite pavement is subjected to (a) the temperature load only and the AC layer has short-term modulus E_{ACT} and (b) the traffic load only and the AC layer has short-term modulus E_{ACL} . The combined PCC top stress at the edge of the slab using the *2-moduli approach* is compared against the sum of stresses from case (a) and case (b). The results are presented in Table 3-18 below.

Table 3-18: Deflections and stresses at the top of the PCC layer at slab edge.

	Location, in		Deflection, in	Rotation		Longitudinal Stress, psi
	X	Y		θ_y	θ_x	
Three elastic solution						
# 1	90	0	-0.0077	0.00	0.00	108.74
# 2	90	0	-0.0077	0.00	0.00	-138.36
# 3	90	0	0.0038	0.00	0.00	204.06
Combined stress						451.17
Viscoelastic FE solution						
	90	0	0.0038	0.00	0.00	451.12
E_{ACT}, temperature load only						
	90	0	-0.0077	0.00	0.00	108.74
E_{ACL}, traffic load only						
	90	0	0.0033	0.00	0.00	284.05
						392.79
% Difference						14.86%

The difference between the stresses from the two approaches, which was 14.86%, clearly demonstrate that the stress from individual traffic and temperature loads cannot simply be added to obtain the combined stress. This phenomenon is due to the non-linear behavior of the slab-foundation interaction.

3.3.7 Comparison of the Stress Solution using the 2-Moduli Approach with the Stress Solution using the MEPDG Process

The stresses obtained using the *2-moduli approach* are compared with the stresses obtained using the MEPDG procedure in order to assess the difference between the two procedures. The MEPDG considers the temperature distribution present in the layers of the pavement to be a step

function of time with duration of one hour. In this example, the temperature distribution with the maximum temperature difference between the top of the AC layer and the bottom of the PCC layer was selected for each month over two years of data. The stress in the pavement was then computed using the selected temperature distribution for each month in combination with the traffic loading. The MEPDG employs neural networks (NNs) to compute the stresses in rigid and composite pavements. These NNs are trained using a factorial of ISLAB2000 cases. Therefore, to maintain consistency with the MEPDG, ISLAB2000 cases were executed such that the composite pavement was subjected to a combination of the temperature distribution corresponding to each month of the analysis and traffic loading.

Consider the three-layered composite pavement presented above. Twenty-four cases corresponding to twenty-four months are analyzed such that the pavement is subjected to the SADW load given previously and the selected temperature distribution with maximum gradient for each month. The properties of the constituent layers of the composite pavement are given in Table 3-19. The AC layer is represented using the *2-moduli approach* such that (a) the short-term modulus *EACL* is dependent on the vehicle loading rate and (b) the short-term modulus *EACT* is dependent on one hour of temperature loading. Also, both *EACL* and *EACT* for each month are calculated using the 3rd quintile AC temperatures at the mid-depth of the AC layer for the corresponding month.

Table 3-19: Layer properties for the composite pavement.

Layer	Thickness, h (in)	Layer modulus, E (psi)	Poisson's ratio, M	Unit weight, γ (lb/in ³)	Coefficient of thermal expansion, α (1/°F)
AC	2	<i>EACT</i>	0.15	0.087	1.00E-13
		<i>EACL</i>			
PCC	7	4.0E+06	0.15	0.087	5.50E-06
Base	0	4.0E+04	0.15	0.087	5.50E-06

ISLAB2000 cannot currently analyze a three-layered system if both the layer interfaces are fully bonded. While this is rarely a limitation for the analysis of rigid pavements, it introduces some limitation when fully bonded composite pavements are analyzed. Therefore, to maintain compatibility with ISLAB2000, the thickness of the base layer of the composite pavement is set to zero. The stresses obtained using the *2-moduli approach* and by executing the ISLAB2000 case for replicating the MEPDG procedure are presented in Figure 3-35. The stress is computed at the bottom of the PCC layer at the edge of the slab.

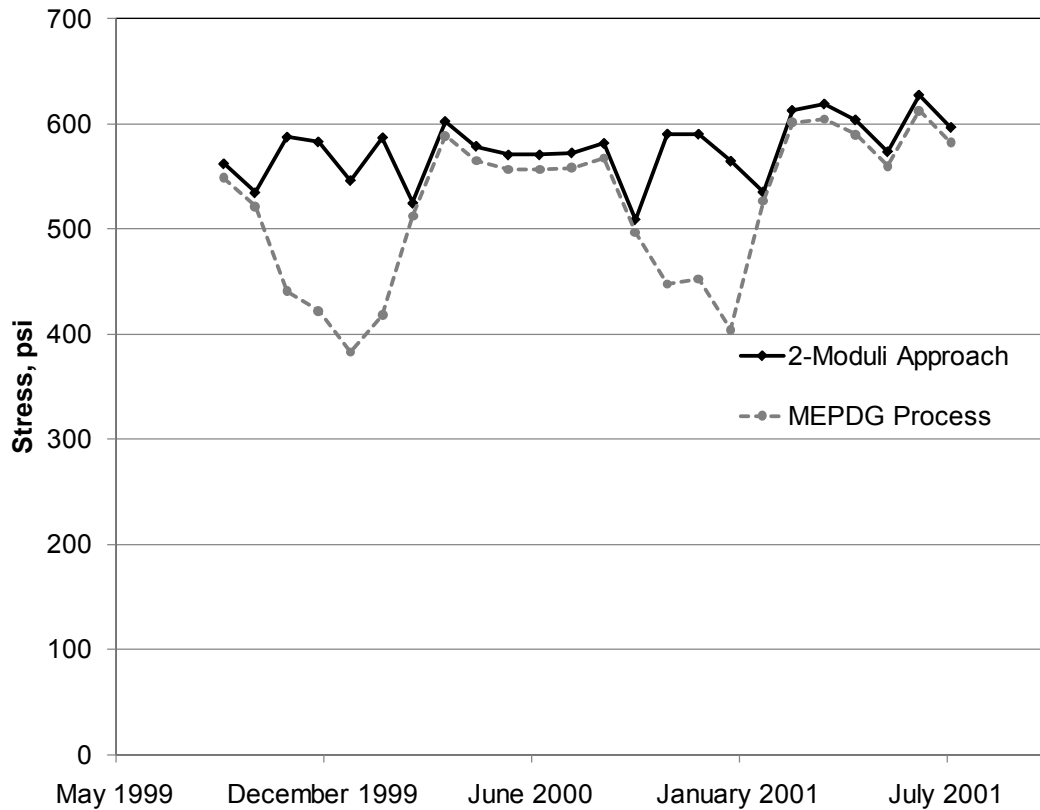


Figure 3-35: Comparison of stress using the 2-moduli approach and the MEPDG procedure.

A difference between the stresses from the *2-moduli approach* and the MEPDG procedure is observed. There could be several factors that contribute to this difference. The MEPDG uses a single traffic loading based AC dynamic modulus (*EACL*) whereas the 2-moduli approach employs moduli *EACT* and *EACL*. This may cause a difference between the self-equilibrating stresses present in a layer due to the non-linear-strain-causing temperature component, which directly affects the total stress at any point in the pavement.

3.4. Development of a Framework for Implementation of the 2-Moduli Approach into MEPDG

The objective of this research is to develop a framework for the structural analysis of composite pavements, which can be implemented into the existing or future versions of the Mechanistic Empirical Pavement Design Guide (MEPDG). The *2-moduli approach* presented in the last section is an attractive alternative to the elastic analysis currently implemented by the MEPDG and the more rigorous viscoelastic finite element (FE) model. As was discussed previously, a direct implementation of a FE solution into the MEPDG is not feasible due to the computational time constraint.

The current structural analysis of composite pavements implemented into the MEPDG utilizes rapid solutions that are developed based on the results of a factorial of ISLAB2000 runs. In

order to accommodate a large number of design parameters in the proposed *2-moduli approach*, the following techniques were adopted (*AASHTO 2008*):

1. Replacement of the structural system by a combination of two simpler systems
2. Equivalency techniques to reduce the number of independent input parameters.

Part 3.2 provides the details of the techniques employed by the MEPDG for the simplification of stress analysis in the existing fatigue cracking distress models for rigid and composite pavements. In this section, similar methods are introduced for the simplification of the stress analysis using the *2-moduli approach* presented in Part 3.4. Further, examples are presented to verify the proposed simplification and its compatibility with the MEPDG framework.

3.4.1 Simplification of the Structural System

The MEPDG employs a framework of artificial neural networks (NNs) to predict the stress solutions for rigid and composite pavements under traffic loading, temperature distribution, or their combinations (*AASHTO 2008*). The NNs are based on a combination of two simpler systems presented in the Part 3.2 section entitled *MEPDG Neural Networks for Computing PCC Stresses* to compute stresses in the original multi-slab system. A similar approach is adopted for the development of a MEPDG compatible framework that shall incorporate the stress solutions obtained using the *2-moduli approach*.

The original multi-slab composite pavement system consists of one or more connected pavement slabs and a shoulder that provides edge support to the slab through load transfer between the pavement slab and the shoulder (refer to Figure 3-2a). The original system is subjected to an axle load acting over a tire footprint area and a temperature distribution, which varies throughout the depth of the pavement. The asphalt concrete (AC) layer of the composite pavement is characterized using the short-term AC modulus *EACL* when the pavement is subjected to the axle load and the long-term AC modulus *EACT* when the pavement is subjected to temperature distribution.

A single slab system—system A (refer to Figure 3-2b)—is the first system used to simplify the representation of the original multi-slab pavement. System A is subjected to three separate loading regimes as follows:

- Temperature curling only
- Combined axle loading and temperature curling
- Axle loading only

For computing the stresses corresponding to the combined axle loading and temperature curling load regime, the boundary value problem (BVP) detailed in the Part 3.4 section entitled *Stress Computation Procedure using the 2-Moduli Approach* is used. The AC layer of the composite pavement system A is represented using the short-term modulus *EACL* when the pavement is subjected to the axle load and the long-term modulus *EACT* when the pavement is subjected to the temperature distribution. For computing the stresses due to temperature curling only and axle loading only, either the FE code presented in Part 3.3 or ISLAB2000 may be used. The footprint of the axle load for system A is considered to be 7 in by 7 in.

A two-slab system—system B (refer to Figure 3-2c)—is the other system used to simplify the representation of the original multi-slab pavement. Similar to system A, the details of system B are not repeated here. System B is used to account for the effect of tire footprint geometry and shoulder support. Since a curling analysis of system B is not required, the AC layer of the composite pavement of system B is represented using the short-term modulus *EACL* only. Again, either the FE code or ISLAB2000 may be used for computing the stress due to axle loading only.

Similar to the total stress obtained using the MEPDG procedure (Equation (3-23)), the stress in the original multi-slab composite system is related to the stress in systems A and B as follows:

$$\sigma_{Tot} = \sigma_1^A(0, T) + LTE * [(\sigma_3^A(P, T^*) - \sigma_2^A(0, T^*)) - \sigma^A(P, 0) + \sigma^B(0)] \quad (3-122)$$

where:

σ_{Tot} = stress in the original multi-slab composite pavement

$\sigma_1^A(0, T)$ = stress in system A due to temperature curling only and is equal to the stress from the first elastic BVP of the *2-moduli approach*

$\sigma_2^A(0, T^*)$ and $\sigma_3^A(P, T^*)$ = stresses in system A due to the combined axle loading and temperature curling and are equal to the stresses from the second and third elastic BVPs of the *2-moduli approach*, respectively

$\sigma^A(P, 0)$ = stress in system A due to axle loading only

$\sigma^B(0)$ = stress in system B when the shoulder provides no edge support

LTE = load transfer efficiency between the pavement slab and the shoulder

Equation (3-122) is verified using a 15 ft long by 12 ft wide composite pavement placed on an elastic Winkler foundation. The modulus of subgrade reaction for the Winkler foundation is equal to 100 psi/in. The material properties of the constituent layers are presented in Table 3-20. Both of the layer interfaces are fully bonded. The stresses $\sigma^A(P, 0)$ and $\sigma^B(0)$ are computed using projects designed in ISLAB2000.

Table 3-20: Layer properties for the composite pavement.

Layer	Thickness, h (in)	Layer modulus, E (psi)	Poisson's ratio, μ	Unit weight, γ (lb/in ³)	Coefficient of thermal expansion, α (1/°F)
AC	4	<i>EACT</i> = 39448.9	0.15	0.087	1.65E-05
		<i>EACL</i> = 2.0E+05			
PCC	8	4.0E+06	0.15	0.087	5.50E-06
Base	0	4.0E+04	0.15	0.087	5.50E-06

In this example, the thickness of the base layer is purposely selected to be zero inches. This is done to maintain compatibility with ISLAB2000 since ISLAB2000 is not capable of analyzing fully bonded three-layered systems. However, it must be noted that other options such as

combining the thickness of layers 2 and 3 (while maintaining the exact same properties for the two layers) can also be used to maintain compatibility with ISLAB2000.

The composite pavement is subjected to a non-linear temperature distribution given in Table 3-21 below.

Table 3-21: Temperature profile for the composite pavement.

Layer		No. of temperature data points										
		1	2	3	4	5	6	7	8	9	10	11
AC	Reference temperature = 55.90 °F											
	Depth, in	0.0	1.0	2.0	3.0	4.0						
	Temp., °F	90.9	86.0	81.0	76.4	71.8						
PCC	Reference temperature = 55.90 °F											
	Depth, in	0.0	0.8	1.6	2.4	3.2	4.0	4.8	5.6	6.4	7.2	8.0
	Temp., °F	71.8	69.0	66.9	64.8	63.0	61.4	60.0	58.7	57.6	57.0	55.9

The axle load present on the slab is in the form of single axle dual wheel (SADW) load with a total load of 18000 lbs. The tire footprint is 9 in by 5 in and the load is applied at an offset, s , from the longitudinal edge of the slab. A uniform mesh of 6 in by 6 in elements is generated on the slab. Figure 3-36 presents the mesh and the loading configuration of the composite pavement.

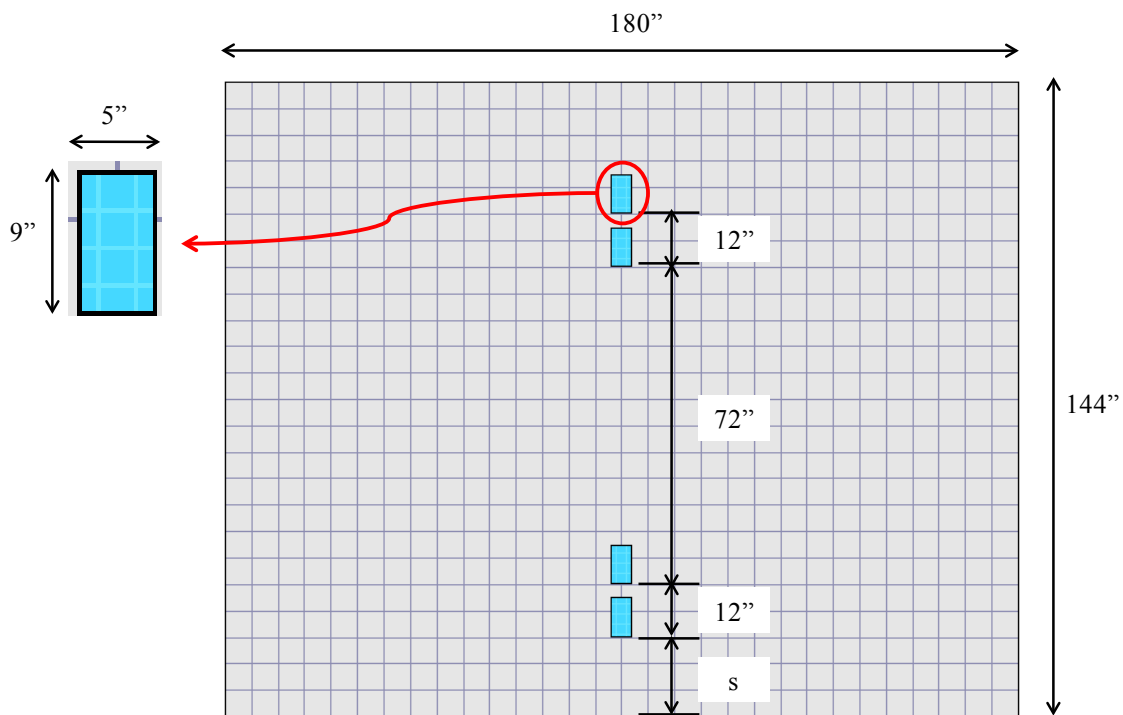


Figure 3-36: The original composite pavement system.

System A is the first simplified structural system with slab dimensions, layer properties, axle type, total axle load, wheel offset, and non-linear temperature distribution exactly the same as that of the original composite pavement. However, the tire footprint for system A is selected as a square with 7 in sides. The schematic of system A is shown in Figure 3-37.

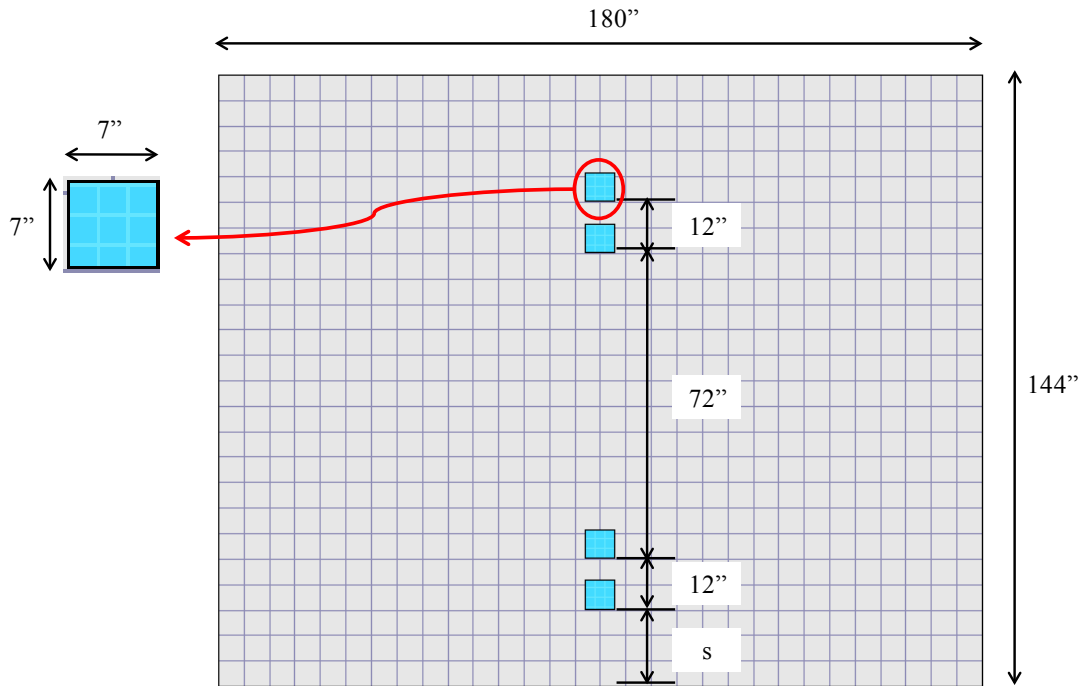


Figure 3-37: System A.

System B, the other simplified structural system, is considered as a single slab with layer properties, axle type, total axle load, wheel offset, and load footprint geometry exactly the same as that of the composite pavement. However, the dimensions for the slab in system B are selected as 30 ft long by 12 ft wide to ignore slab size effects. The schematic of system B is shown in Figure 3-38.

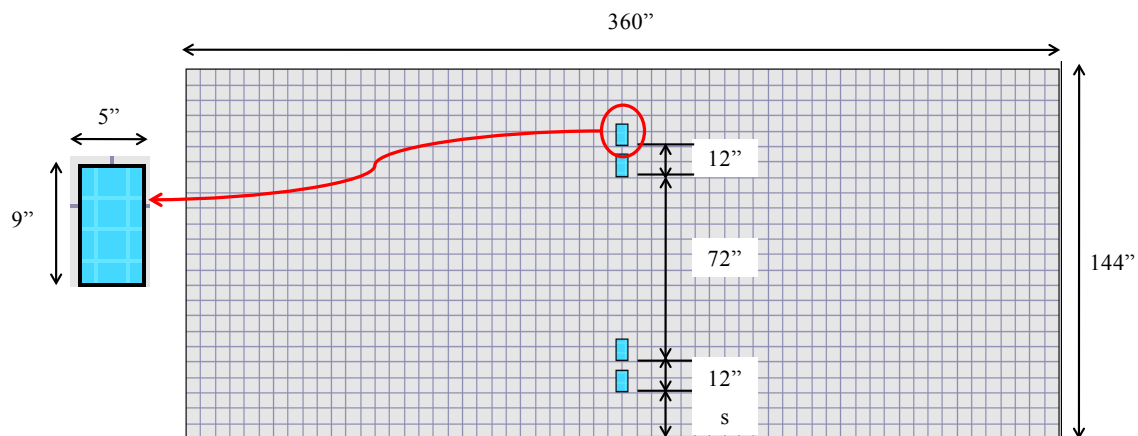


Figure 3-38: System B.

A factorial of 98 cases was considered by varying the offset s (i.e., distance of the axle load from the slab edge) and the thickness of the PCC layer. The offset is varied from 0 to 24 in (0, 2, 4, 6, 12, 18, and 24). The thickness of the PCC layer is varied from 2 to 15 in (2, 3, 4, 5, 6, 7, 8, 9, 10, 11, 12, 13, 14, and 15). The stress at the bottom of the PCC layer in the original composite pavement was calculated using the combined stress procedure detailed in Part 3.4 (Equation (3-110)) and it was verified against the stress obtained from systems A and B using Equation (3-122). The comparison of the stresses is presented in Figure 3-39.

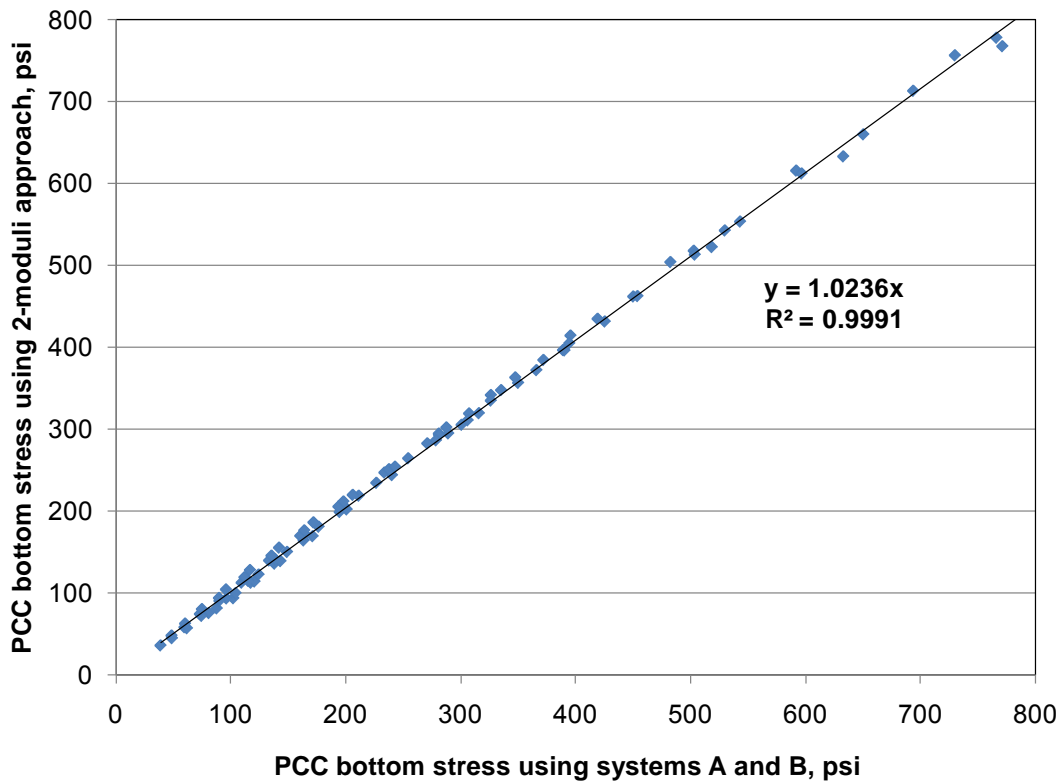


Figure 3-39: Comparison of PCC bottom stresses in the original composite pavement system using the 2-moduli approach and simplified systems A and B.

A very good match is observed between the stresses obtained using the two methods mentioned above. This implies that similar to the MEPDG, simplified structural systems can be used to represent a composite pavement system for computing stresses using the 2-moduli approach developed in this research.

Another technique employed by the MEPDG to simplify stress analysis is the use of equivalency conditions to analyze single layer systems in place of multi-layered pavement systems. Using this technique, the number of independent input parameters required for the analysis of multi-layered pavement can be substantially reduced. This was a significant contribution towards the development and training of the MEPDG neural networks. The following section presents the application of this technique for computation of stresses using the 2-moduli approach.

3.4.2 Equivalency Techniques for Multi-Layered Pavements

The stresses in a multi-layered pavement subjected to a combination of traffic loads and temperature distribution are dependent on several factors (*AASHTO 2008*). The MEPDG identifies up to 30 input parameters for the distress model of fatigue cracking in jointed plain concrete pavements (JPCP). These parameters include but are not limited to slab geometry, material properties of the constituent layers, foundation properties, temperature distribution, load geometry and properties, joint spacing, and load transfer efficiency. In the case of composite pavements, there are additional input parameters due to the presence of a viscoelastic asphalt concrete (AC) layer that influence the distress model of fatigue cracking for composite pavements.

In order to reduce the number of input parameters required for the analysis, the solution of a multi-layered pavement is expressed in terms of the solution of a simpler equivalent system. The equivalent system is generally selected as a single layer slab-on-grade. Finally, using equivalency conditions discussed below, the deflection and stress in the multi-layered pavement can be computed in terms of the deflection and stress in the equivalent single layer system, respectively. This technique has been adopted in the MEPDG for the analysis of rigid and composite pavements.

The equivalency between any two pavement systems is established based on the following criteria (*Korenev and Chernigovskaya 1962; Ioannides et al. 1992; and Khazanovich 1994*):

1. Equivalency of slab stiffness, $D = \frac{E h^3}{12(1 - \mu^2)}$
2. Equivalency of Korenev's non-dimensional temperature gradient, $\phi = \frac{2\alpha(1 + \mu)l^2}{h^2} \frac{k}{\gamma} \Delta T$
3. Equivalency of radius of relative stiffness, $l = \sqrt[4]{\frac{D}{k}}$, and
4. Equivalency of normalized load ratio, $q^* = \frac{P}{LW\gamma h}$

where:

D = stiffness of the slab

h and γ = thickness and unit weight of the layer, respectively

E and μ = Young's modulus and Poisson's ratio of the layer

α = coefficient of thermal expansion of the layer

k = modulus of subgrade reaction

ΔT = equivalent linear temperature gradient given by Equation (3-82)

P = applied axle load, and

L and W = length and width of the slab, respectively

If the above mentioned equivalency conditions are satisfied, then the deflections and stresses in the two pavements are related as follows:

$$w_1 = \frac{\gamma_1 h_1 k_2}{\gamma_2 h_2 k_1} w_2 \quad (3-123)$$

$$\sigma_1 = \frac{h_2 \gamma_1}{h_1 \gamma_2} \sigma_2 \quad (3-124)$$

where:

w = deflection of the pavement

σ = stress in the pavement

subscripts 1 and 2 = pavement systems 1 and 2, respectively

A simple example to verify the applicability of equivalency conditions for the stress analysis using the *2-moduli approach* is presented next. The original three-layered composite pavement system, placed on an elastic Winkler foundation, is loaded under a SADW wheel load at an offset of 2 in from the slab edge (Figure 3-36). The modulus of subgrade reaction for the Winkler foundation is equal to 100 psi/in. The properties of the constituent layers are given in Table 3-20. Both of the layer interfaces are fully bonded. The pavement is also subjected to the non-linear temperature distribution given in Table 3-21.

Corresponding to the multi-layered systems 1 and 2 of the BVPs described in Part 3.4, two equivalent single layer slabs (SL1 and SL2) are obtained. Slab SL1 corresponds to the long-term AC modulus E_{ACT} and slab SL2 corresponds to the short-term AC modulus E_{ACL} . Both the slabs are placed on an elastic Winkler foundation with a coefficient of subgrade reaction equal to 100 psi/in.

Using the equivalency of slab stiffness, either the thickness or the Young's modulus of the equivalent single layer slab can be computed. For this example, the Young's modulus of the equivalent single layer slab E_{eq} is assumed to be known and the corresponding thickness h_{eq} is calculated as follows:

$$h_{eq} = \sqrt[3]{\frac{1}{E_{eq}} \left[\begin{aligned} & E_{AC} h_A^3 + E_{PCC} h_{PCC}^3 + E_{Base} h_{Base}^3 + \\ & E_A h_A \left(\frac{h_A}{2} - x \right)^2 + E_{PCC} h_{PCC} \left(h_{AC} + \frac{h_{PCC}}{2} - x \right)^2 \\ & + E_{Base} h_{Base} \left(h_{AC} + h_{PCC} + \frac{h_{Base}}{2} - x \right)^2 \end{aligned} \right]} \quad (3-125)$$

where:

x = distance of the neutral axis from the top of the AC layer

The unit weight of the equivalent single layer slab γ_{eq} is calculated as:

$$\gamma_{eq} = \frac{(\gamma_{AC}h_{AC} + \gamma_{PCC}h_{PCC} + \gamma_{Base}h_{Base})}{h_{eq}} \quad (3-126)$$

The properties of the slabs SL1 and SL2 are presented in Table 3-22 where the thickness and the unit weight are computed using equations (125) and (126), respectively.

Table 3-22: Layer properties for slabs SL1 and SL2.

	Young's modulus, (psi)	Poisson's ratio	Coefficient of thermal expansion, (1/°F)	Thickness, (in)	Unit weight, (lb/in ³)
SL1	4.0E+06	0.15	5.50E-06	8.09	0.1290
SL2	4.0E+06	0.15	5.50E-06	8.43	0.1238

Slab SL1 is subjected to an equivalent linear temperature gradient calculated using the non-linear temperature distribution present in the three-layered composite pavement system (Table 3-21) and Equation (3-82). Since SL1 corresponds to the long-term AC modulus E_{ACT} and is subjected to the temperature gradient only, stresses in slab SL1 are computed using the first BVP presented in Part 3.4 section entitled *Stress Computation Procedure using the 2-Moduli Approach* for temperature curling only.

On the other hand, slab SL2 corresponds to the short-term AC modulus E_{ACL} and is subjected to the fictitious force corresponding to the temperature gradient in slab SL1, which is computed using the second BVP presented in the Part 3.4 section entitled *Stress Computation Procedure using the 2-Moduli Approach*. Slab SL2 is also subjected to the SADW load acting on the three-layered composite pavement system. The axle type, axle load, and wheel offset of the SADW load acting on slab SL2 are exactly the same as that on the three-layered composite pavement system. The stress in slab SL2 under the sum of the fictitious force and the SADW load is computed using the third BVP presented in the Part 3.4 section entitled *Stress Computation Procedure using the 2-Moduli Approach*.

The bending stresses obtained at the bottom of slabs SL1 and SL2 are transformed to the bending stress at the bottom of PCC layer in the three-layered composite pavement using equations (88) and (89) as follows:

$$\sigma_{3LS} = \beta * \sigma_{SL} \quad (3-127)$$

$$\beta_1 = \frac{2 * (h_{AC} + h_{PCC} - x_1) E_{PCC}}{h_{eq1} E_{eq1}} \quad (3-128)$$

$$\beta_2 = \frac{2 * (h_{AC} + h_{PCC} - x_2) E_{PCC}}{h_{eq2} E_{eq2}} \quad (3-129)$$

where:

σ_{3LS} = stress in the three-layered system

σ_{SL} = stress in the equivalent single layer slab

β = factor that converts the linear bending stresses at the bottom of the equivalent single layer slab to the linear bending stresses in the multi-layered slab at the depth of interest z

The deflections and stresses obtained using the stress computation procedure presented in Part 3.4 for the three-layered composite pavement system are compared to the deflections and stresses obtained for the equivalent single layer slabs SL1 and SL2. Table 3-23 presents the deflections and stress at the bottom of the PCC layer at slab edge.

Table 3-23: Deflections and stress at the bottom of the PCC layer at slab edge.

	Location, in		Deflection, in	Longitudinal stress, psi		
	X	Y		σ_{SL}	β	σ_{3LS}
Three elastic solution – Three-layered composite pavement						
# 1	90	0	0.0188			136.19
# 2	90	0	0.0188			-101.04
# 3	90	0	0.0424			180.99
Combined stress						418.22
Three elastic solution – Equivalent single layer slabs SL1 and SL2						
SL1: # 1	90	0	0.0188	136.73	0.996	136.191
SL2: # 2	90	0	0.0188	-102.73	0.983	-101.038
SL2: # 3	90	0	0.0424	184.03	0.983	180.993
Combined stress						418.221
% Difference						0.000%

The combined stress in the three-layered composite pavement exactly matches the combined stress obtained from the equivalent single layer slabs SL1 and SL2. This implies that the stress computation procedure, presented in Part 3.4, is capable of analyzing the multi-layered system through a combination of equivalent single layer systems.

3.5. The 2-Moduli Approach in Summary

Composite pavements are complex structures incorporating both asphalt and Portland cement concrete (PCC) layers. Composite pavement behavior exhibits features of both rigid and flexible pavements. Because of this, a structural analysis of composite pavements is a challenging program. This research concentrated on improving the structural modeling of stress analysis for prediction of PCC fatigue cracking compatible with the MEPDG PCC fatigue cracking modeling. A summary of the research findings is presented below.

3.5.1 Research Findings

The main findings of this research work can be summarized as follows:

- The use of a single load duration-dependent AC dynamic modulus to characterize the behavior of the AC layer seems insufficient for composite pavements subjected to a combination of traffic loads and temperature curling because a significant difference was found in the AC dynamic modulus when a composite pavement is subjected to typical traffic loads and to one hour of temperature loads.
- A finite element (FE) model was developed to analyze a composite pavement placed on a Winkler foundation that incorporates elastic and viscoelastic layers. The FE model has the capability to analyze pavements subjected to traffic loads and temperature curling. The FE model was validated against semi-analytical solutions.
- A stress computation procedure was developed to calculate stresses in the composite pavement subjected to a combination of traffic loads and temperature curling using two load duration-dependent AC moduli. The AC moduli were computed using the existing MEPDG procedure for calculating the dynamic modulus of the AC layer.
- The stress computation procedure based on the *2-moduli approach* demonstrated that the MEPDG may significantly underestimate the stress in composite pavements subjected to a combination of traffic loading and temperature curling. Further investigation of this issue is required.

3.5.2 Recommendations for the Future Research

Based on the findings of this research, the following recommendations for the future research are made:

- The procedure for computing the AC dynamic modulus was originally developed for flexible pavements (AC layer placed directly on top of the base layer). Modifications to this procedure are required for the analysis of composite pavement due to the presence of a stiff Portland cement concrete (PCC) layer between the AC layer and the base.
- In the case of temperature curling analysis, both the MEPDG and the proposed FE model assume the reference temperature of the AC layer as equal to the temperature at the bottom surface of the PCC layer. This assumption needs to be investigated and modified, if required.
- The FE model developed in this research is an extension of the state-of-the-art pavement computational package ISLAB2000 in terms of viscoelastic material modeling. However, not all features of ISLAB2000 are currently implemented in the FE model. Future versions of the FE code require complete merger with ISLAB2000.
- For merging the results of this research with the MEPDG fatigue cracking model for composite pavements, rapid solutions based on the stress computation procedure using the *2-moduli approach* should be generated.

It has been observed by many researchers that the subgrade behavior of the Winkler foundation is load rate-dependent. The apparent subgrade stiffness is much higher under the fast moving axle loads than during the slow developing temperature curling and moisture warping. Therefore, it may be possible to extend a similar *2-moduli approach* to the subgrade modulus in order to overcome this limitation.

Chapter 4. Design and Analysis of TICP

4.1. HMA-PCC Rutting Models

One advantage of the timing of the TPF-5(149) project is that it ran concurrently with the SHRP2 R21 project, which examined the suitability of the MEPDG for HMA-PCC design and analysis. One recommendation made by the R21 project was that while the MEPDG was found to adequately predict rutting performance for Level 1 inputs, for Level 3 inputs the MEPDG underestimated the extent of permanent deformation in rutting relative to field data (SHRP2 2012). Hence, a dual objective for the project research was to:

1. investigate the MEPDG rutting model and the CalME rutting model and
2. develop a procedure to incorporate the CalME rutting model into the MEPDG framework that provides reasonable rutting prediction for Level 3 inputs.

The overall goal was to provide a HMA-PCC design and analysis procedure for rutting for pavement engineers that does not require uncommon inputs (most projects do not contain Level 1 detail) and does not force the user outside of the MEPDG framework. The following subsections describe this effort.

4.1.1 MEPDG Rutting Model

As detailed in previous task reports, the MEPDG divides the layers of the pavement system into sublayers, where the thickness of each sublayer is determined from the layer material properties, overall layer thickness, and the position of the sublayer relative to the thickness of the pavement system (NCHRP 2004). The pavement response in each sublayer is calculated using elastic layer theory (JULEA). Furthermore, the MEPDG uses the Enhanced Integrated Climate Model (EICM) to calculate hourly temperature and moisture conditions through the sublayers of the pavement structure and adjust sublayer modulus values accordingly (Larson and Dempsey 1997).

Before detailing how the MEPDG models rutting, the temperature quintile concept for HMA sublayers should be briefly introduced. HMA sublayer temperatures are combined into five quintiles for each month of the project analysis. A normal distribution is assumed for the frequency distribution of HMA sublayer temperatures (Figure 4-1).

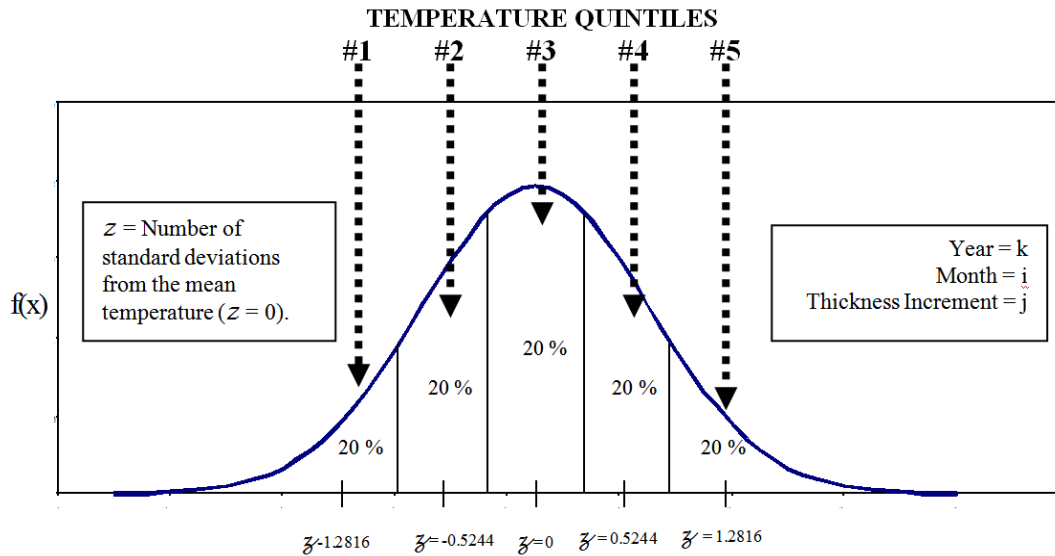


Figure 4-1: Temperature quintiles used by MEPDG to determine HMA sublayer dynamic modulus (from AASHTO 2008).

The average temperature within each quintile of a sublayer for each month is used to determine the dynamic modulus of that sublayer. It is important to note that traffic is assumed to be equal within each of the five temperature quintiles; hence, for HMA projects, the MEPDG does not relate hourly truck volumes directly to the hourly temperatures (AASHTO 2008).

Furthermore, EICM calculates the temperatures within each unbound sublayer. This calculation is used, for example, to modify the resilient modulus of sublayers that experience freeze-thaw. EICM also calculates the average moisture content in the unbound sublayers for each month of the analysis period; this calculation is used to adjust the resilient modulus of each unbound sublayer for each month throughout the analysis period (Larson and Dempsey 1997; NCHRP 2004).

Permanent deformation in the form of HMA rutting is caused by the plastic or permanent vertical deformation in the layers of the pavement system. Given sublayer properties and associated temperature quintiles, the MEPDG uses sublayer characteristics to determine the maximum permanent deformation within each sublayer from horizontal and vertical strains at critical locations through the sublayer. Hence, according to the MEPDG, rutting for a given season is the sum of the plastic vertical deformations within each layer (AASHTO 2008).

The MEPDG model for rutting uses the plastic vertical strain under specific pavement conditions for the total number of trucks within that condition. As conditions vary on a monthly basis, the MEPDG uses the so-called strain hardening approach to incorporate plastic vertical strains within each month in a cumulative deformation subsystem. The accumulation of plastic deformation is measured in the laboratory using repeated load triaxial tests for both HMA mixtures and unbound materials, and the laboratory-derived relationship is adjusted to match rut depth observed in the field. The expression for permanent vertical deformation in the HMA surface layer, as detailed in AASHTO (2008), is then

$$\Delta_{p(HMA)} = \varepsilon_{p(HMA)} h_{HMA} = \beta_{1r} k_z \varepsilon_{r(HMA)} 10^{k_{1r}} n^{k_{2r} \beta_{2r}} T^{k_{3r} \beta_{3r}} \quad (4-1)$$

where

- $\Delta_{p(HMA)}$ = Accumulated permanent or plastic vertical deformation in the HMA layer/sublayer, in.
 $\varepsilon_{p(HMA)}$ = Accumulated permanent or plastic axial strain in the HMA layer/sublayer, in/in.
 $\varepsilon_{r(HMA)}$ = Resilient or elastic strain calculated by the structural response model at the mid-depth of each HMA sublayer, in/in.
 $h_{(HMA)}$ = Thickness of the HMA layer/sublayer, in.
 n = Number of axle load repetitions.
 T = Mix or pavement temperature, °F.
 k_z = Depth confinement factor.
 k_{1r}, k_{2r}, k_{3r} = Global field calibration parameters (from the NCHRP 1-40D recalibration; $k_{1r} = -3.35412$, $k_{2r} = 0.4791$, $k_{3r} = 1.5606$).
 $\beta_{1r}, \beta_{2r}, \beta_{3r}$ = Local or mixture field calibration constants; for the global calibration, these constants were all set to 1.0.

and where

$$k_z = (C_1 + C_2 D) 0.328196^D \quad (4-2)$$

$$C_1 = -0.1039(H_{HMA})^2 + 2.4868H_{HMA} - 17.342 \quad (4-3)$$

$$C_2 = 0.0172(H_{HMA})^2 - 1.7331H_{HMA} + 27.428 \quad (4-4)$$

- D = Depth below the surface, in.
 H_{HMA} = Total HMA thickness, in.

Furthermore, the model adopted by MEPDG for deformation in unbound sublayers (including the foundation), as described in AASHTO (2008), is

$$\Delta_{p(soil)} = \beta_{s1} k_{s1} \varepsilon_v h_{soil} \left(\frac{\varepsilon_o}{\varepsilon_r} \right) e^{-\left(\frac{\rho}{n}\right)^\beta} \quad (4-5)$$

where

- $\Delta_{p(Soil)}$ = Permanent or plastic deformation for the layer/sublayer, in.
 n = Number of axle load applications.
 ε_o = Intercept determined from laboratory repeated load permanent deformation tests, in/in.

- ε_r = Resilient strain imposed in laboratory test to obtain material properties ε_o , β , and ρ , in/in.
 ε_v = Average vertical resilient or elastic strain in the layer/sublayer and calculated by the structural response model, in/in.
 h_{Soil} = Thickness of the unbound layer/sublayer, in.
 k_{sl} = Global calibration coefficients; $k_{sl}=1.673$ for granular materials and 1.35 for fine-grained materials.
 β_{sl} = Local calibration constant for the rutting in the unbound layers; the local calibration constant was set to 1.0 for the global calibration effort.

and where

$$\text{Log}\beta = -0.61119 - 0.017638(W_c) \quad (4-6)$$

$$\rho = 10^9 \left(\frac{C_o}{(1 - (10^9)^\beta)} \right)^{\frac{1}{\beta}} \quad (4-7)$$

$$C_o = \text{Ln} \left(\frac{a_1 M_r^{b_1}}{a_9 M_r^{b_9}} \right) = 0.0075 \quad (4-8)$$

- W_c = Water content, percent.
 M_r = Resilient modulus of the unbound layer or sublayer, psi.
 $a_{1,9}$ = Regression constants; $a_1=0.15$ and $a_9=20.0$.
 $b_{1,9}$ = Regression constants; $b_1=0.0$ and $b_9=0.0$.

4.1.2 CalME Rutting Model

To predict rutting, CalME uses a modified version of the shear-based procedure developed by Deacon et al (2002) to predict accumulated rut depth in HMA layers (Ullidtz et al 2008). This model considers the effects of temperature, material properties, load levels, and speed. Furthermore, it makes use of fundamental physical properties and a theoretical model to predict pavement response caused by a load on the pavement.

CalME follows an increment-recursive (IR) procedure when simulating pavement performance, wherein material properties are updated for each time increment by considering the changes in environmental conditions, traffic characteristics, and HMA stiffness. Calculated damage (permanent deformation for rutting, stiffness change otherwise) for each time increment is recursively accumulated to be able to predict the pavement condition at any point in time. The IR mechanism has been found to be an effective approach for considering damage accumulation (Ullidtz et al 2006).

The CalME model for rutting has been adopted for this work and is described in the subsections below, which also describe the models, at times, in terms of their incorporation into the TPF-5(149) procedure to avoid repeating this information in multiple locations. The CalME

procedure has been slightly modified in the sense that MEPDG project inputs are used to develop calibration coefficients, which are detailed in the course of describing the full coupling of the CalME and MEPDG procedures in Section 4.1.3.

Rut Depth

In order to calculate the permanent deformation in an AC sublayer, the elastic shear strain γ_e for a given increment is calculated as

$$\gamma^e = \frac{\tau_{xz}}{E_{dam} / (1 + \nu)} \quad (4-9)$$

where E_{dam} is the damaged modulus; ν is Poisson's ratio; and τ_{xz} is the shear stress calculated using a layered elastic analysis program at 50 mm below the tire edge.

Furthermore, the effective number of load applications N_0 that are required to produce the condition at the beginning of the increment are calculated. The total number of load applications N_{tot} is the sum of effective number of load applications and the number of load applications during the current increment.

$$N_{tot} = N_0 + N \quad (4-10)$$

The inelastic shear strain in the asphalt layer, γ_i , for the total number of load applications during the current increment is

$$\gamma^i = \exp\left(A3 + \alpha3 * \left[1 - \exp\left(-\ln(N_{tot})/\gamma3\right) * \left(1 + \ln(N_{tot})/\gamma3\right)\right]\right) * \exp\left(\beta3 * \tau_{xz} / \tau_{ref}\right) * \gamma^e \quad (4-11)$$

where τ_{ref} is a reference shear stress (0.1 MPa \approx atmospheric pressure) and $A3$, $\alpha3$, $\beta3$, and $\gamma3$ are calibration coefficients, which take values that correspond to the HMA mix design for the upper lift of the TICP. This calibration can be conducted using laboratory-derived values or can be correlated using in-field estimates, as done for the CalME-MEPDG coupling below (Table 4-2).

The permanent deformation for each AC sublayer, dp , is

$$dp = K * h * \gamma^i \quad (4-12)$$

where h is the thickness of the AC sublayer and K is a calibration constant = 1.4. The total rut depth is calculated by adding the permanent deformation for all AC sublayers.

Fatigue Damage

The damaged modulus, E_{dam} , for a particular month is calculated based on the damage w from the previous month. For the very first month of analysis (traffic open month), the pavement is assumed to be undamaged ($w = 0$).

$$\log(E_{dam}) - \delta = (\log(E_i - \delta)) * (1 - w_{(month-1)}) \quad (4-13)$$

where *month* represents the current month of analysis; E_i is the modulus of intact material; and δ is a material constant.

Using the damaged AC modulus, modulus for other layers, and structural information, strain and shear stress is calculated in the AC layer using layered elastic analysis (LEA). For the combined MEPDG/CALME procedure of TPF-5(149) for TICP design, the program MnLayer is used to calculate the elastic strain either at 100 mm into the AC layer or at the bottom of the AC layer if its thickness is less than 100 mm. This agrees with CalME assumptions that rutting is confined to the upper 100 mm of the asphalt layers (Ullidtz et al 2008). Similarly, the shear stress is calculated either at 50 mm into the AC layer or at half the depth of the AC layer if its thickness is less than 100 mm. Five different positions of traffic wander for each axle weight are considered to obtain the shear stresses and strains.

The next step involves the calculation of allowable number of load repetitions, MN_p , which is defined as

$$MN_p = A2 * \left(\frac{\mu\epsilon_{xx}}{\mu\epsilon_{ref}} \right)^{\beta2} * \left(\frac{E_{dam}}{E_{ref}} \right)^{\gamma2} * \left(\frac{E_i}{E_{ref}} \right)^{\delta2} \quad (4-14)$$

where E_{ref} is the reference asphalt modulus; $\mu\epsilon_{ref}$ is the reference asphalt strain in microstrains; $\mu\epsilon_{xx}$ is the horizontal strain; and $A2$, $\beta2$, $\gamma2$, and $\delta2$ are calibration coefficients. The CalME procedure was developed for flexible pavements requires the horizontal strain to be computed at the bottom of the HMA layer; for TPF-5(149) adoption of CalME for the MEPDG framework, the horizontal strain is instead computed at the mid-depth of the HMA layer. The calibration coefficients are developed from laboratory tests; in the case of the TPF-5(149) procedure detailed below, these coefficients are correlated to known properties of the pavement system from MEPDG intermediate files (Table 4-1).

It is now necessary to calculate MN_0 , the effective allowable number of load applications that would reproduce the condition at the beginning of the increment

$$MN_0 = 3 * MN_p * (w)^{1/\alpha2} \quad (4-15)$$

Note that the damage w used in this calculation is from the previous increment and $\alpha2$ is a calibration parameter. The total number of load applications for the current increment, MN_{tot} , is

$$MN_{tot} = MN_0 + \left(\frac{N}{10^6} \right) \quad (4-16)$$

given that,

$$N = 30 \cdot N_{IN} \cdot \left(\frac{1}{n_{qt}} \right) \cdot \left(\frac{1}{n_{lp}} \right) \quad (4-17)$$

where N_{IN} is the number of load applications from the traffic file, n_{qt} is the number of quintile temperatures in a single month, and n_{lp} is the number of load positions used.

Finally, the damage w in the current increment corresponding to the total number of load applications, MN_{tot} , is calculated as

$$w = \left(\frac{MN_{tot}}{3 * MN_p} \right)^{\alpha^2} \quad (4-18)$$

where both MN_{tot} and MN_p are in millions (10^6) of load applications.

The damage is then calculated for the next increment of axle weights, axle types, load positions, and quintile temperatures in a single month. Finally, it is calculated for each month in the pavement design life, in a similar manner.

4.1.3 TPF-5(149) M-E Design to Mitigate Rutting in TICP

The procedure developed under TPF-5(149) to design TICP and better account for rutting 1) employs the input files generated by executing a MEPDG project and 2) calculates the rut depth in an AC overlaid PCC pavement based on the CalME rutting model developed at the University of California-Davis. The rut-depth calculation is a three-step process which involves:

1. Computation of fatigue damage;
2. Calculation of rut depth based on fatigue damage;
3. Extracting information from intermediate MEPDG project files to be used as inputs for the above calculations.

The following subsections describe the specific steps to be employed when incorporating the CalME rutting procedure into an MEPDG project for a TICP.

Create and run MEPDG for TICP project file

The first step in the modified TPF-5(149) procedure is to create a HMA-PCC project file in the MEPDG program that best describes the desired TICP project. Once the project is created, the project file should be run to completion. Doing so creates traffic and climate analysis files that are necessary to augment the MEPDG analysis with the CalME rutting model.

Run TPF-5(149) program to read MEPDG inputs for CalME calibration

The next step is to run the TPF-5(149) program, which will read intermediate MEPDG project files to create calibration coefficients for the CalME fatigue and rutting models, detailed in

Sections 2.2.1 and 2.2.2 respectively. Table 4-1 provides example values for these coefficients for three HMA mix designs for the calculation of fatigue damage. These coefficients were calculated based on laboratory data for the HMA mixes of the HVS (PG 64-28 PM and RHMA-G) and MnROAD (PG 64-34) test sections by using nonlinear regression obtained by the University of California-Davis under the SHRP2 R21 project. In the combined MEPDG/CalME program for TPF-5(149), these calibration parameters are extracted directly from the MEPDG intermediate files.

Table 4-1: Model coefficients for CalME fatigue model.

HMA Mix	A2	β_2	γ_2	δ_2
PG 64-28 PM	1.9166	2.6490	0	4.2084
RHMA	0.3593	3.9425	0	1.7189
PG 64-34	0.7546	3.3804	0	2.2463

Table 4-2 describes values for these coefficients for the same HMA mix designs for the rut depth calculation.

Table 4-2: Model coefficients for CalME rutting model.

HMA Mix	A3	α_3	β_3	γ_3	τ_{ref}
PG 64-28 PM	1.9166	2.6490	0	4.2084	0.1
RHMA	0.3593	3.9425	0	1.7189	0.1
PG 64-34	0.7546	3.3804	0	2.2463	0.1

The input files necessary to develop these calibration coefficients are detailed in the following step-by-step procedure. The input files listed below are extracted from the outputs generated by executing a MEPDG project. The extraction process is simplified by executing the program from the compiled and built source code 'NewCivilGUI.jar'. The program extracts required information from the structural, traffic, and temperature files of a MEPDG project (Figure 4-2).

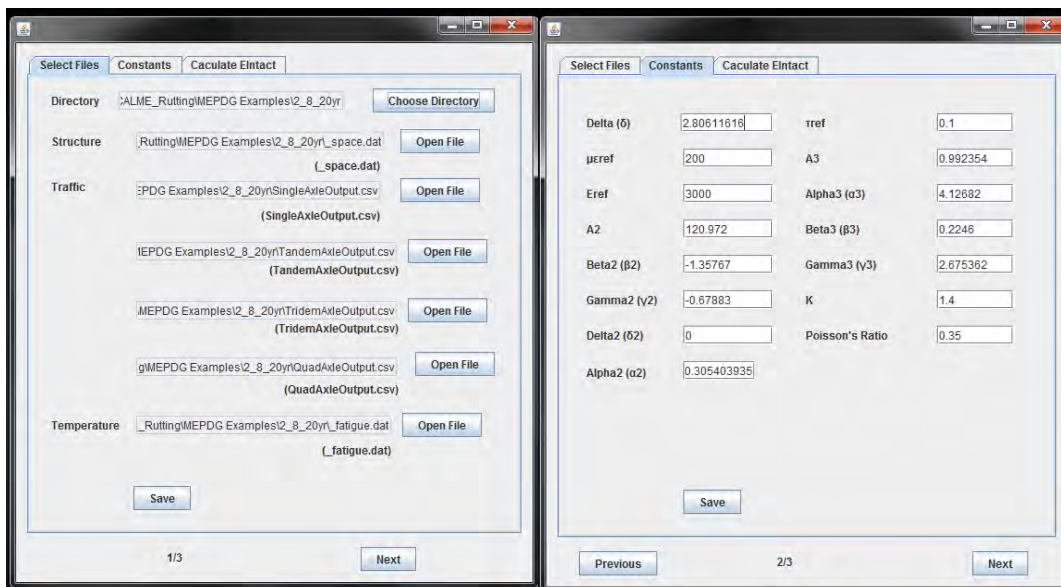


Figure 4-2: GUI for extracting MEPDG project input information (at left) and extracting calibration constants (at right).

The constants for the calculation of AC dynamic modulus are also extracted from the MEPDG temporary files and saved (Figure 4-2). The user may overwrite these constants before saving them, if required. The following subsections describe each of the input files containing the required data for the TPF-5(149) pavement design procedure.

Step 1: Structural Inputs from _space.dat

The MEPDG temporary file “_space.dat” is used for reading the number and thicknesses of the AC sublayers. Figure 4-3 presents the thicknesses of sublayers AC1, AC2, and AC3 as highlighted in rows # 3 to 5. Also, note the total number of months as highlighted in row 10 of the example file.

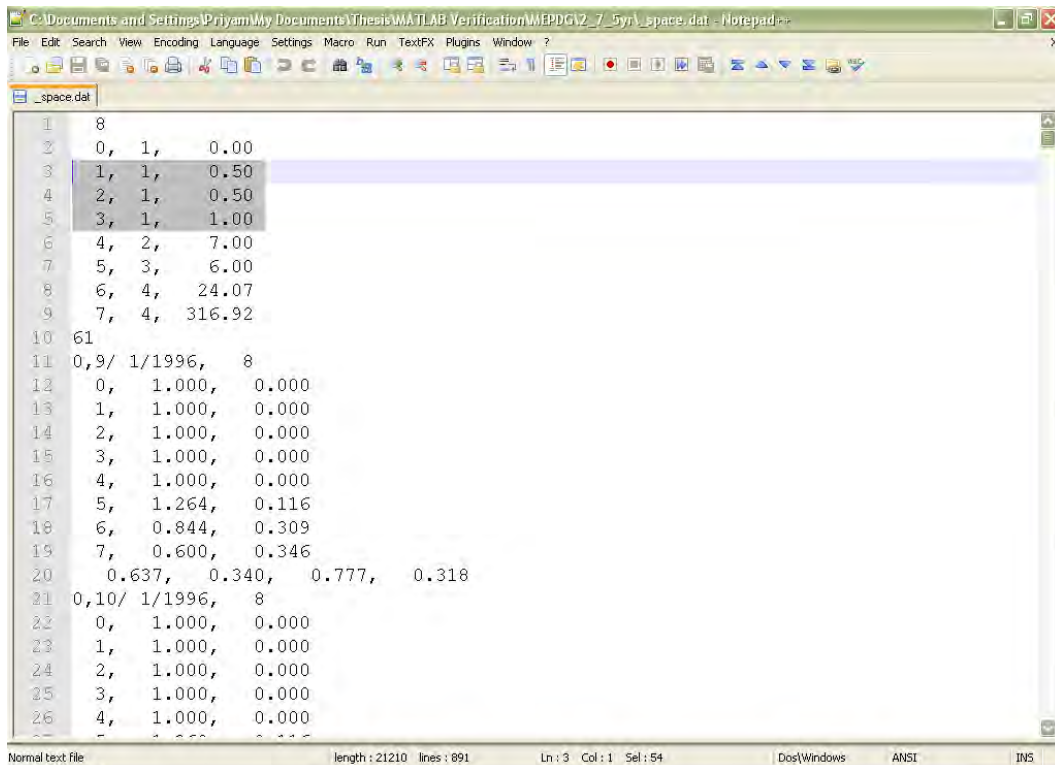


Figure 4-3: MEPDG file "_space.dat", specifying pavement structure.

Step 2: Traffic Open Timing from MonthlySeasonPattern.txt

The MEPDG file “MonthlySeasonPattern.txt” is used for reading the number of months between construction and traffic open as highlighted in rows # 4. Subtract the number of months between construction and traffic open from the total number of months (highlighted in Figure 4-4) to obtain the number of months for actual analysis.

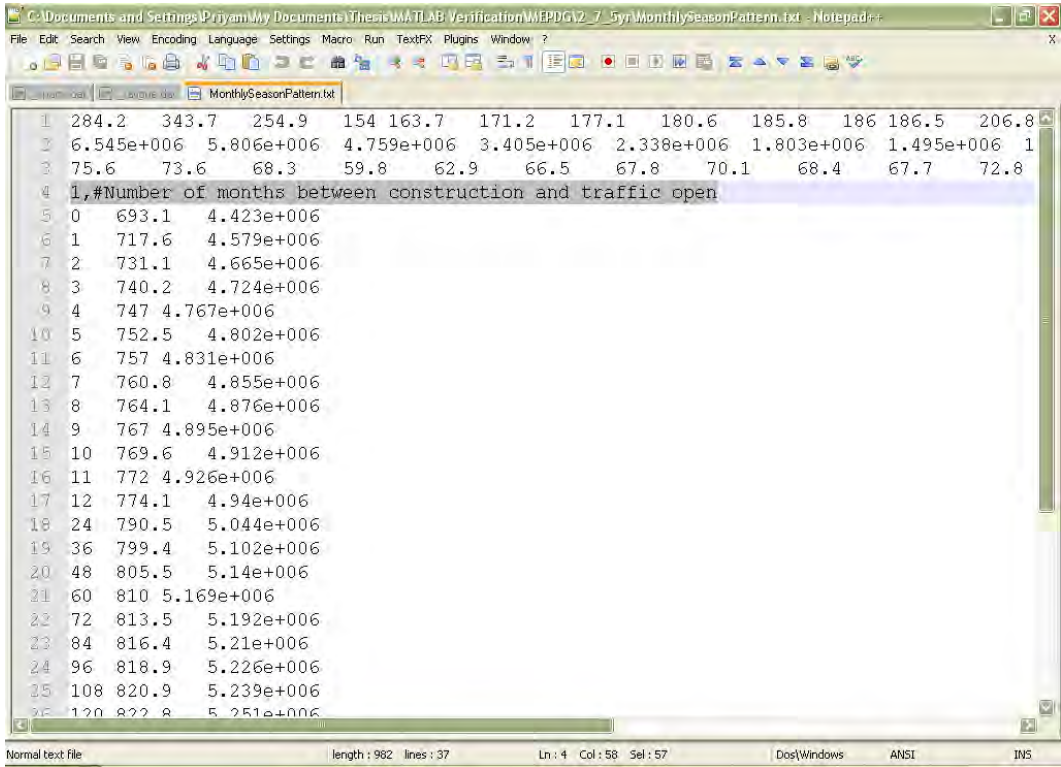


Figure 4-4: MEPDG input file specifying number of months between construction and traffic open.

Step 3: Temperature Data from _fatigue.dat

The MEPDG temporary file “_fatigue.dat” is used for reading monthly quintile temperatures corresponding to each sublayer of AC. Skip records corresponding to the number of months between construction and traffic open. Figure 4-5 presents the five quintile temperatures (T1, T2, T3, T4, and T5) for sublayer AC1 highlighted in row # 8 for the month of October 1996.

Line	Temp	Pos	Q1	Q2	Q3	Q4	Q5	Q6	Q7	Q8	Q9	Q10
1	0, 9/ 1/1996,	10										
2	0,	1,	50.2,	58.1,	65.8,	73.8,	89.7,	67.55,	14.23			
3	1,	1,	50.9,	58.4,	65.9,	73.5,	88.6,	67.46,	13.60			
4	2,	1,	51.9,	58.9,	66.1,	73.0,	86.4,	67.25,	12.50			
5	3,	1,	53.2,	59.5,	66.1,	72.1,	83.8,	66.93,	11.07			
6	0,10/ 1/1996,	10										
7	0,	1,	35.8,	45.1,	52.4,	59.7,	73.8,	53.37,	13.68			
8	1,	1,	36.4,	45.5,	52.6,	59.6,	72.9,	53.41,	13.14			
9	2,	1,	37.6,	46.2,	53.1,	59.5,	71.3,	53.54,	12.17			
10	3,	1,	39.1,	47.2,	53.6,	59.2,	69.3,	53.67,	10.89			
11	1,11/ 1/1996,	10										
12	0,	1,	19.4,	27.1,	32.6,	39.0,	48.2,	33.28,	10.44			
13	1,	1,	20.0,	27.5,	32.8,	38.9,	47.8,	33.41,	10.03			
14	2,	1,	21.0,	28.0,	32.9,	39.0,	47.2,	33.62,	9.44			
15	3,	1,	22.5,	28.8,	33.1,	39.0,	46.4,	33.96,	8.60			
16	1,11/16/1996,	10										
17	0,	1,	9.4,	21.3,	25.5,	29.7,	38.3,	24.84,	10.35			
18	1,	1,	10.1,	21.6,	25.7,	29.7,	38.2,	25.04,	10.05			
19	2,	1,	11.5,	22.2,	25.9,	29.8,	37.6,	25.39,	9.40			
20	3,	1,	13.2,	22.9,	26.5,	29.8,	36.9,	25.86,	8.55			
21	1,12/ 1/1996,	10										
22	0,	1,	14.4,	23.5,	26.3,	29.1,	33.6,	25.36,	6.74			
23	1,	1,	15.0,	23.7,	26.3,	28.9,	33.4,	25.46,	6.45			
24	2,	1,	16.0,	24.0,	26.4,	28.8,	32.9,	25.64,	5.93			
25	3,	1,	17.5,	24.6,	26.5,	28.6,	32.3,	25.91,	5.18			
26	1,12/16/1996,	10										
27	0,	1,	-4.6,	6.9,	11.8,	16.6,	23.9,	10.98,	9.95			
28	1,	1,	4.0,	7.4,	11.8,	16.7,	23.7,	11.18,	9.65			

Figure 4-5: MEPDG input file for temperature.

*Step 4: Traffic Data from *.AxleOutput.csv*

The MEPDG temporary files “SingleAxleOutput.csv”, “TandemAxleOutput.csv”, “TridemAxleOutput.csv”, and “QuadAxleOutput.csv” are used for reading the number of load applications due to single axle, tandem axle, tridem axle, and quad axle, respectively. The values in the .csv files are listed for an average day in a month. Also, since the monthly temperatures are divided into five quintiles and four load positions are assumed, each cell has to be multiplied with $(30 \times 0.2 \times 0.25)$ to obtain the number of load applications for one month, one quintile temperature, and one load position. The columns of the .csv file denote the weights of an axle. Figure 4-6 presents the input file for single axle.

	A	B	C	D	E	F	G	H	I	J	K	L	M	N	O
1	2006	October	135.743	109.003	150.224	127.212	136.22	167.881	196.658	220.55	200.342	158.581	104.109	69.438	49.8029
2	2006	November	135.931	109.062	150.184	127.203	136.121	167.768	196.5	220.586	200.338	158.704	104.114	69.4518	49.8029
3	2006	December	135.916	109.031	150.238	127.11	136.19	167.728	196.514	220.587	200.418	158.645	104.143	69.4409	49.8029
4	2007	January	135.902	109.017	150.252	127.213	136.117	167.699	196.485	220.633	200.327	158.669	104.171	69.4754	49.8029
5	2007	February	135.785	109.003	150.194	127.227	136.291	167.699	196.549	220.646	200.413	158.599	104.106	69.4487	49.8035
6	2007	March	135.83	109.003	150.18	127.096	136.179	167.737	196.604	220.732	200.337	158.674	104.113	69.4478	49.8305
7	2007	April	135.785	108.887	150.659	127.259	136.163	167.648	196.48	220.605	200.346	158.584	104.097	69.4484	49.8029
8	2007	May	135.902	109.017	150.297	127.1	136.173	167.685	196.542	220.618	200.374	158.599	104.151	69.4895	49.8167
9	2007	June	135.93	109.017	150.238	127.119	136.213	167.82	196.571	220.605	200.248	158.607	104.114	69.4522	49.817
10	2007	July	135.906	109.017	150.242	127.114	136.194	167.722	196.552	220.63	200.377	158.613	104.114	69.466	49.817
11	2007	August	135.929	109.003	150.224	127.11	136.22	167.727	196.458	220.66	200.363	158.651	104.153	69.4487	49.817
12	2007	September	135.902	109.017	150.294	127.17	136.211	167.705	196.5	220.573	200.349	158.694	104.1	69.438	49.8063
13	2007	October	141.173	113.363	156.233	132.3	141.669	174.596	204.524	229.372	208.355	164.924	108.274	72.2155	51.795
14	2007	November	141.368	113.424	156.191	132.291	141.566	174.478	204.36	229.409	208.352	165.052	108.278	72.2298	51.795
15	2007	December	141.353	113.392	156.247	132.195	141.637	174.437	204.375	229.411	208.435	164.991	108.308	72.2185	51.795
16	2008	January	141.338	113.378	156.262	132.301	141.562	174.406	204.344	229.458	208.34	165.015	108.338	72.2543	51.795
17	2008	February	141.217	113.363	156.201	132.316	141.743	174.407	204.411	229.472	208.43	164.943	108.27	72.2266	51.7956
18	2008	March	141.263	113.363	156.187	132.18	141.626	174.446	204.468	229.561	208.35	165.021	108.278	72.2256	51.8236
19	2008	April	141.217	113.242	156.686	132.349	141.61	174.353	204.339	229.429	208.36	164.927	108.26	72.2262	51.795
20	2008	May	141.338	113.378	156.308	132.184	141.619	174.392	204.404	229.443	208.389	164.942	108.317	72.269	51.8093
21	2008	June	141.367	113.378	156.248	132.204	141.661	174.533	204.433	229.429	208.258	164.951	108.278	72.2302	51.8097
22	2008	July	141.342	113.378	156.252	132.198	141.641	174.431	204.414	229.455	208.392	164.958	108.278	72.2445	51.8097
23	2008	August	141.367	113.363	156.233	132.194	141.669	174.435	204.316	229.487	208.377	164.997	108.319	72.2266	51.8097
24	2008	September	141.338	113.378	156.306	132.256	141.659	174.413	204.36	229.396	208.363	165.042	108.264	72.2155	51.7986
25	2008	October	146.819	117.898	162.482	137.592	147.335	181.58	212.705	238.547	216.689	171.521	112.605	75.1041	53.8667
26	2008	November	147.022	117.961	162.429	137.592	147.228	181.457	212.524	238.586	216.685	171.652	112.609	75.119	53.8667

Figure 4-6: One of three MEPDG files used to obtain traffic inputs.

Step 5: Dynamic Modulus Parameters from HMA1.tmp*

The constants for the calculation of AC dynamic modulus are read from the MEPDG temporary files “HMA1Input.tmp” and “HMA1Output.tmp”. The file HMA1Input.tmp includes constants MaaT, reference temperature TR, A, and VTS (in this exact order) as shown at left in Figure 4-7. The location of the constants in the file seems fixed. The file HMA1Output.tmp includes constants i , α , β , γ , and c as shown at right in Figure 4-7. The location of the constants in the file is at line 21; this has been confirmed for several MEPDG cases and appears to be an MEPDG standard.

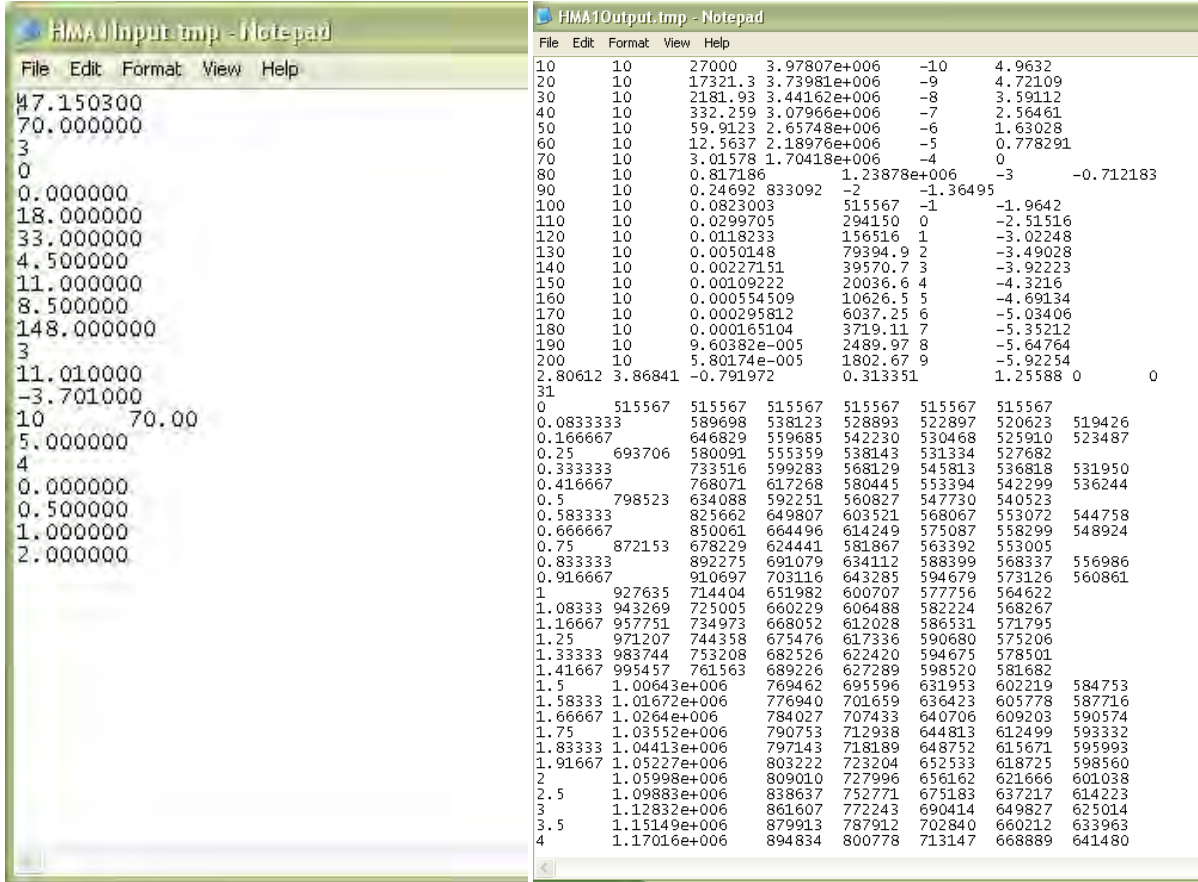


Figure 4-7: MEPDG files used to obtain dynamic modulus of AC layer.

Step 6: Layer Moduli from layermodulus.tmp

The MEPDG temporary file “layermodulus.tmp” is used for reading the layer modulus for all layers corresponding to each month of the pavement design life. This file is illustrated in Figure 4-8.

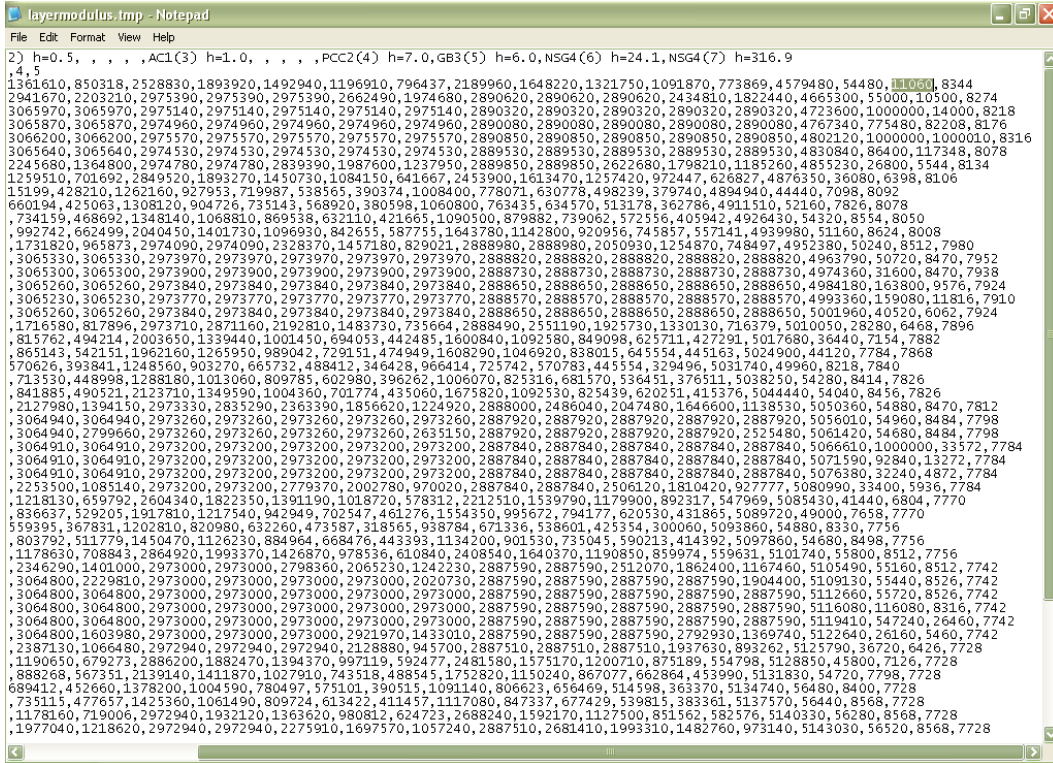


Figure 4-8: MEPDG temporary file describing monthly modulus values for all layer and sublayers in the TICP project.

Step 6 is the final step in the process of intermediate inputs prior to running the TPF-5(149) program for rutting.

Run TPF-5(149) Program to Supplement MEPDG Results with Predicted Rutting Depth Results from CalME

After the provision of appropriate calibration coefficients to the CalME models for a given project, the TPF-5(149) program then conducts the CalME rutting analysis and creates modified project output files. These files detail predicted rutting for the HMA-PCC project according to CalME.

4.1.4 Validation of TPF-5(149) Procedure for Rutting in TICP

The research team used two sources of existing HMA-PCC rutting data to validate the incorporation of the CalME rutting model into the MEPDG framework: full-scale accelerated testing data from the SHRP2 R21 project and HMA-PCC test section data from the MnROAD facility. The following subsections describe validation efforts using those datasets.

UCPRC Heavy Vehicle Simulator (HVS) SHRP2 R21 Data

The University of California Pavement Research Center (UCPRC) Heavy Vehicle Simulator (HVS) is a mobile load frame that uses a full-scale wheel (dual or single) to traffic the pavement

test section. This subsection describes an example of HVS testing of a TICP section at UCPRC (Section 609HB) conducted under the SHRP2 R21 project (SHRP/ARA 2012).

HVS Test Procedure

The trafficked test section is 8 m (26.4 ft) long, of which 1 m (3.3 ft) on each end are used for turnaround of the wheel and are generally not included in analysis and reporting of results. This wheelpath length permits the testing of one slab of jointed PCC of up to approximately 6 m (19.8 ft) with the trafficking including both joints and the entire slab. The specifications and a photograph of the HVS are shown in Figure 4-9.

Overall weight		59,646 kg
Load weight of the test wheel tire		20-100 kN with truck tire 20-200 kN with aircraft tire
Dimensions of tested area of pavement		1.5 m × 8 m maximum
Velocity of the test wheel		10 km/hr maximum
Maximum trafficking rate		1000 repetitions/hr
Average trafficking rate		750 repetitions/hr
Average daily repetitions		16,000
Dimensions:	Length	22.56 m
	Width, overall	3.73 m
	Height	3.7 m
	Wheel base	16.7m
Number of axles		3 (1 in rear, 2 in front)

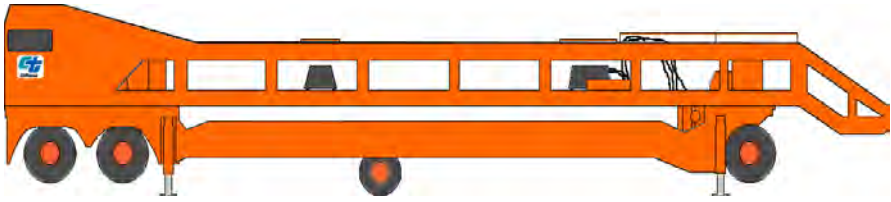


Figure 4-9: The HVS apparatus at UCPRC.

The sections tested to verify the rutting model were assigned a failure criterion of an average maximum rut of 12.5 mm (0.5 in.) over the full monitored section. Testing was continued past a 12.5-mm average rut depth until the rutting accumulation rate stabilized. The HVS loading program for the example is summarized in Table 4-3. Tire pressure was constant at 690kPa (100 psi) for the test section.

Table 4-3: HVS loading program for example section.

Section	Mix type	As-built Thickness (mm)	Wheel Load (kN)	Temperatures at 50 mm (2 in.)		Total Repetitions
				Average (°C)	SD (°C)	
609HB	PG 64-28 PM	116	40	49.5	1.1	63,750
			60			

The pavement temperature at 50 mm (2.0 in.) depth was maintained at 50°C±4°C (122°F±7°F) to assess rutting potential under typical pavement conditions. Heaters were operated inside the temperature control box to maintain the pavement temperature. The pavement surface received no direct rainfall as it was protected by the temperature control unit. The sections were tested predominantly during the wet season, however, measures were taken to keep water from entering the pavement structure inside the temperature control box, and there was an extensive drainage system placed around the entire set of pavement test sections. In addition, plastic sheets were placed on the surface to keep water out of the pavement.

HVS Test Temperature and Loading Conditions

All HVS sections were monitored closely. The following examples for Section 609HB detail the monitoring of load history and temperature at UCPRC. Figure 4-10 illustrates the HVS loading history for the example section.

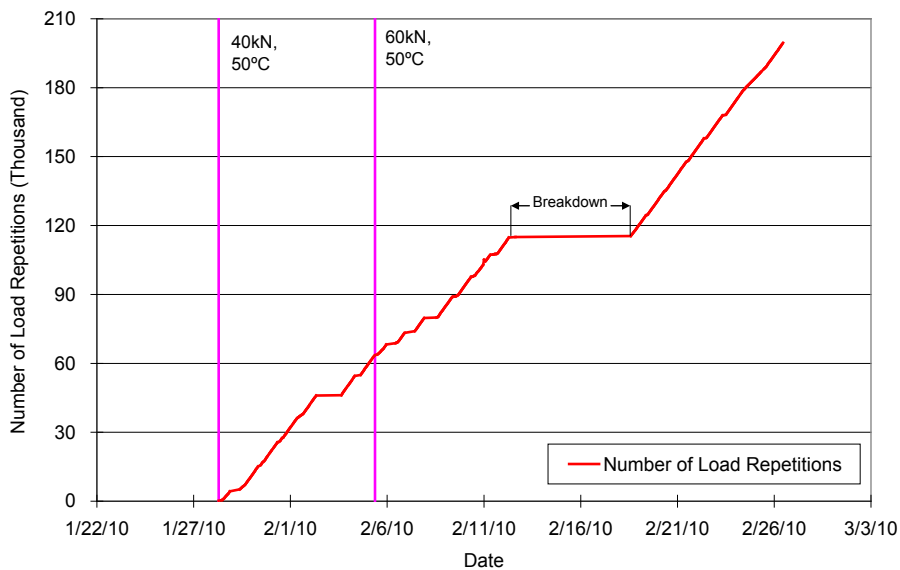


Figure 4-10: Section 609HB load history.

Outside air temperatures for the example section are summarized in Figure 4-11. Vertical error bars on each point on the graph show daily temperature range. Hence, for Section 609HB, temperatures ranged from 1.4°C to 20.9°C (34.5°F to 69.6°F) during the course of HVS testing, with a daily average of 10.6°C (51.1°F), an average minimum of 6.7°C (44.1°F), and an average maximum of 15.5°C (59.9°F).

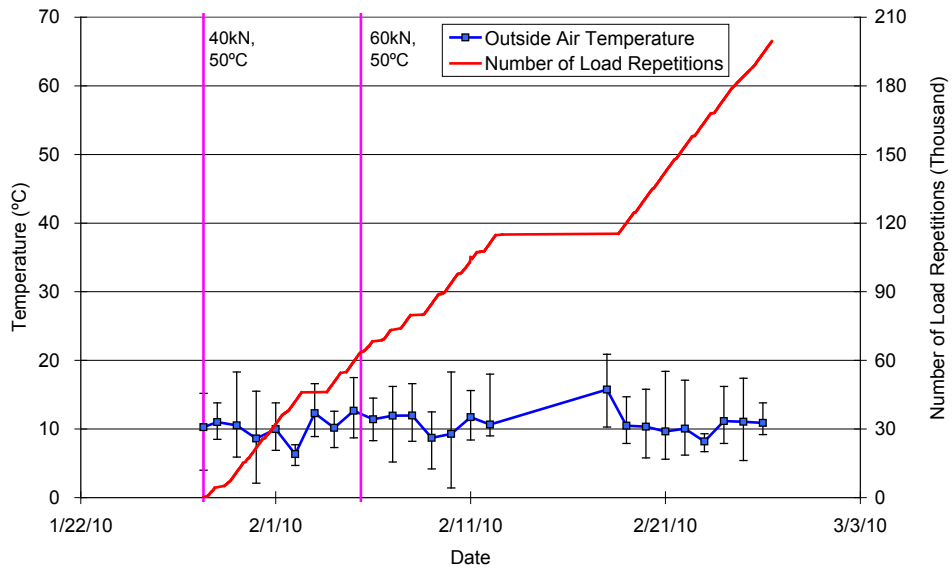


Figure 4-11: Daily average outside air temperatures.

During the test, air temperatures inside the temperature control unit at Section 609HB ranged from 15.6°C to 52.9°C (60.1°F to 127.2°F) with an average of 41.1°C (106°F) and standard deviation of 2.6°C (4.7°F). The daily average air temperatures recorded in the temperature control unit, calculated from the hourly temperatures recorded during HVS operation, are shown in Figure 4-12. Vertical errors bars on each point on the graph show daily temperature range.

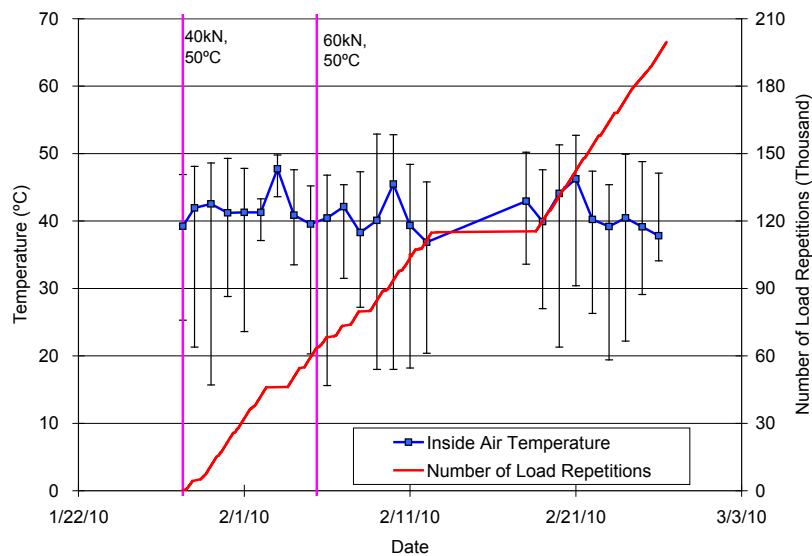


Figure 4-12: Daily average inside air temperatures.

Daily averages of the surface and in-depth temperatures of the asphalt concrete layers of Section 609HB are listed in Table 4-4 and shown in Figure 4-13. Similar tables were constructed for other sections involved in the SHRP2 R21 tests at UCPRC. Pavement temperatures decreased

slightly with increasing depth in the pavement, which was expected as there is usually a thermal gradient between the top and bottom of the asphalt concrete pavement layers.

Table 4-4: Section 609HB temperature summary for air and pavement.

Temperature	Average (°C)	Std Dev (°C)	Average (°F)	Std Dev (°F)
Outside air	10.6	1.8	51.1	3.2
Inside air	41.1	2.6	106.0	4.7
Pavement surface	47.8	2.0	118.0	3.6
- 25 mm below surface	49.7	1.3	121.4	2.4
- 50 mm below surface	49.5	1.1	121.1	2.0
- 90 mm below surface	48.6	0.9	119.5	1.7
- 120 mm below surface	47.5	0.9	117.4	1.7

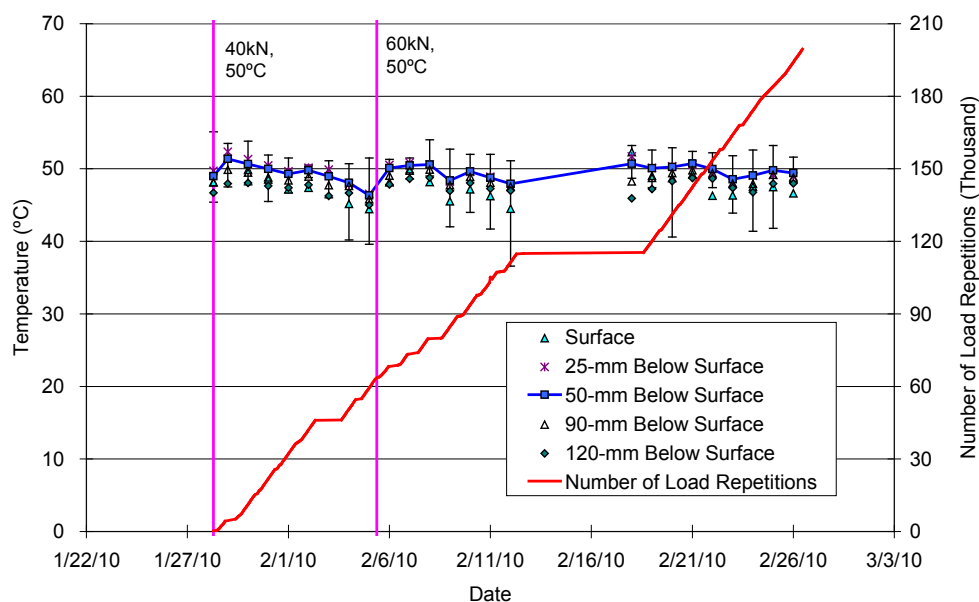


Figure 4-13: Daily average temperatures at surface and various depths of Section 609HB.

HVS Rutting Measurements

The section was monitored closely through its load history to determine strain and deformation of the section at regular intervals. Plastic strain was computed using temperature at 50 mm depth of the asphalt concrete and the temperature gradient. Permanent deformation at the pavement surface (rutting) was monitored with a surface profilometer and strain gauges at 50 mm depth in the asphalt in the sections with thicker HMA layers (strain gauges placed between the two lifts of HMA used to construct the surface layer). The profilometer is a stand-alone moveable device with a traveling downward-shooting vertical laser, which is used to take surface profiles transverse to the direction of the HVS wheel track. Transverse profiles are taken at 0.5-m (1.15-ft) intervals along the test section.

The profilometer, as illustrated in Figure 4-14, was used to determine average maximum rut depth, average deformation, location and magnitude of the maximum rut depth, and rate of rut development. This discussion for this example will focus on average deformation.

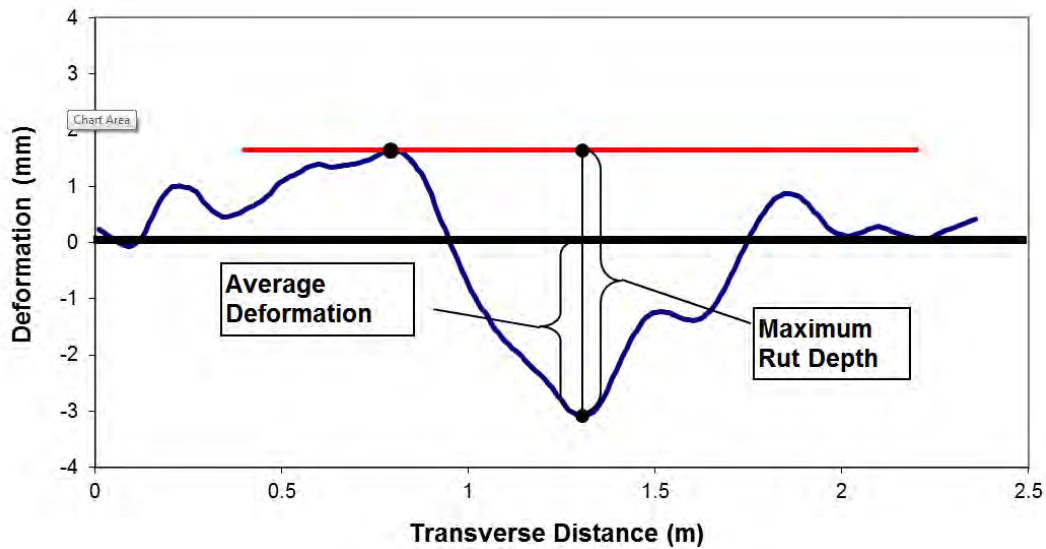


Figure 4-14: Illustration of maximum rut depth and average deformation of a leveled profile.

The average transverse cross-section for the example section discussed here is illustrated in Figure 4-15. Note the evolution of rut depth of the course of repeated loading.

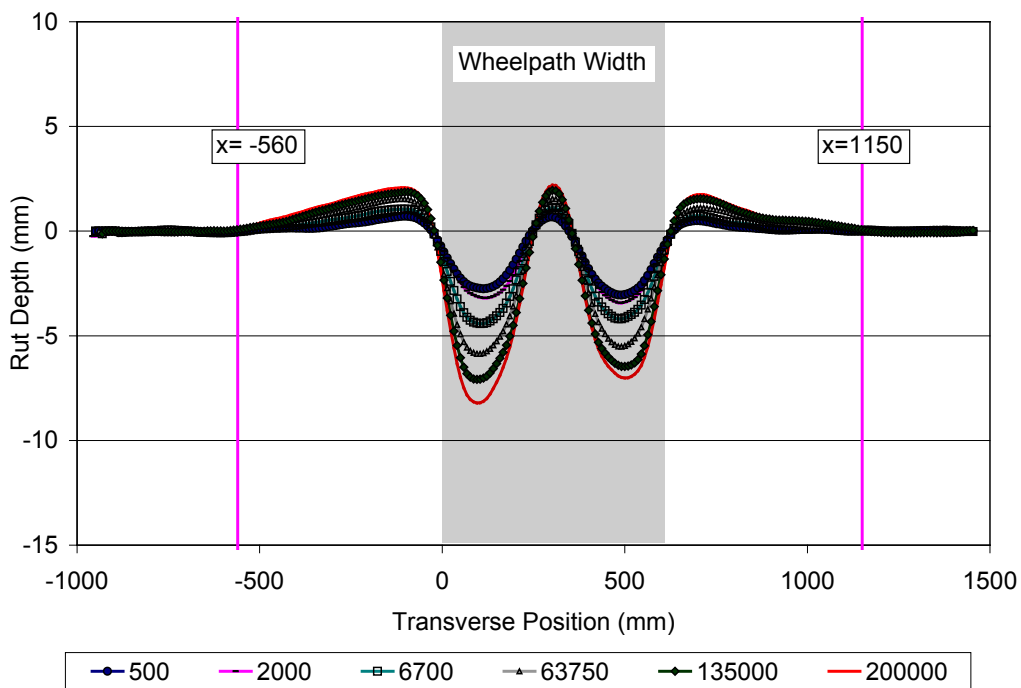


Figure 4-15: Evolution of Section 609HB rutting profile.

During HVS testing, rutting usually accumulates at a faster rate initially due to fast reduction of air voids (densification). Thereafter, it diminishes as trafficking progresses until reaching a steady state. This initial phase is referred to as the “embedment” phase. Figure 4-16 describes the development of average deformation with load repetitions, with an embedment phase only apparent at the beginning of the experiment (i.e. the first 15000 repetitions). Error bars on the average reading indicate that there was high variation along the length of the section which was a result of the HMA blocks removed for CT image evaluation.

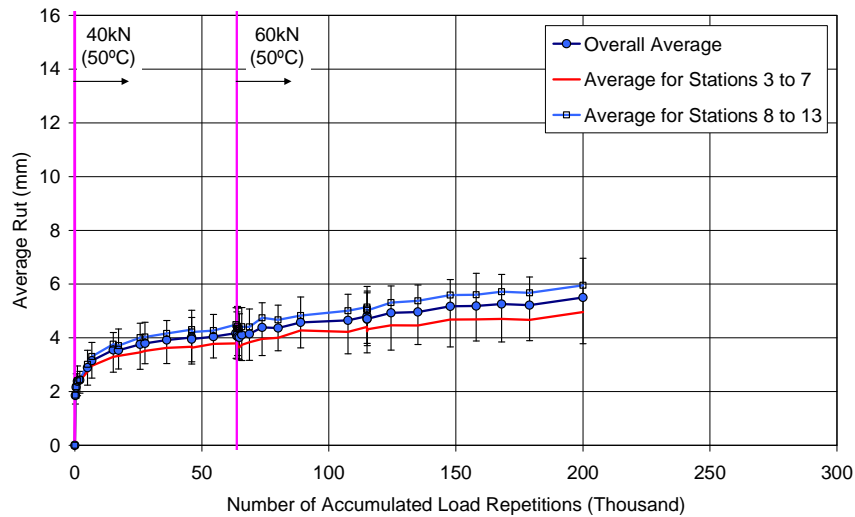


Figure 4-16: Average deformation for Section 609HB.

Apart from rutting, no other distresses were observed on the section. A summary of results from all four HVS sections at UCPRC for the SHRP2 R21 project are illustrated in Figure 4-17. These results are provided for later validation of the TPF-5(149) procedure.

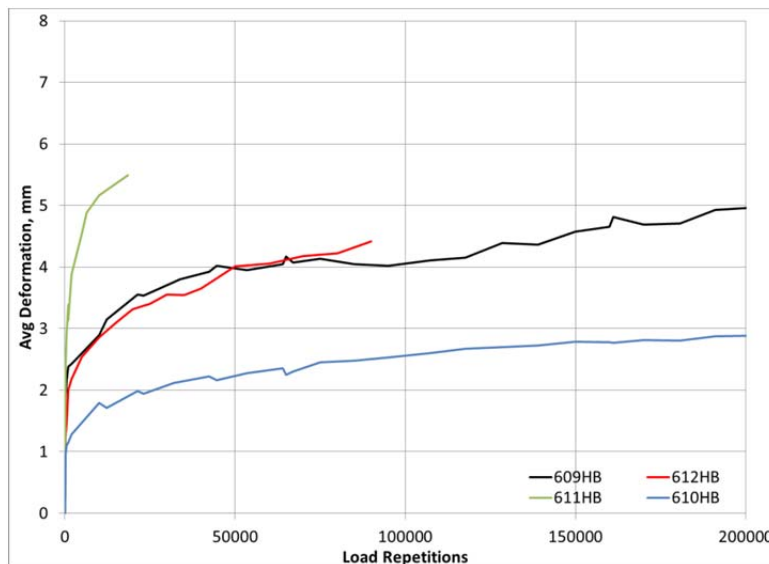


Figure 4-17: Summary of measured rutting (average deformation) observed at the UCPRC facility for HVS testing.

TPF-5(149) Predicted Rutting for HVS Test Sections

The research team developed MEPDG project files for each of the four SHRP2 R21 test sections at UCPRC, and using the method described in Section 2.3, these project files were used as project inputs for the TPF-5(149) procedure. The measured rutting (in average deformation) for each of these projects relative to HVS load repetitions is illustrated in Figure 4-18.

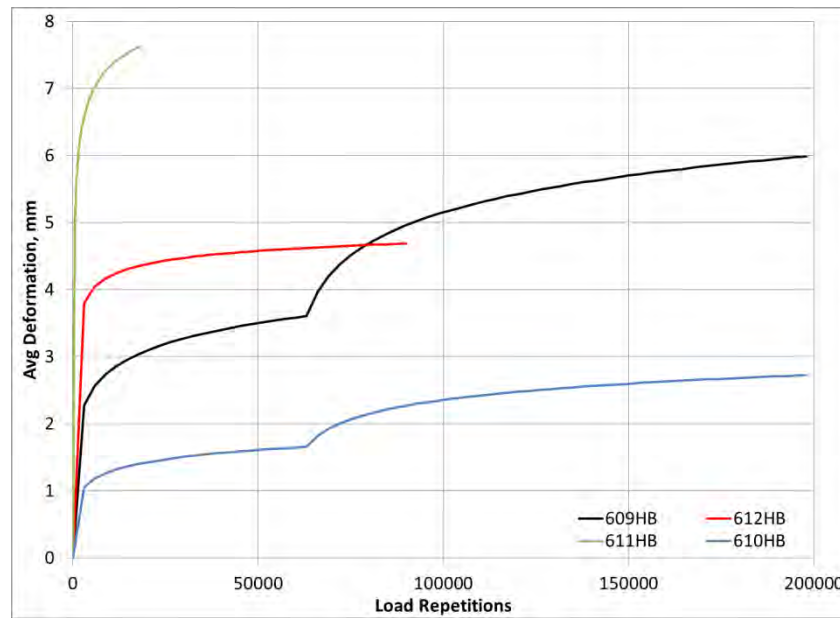


Figure 4-18: Summary of predicted rutting (average deformation) from TPF-5(149) procedure described in this report.

In validating the TPF-5(149) using measured rutting (Figure 4-17), the research team used MPEDG project files developed by ARA, Inc, that assumed basic Level 3 inputs for all MEPDG material parameters (H. Von Quintus, personal communication, 2012). In this light, the predicted rutting (Figure 4-18) is reasonable. The goal of the TPF-5(149) procedure is to operate within the MEPDG framework and provide a better model for rutting. By producing reasonable curves for the HVS sections, the TPF-5(149) procedure is validated.

The SHRP2 R21 project used CalME only to evaluate rutting in HMA-PCC, and R21 illustrated that with further calibration, the CalME rutting predictions for HMA-PCC improved. As the CalME rutting model was incorporated into the MEPDG framework without modification to the model itself, tuning the TPF-5(149) procedure is simply a case of modifying the MEPDG project files. Hence, further calibration of the MEPDG project files – including tuning the material properties of the HMA to, in turn, modify the CalME calibration coefficients – would bring the permanent deformation in rutting curves of Figure 4-18 closer to the HVS measured results of Figure 4-17.

MnROAD TICP Test Section Measured Rutting

As part of TPF-5(149), TICP full-scale test sections were constructed at MnROAD. This includes Cells 106 and 206 at MnROAD, which have been extensively detailed in earlier task

reporting. These cells feature a 2-inch HMA overlay over a 5-inch JPCP slab. The cells are identical in cross-section and materials other than 106 using 1-inch dowels, while 206 is undoweled; Table 4-5 summarizes the design of Cells 106 and 206.

Table 4-5: MnROAD Cell 106/206 design in summary.

Section	HMA overlay	PCC slab	Base	Subbase	Subgrade	JPCP panel size	Doweling	Construction date
106	2" PG 64-34	5" (Mesabi 4.75 mm Super P)	6" Class 1 Stabilized Aggregate	6" Class 5	Clay	15' x 12'	1" dia dowels	Oct 08
206	2" PG 64-34	5" (Mesabi 4.75 mm Super P)	6" Class 1 Stabilized Aggregate	6" Class 5	Clay	15' x 12'	None	Oct 08

Since construction, Cells 106 and 206 have been included in the varied tests conducted on all pavement test sections at MnROAD. Among these measurements are rutting profiles in average deformation. These profiles are created using an ALPS laser profilometer in a manner similar to that of UCPRC detailed in Section 2.4.1.

The research team developed MEPDG project files for Cells 106 and 206. Default (Level 3) values for the MEPDG were assumed for project files; HMA material properties were adopted from testing by UCPRC for CalME. Using the method described in Section 2.3, these project files were used as a project input for the TPF-5(149) procedure. The measured rutting (in average deformation) for Cells 106 and 206 over time (months since construction) is illustrated in Figure 4-19.

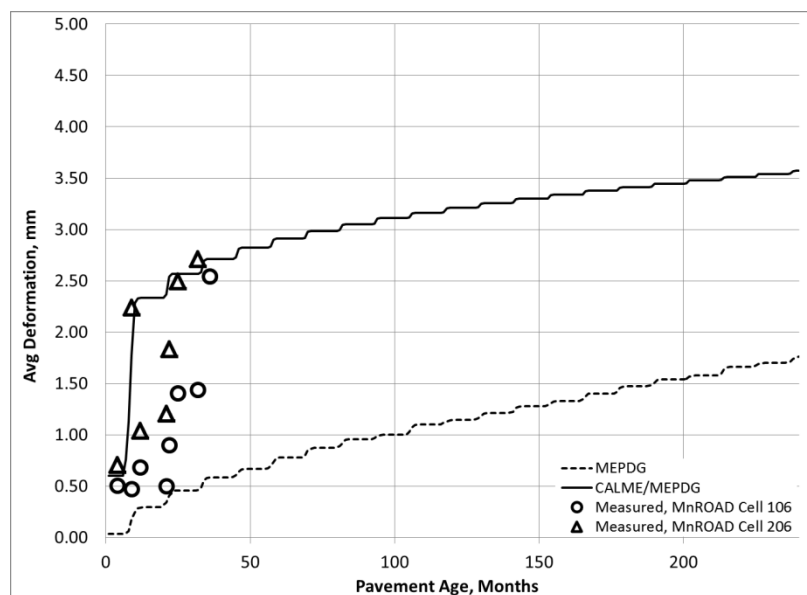


Figure 4-19: Comparison of TPF-5(149) procedure and unmodified MEPDG procedure predictions for rutting (average deformation) and observed rutting at MnROAD Cells 106 and 206.

One of the first observations to be made from Figure 4-19 is the underprediction for rutting in HMA-PCC by the MEPDG in this case. However, a difficulty of Figure 4-19 is the measured rutting data itself, which is muddled by natural variability in measurements. In general, a trend in rutting for either test section is difficult to determine from the data, and as a result a comparison with rutting predictions is not informative.

MnROAD contains other HMA-PCC pavements with rutting data that may be of assistance. Figure 4-20 illustrates average deformation in rutting measured on Cell 70 at MnROAD, which was constructed for the SHRP2 R21 project.

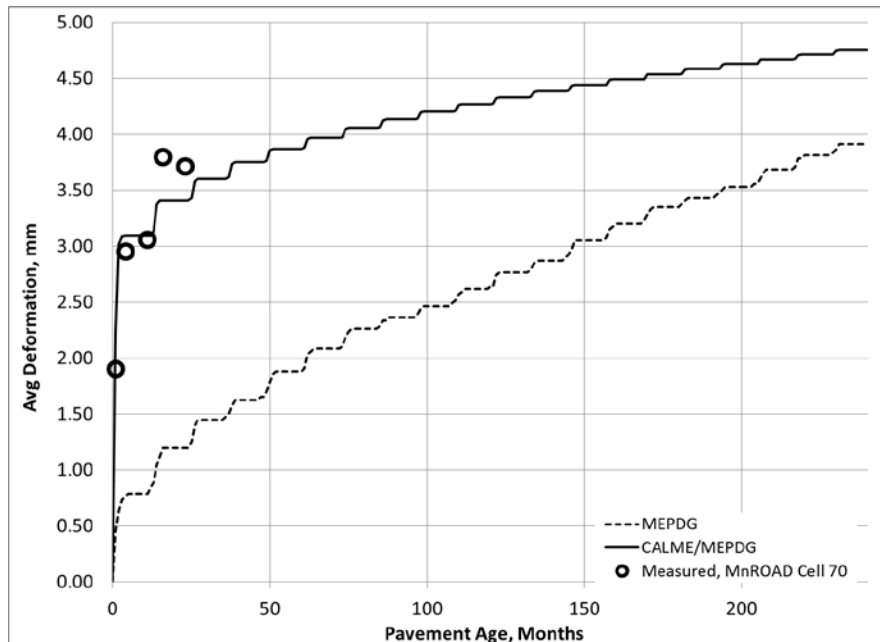


Figure 4-20: Comparison of TPF-5(149) procedure and unmodified MEPDG procedure predictions for rutting (average deformation) and observed rutting at MnROAD Cell 70.

Again, while there is some variability in the data set illustrated in Figure 4-20, a trend is much easier to spot in this data set. For Cell 70, the TPF-5(149) procedure appears to capture rutting behavior for its early life. In the cases of Cells 106/206 and Cell 70, continued monitoring at MnROAD will help evaluate the effectiveness of the TPF-5(149) procedure.

Overall, the validation of Figure 4-19 and Figure 4-20 indicates that the TPF-5(149) procedure is an attractive alternative to the exclusive use of MEPDG. It should also be noted that the analysis using TPF-5(149) above assumed Level 3 inputs, and thus it could be further calibrated and modified to resemble MnROAD Cell 106/206 and Cell 70 conditions.

4.1.5 Sensitivity Analysis of TPF-5(149) Procedure for Rutting in TICP

Given that both the MEPDG and CalME rutting model have been subjected to extensive review and sensitivity analysis, the need for an in-depth sensitivity analysis of the TPF-5(149) procedure was not a critical concern for the work of Task 5. However, the research team undertook a brief analysis of rutting performance sensitivity to two important parameters: HMA thickness and

climate. Other than these two parameters, the sensitivity study assumed structural properties of an HMA-PCC pavement with 2 inches (50 mm) HMA over 7 inches (175 mm) JPCP. Furthermore, the analysis assumed MEPDG defaults for material properties (Level 3 inputs) for all projects. Assumed traffic was 2000 AADTT.

Climate

Figure 4-21 illustrates the sensitivity of rutting predictions to climate for 5 locations. Each of these locations corresponds to EICM climate files (*.icm) for Seattle, WA; Pullman, WA; Sacramento, CA; San Francisco, CA; and Minneapolis-Saint Paul, MN.

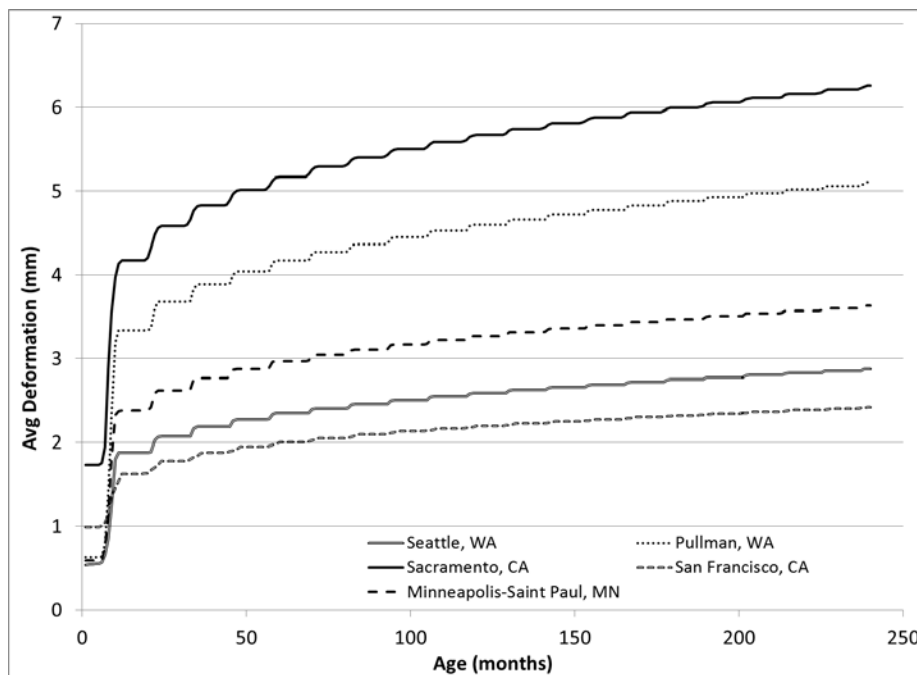


Figure 4-21: TPF-5(149) procedure for rutting, sensitivity to climate.

Climate is an influential parameter on rutting performance. This behavior is in keeping with other M-E models for rutting, and thus the TPF-5(149) procedure performs acceptably in this regard. Furthermore, it should be noted that in this analysis, the asphalt mix properties are kept constant, which obviously does not mirror in-field conditions, wherein the properties would change along with climate conditions.

Pavement Thickness

Figure 4-22 illustrates the sensitivity of TPF-5(149) procedure predictions for rutting to 4 levels of HMA thickness. The projects in Figure 4-22 were developed for an EICM climate file developed from weather data for Sacramento International Airport (SMF) in Sacramento, CA. For projects examining sensitivity to HMA thickness, PCC thickness was held at a constant 7 inches (175 mm).

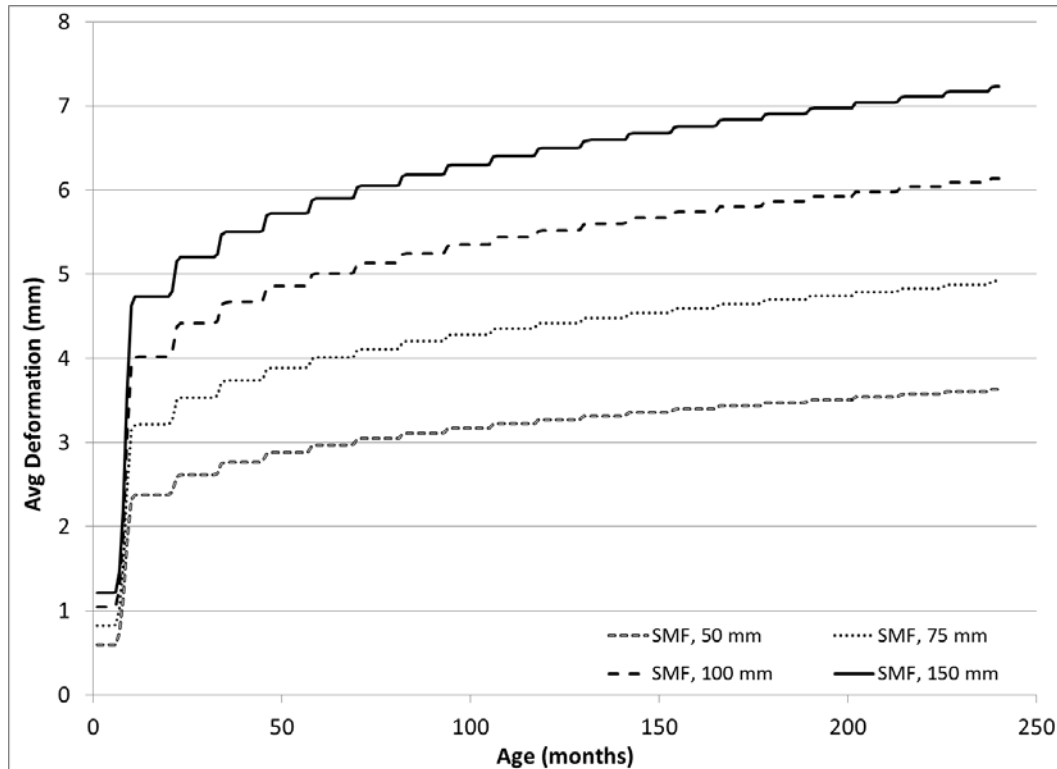


Figure 4-22: TPF-5(149) procedure for rutting, sensitivity to HMA overlay thickness.

As with climate, the objective of the HMA thickness sensitivity study is merely to validate the TPF-5(149) procedure against M-E expectations. Here as overlay thickness increases, so does the extent of rutting. This agrees with HVS testing experience observed under the SHRP2 R21 project (SHRP 2012).

4.2. HMA-PCC Reflective Cracking Models

In HMA-PCC composites such as TICPs, localized high stresses at the base of the HMA overlay above joints/cracks can result in cracks that propagate through the overlay thickness. These cracks can be caused by various phenomena, most notably the displacement of cracks or joints in the underlying PCC pavement (due to traffic loading or temperature) and the deformation of the overlay due to thermal effects. The initiation and propagation of cracking in the overlay due to preexisting cracks/joints in the rigid pavement is known as reflective (or reflection) cracking.

As state, local, and federal interest in composite pavements increases, so does research in the mechanistic-empirical (M-E) modeling of reflective cracking. Some of these models include:

- CRACKTIP, a two-dimensional finite element model developed for HMA overlays by Jayawickrama and Lytton (1987), is capable of modeling reflective cracking for HMA-PCC in the presence of traffic loads (not thermal effects).
- The Computer Aided Pavement Analysis (CAPA) program developed by Scarpas et al (1993) included the ability to investigate the response of the HMA overlay to both thermal and traffic loads and the propagation of fracture through the overlay.

- Kohale and Lytton (2000) developed an M-E model for overlay design involving interlayer techniques.
- Ullidtz et al (2006) developed a reflection cracking model for the California Mechanistic-Empirical Design (CalME).
- NCHRP (2010) recently released a reflective cracking model developed under NCHRP Project 1-41 specifically to update the MEPDG procedure for HMA-PCC design and analysis (NCHRP 2010).

Additional M-E models for reflective cracking are detailed in Bennert (2011).

Given the modification of the MEPDG using the CalME rutting model for TPF-5(149), the research team considered an investigation of the CalME reflective cracking model and possible modification of the MEPDG similar to the TPF-5(149) procedure for rutting. After discussions with the technical panel, the NCHRP 1-41 model was not considered for the modeling of reflective cracking in TICP for TPF-5(149). As a part of Task 5, the research team:

- Reviewed the original MEPDG reflective cracking model;
- Reviewed the CalME reflection cracking model;
- Developed reflection cracking procedure for TPF-5(149) using MEPDG framework and CalME reflective cracking model.

These efforts are detailed in the following subsections, which also include a brief overview of the original MEPDG reflective cracking model.

4.2.1 Original MEPDG Reflective Cracking Model

The MEPDG predicts reflection cracks in HMA overlays of HMA-PCC projects using a regression model derived from empirical data. The MEPDG does not specify a severity level to be associated with predicted reflection cracking. This regression Equation 5-estimates the percentage of area of cracks that propagate through the overlay, RC , as a function of time, t , using a sigmoid function

$$RC = \frac{100}{1 + e^{a(c)+bt(d)}} \quad (4-19)$$

where a and b are regression fitting parameters defined through a calibration process and parameters c and d are defined by the user to describe cracking progression. The parameters a and b are a function of the effective HMA overlay thickness, H_{eff} , which is a function of the overlay thickness and a rating of the load-transfer efficiency.

$$a = 3.5 + 0.75(H_{eff}) \quad (4-20)$$

$$b = -0.688684 - 3.37302(H_{eff})^{-0.915469} \quad (4-21)$$

Values assigned for H_{eff} can be found in AASHTO (2008).

Table 4-6: Assigned values for H_{eff} , c , and d in original MEPDG reflective cracking model (from AASHTO 2008).

Pavement Type	H_{eff}	c	d	
			(to delay cracking by 2 years)	(to accelerate cracking by 2 years)
Rigid-Good Load Transfer	$H_{eff} = H_{HMA} - 1$	---	---	---
Rigid-Poor Load Transfer	$H_{eff} = H_{HMA} - 3$	---	---	---
Effective Overlay Thickness, H_{eff}, inches	---	---	---	---
<4	---	1.0	0.6	3.0
4 to 6	---	1.0	0.7	1.7
>6	---	1.0	0.8	1.4

The user-defined cracking progression parameters c and d can be used to accelerate or delay the amount of reflection cracks. The model is very sensitive to these parameters, and as a result of their being arbitrarily assigned for the release of MEPDG and left to the user to refine, the original MEPDG reflective cracking model is essentially uncalibrated and to be implemented with caution. Thus reflective cracking was incorporated into the MEPDG as a placeholder, assuming that either the model would be calibrated or revised entirely (which was the result of NCHRP 1-41).

4.2.2 CalME Reflective Cracking Model

The CalME model assumes that debonding occurs quickly after a HMA-PCC pavement is opened to traffic, and thus the HMA layer is effectively a flexural beam through the life of the HMA-PCC pavement. In this arrangement, the crack tip strain, ε , is the maximum bending strain at the bottom of the HMA layer. The CalME reflection cracking model is based on regression models for crack tip strains; these regression models are based on a large factorial of cases (i.e. pavement systems and applied traffic loads) solved using the finite element method (Wu 2005). Hence, the crack tip strain is a function of traffic and pavement structural properties and is defined as

$$\varepsilon = \alpha \times E_{an}^{\beta_1} \times E_{bn}^{\beta_2} \times (a_1 + b_1 \times \ln(LS_n)) \times \exp(b_2 \times H_{an}) \times (1 + b_3 \times H_{un}) \times (1 + b_4 \times E_{un}) \times \sigma_n \quad (4-22)$$

where

$$\begin{aligned} E_{an} &= E_a / E_s, E_{bn} = E_b / E_s, E_{un} = E_u / E_s, \sigma_n = \sigma_o / E_s, \\ LS_n &= LS / a, H_{an} = H_a / a, H_{un} = H_u / a \end{aligned} \quad (4-23)$$

and where E_a is the modulus of the HMA overlay; H_a is the thickness of the HMA overlay; E_u is the modulus of the PCC slab; H_u is the thickness of the PCC; E_b is the modulus of the base/sub-base; E_s is the modulus of the subgrade; LS is the crack spacing; σ_o is the tire pressure; and

a is the radius of the loaded area for one wheel.

It is important to note that loading conditions considered do not include thermal loads – this is a modeling simplification specific to California, where pavements do not experience temperatures that are extremely low compared to construction temperatures. For these conditions, Caltrans is confident that thermal strains induced by temperature variation in the HMA layer are not significant and thus thermal loads are excluded from the CalME reflection cracking model.

To predict reflection cracking, the crack tip strain, ε , from Eq. 4.2.4 is used with the incremental damage model, which has the format

$$\log(E_{dam}) - \delta = \frac{\alpha(1 - \omega)}{1 + \exp(\beta + \gamma \log(tr))} \quad (4-24)$$

where tr is reduced time in seconds and δ , α , β , and γ are calibration constants. For this approach, which is similar to the fatigue damage discussion for rutting in Section 2.2.2, the damage, ω , is defined as

$$w = \left(\frac{MN_{tot}}{MN_p} \right)^\alpha \quad (4-25)$$

where MN_{tot} is the current number of load repetitions and the allowable number of load repetitions, MN_p , is defined as

$$MN_p = A \cdot \left(\frac{\mu\varepsilon}{\mu\varepsilon_{ref}} \right)^\beta * \left(\frac{E_{dam}}{E_{ref}} \right)^{\beta/2} = A' \cdot \left(\frac{SE}{SE_{ref}} \right)^{\beta/2} \quad (4-26)$$

and where E_{ref} is the reference asphalt modulus; $\mu\varepsilon_{ref}$ is the reference asphalt strain in microstrains; $\mu\varepsilon$ is the strain at the bottom of the asphalt layer; SE and SE_{ref} are strain energies; and A , A' , and β are calibration coefficients.

In addition to being an incremental damage approach, the CalME model benefits from its simplicity and ease of implementation. As noted earlier, it does not account for thermal loads, and it also does not account for load transfer at joints (i.e. doweling) or severity levels in cracking. Despite these drawbacks, there is much utility in the CalME approach. First, it benefits from having been validated using HVS data from the SHRP2 R21 project. In addition, it uses a framework that is similar to that of rutting (detailed in Section 2.2.2) and fatigue cracking.

4.2.3 TPF-5(149) Procedure for Predicting Reflective Cracking in TICP

Modified CalME Reflection Cracking Model for TPF-5(149)

The research team developed a modified CalME reflection cracking model for a procedure similar to the rutting procedure developed for TPF-5(149) and described in Chapter 2. As in the TICP rutting model, CalME is once again combined with MEPDG to augment typical MEPDG

results with more specific results concerning reflective cracking. In this case, the CalME model for reflection cracking has been slightly modified to account for:

- Thermal loading;
- Joint load transfer (i.e. dowels); and
- Two severity levels of cracking: Low + Medium + High (L+M+H) and Medium + High (M+H), where notation is borrowed from NCHRP 1-41 conventions.

These modifications remedy the few issues the research team had in applying the HMA-PCC projects outside of the state of California. As noted in Section 4.2.2, the CalME reflective cracking model is very useful: it is both simple and direct, and it has been well documented. Thus its modification and incorporation into the TPF-5(149) approach is relatively straightforward.

To modify CalME, the research team consulted a methodology developed by Bennert (2011). The incremental damage approach for reflective cracking described in Section 4.2.2 is modified so that the calculated damage is a function of both thermal loads and axle loads. Two levels of total damage are considered for the two severity levels of cracking (L+M+H and M+H).

L+M+H Severity Reflective Cracking Model

To begin, Low, Medium, and High reflective cracking RC_{LMH} is defined similar to the CalME definition for reflective cracking, such that

$$RC_{LMH} = \frac{100}{1 + \left(a_1 \frac{DAM_{LMH}}{h_{HMA}} \right)^{b_1}} \quad (4-27)$$

where h_{HMA} is the HMA overlay thickness; a_1 and b_1 are calibration constants (determined to be 0.05 and -6, respectively); and DAM_{LMH} is the total damage leading to Low, Medium, and High severity cracking. DAM_{LMH} can be further defined as

$$DAM_{LMH} = \frac{DAM_{LMH}^{temp}}{DAM_0^{temp}} + \frac{DAM_{LMH}^{load}}{DAM_0^{load}} \quad (4-28)$$

where parameters corresponding to damage due to thermal effects have the superscript *temp*, parameters corresponding to damage due to axle loads have the superscript *load*, and the subscript *0* indicates a damage scaling parameter. Each of the parameters in Equation (4-29) is defined below in more detail.

The damage due to axle load repetitions is based on Equations (4-27) and (4-28) above and has the form

$$DAM_{LMH}^{load} = \omega \quad (4-29)$$

It should be noted that a determination of the allowable number of load repetitions using Equation (4-27) requires the use of critical strains from Equation (4-25). As Equation (4-23) was developed for undoweled HMA-PCC pavements, to account for the effect of reduction in the pavement deflections and corresponding reduction in asphalt strains, the following correction was introduced

$$\varepsilon_{doweled} = \psi \varepsilon_{undoweled} \quad (4-30)$$

where $\varepsilon_{undoweled}$ is the strain from Equation (4-23) and ψ is a correction factor (assumed to be equivalent to 0.8 for this study). To determine load-induced portion of the damage, Equation (4-23) was used to predict critical HMA strains. Equation (4-23) requires a single modulus of elasticity. The MEPDG input is the subgrade resilient modulus for the optimum moisture content, but the MEPDG later subdivides the subgrade in several sublayers and adjusts the moduli for each sublayer based on the sublayer moisture content for each month. It should be also noted that the MEPDG does not adjust the moduli for the stress level sensitivity which is built-in into the MEPDG E-to-k conversion for rigid pavements.

To provide an input into Equation (4-23), these moduli, preferably adjusted to the stress level, should be combined back into one composite modulus, which is not a trivial task. To address this issue, it was decided not use the elastic moduli of the individual sublayer, but rather composite k-values from the rigid part. These values were converted to composite E using the relationships between the backcalculated E and k-values established by Khazanovich et al. (2001), based on the several hundred LTPP test sections.

$$k = 0.296 E_{subgr} \quad (4-31)$$

Furthermore, the damage load scaling factor, adopted from CalME initiation damage, is defined as

$$DAM_0^{load} = \frac{0.54}{1 + \left(1 + \frac{h_{HMA}}{10}\right)^{-0.9}} \quad (4-32)$$

The damage due to thermal effects has the form

$$DAM_{LMH}^{temp} = \sum \frac{n(\Delta T_i)}{N(\Delta T_i)} \quad (4-33)$$

where ΔT_i is the difference between the daily maximum and minimum temperatures at the top of the PCC layer, as predicted by EICM; $n(\Delta T_i)$ is the number of days ΔT_i occurs; and $N(\Delta T_i)$ is the allowable number of joint openings associated with change in PCC temperature ΔT_i . $N(\Delta T_i)$ is adopted from Bennert (2011), German and Lytton (1979), and Zhou and Scullion (2005) and is defined as

$$N(\Delta T_i) = k_1 (\Delta T_i)^{k_2} (\Delta L_i)^{k_3} \quad (4-34)$$

where ΔL_i is the joint movement and k_1 , k_2 , and k_3 are material specific coefficients that are determined using the Texas Transportation Institute (TTI) overlay testing device. Bennert (2011) reported example values for these coefficients for several mixtures used in New Jersey HMA overlays of JPCP. This study adopted the respective values 2.10×10^{-7} , 1.3, and -2 for k_1 , k_2 , and k_3 .

Furthermore, the model adopts the relationship developed by Bennert (2011) between the joint movement, ΔL_i , and the change in temperature ΔT_i .

$$\Delta L_i = \beta \alpha_{PCC} L \Delta T_i \quad (4-35)$$

where α_{PCC} is the coefficient of thermal expansion of the PCC layer, L is the joint spacing, and β is the PCC-base friction coefficient (assumed to be 0.5 for this study, a value commonly assumed for granular bases). Finally, the damage scaling factor for temperature is assumed to be equivalent to 1.

M+H Severity Reflective Cracking Model

The use of the critical HMA strain, defined by Equation (4-25), to relate traffic loading and reflective cracking is reasonable to describe the stages of crack initiation and propagation (i.e. the development of Low severity cracking). However, after the crack has propagated, the strains disappear and, therefore, cannot be used to determine crack deterioration (i.e. the progression from Low to Medium and High severity).

In this study, a different mechanistic parameter was selected: differential energy of subgrade deformation, DE , which is used by the MEPDG to characterize the development of joint faulting. It was hypothesized that crack deterioration is caused by excessive vertical deflections of the crack edges, which in turn causes high shear stress at the HMA-PCC interface and high differential deflections of the crack edges. The use of DE addresses both of these mechanistic concerns as DE , for one load application, is defined as follows

$$DE = k \frac{\delta_l + \delta_u}{2} (\delta_l + \delta_u) \quad (4-36)$$

where δ_l is the deflection of the loaded-side of the joint (crack); δ_u is the deflection of the unloaded-side of the joint (crack); and k is the coefficient of subgrade reaction. The procedure for the adoption of DE is adopted from the MEPDG faulting model, modified for HMA-PCC pavements in the work of Task 5 as described in section 4.4.

As only a portion of the total number of cracks can be both Medium and High severity, the following functional form is adopted for the expression for the Medium and High severity level reflective cracking

$$RC_{MH} = \frac{RC_{LMH}}{1 + (a_2 \sum DE)^{b_2}} \quad (4-37)$$

where a_2 and b_2 are calibration coefficients (determined for this study to be 8×10^{-6} and -0.34, respectively).

There are a number of advantages to the TPF-5(149) approach for reflective cracking. The first advantage is that the approach adopts the MEPDG sigmoidal model, detailed in Section 4.1. Furthermore, it generalizes the CalME model by accounting for the effect of temperature variations and load transfer efficiency, both of which were observed by Bennert (2011) important factors in the development of reflective cracking. Finally, it adopts mechanistic modeling of JPCP joint faulting to characterize deterioration of cracking from Medium to High severity.

Modification of TPF-5(149) Companion Program to the MEPDG

Note that the TPF-5(149) procedure works within the MEPDG framework. Hence, all inputs required for the TPF-5(149) procedure for reflective cracking are taken from MEPDG project inputs in a manner similar to that described in Section 2.3. Both the rutting and reflective cracking procedures are now part of the same companion program to the MEPDG. Thus, for any given TICP project file, a MEPDG user can run the TPF-5(149) companion program to receive modified rutting and reflective cracking predictions according to the models described in this report.

4.2.4 Validation of TPF-5(149) Procedure for Reflection Cracking

To validate the developed procedure, the TPF-5(149) research team used readily available reflective cracking data to evaluate the fitness of the procedure. As the CalME model had been extensively calibrated and validated against HVS data, the validation of the TPF-5(149) procedure is limited to recent reflective cracking data from MnROAD.

Furthermore, given that the original MEPDG uses the same MEPDG project files required for the TPF-5(149) procedure (as all accommodate the MEPDG framework), the research team also ran the original MEDPG for the project file describing MnROAD Cells 106 and 206. This validates the TPF-5(149) procedure against the existing reflective cracking model for the MEPDG.

As noted in the validation of the TPF-5(149) procedure for rutting in Section 2.4.1, TICP full-scale test sections were constructed at MnROAD Cells 106 and 206. These test sections have been described in earlier task reporting and are summarized in Table 4-5. Regular monitoring of Cells 106 and 206 has included surveys of reflective cracking according to crack length and severity level. Severity of cracking is denoted as Low (L), Medium (M), and High (H); these abbreviations may be adopted in the subsections to follow.

Figure 4-23 illustrates a comparison of collected MnROAD observed M+H reflective cracking with M+H reflective cracking predicted by the TPF-5(149) procedure using MPEDG project files describing Cells 106 and 206 (with a 20-year service life). Figure 4-23 also includes reflective cracking predictions for Cells 106 and 206 using the original MEPDG procedure for reflective

cracking. Note that as the original MEPDG reflective cracking model does not consider joint load transfer, the predicted reflective cracking for these test sections is identical. Furthermore, while the original MEPDG model does not specify the severity of cracking it predicts, based on the results for the project file, it is assumed it predicts M+H level severity cracking, and thus these results are included.

Given that reflective cracking data has only been collected for two years, a validation of the model for the first 24 months of the predicted performance is illustrated in Figure 4-24. Figure 4-24 also includes predicted reflective cracking according to the original MEPDG procedure.

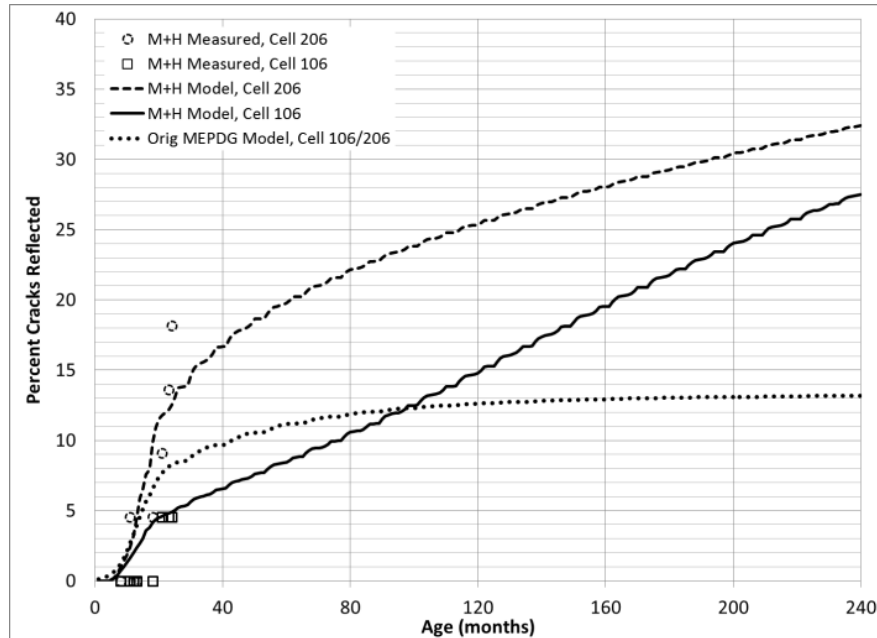


Figure 4-23: TPF-5(149) procedure predicted 20-year M+H severity reflective cracking performance for MnROAD Cells 106 and 206.

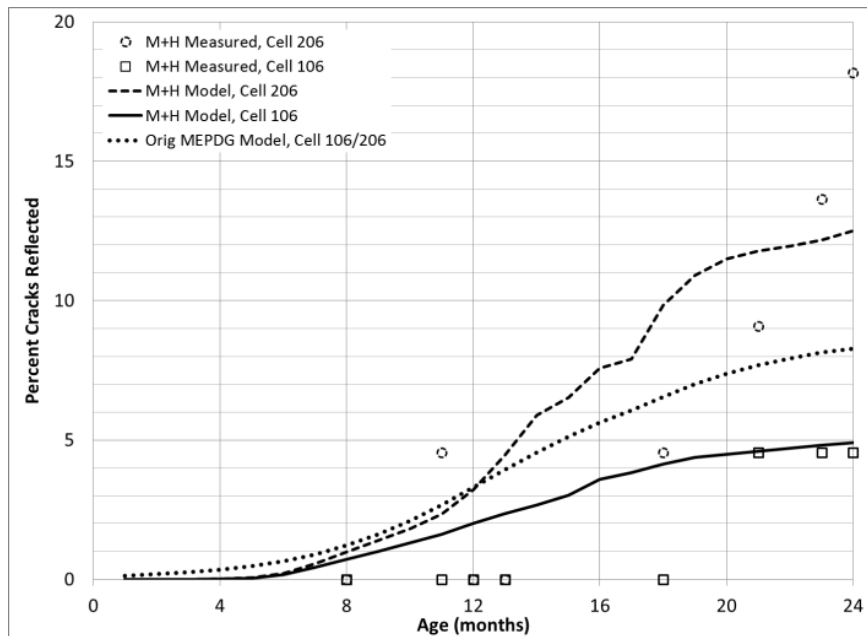


Figure 4-24: The first two years of MnROAD Medium and High (M+H) severity reflection cracking data versus TPF-5(149) modeled M+H performance and Original MEPDG modeled performance.

For both projects (which differ only in the presence of doweling), the data appears to validate the TPF-5(149) procedure. In the model predictions and the observed M+H reflective cracking data, the effect of the 1-inch dowels in Cell 106 is apparent. This agrees with expectations: as noted earlier, one advantage of the TPF-5(149) procedure is that in addition to considering axle loads for M+H severity reflective cracking, it has modified the CalME procedure to include LTE in the model. This result confirms the influence of that new information in the model. In summary, the model properly describes the experimental data. Furthermore, the TPF-5(149) model seems to reproduce the trend in the data of Figure 4-24 relative to the original MEPDG reflective cracking model.

Including Low severity cracking data, and corresponding predictions for L+M+H reflective cracking, results in much higher predicted and observed cracking in Cells 106 and 206, as illustrated in Figure 4-25. As was the case for M+H reflective cracking data, L+M+H data is available for the first two years of Cells 106 and 206, hence a validation of the model for the first 24 months of the predicted L+M+H performance is illustrated in Figure 4-26.

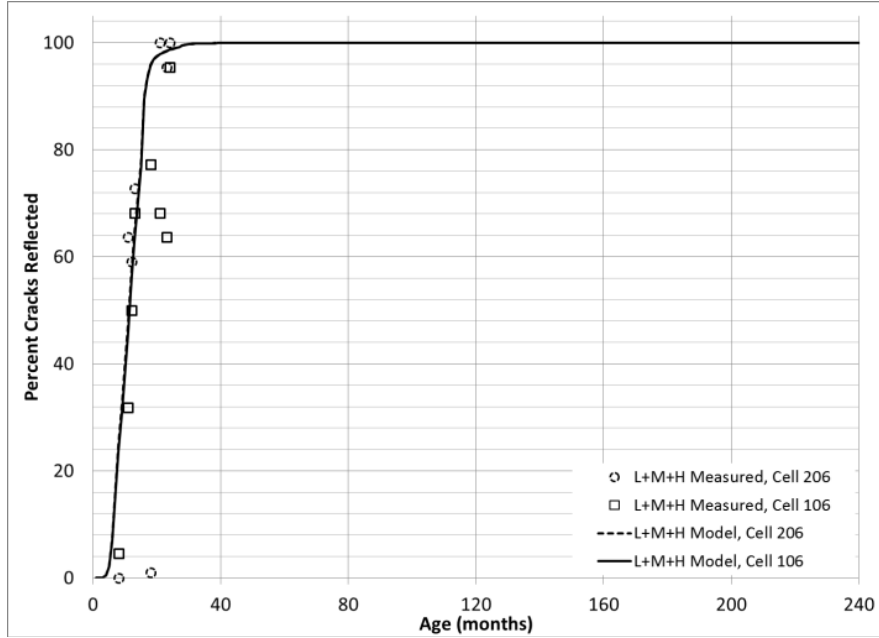


Figure 4-25: Predicted 20-year Low, Medium, and High (L+M+H) severity reflective cracking performance for MnROAD Cells 106 and 206 according to TPF-5(149) procedure.

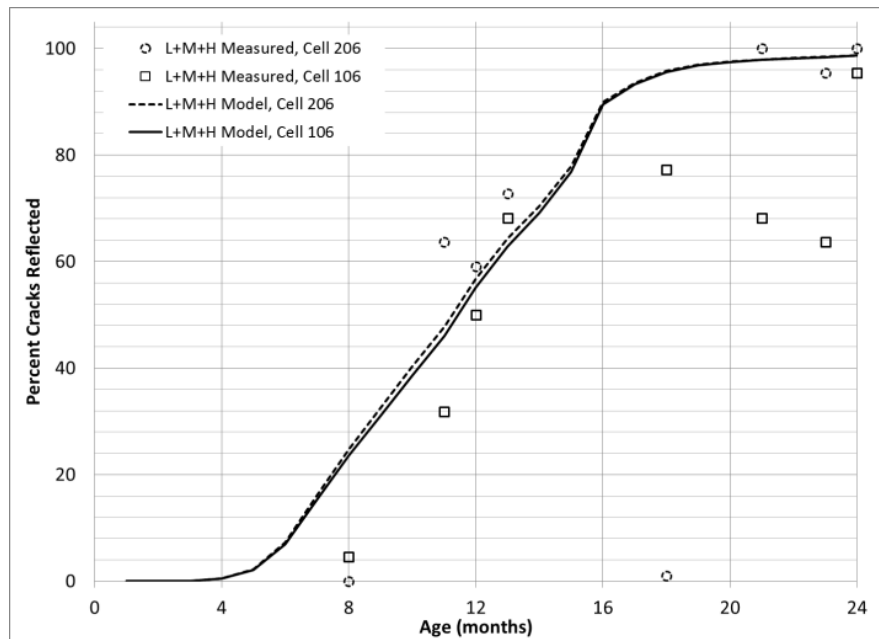


Figure 4-26: First two years of MnROAD Low, Medium, and High (L+M+H) severity reflection cracking data versus TPF-5(149) modeled L+M+H performance.

As the L+M+H model considers thermal effects, we anticipate that model predictions would far exceed those of the M+H case over the service life of the projects. This expectation is upheld in a comparison of Figure 4-23 and Figure 4-25. Furthermore, in Figure 4-25 (and Figure 4-26) the presence of doweling does not appear to mitigate overall cracking; the model prediction in this regard is upheld by observed reflective cracking for the first 24 months of Cells 106 and 206. As

noted above, the TPF-5(149) model of L+M+H reflective cracking includes thermal effects, and thus for these severity levels the Low cracking due to thermal effects predominate. Again, this model prediction appears to be validated by the available MnROAD data.

Both the model and the MnROAD field data show that Low severity cracking can be expected within a few years after opening to traffic. Therefore, saw-and-sealing should be recommended to eliminate this distress.

Overall, the TPF-5(149) procedure clearly represents an improvement on the existing MEPDG procedure. Furthermore, given these results and the TPF-5(149) project's accommodation of the MEPDG, it is a possible candidate for incorporation into the new AASHTO DARWin-ME program. However, for the TPF-5(149) procedure to be considered as a serious model for reflective cracking, more work needs to be done in terms of calibration, validation, and sensitivity analysis. The following section describes a brief sensitivity analysis conducted during Task 5 to address this concern.

4.2.5 Sensitivity Analysis of TPF-5(149) Procedure for Reflection Cracking

As was the case for the sensitivity analysis of the rutting procedure of Section 4.1.5, both the MEPDG and CalME rutting model have been subjected to extensive review and sensitivity analysis. However a difference in the reflective cracking case is that the CalME model has been modified to account for thermal effects, LTE, and two levels of cracking severity.

The research team undertook a brief analysis of reflective cracking performance sensitivity to two important parameters: HMA thickness and climate. Other than these two parameters, the sensitivity study assumed a HMA-PCC pavement with a 2-inch HMA overlay of a 7-inch JPCP. Furthermore, the analysis assumed MEPDG defaults for material properties (Level 3 inputs) for all projects. All projects are assumed to be doweled unless otherwise indicated. Assumed traffic was 2000 AADTT.

Climate

Figure 4-27 and Figure 4-28 illustrate the sensitivity of reflective predictions to climate for 5 locations in M+H severity and L+M+H severity. Each of these locations corresponds to EICM climate files (*.icm) for Seattle, WA; Pullman, WA; Sacramento, CA; San Francisco, CA; and Minneapolis-Saint Paul, MN.

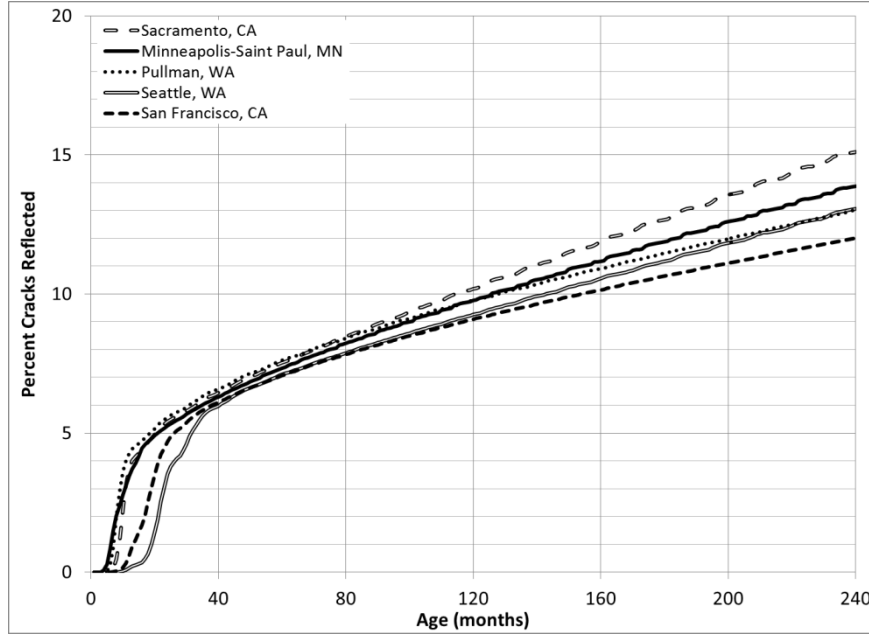


Figure 4-27: Influence of climate file on TPF-5(149) procedure for M+H reflective cracking.

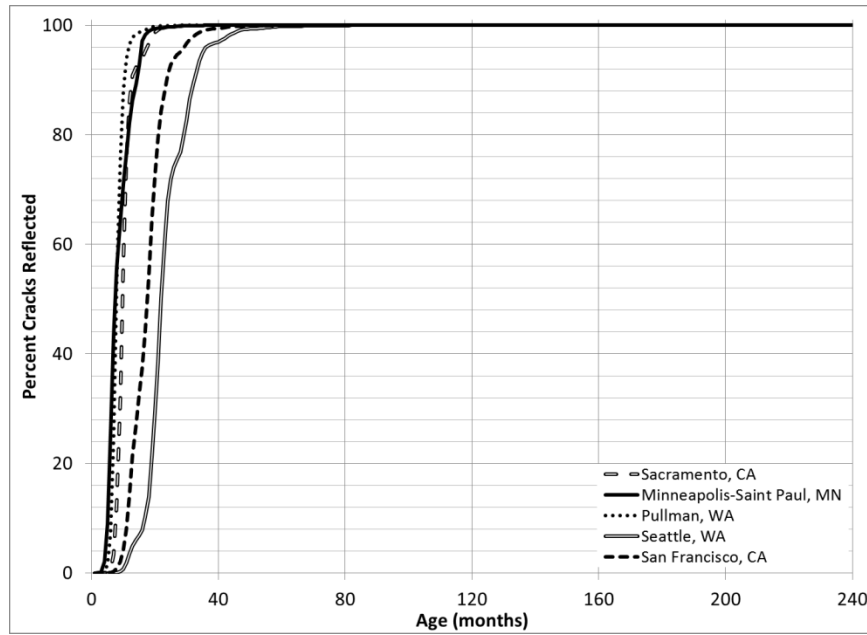


Figure 4-28: Influence of climate file on TPF-5(149) procedure for L+M+H severity reflective cracking.

A comparison of Figure 4-27 and Figure 4-28 immediately describes the sensitivity of Low severity cracking to climate and, by extension, the inclusion of thermal effects in the Low severity reflective cracking model. The sensitivity of the model is more easily identified in Figure 4-29.

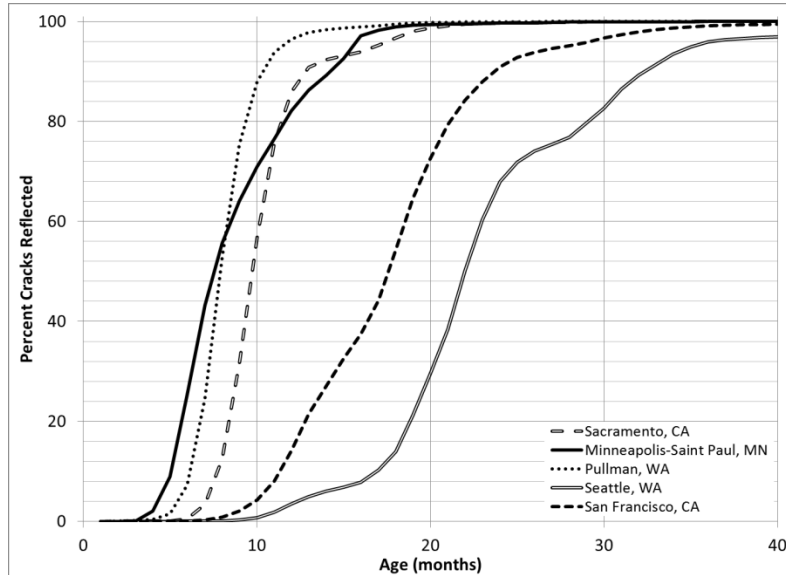


Figure 4-29: First 40 months of predicted L+M+H severity reflective cracking by TPF-5(149) procedure for five climate files.

It can be seen in Figure 4-29 that the onset of 20% L+M+H cracking is predicted to occur 13 months later in Seattle than it is in Minneapolis. Furthermore, the percent L+M+H cracking associated with pavements of 10 months of age for different climates ranges from 1% (for Seattle) to 88% (for Pullman). Thus, whereas M+H cracking (whose model does not include thermal effects) occurs for all climates at the same percentage of incidence within a few months, for L+M+H cracking the onset and extent of cracking can differ by over a year for different climates. This observation not only confirms that the TPF-5(149) procedure is sensitive to climate, it also validates the inclusion of thermal effects in the L+M+H reflective cracking model developed under TPF-5(149).

Pavement Thickness

Figure 4-30 and Figure 4-31 illustrates the sensitivity of TPF-5(149) procedure predictions for M+H and L+M+H reflective cracking to three levels of HMA thickness. These projects were developed for an EICM climate file developed from weather data for Minneapolis-Saint Paul International Airport (MSP) in Minneapolis, MN. For projects examining sensitivity to HMA thickness, PCC thickness was held at a constant 7 inches (175 mm).

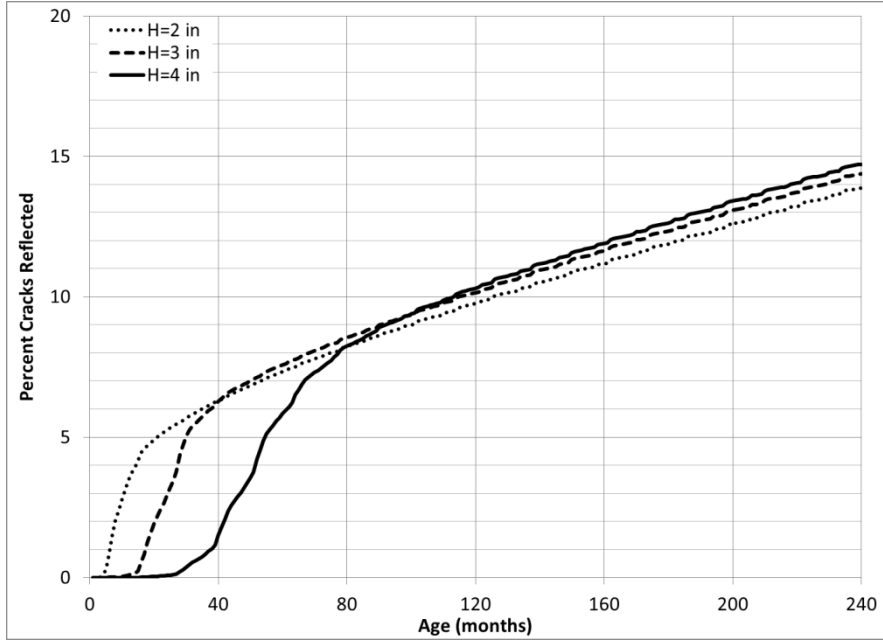


Figure 4-30: Influence of HMA overlay thickness on TPF-5(149) procedure for M+H severity reflective cracking.

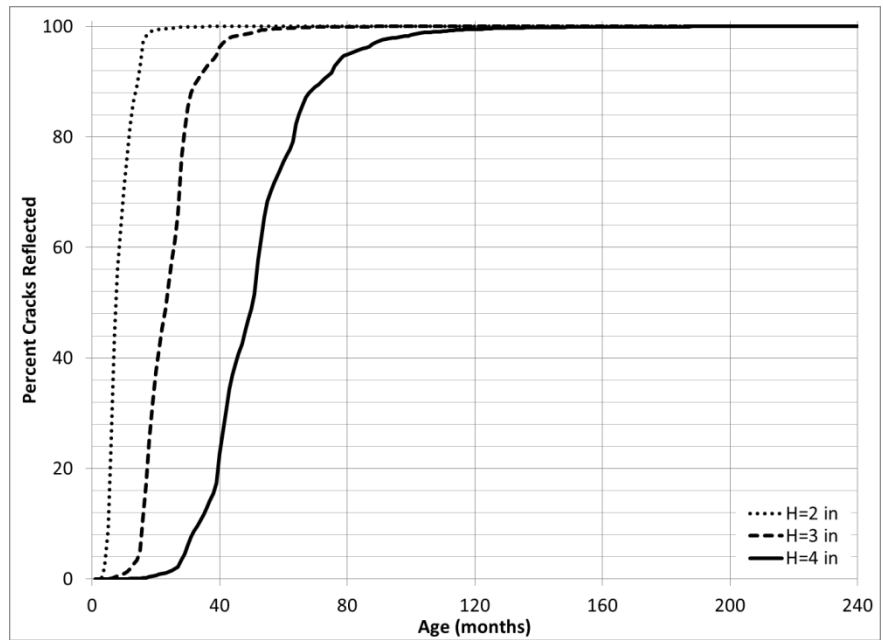


Figure 4-31: Influence of HMA overlay thickness on TPF-5(149) procedure for L+M+H severity reflective cracking.

The sensitivity of both the M+H and L+M+H models to HMA overlay thickness prompts two key observations. First, total reflective cracking over the service life of the pavement will not be reduced significantly by increased overlay thickness. However, an increase in overlay thickness does significantly mitigate (by nearly 1/6th of the pavement service life in the example above) the predicted onset of initial reflective cracking. The sensitivity of the model in this regard is

supported by other models and observations of in-field reflective cracking, which have been used to support regular maintenance and renewal of HMA-PCC systems.

Joint Load Transfer

It should be noted that the study of Cells 106 and 206 in Section 4.1.5 is itself a sensitivity study of the model to the presence of doweling. As noted earlier, for M+H cases in Figure 4-23, the model is sensitive to the presence of dowels while being insensitive to LTE in L+M+H cases, represented by Figure 4-25. Note again that Cell 106 has 1-inch dowel at transverse joints, and Cell 206 is undoweled. The sections are otherwise identical.

However, it may be so that for less severe climates, there is some sensitivity in the L+M+H reflective cracking model. To test this, given the results of the sensitivity analysis for climate, the Seattle climate file was used for a brief study of sensitivity to joint load transfer (or simply LTE). Predicted M+H and L+M+H severity cracking by the TPF-5(149) procedure for projects in Seattle with and without 1-inch dowels are presented in Figure 4-32 and Figure 4-33, respectively.

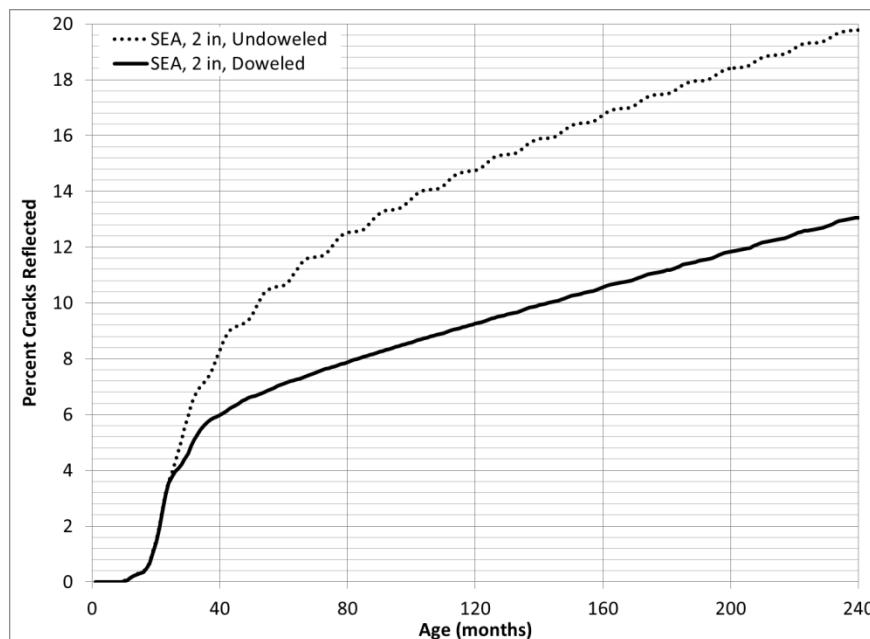


Figure 4-32: Influence of dowels on TPF-5(149) procedure for M+H severity reflective cracking for project using Seattle, WA, climate file.

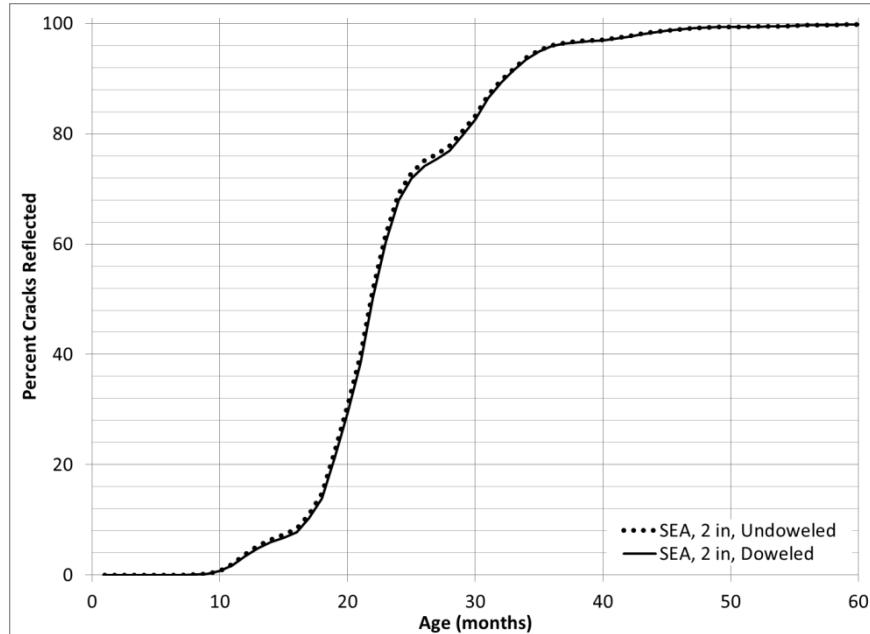


Figure 4-33: Influence of dowels on TPF-5(149) procedure for L+M+H severity reflective cracking for project using Seattle, WA, climate file.

As in the case with the MnROAD results, Figure 4-32 confirms the sensitivity of the M+H cracking model to LTE, which is to be expected given that the M+H model considers only axle loads. Figure 4-33 shows that even for projects with less severe climatic conditions than those of MnROAD, L+M+H predictions remain fairly insensitive to LTE. While this is to be expected given the predominance of Low severity cracking, it illustrates that even for less severe climates, thermal effects will contribute to damage far more than axle loads in the L+M+H model.

4.3. JPCP Cracking Models for HMA-PCC

Many HMA overlays fail prematurely due to transverse cracking in the PCC layer reflecting through the asphalt. The MEPDG identifies transverse cracking in the PCC layer as a major distress that is important to control. The MEPDG assumes that a transverse crack developed in the PCC layer will eventually propagate through the HMA layer over time and traffic. Figure 4-34 illustrates the propagation of a fatigue crack in the PCC layer to the top of the HMA layer.

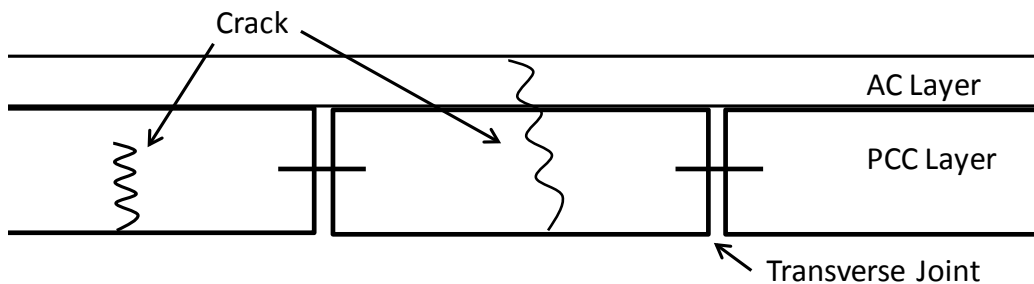


Figure 4-34: Propagation of fatigue cracking in a composite pavement.

For HMA-PCC projects, the MEPDG uses a separate distress model to compute reflective cracking, as detailed in Chapter 3. However, the MEPDG currently uses only the existing model for JPCP in determining the extent of transverse cracking in the PCC layer. Although the JPCP cracking model is quite robust and comprehensive, there is a concern that the HMA characterization used in the model may be inadequate.

The work of Task 5 included a review of the existing JPCP transverse cracking model and a modification of this model for HMA-PCC projects. Task 5 also included a brief validation and sensitivity analysis. These efforts are detailed in the following subsections.

4.3.1 MEPDG Transverse Cracking Model for JPCP

The MEPDG distress model for predicting transverse cracking in JPCP has the form

$$TCRACK = (CRK_{Bottom-up} + CRK_{Top-down} - CRK_{Bottom-up} \cdot CRK_{Top-down}) \cdot 100\% \quad (4-38)$$

$$CRK = \frac{100}{1 + FD^{-1.68}} \quad (4-39)$$

$$FD = \sum \frac{n_{t,j,k,l,m,p}}{N_{t,j,k,l,m,p}} \quad (4-40)$$

$$\log(N_{t,j,k,l,m,p}) = C_1 \cdot \left(\frac{MR}{\sigma_{t,j,k,l,m,p}} \right)^{C_2} \quad (4-41)$$

where *TCRACK* is the total transverse cracking (percent; all severities); *CRK* is the percentage of bottom-up or top-down PCC cracking; *FD* is the fatigue damage; *n* is the applied number of load applications at conditions *t, j, k, l, m, and p*; *N* is the allowable number of load applications at conditions *t, j, k, l, m, p*; *t, j, k, l, m, and p* are conditions relating to the age, month, axle type, load level, temperature difference, and traffic path, respectively; *MR* is the modulus of rupture of PCC; *σ* is the applied stress at conditions *t, j, k, l, m, and p*; and *C₁* and *C₂* are calibration constants (*C₁* = 2.0; *C₂* = 1.22).

4.3.2 Modifications to JPCP Transverse Cracking Model for HMA-PCC Projects and Incorporation into the MEPDG

Equation (4-41) implies that cracking in the PCC layer is a function of the “applied stress” and thus depends on the various factors related to traffic loads and temperature gradients. Accurate computation of the stress at the critical location in the PCC layer is an important step in the calculation of fatigue cracking.

To compute structural responses such as stresses, strains, and displacements, constitutive relationships for each layer in the structural model should be provided. Asphalt is a viscoelastic

material; its structural responses depend not only on the magnitude of the applied load but on the load duration as well. However, conducting a viscoelastic analysis for each combination of site and loading conditions required by the MEPDG damage computation process would be computationally prohibitive. In order to simplify the structural analysis, the MEPDG treats asphalt layers as elastic, but to account for the viscoelastic behavior of the asphalt layer, the MEPDG assumes that the asphalt modulus of elasticity is equal to the load duration-dependent dynamic (complex) modulus.

The loading duration for traffic loads depends on the vehicle speed. If vehicle speed is approximately 60 mph, then the loading duration ranges between 0.01 sec and 0.05 seconds. However, the duration of temperature loading is significantly longer. The MEPDG analysis of flexible pavements ignores temperature-induced asphalt stresses and strains for all the distress models except the low-temperature cracking model. In the low-temperature cracking model, the temperature-induced stresses are accounted for but asphalt material is characterized differently and the axle load-induced stresses are ignored. Therefore, the MEPDG framework used to account for the viscoelastic behavior of asphalt layers in the design of flexible pavements can be considered reasonable.

The situation is quite different in the case of asphalt overlays of concrete pavements because the MEPDG implicitly accounts for both traffic and temperature induced stresses and strains in the asphalt layer. The MEPDG recognizes that there is an interaction between temperature curling and deformations due to traffic loading for the JPCP and HMA overlays of JPCP. Moreover, the loading durations of temperature gradients and fast moving traffic loads are significantly different. Therefore, for the case of asphalt overlays of JPCP in the MEPDG framework, the characterization of the HMA layer using a single dynamic modulus may be an oversimplification.

The MEPDG distress model for predicting transverse cracking in the PCC layer of an HMA overlaid JPCP was adopted directly from the fatigue cracking model of a new JPCP detailed in Section 4.1. Under Task 4 of TPF-5(149), an approximate two-moduli analysis for the prediction of the critical concrete stresses was developed. However, a direct implementation of that method was not feasible due to a need to re-train a portion of the MEPDG neural networks and replace the current temperature distribution linearization procedure. These activities will be a subject of future research. A simplified procedure for TPF-5(149) was instead adopted.

For each combination of traffic loading and temperature distribution throughout the composite pavement system, three stresses were computed using the MEPDG.

1. The first stress, $\sigma(E_{red}, \Delta T)$, was computed using the current MEPDG HMA complex modulus and zero temperature gradient;
2. the second, $\sigma(E_{red}, 0)$, was calculated using the reduced HMA modulus to account for longer duration of curling process and the actual temperature gradient;
3. and the third and final stress, $\sigma(E^*, 0)$, was calculated using the reduced HMA modulus and zero temperature gradient.

These stresses were combined for the subsequent fatigue analysis according to

$$\sigma_{\text{comb}} = \sigma(E_{\text{red}}, \Delta T) - \sigma(E_{\text{red}}, 0) + \sigma(E^*, 0) \quad (4-42)$$

where E^* is the MEPDG HMA complex modulus currently used HMA overlay cracking analysis and E_{red} is the reduced modulus. Currently, the reduced modulus is assumed to be 50% of the complex modulus.

4.3.3 Sensitivity Analysis of Modified MEPDG JPCP Transverse Cracking Model

The research team undertook a brief sensitivity analysis of the modified transverse cracking performance relative to two important parameters: HMA overlay thickness and climate. Other than these two parameters, the sensitivity study assumed a HMA-PCC pavement with 2 inches (50 mm) HMA over 7 inches (175 mm) JPCP. Furthermore, the analysis assumed MEPDG defaults for material properties (Level 3 inputs) for all projects. Assumed traffic was 2000 AADTT.

To begin, a number of JPCP projects were created to assess the effect of the HMA overlay on overall PCC transverse cracking performance. These JPCP projects (for a 7-inch, 8-inch, and 9-inch slab) were run using the original MEPDG. The HMA-PCC project was run using both the original MEPDG procedure and the TPF-5(149) procedure for PCC transverse cracking developed in Task 5. Figure 4-35 and Figure 4-36 present the predicted PCC transverse cracking for these cases.

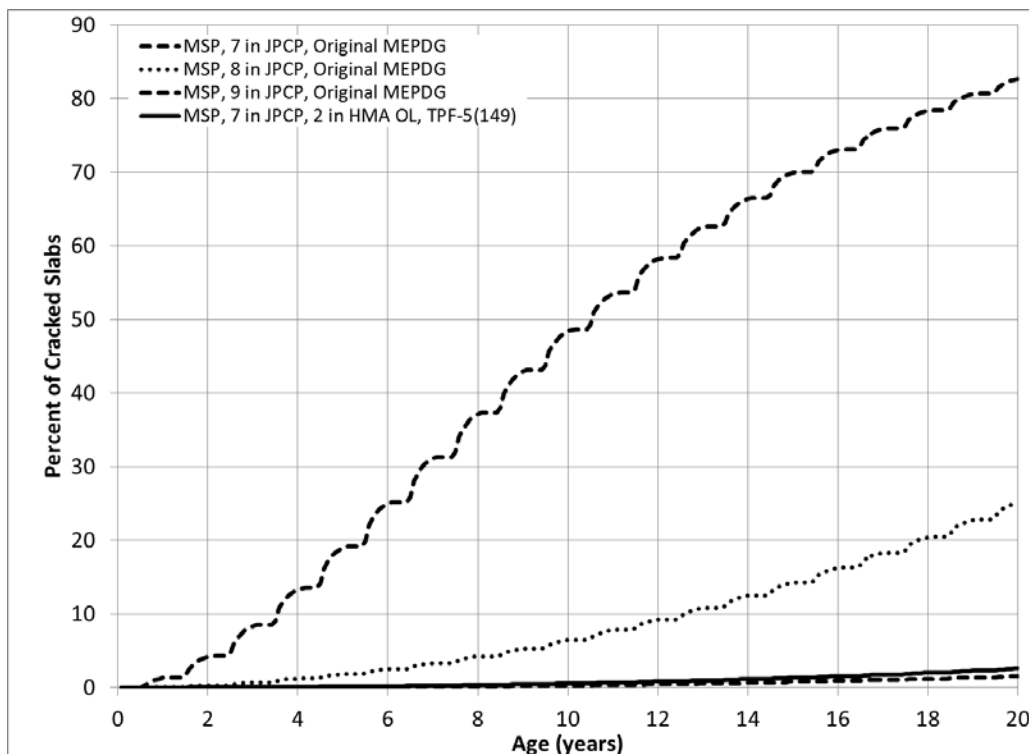


Figure 4-35: Predicted JPCP transverse performance for three JPCP projects (according to original MEPDG) and a HMA-PCC project (according to TPF-5(149) procedure).

As expected, a presence of an overlay reduces PCC cracking. Figure 4-35 shows, however, that this effect can be very pronounced. The MEPDG predicts that after 10 years a 7-in thick JPCP would exhibit 50 percent of cracked slabs while a TICP would have almost negligible amount of cracking. An 8-in JPCP would also exhibit higher cracking than the composite pavement and only 9-in JPCP would have lower cracking. This behavior can be explained by the fact that presence of a HMA overlay significantly reduces temperature gradients in the PCC layer (i.e. it is “thermally insulated”) thus reducing fatigue damage. It should be noted that a similar trend produced by the original MEPDG cracking model for HMA overlays.

Furthermore, Figure 4-36 shows that the original MEPDG model predicts even lower cracking in the composite pavements compared to a 9-in JPCP under the same site conditions.

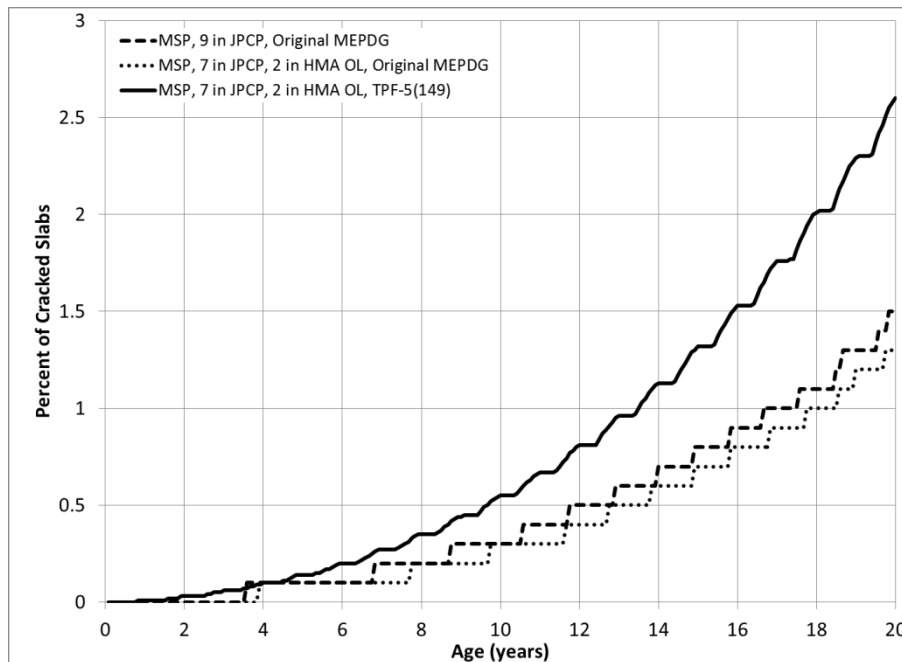


Figure 4-36: Comparison of 9-inch JPCP project and model predictions for PCC transverse cracking according to original MEPDG and TPF-5(149) procedures.

Figure 4-37 illustrates the sensitivity of transverse cracking predictions for the PCC layer to climate for 3 levels of HMA overlay thickness (and in turn composite pavement thickness). For each of these cases, the PCC thickness is a constant 7 inches.

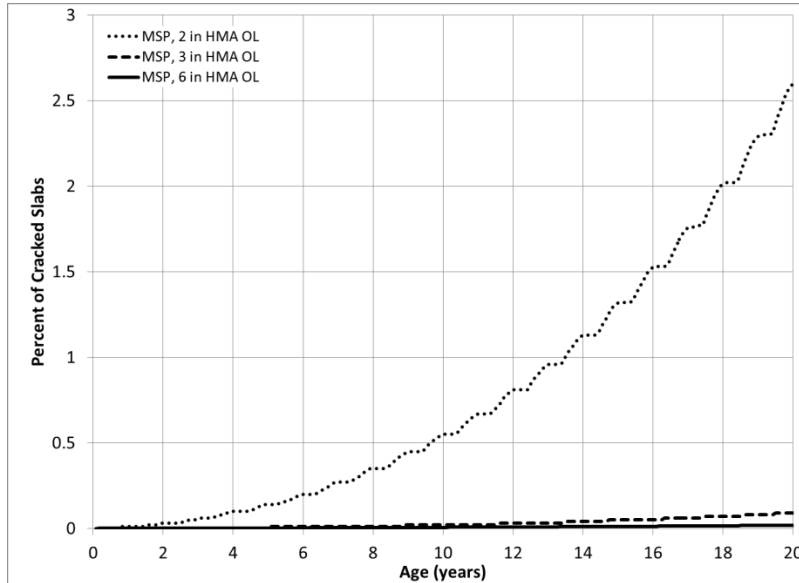


Figure 4-37. Influence of HMA overlay thickness on predicted JPCP transverse cracking for a HMA-PCC project.

As expected, an increase in HMA overlay thickness decreases cracking. It should be noted that this trend (a decrease in PCC cracking with an increase in HMA thickness) was experimentally confirmed at HVS testing conducted under the SHRP2 R21 project. It is also worth considering, however, that both HVS testing and the analysis from this study concluded that an increase in HMA thickness increases HMA rutting

Figure 4-38 illustrates the sensitivity of transverse cracking predictions for the PCC layer to climate for 4 locations. Each of these locations corresponds to EICM climate files (*.icm) for Seattle, WA; Pullman, WA; San Francisco, CA; and Minneapolis-Saint Paul, MN.

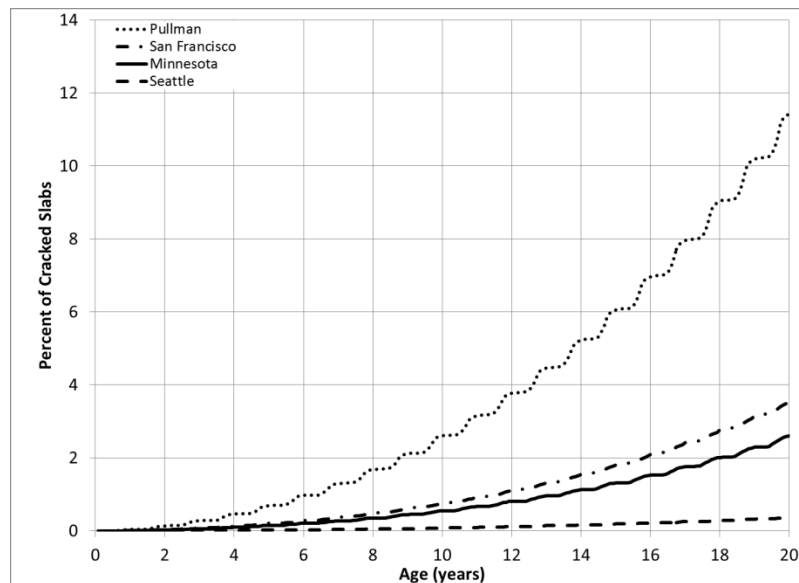


Figure 4-38: Influence of climate on JPCP transverse cracking for a HMA-PCC project.

It can be observed that the cracking prediction is sensitive to the climate data, as it was discussed in the previous task reports.

4.3.4 Confirmation of TPF-5(149) Modifications to MEPDG JPCP Transverse Cracking Model for HMA-PCC Projects

Figure 4-39 illustrates a comparison of predicted JPCP transverse cracking for HMA-PCC projects in Minneapolis, MN, and Pullman, WA using the original MEPDG and the modified MEPDG that utilizes the JPCP transverse cracking revised during the work of Task 5. These projects assume a cross-section of a 2-inch HMA overlay of 7-inch JPCP with Level 3 inputs.

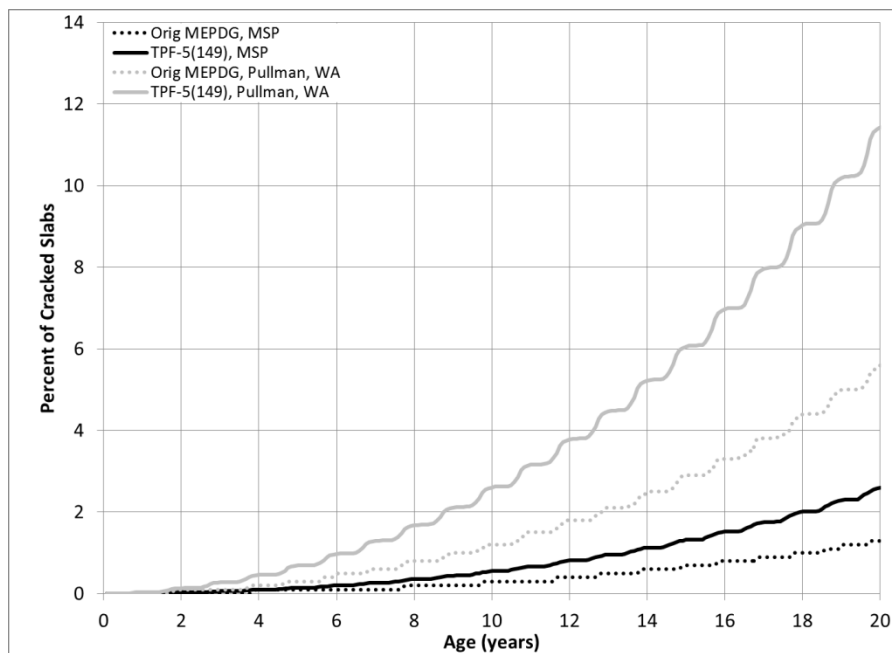


Figure 4-39. Predicted JPCP transverse cracking in HMA-PCC projects for Minneapolis, MN, and Pullman, WA, according to the original and TPF-5(149) modified MEDPG.

Both models produce the same trends. It is possible that the developed TPF-5(149) procedure may not be conservative enough. At the same time, as it was observed from the analysis of MnROAD Cells 106 and 206, the original MEPDG model may produce higher cracking than the TPF-5(149) model. More comparison with field performance data is needed to establish what model is better. Meanwhile, it is recommended to run both models and use a more conservative prediction.

Figure 4-40 compares transverse cracking prediction for Cells 106 and 206 using the original MEPDG procedure and the TPF-5(149) model.

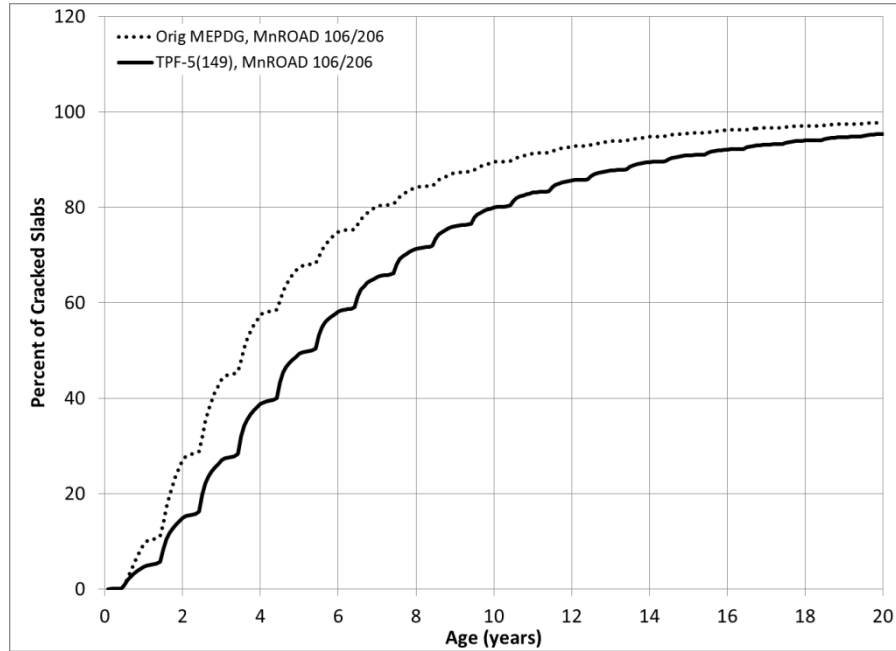


Figure 4-40. Predicted transverse cracking in MnROAD Cells 106 and 206 according to the original MEPDG and TPF-5(149) procedures

As shown in Figure 4-40, both models predict a high percentage of cracking two years after construction. This somewhat agrees with field observations, as structural performance of both cells was reported by MnROAD to be poor and they were reconstructed after three years of service.

At the same time, the main structural distress in the PCC layer was longitudinal and not transverse cracking. Currently, the MEPDG does not have a model for the prediction of longitudinal cracking in JPCP and HMA-PCC. However, a predicted high transverse cracking fatigue damage can be used as an indirect estimate of the longitudinal cracking damage. Since both models predict high fatigue damage, one can conclude that both models predicted poor performance for both Cells 106 and 206.

4.4. JPCP Faulting Models for HMA-PCC

The faulting model in the current MEPDG is for newly constructed JPCP pavements only; thus, a faulting model has not been implemented for HMA-PCC projects. One of the reasons for this is that for conventional HMA-PCC pavements, faulting does not develop until reflective cracks propagate, which then complicates observation of cracking that can be directly attributed to faulting. Furthermore, faulting data is typically not collected for HMA-PCC.

Nevertheless, given the popularity of saw-and-seal techniques for HMA-PCC and the recommendation of saw-and-seal for HMA-PCC by the SHRP2 R21 project, there is a need to quantify the benefits of the use of dowels in terms of design and analysis. As noted earlier, the MEPDG does not provide this, and therefore the work of Task 5 included the modification of the

MEPDG faulting model for HMA-PCC and the incorporation of this modified model into the existing MEPDG framework for HMA-PCC projects.

4.4.1 MEPDG JPCP Faulting Model

The mean transverse joint faulting is predicted using incremental approach as illustrated in Figure 4-3. A faulting increment is determined each month and the current faulting level affects the magnitude of increment. The faulting at each month is determined as a sum of faulting increments from all previous months in the pavement life since the traffic opening using the following model:

$$Fault_m = \sum_{i=1}^m \Delta Fault_i \quad (4-43)$$

$$\Delta Fault_i = C_{34} * (FAULTMAX_{i-1} - Fault_{i-1})^2 * DE_i \quad (4-44)$$

$$FAULTMAX_i = FAULTMAX_0 + C_7 * \sum_{j=1}^m DE_j * \text{Log}(1 + C_5 * 5.0^{EROD})^{C_6} \quad (4-45)$$

$$FAULTMAX_0 = C_{12} * \delta_{curling} * \left[\text{Log}(1 + C_5 * 5.0^{EROD}) * \text{Log}\left(\frac{P_{200} * WetDays}{P_s}\right) \right]^{C_6} \quad (4-46)$$

where C_{12} , C_{34} , C_5 , C_6 , and C_7 are calibration constants and

$Fault_m$	= Mean joint faulting at the end of month m , inches
$\Delta Fault_i$	= Incremental change (monthly) in mean transverse joint faulting during month i , inches
$FAULTMAX_i$	= Maximum mean transverse joint faulting for month i , inches
$FAULTMAX_0$	= Initial maximum mean transverse joint faulting, inches
$EROD$	= Base/subbase erodibility factor
DE_i	= Differential deformation energy accumulated during month i
$\delta_{curling}$	= Maximum mean monthly slab corner upward deflection PCC due to temperature curling and moisture warping
PS	= Overburden on subgrade, pounds
$P200$	= Percent subgrade material passing #200 sieve
$WetDays$	= Average annual number of wet days (greater than 0.1 inch rainfall)
FR	= Base freezing index, defined as the percentage of time the top base temperature is below freezing (32 °F) temperature.

Khazanovich et al (2004) and AASHTO (2008) further describe the differential energy concept used to define parameter DE_i (which accounts for joint load-transfer efficiency, aggregate interlock, and the presence and type of joint dowels). Furthermore, calibration coefficients C_{12} and C_{34} are related to the base freezing index, FR , as follows

$$C_{12} = C_1 + C_2 * FR^{0.25} \quad (4-47)$$

$$C_{34} = C_3 + C_4 * FR^{0.25} \quad (4-48)$$

where C_1 through C_4 are calibration constants and the base freezing index, FR, is defined as the percentage of time the top base temperature is below freezing (32 °F) temperature.

The functional form of the model reflects the hypothesis that faulting potential for a given pavement structure depends on the extent of slab curling, the erodibility of the base material, and the presence of fines and free water in the subgrade. Faulting potential decreases with an increase of overburden pressure on the subgrade. The rate of faulting development depends on the current faulting level, and that rate decreases as faulting increases. Eventually the faulting stabilizes at a certain level.

4.4.2 Modifications of MEPDG Faulting Model for HMA-PCC and Incorporation into the MEPDG Procedure

Two major modifications of the MEPDG faulting model were implemented during the work of Task 5.

- The composite HMA-PCC structure was replaced by an equivalent single layer system.
- The load transfer efficiency characterization was modified.

Equivalent Single-Layer Pavement

For a fully bonded PCC-base system, the neutral axis of the bonded system, assuming the origin is at the top of the PCC layer, is given as follows:

$$x = \frac{\int_0^h E(z)zdz}{\int_0^h E(z)dz} = \frac{E_{PCC}h_{PCC}\left(\frac{h_{PCC}}{2}\right) + E_{Base}h_{Base}\left(h_{PCC} + \frac{h_{Base}}{2}\right)}{E_{PCC}h_{PCC} + E_{Base}h_{Base}} \quad (4-49)$$

where x is the location of the neutral axis from the top of PCC layer. The thickness and modulus of the equivalent single-layer slab can be established in terms of the thicknesses and moduli of the corresponding multi-layered slab as follows:

$$E_{eff}h_{eff}^3 = E_{PCC}h_{PCC}^3 + E_{base}h_{base}^3 + 12\left[E_{PCC}h_{PCC}\left(\frac{h_{PCC}}{2} - x\right)^2 + E_{Base}h_{Base}\left(h_{PCC} + \frac{h_{Base}}{2} - x\right)^2\right] \quad (4-50)$$

For a fully bonded HMA-PCC-base system, the neutral axis x is located as follows, assuming the origin is located at the surface of the HMA overlay:

$$x = \frac{\frac{E_{HMA}}{E_{PCC}}\frac{h_{HMA}^2}{2} + h_{PCC}\left(h_{HMA} + \frac{h_{PCC}}{2}\right) + \frac{E_{Base}}{E_{PCC}}h_{Base}\left(h_{HMA} + h_{PCC} + \frac{h_{Base}}{2}\right)}{\frac{E_{HMA}}{E_{PCC}}h_{HMA} + h_{PCC} + \frac{E_{Base}}{E_{PCC}}h_{Base}} \quad (4-51)$$

where and E_{eff} , E_{HMA} , E_{PCC} , and E_{Base} are the Young's moduli of the effective composite system, HMA overlay, PCC layer, and base layers, respectively, and h_{eq} , h_{HMA} , h_{PCC} , and h_{Base} are the thicknesses of the effective composite slab, HMA overlay, PCC layer, and base layers, respectively.

One check of the solution for the neutral axis in the three-layer PCC system is to consider that if $E_{HMA} = E_{PCC}$, Equation (4-46) will reduce to Equation (4-44), which represents the location of the neutral axis in a single-layer PCC over base layer system. The thickness and modulus of the equivalent single-layer slab for the three-layer system can be established as in Equation (4-45), where

$$E_{eff}h_{eff}^3 = E_{HMA}h_{HMA}^3 + E_{PCC}h_{PCC}^3 + E_{Base}h_{Base}^3 + 12 \left[E_{HMA}h_{HMA} \left(x - \frac{h_{HMA}}{2} \right)^2 + E_{PCC}h_{PCC} \left(h_{HMA} + \frac{h_{PCC}}{2} - x \right)^2 + E_{Base}h_{Base} \left(h_{HMA} + h_{PCC} + \frac{h_{Base}}{2} - x \right)^2 \right] \quad (4-52)$$

All variables in Equation (4-47) are defined above for Equation (4-46).

Load Transfer in a HMA-PCC System

For transverse joints, the total deflection LTE includes the contribution of three major mechanisms of load transfer:

- load transfer by PCC aggregates;
- load transfer by joint dowels (if applicable); and
- joint transfer by the base/subgrade.

In the MEPDG, the combined LTE for a JPCP project is defined as

$$LTE_{joint} = 100 \left(1 - (1 - LTE_{dowel} / 100)(1 - LTE_{agg} / 100)(1 - LTE_{base} / 100) \right) \quad (4-53)$$

where LTE_{joint} is the percentage of total joint LTE; LTE_{dowel} is the percentage of joint LTE if dowels are the only mechanism of load transfer; LTE_{base} is the percentage of joint LTE if the base is the only mechanism of load transfer; and LTE_{agg} is the percentage of joint LTE if aggregate interlock is the only mechanism of load transfer.

For composite pavements, the HMA overlay also provides load transfer until the reflective crack propagates to the surface. To account for this effect, Equation (4-48) has been modified to become

$$LTE_{joint} = 100 \left(1 - \left(1 - \frac{LTE_{dowel}}{100} \right) \left(1 - \frac{LTE_{agg}}{100} \right) \left(1 - \frac{LTE_{base}}{100} \right) \frac{RC_{LMH}}{100} \right) \quad (4-54)$$

where RC_{LMH} is the total reflective cracking, defined in Equation (4-10). Equation (4-49) – i.e. the modification of Equation (4-48) – states that the HMA overlay:

1. dominates the joint load transfer until the cracks propagate and

2. does not directly contribute to the load transfer after all reflective cracks (100 percent) propagate to the surface

4.4.3 Validation and Sensitivity Analysis of Modified MEPDG Faulting Model for HMA-PCC

Faulting data are not routinely collected for composite pavements. To validate the model, the predictions were compared with the predictions of the field-calibrated faulting model for new JPCP pavements as well as through the analysis of sensitivity of the predictions to the input parameters. Since the faulting prediction is especially important for saw-and-seal pavements, this type of joint is considered below.

Figure 4-41 presents a comparison of the predicted faulting a 2-inch HMA overlay of 7-inch undoweled JPCP with the predicted faulting for 8-inch and 9-inch thick new undoweled JPCP projects.

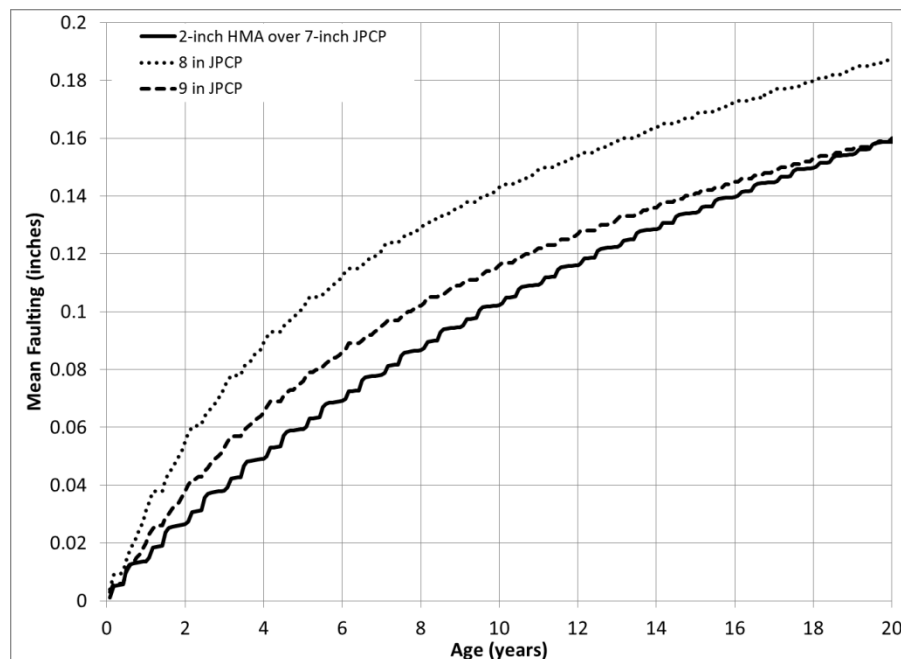


Figure 4-41: Comparison of predicted faulting for HMA-PCC and JPCP projects using MEPDG modified according to TPF-5(149).

One can observe in Figure 4-41 that the predicted faulting for the HMA-PCC project is lower than for the 8-inch JPCP and is comparable with the predicted faulting for the 9-in JPCP. Such behavior might be expected, because although the replacement of the top two inches of PCC with HMA increases the flexibility of the pavement, the presence of an HMA layer decreases temperature gradients throughout the PCC slab thickness. Also, the HMA layer seals off the PCC surface thus reducing the PCC shrinkage. It should be also noted that the PCC cracking models for the same site conditions also predicted similar cracking for the HMA-PCC and 9-inch thick JPCP.

Figure 4-42 compares the predicted faulting for HMA-PCC projects in Minneapolis, MN, and Pullman, WA, whose cross-section is a 2-inch HMA overlay of 7-inch JPCP with Level 3 inputs assumed otherwise.

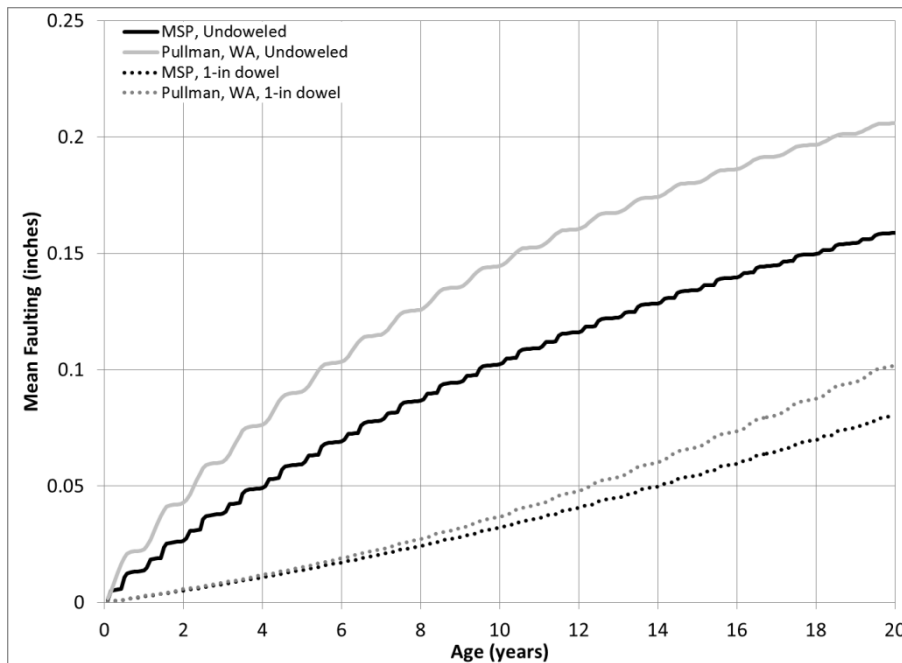


Figure 4-42: Effect of 1-inch dowels in HMA-PCC projects for Minneapolis, MN, and Pullman, WA.

The presence of doweling for these projects mitigates predicted faulting by nearly one-third for these cases. For both locations, the presence of dowels significantly reduces the predicted faulting. This trend was expected, as the presence of dowels significantly improves the load transfer efficiency of the PCC joint.

Figure 4-43 and Figure 4-44 demonstrate the effect of climate on faulting prediction for doweled and undoweled HMA-PCC pavements, respectively. Here the projects assume a cross-section that is 2-inch HMA overlay of 7-inch JPCP, and MEPDG Level 3 default parameters are otherwise assumed. The projects are associated with four EICM climate files: Minneapolis, MN; Seattle, WA; Pullman, WA; and San Francisco, CA.

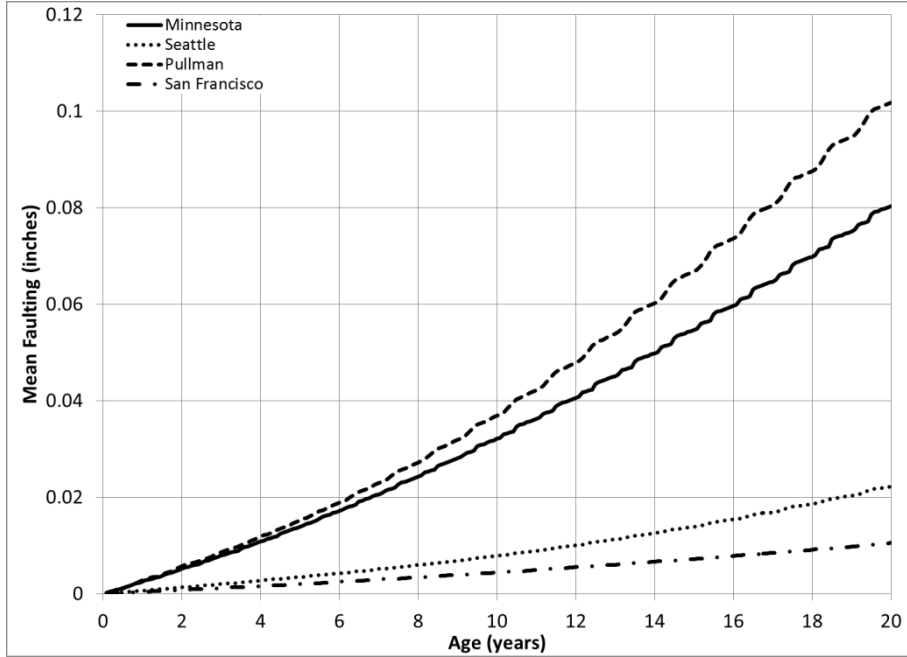


Figure 4-43: Influence of climate on predicted faulting in HMA-PCC using TPF-5(149) modified MEPDG for HMA-PCC project with 1-inch dowels.

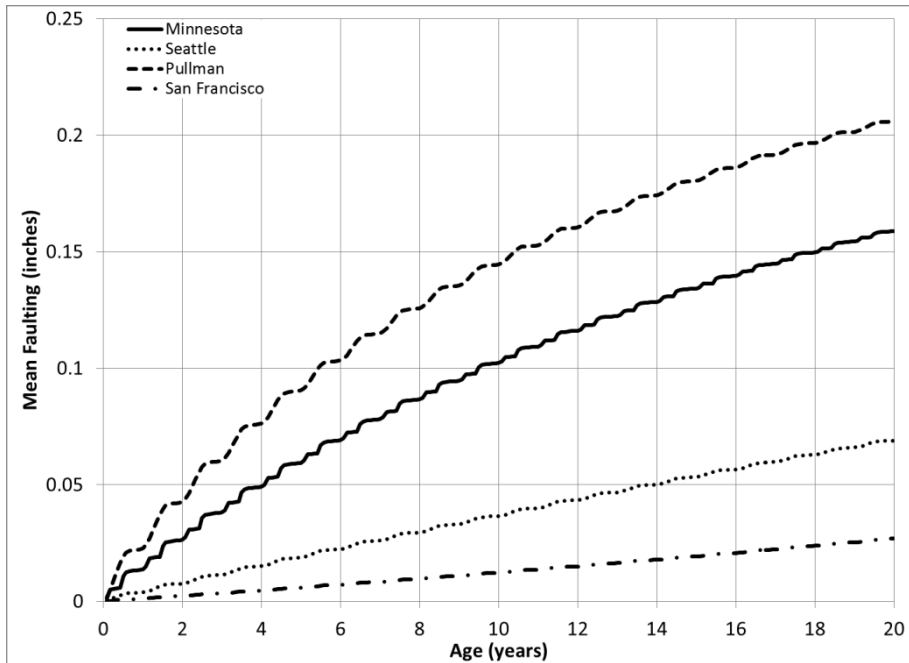


Figure 4-44: Influence of climate on predicted faulting in HMA-PCC using TPF-5(149) modified MEPDG for HMA-PCC project without dowels.

As expected, the predicted faulting is lower in a milder climate, provided that other design features and site conditions remain fixed from project to project. This is true for both doweled and undoweled composite pavements. It should be noted, however, that Figure 4-43 and Figure

4-44 illustrate only the effect of climate *and not* location. The subgrade properties for these locations can be different and this may significantly affect the relative magnitude of faulting for the same design features and traffic.

Finally, Figure 4-45 and Figure 4-46 describe the influence of HMA overlay thickness on faulting predictions for doweled and undoweled projects, respectively. For these projects, we assume a cross-section that is 2-inch HMA overlay of 7-inch JPCP, and MEPDG Level 3 default parameters are otherwise assumed. The projects are associated with an EICM climate file for Minneapolis, MN.

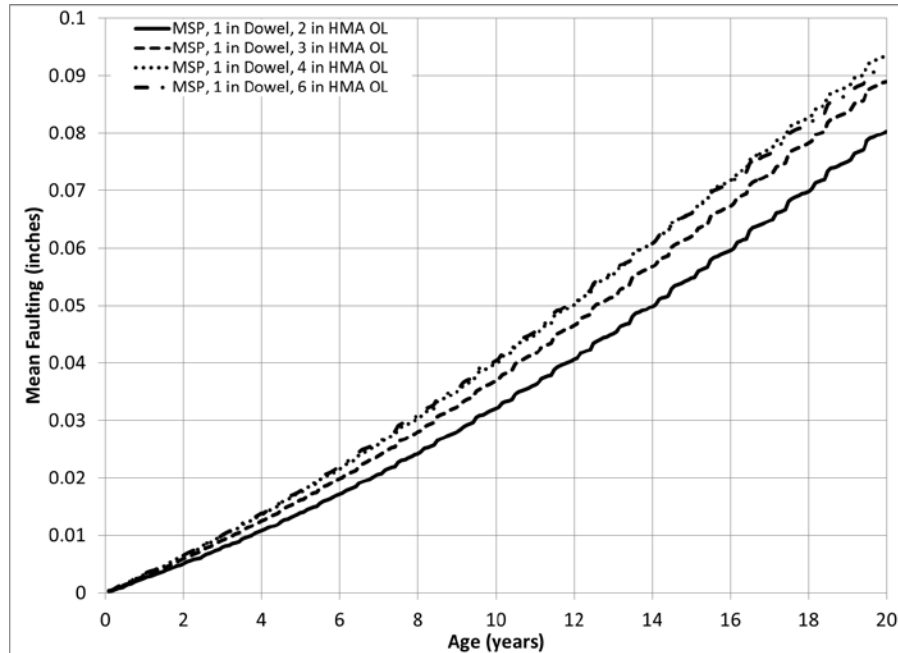


Figure 4-45: Influence of HMA overlay thickness on predicted faulting in HMA-PCC using TPF-5(149) modified MEPDG for HMA-PCC project with 1-inch dowels.

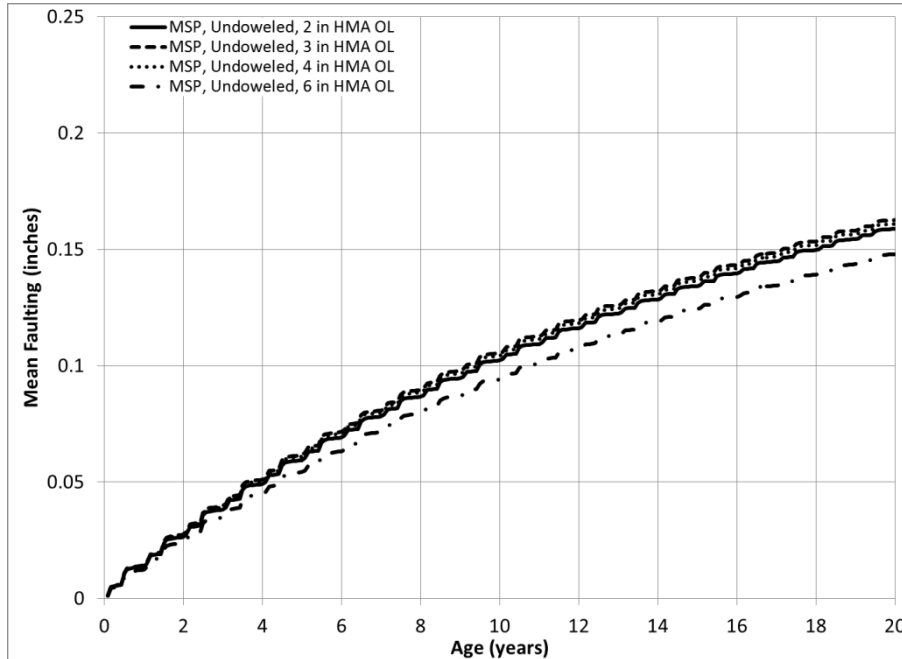


Figure 4-46: Influence of HMA overlay thickness on predicted faulting in HMA-PCC using TPF-5(149) modified MEPDG for HMA-PCC project without dowels.

One can observe in Figure 4-45 and Figure 4-46 that an increase in the HMA overlay thickness over two inches does not appreciably reduce faulting. The HMA overlay is less stiff than concrete and its relative contribution to slab rigidity is not very significant. At the same time, the HMA layer has a high coefficient of thermal expansion. Making the HMA layer thicker increases the “thermal moment” on the PCC slab; under certain conditions it may even increase faulting.

In summary, the analysis presented above demonstrates robustness of the faulting model. However, to fully validate the model, field performance data should be collected to enable comparison with the model predictions.

4.5. Guidelines to TPF-5(149) Procedure for Design and Analysis of TICP

The work of Task 5 developed four separate programs that allow an MEPDG user to interface with the MEPDG project and intermediate files for a TICP project to develop revised rutting, reflective cracking, faulting, and transverse cracking predictions to use in design and analysis. The following outline describes the steps a general user would take in creating an MEPDG project creation and running the TPF-5(149) programs to obtain modified performance results according to the TPF-5(149) procedure.

4.5.1 Creating MEPDG Project File

The first step is the basic creation of an MEPDG project.

1. Design Type: Select “Overlay.” (Although TICP is a newly constructed composite pavement and not an overlay of an existing JPCP, this is the proper Design Type to select

until the MEPDG is modified by AASHTO to include newly constructed HMA-PCC projects.)

2. Pavement Type: Select “HMA/JPCP” for AC/JPC
3. Design Life: Select desired life of pavement.

Once a project file has been initiated, the user must select all design inputs for a trial design. The unique inputs for a TICP composite pavement are as follows.

1. Design reliability and performance for composite pavements:
 - a. Design reliability should be based on traffic level of the highway. Higher traffic levels warrant higher reliability levels (95% to 99%).
 - b. Structural fatigue cracking should range between 5% and 15% JPCP transverse fatigue cracking
 - c. Smoothness (Terminal IRI) should be based on traffic level of the highway. Higher traffic levels warrant lower terminal smoothness levels (~150 in/mile).
 - d. Permanent deformation (rutting of HMA only which is total also) should be ~0.50-in mean wheel path
 - e. Joint faulting for “bare” JPCP comparisons: 0.15 to 0.20 in.
 - f. Initial IRI: The initial IRI for HMA/PCC composite pavements can be very low due to the multiple layering of the pavement. Initial IRI values as low as 35 in/mile have been achieved, with routine values from 40 to 50 in/mile.
 - g. Type and thickness of HMA surface layer. The type depends on the design objectives. If reducing noise levels to a minimum are required, then some type of porous asphalt surface can be used. Thickness should be the minimum possible to provide durability and surface characteristics desired for a given truck traffic and climate. In warmer weather locations, a thinner surfacing is feasible, such as 1 in, but for colder weather and heavier traffic, up to 3 in total may be required.
2. Type (JPCP) and thickness of the PCC layer. This is the load carrying capacity layer for the composite pavement. The trial design should start with a typical thickness used for bare pavement. Depending on the thickness of the HMA surface, the slab thickness may be reduced by 1 to 3 inches of concrete.
3. Joint design. Joint design includes joint spacing and joint load transfer.
 - a. Joint load transfer requirement is similar to bare JPCP design in that dowels of sufficient size are required to prevent erosion and faulting for any significant level of truck traffic. The greater the dowel diameter the higher the joint LTE and the more truck loadings the pavement can carry to the terminal level of faulting.
 - b. Simplified dowel design: the dowel diameter should be at least 1/8 the slab thickness
 - c. Low volume roadways where dowels would not normally be used for bare JPCP do not require dowels for composite pavement. This is true for residential or farm to market streets where JPC or RCC is used as the lower layer. When dowels are not used, it is highly recommended to reduce the joint spacing to 10 ft to reduce reflection cracking severity and increase joint LTE.
4. Concrete slab recommendations:
 - a. Typical concrete used in bare JPCP can be used for TICP with no changes. There are no special requirements different than that for bare pavement.

- b. Lower cost concrete based on local aggregates or recycled concrete. The strength, modulus of elasticity, CTE, and drying shrinkage of the concrete can be varied as inputs.
- c. The SHRP2 R21 MnROAD test sections showed that recycled concrete from a local roadway or local aggregates can be used for the lower layer. Both of these alternatives provided sustainability advantages and cost savings.
- d. Base layer and other sublayers should be selected similar to bare JPCP or CRCP designs based on minimizing erosion, construction ease, and cost effectiveness. No attempts should be made to reduce the friction between the slab and the base because as friction helps control erosion and pumping and reduces stress in the slab.

At this point, the user should have a full project file created.

4.5.2 Execute MEPDG Analysis for TICP Project

In the second step, the user runs the MEPDG program for the created TICP project file (or more generally, an HMA-over-JPCP project file). The MEPDG software performs traffic and EICM (climatic) analysis and creates intermediate project files, which later will be used in the TPF-5(149) analysis.

4.5.3 Execute TPF 5(149) Analysis for TICP Project

In the third step, the user will implement the TPF-5(149) procedure to revise MEPDG predicted performance for the HMA-PCC distresses discussed earlier in this report. The designer may choose to execute any or all of the following models:

- TPF-5(149) rutting model
- TPF-5(149) JPCP cracking model
- TPF-5(149) faulting model
- TPF-5(149) reflective cracking model (if the saw-and-seal option is not selected)

Each model will predict the corresponding distress for every month of the pavement design life.

4.5.4 Interpret Design Outputs

After the TPF-5(149) analysis is complete, the designer should compare the predicted level of distresses with distresses with the specified performance threshold values. The designer can use either MEPDG or the TPF-5(149) procedure. The following basic checks will assist the user in determining an adequate structural design for a given TICP project:

1. Transverse fatigue cracking, IRI, and HMA rutting must all meet the design reliability requirements for a trial design to be feasible.
2. If any of these do not “Pass” at the reliability level, a modification in the design is required. Some guidelines are as follows for making modifications:
3. For excess transverse cracking of JPCP, increase slab thickness, shorten joint spacing, add a tied PCC shoulder or 1-ft widened slab, use a stabilized base course, increase PCC

strength (with appropriate change in the modulus of elasticity), or use different aggregate source (one with lower CTE).

4. For excess rutting of HMA surface, modify binder grade, modify mixture parameters such as as-built air voids and binder content, and reduce layer thickness. If these changes are not effective or acceptable, program a surface removal and replacement at the point of predicted rutting reaching the critical level.
5. For excess IRI, reduce JPCP and HMA rutting, or require a smoother initial pavement.
6. For excess Medium and High severity reflective cracking, select saw-and-seal, use dowels, increase HMA thickness, or modify mixture parameters.

4.6. Design and Analysis Discussion and Conclusions

As detailed in the report, examining the design and analysis of TICP was a challenging research objective for the TPF-5(149) project, and its completion and the results produced are potentially very useful to the design and analysis of HMA-PCC pavement, in particular TICP. Where other research projects have assessed the fitness of certain models or design procedures for HMA-PCC (let alone TICP), few of them have both 1) modified existing models or developed new models for HMA-PCC and 2) tailored those efforts to accommodate the MEPDG framework (i.e. project creation and structural/material inputs). In this way, the TPF-5(149) project is not only singular for advancing the design and analysis of HMA-PCC, it is especially valuable in having done so for the MEPDG, the most popular and readily available M-E design tool for pavement engineers.

The research accomplished on the design and analysis of TICP can be summarized in terms of the models and procedures that were modified for the sake of TPF-5(149):

1. The CalME rutting procedure was reviewed and modified slightly. This procedure was then incorporated into the MEPDG framework using an accessible, “one button” program for general MEPDG users.
2. The CalME model for reflective cracking was reviewed, and a TPF-5(149) model for reflective cracking was developed based on this review of the CalME procedure. This model is also incorporated into an user-friendly program that interfaces with the MEPDG in a manner similar to that of the CalME rutting procedure.
3. The MEPDG model for JPCP transverse cracking was reviewed and modified so that HMA-PCC projects run in the MEPDG accommodate for transverse fatigue cracking in the PCC layer. As with earlier models, a user-friendly program was developed to interface with an existing MEPDG project file for a TICP project (or general HMA-PCC project).
4. The MEPDG model for JPCP joint faulting was reviewed and modified so that HMA-PCC projects run in the MEPDG account for joint faulting. As with earlier modifications, this model is associated with a user-friendly program to interface with the MEPDG.

There are a number of benefits to this comprehensive review and modification of models associated with key distresses in HMA-PCC pavements.

- The proposed models utilize the MEPDG framework, but also incorporate the results of research conducted outside of the MEPDG development.

- The designer is given a choice of performance models, and this choice comes with the convenience of not requiring different input parameters per choice. At the same time, the modified models enable the designer to incorporate the results of different material characterization procedures (such as the CalME rutting test protocol and the TTI overlay tester) in the design process.
- The proposed models enable the designer to quantify the effect of dowels on the long-term performance of composite pavements, which cannot be done with the current MEPDG models.

Finally, the TPF-5(149) research has further supported HMA-PCC design concepts using M-E modeling. As illustrated in the report, increasing HMA overlay thickness reduces JPCP cracking, delays the onset of reflective cracking, and slows the rate of progression of reflective cracking, and reduces faulting. However, as shown by the TPF-5(149) procedure and supporting SHRP2 R21 data, increasing HMA overlay thickness also increases rutting. Furthermore, the M-E models developed in TPF-5(149) allow for recommendations on the use dowels in HMA-PCC. The study found that joint load transfer in the PCC layer delays the onset of reflective cracking; slows the rate of reflective cracking; and reduces faulting.

Chapter 5. Construction Practices for HMA-PCC Composite Pavements

Asphalt overlay construction on concrete pavements requires careful attention to all phases of the process to achieve acceptable performance. Appropriate construction practices must be observed during casting of the concrete slab, as well as during construction of the hot mix asphalt (HMA) overlay. Even though the Portland cement concrete (PCC) pavement will not be the final riding surface for the road, proper design and construction is important to ensure the success of the overall pavement system. The underlying PCC pavement can be either a standard PCC pavement, such as a jointed plain concrete pavement (JPCP), or a roller compacted concrete pavement (RCC). Following proper HMA mix selection, good construction practices, such as proper mixing and placement temperatures, adequate compaction, well defined quality control and quality assurance (QC/QA) procedures will help ensure the best possible overlay performance. Due to regularly spaced PCC joints below and high stresses within the HMA overlay, poor performance (reflective cracking and rutting) of the HMA overlay is not uncommon.

The performance of HMA overlays on PCC is often a compromise between strategies used to minimize reflective cracking and HMA rutting. These design strategies, which will affect construction, include selecting the mix to favor rutting or cracking performance, reducing the percentage of reflective cracks in the HMA surface, retarding the rate at which the reflective cracks appear and propagate, and enhancing the appearance of the expected cracks at the surface. Specific proprietary reflective crack control treatments, such as use of fabrics, are beyond the scope of this document. Agency policies, such as using thin HMA surfacing on PCC pavements, acknowledge the limited lifetime of the overlay, and are made for non-structural purposes, such as noise or safety.

Under this study, the research team interviewed the following experts:

Expert	Contractor	Phone Number
Dr. Shiraz Tayabji	Fugro Consultants, Inc.	410-302-0831
Stewart Krummen	CS McCrossan	763-315-1325/612-919-0718
Dean Allen	RL Brosamer	925-627-1700
Dale Criswell	Teichert Construction	916-645-4829
Chris Hundley	Tullis, Inc.	530- 241-5105

The information gleaned from the experts during these interviews has been incorporated into the body of the document. Summaries of sample interviews are presented in Appendix A.

The following elements of HMA overlay construction on PCC pavements will be discussed: construction of standard PCC and roller compacted (RCC) pavements, HMA delivery and placement, mat compaction, joint compaction, and quality control and quality assurance (QC/QA). Numerous detailed references are cited for those wishing further information.

5.1. Construction Practices for HMA-PCC Composite Pavements

5.1.1 JPCP Construction

Khazanovich and Darter (2004) provided much useful information on the design of a high quality concrete pavement. To ensure a high quality HMA over PCC pavement system, it is important to begin by ensuring quality of the underlying layers. The horizontal and vertical variations in subsurface soil types, moisture contents, densities, and water table depths should be considered during the pavement design process to help ensure that the pavement structure will be supported by a uniform and consistent platform. These elements can be quantified through the implementation of proper field (subsurface investigation) and laboratory testing programs. More important, preparation of the subgrade prior to the placement of the paving layers and special subsurface conditions, such as swelling soils and frost-susceptible soils, must be identified and considered in pavement design.

It is recommended that subgrades for PCC pavement construction have a minimum CBR of 6 percent in the top 300 mm in order to provide stability and uniformity for the base paving operations. However, several European countries require a higher minimum level of subgrade support. For instance, Spain requires a minimum CBR of 10, below which the subgrade must be removed; if the CBR is between 10 and 20, a granular subbase layer is required (Darter, 1993). Similarly, Germany specifies a minimum subgrade bearing value of 45 MPa, determined using a modified plate load test (Larson et al., 1993). Austria also specified a minimum bearing value for its subgrades (35 MPa), below which soil replacement or stabilization is required (Darter, 1993). A dynamic cone penetrometer (DCP), a long, narrow device that can be driven into the subgrade to estimate the in place CBR of the soil, can also be used for construction control.

Often the native or imported embankment is unable to provide those qualities. In such cases, the following techniques can be used to improve the strength and uniformity and reduce the climatic variation of the foundation on pavement performance:

1. Stabilization of weak soils (highly plastic or compressible soils).
2. Thick granular layers.
3. Subsurface drainage systems.
4. Geotextiles.
5. Soil encapsulation.

Stabilization of the existing subgrade is one method of addressing problem soils. The following types of stabilizers are commonly used (Carpenter et al. 1992):

- Lime stabilization (soils must be reactive with lime)
- Cement stabilization
- Fly ash stabilization (similar to cement – used quite a bit in MN, especially in counties)
- Asphalt stabilization (granular soils only)

The type of stabilizing agent to be used is strongly dependent on the type of subgrade. Lime stabilization is appropriate for medium-, moderately fine-, and fine-grained soils with moderate to high plasticity, but most suited to soils with plasticity index (PI) greater than 10 and more than

25 percent passing No. 200 sieve. Cement stabilization is appropriate for coarse-, medium-, and fine-grained soils having low to moderately high plasticity, but most suited to sandy soils with $PI < 30$, fine-grained soils with $PI < 20$ and $LL < 40$, and coarse-grained soils with $PI > (20 + [50 - \text{finest content}])$. Asphalt stabilization is generally suited to medium- and coarse-grained soils with low plasticity and suited to sands with less than 25 percent passing the number 200 sieve and $PI < 6$ or coarse grained material with less than 15 percent passing the number 200 sieve and $PI < 6$. Additional information on the selection and mix design of stabilizing agents are found in references (Portland Cement Association, 1995; Portland Cement Association, 1992; Asphalt Institute, 1997; Barenberg and Thompson, 1976).

Another critical consideration in the preparation of the subgrade is the potential for frost heave. Where frost heave is a problem, susceptible soils should be replaced with a nonfrost-susceptible material. Alternatively, the addition of a select nonfrost-susceptible material over the problem soil may be effective, with the result of raising the grade line above natural ground (FHWA, 2001). Many Northern European countries place thick granular layers (203 to 508 mm) between the subgrade and the base course to help control frost heave (Darter, 1993). The layer thickness required for frost protection is generally taken as one-half to three-fourths of the depth of the local frost penetration. Finally, subcutting, remixing, and recompacting suitable quality soils will increase the level of support and decrease problems due to nonuniformity of the in-place material.

In addition to frost heave, swelling (or expansive) soils represent another potential subgrade problem. These soils exhibit significant volume changes in reaction to changing moisture contents. Possible solutions for these types of soils include removal, placement of a more suitable material, compaction at water contents 1 to 2 percent above optimum, compaction to 102 percent of optimum using ASTM T-99, and lime or cement stabilization (Okamoto et al., 1991; Lehmann, 2001). More exotic treatments (such as membrane encapsulation) may be required for severe swelling soils.

After the subgrade is properly prepared, the base and subbase must be addressed. Concrete pavements use one or more base and subbase courses to fulfill a number of requirements. The base layers are placed on the finished roadbed. The two main requirements of the base for a concrete pavement are the following:

1. Serve as a construction platform for the concrete slab so that the pavers will have a stable platform on which to operate to produce a smooth pavement. Smoothness of the surface requires smoothness of the sub-layers.
2. Provide a uniform support for the concrete slab that will not erode and result in loss of support.

Therefore, the base must be constructed to the proper elevation along the grade, contain the specified ingredients, and the proper compaction and/or strength to achieve this high durability.

The grade has to be checked and corrected as needed prior to placement of the concrete. If the grading operations or construction traffic disturb density of the base, additional compaction is required to correct it.

Following construction of the base, paving can begin. If a slipform paving is used, it is recommended to provide a base layer 600 mm wider on each side than the traffic lanes to accommodate the slipform tracks. Special attention should be paid to prevent crushing of edge drains with the slipform paver. Edge drains can be installed beyond the edge of the base or after the traffic lanes are paved (FHWA, 2001).

Proper curing is important for pavements which will be overlain with asphalt because curing ensures adequate strength and integrity of the concrete. Contractors should consider modifying the curing regime to account for the fact that the HMA must bond to the PCC surface. An asphalt based prime coat could be applied to the wet PCC surface to ensure a good bond, but this could also interfere with the saw-cutting operation if it were not dry in time. Alternately, conventional cure compound could be used, but this may need to be removed by sandblasting in order to ensure good bond. If adequate bond is not achieved, there is a risk for early delamination of the HMA layer from the PCC. The concrete mixture must have a lower w/c ratio and sufficient cement content to provide a low abrasion surface. The entrained air content must be such that for the prevailing climate no scaling or spalling will develop due to freeze thaw.

In addition, water curing will result in a much lower built in temperature gradient during construction on sunny days which will reduce the occurrence of corner breaks and some transverse, longitudinal, and diagonal cracks. The zero-stress temperature of the PCC will also be lower resulting in less joint and crack opening.



Figure 5-1: Curing of concrete pavements is critical; water cure eliminates built-in temperature gradients, high zero-stress temperature, and excessive shrinkage.

Conventional concrete pavements are textured to ensure a proper ride surface. In the case of concrete pavements overlain with asphalt, the wear surface will be HMA, so the texture of the PCC does not play the same role as in conventional concrete. The PCC could either be left untextured, or given a modified texture to allow for better interlock with the HMA overlay.

When transverse joint dowels do not have proper horizontal or vertical alignment the joint can lock up and the result will be random cracking near the joint. These cracks will often open up and spall and require full depth replacement of the joint and or adjacent slabs. There is much controversy over current specifications requiring certain tolerances because of lack of data to support them. There has not been the capability to measure the alignment until just recently. The MIT Scan technology has become available that makes it possible to locate dowel bars and tie bars within about 2 mm of their vertical or horizontal alignment and this technology is likely to change both specifications over the next few years (Lehmann, 2001).

When tie bars across longitudinal joints do not have adequate positioning the joint could open up over time resulting in a safety situation where motorcycle or other tires would have safety problems. Again, there is controversy over what is adequate alignment of tie bars. One criterion is that they must not be closer than 50 mm from top or bottom of the PCC slab to avoid spalling.



Figure 5-2: Dowels can be placed within acceptable tolerances, field measurement every day is critical.



Figure 5-3: Tie bar placement is important and should be measured every day.

The construction of the transverse joint requires that the depth of the saw-cut in a slab be deep enough to ensure the formation of the crack beneath it. However, in order to achieve maximum joint sawing production rates, it is desirable to saw to the minimum depth necessary to ensure the formation of the crack. Also, on non-doweled joints, it is desirable to limit the depth of sawing in order to provide a greater aggregate interlock load transfer.

Conventional practice has been to saw transverse joints to a depth of 25 percent of the slab thickness for transverse joints and 33 percent (or greater) for longitudinal joints. While this depth has worked well in most cases, the type of underlying base course may also have an effect on the required depth of sawing. Stabilized bases produce more friction between the slab and the base, and therefore can induce larger tensile stresses in the slab. In addition, slabs placed on permeable bases often end up slightly thicker than the design thickness due to the open texture of the base course material. Thus, to ensure the formation of the crack, the saw-cut depth of transverse joints may need to be greater for slabs placed on stabilized and permeable bases (33 percent of the slab thickness).

Another way to address the problem associated with friction caused by stabilized bases is to notch the surface of the treated base course at the prescribed transverse joint spacing to ensure the formation of the cracks at that location in the treated base. This practice is routinely conducted in Germany on their cement-treated bases. After placement of the pavement on top of the base, Germany specifies that the joints in the PCC slab be sawed to 30 percent of the slab thickness (Darter, 1993; Larson et al., 1993).

For initial saw cutting operations, most joints are sawed to a width of 3 mm prior to widening for joint reservoir. Some saw blade manufacturers now produce a blade that can produce the initial saw cut and the reservoir saw cut in a single pass.

A critical aspect of the joint sawing operations is the timing of the actual sawing of the slab. If this sawing is performed too early (i.e., before the slab has hardened sufficiently), spalling or raveling of the joint can occur. On the other hand, if the joint sawing is performed too late (after the development of internal slab stresses), uncontrolled cracking will develop. Since the

occurrence of the latter is of more critical concern than the former, it is desirable to begin sawing as soon as possible, generally within 4 to 12 hours.

The far limit, or the latest time that sawing can be done to prevent the occurrence of random cracking, is dependent upon the development of restraint stresses in the slab. These restraint stresses primarily are made up of frictional restraint stresses and thermal curling stresses. During the first 24 hours of paving, the concrete slabs are very sensitive to the development of restraint stresses. Field observations and testing has shown that a primary indicator of the latest time that sawing can be performed is when the temperature of the concrete surface cools more than 8 °C. However, because of the difficulty in determining that time, and because the surface may cool off very rapidly (due to late afternoon cooling, rain shower, and so on), it is recommended that joint sawing be performed as soon as the concrete can be sawed without significant raveling of the joints. This is particularly true for slabs placed on stabilized bases, since these pavements can develop greater frictional restraint stresses. Additional time for saw cutting may be made available if paving is performed at night or very early in the morning (completing by 10 or 11 a.m.) to minimize the development of temperature gradients through the slab (Okamoto et al. 1991).

In the past, some agencies have used skip joint sawing procedures, in which only every second or third joint is initially sawed. This is usually done in an effort to keep up with the paving operation, and the skipped joints are sawed later. However, this practice can result in the development of transverse cracks at or near the joints that were skipped, particularly on slabs over stabilized bases. Also, the joints sawed first are typically wider, creating non-uniform joint movements and variable performance of joint sealants.

The need for sealing of joints in JPCP has been questioned and some highway agencies in North America have stopped sealing of these joints. When joints are not sealed, it is advantageous to cut the joint very narrow. A saw blade of 2 mm has been used in Chile to saw transverse joints with good success (e.g., low noise).

Taking care in the construction of joints will help to ensure pavement smoothness. Field studies have clearly shown that pavements that are built smoother will remain smoother over their design life and last longer than those built rougher (Smith et al. 1997). Reasons for this finding are several:

- Initial smoothness can only be achieved through quality construction of all layers from the subgrade up, uniform concrete production; accurate string line and grade control.
- Initial smoothness requires a uniformly moving construction process with no delays of concrete delivery.
- The contractor must take more care in all aspects of the construction process (steady forward motion of the paver, adequate internal vibration for proper consolidation of the concrete, timely texturing, curing, and joint sawing) to achieve a smooth pavement.

The International Roughness Index (IRI) in recent years has become the standard for expressing pavement roughness. Data from Khazanovich et al. (1997) indicate that initial IRI values less than 0.63 m/km (40 in/mi) represent good initial smoothness levels. However, the achievement

of lower initial roughness levels is quite common given the recent improvements in paving technology and the more widespread use of smoothness specifications.

Smoothness specifications with strong pay incentives are strongly recommended (contractors in the US can receive up to 8 percent extra pay for many projects). This has led to improved paving operations and very smooth pavement surfaces to serve roadway users for many years into the future. European specifications lack of bonuses offered to contractors. Use of warranties is much more common in Europe than in the US.

The following factors govern the construction of a smooth PCC pavement (Grogg and Smith, 2001):

- PCC material and mix design. The mix design needs to be optimized to provide workability and ease of finishing without jeopardized strength. The mix produced by the contractor should be uniform and adherent to the mix design. Inconsistent mix will change the hydraulic forces of the pavement acting on the paver and alter the final pavement profile.
- Grade control. Smooth pavement cannot be constructed without a tight grade control. Grade control should be performed on all stages of the pavement construction starting from subgrade preparation and finishing when the final pavement profile is provided. The grades of stakes and string lines should be checked by surveying equipment. Two string lines should be used. It is preferably to construct the string lines of aircraft cable and space supports for them not more than 8 m apart. Special attention should be paid to areas where string lines begin and end to provide a smooth transition. The string lines should be monitored and maintained during construction. String lines might be unintentionally displaced as a result of:
 - Placing a foreign object on it
 - Workers bumping on it while crossing
 - PCC delivery operation

If such an event occurs, the string line should be re-installed using surveying equipment. Just a visual inspection might be inadequate.

- Paving speed and material delivery rate. It is crucially important to harmonize delivery of PCC with the speed of paving operations. Maintaining a constant speed of the paving train reduces changes in hydraulic forces acting on it from the plastic PCC. The number of paver's stops during paving should be reduced to the absolutely necessary minimum. Therefore the production rate of the plastic PCC should be adequate. Shortage of the plastic concrete will cause slowing down or stoppage of the paver. Oversupply of the plastic concrete may create different degrees of concrete workability. In both cases, paving and finishing processes will be jeopardized.
- PCC head in front of the paver. It is important to ensure that PCC mix is spreading uniformly across the base and avoid moving mounds of plastic PCC. A constant head should be kept above the strike-off bar to avoid changing in the hydraulic forces acting on the bottom of the paver.
- Embedded items. Dowel bars, tie bars, and reinforcing steel create challenges in producing a smooth pavement. It is important to apply an adequate pressure when the

PCC is extruded from the back of the paver. Too low pressure would prevent consolidation of concrete around steel whereas too high pressure would move it downward followed by settlement or rebound of steel and resulting in dips or bumps in the pavement, respectively. It is also very important to avoid contact between the embedded steel and vibrators.

- Curing and environmental conditions (see section above).
- Equipment maintenance. It is crucial to keep equipment well-maintained and clean to minimize stoppage in paving.
- Trained workforce. All crew members should know and understand their roles in the paving process and effects their actions might have on the pavement smoothness.
- Finally, it has been found in the US over the past 20 years that incentives/disincentives to the contractor has a very major effect on achieving very smooth pavements. Up to 8 percent of the contract bid is paid to contractors who build very smooth pavements. This has revolutionized the paving operations and resulted in longer lives and more comfort to highway users.



Figure 5-4: Quality construction is critical and contractor pay incentives are very helpful.

The following table provides a useful checklist of required activities for the design and construction of a successful concrete pavement.

Table 5-1: Checklist of design and construction activities for concrete pavements (adapted from Grogg and Smith, 2001).

No	Item	Yes	No	NA
1	Collect information on site conditions			
1.1	<i>Evaluate subgrade properties</i>			
1.1.1	Have soil samples been collected along the grade?	<input type="checkbox"/>	<input type="checkbox"/>	<input type="checkbox"/>
1.1.2	Have soil samples been tested properly?	<input type="checkbox"/>	<input type="checkbox"/>	<input type="checkbox"/>
1.1.3	Has the soil class been determined along the grade?	<input type="checkbox"/>	<input type="checkbox"/>	<input type="checkbox"/>
1.1.4	Is the subgrade expansive or frost heave susceptible?	<input type="checkbox"/>	<input type="checkbox"/>	<input type="checkbox"/>
1.1.5	Is the depth to the water table known?	<input type="checkbox"/>	<input type="checkbox"/>	<input type="checkbox"/>
1.1.6	Will the concrete be subjected to external sulfate attack?	<input type="checkbox"/>	<input type="checkbox"/>	<input type="checkbox"/>
1.2	<i>Collect traffic data</i>			
1.2.1	Has the number of heavy trucks over design life been estimated?	<input type="checkbox"/>	<input type="checkbox"/>	<input type="checkbox"/>
1.2.2	Is the number of equivalent single axle loads known?	<input type="checkbox"/>	<input type="checkbox"/>	<input type="checkbox"/>
1.2.3	Has the axle load spectra been measured on site?	<input type="checkbox"/>	<input type="checkbox"/>	<input type="checkbox"/>
1.2.4	Has lane distribution of trucks been measure? Lateral offset from edge of slab?	<input type="checkbox"/>	<input type="checkbox"/>	<input type="checkbox"/>
1.3	<i>Collect climate information</i>			
1.3.1	Is average annual precipitation known?	<input type="checkbox"/>	<input type="checkbox"/>	<input type="checkbox"/>
1.3.2	What is an average number of air freeze-thaw cycles?	<input type="checkbox"/>	<input type="checkbox"/>	<input type="checkbox"/>
1.3.3	What is an average annual air temperature?	<input type="checkbox"/>	<input type="checkbox"/>	<input type="checkbox"/>
1.3.4	What is freezing index (estimate depth of frost)?	<input type="checkbox"/>	<input type="checkbox"/>	<input type="checkbox"/>
1.3.5	Will be de-icing materials applied over pavement service life?	<input type="checkbox"/>	<input type="checkbox"/>	<input type="checkbox"/>
1.4	<i>Evaluate source of aggregates for concrete and base</i>			
1.4.1	Do local aggregates have sufficient freeze-thaw resistance?	<input type="checkbox"/>	<input type="checkbox"/>	<input type="checkbox"/>
1.4.2	Do local aggregates exhibit adequate wearing resistant?	<input type="checkbox"/>	<input type="checkbox"/>	<input type="checkbox"/>
1.4.3	Is it possible to have chemical incompatibility with cement?	<input type="checkbox"/>	<input type="checkbox"/>	<input type="checkbox"/>
1.4.4	Are the aggregates susceptible to freeze-thaw?	<input type="checkbox"/>	<input type="checkbox"/>	<input type="checkbox"/>
2	Design PCC Mix			
2.1	<i>Select target PCC properties</i>			
2.1.1	What is the target PCC flexural strength?	<input type="checkbox"/>	<input type="checkbox"/>	<input type="checkbox"/>
2.1.2	What is the target PCC modulus of elasticity?	<input type="checkbox"/>	<input type="checkbox"/>	<input type="checkbox"/>
2.1.3	What is the coefficient of thermal expansion?	<input type="checkbox"/>	<input type="checkbox"/>	<input type="checkbox"/>
2.1.4	What is the ultimate shrinkage?	<input type="checkbox"/>	<input type="checkbox"/>	<input type="checkbox"/>
2.2	<i>Select PCC mix proportion</i>			
2.2.1	Was PCC mix design optimized considering PCC target properties, workability, and cost?	<input type="checkbox"/>	<input type="checkbox"/>	<input type="checkbox"/>
2.2.2	Has a procedure been developed to modify the PCC mix proportion if strength, or workability are encountered?	<input type="checkbox"/>	<input type="checkbox"/>	<input type="checkbox"/>

No	Item	Yes	No	NA
2.2.3	Are any cementitious replacements of cement (fly ash, slags) used?	<input type="checkbox"/>	<input type="checkbox"/>	<input type="checkbox"/>
2.2.4	Are water-reducing admixtures required?	<input type="checkbox"/>	<input type="checkbox"/>	<input type="checkbox"/>
2.2.5	Are air-entrained admixtures required?	<input type="checkbox"/>	<input type="checkbox"/>	<input type="checkbox"/>
2.3	<i>Check mix compatibility/durability</i>			
2.3.1	Is it possible that a chemical reaction between the alkalis in Portland cement and carbonate/dolomite aggregates will take place?	<input type="checkbox"/>	<input type="checkbox"/>	<input type="checkbox"/>
2.3.2	Is it possible that a chemical reaction between the alkalis in Portland cement and silica in aggregate (ASR) will take place?	<input type="checkbox"/>	<input type="checkbox"/>	<input type="checkbox"/>
2.3.3	Is the mix resistant to external sources of sulfates from groundwater or deicing chemicals?	<input type="checkbox"/>	<input type="checkbox"/>	<input type="checkbox"/>
2.3.4	Is percentage of entrained air voids sufficient for local climate?	<input type="checkbox"/>	<input type="checkbox"/>	<input type="checkbox"/>
3	Construction			
3.1	<i>Subgrade preparation</i>			
3.1.1	Has a subgrade been graded for uniformity and compacted sufficiently to exhibit sufficient strength for placement of upper layers (e.g., CBR > 6 %)?	<input type="checkbox"/>	<input type="checkbox"/>	<input type="checkbox"/>
3.1.2	Has a subgrade been trimmed to grade?	<input type="checkbox"/>	<input type="checkbox"/>	<input type="checkbox"/>
3.1.3	Has a base layer been constructed and trimmed to grade?	<input type="checkbox"/>	<input type="checkbox"/>	<input type="checkbox"/>
3.1.4	Has a base layer been constructed sufficiently stable?	<input type="checkbox"/>	<input type="checkbox"/>	<input type="checkbox"/>
3.1.5	Are stable and sufficiently wide track lines provided for paver's operation?	<input type="checkbox"/>	<input type="checkbox"/>	<input type="checkbox"/>
3.2	<i>Grade control</i>			
3.2.1	Has a procedure for control of the pavement profile been developed?	<input type="checkbox"/>	<input type="checkbox"/>	<input type="checkbox"/>
3.2.2	Has a quality control procedure the finished grade of the all pavement layers (subgrade, subbase, base, and PCC) been developed?	<input type="checkbox"/>	<input type="checkbox"/>	<input type="checkbox"/>
3.2.3	Have the design features of the roadway (grade, super-elevation, transition, railroad crossing, etc.) been accounted for in the layout and staking of the pavement?	<input type="checkbox"/>	<input type="checkbox"/>	<input type="checkbox"/>
3.3	<i>PCC paving</i>			
3.3.1	Has a quality control plan for checking the consistency of designed and produced mix been developed?	<input type="checkbox"/>	<input type="checkbox"/>	<input type="checkbox"/>
3.3.2	Has a quality control plan for checking the mix workability, segregation, or finishing problem been developed?	<input type="checkbox"/>	<input type="checkbox"/>	<input type="checkbox"/>
3.3.3	How will the PCC mix formula be adjusted if workability of	<input type="checkbox"/>	<input type="checkbox"/>	<input type="checkbox"/>

No	Item	Yes	No	NA
	finishing problems are encountered?			
3.3.4	Will the PCC plant and delivery vehicles provide sufficient amount of concrete with required frequency?	<input type="checkbox"/>	<input type="checkbox"/>	<input type="checkbox"/>
3.3.5	Has the paving and vibration operations adjusted to accommodate presence of dowels or steel reinforcement?	<input type="checkbox"/>	<input type="checkbox"/>	<input type="checkbox"/>
3.3.6	Are the ranges of the environmental conditions (air temperature, humidity, wind speed) acceptable?	<input type="checkbox"/>	<input type="checkbox"/>	<input type="checkbox"/>
3.3.7	Is equipment cleaned of old concrete on a regular basis?	<input type="checkbox"/>	<input type="checkbox"/>	<input type="checkbox"/>
3.3.8	Is a proper curing medium been applied to the PCC layer as soon as practical?	<input type="checkbox"/>	<input type="checkbox"/>	<input type="checkbox"/>
3.3.9	Have been joints sawed at the right time window?	<input type="checkbox"/>	<input type="checkbox"/>	<input type="checkbox"/>
3.3.10	Is there a plan to check the alignment of dowel bars?	<input type="checkbox"/>	<input type="checkbox"/>	<input type="checkbox"/>
3.3.11	Is there a plan to check the alignment of the tie bars?	<input type="checkbox"/>	<input type="checkbox"/>	<input type="checkbox"/>
3.4.12	Is there a plan to check the depth of the joint sawing and timing?	<input type="checkbox"/>	<input type="checkbox"/>	<input type="checkbox"/>
3.4	<i>Sub-drainage (if used)</i>			
3.4.1	Is there a plan to video check the longitudinal and transverse pipes	<input type="checkbox"/>	<input type="checkbox"/>	<input type="checkbox"/>
3.4.2	Are the outlets higher than the bottom of the ditch line?	<input type="checkbox"/>	<input type="checkbox"/>	<input type="checkbox"/>
3.4.3	Are there durable outlets for the lateral drain pipes that will not clog?	<input type="checkbox"/>	<input type="checkbox"/>	<input type="checkbox"/>
3.4.4	Is there plan to check the density of materials around the longitudinal drain pipes?	<input type="checkbox"/>	<input type="checkbox"/>	<input type="checkbox"/>
4	Joint seals			
4.1	<i>Installation of seals</i>			
4.1.1	Is there a plan to check the adequacy of the joint sealants?	<input type="checkbox"/>	<input type="checkbox"/>	<input type="checkbox"/>
5	Future preservation of pavement			
5.1	<i>Joint seals</i>			
5.1.1	Is there a plan for regular maintenance of joint seals?	<input type="checkbox"/>	<input type="checkbox"/>	<input type="checkbox"/>
5.1.2	Is there a plan for spall repairs?	<input type="checkbox"/>	<input type="checkbox"/>	<input type="checkbox"/>
5.1.3	Is there a plan for slab replacement for JPCP?	<input type="checkbox"/>	<input type="checkbox"/>	<input type="checkbox"/>
5.6.4	Is there a plan for full-depth repair of CRCP?	<input type="checkbox"/>	<input type="checkbox"/>	<input type="checkbox"/>

5.1.2 RCC Construction

As an alternative to conventional concrete pavements, such as JPCP, roller compacted concrete (RCC) pavements can be used. RCC is a type of concrete with very little water in the mix. This concrete has zero slump, and therefore cannot be placed using conventional placement techniques. Because of its low water content, RCC is relatively high strength and very durable. RCC pavements do not need to be formed or finished, but as a result, they do not have a smooth surface. RCC pavements are not suited for typical highway paving applications due to low ride

quality which results from this surface (Portland Cement Association, 2012). Instead, they are typically used in industrial applications, such as container terminals and ports, or for temporary road ways where quick construction and high strength are the only criteria. However, surface quality is not a problem for concrete pavements which will be overlain with HMA, because the HMA provides the smooth surface.

An additional advantage to using RCC in concrete pavements with an HMA overlay is that RCC is cast using the same equipment as HMA. This means that only one set of equipment must be mobilized to the job site for the paving operation. In a conventional asphalt overlay job, both PCC and HMA paving equipment are needed. Construction costs are also lower for RCC pavements than PCC pavements because there is no need for finishing, and joint spacing is much larger, which decreases the amount of labor needed to cut joints, and leaner mixes can be used, reducing material costs (Portland Cement Association, 2012). It is important to note that RCC cannot be used in conjunction with dowel bars, so RCC is not suitable for pavement systems where dowel bars are required. However, RCC also has much higher strengths than typical pavements, and therefore may be used in some instances without dowel bars where a conventional pavement would require them (Portland Cement Association, 2012).

The first recorded use of RCC was in Canada in the 1970's, when logging companies needed low cost, durable platforms for storage and to unload logging trucks. In this application, RCC was found to be extremely durable despite heavy loads, a harsh climate and very little maintenance (Piggott, 1999). Since then, RCC has become common for use in industrial situations, temporary roads (particularly for the military), parking, staging areas, and low-speed roads (where the surface roughness does not pose as large of a problem) (Portland Cement Association, 2012).

RCC Pavement Design

The design of an RCC pavement is not very different from that of a conventional concrete pavement: the goal is to find the thickness required to minimize damage. For RCC pavements, the main failure mode is fatigue. Therefore, RCC pavements are designed to prevent fatigue failure by ensuring that the concrete used has a sufficiently high modulus of rupture to resist the stresses induced by the predicted loads. An analysis is conducted to determine the load cases which will produce the highest stresses and how much fatigue damage will be induced by those stresses (Luhr, 1995). The pavement thickness is selected to ensure that the pavement will have adequate strength and fatigue capacity. This thickness can be determined using either the procedure outlined by the Portland Cement Association (1987), or the computer program *RCC-Pave* (PCA 2002). Typical thicknesses used range from 6-15 inches (Rao et al. 2011).

RCC Mix Design

There is no one specific, accepted mix design method for RCC pavements, though several approaches exist (ex. ACI 1995, Marchand 1997). To ensure that a mix will perform as required, laboratory specimens of any potential mixes should be evaluated (Luhr, 1995). When designing an RCC mix, the main requirement is that there be a sufficient amount of paste to cover all aggregates and bond them together without voids between the aggregates. The overall water content of the mix must be low enough that the mix can support the compactor. However,

there must be a sufficient amount of moisture in the mix that it can still be spread using a vibratory paver (Portland Cement Association, 2012).

Given that the aggregate is the main constituent of an RCC mix, it is important that quality aggregate and a proper gradation be used. Quality aggregates used in standard ready mix concrete are often acceptable, as long as the proper gradation can be achieved. The American Concrete Institute and the Portland Cement Association recommend that the following gradation be used. This gradation ensures that the required density will be achieved. The nominal aggregate size is limited to ¾ inch in an effort to mitigate segregation. A higher fines content is required to ensure that the mix will be stable enough to tolerate the weight of the compactor while it is still plastic. However, this can result in cost savings as it often eliminates the need for aggregate washing (Portland Cement Association, 2012).

Table 5-2: Recommended aggregate gradation for RCC mixes (from ACI 1995).

Sieve Size		Percent Passing	
Inch	Millimeter	Minimum	Maximum
3/4"	19	100	100
1/2"	12.5	70	90
3/8"	9.5	60	85
#4	4.75	40	60
#8	2.36	35	55
#16	1.18	20	40
#30	0.6	15	35
#50	0.3	8	20
#100	0.15	6	18
#200	0.075	2	8

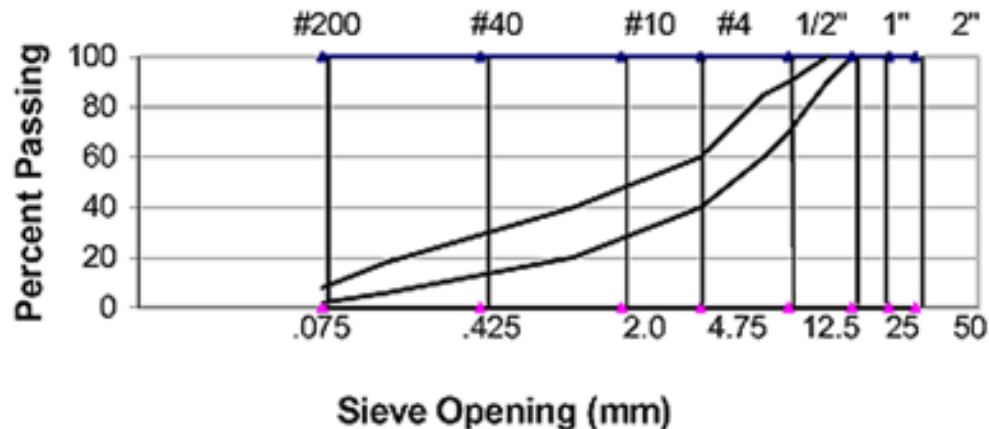


Figure 5-5: Recommended aggregate gradation for RCC (from ACI 1995).

Only the minimum amount of cementitious material which is necessary to ensure adequate strength should be used. This reduces the overall cost of RCC, which is often selected as a paving material due to its cost savings (Luhr, 1995).

RCC Construction

Like any concrete pavement, construction begins by preparing a proper base and subgrade. The subgrade must be graded and compacted using standard procedures for a typical pavement. A crushed stone base is then placed. Together, the base and subgrade create a stable foundation on which the RCC can be placed (Luhr, 1995).

RCC is paved in a manner similar to asphalt. All of the ingredients are mixed in a rotating mixer and loaded into a dump truck to be hauled to the site (Luhr, 1995). The dump truck is covered to reduce moisture loss, but during hot weather, additional water may need to be added to the mix to account for evaporation during transport (Portland Cement Association 2012). The dump truck empties the mix into either a conventional or high density paver (Luhr, 1995). Depending on the specification being used on a specific job, RCC must have a density that is at least 98% of optimal as measured by the modified proctor test (Portland Cement Association, 2012). Though high density pavers are capable of achieving a more compacted mix than standard pavers, they cannot meet the required density of RCC. Therefore, compaction is necessary regardless of the type of paver used.



Figure 5-6: Typical RCC paving operation: dump truck unloads mix into an asphalt paver, a roller follows close behind to ensure adequate compaction (from Portland Cement Association, 2012).

Proper compaction of RCC is required to achieve performance in terms of strength and durability. Figure 5-7 shows how dramatically strength can decrease if proper compaction is not achieved. Typically, a smooth wheel, vibrating roller is used to compact the concrete, though occasionally pneumatic tire rollers are used for the final pass to provide a better finish. The

rolling pattern to be used for compaction should be determined and tested before paving begins to ensure that proper densities will be achieved (Luhr, 1995).

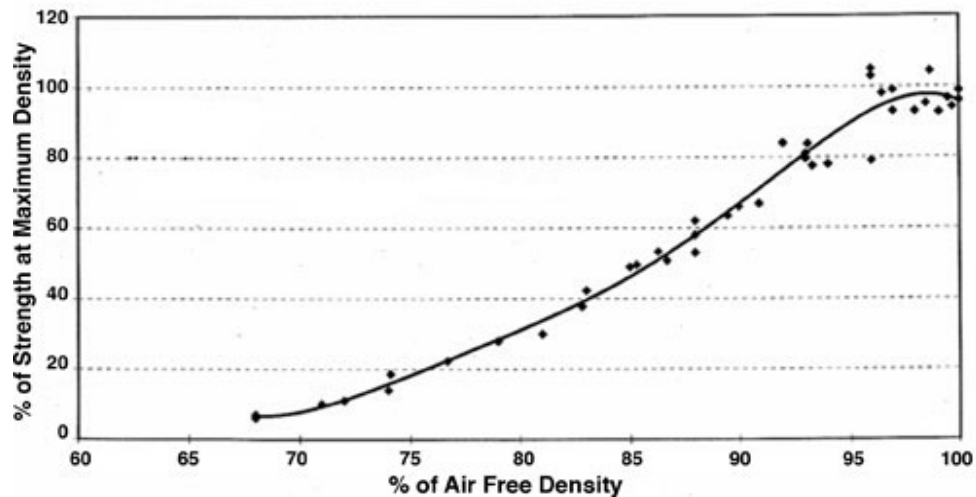


Figure 5-7: Relation between compaction (measured as % air free density) and strength (from Schrader, 1992).

Factors such as compaction time and technique, concrete mix properties and lift size will influence the amount of compaction which is achieved. Inadequate compaction (and therefore insufficient strength can be caused by any of the following (Portland Cement Association, 2012):

- Delaying the start of the compaction process
- Segregation of the aggregate within the mix
- Rollers which cannot provide sufficient compaction
- Lifts which are too thick
- Low moisture content of the mix
- Overcompaction due to excess rolling

If loads of adjacent materials from different trucks are placed less than an hour apart, then the joint between the material is not considered to be cold. When constructing such a joint (sometimes called a fresh joint), the material from both sides of the joint should be blended together prior to full compaction. This can be accomplished by using specific types of rolling patterns. For a cold joint, where more than one hour elapses between placement of adjacent loads of material, the set material should be cut to create a vertical surface at the edge. Grout should be applied to this face directly before the new adjacent material is placed to ensure that the set and plastic concretes form a good bond (Luhr, 1995).

As with any concrete, curing is one of the most important steps to ensure that the desired properties are achieved. If the RCC dries rather than curing, the following can occur:

- Drying shrinkage cracks on the surface
- Incomplete hydration, especially on the surface, resulting in decreased strength and durability
- Increased dust on the surface

RCC can be cured using conventional cure methods such as water cure or cure compound. Standard PCC cure compounds which follow the ASTM C 309 specification can be used on RCC, but they require an application rate which is 1.5 to 2 times greater to account for the surface texture of the RCC. For RCC, the cure compound is generally applied in two lifts, which are perpendicular to each other. Other standard cure techniques for concrete, such as covering with plastic sheeting or wet burlap can be used with RCC. However, RCC is generally used for paving large areas, where covering is not feasible (Portland Cement Association, 2012). When RCC will be used in conjunction with HMA overlays, the bituminous tack coat can be used in place of cure compound and can be applied as soon as compaction is complete (Luhr, 1995).

Less cracking is seen in RCC compared with conventional PCC because of the lack of bleed water which results from the low water/cement ratios used in RCC (Luhr 1995). In instances where cracking is not a concern, RCC is not saw cut and shrinkage cracks are allowed to form naturally; typically this results in a joint spacing of between 20-70 ft (Luhr, 1995; Portland Cement Association, 2012). This would not be desirable in a pavement which will receive an HMA overlay due to the potential for reflection cracking. Instead, joints can be saw cut to eliminate random cracks.

In RCC, joints are timed and cut using conventional techniques (Portland Cement Association, 2012), though compaction must be complete before saw cutting begins (Luhr, 1995). Saw cuts should not be deeper than $\frac{1}{4}$ of the pavement thickness. If a thin early entry saw is used, the cut should not be more than 1-1.25 inches deep. Transverse joint spacing is every 15-20 feet for pavements less than eight inches thick. For pavements more than eight inches thick, transverse joint spacing (in feet) = 3 or 4 * pavement thickness (in inches). Longitudinal joints are generally spaced closer than transverse joints in RCC because loading in the longitudinal direction causes hinge action. Longitudinal joint spacing is every 15-20 feet for pavements less than eight inches thick. For pavements more than eight inches thick, longitudinal joint spacing (in feet) = 2.5 * pavement thickness (in inches) (Portland Cement Association, 2012). It has been found that, for HMA over RCC pavements, shorter joint spacing (every 10 ft) results in less reflected cracking (Rao et al, 2011).

The HMA layer can be placed on the RCC as soon as joints have been sawn. Non-truck traffic can be allowed on the roadway as soon as it can be tolerated by the HMA layer.

5.1.3 HMA Overlay Construction

This section discusses HMA construction subsequent to pre-overlay repair. In-service PCC pavements will generally require pre-overlay treatment for best performance such as replacing and repairing slabs, stabilizing slabs, and preparing joints. HMA overlays constructed on newly designed and built HMA/PCC and in-service PCC pavements will generally follow comparable construction processes. However, depending on the design selection, the overlay may be

conventional HMA with the goal of maximum service life, or it may be constructed as a sacrificial layer for ride and noise purposes.

The HMA overlays may be structural, consisting of dense graded or gap graded/stone matrix asphalt (SMA), or functional, consisting of open graded mixes for noise and/or splash-spray control, and may contain rubber or polymer modifiers.

HMA overlay performance can be enhanced through best practice measures throughout the construction process. These practices are aimed at maximizing cracking and rutting performance of the HMA overlay, irrespective of any crack control measures. For instance, saw and seal techniques (described at the end of this section) performed at the time of HMA overlay construction have been found in numerous studies to be one of the best performing strategies to address reflective cracking (Rao, 2011). Using these best practices, like the saw and seal technique, does not relinquish the contractor from using other best construction practices.

Pre-Overlay Treatments

Prior to placement of the HMA overlay on existing PCC pavements, rehabilitation treatments should be performed to restore a smooth profile and minimize joint movement. Examples of these treatments include joint sealing, diamond grinding, dowel bar retrofitting, slab sub-sealing and jacking, full and partial depth slab repairing, cracking and seating, and rubblizing. These specific topics are out of the scope of this section and may be found elsewhere.

Surface Preparation

The first step toward ensuring pavement performance is to provide the maximum bond between the PCC (new or existing) and the HMA overlay. Poor initial bonding or the loss of bonding between the HMA overlay and PCC pavement may result in several distresses, such as slippage cracking, as well as compaction difficulty (Leng et al., 2009, West et al., 2005). Strong interlayer bonding may be achieved through one or a combination of the following methods: 1) texturing the PCC surface to provide added bond potential, 2) cleaning the PCC surface, and 3) placing a tack coat with the proper type and quantity on the PCC surface (Leng et al. 2009).

Surface texturing can be provided by transverse or longitudinal tining or surface milling. Tining does not allow for significant connection between PCC and HMA and milling was found to provide the highest shear strength in laboratory tests (Leng et al., 2009). Subsequent to texturing and other pre-overlay repairs, clean the surface with mechanical brooms and air blowing and use water flushing where needed (MLRRB, USACE). Other studies have shown that air blasting is preferred to mechanical brooms if only one method is chosen (Leng et al. 2009).

Some agencies utilize a chip seal type SAMI alone or in combination with a leveling course for use on the PCC surface to act as a reflective crack control strategy prior to the HMA overlay. Use of a reflective crack relief interlayer mix RCRI, consisting of one inch of fine aggregate bound with a highly elastic polymer modified binder was shown to be statistically the best performer in mitigating reflective cracking, in an extensive study of composite pavement performance in New Jersey (Bennert, 2011).

Various studies have been performed looking at tack coat optimization for overlays on PCC (Al Qadi, 2008) and HMA (Mohammed, 2005). This study found that SS-1h (or SS-1hP) spread at a rate of 0.2 gal/yd² (residual) provided the greatest shear strength between layers and best overall pavement performance. Uniform coverage of the tack coat without ribbons or “zebra stripes” is critical to achieving maximum bond strength.

HMA Delivery and Placement

Guidelines for delivery, placement, and compaction of HMA overlays on either existing or new PCC vary little from sound practice recommendations for paving HMA on HMA. The goal is providing a uniform spread quantity and quality of HMA to maximize smoothness and minimize segregation during placement, prior to compaction.

Maintaining elevated mix temperatures is primary to proper placement and compaction, so the following factors should be considered when developing a delivery strategy:

- delivery haul length
- truck type
- mix type
- ambient temperature
- wind.

Lower than desired temperatures make placement more difficult, and can lead to mix segregation, which has been shown to affect mix fatigue performance adversely (Khedaywi 1996). This is very important over moving PCC joints, as reflective cracking models have been developed that are based on fatigue failure modes (Wu et al 2006).

The following list highlights several best construction practices for HMA placement (MLRRB).



Figure 5-8: End dump of HMA into paver hopper (Mahoney, Pavement Interactive.com).

- The truck bed should be raised before opening the tailgate if using end-dump trucks so the mix slides against the tailgate as shown in . This minimizes segregation.
- Let the paver move forward toward the HMA delivery truck to eliminate mat indentations. Avoid having the truck back up into the paver. The paver should stop during the exchange of material. Following emptying the HMA, the truck should drive away smoothly without jerking the paver.
- Bring the paver to paving speed as quickly as practicable to maintain constant head in front of the screed. Maintain sufficient mix in the hopper so that slat conveyors are never visible, but do not overflow the hopper. Only raise paver wings when necessary to eliminate a buildup of cold mix in the hopper corners.
- Maintain a constant head of material on the paver augers through constant speed and continuous operation. Material level should be at the same height or slightly above the auger shaft, as shown in Figure 5-9.



Figure 5-9: HMA head in auger (Mahoney, Pavement interactive.com).

A constant head at the augers results in minimal movement of the screed and helps maintain consistent mix height and mat smoothness. Variations in head affect screed movement and mat thickness, as shown in Figure 5-10.

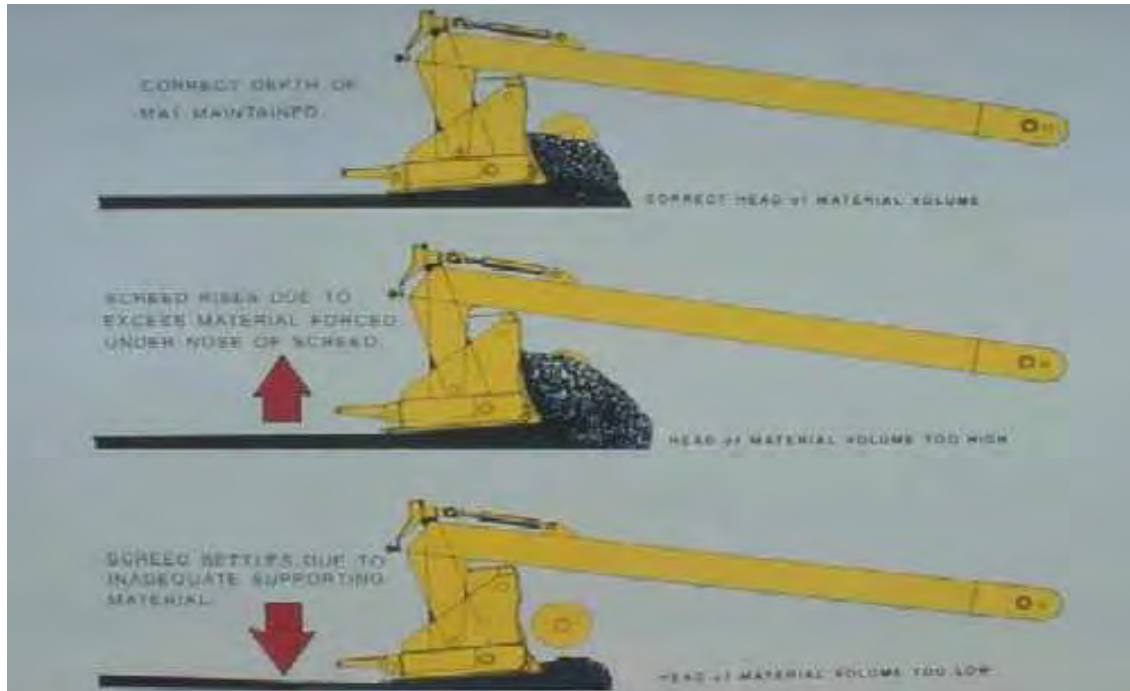


Figure 5-10: Screed movement with material head variation.

Mat Compaction

Mat compaction (density) is considered the most important factor in determining HMA performance. Compaction to six percent or less air voids increases fatigue life, reduces rutting, decreases oxidation and aging, and moisture damage (Benson and Scherocman, 2006). Lift thickness, mix properties, and environmental conditions are key factors that affect the ability of the contractor to achieve density in the HMA layer (Decker, 2006).

With HMA overlays on PCC, thin functional overlays (< 1.5 in.) may be placed as well as thicker structural overlays (> 2in.), which require greater attention during compaction, particularly in colder weather. Properties of the aggregate and asphalt binder (including use of modifiers) have an impact on the ability of the contractor to achieve density. It is well known that mixes made with coarse, angular aggregates may be more difficult to compact than mixes made with rounded materials. As a result, the coarser mixes may cool before density can be achieved (Decker, 2006).

Because it is affected by mixing temperature and delivery, the HMA mat temperature must be sufficient to obtain the required HMA density. Mat temperature are affected by numerous factors including haul time, mix type, ambient temperature, ground/PCC temperature, and wind.

When placed on PCC, HMA overlays are subject to higher levels of compressive energy due from truck traffic. The highly rigid PCC (modulus greater than 4,000,000 lb/in²) leads to the HMA layer absorbing more load energy due to higher confinement effects and lack of dissipation throughout the pavement system. Rutting levels of comparable mixes placed on PCC versus on HMA have been measured at 15 to 20 percent higher. With the increased stresses placed on

HMA in composite systems, makes meeting compaction specifications even more critical than in “conventional” HMA/HMA overlays or full depth paving.

Joint Compaction

Proper HMA joint compaction is critical in composite pavements with HMA surfacing due to the high degree of PCC movement beneath the HMA. Poor compaction of longitudinal joints typically results in joints cracking, opening, and raveling of the adjacent material. Joint density is determined by three primary factors 1) density on the outside edge of the first paved lane (cold side – free edge) 2) degree of compaction of the joint which requires some overlap to ensure adequate material and 3) degree of compaction of the second paved lane (hot side) (Brown, 2006). In composite pavements, even if saw and seal will be performed, having as high density as possible in the HMA surrounding the sealed saw cut will facilitate longer life of the treatment. Figure 5-11 shows a typical poor performing longitudinal joint.



Figure 5-11: Raveled longitudinal joint (Brown, 2006).

Compaction of the free unsupported edge can be problematic. The type of roller used and its position in regard to the unsupported edge of the pavement significantly affects the amount of density that can be obtained. A pneumatic (rubber) tire roller normally cannot be used within about 150 mm (6 in.) of the unsupported edge of the lane without pushing the mix sideways due to the high pressure in the rubber tires (Benson and Scherocman 2006, Brown 2006). It is recommended that a steel wheel roller extend over the edge of the lane by approximately 6 in. as shown in Figure 5-12 (Benson and Scherocman 2006).



Figure 5-12: Proper rolling of free edge (Benson and Scherocman 2006).

The second factor for durable longitudinal joints relates to the amount of HMA placed at the interface between the two adjacent mats. Two factors are involved in this – the height of the uncompacted hot mat and the amount of overlap onto the cold mat. The height of overlap onto the cold side depends upon the thickness of the uncompacted mat on the hot side. Given that mix compacts approximately 25 percent (1/4 in. per in. thickness) the overlap needs to be high by the amount of compaction expected to occur so adequate material is present (Benson and Scherocman 2006). The amount of overlap onto the cold side (transversely) is critical. There should be no gaps by the paver and even given variability of the paver, there should always be some overlap. Augers must adequately push HMA against the free edge when placing the second lane. Any screed extensions must be assessed for sufficient material placement at the joint (Brown, 2006). The amount of transverse overlap needed is in the range of 25 mm (1 in.) to 40 mm (1½ in.) for proper longitudinal joint construction. If proper overlap is established, raking or luting the joint is not necessary (Benson and Scherocman 2006). Figure 5-13 shows proper overlap.



Figure 5-13: Proper overlap of hot mat onto cold mat (Benson and Scherocman 2006).

The final issues for constructing well performing longitudinal joints is placement of adequate material on the hot side and proper rolling of the joint. Sufficient material must be placed to allow for 20 to 25 percent compaction of the hot mat. Unfortunately, the tendency by contractors to place less material along the hot mat, to produce a smooth joint, results in too little material along the joint. Once the hot mat is compacted to the level of the cold mat, a steel wheel roller will bridge over this material and compaction will cease at the joint. A rubber tire roller can be used successfully to further densify the mat in low spots (Brown 2006).

It is recommended to place either a steel wheel roller or a pneumatic tire roller, a short distance (6 in.) over the top of the joint from the hot side of the joint. For a rubber tire roller, the center of the outside tire of the roller, at the end of the roller with an even number of tires, is placed directly over the top of the longitudinal joint. Placing the roller in this position permits proper compaction of the mix at the joint as well as compaction of the mix on the hot mat (Benson and Scherocman 2006). Figure 5-14 shows this roller placement.



Figure 5-14: Rolling of hot mat for joint compaction (Benson and Scherocman 2006).

Sawing and Sealing HMA Overlays at PCC Joints

As part of the recent SHRP2 R21 project, R21 research engineers assisted the Illinois Tollway Association in developing a specification for the sawing and sealing of joints in the AC overlay of a newly constructed PCC pavement (Rao et al 2011). This specification describes the saw cutting, cleaning, drying, and sealing of transverse joints in new AC overlay surfaces. More information on the saw and seal operations promoted by the SHRP2 R21 project can be found in Rao et al (2011). A few illustrations of the saw-and-seal procedure are provided in Figure 5-15.



Figure 5-15: Sawing joints in the AC layer which correspond to the joints in the underlying PCC layer (left) and sealing the newly sawn joints (from Rao et al 2011).

For the Illinois Tollway AC-PCC, the joints cut for the 3-inch AC overlay were to be $\frac{1}{2}$ inch wide by $\frac{5}{8}$ inch deep. Each sawed AC overlay joint was required to be within 0.5 inches of the transverse joints in the JPCP below – as illustrated in Figure 5-16 and later described below in discussing the effectiveness of sawing and sealing, sawed joint locations have been shown to be critical to well-formed joints in AC-PCC.



Figure 5-16: Illinois tollway saw-and-seal (Elsefi 2011).

The sealant used was required to meet ASTM D-3405 with the modifications that penetration at 77 deg F be 90-150 and that the sealant pass bond testing at -20 deg F. Furthermore, the specification required that the sealant density be between 9.0 and 9.35 lb/gal. The bond breaker tape used was required to be not more than 1/8 inch narrower than the joint saw cut. The SHRP2 R21 report can be consulted for specifications on the saw, compressor, and heat lance used (Rao et al 2011).

The construction specification requires that saw joints were cut in the AC overlay no earlier than 48 hours after paving of the overlay. Saw cutting was performed as indicated above. Of particular note in the construction specifications was the requirement for the finished joint to be

well-cleaned upon completion. This ensured an acceptable seal on the joint. Sealing was conducted during daylight hours and only in favorable weather. More information on the saw and seal operations promoted by the SHRP2 R21 project can be found in Rao et al (2011).

Effectiveness of “Saw and Seal” Treatment for AC Overlays

Two recent projects have examined the effectiveness of sawing and sealing in HMA/PCC. The first was a study conducted by the Louisiana DOT to evaluate the saw and seal method in terms of pavement performance and cost (Elseifi 2011). The study involved the survey of 15 saw-and-sealed pavements throughout Louisiana over the course of six to 14 years. These saw-and-sealed pavements were compared with neighboring pavement sections that did not use sawing and sealing for the HMA overlay. The report concluded that the use of sawing and sealing extended the pavement service life by an average of four years, and was judged a cost-effective alternative for HMA overlays. Elseifi et al. also included finite element analysis of an HMA/PCC section to determine the mechanics of how saw and seal treatments minimize reflective cracking. The analysis determined that the constructed joints in the HMA allow the HMA slab to move with the underlying PCC slab as it expands and contracts.

The second study was conducted as a portion of the SHRP2 R21 Composite Pavement project; the R21 team conducted a survey of composite pavement project in the European Union (Rao et al. 2010). The SHRP2 effort included meeting with pavement experts from various countries and transportation agencies to discuss their paving techniques and experience and to survey their existing composite pavements. This survey included a number of HMA/PCC pavements that utilized the saw and seal method, which has been regularly applied to pavements in Germany since the early 1990s.

The SHRP2 team surveyed many sections featuring stone-matrix asphalt (SMA) overlays of PCC pavements along the A93 motorway, south of Munich, in 2008. For one section, illustrated in Figure 5-9, a 3-cm layer of SMA was placed over a 26 cm two-layer PCC pavement in 1995-1996. The SMA was a gap-graded mix with a maximum aggregate size of 8 mm. The saw and seal work showed little surface distress and looked outstanding and of very high quality. The longitudinal joints between PCC slabs had propagated up through the SMA, both between the inner/outer slabs and between inner/shoulder slabs. The only significant maintenance that had been done was to place a few patches at transverse joints where the SMA had debonded from the PCC surface and cracked. These rectangular repairs can be seen in Figure 5-17.



Figure 5-17: SMA over PCC along A93 in Germany, rectangular patch repair visible next to red traffic diversion truck (Rao SHRP 2010).

The R21 research team learned that the use of SMA over JPCP in Germany and other countries has used sawing and sealing for approximately 15 years. In the European experience, reflection cracking was found to be a problem when JPCP is used, and the JPCP joints reflected through to the surface unless the saw and sealing technique was used above transverse and longitudinal joints. Furthermore, experts in Germany claimed that the use of sawing and sealing of SMA over CRCP was effective in minimizing reflection cracking. As a result of the tour of European HMA/PCC composites, the SHRP2 R21 project recommended saw and seal to handling reflection cracking for an HMA overlay, be it SMA, Superpave, rubberized surfacing, etc. (Rao et al. 2010).

Quality Control and Quality Assurance

Quality Control and Quality Assurance (QC/QA) for HMA paving in composite pavement systems is comparable to that performed for conventional HMA full depth and overlay paving. However, with the added environmental stresses and strains and the increased traffic energy imparted to the pavement by the truck traffic, sufficient mix density, minimal segregation, and adequate joint density become even more important.

Quality assurance specifications are defined by the TRB glossary as (Burati 1995): ***Quality assurance specifications***—Also called ***QA/QC specifications*** or ***QC/QA specifications***. A combination of end result specifications and materials and methods specifications. The contractor is responsible for QC (process control), and the highway agency is responsible for acceptance of the product. [QA specifications typically are statistically based specifications that use methods such as random sampling and lot-by-lot testing, which let the contractor know if

the operations are producing an acceptable product.] Detailed descriptions of the QC/QA process are found in (Hand and Epps 2006 and Burati 1995).

Statistically based QC/QA is used by most states to evaluate mix quality during construction. Constructed characteristics such as smoothness, binder content, in-place density, and gradation are measured and the contractor is paid for the quality provided. To quantify the measurements of these mat and mix properties, the percent within specification limits (PWL) for each parameter is commonly used. The contractor is then paid based on performance through Pay Factors and incentives and disincentives which proportion the contracted pay depending on quality. To make the process more manageable, QC/QA specifications typically utilize a composite pay factor that includes many quality measurements, and often in-place density is given the most value (Hand and Epps 2006). For composite pavements, joint saw and seal quality can be measured and rejected if quality does not meet specifications, such as joint not properly filled, sealant not bonding, and sealant contaminated (Rao, 2011).

The main components of a QC/QA statistical system include

- acceptance sampling,
- comparison testing (f-testing (mean) and t-testing (variance)),
- quality-level analysis (PWL determination), and
- pay factor determination.

QC sampling and testing is normally the responsibility of the contractor (or the representative) and is performed randomly at a high frequency based on subplot size. Sublot size is determined from lot size (for example lot size is 5000 tons and subplot is 1000 tons).

QA sampling and testing is performed by the agency, or the contractor samples and the agency (or representative) performs the assurance tests. A view of the process is shown in Figure 5-18. Variability is present in all stages of this process and adds risk to the agency and contractor. The goal is to minimize this variability and balance the risk to the contractor and agency.

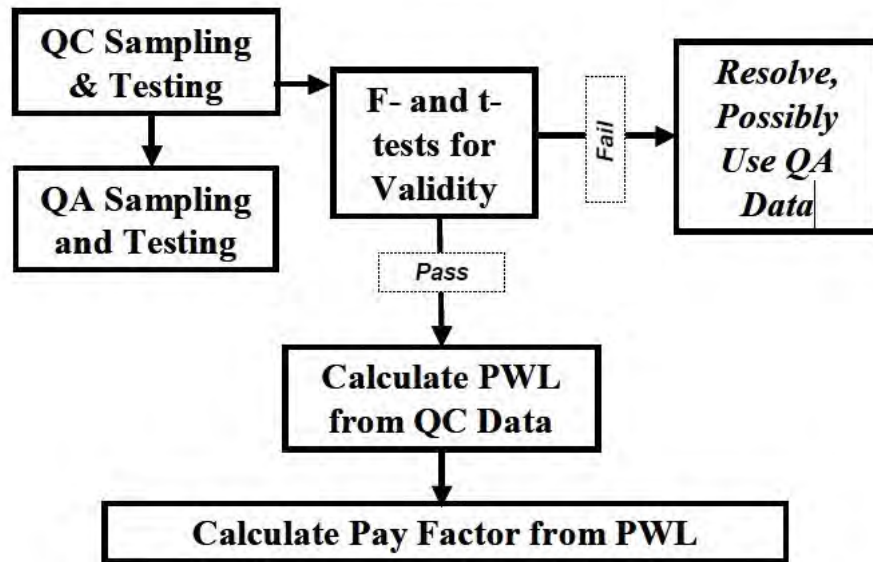


Figure 5-18: View of statistical QC/QA process (Hand and Epps 2006).

A key issue in QC and QA is the sampling process. This process has to be conducted properly so that the sample is representative of the placed mat. There are two phases of the sampling operation – selecting the sampling location and acquiring the material. FHWA supplement 23CFR637 recommends obtaining a sample as close to the work as possible. This means potentially sampling in the completed mat to ensure the mixture is most representative of the paved roadway. However, this disturbs the paved surface and contractors want to avoid potential penalties for smoothness (Elseifi, 2009). For example, Michigan DOT has a procedure that presents little damage to the paved surface while obtaining representative samples. Plates with affixed wires are put randomly beneath the to-be-placed lift. The material is shoveled out with a specially designed shovel from above the plates until sufficient quantities are obtained and back-fill HMA is replaced. Figure 5-19 and Figure 5-20 shows part of this process. Overall, many states successfully sample from the back of the paver and this is recommended (Elseifi, 2009).



Figure 5-19: Plates randomly placed under HMA mat.



Figure 5-20: Shoveling material from above plates.

For PWL determination, some specifications use just QC data, some use QA only, and others use a pooled combination of QC and QA data. Using QC data alone is recommended. Specification limits are normally selected using engineering judgment and a current limitation is the not yet fully known relationship between measured quality of the pavement and long term performance of the pavement. This makes it impossible to rationally determine life cycle costs and equitably develop pay factors (Hand and Epps 2006).

Hand and Epps, 2006 recommend the following to minimize variability throughout the sampling and testing process:

- Require all laboratories conducting QC and QA testing to be AASHTO accredited;
- Require all technicians working of QC/QA projects to be certified, preferably by a national (NICET), regional (WAQTC), or state agency;
- Select sampling locations and sampling/splitting methods that result in the lowest amount of variability;
- Select test methods that result in the lowest amount of variability;
- Eliminate options within test methods to reduce between laboratory variability; and
- Use only QC rather than pooled QC and QA data.

“Each and every selection ultimately has an impact on final acceptance and payment. Therefore it is extremely important that QC/QA specifications be developed based on knowledge of all these items as well as experience with variation in each”

5.2. AC Mix Design for HMA-PCC

Rehabilitation of existing PCC pavements with AC overlays involves placing one or more layers of AC over the PCC. The AC may be placed directly on the existing PCC or placed over a broken or rubblized PCC layer (Figure 4-21).

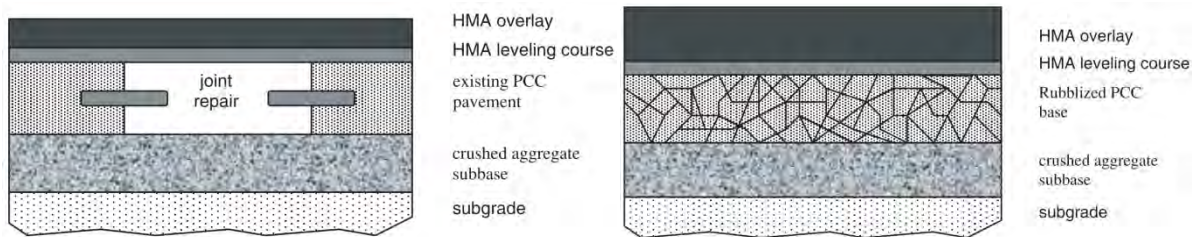


Figure 5-21: Examples of AC overlays to rehabilitate existing rigid pavements, here for a repaired PCC slab (at left) and rubblized PCC pavement (at right) (from Christensen and Bonaquist 2011).

The use of AC overlays on existing or rubblized PCC pavements involves placing an AC surface course, and possibly a thin leveling course of variable thickness to improve smoothness prior to placing the AC layers. The following subsections describe a few general details of asphalt concrete paving materials and details specifically describing materials/conditions of note for AC overlay surface or thin leveling layers. In general, much of the AC mix design selection process for AC overlays of PCC is identical to the process used for partial- or full-depth AC pavements. As a result, where appropriate, the guidelines will address special considerations for AC-PCC.

5.2.1 Important Performance Concerns for AC-over-PCC

Several important factors should be considered when selecting an AC mixture for the repair or rehabilitation of existing PCC pavements. These include:

- Rut resistance;
- Reflective cracking resistance;
- Raveling resistance;

- Noise suppression;
- Top-down cracking resistance to traffic loads and low temperatures; and
- Skid resistance.

Balancing these factors is necessary in AC mix design. Mix design properties for AC overlays will be considered in light of these important factors, though there may be overlap. For example, stiffer mixes have better rutting resistance but worse fatigue resistance for a given strain, while the reverse is true for softer mixes.

Rut Resistance

The required rut resistance of a mixture depends on the traffic level and the location of the mixture in the pavement structure. Pavements with higher traffic levels require greater rut resistance than pavements with low traffic volumes. Surface and intermediate layers require greater rut resistance than base layers. Extensive studies of the effect of asphalt overlay parameters, including properties of AC mix design, are detailed in Von Quintus et al (2012).

Reflective Cracking Resistance

Reflective cracking is one of the primary forms of distress in AC overlays of PCC pavements. Reflected cracks degrade ride quality and introduce water and debris through these cracks into the pavement system, which exacerbates the deterioration of the overlay. The mitigation of reflective cracking is an important consideration in the mix design of AC to be used in composite pavements, and an increasing amount of research in this field is being developed to address this issue both in modeling and AC mix design (Lytton et al 2010; Hu et al 2010; Bennert 2009).

It should be noted that for thinner overlays, the need to mitigate reflective cracking, in a certain sense, competes with the need to mitigate rutting. Where a mix should be stiffer to resist rutting, it should also be more compliant and tougher to minimize cracks reflective through the overlay because for thin overlays, increases in the mix stiffness have little or no effect on the tensile and shear strains (Harvey et al 2004). On the other hand, for thicker overlays, greater stiffness of the mix results in better rutting resistance and the greater stiffness combined with the thickness can reduce the tensile and shear strains. For thicker overlays, the effect of reducing the tensile strain has more effect on the fatigue life than does the lower fatigue for a given strain of a stiffer mix.

This concept is illustrated in Figure 5-22, which compares the logarithm of the tensile strain in a beam test with the number of load repetitions for permutations of beam specimens cut from pavements with thick and thin AC layers (T and t respectively) and mixes with stiff binders and soft binders (S and s respectively). It can be seen in the figure that for a given strain, the softer binder has a longer fatigue life, and that for the thin overlay increasing the stiffness of the binder does not change the tensile strain much, resulting in a lower fatigue life (y -axis) for the stiffer binder (NtS). However, it can be that for the thick overlay (T), the stiff binder has a larger effect on the tensile strain, and the reduced strain results in a greater fatigue life for the stiff binder (NTS). For many binders, one can substitute cold and hot temperatures for the same binder in place of stiff and soft binders, respectively, in the figure.

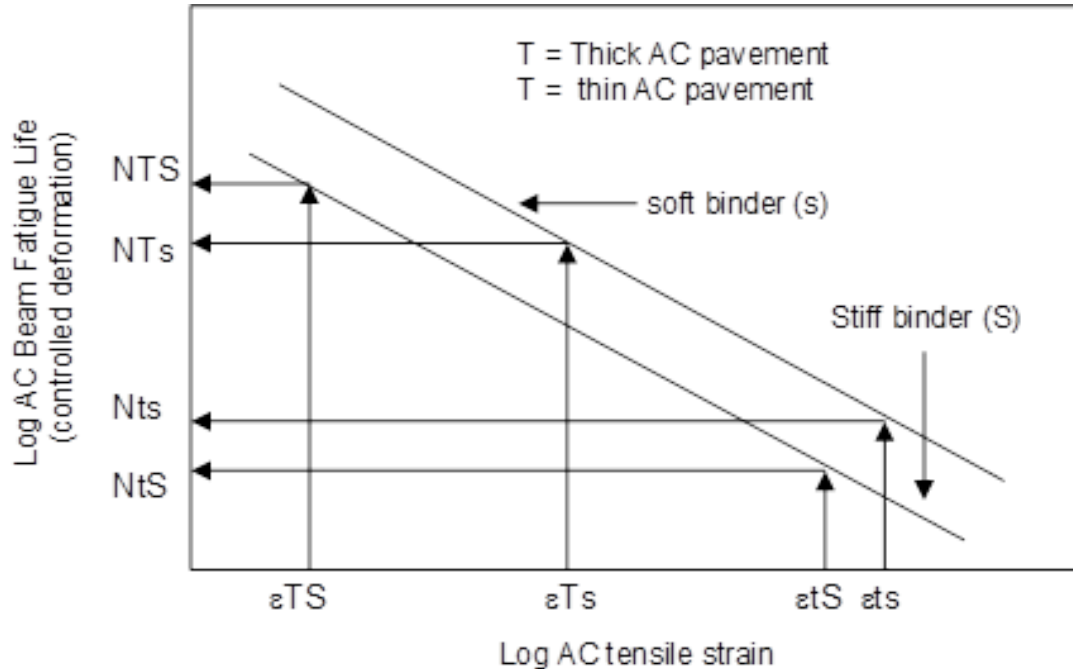


Figure 5-22: Illustration of net effects of binder stiffness and overlay thickness on fatigue life [from Harvey et al. 2004].

This consideration complicates the selection of the appropriate mix for an AC overlay, discussed later in Section 4.3.

Raveling Resistance

Raveling resistance mitigates the disintegration of an AC mixture due to exposure to the combined effects of weathering and traffic. AC surface courses have the most severe exposure, because they are subjected directly to damage by both traffic loading and the environment. Mixtures subjected to more severe exposure conditions must have greater durability. One of the best ways to increase durability of dense-graded and SMA wearing courses is to get good compaction during construction, which limits the ability of water and air to enter into the mix.

Noise Suppression

Noise reduction has been a major concern for pavement engineers in Europe for many decades, and in the past decade noise from roadway traffic has become an issue of growing concern in the United States. Roadway noise is generated by many sources, but the most predominant source (for highway speeds) is tire/pavement interaction (Bernhard and Wayson 2005). The design of AC mixes to mitigate noise considers factors such as permeability, macrotexture, roughness, and durability (Ongel et al 2007).

Top-Down Cracking Resistance

Another important consideration related to traffic loading is the resistance of the AC overlay to fatigue cracking at the surface, or top-down cracking. Pavements with higher traffic levels

require overlays with greater resistance to fatigue cracking (Roque et al 2010). In addition, for AC overlays in the northern United States and Canada, mix design must consider low-temperature cracking, which is the primary distress for AC pavements in these climates (Marasteanu et al 2004). One of the most important mixture design factors affecting fatigue resistance in either regard is the effective binder content of the AC mixture.

Skid Resistance

The skid resistance of a pavement is an important given the correlation between low pavement skid resistance and accident rates (Masad et al 2007). Pavement skid resistance is typically measured in the field in terms of a friction or skid number, where higher values correspond to increased friction and reduced stopping distances. The mechanism of skid resistance is generally considered in terms of pavement microtexture and macrotexture (Ongel et al 2007). Given that the skid resistance of a pavement can change over time, it is very important that the AC mix design carefully consider desired surface friction both at opening to traffic and throughout the service life of the pavement.

In this respect, aggregate gradation has been identified as the most important design parameter in providing adequate skid resistance at highway speeds (texture wavelengths between 0.5 and 50 mm), (Masad et al 2007; Ongel et al 2007), while microtexture (texture wavelengths less than 0.5 mm) is largely controlled by aggregate source and crushing. Keeping binder contents at a level that results in no “bleeding” or expulsion of asphalt to the surface, is also very important for maintaining skid resistance, because thick films of asphalt at the surface in the wheelpaths become very slippery when they are cold and wet.

5.2.2 Asphalt Concrete Mixtures for AC-PCC

AC mixtures are typically classified by whether or not the mix must be heated prior to transport; the manner of placement; and the use of compaction. The most common type of AC is hot-mix asphalt (HMA), which must be thoroughly heated during mixing, transport, placement, and compaction. The asphalt binder used in HMA is quite stiff at room temperatures, so that once this type of AC cools it becomes stiff and strong enough to support heavy traffic. These guidelines summarize detailed design procedures for five types of HMA mixtures: dense-graded asphalt (DGHMA), polymer-modified DGHMA, stone matrix asphalt (SMA), open-graded friction course asphalt (OGFC), and rubberized gap-graded asphalt. Warm-mix asphalt (WMA) is also discussed, although warm mix is primarily a compaction aid and does not have much effect on final mix properties in service.

Dense-Graded HMA

Dense-graded HMA mixtures are the most commonly used mixtures in the United States. They can be used in any layer of the pavement structure for any traffic level. Traffic level is a direct consideration in the design of dense-graded mixtures. Aggregate angularity, fine content, binder grade, compactive effort, and some volumetric properties vary with traffic level in the dense-graded mixture design procedure. Dense-graded mixtures also provide the mixture designer with the greatest flexibility to tailor the mixture for the specific application (Christensen and Bonaquist 2011).

For instance, dense-graded mixtures can also be designed as fine or coarse mixtures. Fine mixtures generally have a gradation that plots above the maximum density line (when the gradation is plotted with sieve sizes raised to the 0.45 power) while coarse mixtures plot below the maximum density line. The sieve sizes used in the definition of fine and coarse mixtures in AASHTO M 323 is summarized in Table 5-3.

Table 5-3: Sieve sizes used to define fine and coarse mixes in AASHTO M 323 (from Christensen and Bonaquist 2006).

Nominal Maximum Aggregate Size	Primary Control Sieve	Percent Passing
37.5 mm	9.5 mm	≥ 47
25.0 mm	4.75 mm	≥ 40
19.0 mm	4.75 mm	≥ 47
12.5 mm	2.36 mm	≥ 39
9.5 mm	2.36 mm	≥ 47

For each nominal maximum aggregate size, a primary control sieve has been identified. If the percent passing the primary control sieve is equal to or greater than the specified value in Table 5-3, the mixture classifies as a fine mixture; otherwise it classifies as a coarse mixture. Fine mixtures have smoother surface texture, lower permeability for the same in-place density, and can be placed in thinner lifts than coarse mixtures, a feature that might be advantageous for thin AC overlays of PCC. However, because of generally greater surface area, they often require more binder than coarse mixes, increasing the cost of the mix.

A survey of 26 state highway departments found that the majority of the states surveyed use either a 9.5mm Superpave Performance Grade (PG) mix over a 12.5mm Superpave mix or a 12.5mm Superpave mix over a 19mm Superpave mix for HMA overlays of existing concrete pavements. Generally, the LTPPBinder recommendation for the PG grade of the binder was used by the states (Bennert 2009). The PG binder grade controls the high temperature properties related to rutting and the low temperatures properties related to top-down low temperature cracking.

Polymer Modified Dense-Graded Asphalt

Binder selection is a very important issue to improve the response of an AC mixture to climatic conditions, and in this regard conventional asphalts are not necessarily the most appropriate choice for surfaces exposed to extreme weather conditions. While climate determines the performance grade of binder that will be used for the mixture type, polymer modified asphalts can provide the additional flexibility needed to withstand thermal stresses in cold climates and still maintain adequate stiffness to help resist rutting (Terrel and Epps 1989; Shuler et al 1987). The use of polymer additives to modify the performance of an AC mixture is a common practice in paving, and these modified asphalts are as applicable to AC overlays of PCC as they are full-depth asphalt paving.

Open-Graded Friction Course (OGFC)

OGFC is an open-graded mixture with a high air void content. The high air void content and open structure of the mixture provides macrotexture and high permeability to drain water from the tire-pavement interface. This minimizes the potential for hydroplaning, improves wet weather skid resistance, and reduces splash and spray.

Other benefits of OGFC include reduced noise levels, improved wet weather visibility of pavement markings, and reduced glare. OGFCs are made with durable, polish-resistant aggregates and usually contain modified binders and fibers to increase the binder content and improve their durability (Christensen and Bonaquist 2011). OGFCs, though generally more expensive than dense-graded mixtures, are placed in a thin 30 to 60 mm thick lift over a dense-graded or gap-graded lift (Ongel et al 2007).

Rubberized Gap-Graded Asphalt (RHMA-G or ARFC)

Gap-gradations are primarily used for rubberized binders to provide empty space in the gradation to accommodate the rubber particles or heavily polymer modified binders. They are densely compacted to maximize rut resistance and durability. The principal design consideration in gap-graded AC mixtures is to maximize the contact between particles in the coarse aggregate fraction of the mixture. This fraction provides stability and shear strength to the mixture. The coarse aggregate fraction is then essentially glued together by a binder-rich mastic consisting of a properly selected asphalt binder, and mineral filler and/or fibers in SMA mixes. The fibers are included to minimize draindown of the binder from the mixture during transportation, handling and placement.

The advantages of GGHMA mixtures over dense-graded mixtures include (1) increased resistance to permanent deformation, cracking, and aging and (2) improved durability, wear resistance, low-temperature performance, and surface texture (Christensen and Bonaquist 2011). GGHMA mixtures generally cost more than dense-graded mixtures due to their higher binder content, high filler content, stringent aggregate requirements, and the use of polymer-modified binders and fibers.

The use of rubber reclaimed from waste tires is one means of both accommodating modifications to the binder and reducing the cost of the mix. These gap-graded rubberized hot mix asphalt (RHMA-G) are often used in the top 60 mm (2.4 inches) layer of pavements in California (Coleri et al 2012) and in thickness of 38-50 mm (1.5 to 2.0 inches) of composite pavements in Arizona, where they are referred to as an asphalt rubber friction course (ARFC) when used with a more open gap-graded gradation (Scofield and Donovan 2003; Kaloush et al 2009).

Stone Matrix Asphalt (SMA)

During the past 20 years, stone-matrix asphalt (SMA) has become increasingly common in the United States and Europe. SMA is a special type of GGHMA designed specifically to hold up under very heavy traffic. SMA is composed of high-quality coarse aggregate, combined with a large amount of mastic composed of a high-performance asphalt binder, mineral filler, and a small amount of fibers. The aggregate used in SMA contains a large amount of coarse aggregate

and a large amount of very fine material (called mineral filler), but not much sand-sized material. A well-developed coarse aggregate structure in combination with a relatively large volume of high performance binder helps ensure that a properly designed SMA mixture will exhibit excellent performance. SMA is usually only used on very heavily trafficked roadways, where its excellent performance makes it cost-effective despite the high initial investment required to construct SMA pavements (Rao et al 2011; Christensen and Bonaquist 2011). They are typically placed as a highly durable surface course that is 60 mm or less in thickness because of their high cost.

Warm Mix Asphalts

Warm-mix asphalt (WMA)—has recently become increasingly popular. A hot mix becomes a warm mix when an additive is used during the mixing process that increases the workability of the mix at lower temperatures. Otherwise, there is little or no difference from hot mix. In this type of mixture, various different methods are used to significantly reduce mix production temperature by 30 to over 100°F. Warm mix additives are generally grouped into the following three categories:

1. using chemical additives to lower the high-temperature viscosity of the asphalt binder, referred to as chemical additives;
2. techniques involving the addition of water to the binder, causing it to foam, referred to as mechanical foaming when water is injected; and
3. using chemical additives that produce water in the binder causing it to foam, referred to as chemical foaming agents.

WMA has several benefits, including potentially lower costs (depending on fuel use and additive costs), lower emissions and improved environmental impact, and potentially improved performance because of decreased age hardening. There is some concern that WMA might in some cases be more susceptible to moisture damage, but this has yet to be clearly demonstrated. Furthermore, given its relatively recent adoption, the long-term performance of WMA is as yet uncertain and undocumented, but preliminary indications suggest there is much potential for the application of WMA in AC-PCC (Jones et al 2009).

5.2.3 AC Overlay Mix Design Selection

The selection of an appropriate AC mixture for AC-PCC is a difficult decision that involves consideration of cost, traffic, climate, construction, and performance concerns. Although the types of mixtures to be used in a project are usually selected during the design phase, it is important that mixture designers understand the rationale behind the selection of mixtures for specific applications.

In general, the pavement designer should follow a process for the AC overlay mix design that is similar to the method described in NCHRP Report 673 for general asphalt design according to the Superpave method as follows:

1. Gather Information
2. Select Asphalt Binder

3. Determine Compaction Level
4. Select Nominal Maximum Aggregate Size
5. Determine Target VMA and Design Air Void Content
6. Calculate Target Binder Content
7. Calculate Aggregate Content
8. Proportion Aggregates for Trial Mixtures
9. Calculate Trial Mix Proportions by Weight and Check Dust/Binder Ratio
10. Evaluate and Refine Trial Mixtures
11. Compile Mix Design Report

Most of these steps are straightforward and easily accomplished. However, Steps 8 through 10 are more complicated and require some experience in order to perform them proficiently. The reader is referred to NCHRP Report 673 for more detail and references on this process, including a developed spreadsheet for AC mix design (Christensen and Bonaquist 2011).

Given that different applications require different mix designs, the pavement designer must consider desired performance (e.g. design life), climate, and traffic volumes together to best select an appropriate mix design for the AC overlay of a PCC pavement. The following subsections provide comments and recommendations on AC mixtures based on performance concerns for the constructed AC overlay, with comments addressing design life, traffic, and/or climate where appropriate.

Rutting

For dense-graded mixtures, aggregate angularity, binder grade, compactive effort, and some volumetric properties are selected depending on traffic level and layer depth to provide adequate rut resistance. Crushed faces and rough surface texture are the most important properties controlling rutting. GGHMA and OGFC mixtures are designed to ensure stone-on-stone contact to minimize the potential for rutting. Binder grade for these mixtures is also selected considering environment and traffic level using the PG specification. Polymer modified binders will often improve rutting resistance. The PG binder specification is currently undergoing review to consider the greater elastic recovery under repeated loading of polymer modified binders compared to conventional binders. In general, thin overlays on concrete will generally not rut as much as thicker overlays on concrete or overlays placed on asphalt due to shear restraint from the underlying PCC slab (Coleri et al 2012).

Reflective Cracking

Bennert (2009) found that the time for reflective cracking to appear is partially dependent on the low temperature PG grade of the binder used. Figure 5-23 illustrates the low temperature PG grade recommended by LTPPBind for locations in the United States.

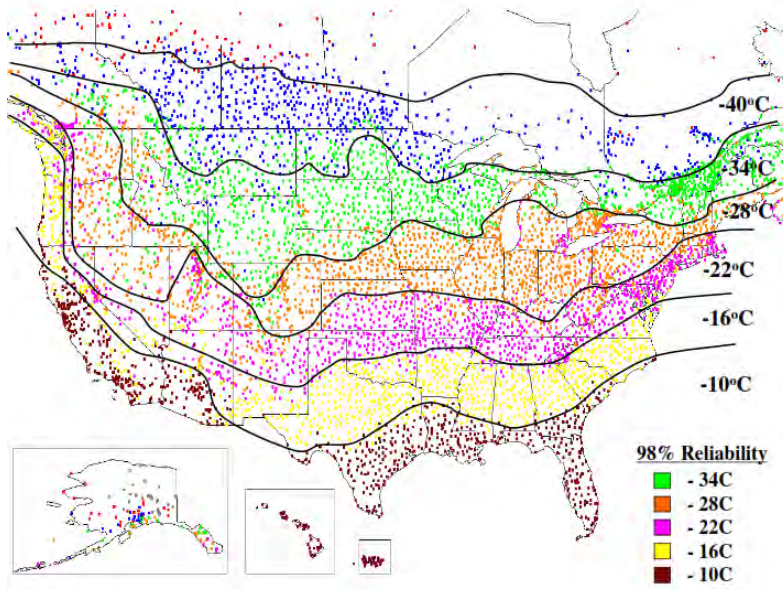


Figure 5-23: Recommended low temperature PG grade from LTPPBind (from Bennert 2009).

Likewise, Figure 5-23 describes the same recommendations as those of Figure 5-24, superimposed on a map illustrating the time until reflective cracking is generally observed in AC overlays of PCC pavements. From these figures, it can be seen that states using low temperature PG grades between -10°C and -16°C had the longest time before reflective cracking was observed, most likely because they had the warmest winters. Bennert (2009) observed that lower recommended low temperature PG grades for a given climate correspond to less time before the occurrence of reflective cracking.

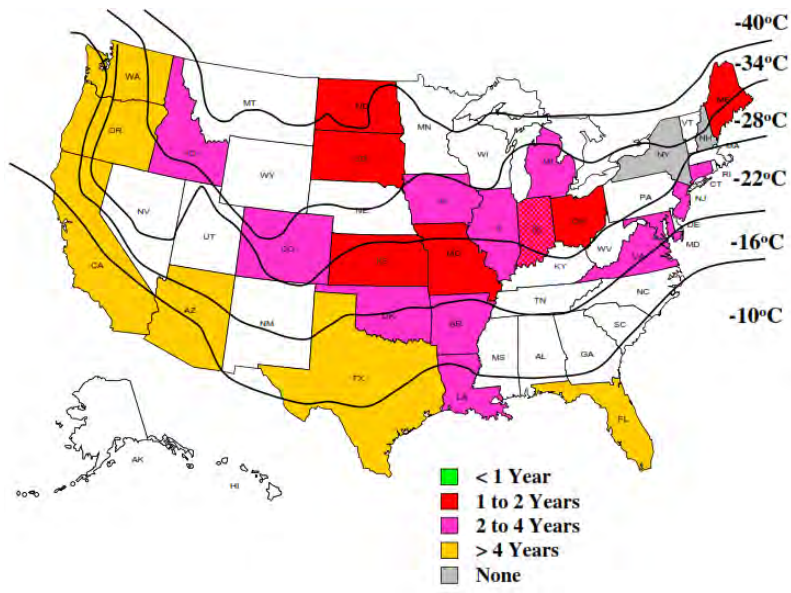


Figure 5-24: Time in years until reflective cracking occurs in AC overlays of PCC pavements and recommended low temperature PG grade from LTPPBind (from Bennert 2009).

Bennert (2009) also found that states using a binder with a PG low temperature grade lower than that recommended by LTPPBind by one or two grades had a longer pavement life before reflective cracking was observed. Conversely, composite pavements in states that used a binder with a PG low temperature grade higher than that recommended by LTPPBind by one or two grades had a shorter pavement life before reflective cracking was observed.

As noted in the overview of performance concerns for AC overlay mix design, rutting and reflective cracking are often considered alongside each other given their somewhat contradictory needs from a mix design point of view for thinner overlays. Recent work at the Texas Transportation Institute (TTI) involved the use of an AC overlay tester, which can be used to simulate horizontal opening and closing of joints or cracks in the pavement below the asphalt overlay (Figure 5-25). This allows the resistance of an asphalt mixture to reflective cracking to be measured using specimens that are easier to obtain than the currently used four point beam samples.

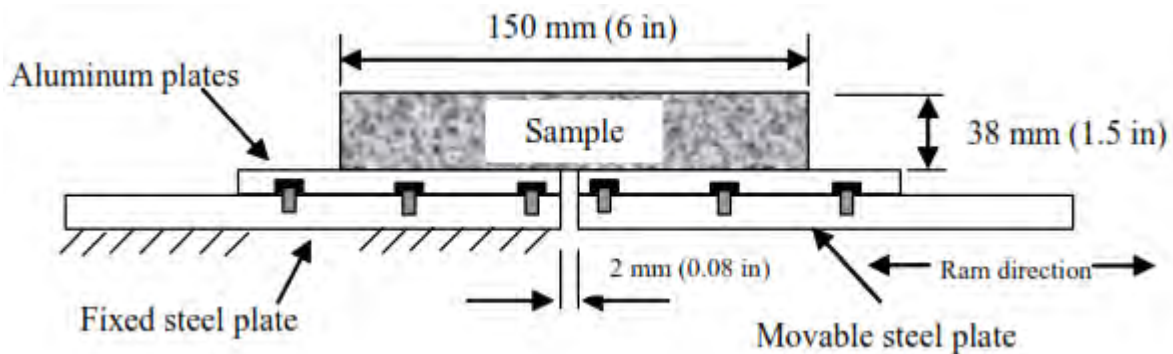


Figure 5-25: TTI overlay tester to investigate mix design influence on reflective cracking (from Zhou and Scullion 2003).

Using the overlay tester to examine in place overlays, Zhou and Scullion (2003) determined that overlays designed with stiffer binders had less resistance to reflective cracking than those using softer binders. Furthermore, Zhou et al (2006) developed an HMA mix design selection procedure for overlays that accounted for both reflective cracking and rutting concerns. This procedure is outlined in Figure 5-26. Using this procedure, Zhou et al developed recommendations for the binder content for HMA overlay mixes, illustrated in Figure 5-26.

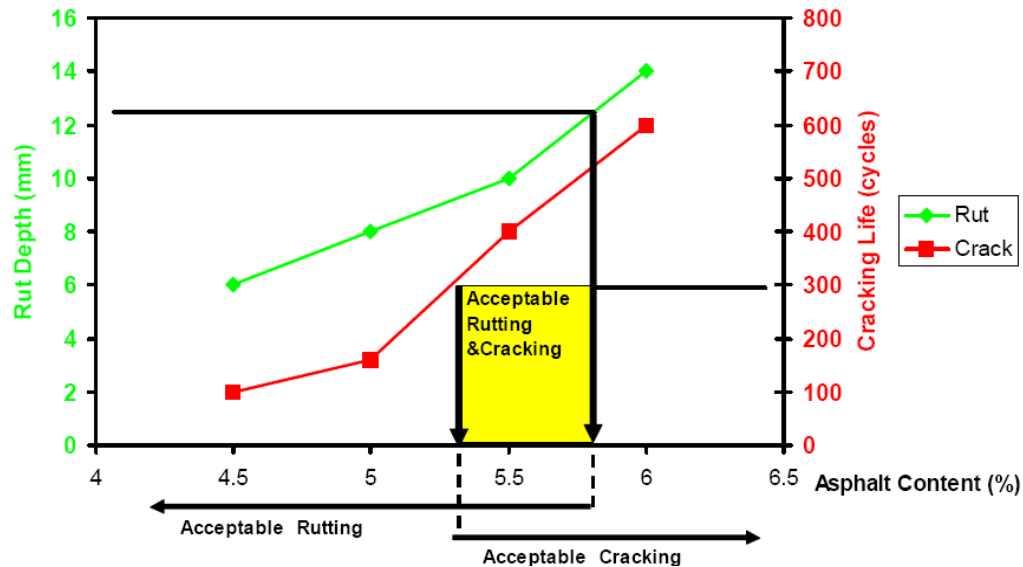


Figure 5-26: Overlay binder content to optimize resistance to rutting and fatigue cracking from Zhou et al (2006).

Raveling

NCHRP Report 567 summarizes the relationships among AC composition and performance in raveling. For the most durable mixes—ones with good fatigue resistance and low permeability to air and water—high binder contents are needed, along with a reasonable amount of fine material in the aggregate. Perhaps most importantly, the mix should be well compacted during construction. In general, both the binder content and the amount of fines in the aggregate blend will increase with decreasing aggregate nominal maximum aggregate size (NMAS). This is one of the reasons that smaller NMAS mixtures are used in surface courses (Christensen and Bonaquist 2006). The effective binder content of GGHMA mixtures is very high due to the gap-graded structure of these mixtures.

OGFC mixtures typically incorporate modified binders and fibers to increase the binder content of these mixtures and improve their durability. If OGFC is selected, high-speed traffic is an important consideration because it helps keep the pores from clogging with debris, however in general raveling will become a problem for OGFC within about 8-12 years depending on traffic and winter maintenance (Ongel et al 2007; Sandberg and Eismont 2002).

Noise and Skid Resistance

Both OGFC and rubberized gap-graded mixes perform equally well in reducing noise and improving skid resistance if their initial air-voids are similar, however, rubberized gap-graded mixes typically densify under traffic and lose some of the noise reducing properties (Ongel et al 2007). Whereas OGFC can reduce hydroplaning and spray and splash and hence improve safety, its high permeability may lead to increased raveling relative to the performance of less permeable polymer-modified dense-graded and rubberized gap-graded mixes. OGFC mixes have been found to lose their noise-reducing advantage over a typical dense-graded mix within 7

years of placement due to clogging and distresses at the pavement surface (Ongel et al 2007), which is improved if the open-graded mix has a rubberized asphalt binder (Lu et al 2010).

Another important consideration for OGFC in mitigating noise and improving skid resistance is climate. The open structure of OGFCs causes these mixtures to freeze more quickly than dense-graded and GGHMA mixtures, resulting in the need for earlier and more frequent application of deicing chemicals. The SHRP2 R21 project discussed these difficulties in its tour of European composite pavements, where engineers from countries with freeze-thaw cycles discussed OGFC difficulties in AC-PCC applications (Rao et al 2011). Additionally, sand should not be used with the deicing chemicals because the sand will plug the pores of the OGFC, decreasing their effectiveness in both noise and skid resistance. Finally, as SMA mixes are generally impermeable, they do not reduce the air pumping mechanism of tire/pavement noise. Their noise level primarily depends on their macro texture and the tire vibration mechanism.

Top-Down Cracking Resistance

To resist load-related top-down cracking, Christensen and Bonaquist (2011) recommend dense-graded mixtures of smaller nominal maximum aggregate size and GGHMA mixtures should be considered for high traffic levels. The dense-graded mixture design procedure provides the flexibility to increase the design VMA requirements up to 1.0% to produce mixtures with improved fatigue resistance and durability. Increasing the VMA requirement increases the effective binder content of these mixtures over that for normal dense-graded mixtures. SMA mixes have also been shown to perform very well in terms of resistance to top-down cracking. For resistance to low-temperature cracking, established PG binder specifications can be followed to mitigate this distress for AC overlays in a manner consistent with that of full-depth AC pavements.

Chapter 6. Life Cycle Cost Analysis Case Studies

A conceptual life cycle cost analysis (LCCA) sensitivity study was performed to evaluate the cost and structural reasonableness of thermally insulated concrete pavement (TICP) structures that are economically viable compared with jointed plain concrete pavement (JPCP).

Three cases were considered for this life cycle cost analysis of TICPs. The first two cases were based on California conditions. For these cases, the discount rate, LCCA periods, material costs, pavement designs, and maintenance and rehabilitation (M & R) practices were based on current Caltrans practices. Caltrans Case 1 involved reconstruction of truck lanes and maintenance of passenger lanes on an existing JPCP freeway. Caltrans Case 2 involved construction of two lanes on a new roadbed in order to convert a highway into a dual carriageway freeway.

A spreadsheet was built so that, given an array of assumptions, the construction and maintenance costs of TICP could be considered relative to those of JPCP. Considered in this sensitivity analysis were the cost of HMA relative to the cost of PCC, traffic handling costs during construction, and different TICP designs. The layer types and thicknesses in the JPCPs and the underlying concrete layer in the TICP were based on the Caltrans Highway Design Manual. The third case, MN Case 3, considered construction of a new TICP on a major highway or Interstate. The pavement design was based on Minnesota climatic conditions and typical Minnesota Department of Transportation (MnDOT) design guidelines.

Within each case study, three measures were evaluated for reasonableness:

- PCC thickness requirement: the thickness of the Portland cement concrete (PCC) in the TICP pavement that resulted in same net present value (NPV) for the TICP as for the JPCP. These thicknesses were compared with assumed plausible minimum thicknesses necessary to provide required service lives.
- TICP PCC cost reduction requirement: if the TICP and JPCP PCC thicknesses remained equal, the reduction in cost of the TICP PCC as a percentage of the cost of JPCP PCC that resulted in the same NPV for TICP and JPCP.
- Life extension: the increase of PCC life in the TICP pavement beyond the normal PCC service life caused by including a hot-mix asphalt (HMA) overlay from initial construction. The HMA overlay would be expected to reduce temperature gradients in the PCC, therefore reducing stresses and increasing the cracking life of the PCC. The PCC thickness in the TICP pavement was the normal PCC thickness for JPCP. The maximum reasonable life extension was assumed to be 70 percent.

It must be emphasized that this was a conceptual study that intended to evaluate the plausibility of TICP PCC thickness reductions relative to JPCPs, TICP PCC cost reductions relative to JPCP PCC costs, and life extensions of PCC in TICPs that were economically competitive with JPCPs.

6.1. Background Information for Caltrans Case Studies

A LCCA was considered for both TICPs and JPCPs in the context of the following two case studies:

- Case 1: Lane replacement of truck lanes in Southern California as TICP instead of JPCP. This project was based on the scope of a real project on I-15 near Devore (District 8).
- Case 2: Convert multi-lane highway in Northern California into divided highway by adding new direction with TICP instead of JPCP. This project was roughly based on the scope of a real project on State Route 70 near East Nicholas (District 3).

Two basic TICP designs were considered to represent different initial design lives. Design 1 was composed of a thicker concrete slab and a thicker asphalt overlay. Design 2 was composed of a thinner slab and thinner asphalt overlay. Based on the Caltrans LCCA Manual and Highway Design Manual, Design 1 was intended to provide 50 years of service until the first major intervention is required and is referred to as having a 40-year design life. Design 2 was intended to provide 30 years of service until the first major intervention is required and is referred to having a 20-year design life. Both conventional hot mix asphalt (HMA) and rubberized hot mix asphalt (RHMA) were considered as the top layer for the TICPs.

All cost data for the initial construction were taken from the 2009 Caltrans Construction Cost Data Book, for the appropriate district, using data for similar size projects. The JPCP designs and the PCC and base thicknesses underlying the TICPs came from the current Caltrans Highway Design Manual. The annual maintenance costs, design lives, analysis periods, and future maintenance and rehabilitation treatments and costs were taken from the current version of the Caltrans Life Cycle Cost Analysis Manual for the appropriate climate region and design life for JPCP and Composite pavement types. The discount rate used was four percent, as required by the Caltrans Life Cycle Cost Analysis Manual. Traffic control costs for future annual maintenance, maintenance, and rehabilitation were assumed to be included in the costs used from the Caltrans LCCA Manual. Only costs for the mainline were considered, no shoulder costs were considered because it was assumed that shoulder reconstruction and maintenance would be similar for all alternatives. The following cost data apply to both Caltrans case studies:

Asphalt and PCC Costs. Two scenarios were considered regarding the prices of asphalt and PCC for the LCCAs. The first, referred to as the 1:1 case, assumed that the HMA, RHMA, and PCC costs were those typical of these materials in California in 2009. The second scenario, referred to as the 0.8:1 case, assumed that HMA costs were 80 percent of the 2009 cost. The following values were used as the cost basis for HMA, RHMA, and PCC:

HMA overlays and HMA base:

- \$80/ton = \$192/m³ for 1:1 case
- \$154/m³ for 0.8:1 case

RHMA overlays:

- \$100/ton = \$240/m³ for 1:1 case
- \$192/m³ for 0.8:1 case

PCC:

- \$190/m³

For the life extension cases where the PCC layer has equal thickness in both the new JPCP and TICP pavements, the cost of the PCC was assumed to be the same. This may be a conservative assumption because one of the benefits of TICP is that the PCC layer is not exposed to the extreme environmental stresses or tire wear that a typical JPCP surface must be durable against. This implies that it would be possible to decrease the cost of composite pavements by either decreasing the thickness of the PCC layer or by decreasing the cost of the cement or aggregates in the PCC layer. A reduction in cost of the TICP PCC layer could be accomplished by increasing the percentage of supplementary cementitious materials in the total cementitious volume, by substituting recycled concrete aggregates for conventional coarse aggregates, or by allowing a higher percentage of fine, soft, spall, or slate in the coarse aggregate.

Traffic Control Costs. For second reconstructions only, two traffic control costs of 15% and 50% of the total pavement construction costs were considered, based on analyses of similar long-life pavement rehabilitation projects completed by the University of California Pavement Research Center (UCPRC), as follows:

- I-15 Devore, continuous closure, intermediate between rural and urban: 16%
- I-710 Long Beach, 55 hour weekends, urban: 63%
- I-80 Truckee, continuous closure, rural: 7%
- I-10 Pomona, 55 hour weekend and nighttime, urban: 12%

Mobilization Costs. A mobilization cost of \$400,000 was applied to the initial construction and to future reconstructions. Mobilization was assumed to be included in the costs for future annual maintenance and rehabilitation taken from the Caltrans LCCA Manual for those activities.

6.2. Reconstruction of truck lanes on I-15 in California

History. Caltrans Case 1 involved the lane replacement of truck lanes and rehabilitation or maintenance of the passenger lanes in an existing freeway. The existing JPCP pavement was approximately 40 years old and consisted of 230 mm (9 in) of non-doweled concrete slabs over 100 to 150 mm (4 in to 6 in) of cement-treated base on aggregate subbase.

Project Scope. The total reconstruction project length was 4.5 km with 2 km with 3 lanes and 2.5 km with 4 lanes in each direction. Truck lanes consisted of 4-4.5 km lanes totaling 18 lane-km (11.2 lane-miles) and passenger car lanes consisted of 2-2 km lanes and 4-2.5 km lanes totaling 14 lane-km (8.7 lane-miles). It was assumed that the existing JPCP in the passenger car lanes never needed reconstruction, only normal maintenance for concrete (JPCP) or asphalt (TICP) surfaces, in perpetuity. In the passenger car lanes, it was assumed that a maintenance treatment other than annual maintenance was needed every 20 years for up to 100 years for PCC surfaces and then every 15 years, and every 15 years for HMA surfaces following the initial service life (50 or 30 years). The high annual maintenance cost of the TICP pavement reflects periodic asphalt resurfacing during the initial service life without explicitly identifying when these will occur.

The existing grade was maintained across all lanes for the JPCP designs. For the TICP designs, the new PCC surface in the truck lanes matched the grade of the existing JPCP in the passenger lanes, and all lanes were overlaid with the same thickness of HMA or RHMA. In the truck lanes,

the existing pavement was excavated to the depth required for the new base and PCC layers, and the top of the remaining existing aggregate base layer was recompact. The base was assumed to be HMA. The subgrade was assumed to be Type II soil (lean clay). Costs of constructing the base were the same for JPCP and TPCP because the thicknesses were assumed equal for this case, although this assumption might not be true for all JPCP and TPCP comparisons.

The passenger car lanes were 3.6 m (12 ft) wide and the truck lanes were 4.2 m (14 ft) wide. Caltrans designs assume joint spacings of 3.6, 3.9, 4.2, 4.5 m (12, 13, 14, 15 ft), with 11 dowels per joint for 3.6 m lanes and 13 dowels for 4.2 m lanes. Dowel costs were included in the PCC cost. The 40-year design ESALs were 55 million, and the traffic index was 14.5. The 20-year design ESALs were 22 million, and the traffic index was 13.

JPCP Design. The JPCP design per Table 623.1G of the Highway Design Manual for doweled JPCP with a nominal 40-year design life was the following:

- 300 mm (12 in) PCC
- 150 mm (6 in) HMA base

The maintenance and rehabilitation schedule was assumed as shown in Table 6-1.

Table 6-1: Caltrans Case 1 JPCP maintenance and rehabilitation schedule.

Truck lane				
Item	Year	Cost/ln-mi	Design Life	Annual Maintenance Cost/ln-mi
Initial JPCP	0	Calculated elsewhere	45	\$800
CPR-C	45	\$89,000	5	\$3000
CPR-B	50	\$106,000	10	\$1500
Reconstruct JPCP **	60	Same as Year 0	45	\$800

Passenger lane				
Item	Year	Cost/ln-mi	Design Life	Annual Maintenance Cost/ln-mi
CPR-C	0	\$89,000	20	\$3000
CPR-C	20	\$89,000	20	\$3000
CPR-C	40	\$89,000	15* or 20**	\$3000
CPR-B**	60	\$106,000	15	\$1500

** for 55 year analysis period, ** for 75 year analysis period*

Special notes for this project and for Table 6-1 include the following:

- Concrete Pavement Rehabilitation B involves pavement grinding, moderate slab replacement, spall repair, & joint seal repair. It is for JPCP projects with a total number of slabs in the lane that were replaced or exhibit third stage rigid cracking between 2 and 5%.

- Concrete Pavement Rehabilitation C involves pavement grinding, minor slab replacement, spall repair, & joint seal repair. It is for JPCP projects with a total number of slabs in the lane that were replaced or exhibit third stage rigid cracking of 2% or less.

TICP Design 1. The pavement design per Table 623.1G of the Highway Design Manual for doweled JPCP with a nominal 40-year design life was:

- 300 mm (12 in) PCC (PCC thickness was solved for in TICP PCC thickness analysis cases)
- 150 mm (6 in) HMA base

The following two asphalt overlays were considered:

- 105 mm (4 in) HMA
- 75 mm (3 in) RHMA

The maintenance and rehabilitation schedule was assumed as shown in Table 6-2.

Table 6-2: Caltrans Case 1 TICP Design 1 maintenance and rehabilitation schedule.

Item	Year	Cost/ln-mi	Design Life	Lanes	Annual Maintenance Cost/ln-mi
Initial TICP	0	Calculated	50 + LE*	Reconstruct PCC/base in truck lanes (18 ln-km) and overlay all lanes (32 ln-km)	\$4800**
FO+JPCP SR	50 + LE*	\$91,000	8	Truck lanes (18 ln-km)	\$700
75 mm Overlay	50 + LE*	Calculated	15	Passenger lanes (14 ln-km)	\$4800
FO+JPCP SR	50 + LE* + 8	\$91,000	7	Truck lanes (18 ln-km)	\$700
Repeat TICP	50 + LE* + 15	Same as initial TICP	50 + LE*	Truck lanes (18 ln-km)	\$700
75 mm Overlay	50 + LE* + 15	Calculated	15	Passenger lanes (14 ln-km)	\$4800

** Life Extension (LE) additional years solved for in life extension analyses, equal to zero in TICP PCC thickness analyses.
 ** Annual maintenance cost for TICP and other longer life overlays includes cost of patching and other late-life maintenance, cost of periodic replacement of the overlay for long design lives of the TICP overlays. This value comes from the Caltrans LCCA Manual.*

TICP Design 2. The pavement design per Table 623.1G of the Highway Design Manual for doweled JPCP with a nominal 20-year design life was:

- 255 mm (10 in) PCC (PCC thickness is solved for in thickness changes cases)
- 150 mm (6 in) HMA base

The following four asphalt overlays were considered:

- 30 mm (1.2 in) HMA
- 45 mm (1.8 in) HMA
- 30 mm (1.2 in) RHMA
- 45 mm (1.8 in) RHMA

The maintenance and rehabilitation schedule was assumed as shown in Table 6-3.

Table 6-3: Caltrans Case 1 TICP Design 2 maintenance and rehabilitation schedule.

Item	Year	Cost/ln-mi	Design Life	Lanes	Annual Maintenance Cost/ln-mi
Initial TICP	0	Calculated	30 + LE*	Reconstruct PCC/base in truck lanes (18 ln-km) and overlay all lanes (32 ln-km)	\$4800***
FO+JPCP SR	30 + LE*	\$91,000	8	Truck lanes (18 ln-km)	\$700
30 or 45 mm Overlay**	30 + LE*	Calculated	15	Passenger lanes (14 ln-km)	\$4800
FO+JPCP SR	30 + LE* + 8	\$91,000	7	Truck lanes (18 ln-km)	\$700
Repeat TICP	30 + LE* + 15	Same as initial TICP	30 + LE*	Truck lanes (18 ln-km)	\$700
30 or 45 mm Overlay**	30 + LE* + 15	Calculated	15	Passenger lanes (14 ln-km)	\$4800
30 or 45 mm Overlay**	30 + LE* + 15 + 15	Calculated	15	Passenger lanes (14 ln-km)	\$4800

* Life Extension (LE) additional years solved for in life extension analyses, equal to zero in TICP PCC thickness analyses.
 ** Overlay thickness same as original TICP overlay thickness
 *** Annual maintenance cost for TICP and other longer life overlays includes cost of patching and other late-life maintenance, cost of periodic replacement of the overlay for long design lives of the TICP overlays. This value comes from the Caltrans LCCA Manual

6.2.1 Caltrans I-70 Case Study Results

TICP PCC Thickness Analyses. The results of the analyses of the thickness requirement for the TICPs PCC are shown for 1:1 cost scenarios in Table 6-4 and for 0.8:1 cost scenarios in Table 6-5. The tables show the TICP PCC thicknesses that make the NPV of the TICP pavements equal to the NPV of the JPCP pavement. It can be observed that the Design 2 TICPs resulted in a thicker allowable PCC layer than the Design 1 TICPs. This is because the lower initial cost of constructing Design 2 TICP more than compensates for the later cost of reconstructing the truck lanes a second time with the Caltrans official discount rate of four percent.

Assuming that an absolute minimum possible thickness for the PCC in the TICP pavements is 175 mm (7 in), it can be seen that most of the Design 2 TICPs are potentially viable when the costs are at 2009 levels for both HMA and PCC. If the cost of HMA drops to 80% of its 2009 cost with no change in the cost of PCC, then the results indicate that there is a significant improvement in the allowable PCC thicknesses in the TICPs.

Assuming that 70% is the minimum cost of TICP PCC relative to JPCP PCC, half of the TICPs have equal NPV to the JPCPs with 1:1 cost scenarios and two thirds of the TICPs have equal NPV to the JPCPs with 0.8:1 cost scenarios. An equal NPV between TICP and JPCP is more likely achieved with a thinner asphalt overlay and with an HMA rather than an RHMA overlay.

Table 6-4: Caltrans Case 1: Change of PCC thickness in TICP pavement for same NPV as JPCP with 1:1 costs.

Traffic Handling Cost on M&R (% pave cost)	HMA/RHMA type, thickness (mm)	TICP Design No.	Max TICP PCC thickness for equal NPV (mm)	Cost of TICP PCC relative to JPCP PCC for equal NPV and PCC thickness in JPCP and TICP
15	HMA 105	1	136	45%
15	RHMA 75	1	153	51%
15	HMA 30	2	207	81%
15	HMA 45	2	180	71%
15	RHMA 30	2	193	76%
15	RHMA 45	2	160	63%
50	HMA 105	1	141	47%
50	RHMA 75	1	159	53%
50	HMA 30	2	218	85%
50	HMA 45	2	192	75%
50	RHMA 30	2	205	80%
50	RHMA 45	2	173	68%

Table 6-5: Caltrans Case 1: Change of PCC thickness in TICP pavement for same NPV as JPCP with 0.8:1 costs.

Traffic Handling Cost on M&R (% pave cost)	HMA/RHMA type, thickness (mm)	TICP Design No.	Max TICP PCC thickness for equal NPV (mm)	Cost of TICP PCC relative to JPCP PCC for equal NPV and PCC thickness in JPCP and TICP
15	HMA 105	1	171	57%
15	RHMA 75	1	185	62%
15	HMA 30	2	217	85%
15	HMA 45	2	196	77%
15	RHMA 30	2	207	81%
15	RHMA 45	2	180	71%
50	HMA 105	1	175	58%
50	RHMA 75	1	190	63%
50	HMA 30	2	229	90%
50	HMA 45	2	208	82%
50	RHMA 30	2	218	85%
50	RHMA 45	2	192	75%

Life Extension Analyses. The results of the life extension analyses are shown for the 1:1 cost ratios between HMA and PCC in Table 6-6 and for the 0.8:1 cost ratios between HMA and PCC in Table 6-7. The results indicate that except for thin overlays on Design 2 TICPs, a more than 70% increase in the life of the PCC layer in the TICP must be achieved to be economically competitive with JPCP. This is because the initial cost of constructing a full scale PCC pavement with the additional overlay is not compensated for sufficiently in later years by the reduced maintenance and rehabilitation costs, with this discount rate. The results do not change significantly by reducing the HMA costs to 80% of 2009 values while holding PCC costs at 2009 values because most of the initial cost of the TICP is in the PCC layer.

Table 6-6: Caltrans Case 1: Change of PCC life in TICP pavement for same NPV as JPCP with 1:1 costs.

Traffic Handling Cost on M&R (% pave cost)	JPCP PCC thickness (mm)	TICP PCC thickness (mm)	HMA/RHMA type, thickness (mm)	TICP Design No.	TICP % PCC life change for same NPV
15	300	300	HMA 105	1	>70%
15	300	300	RHMA 75	1	>70%
15	300	255	HMA 30	2	37%
15	300	255	HMA 45	2	70%
15	300	255	RHMA 30	2	54%
15	300	255	RHMA 45	2	>70%
50	300	300	HMA 105	1	>70%
50	300	300	RHMA 75	1	>70%
50	300	255	HMA 30	2	27%
50	300	255	HMA 45	2	64%
50	300	255	RHMA 30	2	44%
50	300	255	RHMA 45	2	>70%

Table 6-7: Caltrans Case 1: Change of PCC life in TICP pavement for same NPV as JPCP with 0.8:1 costs.

Traffic Handling Cost on M&R (% pave cost)	JPCP PCC thickness (mm)	TICP PCC thickness (mm)	HMA/RHMA type, thickness (mm)	TICP Design No.	TICP % PCC life change for same NPV
15	300	300	HMA 105	1	>70%
15	300	300	RHMA 75	1	>70%
15	300	255	HMA 30	2	24%
15	300	255	HMA 45	2	54%
15	300	255	RHMA 30	2	37%
15	300	255	RHMA 45	2	>70%
50	300	300	HMA 105	1	>70%
50	300	300	RHMA 75	1	>70%
50	300	255	HMA 30	2	17%
50	300	255	HMA 45	2	44%
50	300	255	RHMA 30	2	30%
50	300	255	RHMA 45	2	67%

6.3. Construction of New Pavement lanes on State Route 70 in California

Project Scope. This case involved the construction of two new pavement lanes on virgin ground creating a dual carriageway where a two lane highway existed. The total project length was 10 km (6.2 miles). Truck lanes totaled 10 lane-km (6.2 lane-miles) and passenger car lanes totaled

10 lane-km (6.2 lane-miles). It was assumed that once the new JPCP was constructed, the passenger car lanes would never need reconstruction, only normal maintenance for concrete surfaces, in perpetuity. Similarly, it was assumed that the passenger car lanes for the TICP would only require normal maintenance for asphalt surfaces, in perpetuity. In the passenger car lanes, it was assumed that a maintenance treatment other than annual maintenance was needed every 20 years for up to 100 years for PCC surfaces, and every 15 years for HMA following the initial service life (50 or 30 years). The high annual maintenance cost of the TICP pavement reflects periodic resurfacing during the initial service life without explicitly identifying when these would occur during that initial period.

The subgrade is assumed to be Type II soil (lean clay). Site preparation costs were ignored for Case 2, as these costs were similar for both JPCPs and TICPs. The passenger car lanes were 3.6 m (12 ft) wide and the truck lanes were 4.2 m (14 ft) wide. Caltrans designs assume joint spacings of 3.6, 3.9, 4.2, 4.5 m (12, 13, 14, 15 ft), with 11 dowels per joint for 3.6 m lanes and 13 dowels for 4.2 m lanes. Dowel costs were included in the PCC cost. The 40-year design ESALs were 55 million, and the traffic index was 14.5. The 20-year design ESALs were 22 million, and the traffic index was 13.

JPCP Design. The pavement design per Table 623.1G of the Highway Design Manual for doweled JPCP with a nominal 40-year design life was the following:

- 255 mm (10 in) PCC
- 150 mm (6 in) lean concrete base (LCB)
- 210 mm (8.5 in) aggregate subbase (ASB)

The maintenance and rehabilitation schedule was assumed as shown in Table 6-8.

Table 6-8: Caltrans Case 2 JPCP truck lane maintenance and rehabilitation schedule.

Truck lane				
Item	Year	Cost/ln-mi	Design Life	Annual Maintenance Cost/ln-mi
Initial JPCP	0	Calculated elsewhere	45	\$800
CPR-C	45	\$89,000	5	\$3000
CPR-B	50	\$106,000	10	\$1500
Reconstruct JPCP *	60	Same as Year 0	45	\$800

Passenger lane				
Item	Year	Cost/ln-mi	Design Life	Annual Maintenance Cost/ln-mi
Initial JPCP	0	Calculated elsewhere	45	\$800
CPR-C	45	\$89,000	20	\$3000
CPR-C *	65	\$89,000	20	\$3000

** for 75 year analysis period*

Special notes for this project and for Table 6-8 include the following:

- Concrete Pavement Rehabilitation B involves pavement grinding, moderate slab replacement, spall repair, & joint seal repair. It is for JPCP projects with a total number of slabs in the lane that were replaced or exhibit third stage rigid cracking between 2 and 5%.
- Concrete Pavement Rehabilitation C involves pavement grinding, minor slab replacement, spall repair, & joint seal repair. It is for JPCP projects with a total number of slabs in the lane that were replaced or exhibit third stage rigid cracking of 2% or less.

TICP Design 1. The pavement design per Table 623.1G of the Highway Design Manual for doweled JPCP with a nominal 40-year design life was the following:

- 255 mm PCC (10 in) (PCC thickness is solved for in thickness changes cases)
- 150 mm (6 in) LCB
- 210 mm (8.4 in) ASB

The following two asphalt overlays were considered:

- 105 mm (4 in) HMA
- 75 mm (3 in) RHMA

The maintenance and rehabilitation schedule were assumed as shown in Table 6-9.

Table 6-9: Caltrans Case 2 TICP Design 1 maintenance and rehabilitation schedule.

Item	Year	Cost/ln-mi	Design Life	Lanes	Annual Maintenance Cost/ln-mi
Initial TICP	0	Calculated	50 + LE*	Reconstruct PCC/base in truck lanes (18 ln-km) and overlay all lanes (32 ln-km)	\$4800**
FO+JPCP SR	50 + LE*	\$91,000	8	Truck lanes (18 ln-km)	\$700
75 mm Overlay	50 + LE*	Calculated	15	Passenger lanes (14 ln-km)	\$4800
FO+JPCP SR	50 + LE* + 8	\$91,000	7	Truck lanes (18 ln-km)	\$700
Repeat TICP	50 + LE* + 15	Same as initial TICP	50 + LE*	Truck lanes (18 ln-km)	\$700
75 mm Overlay	50 + LE* + 15	Calculated	15	Passenger lanes (14 ln-km)	\$4800

** Life Extension (LE) additional years solved for in life extension analyses, equal to zero in TICP PCC thickness analyses.
 ** Annual maintenance cost for TICP and other longer life overlays includes cost of patching and other late-life maintenance, cost of periodic replacement of the overlay for long design lives of the TICP overlays. This value comes from the Caltrans LCCA Manual.*

TICP Design 2. The pavement design per Table 623.1G of the Highway Design Manual for doweled JPCP with a nominal 20-year design life is the following:

- 225 mm (9 in) PCC (PCC thickness is solved for in TICP PCC thickness analyses)
- 120 mm (4.7 in) LCB (assumed to be 150 mm (6.0 in) for cost calculations)
- 180 mm (7 in) ASB (assumed to be 210 mm (8.3 in) for cost calculations)

The following four asphalt overlays were considered:

- 30 mm (1.2 in) HMA
- 45 mm (1.8 in) HMA
- 30 mm (1.2 in) RHMA
- 45 mm (1.8 in) RHMA

The maintenance and rehabilitation schedule were assumed as shown in Table 6-10.

Table 6-10: Caltrans Case 2 TICP Design 2 maintenance and rehabilitation schedule.

Item	Year	Cost/ln-mi	Design Life	Lanes	Annual Maintenance Cost/ln-mi
Initial TICP	0	Calculated	30 + LE*	Reconstruct PCC/base in truck lanes (18 ln-km) and overlay all lanes (32 ln-km)	\$4800***
FO+JPCP SR	30 + LE*	\$91,000	8	Truck lanes (18 ln-km)	\$700
30 or 45 mm Overlay**	30 + LE*	Calculated	15	Passenger lanes (14 ln-km)	\$4800
FO+JPCP SR	30 + LE* + 8	\$91,000	7	Truck lanes (18 ln-km)	\$700
Repeat TICP	30 + LE* + 15	Same as initial TICP	30 + LE*	Truck lanes (18 ln-km)	\$700
30 or 45 mm Overlay**	30 + LE* + 15	Calculated	15	Passenger lanes (14 ln-km)	\$4800
30 or 45 mm Overlay**	30 + LE* + 15 + 15	Calculated	15	Passenger lanes (14 ln-km)	\$4800

* Life Extension (LE) additional years solved for in life extension analyses, equal to zero in TICP PCC thickness analyses.
 ** Overlay thickness same as original TICP overlay thickness
 *** Annual maintenance cost for TICP and other longer life overlays includes cost of patching and other late-life maintenance, cost of periodic replacement of the overlay for long design lives of the TICP overlays. This value comes from the Caltrans LCCA Manual

6.3.1 Caltrans State Route 70 Case Study Results

TICP PCC Thickness Analyses. The results of the thickness change analyses for the 1:1 cost scenario are shown in Table 6-11 and for the 0.8:1 cost scenario in Table 6-12. The results show that Design 2 TICP resulted in a thicker allowable PCC thickness in the TICPs than the Design 1 TICP. This is because the lower initial cost of constructing Design 2 TICPs more than compensated for the later cost of reconstructing the truck lanes a second time with the Caltrans official discount rate of four percent.

Assuming that an absolute minimum thickness for the PCC in the TICPs was 125 mm (5 in), it can be seen that most of the Design 2 scenarios were potentially viable when the HMA and PCC costs were at 2009 levels. If the cost of the HMA dropped to 80% of its 2009 costs and the PCC

costs remained the same, then the results indicated that there could be a significant improvement in the allowable TICP PCC thicknesses. The Design 1 TICP PCC thicknesses were generally below a reasonable minimum thickness for the PCC layer.

Assuming that 70% is the minimum cost of TICP PCC relative to JPCP PCC, none of the TICPs had equal NPV to the JPCPs with 1:1 cost scenarios, and none of the TICPs had equal NPV to the JPCPs with 0.8:1 cost scenarios.

Table 6-11: Caltrans Case 2 Change of PCC thickness in TICP pavement for same NPV as JPCP with 1:1 costs.

Traffic Handling Cost on M&R (% pave cost)	HMA/RHMA type, thickness (mm)	TICP Design No.	Min. TICP PCC thickness for equal NPV (mm)	Cost of TICP PCC relative to JPCP PCC for equal NPV and PCC thickness in JPCP and TICP
15	HMA 105	1	91	36%
15	RHMA 75	1	103	40%
15	HMA 30	2	144	56%
15	HMA 45	2	126	49%
15	RHMA 30	2	135	53%
15	RHMA 45	2	113	44%
50	HMA 105	1	111	44%
50	RHMA 75	1	123	48%
50	HMA 30	2	166	65%
50	HMA 45	2	149	58%
50	RHMA 30	2	158	62%
50	RHMA 45	2	136	53%

Table 6-12: Caltrans Case 2 Change of PCC thickness in TICP pavement for same NPV as JPCP with 0.8:1 costs.

Traffic Handling Cost on M&R (% pave cost)	HMA/RHMA type, thickness (mm)	TICP Design No.	Min. TICP PCC thickness for equal NPV (mm)	Cost of TICP PCC relative to JPCP PCC for equal NPV and PCC thickness in JPCP and TICP
15	HMA 105	1	113	44%
15	RHMA 75	1	122	48%
15	HMA 30	2	151	59%
15	HMA 45	2	137	54%
15	RHMA 30	2	144	56%
15	RHMA 45	2	126	49%
50	HMA 105	1	133	52%
50	RHMA 75	1	142	56%
50	HMA 30	2	173	68%
50	HMA 45	2	159	62%
50	RHMA 30	2	166	65%
50	RHMA 45	2	149	58%

Life Extension Analyses. The results of the life extension analyses are shown for the 1:1 cost scenarios in Table 6-13 and for the 0.8:1 cost scenarios in Table 6-14. The results indicate that life extension, even up to 70%, for the TICP PCC layer did not result in them being economically competitive. This is because, with the assumed discount rate, the initial cost of constructing equal amounts of PCC in both the JPCP and TICP pavements overwhelmed any future maintenance and rehabilitation savings. The primary difference between Case 1 and Case 2 in this regard was that in Case 1, the passenger lanes made use of existing JPCP lanes which were simply overlaid and did not include the cost of constructing new PCC layers for the TICP in the passenger lanes.

Table 6-13: Caltrans Case 2 Change of PCC life in TICP pavement for same NPV as JPCP with 1:1 costs.

Traffic Handling Cost on M&R (% pave cost)	JPCP PCC thickness (mm)	TICP PCC thickness (mm)	HMA/RHMA type, thickness (mm)	TICP Design No.	TICP % PCC life change for same NPV
15	255	255	HMA 105	1	>70%
15	255	255	RHMA 75	1	>70%
15	255	225	HMA 30	2	>70%
15	255	225	HMA 45	2	>70%
15	255	225	RHMA 30	2	>70%
15	255	225	RHMA 45	2	>70%
50	255	255	HMA 105	1	>70%
50	255	255	RHMA 75	1	>70%
50	255	225	HMA 30	2	>70%
50	255	225	HMA 45	2	>70%
50	255	225	RHMA 30	2	>70%
50	255	225	RHMA 45	2	>70%

Table 6-14: Caltrans Case 2 Change of PCC life in TICP pavement for same NPV as JPCP with 0.8:1 costs.

Traffic Handling Cost on M&R (% pave cost)	JPCP PCC thickness (mm)	TICP PCC thickness (mm)	HMA/RHMA type, thickness (mm)	TICP Design No.	TICP % PCC life change for same NPV
15	255	255	HMA 105	1	>70%
15	255	255	RHMA 75	1	>70%
15	255	225	HMA 30	2	>70%
15	255	225	HMA 45	2	>70%
15	255	225	RHMA 30	2	>70%
15	255	225	RHMA 45	2	>70%
50	255	255	HMA 105	1	>70%
50	255	255	RHMA 75	1	>70%
50	255	225	HMA 30	2	>70%
50	255	225	HMA 45	2	>70%
50	255	225	RHMA 30	2	>70%
50	255	225	RHMA 45	2	>70%

6.4. Construction of Two Lanes on a Major Highway or Interstate in Minnesota

Background, Assumptions, and Scope. This LCCA focused on construction, maintenance, and rehabilitation costs of TICPs and JPCPs. Similar to the Caltrans case studies, this LCCA was completed with a NPV calculation that considered life cycle costs that were unique to each pavement type and disregarded costs that were common across all pavement types. The following inputs, typical of Minnesota, were considered for this LCCA, which compared the economic viability of TICP and JPCP:

- Analysis period (total years of pavement life with typical maintenance and rehabilitation (M & R) schedules)
- Discount rate
- Pavement lane-miles
- Pavement lane width
- JPCP concrete thickness
- TICP concrete thickness
- TICP asphalt thickness
- Mobilization charges that reflect the difference in mobilizing equipment for composite pavement construction
- M & R schedules for the average rigid and asphalt pavements
- Unit cost of concrete
- Unit cost of asphalt

The following items were not considered for this LCCA:

- Removal of existing pavement
- Subgrade and base preparation
- Shoulder construction, including preparation and materials
- Dowel bars
- Jointing
- Concrete or asphalt placement costs
- Engineering costs

Additionally, items that could vary depending on the length of time for pavement construction and/or location of construction (urban vs. rural) were not considered in the LCCA:

- Traffic handling
- User costs

Finally, costs of annual maintenance performed on the pavements between minor and major rehabilitation projects were not considered.

The assumptions for the LCCA inputs were based on values provided by the Minnesota Department of Transportation (MnDOT) and information collected from construction of a test section of TICP at the Minnesota Road Research Center (Mn/ROAD) in May of 2010. The

inputs for the LCCA are shown below, and each is followed by an explanation or reference. Four of the inputs were varied to show their impacts on total NPV, and these were discount rate, cost of concrete, cost of asphalt, and cost of concrete in TICP relative to the cost of concrete in JPCP.

- Analysis period = 50 years (typical LCCA period for MnDOT projects)
- Discount Rates = 2.8 and 5.0 (Survey of Caltrans, MnDOT, and Washington State Department of Transportation indicated discount rates of 4.0 and 2.8 for a given year. 5.0 was assumed to be a maximum discount rate and 2.8 was considered to be a minimum discount rate.)
- Design lane length = 6.2 mi (10 km) (Similar to the lane length in Case 2 by Caltrans)
- Truck lane width = 13.5 ft (4.1 m) (MnDOT standard truck lane width)
- Passenger lane width = 12 ft (3.6 m) (MnDOT standard passenger lane width)
- JPCP concrete thickness = 9 in (229 mm) (typical MnDOT JPCP thickness)
- TICP concrete thickness = 7 in (178 mm) which is a typical concrete thickness used in European composite pavements
- TICP asphalt thickness = 3 in (76 mm)
- Mobilization charges:
 - JPCP = \$107,000
 - TICP = \$157,000

Additional considerations not included in the above are discussed below.

TICP Mobilization. The \$50,000 premium for TICP mobilization is based on a recommendation from the Minnesota contractor who built the TICP test section. The additional cost is attributed to additional pavers and/or additional aggregate silos for mobile concrete batch plants required for composite pavement construction.

Minor and major maintenance and rehabilitation costs. Table 6-15 and Table 6-16 show M & R schedules for high-volume bituminous and concrete pavements based on MnDOT’s recommendations (MnDOT Engineering Services Technical memorandum No. 04-19-MAT-02, September 7, 2004) and M & R data provided by MnDOT’s pavement management division from 30 years of MnDOT’s experience with minor and major M&R projects on JPCPs and JPCPs with asphalt overlays. It was assumed that the TICP required the same M & R procedures as a high-volume, conventional bituminous pavement.

Table 6-15: MN Case 3 bituminous pavement M & R schedule for ESALs > 7 million.

Pavement Age	Treatment
0	initial construction
7	crack fill
15	mill and overlay
20	crack fill
27	mill and overlay
32	crack fill
40	mill and overlay
45	crack fill
50	end of analysis period (no residual value)

Table 6-16: MN Case 3 concrete pavement M & R schedule.

Pavement Age	Treatment
0	initial construction
17	minor re-seal and minor CPR (partial depth repairs)
27	Minor CPR (partial depth repairs) and some full depth repairs
40	major CPR (Full depth repair and diamond grind)
50	end of analysis period (no residual value)

CPR=concrete pavement restoration

Unit costs of concrete and asphalt. Three levels of material cost were assumed for both concrete and asphalt. The potential range of costs was based on typical MnDOT estimating quantities as well as bid prices provided by contractors who submitted bids to build the TICP test section. Concrete and asphalt costs and their designations as low, medium, or high are shown in Table 6-17.

Table 6-17: MN Case 3 range of concrete and asphalt costs used for the LCCA.

Concrete or Asphalt \$ per yd ³ (m ³)	Price designation
38 (50)	Low
115 (150)	Medium
230 (300)	High

Cost of TICP concrete as a percentage of JPCP concrete. One of the benefits of composite pavements is that the concrete layer has an HMA layer protecting it to some degree from the extreme environmental stresses and tire wear that a typical JPCP surface must endure. This implies that it would be possible to decrease the cost of composite pavements by either decreasing the thickness of the concrete layer or by decreasing the cost of the cement or aggregates in the concrete layer. A reduction in cost of the TICP PCC layer could be accomplished by increasing the percentage of supplementary cementitious materials in the total cementitious volume, by substituting recycled concrete aggregates for conventional coarse aggregates, or by allowing a higher percentage of fine, soft, spall, or slate in the coarse aggregate. Decreasing the cost of concrete is not limited to these examples. In a region with low aggregate quality where it is necessary to haul aggregates long distances from an acceptable source, TICP pavement construction could potentially allow the use of aggregates closer to the construction site, which would decrease the project's cost.

6.4.1 Minnesota Case Study Results

The Minnesota LCCA analysis considered the economic viability of building TICPs if the cost of the TICP concrete was 25%, 50%, 75%, or 100% the cost of the JPCP concrete.

Figure 6-27 shows how the ratio of NPV of TICP to JPCP depended on asphalt cost, JPCP concrete cost, TICP concrete cost as a percentage of JPCP concrete cost, and discount rate. The low, medium and high designations in the top left plot indicate the cost of JPCP concrete, and these designations are typical for all plots. The data in the top row of plots was calculated with a discount rate of 2.8, and the data in the bottom row of plots was calculated with a discount rate of 5.0. The horizontal line in all the plots at a TICP/JPCP ratio of 1.0 indicates that the NPVs of TICP and JPCP were equal. Ratios above this line indicate it is more cost competitive to build

JPCPs and ratios below this line indicate that it is more cost competitive to build composite TICPs. The following trends can be observed in Figure 6-27.

- As the cost of JPCP concrete increases, TICP become more cost competitive with JPCP.
- If the cost of JPCP concrete is low, it is almost never cost competitive to build TICP instead of JPCP pavements. This remains true despite the discount rate, cost of asphalt, and decrease in concrete cost for TICP concrete.
- If the cost of TICP concrete is equal to 100% of the cost of JPCP concrete, it is almost never cost competitive to build TICPs rather than JPCPs. At best, the NPV of the TICP equals the NPV of the JPCP.
- As the cost of asphalt increases, the cost of TICP concrete must decrease relative to the cost of JPCP concrete in order for TICP to remain cost competitive with JPCP. Table 6-18 shows the NPV breakeven range for the cost of TICP concrete relative to JPCP concrete for asphalt and JPCP concrete costs that are low, medium, and high. Realistically, if the cost of TICP concrete must be less than 60% of the cost of JPCP concrete in order for TICP to be cost competitive with JPCP, it is an unrealistic cost to achieve.
- An increase in discount rate increases the likelihood that TICP will be cost competitive with JPCP. In Table 6-18, the range of TICP concrete costs as a percentage of JPCP concrete costs results from the two discount rate values.

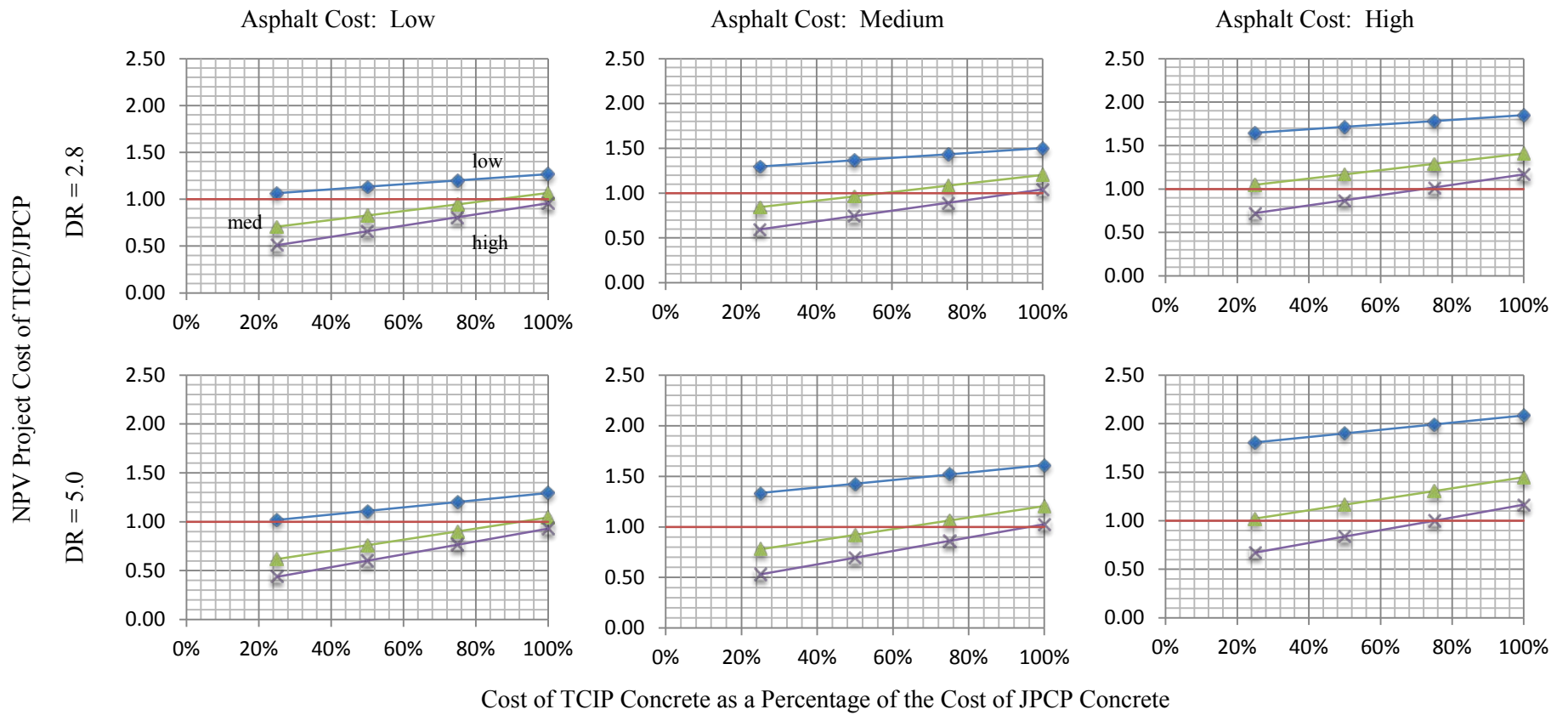


Figure 6-1: The ratio of the NPV of TICP to the NPV of JPCP, which are dependent on asphalt cost, JPCP concrete cost, TICP concrete cost as a percentage of JPCP concrete cost, and discount rate.

Table 6-18: MN Case 3 breakeven range for the cost of TICP concrete as a percentage of JPCP concrete.

Concrete Cost	Asphalt Cost		
	Low	Med	High
Low	20-25%	Never	Never
Med	86-92%	58-64%	<25%
High	> 100%	92-96%	72-67%

6.5. Structural Analysis and LCCA

In the previous sections, a framework for the LCCA analysis was presented based on various performance assumptions. However for each site conditions, these assumptions need to be checked using the performance prediction models developed under TPF-5(149) and presented in previous chapters.

For example, for pavement projects set in Sacramento, CA, the long-term performance of the majority of TICP (described above in tables such as Table 6-4) could not match the performance of a 300 mm thick PCC pavement. Only TICP with 190 mm PCC and 75 mm thick AC surface layer was found to exhibit similar structural performance under similar traffic. This means that if the general construction cost (per cubic yard, for instance) of the PCC layer of the TICP is the same as the cost of the PCC layer in the JPCP and the cost of the AC layer is 80 percent of the 2009 cost (as assumed earlier), then only this TICP will be a cost-effective alternative to JPCP. However, if construction costs for the PCC layer are reduced, then other design alternatives may also cost competitive.

Similarly, for Minnesota conditions, a 9-inch JPCP project demonstrated the same predicted structural performance as a 2-inch AC over 7-inch PCC TICP, as was illustrated in Section 4.3. Using the LCCA presented above, this design may not be cost effective, depending on the costs of construction, particularly material costs. Therefore, only the LCCA with site specific cost data combined with detailed structural modeling for the site conditions can provide information on the feasibility of TICP as a cost-effective alternative to JPCP.

Chapter 7. Conclusions and Recommendations

The FHWA Pooled Fund Project TPF-5(149) Thermally Insulated Concrete Pavement project, focused on the design, cost analysis, construction, and analysis of AC overlays of newly constructed PCC pavements. The title of the project refers to the idea, at the outset, that the AC overlay provided a kind of thermal insulation to reduce the severity of thermal gradients, and their associated deformation (curl), in the PCC layer. While that insulating effect is observed in this study, that observation is far from the major product of this project. Rather, the opportunity to research design and construction for TICP presented an indirect opportunity to develop research products, including models and software for the design and analysis of TICP, that are as applicable to AC overlays of existing PCC as they are AC overlays of newly constructed PCC pavements.

Chapter 2 details the investigation of the MEPDG procedure for AC-PCC projects conducted under this project. This included a comprehensive sensitivity study, spanning thousands of MEPDG project runs, of the effect of climate on the MEPDG performance prediction. Pavement performance was simulated at more than 600 locations across the US using the climatic database data supplied by the MEPDG. It was found that differences in predicted pavement performance among stations with similar environmental conditions were greater than expected, and a significant portion of this difference had to do with non-uniform quality of the climate data in the database and the effect of this data on the EICM and consequently the MEPDG. Research published using TPF-5(149) results represented the first study with extensive, verifiable analysis of this circumstance, and that research recommended that all stations with incomplete data be removed from the database.

Another focus of the project was a better understanding of how mechanistic-empirical models (such as the MEPDG) characterize the response of the AC overlay. This aspect of the project work is described in Chapter 3. The use of a single load duration-dependent AC dynamic modulus seemed insufficient for composite pavements subjected to a combination of traffic loads and temperature curling, as a significant difference was found in the load-duration dependent AC dynamic modulus when a composite pavement is subjected to typical traffic loads and to one hour of temperature loads. Thus, a stress computation procedure, known as the *2-moduli approach*, was developed to calculate stresses in the composite pavement subjected to a combination of traffic loads and temperature curling using two load duration-dependent AC moduli. The stresses computed using the 2-moduli approach and the existing MEPDG procedure were found to be significantly different when composite pavements are subjected to a combination of traffic loading and temperature curling. A framework for the implementation of the proposed stress procedure into the MEPDG was developed, although more research efforts will be required to fully implement the approach into the MEPDG framework.

The research of the project endeavored to assess the current state-of-the-art in M-E models for rutting, reflective cracking, and faulting and to adopt these models/procedures to the MEPDG. The work in reflective cracking is especially important given the challenges discussed in Chapter 4. The developed models were incorporated into a program that interfaces with the MEPDG easily and quickly. In this respect, the TPF-5(149) is far more suitable for design with the

MEPDG, as it can be used alongside the MEPDG without any difficulty for the typical pavement engineer.

Chapters 5 and 6 detail equally important issues in the construction and estimated costs of AC-PCC projects. These issues are coupled in that, as described in Chapter 6, based on the review of the LCCA case studies performed, the cost effectiveness of AC-PCC designs were found to depend very heavily on the costs of construction, particularly material costs, and were less dependent on projected maintenance/rehabilitation costs. Thus, this is one aspect of the TPF-5(149) project that is in need of additional analysis, as, given the dependence on initial construction costs, only LCCA with site specific cost data combined with detailed structural modeling for the site conditions can provide information on the feasibility of TICP as a cost-effective alternative to JPCP.

Overall, as can be verified chapter-by-chapter, while the original intent of the project was the design and construction of TICP, the research results directly addressed important results in the design, analysis, and construction of composite (asphalt-over-concrete) pavements in general. The project recommended extensive revisions and improvements to the MEPDG, and the project work in LCCA represents the first steps in a rigorous assessment of TICP's potential performance and cost benefits.

References

- AASHTO (2008). *Mechanistic-Empirical Pavement Design Guide: A Manual of Practice*. American Association of State Highway and Transportation Officials, Washington, D.C.
- AASHTO T 321. Standard Method of Test for Determining the Fatigue Life of Compacted Hot-Mix Asphalt (HMA) Subjected to Repeated Flexural Bending, *American Association of State Highway and Transportation Officials*, 2007.
- ABAQUS/Standard. Hibbitt, Karlsson & Sorensen Inc. User's Manual, Vol. 1, 10.6.1, 1997.
- ACPA 1994. Slab Stabilization Guidelines for Concrete Pavements. TB018P. American Concrete Pavement Association, Skokie IL.
- ACPA 1995. Joint and Crack Sealing and Repair for Concrete Pavements. Technical Bulletin TB012P. American Concrete Pavement Association, Skokie IL.
- ACPA 2003. Concrete Pavement Repair Manual. JP002P. American Concrete Pavement Association, Skokie IL.
- ACPA, 2006b. Pavement Surface Characteristics: A Synthesis and Guide, Draft Report, American Concrete Pavement Association, April 2006.
- ACPA. 2006a. Concrete Pavement Field Reference – Preservation and Repair. Report EB239P. American Concrete Pavement Association, Skokie IL.
- Al-Qadi, I. L., and M. A. Elseifi. Field Installation and Design Considerations of Steel Reinforcing Netting to Reduce Reflection of Cracks. In *Proceedings of the International RILEM Conference, No. 37, Cracking in Pavements—Mitigation, Risk Assessment, and Prevention* (C. Petit, I. L. Al-Qadi, and A. Millien, eds.), Limoges, France, 2004, pp. 97–104.
- Al-Qadi, I., W. Buttlar, J. Baek, and M. Kim. 2009. Cost-Effectiveness and Performance of Overlay Systems in Illinois -Volume 1: Effectiveness Assessment of HMA Overlay Interlayer Systems Used to Retard Reflective Cracking. Report No. ICT -09-044. Illinois Center for Transportation Springfield.
- Al-Qadi, S. H. Carpenter, Z. Leng, H. Ozer, J. S. Trepanier, Tack Coat Optimization for HMA Overlays: Laboratory Testing, Illinois Department of Transportation, FHWA-ICT-08-023.
- American Association of State Highway and Transportation Officials. Guide for Design of Pavement Structures, Washington, D.C. 1993.
- American Association of State Highway and Transportation Officials. Mechanistic-Empirical Pavement Design Guide, Interim Edition: A Manual of Practice. Washington, D.C. 2008.

- American Association of State Highway and Transportation Officials (2002). AASHTO Standard Practice for Determination of International Roughness Index for Quantifying Roughness of Pavements – AASHTO PP 37, Washington D.C.
- Ameri-Gaznon, M. and D. Little. 1988. Permanent Deformation Potential in Hot mix asphalt Overlays over Portland Cement Concrete Pavements. Report No 452-3F. Texas State Department of Highways and Public Transportation, Austin TX.
- Amini, F. 2005. “Potential applications of paving fabrics to reduce reflective cracking. Jackson State University, Report FHWA/MS-DOT-RD-05-174, Jackson MS.
- ANSYS, Inc. Theory Reference. ANSYS Release 9.0. 4-60, 2004.
- Arudi, R. S., Minkarah, I., Kandula, K., and A. Gosain. Performance Evaluation of Asphalt Overlays on Broken and Seated Concrete Pavements. In Transportation Research Record 1543, TRB, National Research Council, Washington D.C., 1996.
- Arudi, Rajagopal S.; Minkarah, Issam; Kandula, Krishna; Gosain, Archana. 1996. Performance evaluation of asphalt overlays on broken and seated concrete pavements. Transportation Research Record, n 1543, National Research Council, p 55-62.
- Baek, Jongeun, Al-Qadi, Imad L. Finite Element Method Modeling of Reflective Cracking Initiation and Propagation - Investigation of the Effect of Steel Reinforcement Interlayer on Retarding Reflective Cracking in Hot-Mix Asphalt Overlay. In Transportation Research Record 1949, TRB, National Research Council, Washington D.C., 2006 pp32-42.
- Bahia H. U., Anderson D. A., and Christensen D. W. The Bending Beam Rheometer; A Simple Device for Measuring Low-Temperature Rheology of Asphalt Binders. Journal of Association of Asphalt Paving Technologists, Vol. 61, pp. 117-153, 1992.
- Baker, R.F. “New Jersey Composite Pavement Project,” *Highway Research Record*, Number 434, pp. 16-23, 1973.
- Banan M. and Hjelmstad. Data-Based Mathematical Modeling: Development and Application. SRS No. 590, Civil Engineering Studies, University of Illinois, Urbana, IL 1994.
- Baumgardner, R., and D. Mathis. 1989. Concrete Pavement Drainage Rehabilitation, State of the Practice Report. Experimental Project No. 12. Federal Highway Administration, Demonstration Projects Division, Washington D.C.
- Becker, D. Rubblization. Design and Construction Guidelines of Rubblizing and Overlaying PCC Pavements with Hot-Mix Asphalt. National Asphalt Pavement Association, 2006.
- Belshe, M., K. Kaloush, and J. Golden. *The Urban Heat Island Effect and Impact of AR-ACFC Overlays on PCC Pavements*. Asphalt Rubber International Conference, Palm Springs, CA, 2006.

- Bemanian, Sohila; Sebaaly, Peter. 1999. Cost-effective rehabilitation of portland cement concrete pavement in Nevada. Transportation Research Record, National Research Council, n1684, p 156-164.
- Bennert, T. 2009. A Rational Approach to the Prediction of Reflective Cracking in Bituminous Overlays for Concrete Pavements. Dissertation. Rutgers, the State University of New Jersey, New Brunswick.
- Bennert, T., Flexible Overlays for Rigid Pavements. Publication FHWA-NJ-2009-014, New Jersey Department of Transportation, 2010
- Bennert, T.A. (2011). A rational approach to the prediction of reflective cracking in bituminous overlays for concrete pavements. Doctoral thesis. Rutgers University, New Brunswick, New Jersey.
- Bennert, Thomas, and Maher, Ali. Evaluation of Current State of Flexible Overlay Design for Rigid and Composite Pavements in the United States. In Transportation Research Record 1991, TRB, National Research Council, Washington D.C., 2007.
- Bennert, Thomas; Maher, Ali. 2007. Evaluation of current state of flexible overlay design for rigid and composite pavements in the United States. Transportation Research Record, n 1991, National Research Council, p 97-108.
- Bennert, Thomas; Worden, Michael; Turo, Matthew. 2009. Field and laboratory forensic analysis of reflective cracking on Massachusetts Interstate 495. Transportation Research Record, n 2126, National Research Council, p 27-38, 2009.
- Benson, J. S., J. A. Scherocman, Construction of Durable Longitudinal Joints, Transportation Research Circular, E-C105, Factors Affecting Compaction of Asphalt Pavements, September 2006, pp 120-139.
- Bishoff, D., and A. Toepel. 2002. Dowel Bar Retrofit – STH 13 Construction and One-Year Performance Report. WI-07-02. Wisconsin Department of Transportation.
- Blankenship, P. Reflective Cracking Relief Interlayer for Composite Pavements. Asphalt Vol. 22 No. 2. Asphalt Institute, 2007. <<http://www.asphaltinstitute.org>>
- Blankenship, P., Iker, N., DRBohlav, J. Interlayer and Design Considerations to Retard Reflective Cracking. In Transportation Research Record 1896, TRB, National Research Council, Washington D.C., 2004, pp. 177-186.
- Bradley, M., T Larsen, W. Temple, R. Gains, and A. Thomas. 1986. Longitudinal Edge Drains in Rigid Pavement Systems. Report FHWA-TS-86-208. Federal Highway Administration, Washington D.C.
- Brewer, W. Sand Anti-Fracture Mixture on I-35 in Logan County, Oklahoma. Research, Development and Technology Transfer, March 1997.

- Brown, E. R. Basics of Longitudinal Joint Compaction, Transportation Research Circular, E-C105, Factors Affecting Compaction of Asphalt Pavements, September 2006, pp 86-95.
- Burati, J. L., R. M. Weed, C. S. Hughes, H. S. Hill, Publication FHWA-RD-02-095, Clemson University, 1995.
- Butler, W., Bozkurt, D., Dempsey, B. Cost Effectiveness of Paving Fabrics used to Control Reflective Cracking. In Transportation Research Record 1730, TRB, National Research Council, Washington D.C, 2000.
- Button, J. Overlay Construction and Performance Using Geotextiles. In Transportation Research Record 1284, TRB, National Research Council, Washington, D.C, 1989.
- Button, J., and R. Lytton. 2003. Guidelines for Using Geosynthetics with HMA Overlays to Reduce Reflective Cracking. 0-1777-P2. Texas Transportation Institute.
- Button, J., and R. Lytton. 2007. "Guidelines for using geosynthetics with hot mix asphalt overlays to reduce reflective cracking." Transportation Research Record, n 1608, National Academy of Sciences, Washington DC.
- Caltrans. CPB 03-1 Paint Binder (Tack Coat) Guidelines, California Department of Transportation, Construction Procedure Bulletin, 2003.
- Caltrans. MTAG Volume II - Rigid Pavement Preservation 2nd Edition: CHAPTER 2—SURFACE CHARACTERISTICS. Caltrans Division of Maintenance. California Department of Transportation. 2007.
- Ceylan H., Tutumluer E., and Barenberg E. J. Artificial Neural Networks As Design Tools In Concrete Airfield Pavement Design. Proceedings of the 25th International Air Transportation Conference, Austin, Texas, June 14-17, pp. 447-465, 1998.
- Ceylan H., Tutumluer E., and Barenberg E. J. Artificial Neural Network Analyses of Concrete Airfield Pavements Serving the Boeing B-777 Aircraft. Transportation Research Record 1684, National Research Council, Washington, D.C., pp. 110-117, 1999.
- Ceylan H., Tutumluer E., and Barenberg E. J. Effects of Combined Temperature and Gear Loading on the Response of Concrete Airfield Pavements Serving the Boeing B-777 Aircraft. Proceedings of the International Air Transport Conference (IATC), 20th Vision of Air Transportation, San Francisco, California, June 18-21, 2000.
- Ceylan, H., Gopalakrishnan, K., Coree, B., Kota, T., Mathews, R. Rehabilitation of Concrete Pavements Utilizing Rubblization: A Mechanistic Based Approach to HMA Overlay Thickness Design. International Journal of Pavement Engineering, Vol. 9 No. 1. Taylor & Francis Limited, 2008.
- Ceylan, H., Mathews, R., Kota, T., Gopalakrishnan, K., Coree, B. Rehabilitation of Concrete Pavements Utilizing Rubblization and Crack and Seat Methods. Iowa Highway Research

- Board, Iowa Department of Transportation. Center for Transportation Research and Education, Iowa State University, Final Report No. CTRE 02-106, June 2005.
- Ceylan, H., Mathews, R., Kota, T., Goplalkrishnan, K. and B. Coree. 2005. Rehabilitation of Concrete Pavements Utilizing Rubblization and Crack-and-seat Methods. Iowa Highway Research Board Report No. TR-473. Center for Transportation Research and Education. Ames IA.
- Chen T. Determining a Prony Series for a Viscoelastic Material from Time Strain Data. NASA/TM-2000-210123, ARL-TR-2206, Langley Research Center, Hampton, Virginia, 2000.
- Cho, Y.-H., Liu, C., Dossey, T., and B. McCullough. 1998. "Asphalt overlay design methods for rigid pavements considering rutting, reflection cracking, and fatigue cracking." Center for Transportation Research, Report 987-9, University of Texas, Austin TX.
- Chou Y. T. Structural Analysis Computer Programs for Rigid Multicomponent Pavement Structures with Discontinuities - WESLIQID and WESLAYER, Technical Report GL-81-6, U.S. Army Engineer Waterways Experiment Station, May 1981.
- Chowdhury, A., J. Button, and R. Lytton. 2009. Tests of HMA Overlays Using Geosynthetics to Reduce Reflective Cracking. Report No. 0-1777-3. Texas Department of Transportation.
- Christensen, D.W. and R. F. Bonaquist. 2006. Volumetric Requirements for Superpave Mix Design. NCHRP Report 567. National Cooperative Highway Research Program. Transportation Research Board of the National Academies, Washington D.C.
- Christensen, D.W. and R. F. Bonaquist. 2011. A Manual for Design of Hot Mix Asphalt with Commentary. NCHRP Report 673. National Cooperative Highway Research Program. Transportation Research Board of the National Academies, Washington D.C.
- Christopher, B. 2000. Maintenance of Highway Edge Drains. NCHRP Synthesis of Highway Practice 285. Transportation Research Board, Washington D.C.
- Christopher, B., and V. McGuffey. 1997. Pavement Subsurface Drainage Systems. Synthesis of Highway Practice Report Number 239. National Cooperative Highway Research Program. Washington D.C.
- Christory, J.P., Grob, D., Guidoux, Y., Sainton, A. "Composite Pavements: An Example of a 'Shared Technique' for Better Public Spaces and Road Infrastructures", *7th International Conference on Concrete Pavements*, Orlando, FL, Sept. 9-13, 2001.
- Cleveland, G., Button, J., and R. Lytton. 2002. Geosynthetics in Flexible and Rigid Pavement Overlay Systems to Reduce Reflection Cracking. Report No. 1777-1. Texas Transportation Institute.
- Cleveland, G., J. Button, and R. Lytton. 2004. Using Geosynthetics In Overlays to Minimize Reflection Cracking. Project Summary Report 0-1777-S. Texas Transportation Institute.

- Cook R. D., Malkus D. S., and Plesha M. E. Concepts and Applications of Finite Element Analysis. John Wiley & Sons, Inc., 1974.
- Cooper, J., McDougall, J., Lynch, D. Rehabilitation of a Major Urban Freeway Using a Hot Mix Overlay. Proceedings of the Asphalt Paving Technologists Technical Session, Vol. 53. Scottsdale Arizona, 1984.
- Cumbaa, Steven L., and Paul, Harold R. LTRC 211 “Latex Modified Asphalt and Experimental Joint Treatments on Asphaltic Concrete overlays Experimental Project No. 3 Asphalt Additives” Louisiana Transportation Research Center & Louisiana Department of Transportation and Development, June 1988.
- Daleiden, J. F., Simpson, A. L., and Rauhut, J. B., “Rehabilitation Performance Trends: Early Observations from Long-Term Pavement Performance (LTPP) Specific Pavement Studies (SPS),” Report No. FHWA-RD-97-099, 1998
- Daleiden, Jerome F.; Ooten, David A.; Sargent, Mark D. 1995. Rehabilitation of a jointed portland cement concrete pavement on I-35 (southbound) in Kay County, Oklahoma. Transportation Research Record, n 1513, National Research Council, p 61-69.
- Daniel J. S., Kim Y. R., and Lee H. Effects of Aging on Viscoelastic Properties of Asphalt-Aggregate Mixtures. Transportation Research Record, Vol. 1630, pp. 21-27, 1998.
- Darter M. I. et al. Composite Pavement Systems. Draft Interim Report, Project SHRP2 R21, Transportation Research Board, Washington D.C. 2008.
- Darter, M. J. Becker, M. Snyder, and R. Smith. 1985. Portland Cement Concrete Pavement Evaluation System (COPES). NCHRP Report 277. Transportation Research Board, Washington D.C.
- Darter, M., Barenberg, E., and W. Yrjanson. 1985. Joint Repair Methods for Portland Cement Concrete Pavements. NCHRP Report 28. Transportation Research Board, Washington D.C.
- Darter, M.I., and E.J. Barenberg. *Zero-Maintenance Pavement: Field Studies on the Performance Requirements and Capabilities of Conventional Pavement Systems*, Report FHWA-RD-76-105, FHWA, 1976.
- Davids W. G., Turkiyyah G. M., and Mahoney J. EVERFE -- a New Rigid Pavement Finite Element Analysis Tool, Transportation Research Record No. 1629, pp. 69-78, Washington D. C. 1998.
- Deacon, J.A, Harvey, J.T., Guada, I., Popescu, L., and C.L. Monismith (2002). *Analytically based approach to rutting prediction*. Transportation Research Record: Journal of the Transportation Research 1806:1, pp. Transportation Research Board of the National Academies, Washington D.C.

- Deacon, J.A., Harvey, J.T., Guarda, I., Popescu, L., and Monismith, C.L., Analytically based Approach to Rutting Prediction, Transportation Research Record, TRR-1806, Washington, DC, 2002.
- Decker, D. S., State-of-the-Practice for Cold-Weather Compaction of Hot-Mix Asphalt Pavements, Transportation Research Circular, E-C105, Factors Affecting Compaction of Asphalt Pavements, September 2006, pp 27-35.
- Delatte, N. J., Amer, N., Storey, C., *Improved Management of RCC Pavement Technology*, UTCA Report Number 01231, The University Transportation Center for Alabama, February 2003.
- Delatte, Norbert. Simplified Design of Roller Compacted Concrete (RCC) Composite Pavement. *TRB Annual Meeting*, Washington D.C., 2004.
- Dempsey, B.J. Development and Performance of Interlayer Stress-Absorbing Composite in Asphalt Concrete Overlays. In Transportation Research Record 1809, TRB, National Research Council, Washington D.C., 2002.
- Di Benedetto H., Delaporte B., and Sauzeat C. Viscoelastic Modeling and Field Validation of Flexible Pavements. *International Journal of Geomechanics*, March/April, pp. 149-157, 2007.
- Di Benedetto H., Olard F., Sauzeat C., and Delaporte B. Linear Viscoelastic Behavior of Bituminous Materials: From Binders to Mixes. *International Journal of Road Materials and Pavement Design*, Vol. 5, Special Issue, pp. 163-202, 2004.
- Elseifi M. A., Al-Qadi I. L., and Yoo P. J. Three-dimensional Linear Behavior of Bituminous Materials; Experiments and Modeling. *Journal of Engineering Mechanics*, Vol. 132, Issue 2, pp. 172 – 178, 2006.
- Elseifi, M. A., J. Trepanier, H. Wakefield, W. J. Pine, A. Dahhan, Hot-Mix Asphalt Sampling Techniques and Methods of Acceptance – State DOT’s Practice, Presented at 885h Annual Meeting of the Transportation Research Board, Washington, D.C., 2009.
- Elseifi, M.A., Bandaru, R., Zhang, Z., and S. Ismail. 2011. Field Evaluation and Cost-Effectiveness of Saw and Seal Method to Control Reflection Cracking in Composite Pavements. *Transportation Research Record: Journal of the Transportation Research Board*, No. 2227, Transportation Research Board of the National Academies, Washington D.C., p.33-42.
- Federal Highway Administration. Long-life Concrete Pavements in Europe and Canada. Publication No. FHWA-PL-07-027. Federal Highway Administration, Washington D.C., 2007.
- Ferry J.D. Viscoelastic Properties of Polymers. 2nd edition, Wiley Publication, New York 1970.

- FHWA. 1990. Technical Guide Paper on Subsurface Pavement Drainage. Technical Paper 90-01. Federal Highway Administration, Washington D.C.
- FHWA. 1992. Drainable Pavement Systems –Participant Notebook. Demonstration Project 87. FHWA-SA-92-008. Federal Highway Administration, Washington D.C.
- FHWA. 2005. “Pavement Preservation Definitions.” Federal Highway Administration. <<http://www.fhwa.dot.gov/pavement/preservation/091205.cfm>>.
- FHWA. 2006. Pavement Preservation Compendium II. Federal Highway Administration, Washington D.C.
- FHWA/ACPA. 1998. Concrete Pavement Rehabilitation: Guide for Load Transfer Restoration. FHWA-SA-97-103, ACPA Bulletin JP001P. Federal Highway Administration, Washington D.C. and American Concrete Pavement Association, Skokie IL.
- Flexible Pavement Rehabilitation Manual. California Department of Transportation, June, 2001.
- FORTRAN. Visual Numerics, Inc., 1997 <http://www.vni.com>
- Freeman, T. E. 2002. Evaluation of Concrete Slab Fracturing Techniques in Mitigating Reflective Cracking through Asphalt Overlays. Final Report. VTRC 03-R3. Virginia Transportation Research Council, Charlottesville, Virginia.
- Fwa, T. F., The Handbook of Highway Engineering, Taylor & Francis Group LLC, 888 pp., 2006.
- Fwa, T. F.. 2006. The Handbook of Highway Engineering, Taylor & Francis Group LLC, 888 pp.
- Galal, K., Coree, B., Haddock, J., White, T. Structural Adequacy of Rubblized Portland Cement Concrete Pavement. Transportation Research Record 1684, TRB, National Research Council, Washington D. C, 1999.
- Galal, Khaled A., and Chehab, Ghassan R. Implementing the Mechanistic Empirical Design Guide Procedure for a Hot-Mix Asphalt-Rehabilitated Pavement in Indiana. In Transportation Research Record 1919, TRB, National Research Council, Washington D.C., 2005 pp.121-133.
- Galal, Khaled A.; Coree, Brian J.; Haddock, John E.; White, Thomas D. 1999. Structural adequacy of rubblized portland cement concrete pavement: Transportation Research Record, n 1684, National Research Council, p 172-177.
- Gerardo W. F., Brian K. D., and Orlando N. 2008. Composite Pavement Systems: Synthesis of Design and Construction Practices, Report No. FHWA/VTRC 09-CR2, Virginia Tech Transportation Institute, Virginia.

- Gerardo W. F., Brian K. D., and Orlando N. Composite Pavement Systems: Synthesis of Design and Construction Practices, Report No. FHWA/VTRC 09-CR2, Virginia Tech Transportation Institute, Virginia 2008.
- Gharaibeh, N., Darter, M., LaTorre, J., Lippert, D. Performance of Original and Resurfaced Pavements on the Illinois Freeway System. Illinois Highway Research Report IHR 540, University of Illinois, Urbana Champaign, Report No. UILU-ENG-96-2010, 1997.
- Gopal, S. 2010. Bituminous Overlay Strategies for Preventative Maintenance on Pennsylvania Interstate Roadways. Master's Thesis. University of Pittsburg.
- Gordon G. V. and Shaw M. T. Computer Programs for Rheologists. Hanser / Gardner Publication, Munich 1994.
- Guide for the Design of Pavement Structures. American Association of State Highway and Transportation Officials, Washington, D.C., 1993.
- Hakim, B. A. The Importance of a Good Bond between Bituminous Layers. *Proc., 9th International Conference on Design of Asphalt Pavements*, Copenhagen, Denmark, 2002.
- Hall, K. T., Darter, M. I., and Steele, D. A., "Guidelines for Evaluation of Asphalt Overlaid Concrete Pavements," Illinois Highway Research Report IHR 532-3, FHWA-IL-UI-246, 1995.
- Hall, K., and Schutzbach, A. Implementation Feasibility of Asphalt Concrete-Overlaid Portland Cement Concrete Pavement Rehabilitation Guidelines. Transportation Research Record 1568, Transportation Research Board of the National Academies, Washington, D.C., 1997.
- Hall, K., C. Correa, and A. Simpson. 2005. LTPP Data Analysis: Effectiveness of Maintenance and Rehabilitation Options. NCHRP Web Document 47. National Cooperative Highway Research Program, Transportation Research Board, Washington D.C.
- Hall, K., Correa, C., Carpenter, S. and R. Elliot. 2001. Rehabilitation Strategies for Highway Pavements. NCHRP Web Document 35(Project C1-38): Contractor's Final Report. Transportation Research Board, Washington D.C.
- Hall, K., Darter, M., Carpenter, S. Guidelines for Rehabilitation of Asphalt Overlaid Concrete Pavements. Illinois Highway Research Report IHR 532-4, FHWA Report FHWA-IL-UI-247. 1994.
- Hall, K., Darter, M., Carpenter, S., Steele, D. Guidelines for Rehabilitation of Asphalt Overlaid Concrete Pavements. Illinois Highway Research Report IHR 532-3, FHWA Report FHWA-IL-UI-246. 1995.
- Hall, K.T., Darter, M.I., Hoerner, T.E., and L. Khazanovich. 1997. LTPP Data Analysis – Phase I: Validation of Guidelines for k-Value Selection and Concrete Pavement Performance

- Prediction. Report FHWA-RD-96-198. Federal Highway Administration, Washington, D.C.
- Hall, Kathleen T., Darter, Michael I., Elliot, Robert P. Field Testing of AASHTO Pavement Overlay Design Procedures. In *Transportation Research Record 1374*, TRB, National Research Council, Washington D.C., 1992b.
- Hall, Kathleen T., Darter, Michael I., Elliot, Robert P. Field Testing of ASHTO Pavement Overlay Design Procedures. In *Transportation Research Record 1374*, TRB, National Research Council, Washington D.C., 1992.
- Hall, Kathleen T., Darter, Michael I., Elliot, Robert P. Field Testing of AASHTO Pavement Overlay Design Procedures. In *Transportation Research Record 1374*, TRB, National Research Council, Washington D.C., 1992b.
- Hall, Kathleen T., Darter, Michael I., Elliot, Robert P. Revision of AASHTO Pavement Overlay Design Procedures. In *Transportation Research Record 1374*, TRB, National Research Council, Washington D.C., 1992a.
- Hall, Kathleen T., Darter, Michael I., Elliot, Robert P. Revision of AASHTO Pavement Overlay Design Procedures. In *Transportation Research Record 1374*, TRB, National Research Council, Washington D.C., 1992a.
- Hand, A. J. T., Epps, J. A., Fundamentals of Percent Within Limits and Quality Control—Quality Assurance Compaction Specifications, Transportation Research Circular, E-C105, Factors Affecting Compaction of Asphalt Pavements, September 2006, pp 140-162.
- Hanson, D., James, R., and C. NeSmith. 2004. Tire/Pavement Noise Study. NCAT Report 04-02. National Center for Asphalt Technology. Auburn AL.
- Hanson, Douglas I. Construction and Performance of an Ultra Thin Bonded Hot-Mix Asphalt Wearing Course. In *Transportation Research Record 1749*, TRB, National Research Council, Washington D.C., pp. 53-59, 2001.
- Harrington, D. 2008. Guide to Concrete Overlays: Sustainable Solutions for Resurfacing and Rehabilitating Existing Pavements. Second Edition. Center for Transportation Research and Education. Ames IA.
- Harvey, J. and Pyle, T. 2009. Use of Ground Penetrating Radar for Network-Level Measurement of Pavement Structural As-Built Information. 8th National Conference on Asset Management. Portland, OR.
- Harvey, J., M. Bejarano, A. Fantoni, A. Heath and H.-C. Shin. 2000. Performance of Caltrans Hot mix asphalt and Asphalt-Rubber Hot Mix Overlays at Moderate Temperatures – Accelerated Pavement Testing Evaluation. California Department of Transportation.
- Hausmann L. D., Tutumluer E., and Barenberg E. J. Neural Network Algorithms for the Correction of Concrete Slab Stresses from Linear Elastic Layered Programs.

- Transportation Research Record 1568, National Research Council, Washington D.C., pp. 44-51, 1997.
- Heckel, Laura B. IL - PRR - 137 “Rubblizing with Bituminous Concrete Overlay – 10 years’ experience in Illinois” Illinois Department of Transportation, April 2002.
- Hill S. A. The Analytical Representation of Viscoelastic Material Properties using Optimization Techniques. NASA TM-108394, February 1993.
- Hoerner, T.E., K.D. Smith, H.T. Yu, D.G. Peshkin and M.J. Wade. 2001. PCC Pavement Evaluation and Rehabilitation, Reference Manual. NHI Course #131062. National Highway Institute, Arlington, VA.
- Huang Y. H. Pavement Analysis and Design. Prentice Hall, Englewood Cliffs, NJ 1993.
- Ioannides, A.M., L. Khazanovich and J.L. Becque, Structural Evaluation of Base Layers in Concrete Pavement Systems, Transportation Research Record 1370, Transportation Research Board, National Council, Washington, D.C., pp. 20-28.
- Janisch, David W., and Turgeon, Curtis M. MN/PR – 96/27 “Sawing and Sealing in Bituminous Pavements to Control Cracking” Minnesota Department of Transportation, March 1996.
- Jayawickrama, P. W., and R. L. Lytton. Methodology for Predicting Asphalt Concrete Overlay Life Against Reflective Cracking. *Proc., 6th International Conference on the Structural Design of Asphalt Pavements*, Vol. 1, July 1987, pp. 912-924.
- Jayawickrama, P.W. and R.L. Lytton (1987). Methodology for predicting asphalt concrete overlay life against reflection cracking. *Proceedings of the 6th International Conference on the Structural Design of Asphalt Pavements, Vol. I*, University of Michigan, July 13-17, 1987, Ann Arbor, Michigan.
- Johanneck, L., and L. Khazanovich. 2010. Comprehensive Evaluation of Effect of Climate in Mechanistic-Empirical Pavement Design Guide Predictions. Transportation Research Record: Journal of the Transportation Research Board, No. 2170, Transportation Research Board of the National Academies, Washington, D.C., pp. 45-55.
- Johnson A. R. and Quigley C. J. A Viscohyperelastic Maxwell Model for Rubber Viscoelasticity. *Rubber Chemistry and Technology*, Vol. 65, No. 1, pp. 137-153, 1992.
- Johnson A. R. Modeling Viscoelastic Materials Using Internal Variables. *The Shock and Vibration Digest*, Vol. 31, No. 2, pp. 91-100, 1999.
- Johnson A. R., Tessler A., and Dambach M. Dynamics of Thick Viscoelastic Beams. *ASME Journal of Engineering Materials and Technology*, Vol. 119, pp. 273-278, 1997.
- Jones, D., Wu, R., Tsai, B., and J.T. Harvey. 2009. Warm-mix asphalt study: F irst-Level Analysis of Phase 2 HVS and Laboratory Testing and Phase 1and Phase 2 Forensic

- Assessments. Report UCPRC-RR-2009-02. California Department of Transportation, Sacramento, CA.
- Kaloush, K., Biligiri, K., Rodezno, M., Belshe, M., Way, G., Carlson, D., and J. Sousa. 2009. "Asphalt rubber hot mix asphalt friction course overlay as a pavement preservation strategy." In *Efficient Transportation and Pavement Systems*, Al Qadi, S. (ed), pp. 559 – 569, Taylor & Francis Group, London.
- Kandhal, Prithvi S., Jr Lubold Carl, W., Roberts, Freddy L. NCAT No. 89-1 "Water Damage to Asphalt Overlays: Case Histories" National Center for Asphalt Technology, February 1989.
- Karamihas, S., and K. Senn. 2010. Profile Analysis of the LTPP SPS-6 Site in Arizona. UMTRI-2010-17. University of Michigan Transportation Research Institute, Ann Arbor, MI.
- Kerr A. D. Elastic and Viscoelastic Foundation Models. ASME Journal of Applied Mechanics, Vol. 31, No. 3, pp. 491-498, 1964.
- Khazanovich L. and Roessler J. DIPLOBACK: a Neural Networks-Based Backcalculation Program for Composite Pavements. Transportation Research Record 1570, Washington D. C. 1997.
- Khazanovich L. Structural Analysis of Multi-Layered Concrete Pavement Systems. Ph.D. Dissertation, University of Illinois, Urbana, IL 1994.
- Khazanovich L., Selezneva O. I., Yu H. T., and Darter M. I. Development of Rapid Solutions for Prediction of Critical Continuously Reinforced Concrete Pavement Stresses. Transportation Research Record 1778, pp. 64-72, Washington D.C., 2001.
- Khazanovich L., Yu H. T., Rao S., Galasova K., Shats E., and Jones R. ISLAB2000—Finite Element Analysis Program for Rigid and Composite Pavements: User's Guide. ARA Inc., ERES Consultants Division, Champaign IL, 2000.
- Khazanovich, L. and A. Gotlif. 2003. Evaluation of joint and crack load transfer. Report No. FHWA-RD-02-088. Federal Highway Administration, Washington, D.C.
- Khazanovich, L. and A.M. Ioannides, Analytical and Numerical Methods for Multi-Layered Concrete Pavements, Proceedings, 3rd International Workshop on the Design and Evaluation of Concrete Pavements, C.R.O.W. Record 14, pp.113-121, 1994.
- Khazanovich, L., Darter, M., and T. Yu (2004). *Mechanistic-Empirical Model for Transverse Joint Faulting Prediction*. Transportation Research Record: Journal of the Transportation Research Board 1896, pp. 34-45. Transportation Research Board of the National Academies, Washington D.C..
- Khazanovich, L., *Structural Anaysis of Multi-Layered Concrete Pavement Systems*, Ph. D. dissertation, University of Illinois, Urbana-Champaign, IL, 1994.

- Khazanovich, L., Tayabji, S., and M. Darter (2001). *Backcalculation of Layer Parameters for Long Term Pavement Performance (LTPP) Test Sections, Volume I: Slab on Elastic Solid and Slab on Dense-Liquid Foundation Analysis of Rigid Pavements*. Report FHWA-RD-00-086, Federal Highway Administration, Washington, DC.
- Khazanovich, L., Tayabji, S.D., and M.I. Darter. 2001. Backcalculation of Layer Parameters for LTPP Test Sections, Volume I. Report No. FHWA-RD-00-0086. Federal Highway Administration, Washington, D.C.
- Khedaywi, T S, T. D. White, Effect of Segregation on Fatigue Performance of Asphalt Paving Mixtuures, Transportation Research Record: Journal of the Transportation Research Board, No. 1543, Transportation Research Board of the National Academies, Washington, D.C., 1996, pp. 63-70.
- Knuttgen. R. "Pavement Noise." Pavement Interactive. Feb 28, 2008. Web. Nov 7, 2011.
- Koch Materials Company. "Sand Anti-Fracture (SAF) Mixture Trial", 1997.
- Kohale, V. and Lytton, R.L. (2000). *Design of Asphalt Concrete Overlay to Mitigate*
- Kohler, E., Santero, N., and J. Harvey. 2005. Pilot Project for Fixed Segmentation of Pavement Network. Report Number UCPRC-RR-2005-11. University of California Pavement Research Center, Berkeley CA.
- Korenev B. G. and Chernigovskaya E. I. Analysis of Plates on Elastic Foundation, Gosstroiiizdat, Moscow (in Russian), 1962.
- Ksaibati, K., Miley, W., and J. Armaghani. 1999. Rubblization of concrete pavements. Transportation Research Record, n 1684, National Research Council, p 165-171.
- Ksaibati, K., Miley, W., Armaghani, J. Rubblization of Concrete Pavements. In Transportation Research Record 1684, TRB, National Research Council, Washington, D.C., pp. 165-171, 1999.
- Larson, G., and B. J. Dempsey (1997). Enhanced Integrated Climatic Model. Version 2.0. Final report. Department of Civil Engineering, University of Illinois at Urbana–Champaign.
- Larson, R. M., D. Peterson, and A. Correa. 1998. Retrofit Load Transfer, Special Demonstration Project SP-204. FHWA-SA-98-047. Federal Highway Administration, Washington, DC.
- Lee, D., Chatti, D., Baladi, G. Development of Roughness thresholds for Preventive Maintenance of Pavements using PMS Distress and Ride Quality Data. Transportation Research Board, 80th Annual Meeting. Washington D.C., 2001.
- Lee, D., Chatti, D., Baladi, G. Development of Roughness thresholds for Preventive Maintenance Action Aimed at Reducing Dynamic Loads. Transportation Research Board, 81th Annual Meeting. Washington D.C., 2002.

- Lee, J., Chen, D.-H., Stokoe, K., and T. Scullion. 2004. Evaluating Potential for Reflection Cracking with Rolling Dynamic Deflectometer. Transportation Research Record n 1869. p 16-24.
- Leng, Z., I. L. Al-Qadi, S. H. Carpenter, H. Ozer, Interface Bonding Between Hot-Mix Asphalt and Various Portland Cement Concrete Surfaces, Transportation Research Record: Journal of the Transportation Research Board, No. 2127, Transportation Research Board of the National Academies, Washington, D.C., 2009, pp. 20-28.
- Lesieutre G. A. and Govindswamy K. Finite Elements Modeling of Frequency Dependent and Temperature Dependent Dynamic Behavior of Viscoelastic Materials in Simple Shear. International Journal of Solids and Structures, Vol. 33, No. 3, pp. 419-432, 1996.
- Li Z. D., Yang T. Q., and Luo W. B. An Improved Model for Bending of Thin Viscoelastic Plate on Elastic Foundation. Natural Science, Vol. 1, No. 2, pp. 120-123, 2009.
- Loulizi, A., Al-Qadi, I., Bhutta, S., Flintsch, G. Evaluation of Geosynthetics used as Separators. In Transportation Research Record 1687, TRB, National Research Council, Washington, D.C., 1999, pp. 104-111.
- LRRB (Minnesota Local Road Research Board). Best practices for Asphalt Paving. Accessed November 2011. <<http://www.lrrb.org/apg/bestpractice.htm#surface>>
- Lu, Q., Harvey, J.T., and R. Wu. 2010. Investigation of Noise and Durability Performance Trends for Asphaltic Pavement Surface Types: Four-Year Results. Report UCPRC-RR-2010-05. California Department of Transportation, Sacramento, CA.
- Luther, M.S., K. Majidzadeh, and C.-W. Chang. Mechanistic Investigation of Reflection Cracking of Asphalt Overlays. In Transportation Research Record 572, TRB, National Research Council, Washington, D.C., 1976 pp. 111-122.
- Maker B. N., Ferencz R. M., and Hallquist J. O. NIKE3D, A Nonlinear, Implicit, Three-dimensional Finite Element Code for Solid and Structural Mechanics. User's Manual 4-40, 1995.
- Makowski, L., Bischoff, D. L., Blamkenship, P., Sobczak, D., and F. Haulter. Wisconsin Experience with Reflective Crack Relief Projects. In Transportation Research Record 1905, TRB, National Research Council, Washington D.C., 2005.
- Marasteanu M. O. and Anderson D. A. Comparison of Moduli for Asphalt Binders Obtained from Different Test Devices. Journal of the Association of Asphalt Paving Technologists, Vol. 69, pp. 574-606, 2000.
- Marasteanu M. O. and Anderson D. A. Improved Model for Bitumen Rheological Characterization. Eurobitume Workshop on Performance Related Properties for Bituminous Binders, Luxembourg, paper no. 133, 1999.

- Marasteanu M., Velasquez R., Falchetto A. C., and Zofka A. Development of a Simple Test to Determine the Low Temperature Creep Compliance of Asphalt Mixtures. IDEA Program Transportation Research Board, National Research Council, 2009.
- Marasteanu, M.O., Li, X., Clyne, T.R., Voller, V. R., Timm, D.H., and D.E. Newcomb. 2004. Low-temperature cracking of asphalt concrete pavements. Report MN/RC-2004-23. Minnesota Department of Transportation, St. Paul, MN.
- Mase G. E. Continuum Mechanics. The McGraw-Hill Companies, 1970.
- Maser, K., Puccinelli, J., Punnackal, T., and A. Carmichael. 2011. Ground Penetrating Rader (GPR) Analysis: Phase II Field Evaluation. Report FHWA/MT-11-002/8201-001. Montana Department of Transportation, Helena, MT.
- Maser, Kenneth R. Use of Ground Penetrating Radar Data for Rehabilitation of Composite Pavements on High Volume Roads. Submitted to the A2K05-Reliability Subcommittee—Session on Reliability of Roadway Condition Assessment Techniques Using Subsurface Sensing and Imaging Technologies, 2001.
- MATHEMATICA. Wolfram Research, Inc. 1988 <http://www.wolfram.com/mathematica/>
- McCullough, B.F.; Dossey, T.; Cho, Y.-H. 1996. Case study of overlay performance on rigid pavement in Bowie county, Texas. Transportation Research Record, n 1525, National Research Council, p 107-114.
- McKesson, C. L. “Slippery Pavements - Causes and Treatments,” Proc. Assoc. of Asphalt Paving Technologists, Vol. 18, 1949.
- Miller J. S. and Bellinger W. Y., Distress Identification Manual for the Long-Term Pavement Performance Program (Fourth Revised Edition), Federal Highway Administration, Report No. FHWA-RD-03-031, McLean, 2003.
- Miller, J. and W. Bellinger. 2003. Distress Identification Manual for the Long-Term Pavement Performance Program (Fourth Revised Edition). Federal Highway Administration. Report number FHWA-RD-03-031.
- Mohammad, L. N., Elseifi, M. A., Bae, A., Patel, N., Button, J. and J. A. Scherocman. Optimization of Tack Coat for HMA Placement. NCHRP Report 712. National Cooperative Highway Research Program, Transportation Research Board, National Academy of Sciences, Washington D.C., 2012.
- Mohammed, L., Optimization of Tack Coat for HMA Placement, NCHRP Project 9-40, Final Report 712, Louisiana Transportation Center, Louisiana State , 2011.
- Monismith C. L. Analytically Based Asphalt Pavement Design and Rehabilitation: Theory to Practice, 1962-1992. Transportation Research Record No. 1354, pp. 5-26, 1992.

- Monismith C. L. and Secor K. E. Viscoelastic Behavior of Asphalt Concrete Pavement. First International Conference on the Structural Design of Asphalt Pavements, pp. 476-498, 1962.
- Monismith, C., Long, F., Harvey, J. CALIFORNIA'S INTERSTATE-710 REHABILITATION: MIX AND STRUCTURAL SECTION DESIGNS, CONSTRUCTION SPECIFICATIONS (WITH DISCUSSION AND CLOSURE). Journal of the Association of Asphalt Paving Technologists Vol. 70, 2001.
- Moody, E. D. 1994. Field investigations of selected strategies to reduce reflective cracking in hot mix asphalt overlays constructed over existing jointed concrete pavements. Transportation Research Record, n 1449, National Research Council, p 209-217.
- Morian, D. A., Oswalt, J., Deodhar, A. Experience with Cold In-Place Recycling as a reflective Crack Control Technique – Twenty Years Later. In Transportation Research Record 1869, TRB, National Research Council, Washington D.C., 2004.
- Mukhtar, M. T., and B. J. Dempsey. Interlayer Stress Absorbing Composite (ISAC) for Mitigating Reflection Cracking in Asphalt Concrete Overlays. Final Report. Illinois Cooperative Highway and Transportation Series No. 260. Department of Civil Engineering, University of Illinois, Urbana, June 1996.
- National Cooperative Highway Research Program (2010). *Models for Predicting Reflection Cracking of Hot-Mix Asphalt Overlays*. NCHRP Report 669, Transportation Research Board of the National Academies, Washington D.C.
- National Highway Institute (NHI). 1999. Pavement Subsurface Drainage Design. Reference Manual. FHWA-HI-99-028. National Highway Institute, Arlington, VA.
- NCHRP 1-40B, User Manual for M E Pavement Design Guide, National Cooperative Highway Research Program, 2007.
- NCHRP 2004a. Guide for Mechanistic-Empirical Design of New and Rehabilitated Pavement Structures: Part 2. Design Input: Chapter 5 Evaluation of Existing Pavements for Rehabilitation. Transportation Research Board, Washington D.C.
- NCHRP 2004b. Guide for Mechanistic-Empirical Design of New and Rehabilitated Pavement Structures: Part 3 Design Analysis: Chapter 1. Drainage. Transportation Research Board, Washington D.C.
- Nenas K. and Nunn M. E. A Model for Top-down Cracking in Composite Pavements. RILEM 4th International Conference on Cracking in Pavements, Limoges, France, 2004.
- Nenas, K., and Nunn, M. A Model for Top-Down Reflection Cracking in Composite Pavements. 5th International RILEM Conference, Limoges, France, May 2004.
- Nishizawa, T., Fukute, T., Kokubun, T. Study on an Analysis Method for Mechanical Behavior of Composite Pavement, Transportation Research Record 1684, pp. 101-109, 1999.

Ohio DOT

<http://www.dot.state.oh.us/Divisions/HighwayOps/Pavement/Pavement%20Design%20%20Rehabilitation%20Manual/Sect500.pdf> accessed July 2009.

Osseiran, Abdallah H. Crack-and-seat Concrete Pavement Construction Report. Phoenix, Arizona: State of Arizona, 1987

Osswald, T. A. and Menges G. Material Science of Polymers for Engineers. 2nd edition, Hanser Gardner Publication, Inc., OH 2003.

Owusu-Antwi, Emmanuel B., Khazanovich, Lev, Titus-Glover, Leslie. Mechanistic-Based Model for Predicting Reflective Cracking in Asphalt Concrete-Overlaid Pavements. In Transportation Research Record 1629, TRB, National Research Council, Washington D.C., 1998.

Park S. W. and Kim Y. R. Fitting Prony-Series Viscoelastic Models with Power-Law Presmoothing. Journal of Materials in Civil Engineering, Vol. 13, Issue 1, pp. 26-32, 2001.

Park S. W. and Schapery R. A. Methods of Interconversion Between Linear Viscoelastic Material Functions. Part I – A Numerical Method Based on Prony Series, International Journal of Solids and Structures, Vol. 36, pp. 1653-1675, 1999.

Pasternak P. L. Fundamentals of a New Method of Analysis of Structures on Elastic Foundation by Means of Two Subgrade Coefficients. Gosudarstvennoe Izdatel'stvo Literaturny po Stroitel'stvu i Arkhitekture, Moscow (in Russian) 1954.

Pavement Consultancy Services (PCS). Guidelines and Methodologies for the Rehabilitation of Rigid Highway Pavements using Asphalt Concrete Overlays. NAPA and SAPE, Maryland, 1991.

Pavement Consultancy Services (PCS). Guidelines and Methodologies for the Rehabilitation of Rigid Highway Pavements Using Asphalt Concrete Overlays. National Asphalt Pavement Association, Beltsville, Md., June 1991

Pellinen T. K. and Witzak M. W. Stress Dependent Master Curve Construction for Dynamic (Complex) Modulus. Journal of the Association of Asphalt Paving Technologists, 2002.

Pickett, D. and R. Lytton. 1983. Laboratory Evaluation of Selected Fabrics for Reinforcement of Asphaltic Concrete Overlays. Report 261-1. Texas Transportation Institute.

Pierce, L., J. Uhlmeyer, J. Weston, J. Lovejoy, and J. Mahoney. 2003. Ten Year Performance of Dowel Bar Retrofit – Application, Performance, and Lessons Learned. Transportation Research Board, Washington, D.C.

Piggott, R. W. *Roller Compacted Concrete Pavements – A Study of Long Term Performance*, RP366. Portland Cement Association Research and Development, 1999.

- Ping W. V. and Xiao Y. Evaluation of the Dynamic Complex Modulus Test and Indirect Diametral Test for Implementing the AASHTO 2002 Design Guide for Pavement Structures in Florida. Florida Department of Transportation, Report No. FL/DOT/RMC/BC-352-12, January 2007.
- Quality Improvement Series, QIP114A/89, National Asphalt Pavement Association.
- Rajagopal, A., Minkarah, I., Green R., Morse, A. Long-Term Performance of Broken and Seated Pavements. In Transportation Research Record 1869, TRB, National Research Council, Washington D.C., 2004.
- Rao, S., Darter, M.I, Tompkins, D., Vancura, M., Khazanovich, L., Signore, J., Coleri, E., Wu, R., Harvey, J., and J. Vandebossche (2011). Composite Pavement Systems, Final Report with Appendices. Strategic Highway Research Program 2, Transportation Research Board of the National Academies, National Research Council. Washington D.C.
- Reddy J N. An Introduction to the Finite Element Method. McGraw-Hill, Inc., 1984.
- Reflective Cracking. Report, Project No. 7256, Florida Department of Transportation, Tallahassee, Florida.
- Roberts, F. L., P. S. Kandhal, E. R. Brown, D. Lee, and T. W. Kennedy. *Hot Mix Asphalt Materials, Mixture, Design, and Construction*. National Asphalt Pavement Association, Lanham, Md., 1996, p. 562.
- Roberts, L., Kandhal, S., Brown, E., Lee, D., Kennedy, T. Hot Mix Asphalt Materials, Mixture Design and Construction. NAPA Research and Education Foundation. Lanham, Maryland, 1996.
- Rodezno, M., Kaloush, K., Way, G. Assessment of Distress in Conventional Hot-Mix Asphalt and Asphalt-Rubber Overlays on Portland Cement Concrete Pavements Using the new Mechanistic-Empirical Design of Pavement Structures. In Transportation Research Record No. 1929, TRB, National Research Council, Washington, D.C., 2005, pp. 20-27.
- Roque, R., Zou, J., Kim, Y.K, Baek, C., Thirunavukkarasu, S., Underwood, B.S., Guddati, M.N.. 2010. Top-down cracking of hot-mix asphalt layers. NCHRP Web-Only Document 162. National Cooperative Highway Research Program. Transportation Research Board of the National Academies, Washington D.C.
- Rowe G. M., Sharrock M. J., Bouldin M.G., and Dongre R. N. Advanced Techniques to Develop Asphalt Master Curves from the Bending Beam Rheometer. Petroleum and Coal, Vol. 43, No. 1, pp. 54-59, 2001.
- Rumpca, H., Storsten, M. Evaluation of Geosynthetics in Asphalt Overlays of Jointed Concrete Pavements. South Dakota Department of Transportation, Report No. SD95-23-X, June 2000.

- Rutkowski, T., S. Shober, and R. Schmeidlin. 1998. Performance Evaluation of Drained Pavement Structures. Virginia Department of Transportation, Charlottesville, VA.
- Ryell, J., and Corkill, J.T. "Long-Term Performance of an Experimental Composite Pavement", *Highway Research Record*, Number 434, pp. 1-15. 1973.
- Saal R. N. J. and Labout J. W. A. Rheologic Properties of Asphalts. *Rheology: Theory and Applications*, Ed. F. R. Eirich, Vol. II, Academic Press, New York, 1958.
- Saal R. N. J. Physical Properties of Asphaltic Bitumen: Rheological Properties. J. P. Pfeiffer, ed., Elsevier, Amsterdam, The Netherlands, pp. 49-76, 1950.
- Sandberg, U., and J. A. Ejsmont. 2002. Tyre/Road Noise Reference Book. Informex, Kisa, Sweden.
- Sayegh G. Viscoelastic Properties of Bituminous Mixtures. Second International Conference on the Structural Design of Asphalt Pavements, 1967.
- Scarpas, A., Blaauwendraad, J., De Bondt, A. H., and A.A.A. Molenaar (1993). CAPA: A Modern Tool for the Analysis and Design of Pavements. *Proceedings of 2nd International RILEM Conference, Reflective Cracking in Pavements: State of the Art and Design Recommendations*, p. 121-128. Belgian Research Centre for Plastics and Rubber Materials, March 10-12, 1993, Liege, Belgium.
- Schapery R. A. Mechanics of Composite Materials. Vol. 2, Ed. Sendeckyj G. P., Academic Press, New York, pp. 85-169, 1974.
- Scotfield, L. and P. Donovan. 2003. Development of Arizona's Quiet Pavement Research Program. Development of Arizona's Quiet Pavement Research Program, Proceedings of Asphalt Rubber 2003, Brasilia, Brazil.
- Scullion, T. 2006. Using Rolling Deflectometer and Ground Penetrating Radar Technologies for Full Coverage Testing of Jointed Concrete Pavements. Report 0-4517-2. Texas Transportation Institute, College Station TX.
- Scullion, T. and T. Saarenketo, Implementation of Ground Penetrating Radar Technology in Asphalt Pavement Testing, 9th International Conference on Asphalt Pavement, Copenhagen, Denmark, Aug. 17-22, 2002
- Scullion, T., Chen, Y., and Lau, C.L., "COLORMAP-Users Manual with Case Studies," TTI Report 0-1341-1, Texas Transportation Institute, College Station, TX. November 1995.
- Shahin, M. Y., M. I. Darter, and S. D. Kohn, Development of a Pavement Maintenance Management System, Volume I: Airfield Pavement Condition Rating, U. S. Air Force Civil Engineering Center, Technical Report No. AFCEC-TR-76-27, 1976.
- Shahin, M.Y., 1994. Pavement Management for Airports, Roads and Parking Lots, Chapman and Hall, New York, NY, 1994.

- Shuler, T.S., J.H. Collins, and J.P. Kirkpatrick. (1987) Polymer-Modified Asphalt Properties Related to Asphalt Concrete Performance. ASTM STP 941, ASTM, Philadelphia, PA.
- Smith, K. 2009. Concrete Pavement Preservation. California Concrete Pavement Workshop. <http://acpa-southwest.org/wksp100809/Concrete%20Pavement%20Preservation_Smith_1perpage.pdf>
- Smith, K., T. Hoerner, and D. Peshkin. 2008. Concrete Pavement Preservation Workshop. Federal Highway Administration. Washington D.C.
- Smith, K., Von Quintus, H., Killingsworth, B., Barton, R., Kobia, K. Review of Life-Cycle Costing Analysis Procedures. Final Report prepared by: Brent Rauhut Engineering, ADI Group, and submitted by ERES Consultants for Ontario Ministry of Transportation. December, 1998.
- Smith, P. "Past Performance of Composite Pavements", *Highway Research Record* Number 37, pp. 14-30, 1963.
- Sousa, J., J. Pais, R. Saim, G. Way, and R. Stubstad. Mechanistic-Empirical Overlay Design Method for Reflective Cracking. Transportation Research Record 1809, pp. 20-217, 2002.
- Sousa, J., J. Pais, R. Saim, G. Way, and R. Stubstad. *Development of a Mechanistic Overlay Design Method Based on Reflective Cracking Concepts*. Consulpav, Oeiras, Portugal, Aug. 2001.
- Soussou J. E., Moavenzadeh F., Gradowczyk M. H. Application of Prony Series to Linear Viscoelasticity. *Journal of Rheology*, Vol. 14, Issue 4, pp. 573-584, 1970.
- Strategic Highway Research Program (2012). *SHRP2 R21 Composite Pavements Final Report*. In Press. Transportation Research Board of the National Academies, Washington D.C..
- Strategic Highway Research Program 2. *Project R21 Composite Pavement Systems, Phase One Interim Report*. Strategic Highway Research Program, Transportation Research Board, National Research Council, Washington, D.C. 2009.
- SuperPave Overlay of Sand Anti-Fracture Layer over PCCP. Missouri Department of Transportation. Report No. RI97-045, March, 2000a.
- Tabatabaie A. M. and Barenberg E. J. Structural Analysis of Concrete Pavement Systems. *ASCE Transportation Engineering Journal*, Vol. 106, No. 5, pp. 493-506, 1980.
- Tashman, L., Nam, K., and T. Papagiannakis. Evaluation of the Influence of Tack Coat Construction Factors on the Bond Strength between Pavement Layers. Report No. WA-RD 645.1, Washington State Department of Transportation, 2006.

- Tayabji S. D. and Colley B. E. Improved Pavement Joints. Transportation Research Record No. 930, Transportation Research Board, National Research Council, Washington D.C., pp. 69- 78, 1983.
- Terrel, R.L. and J.A. Epps. 1989. "Using Additives and Modifiers in Hot Mix Asphalt,"
- Thomlinson J. Temperature Variations and Consequent Stresses Produced by Daily and Seasonal Temperature Cycles in Concrete Slabs. Concrete Constructional Engineering, Vol. 36, No. 6, pp. 298-307; No. 7, pp. 352-360, 1940.
- Thompson, M. BREAKING/CRACK-AND-SEATING CONCRETE PAVEMENTS. Transportation Research Board. NCHRP Synthesis of Highway Practice, No. 144, 1989.
- Thompson, M. Hot Mix Overlay Design Concepts for Rubblized Portland Cement Concrete Pavements. In Transportation Research Record No. 1684, pp. 147-155, 1999.
- Thompson, M. R. *NCHRP Synthesis of Highway Practice 144: Breaking/Cracking and Seating Concrete Pavements*. TRB, National Research Council, Washington, D.C., March 1989, 39 pp.
- Thompson, Marshall R. 1999. Hot-mix asphalt overlay design concepts for rubblized portland cement concrete pavements. Transportation Research Record, n 1684. National Research Council, p 147-155.
- Timoshenko S. P. and Woinowsky-Krieger S. Theory of Plates and Shells. 2nd edition, McGraw-Hill, NY, 1959.
- Timoshenko S. P. Theory of Elasticity. McGraw-Hill Companies, 3rd Edition, 1970.
- Tompkins, D., L. Khazanovich, and M. Darter, 2010. "2008 Survey of European Composite Pavements." SHRP2 Report S2-R21-RW-1. Second Strategic Highway Research Program. Transportation Research Board, Washington D.C.
- TxDOT http://onlinemanuals.txdot.gov/txdotmanuals/pdm/manual_notice.htm accessed July 2009.
- U.S. Highway 36 - SuperPave Overlay of Sand Anti-Fracture Layer over PCCP. Missouri Department of Transportation. Report No. RI99-042, December, 2000b.
- Ugural A. C. and Fenster S. K. Advanced Strength and Applied Elasticity. Pearson Education, Inc., 2003
- Ullidtz, P., Harvey J., Tsai, B., and Monismith, C., Calibration of Incremental-Recursive Flexible Damage Models in CalME Using HVS Experiments, University of California Pavement Research Center, Report No. UCPRC-RR-2005-06, California, 2006a.

- Ullidtz, P., Harvey J., Tsai, B., and Monismith, C., Calibration of CalME models using WesTrack Performance Data, University of California Pavement Research Center, Report No. UCPRC-RR-2006-14, California, 2006b.
- Ullidtz, P., Harvey, J.T., Tsai, BW, and C.L. Monismith (2008). *Calibration of Mechanistic-Empirical Models for Flexible Pavements Using California Heavy Vehicle Simulators*. Transportation Research Record: Journal of the Transportation Research Board 2087:1, pp. 20-28. Transportation Research Board of the National Academies, Washington D.C.
- Ullidtz, P., Harvey, JT, Tsai, BW, and C.L. Monismith (2006). *Calibration of Incremental-Recursive Flexible Damage Models in CalME Using HVS Experiments*. Report UCPRC-RR-2005-06. University of California, Pavement Research Center. California Department of Transportation, Sacramento, CA.
- UMN Online Lecture 2011
<http://www.me.umn.edu/labs/composites/Projects/Polymer%20Heat%20Exchanger/Cree p%20description.pdf>
- USACE. 2000. Hot-Mix Asphalt Paving Handbook, US Army Corps of Engineers, Document UN-13 CEMP-ET.
- Van der Poel C. A General System Describing the Viscoelastic Properties of Bitumens and its Relation to Routine Test Data. Journal of Applied Chemistry, Vol. 4, Issue 5, pp. 221-236, May 1954.
- Von Quintus, H. and James S. Moulthrop. *Mechanistic-Empirical Pavement Design Guide Flexible Pavement Performance Prediction Models for Montana: Volume I—Executive Research Summary*, Report Number FHWA/MT-07-008/8158-1, Montana Department of Transportation, Research Programs, Helena, Montana, August 2007.
- Von Quintus, H., F. Finn, R. Hudson, and F. Roberts. *Flexible and Composite Structures for Premium Pavements*. FHWA RD-80-154 and 155, Federal Highway Administration, Washington, D.C., 1980.
- Wagoner, Michael P., Butler, William G., Paulino, Glaucio H., Blankenship, Philip. Investigation of the Fracture Resistance of Hot-Mix Asphalt Concrete Using a Compact Disk Shaped Tension Test. In Transportation Research Record 1929, TRB, National Research Council, Washington, D.C., 2005 pp. 183-192.
- Walker, D. Alabama Makes the Case for Rubblization. Asphalt Vol. 21 No. 1. Asphalt Institute, 2006.
- Wang Q. Improvement of Structural Modeling of Flexible Pavements for Mechanistic-Empirical Design, Ph.D. Dissertation, University of Minnesota, December 2007.
- Wen, H., H. Titi, and J. Singh. 2005. Guidelines for the Surface Preparation/Rehabilitation of Existing Concrete and Asphaltic Pavements Prior to an Asphaltic Concrete Overlay. Report #0092-04-05. Wisconsin Highway Research Program, Madison WI.

- West, R., J. Zhang, and J. Moore, Evaluation of Bond Strength between Pavement Layers. NCAT Report 05-08, Auburn, AL, 2005.
- Wienrank, Charles J., Lippert, David L. Illinois Performance Study of Pavement Rubblization. In Transportation Research Circular E-C087: Rubblization of Portland Cement Concrete Pavements, TRB, National Research Council, Washington D.C., January 2006, pp. 75-86.
- Williams, R., Martin, T., Maser, T., McGovern, G. Evaluation of Network Level Ground Penetrating Radar Effectiveness. TRB Annual Meeting, Washington D.C., 2006.
- WisDOT. 2004. Construction and Materials Manual: Chapter 3 Earthwork and Bases: Section 50 Rubblizing Concrete Pavements. Wisconsin Department of Transportation, Madison WI.
- Witczak, Matthew W., and Rada, Gonzalo R. Asphalt Concrete Overlay Design Methodology for Fractured Portland Cement Concrete Pavements. In *Transportation Research Record 1374*, TRB, National Research Council, Washington D.C., 1992.
- Witczak, Matthew W., and Rada, Gonzalo R. Asphalt Concrete Overlay Design Methodology for Fractured Portland Cement Concrete Pavements. In Transportation Research Record 1374, TRB, National Research Council, Washington D.C., 1992.
- Witczak, Matthew W., and Rada, Gonzalo R. Nationwide Evaluation Study of Asphalt Concrete Overlays Placed on Fractured Portland Cement Concrete Pavements. In Transportation Research Record 1374, TRB, National Research Council, Washington D.C., 1992.
- Witczak, Matthew W., and Rada, Gonzalo R. Nationwide Evaluation Study of Asphalt Concrete Overlays Placed on Fractured Portland Cement Concrete Pavements. In Transportation Research Record 1374, TRB, National Research Council, Washington D.C., 1992.
- Wolters, A., T. Hoerner, and K. Smith. 2008. Evaluation of HMA Overlays in Illinois. Report No. 08-021. Illinois Center for Transportation Springfield IL.
- Wolters, Angela S.; Smith, Kurt D.; Peterson, Carol V. 2007. Evaluation of rubblized pavement sections in Michigan. Transportation Research Record, n 2005, National Research Council, p 18-26.
- Wotring, D., Baladi, G., Bower, S., Pavement Distress and Selection of Rehabilitation Alternatives Michigan Practice. 77th Transportation Research Board Annual Meeting, Washington, D.C. 1998.
- WSDOT http://training.ce.washington.edu/wsdot/modules/07_construction/07-2_body.htm accessed July 2009.
- WSDOT. 2005. Quieter Pavements: Options & Challenges for Washington State. Washington State. Washington Department of Transportation, Olympia.
- Wu R. Fatigue Cracking model papers...<Complete Citation>

- Wu, R., Finite Element Analyses of Reflective Cracking in Asphalt Concrete Overlays. PhD Thesis, University of California, Berkeley, 2005.
- Y.H. Huang, Pavement Analysis and Design, PRENTICE HALL, pp.19-21,1993.
- Yoder, E., Witczak, M., Principles of Pavement Design. John Wiley and Sons, NY, 1975.
- Yu. T., D. Peshkin, K. Smith, M. Darter, D. Whiting, and H. Delaney. 1994. Concrete Rehabilitation Users Manual. SHRP-C-412. Strategic Highway Research Program, Washington D.C.
- Zareh A., G. Way, K. Kaloush. "Asphalt-Rubber Open Graded Mix Reduces Tire Pavement Noise", *Proceedings of the Asphalt Rubber Conference*, Palm Springs, CA, pp. 385-398, 2006.
- Zhou, F., and T. Scullion. 2003. Upgraded overlay tester and its application to characterize reflection cracking resistance of asphalt mixtures. Texas Transportation Institute, Report 0-4467-1, College Station TX
- Zhou, F., Hu, S., and T. Scullion. 2006. "Integrated asphalt (overlay) mixture design, balancing rutting and cracking requirements." Texas Transportation Institute Report 0-5123-1, College Station TX.
- Zhou, F; Sun, L. Reflective Cracking in Asphalt Overlay on Existing PCC. Ninth International Conference on Asphalt Pavements, Copenhagen, Denmark, 2002.
- Zienkiewicz O. C. and Taylor R. L. Finite Element Method for Solid and Structural Mechanics, 1st Edition, Elsevier, 1967.
- Zofka A. Investigation of Asphalt Concrete Creep Behavior using 3-point Bending Test. Ph.D. Dissertation, University of Minnesota, 2007.
- Zofka A., Marasteanu M. O., and Turos M. Determination of Asphalt Mixture Creep Compliance at Low Temperatures by Using Thin Beam Specimens. Transportation Research Record No. 2057, Transportation Research Board, pp. 134-139, Washington D. C. 2008.

Appendix A: Construction Practices Survey

Interview with Stewart Krummen

Concrete Division Manager

C.S. McCrossan Construction, Inc

7865 Jefferson Highway
Maple Grove, Minnesota 55369

April 21, 2012

If a concrete contractor were to build identical thickness, side-by-side concrete pavements, but one of the pavements would not need to serve as a wear course (i.e. you would come back in a few weeks and overlay it with 1-2 inches of asphalt), what, operationally, could you or would you do differently? Finishing? Compaction? Paver speed and/or control? Curing? Others?

The concrete would still need to be cured.

We would not need to texture, but still need the texture/curing machine and operator to cure so really little to no savings.

The paver speed and production would be the same as it is limited on mainline paving projects by our plant productivity (simply cannot go faster than we are already without bigger plant).

If the designer was less concerned about sealing the surface, we may be able to eliminate two finishers at a cost of \$1200/day or ~\$0.10/sy

We would not need to have a finisher to imprint the rumble strips saving ~\$0.05/sy

We would not need to seal the pavement which would save ~\$1.00/sy (varies widely depending on type of sealant required from Hot Pour to Pre-Formed)

We would not need to grind for smoothness which may save \$0.05-0.10/sy.

Interview with Shiraz Tayabji, Ph.D., P.E.

Senior Consultant

Fugro Consultants, Inc.

10130 Maxine Street

Ellicott City, Maryland 21042

May 3, 2012

If a concrete contractor were to build identical thickness, side-by-side concrete pavements, but one of the pavements would not need to serve as a wear course (i.e. you would come back in a few weeks and overlay it with 1-2 inches of asphalt), what, operationally, could you or would you do differently?

1. Paver speed and control?

PAVER SPEED AND CONTROL SHOULD BE SAME AS FOR CONVENTION CONCRETE. WE STILL WANT A GOOD QUALITY CONCRETE FOR THE BASE PAVEMENT.

2. Compaction?

COMPACTION SHOULD BE SAME AS FOR CONVENTION CONCRETE. WE STILL WANT A GOOD QUALITY CONCRETE FOR THE BASE PAVEMENT.

3. Finishing?

EXTRA FINISHING IS NOT REQUIRED TO GET THE PCC SURFACE TO BE VERY SMOOTH TO QUALIFY FOR PAY INCENTIVES. PAY INCENTIVE FOR SMOOTHNESS SHOULD BE BASED ON THE FINAL AC SURFACE SMOOTHNESS. HOWEVER PCC EDGES SHOULD BE MAINTAINED VERTICAL AND SLOPPY EDGES MUST NOT BE ALLOWED OR ACCEPTED.

4. Texturing?

TEXTURING SHOULD BE MODIFIED TO ALLOW FOR BETTER INTERLOCKING OF THE AC TO THE PCC SURFACE.

5. Curing?

CURING NEEDS TO BE MODIFIED. NO WAX-BASED CURING. AC NEEDS TO “BOND” TO THE AC SURFACE. SHOULD INVESTIGATE DIRECT APPLICATION OF AN AC-BASED PRIME COAT THAT CAN BE APPLIED ON WET PCC SURFACE THAT CAN EFFECTIVELY SEAL THE PCC SURFACE AND EDGES. BUT IT NEED TO BE DRY IN FEW HOURS TO ALLOW SAWING OPERATION. IF CONVENTIONAL CURING IS USED, IT MAT NEED TO BE REMOVED BY SAND-BLASTING TO ENSURE GOOD BONDING BETWEEN THE AC AND THE PCC SURFACE. OTHERWISE, THERE IS A RISK OF EARLY AC DELAMINATION.

6. Joint sawing

SHOULD FOLLW THE SAME PROCESS AS FOR CONVENTIONAL CONCRETE WITH RESPECT TO TIMING AND DEPTH OF CUT FOR BOTH LONGITUNAL AND TRANSVERSE JOINTS.

7. Others?

JOINT SAWING IN AC MUST BE DONE AS SOON AS POSSIBLE AND OVER THE PCCP JOINTS, OTHERWISE THERE IS A RISK OF REFLECTION CRACKING AT JOINT OFFSET LOCATIONS.

Furthermore, what are your thoughts regarding the use of roller-compacted concrete pavement if it would not be used as the wear coarse?

BEST COMPOSITE SYSTEM WITH RESPECT TO COST AND PERFORMANCE AND CONTRACTOR EXPEDIENCY. AC CONTRACTOR CAN PLACE RCC WITH THE EQUIPMENT HE WILL BE USING FOR THE AC PLACEMENT. HOWEVER, F/T DURABILITY OF THE RCC BELOW AC NEEDS TO BE INVESTIGATED. LESS LENGTH (TIMEWISE) OF LANE CLOSURE IF IT IS REHAB PROJECT.

NOTE: A JOINTED RCCP WILL BEHAVE SIMILARLY TO A JOINTED CONCRETE PAVEMENT, ONLY THE METHOD OF CONSTRUCTION IS DIFFERENT. HOWEVER, RCCP WOULD NOT BE A GOOD OPTION FOR HEAVY TRUCK TRAFFIC ROADWAYS IF DOWEL ARE REQUIRED AT JOINTS. WE CANNOT INSTALL DOWEL BARS IN RCCP.

1. Could the paving be done more quickly?

YES, AS THERE WOULD BE NO NEED TO WAIT FOR CONCRETE TO ATTAIN STRENGTH. THE AC LAYER CAN BE PLACED RIGHT BEHIND THE CONCRETE PLACEMENT AS SOON AS THE RCC JOINT SAWING IS DONE. THIS PRACTICE HAS BEEN USED IN EUROPE (SPAIN) AND IN CANADA. AND NON-TRUCK TRAFFIC CAN BE PUT ON THE ROADWAY AS SOON AS THE AC LAYER IS READY TO BE TRAFFICKED. SO, THE CONSTRUCTION TIME CAN BE REDUCED AND OVERALL COST WOULD BE LOWER, BY 15 TO 20%, DEPENDING ON PROJECT SIZE.

2. Would it require less labor? (running the paver, finishing?)

YES, AN AC PAVER IS STILL REQUIRED PLUS COMPACTION EQUIPMENT.

3. Would the concrete cost less?

YES, DEPENDING ON AVAILABILITY OF NEARBY CONCRETE PLANTS OR CONTRACTOR SET UP PLANT.